204(1), 2026

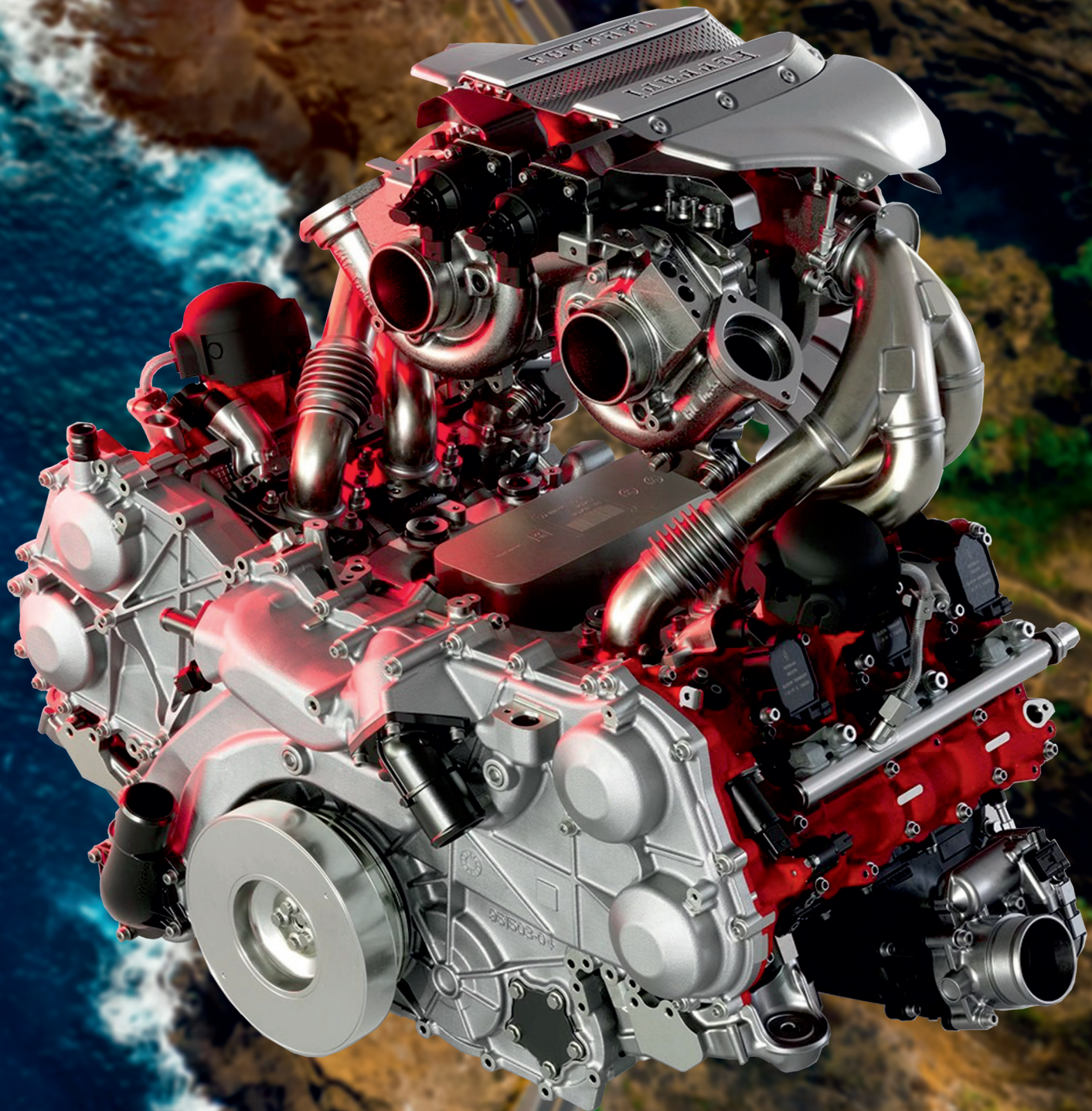

COMBUSTION ENGINES

Cracow University of Technology
Faculty of Mechanical Engineering

Department of Motor Vehicles

www.m4.pk.edu.pl

The Department of Automotive Vehicles is responsible for the "**Automotive Vehicles"** field of study, which combines a passion for the automotive industry with modern technical knowledge.

Specializations in students education:

- Construction and testing of motor vehicles,
- Diagnostics and operation of motor vehicles,
- Power sources and mechatronics of motor vehicles.

Selected laboratory stations for scientific research and teaching:

Chassis dynamometer

Vehicle diagnostics station (SKP)

Accident simulation program

3-Wheel Tilt Vehicle Concept

The concept of a mobile platform with an electric drive

The concept of a hybrid hydrogen-electric vehicle

Industrial hydrogen-powered combustion engine

Research vehicle powered by hydrogen fuel cells (PEM)

Test stand for research of combustion engines

*Since 1993, the Department of Motor Vehicles, in cooperation with the Institute of Forensic Research in Cracow, has offered postgraduate studies in **"Road Accident Expertise"**.*
In 2011, the program received a recommendation from the European Association for Road Accident Investigation and Analysis (EVU).

Politechnika Krakowska im. Tadeusza Kościuszki, Wydział Mechaniczny, Katedra Pojazdów Samochodowych, al. Jana Pawła II 37, 31-864 Kraków, budynek G, tel. +12 6283530, www.m4.pk.edu.pl
e-mail m4sekretariat@pk.edu.pl;

Due to the dynamic development of machine and vehicle powertrains, the "Combustion Engines" scientific journal, while retaining its historical title, currently publishes works related not only to internal combustion engines, but also other powertrains, including hybrid drives, electric drives and fuel cells.

PTNSS Supporting Members
Członkowie wspierający PTNSS

BOSMAL Automotive Research and Development Institute Ltd
Instytut Badań i Rozwoju Motoryzacji BOSMAL Sp. z o.o

Motor Transport Institute
Instytut Transportu Samochodowego

Institute of Aviation
Sieć Badawcza Łukasiewicz – Instytut Lotnictwa

Automotive Industry Institute
Sieć Badawcza Łukasiewicz – Przemysłowy Instytut Motoryzacji

Sieć Badawcza Łukasiewicz – Poznański Instytut Technologiczny

AVL List GmbH

Air Force Institute of Technology
Instytut Techniczny Wojsk Lotniczych

Military Institute of Armoured & Automotive Technology
Wojskowy Instytut Techniki Pancernej i Samochodowej

Toyota Motor Poland Ltd. Sp. z o.o.

RADWAG Balances and Scales
RADWAG Wagi Elektroniczne

FOGO Sp. z o.o.

Horus Energia Sp. z o.o.

John Deere Polska Sp. z o.o.

COMBUSTION ENGINES

A Scientific Magazine

2026, 204(1)

Year LXV

PL eISSN 2658-1442
PL ISSN 2300-9896

Publisher:
Polish Scientific Society of Combustion Engines
61-131 Poznań, ul. J. Rychlewskiego 1, Poland
tel.: +48 61 6475959, fax: +48 61 6652204
E-mail: sekretariat@ptnss.pl
WebSite: http://www.ptnss.pl
Papers available on-line: http://combustion-engines.eu

Contents

Declaration of the original version
The original version of the Combustion Engines journal is the electronic version.

Cover
I – Ferrari F80 engine
(www.motortrend.com);
background (Lukas Rodriguez – pexels.com)
IV – Ducati V2 engine
(www.ducati.com)

Publisher:
Polish Scientific Society of Combustion Engines
61-131 Poznan, ul. J. Rychlewskiego 1, Poland
tel.: +48 61 6475959, fax: +48 61 6652204
E-mail: sekretariat@ptnss.pl
WebSite: http://www.ptnss.pl

The journal is under the patronage of the Transport Committee and the Machine Building Committee of the Polish Academy of Sciences

The journal is registered and listed in the Polish and international database

Papers published in the
Combustion Engines
quarterly receive 70 points as stated by the Notification of the Minister of Science dated 5 January 2024.

Article citation info:
Dopieralski M, Polak F. Cold flow modeling of the combustion chamber for a multi-fuel turbine engine. Combustion Engines. 2026;204(1):3-12. https://doi.org/10.19206/CE-208516

Marcin DOPIERALSKI
Filip POLAK

Combustion Engines
Polish Scientific Society of Combustion Engines

Cold flow modeling of the combustion chamber for a multi-fuel turbine engine

ARTICLE INFO

Received: 22 May 2025
Revised: 30 June 2025
Accepted: 22 July 2025
Available online: 22 September 2025

This article analyses the possibility of using a multi-fuel turbine engine as a primary source in hybrid systems. Turbine engines, thanks to their high efficiency and flexibility in using different types of fuels, can play a key role in integration with hybrid systems that combine electric drive with traditional energy sources. Additionally, different fuels may influence combustion temperatures and soot formation, affecting thermal loads and material degradation. The proposed methodology will consist of conduct a comprehensive review of current models of combustion chambers in turbine engines, focusing on multi-fuel capability and hybrid applications. As a result, it will allow to identify key performance parameters (efficiency, emissions, stability, etc.) and define system requirements for hybrid optimization. The article presents a comparative analysis of which geometry performs best for multi-fuel combustion. The model results were then compared with literature data. The conducted modelling of a multi-fuel combustion chamber intended for use in hybrid turbine systems has shown that the choice of fuel significantly influences combustion behaviour, temperature distribution, and emission profiles. Nevertheless, the developed model provides a solid foundation for future integration into hybrid propulsion architectures, offering adaptability to various fuels and operating regimes.

Key words: *turbine engine, multi-fuel engine, hydrogen, natural gas, hybrid drive*

1. Introduction

The global demand for sustainable and low-emission propulsion systems has intensified the search for alternative fuels and advanced combustion technologies. Gas turbine engines, widely used in power generation and aviation, face increasing pressure to adapt to cleaner energy sources while maintaining high performance and operational reliability. In this context, the combustion of alternative fuels, such as hydrogen, synthetic gases, and biofuels, presents both a promising solution and a complex engineering challenge. The paper [4] describes the challenges of adding hydrogen power to gas turbines, including high production costs, limited infrastructure, and an underdeveloped value chain. All major gas turbine companies are aiming for full hydrogen combustion capability by 2030, and some manufacturers, such as Siemens Energy, are already introducing selected hydrogen-capable models. Technical challenges include the combustion characteristics of hydrogen, in particular, lower ignition energy and higher flame speed [7].

Sample tests have shown that biofuels can offer similar or even better performance compared to conventional fuels, although some biofuels may require modifications to the injectors or combustion chamber. In terms of cost-effectiveness, biofuels and synthetic fuels may be more expensive to produce, but the environmental benefits and potential savings over the long term may make them cost-effective. The use of biofuels, such as biodiesel, in turbine engines can lead to comparable or even better performance compared to conventional fuels. However, some biofuels, especially those with high viscosity, may require modifications to the injectors or combustion chamber to ensure optimal combustion and avoid operational problems [25]. In some cases, especially in aviation, multi-fuel operation allows the engine to be adapted to different weather conditions or missions, which can be important for military operations or specialist missions.

In recent years, research on combustion chambers in turbine engines has focused on optimizing the combustion process to ensure better fuel and air mixing, leading to higher combustion efficiency and lower emissions of harmful chemicals [20]. In the work [20] an analysis of the combustion chamber of a micro gas turbine engine was presented, which can operate on various fuels such as methane, natural gas, and ethanol. The research showed that the appropriate configuration of the outlet holes and the angles of the rotor blades significantly affect the performance of the combustion chamber. High combustion efficiency (over 98% for methane and natural gas) and low emissions of pollutants, such as nitrogen oxides, were key outcomes of this research. In other work, Pasalkar [15] focused on reducing nitrogen oxide (NO_x) emissions in jet engine combustion chambers. By changing design parameters and using computational fluid dynamics (CFD) simulations, researchers significantly reduced NO_x emissions, which is crucial for the sustainable development of fuel technologies [15]. Another article [1] describes the effects of hydrogen-enriched biogas on combustion and emission of a dual-fuel diesel engine. The conclusions of the analysis showed that the addition of hydrogen to biogas significantly reduced carbon dioxide emissions. At 20% H_2 content in biogas, a reduction in CO_2 emissions of up to 56% was observed compared to running the engine on biogas alone.

In the context of hybrid systems, modelling a turbine engine will allow for mapping its operating conditions. Such systems operate in diesel-electric generators or gas-electric generators. Such an application is easier to implement because the turbine operates at a constant speed under different loads, which may suggest that certain operating parameters are much easier to predict. An example of using a turbine as a power generator is shown in Fig. 1. Such an application works as a serial hybrid propulsion called Rex [8]. Modelling a multi-fuel combustion chamber allows for

flexible adaptation to different energy sources, increasing practical application possibilities. With advanced simulation tools, such as Ansys Fluent and Creo-6.0, researchers can accurately analyse the flow of fuel and air, leading to the optimization of the combustion process and the improvement of hybrid systems' efficiency.

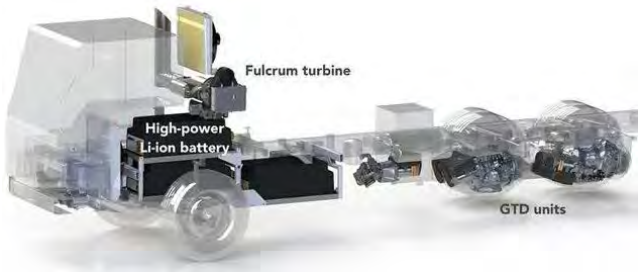

Fig. 1. Application of a turbine as a generator in heavy goods vehicles [14]

2. Research problem

The article describes combustion processes occurring in the chamber of turbine engines. By selecting, among others, the appropriate shape of the combustion chamber, the amount of fuel in the injector and chemical additives, the combustion process can be controlled. The types of combustion are presented: diffusion and laminar, together with examples of their occurrence. Then, the formation of pollutants and their types are described. The emissions of NO_x, CO_2, and particulate matter by gas turbines and reciprocating engines were compared. Ways to reduce gas emissions were proposed, among others, by rearranging the aerodynamics of the combustion chamber, increasing the volume of the primary flame zone, or improving fuel atomization.

The next step is to describe the fuels used to power gas turbines. The main problems of the combustion process are described, including maintaining the initiation of combustion in a very stable flow, or a lack of stability [22]. For example, blends of biofuels with traditional aviation fuels can reduce particulate and CO_2 emissions without significant loss of efficiency. Specific blends, such as bioethanol with jet fuel, have shown a 15% reduction in CO_2 emissions and improved lubricity. The use of hydrogen as a fuel in gas turbines reduces CO_2 emissions by 100% and NO_x by 90% compared to conventional fuels [21]. Additionally, hydrogen as a fuel improves the efficiency of turbines at high temperatures. Other studies have shown that biogas can be effectively used in gas turbines, which allows for a 20–30% reduction in CO_2 emissions. Mixing biogas with natural gas does not significantly affect engine efficiency [16]. The use of gas turbines, for example, as generators or in industry, is discussed. Turbine engines can be used in hybrid motor vehicles as a generator to charge batteries, which allows for increased range and energy efficiency of vehicles.

The following section describes the research stand used for the simulation tests and specifies the operation of the stand, specifying the individual components of the system.

In the research part of the work, the combustion chamber of the tested engine was first modelled in the Ansys Fluent simulation environment. It detailed the calculation of boundary conditions and preparation of the model for the needs of the analysis. The next part included the results of simulation studies of the flow of the working medium through the combustion chamber, taking into account the selection of an appropriate volumetric mesh for the chamber and the simulation of cold air flow. Finally, the results of the simulation were compared with their analysis. The obtained assessment of the numerical analysis allowed for undertaking design changes in the future for the combustion chamber and highlighted further development possibilities of the turbine engine for further research and simulation. The numerical calculations performed using the models and mechanisms available in the Ansys Fluent program can be a starting point for the modernization of the existing research engine. The author will focus on the analysis of the flow through the above-mentioned combustion chamber in order to verify the design solution selected by the team building the turbine engine.

In diffusion combustion, fuel and air mix immediately prior to ignition, and the mixing process continues even after combustion has begun. This type of combustion occurs within the boundary layer where the fuel gas stream meets the still oxidizing environment. A classic example is a candle flame, where a visible glowing zone forms at the point where the amount of fuel and oxidizer is in stoichiometric balance. Depending on the nature of the gas flow, diffusion combustion can be categorized as either laminar or turbulent.

Laminar combustion is represented as molecular. Laminar flame velocity is defined as the propagation rate of the normal flame front relative to the unburned mixture (homogeneous combustible mixture). This is an important property for a mixed flame because it contains basic information about the diffusivity and exothermicity of the combustible hydrocarbon mixture. At a practical level, laminar flame velocity is related to the combustion rate in the chamber, which can affect combustion efficiency and exhaust emissions. Laminar flame speed values can be applied directly in turbulent combustion modelling or used indirectly to validate chemical kinetic models.

The theory shows that the creation of swirl and an internal recirculation zone significantly improves the flame stability in the combustion chamber. On the other hand, the increase in the number of inert gases causes a decrease in the laminar velocity, which causes a deterioration in the flame stability. There are many other models for describing turbulent combustion. Currently, the most commonly used model is the Launder and Spalding model, i.e., the model k-ε, where k denotes the kinetic energy, while the rate of dissipation of kinetic energy. They are described by a two-equation model - the first equation of kinetic energy transport, the second of dissipation. Turbulent viscosity in this model is expressed by the formula ε–ε:

$$u_t = C_\mu * \rho * \frac{k^2}{\varepsilon} \tag{1}$$

where C_μ in the formula means constant, while ρ – density.

The dissipation energy is equal to the energy of large-scale motion, which later transforms into motion with energy of smaller and smaller scale. For the level of fibbers of the smallest scale (Kolmogorov), the energy eventually

dissipates (spreads). Therefore, the dissipation energy is described by the ratio: ρ

$$\varepsilon \sim \frac{u'^3}{l} = \frac{k^{3/2}}{l} \tag{2}$$

where, l – macroscale of turbulence, u' – speed pulsation.

Stability is a key characteristic of the combustion process in turbine engine chambers. Flame stability depends on two main factors: resistance to flame blow-off and resistance to flashback. In combustion chambers, flame blow-off is the primary cause of instability. This occurs when the flow velocity exceeds the flame propagation speed and there is no mechanism in place to stabilize the flame. Stabilization can be achieved by placing an obstruction in the airflow or by generating a swirling motion in the air. This swirl can be produced either by adjusting the air nozzles or by incorporating a swirler into the airstream.

In the exhaust gases, we can find unwanted pollutants that are created in the combustion chamber. There are four main pollutants that occur in the largest quantities [5]:

– unburned hydrocarbons (unburned fuel)
– smoke (carbon particles)
– carbon monoxide
– nitrogen oxides.

Gas turbines emit significantly lower levels of NO_x, CO_2, particulates, and other pollutants compared to reciprocating engines. This difference is due to the distinct combustion methods used: internal combustion engines produce power through thousands of high-temperature explosions within the cylinders, whereas gas turbines operate with a continuous combustion process that maintains a lower and more consistent temperature profile.

To substantially lower CO_2 emissions, achieving maximum net efficiency is essential, as greater efficiency leads to lower specific CO_2 emissions measured in grams per kilowatt-hour (kWh) of energy produced. For illustration, Fig. 2 presents data on the concentration of harmful compounds measured from a turboprop engine.

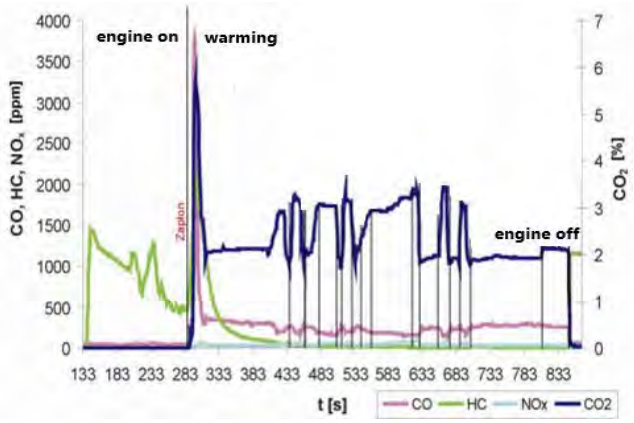

Fig. 2. Content of chemical compounds during measurement of exhaust gas composition concentration in the time domain [13]

When the engine is started, a sharp increase in the concentration of hydrocarbons can be seen, associated with the delivery of the mixture to the combustion chamber. With the initiation of ignition, there is an increase in the amount of carbon monoxide compounds, carbon dioxide, as well as hydrocarbons. The concentrations of the aforementioned compounds decrease in the further stage of engine warm-up [13].

In conditions of optimal excess air coefficient (in the starting range) and high combustion temperature, the greatest amount of NO_x occurs. One way to reduce them is to use a recirculation zone in the combustion chamber (Fig. 3). Its task is to stabilize the flame, lower its temperature, and separate it from the flame tube, which is the internal part of the combustion chamber [5]. The fuel burns with high intensity in a stream of strongly swirled air. The use of lean kinetic flames reduces NO_x emissions compared to diffusion flames (flame temperature exceeds 1900°C). Thanks to the presence of turbulence zones in the combustion chamber, the combustion process can be maintained within wide limits of pressure changes, flow velocity, and mixture composition. Another concept aimed at reducing nitrogen oxides is the use of catalytic combustion. It involves the use of catalysts to accelerate the chemical reaction and initiate the combustion process at very low temperatures, which radically reduces NO_x emissions.

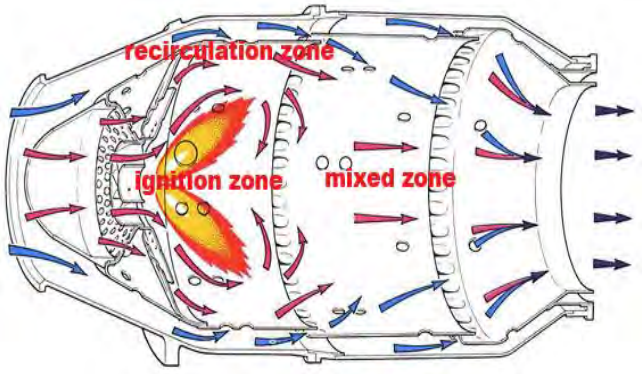

Fig. 3. Individually separated zones in the combustion chamber of a turbine engine [17]

All changes in the combustion chamber must be the result of a compromise between changes in combustion parameters and permissible emission of toxic components. It should be remembered that current standards require a reduction in the components of incomplete combustion – carbon monoxide and unburned hydrocarbons – both fuels ejected from the combustion chamber in the form of droplets or vapours, and products of partial decomposition of hydrocarbons into hydrocarbons with a lower molecular weight.

The most common way of classifying fuels is to divide them into gaseous and liquid fuels, and within gaseous fuels, they can be distinguished according to their calorific value. Table 1 presents the classification of fuels, which is divided into natural gas (mainly methane with small amounts of volatile hydrocarbons and inert gases), and high calorific value gases.

They consist of volatile hydrocarbons with small fractions of inert gases, which are usually very clean and work well in gas turbines. This can be propane, butane, or a mixture of them. They often contain some hydrogen and are usually available as by-products of refineries. Additionally, there are medium calorific value gases. These fuels contain methane additives with a high content of inert substances

(CO_2, N_2), or they are also processing gases or gasifier coal. The latter, i.e., low calorific value gases, contain carbon monoxide and hydrogen diluted with inert components, namely nitrogen and carbon dioxide. They come from the chemical, oil and gas, or steel sectors; many of these fuels cannot be transported or stored, and their main advantage is to reduce the fuel supply in industrial plants in a carbon-constrained environment [11].

Table 1. Classification of fuels for turbine engines [11]

Fuel category	Typical composition	Lower Heating Value [kJ/Nm³]	Typical specific fuels
Ultra/Low LHV gaseous fuels	H_2 < 10% CH_4 < 10% $N_2 + CO_2$ > 40%	< 11,200 (< 300)	Blast furnace gas (BFG), air blown IGCC, biomass gasification
High hydrogen gaseous fuels	H_2 > 50% CH_4 = 0–40%	5,500–11,200 (150–300)	Refinery gas, petrochemical gas, hydrogen power
Medium LHV gaseous fuels	CH_4 = 10–50% $N_2 + CO_2$ = 30–50% H_2 = 10–50%	11,200–30,000	Weak natural gas, landfill gas, coke oven gas, corex gas
Natural gas	CH_4 ≈ 90% C_2H_6 ≈ 5% Inert ≈ 5%	30,000–45,000	Natural gas, liquefied natural gas
High LHV gaseous fuels	CH_4 and higher hydrocarbons C_3H_8 > 10%	45,000–190,000	Liquid petroleum gas (butane, propane), refinery off-gas
Liquid fuels	C_nH_m with n > 6	32,000–45,000	Diesel oil, naphtha crude oils, residual oils, bio-liquids

Hydrogen's relatively low power density compared to other fuels like gasoline or natural gas underscores the difficulties in using it as an energy source. Moreover, hydrogen can cause embrittlement in certain materials, potentially compromising the safety and durability of storage and transport systems, making material compatibility a crucial consideration. When used in fuel cells to produce electricity, hydrogen also suffers energy losses during conversion, which further decreases the overall power density of hydrogen-based systems [2]. Another significant challenge is hydrogen's broad flammability range spanning from 4% to 75% by volume in air, which makes it more prone to ignition than fuels with narrower flammability limits. Additionally, its low ignition energy means it can be ignited by minimal energy sources, such as sparks or hot surfaces. As a result, minimizing ignition sources is critical to safety when working with hydrogen. Finally, the shock wave created by a hydrogen detonation can propagate at very high speeds, causing significant damage to structures and equipment. Therefore, managing and mitigating the risk of detonation is essential in any hydrogen project [2]. The high temperatures and pressures associated with hydrogen combustion can cause wear and damage to engine components. In addition, hydrogen's reactivity poses a risk of corrosion, and its low density creates challenges in fuel injection systems. To address these challenges, special materials are used in engine components exposed to high temperatures and pressures. In addition, corrosion-resistant materials are used in components exposed to hydrogen to mitigate the potential effects of corrosion.

In article [22], a novel concept for a gas turbine engine utilizing pressure gain combustion (PGC) was introduced. This design effectively addressed challenges related to the precise timing of combustion chamber opening and closing. The proposed valve timing system optimized gas flow, enhancing the conversion of high-pressure gas into mechanical energy. The use of rotary combustion chambers allowed for an efficient sealing solution. Notably, the design stands out for its simplicity and potentially low power-to-weight ratio [22]. CFD simulations demonstrated high efficiency and low specific fuel consumption, highlighting the promise of this hybrid gas turbine engine. It achieved a notable energy efficiency of 37% and a specific fuel consumption of just 219.9 g/kWh, all while maintaining a potentially low power-to-weight ratio. The engine's straightforward construction could reduce manufacturing costs compared to traditional engines with isobaric combustion. It incorporates elements common in piston engines, such as fuel injection systems and turbochargers, but eliminates the need for a crankshaft. Additionally, the use of an advanced ceramic sealing system in the rotating combustion chambers further enhances performance [22].

In gas turbine power systems, including hybrid fuel cell plants, transitioning from conventional fuels to pure hydrogen or hydrogen-natural gas blends is a critical development. However, this shift presents several challenges, such as the risk of flashback, acoustic combustion instabilities, higher temperatures on smoke tube walls, and, in some instances, increased nitrogen oxide emissions. The study in [20] focuses on enhancing the efficiency of gas turbine power systems by utilizing pure hydrogen and hydrogen-natural gas mixtures as fuels. The paper examines the operational setup of both premixed combustion chambers and chambers with sequential injection of eco-friendly, energy-efficient steam, specifically for Aquarius-type power plants. The research evaluates the key aerodynamic and energy characteristics of combustion chambers fuelled with hydrogen-containing gases, using conservation and transport equations within a multicomponent reactive system. A four-step chemical reaction model for burning the hydrogen-natural gas mixture was applied, enabling the calculation of optimal parameters for environmentally sustainable combustion systems. The premixed combustion chamber can be recommended only for working with natural gas-hydrogen mixtures with a hydrogen content not exceeding 20% (by volume). An increase in the hydrogen content leads to the formation of flashback zones and fuel combustion inside the swirler channels (Fig. 4). In the case of the combustion chamber of the Vodoley combined-cycle power plant, when operating on pure hydrogen, there are no flashback zones.

In study [17], the impact of hydrogen co-combustion on aircraft engine performance and emissions was examined. Researchers utilized zero-dimensional models of the JetCat P140 RXI and DGEN 380 engines, developed using the GSP (Gas Turbine Simulation Program). Combustion simulations in GSP rely on a real gas model and the NASA Chemical Equilibrium Applications (CEA) equations. The

study evaluated engine performance using Jet A-1 fuel as well as blends containing hydrogen or methane. Simulations were conducted both at ground-level design conditions and during flight at selected altitudes and speeds. Results showed that as the proportion of gas in the fuel mixture increased, there was a slight rise in both thrust and turbine outlet temperature, while specific fuel consumption decreased due to the higher energy content of hydrogen and methane [17]. The performance of JetCat and DGEN 380 engines was calculated for kerosene mixtures with methane or hydrogen. This knowledge will be used to convert these engines to gas fuels. When it comes to fuels and emissions, GSP has limitations related to the set of available chemicals and the zero-dimensional combustion chamber model.

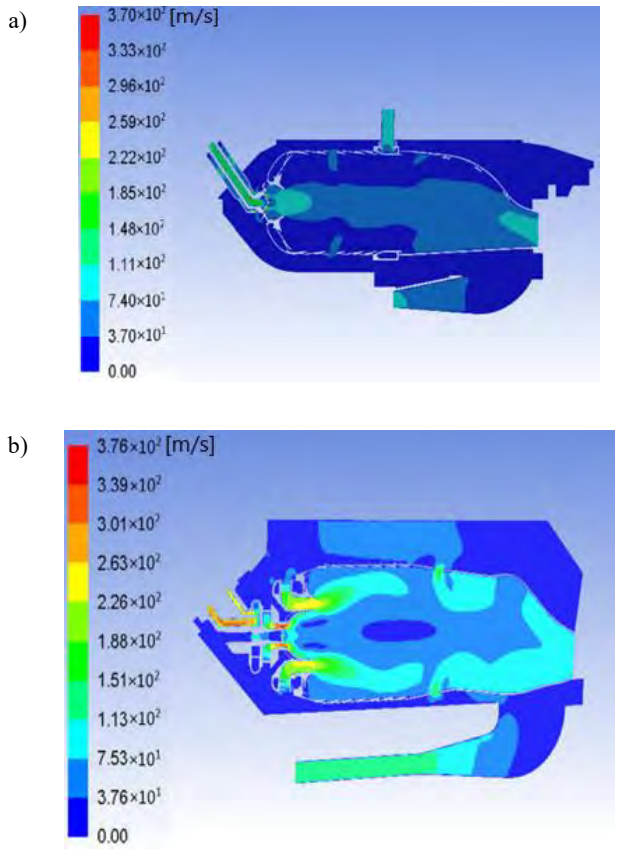

Fig. 4. Contours of velocity values [m/s] inside the combustion chamber with premixing of components (a) and with steam injection (b) [19]

Generalized Spray Combustion (GSC) modelling was also used to predict the performance of JetCat and DGEN engines fuelled with kerosene-methane or hydrogen blends. As the gas content in the fuel increased, both thrust and exhaust gas temperature rose slightly, while specific fuel consumption decreased due to the higher energy content of hydrogen and methane [17]. These results demonstrate the impact of hydrogen co-combustion on engine performance, which is crucial for planning experiments and redesigning fuel systems. Basic aircraft missions were simulated to compare fuel consumption under various conditions. However, accurately modelling off-design operating conditions requires detailed compressor and turbine characterization along with model validation. Additionally, emission predictions necessitate a multireactor approach with the combustion chamber divided into separate zones.

This paper [12] introduces a new mathematical model that incorporates the effects of fuel chemistry on the combustion process in turbine engines. The model was initially validated using tests on the Minijet Rig bench. It can be applied to analyse how various fuel components impact combustion, specifically mixtures of Jet A1 with synthetic paraffinic hydrocarbons C15 and C17 blends added at 10% concentration, and C8 and C11 blends added at 10%. The findings indicated that the variation in the reactivity coefficient (α88/39) between the two fuel types aligns with the experimentally observed differences in combustion behaviour.

3. Description of the tested system and research methodology

The work began with a thorough analysis of the existing literature on combustion chambers in multi-fuel engines and hybrid systems. We focused on research related to combustion mechanisms, fuel efficiency, and emission levels under various operating conditions. The key problems identified were: optimizing the engine's fuel efficiency, reducing harmful emissions, and improving combustion stability when using different fuels (e.g., natural gas, diesel, biofuels).

The first stage was to develop a preliminary design of a test stand for turbine engines based on a radial compressor. The design was created so that in the future it would be possible to conduct analyses of flows in the combustion chamber and to study the concentration of gaseous exhaust components when powered by different fuels. This will allow for the selection of the best fuel supply on the dynamometer, as well as the possibility of powering full-size structures with it. When building a test stand for a radial engine based on a car turbocharger, it was necessary to initially determine the requirements on which the design would be based: selection of an appropriate compressor, design of the combustion chamber, testing of designed elements in numerical analysis programs, design of systems cooperating with the engine, assembly of finished elements and systems on the base. Fig. 5 shows what the stand consists of: housing, wiring, control elements, pressure sensors, oil, control buttons, turbine, combustion chamber, injector, intake duct, ignition system, and fuel (gas).

In order to correctly model the chamber, it was necessary to first determine the values needed to assign boundary conditions. In order to correctly design the combustion chamber, it was necessary to calculate and determine the parameters of the working medium at its inlet. The input data for thermo-gas-dynamic calculations were selected based on the compressor characteristics available on its manufacturer's website.

The next step was to utilize Computational Fluid Dynamics (CFD) software to simulate the combustion process within the chamber. A three-dimensional geometric model of the chamber was created, taking into account all significant physical and chemical parameters. The simulations allowed us to analyse cold flow and heat transfer under various operating conditions.

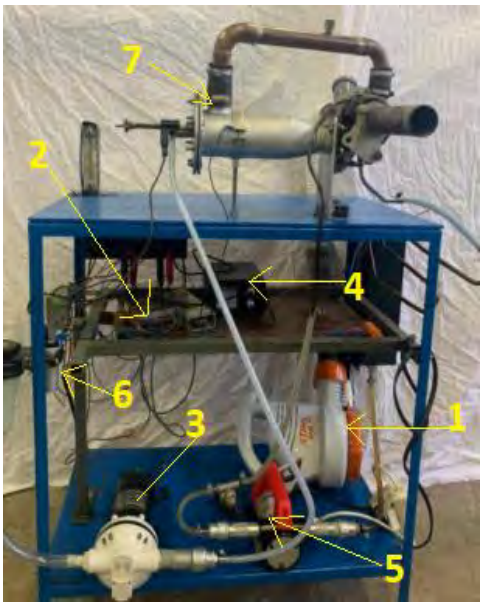

Fig. 5. Miniature jet engine station; 1 – air blower, 2 – control system, 3 – fuel pump, 4 – control display, 5 – oil pump, 6 – ignition system, 7 – turbine engine

One of the most important points in the preparation of a combustion simulation is the selection of a reaction kinetics model. It depends primarily on the fuel used and the available computing power. The article [18] presents simulations of propane combustion based on a one-equation combustion model. Another paper using propane as a fuel uses a five-equation combustion model that includes the following reactions: oxidation of propane, oxidation of carbon monoxide, oxidation of hydrogen, and conversion of carbon monoxide with water vapor [26]. In the articles [9,26] simulations were made using the one-equation Westbrook-Dryer model. The Ansys Fluent program allows simulation of kinetic and diffusion combustion. Depending on the selected model, the approach differs from the point of view of the „solver" according to the division in the user manual [3].

4. Assumptions for numerical modelling

After the first engine start-up, it turned out that the compressor was working at a point other than the one originally selected for calculations. The compression ratio was 2.5, while the rotational speed was about 168,000 rpm. The mass air flow rate measured at the engine inlet was 0.11 kg/s. The actual operating point was plotted on the compressor characteristic, which is shown in Fig. 6.

The photos of the stand shown in Fig. 5 show that the air inlet to the combustion chamber is connected to the air outlet from the compressor diffuser by a copper connector. At first glance, it seems to cause total pressure losses. Consequently, assuming the air parameters at the inlet to the combustion chamber as equal to those at the compressor outlet seems to be too much of an oversimplification. According to the author of this paper, first performing simple simulations of the flow through the aforementioned connector will allow us to estimate, with an acceptable degree of uncertainty, the thermodynamic parameters of the air flowing into the combustion chamber.

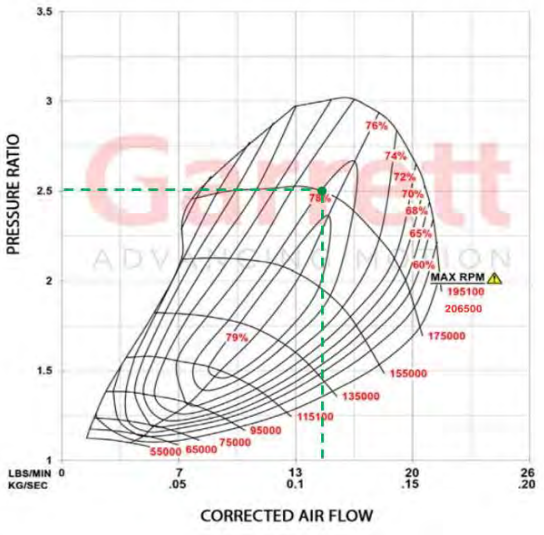

Fig. 6. Selected point of the turbocharger operating characteristic [24]

The study began with the discretization of the computational domain of the copper connector, which links the air inlet to the combustion chamber with the outlet from the compressor diffuser. The size and quality of the computational mesh significantly influence the effectiveness of numerical methods. Simulation results are highly sensitive to the number of mesh elements – generally, the more elements used, the higher the accuracy of the results. However, excessively refined meshes drastically increase computational requirements and do not always yield significantly improved precision. Therefore, a mesh independence study is conducted to assess how variations in mesh density affect the results. The goal of this approach is to determine the coarsest mesh that still captures the key physical phenomena within the studied system.

Two polyhedral meshes were prepared for the analysis. The first consisted of 19,570 elements with an orthogonal quality value of 0.52. The second, more refined mesh contained 30,302 elements and had an orthogonal quality of 0.35. An example of one of the generated meshes is shown in Fig. 7.

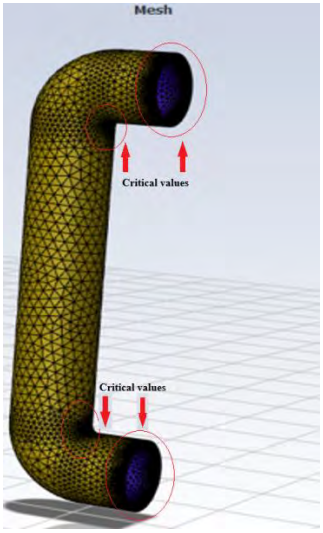

Fig. 7. Example of a connector mesh created in Ansys Fluent

Due to the lack of information about pressure and velocity in the outlet cross-section of the connector, an "outflow" boundary condition was applied at the domain's exit. A drawback of this condition is the necessity to define a "velocity inlet" boundary condition at the domain entrance.

The input data for the calculations are summarized in Table 2.

Table 2. Input data of the model being tested

Parameter	Value [unit]
$\dot{m}$ (compressor air mass flow rate)	0.11 $[\frac{kg}{s}]$
T_2(measured air temperature at pipe inlet/compressor outlet)	448.15 [K]
p_2(air pressure at pipe inlet/compressor outlet)	202600 [Pa]
R (gas constant for air)	287 $[\frac{J}{kg*K}]$
D (diameter of the connecting pipe cross-section)	0.034 [m]

Using the Clapeyron equation, the air density in the cross-section behind the compressor can be calculated:

$$\rho_{pow} = \frac{p_2}{R*T_2} = [\frac{Pa}{\frac{J}{kg \cdot K} \cdot K} = \frac{\frac{N}{m^2}}{\frac{N \cdot m}{kg}} = \frac{kg}{m^3}] \quad (3)$$

$$\rho_{pow} = \frac{202600}{287 \cdot 448.15} = 1.575 \ \frac{kg}{m^3}$$

Having calculated the air density, the velocity can be determined from the flow continuity equation:

$$\dot{m} = \rho_{pow} \cdot v \cdot A \quad (4)$$

where: A – cross-sectional area perpendicular to the direction of movement, v – flow velocity.

We determine the cross-sectional area of the pipe from the equation:

$$A = \pi \cdot (\frac{D}{2})^2 \quad (5)$$

$$A = 3.14 \cdot \left(\frac{0.034}{2}\right)^2 = 0.00091 \ m^2$$

Therefore:

$$v = \frac{\dot{m}}{\rho_{pow} \cdot A} = [\frac{\frac{kg}{s}}{\frac{kg}{m^3} m^2} = \frac{kg}{s} * \frac{m}{kg} = \frac{m}{s}] \quad (6)$$

$$v = \frac{0.11}{1.575 \cdot 0.00091} = 76.75 \frac{m}{s}$$

In the Ansys Fluent Solution program, a boundary condition was given at the pipe inlet – the calculated velocity was 76.75 m/s. Additionally, the static pressure value was entered as 250,000 Pa. The k – omega SST turbulence model was adopted for the calculations.

As a result of the analysis, pressure losses due to air flow through the connector were estimated. For this purpose, the relationship was used:

$$\frac{p_{inl} - p_{out}}{p_{inl}} \cdot 100 \ \% \quad (7)$$

where: p_{inl} – air pressure at the chamber inlet, p_{out} – air pressure at the outlet to the chamber.

The combustion chamber was modelled based on the technical data available in the research engine documentation. The CAD model of the chamber was made using the SolidWorks program (Fig. 8).

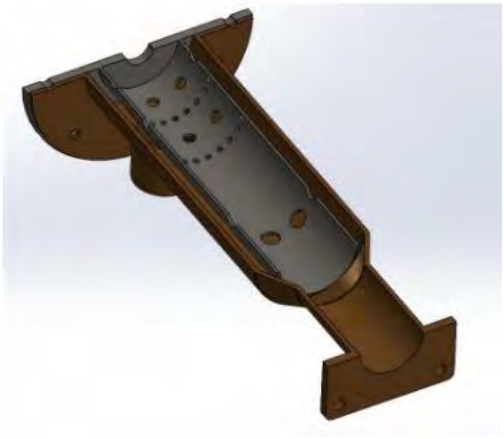

Fig. 8. Combustion chamber cross-section model

When selecting an appropriate combustion model, flame stability should be taken into account. On the one hand, an increase in the number of inert gases causes a decrease in the laminar combustion velocity, which means a deterioration in flame stability. However, the creation of a swirl and an internal recirculation zone significantly improves this stability. The selection of boundary conditions and the turbulence or combustion model strictly depends on the expected simulation results and how complex the simulation will be. It was decided to select the non-premixed combustion diffusion model due to the possibility of selecting the equation used to determine the temperature, defining the parameters of the unburned and burned medium, determining the reaction progress equation and the progress variable at the inlets and outlets, and the option of selecting the flame propagation speed model. When generating the mesh of the tested combustion chamber, it was decided to compare both types of meshes (unstructured and hybrid) and decide which one would be used for CFD analysis. It was decided to discretize the "fluid" domain, which contains the internal volume of the combustion chamber. For this purpose, a chamber volume was created in ANSYS Space Claim (Fig. 9) by replacing the chamber body with a fluid-filled structure of a given volume.

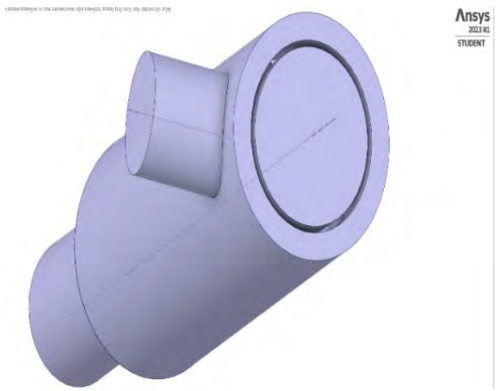

Fig. 9. Ready domain in the form of combustion chamber volume

For comparison purposes with the polyhedra mesh, a poly-hexcore mesh was generated in the next step. For this mesh, a min. Orthogonal Quality = 0.4. In the vicinity of the walls of the fire tube chamber, it was noted that there was a step change in volume of 1:8. This can cause numerical errors during solution. The hexcore mesh also obtained a larger number of elements, which would increase the calculation time of the program. A summary of both meshes is shown in Table 3. The most advantageous mesh parameters were demonstrated by the Polyhedral mesh. It was decided to select this mesh for further numerical tests of the combustion chamber. Also, compared to the Poly-hexcore mesh, it has a smaller number of elements, which will allow for shorter calculation times. The generated mesh meets the requirements for a good quality mesh - all parameters are within the ranges of permissible coefficient values, and the use of an increase in the mesh perpendicular value to 0.4 allowed for a reduction in skewness while maintaining good mesh quality.

Table 3. Input data of the model being tested

Grid type	Skewness	Orthogonal Quality	Number of elements
Polyhedra	0.5984901	0.4	254009
Poly-hexcore	0.79976186	0.4	398248

After the first attempt to simulate cold flow through the combustion chamber, it was checked that the Y+ parameter (dimensionless distance factor from the wall) reached maximum values of about 250 in the lower parts of the body, so it does not exceed acceptable values (about 500) and there is no need to compact the grid.

5. Simulation results and analysis

This part of the paper presents the results of CFD analyses for the previously selected settings in the Ansys Fluent program. Due to the significant computational cost and model complexity, it was decided to start the numerical studies by modelling the flow of the working medium through the chamber, without the combustion process (so-called cold flow). After completing the analysis, the simulation results were developed in the CFD Post post-processor. The first result of the analysis shows a map of the streamline distribution inside the combustion chamber (Fig. 10). It is clearly visible that some of the air flows into the interior of the glow tube through the holes and is swirled. The rest of the air flows around the outer part of the glow tube. Initially, it can be stated that this flow is close to the theoretical one. For a more accurate visualization of the flow through the chamber, the velocity vectors were projected onto the plane of symmetry of the chamber (Fig. 10).

The highest values are obtained in the holes from the glow tube and at the narrowing of the outlet from the chamber. The obtained velocities reach maximum values of approximately. 100 m/s, which is a realistic value. In the primary zone of the chamber, the formation of small recirculation vortices can be seen on the velocity vector maps near the areas of the tube holes. This increases the turbulence of the micro flow scale needed for an effective mixing process, however, in the author's opinion, the vortices created as a result of the simulation are insufficient to fulfil their function. The increase in velocity and the reflection of the airflow from the small openings lead to the formation of backflow, which causes air to recirculate into the mixing zone. Distributed large holes lead to the formation of cold areas in the flow, which are a result of cold streams, which can be a result of generating additional thermal stresses [12].

Comparing the results obtained with those presented in [10] for the GTD 350 turboshaft engine, which has a combustion chamber of a similar type, it can be seen that large symmetrical pairs of air vortices, which are recirculation zones, are formed in it. In the case under review, such vortices are absent. There is a lack of air vortices that would keep the flame “in place”. The increase in velocity and the reflection of the air stream from small holes lead to the formation of a reverse flow, which causes air recirculation to the mixing zone.

a)

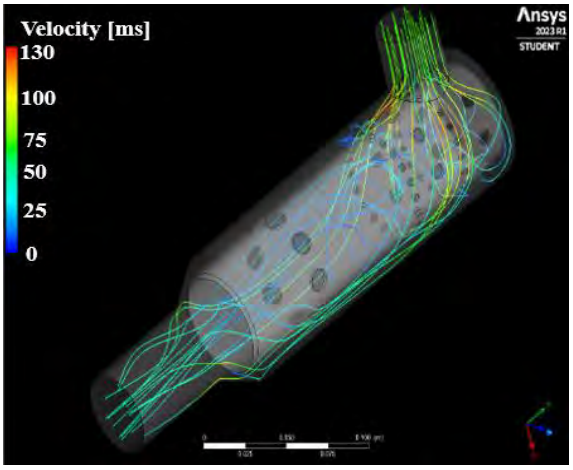

b)

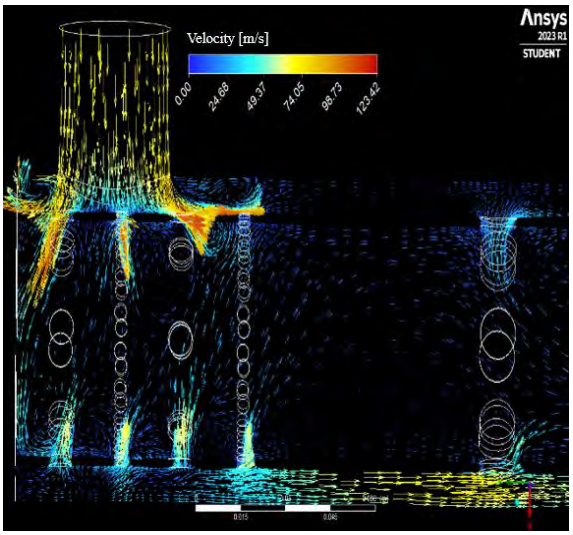

Fig. 10. Maps: a) view of the velocity line layout inside the pipe, b) velocity vector map for the tested chamber

In the further dilution zone, the formation of undesirable vortex zones can be observed. The flow is disturbed there. The velocity in the upper part of the combustion chamber outside the glow tube has significantly lower values than in the lower part.

In the case of velocity distribution, a lack of symmetry can be seen on both sides of the glow tube. The lack of symmetry on both sides of the flame tube in a gas turbine engine combustion chamber can lead to uneven temperature distribution, affecting efficiency and component durability. In article [6], the design of the flame tube in micro gas turbines was analyzed. The authors emphasized key dimensions, such as the total length of the flame tube, which can influence flow symmetry and the combustion process. This thesis [23] demonstrated that combustion primarily occurs within the combustion chamber. When a shorter combustion chamber was used, flames were present in the initial phase, suggesting that asymmetry may influence the combustion process. In the upper part of the combustion chamber, the air is accelerated through small holes, while at the bottom, the increase in velocity has much smaller values. However, before this, the flow velocity drops to zero, which does not favour changes in pressure at the chamber inlet. A compromise should be sought between a large number of small holes and a smaller number of larger holes. A large number of small holes allows for a uniform circumferential temperature distribution; on the other hand, it clearly inhibits the main flow (the flow velocity decreases). On the other hand, too sparsely distributed large holes lead to the formation of cold areas in the flow, which are a result of cold streams, which can be a result of generating additional thermal stresses, e.g., on the turbine blades. In the analysed chamber, the temperature distribution is omitted due to the fact that hot exhaust gases reach the diffuser of the centripetal turbine, which is resistant to this type of disturbance. It can be concluded that the flow through the holes of the glow tube not only depends on their size and pressure drop, but also on the geometry of the holes and the flow conditions in their vicinity.

6. Summary and remarks

1) In the context of research into new fuel technologies, multi-fuel engines can be tested for their performance and combustion efficiency of different fuel types, which can lead to innovations in the field of power supply.
2) It is worth noting that the use of multi-fuel engines may require special design and technological solutions to enable efficient combustion of various substances, as well as maintain the necessary performance parameters.
3) The use of a multi-fuel turbine engine in hybrid systems brings a number of benefits due to its dimensions and the process of preparing it for the combustion process. By using different fuels, it is possible to adapt to the types of fuel available in a given region, which can reduce operating costs and dependence on a single fuel source (e.g. diesel oil, gas, biofuel).
4) The conclusions indicate that multi-fuel turbine engines have the potential to greatly enhance the energy efficiency and environmental impact of hybrid systems, presenting new possibilities for future mobility solutions. In research focused on emerging fuel technologies, these engines can be evaluated for their efficiency and combustion performance with various fuel types, potentially driving innovations in power generation. It is important to highlight that employing multi-fuel engines may demand specialized design and technological approaches to ensure efficient combustion of diverse fuels while maintaining the required performance standards.
5) Analysing the flow velocity distribution, in the author's opinion, the geometry of the glow tube should be changed by using a less frequent arrangement of smaller holes, the diameters should be selected so that the air flow velocities are equal in the upper and lower parts of the chamber, so as to obtain flow symmetry. Additionally, it may be necessary to slightly enlarge the holes in the primary zone, which would result in the possibility of creating larger air turbulence zones.
6) The usefulness of numerical simulations in identifying and shaping mixing and combustion zones has been demonstrated. As a result of the conducted research, the conditions and methods for forming a combustible mixture enabling efficient operation of a pulsating combustion chamber (particularly suitable for heating applications) were determined. The considerations presented in this study may serve as a starting point for the aforementioned extensive research program involving modern measurement techniques.

Acknowledgements

This work was financed/co-financed by the Military University of Technology under the research project UGBWIM__22012025_15.

Nomenclature

CEA	chemical equilibrium applications	GSC	generalized spray combustion
CFD	computational fluid dynamics	GSP	gas turbine simulation program

Bibliography

[1] Ahmed SA, Zhou S, Tsegay S, Ahmad N, Zhu Y. Effects of hydrogen-enriched biogas on combustion and emission of a dual-fuel diesel engine. Energy Sources Part A. 2020:46(1): 5644-5659. https://doi.org/10.1080/15567036.2020.1736694

[2] Algayyim SJM, Saleh K, Wandel AP, Fattah IMR, Yusaf T, Alrazen HA. Influence of natural gas and hydrogen properties on internal combustion engine performance, combustion, and emissions: a review. Fuel 2024;362:130844. https://doi.org/10.1016/j.fuel.2023.130844

[3] ANSYS Fluent Tutorial Guide. 2016. www.ansys.com

[4] Bhuiyan MMH, Siddique Z. Hydrogen as an alternative fuel: a comprehensive review of challenges and opportunities in production, storage, and transportation. Int J Hydrogen Energy. 2025;102:1026-1044. https://doi.org/10.1016/j.ijhydene.2025.01.033

[5] Bulewicz E, Dyjakon A. Spalanie i Paliwa (in Polish). Wroclaw University of Technology Publishing House. Wroclaw 2008.

[6] Czarnecki M. Small scale gas turbine combustor sizing. Autobusy – Technika, Eksploatacja, Systemy Transportowe 2019;20(1-2):180-184. https://doi.org/10.24136/atest.2019.032
[7] Decarbonisation pathways for gas turbines – Modern Power Systems. https://www.modernpowersystems.com/analysis/decarbonisation-pathways-for-gas-turbines/?utm_source=chatgpt.com&cf-view&cf-closed&cf-view&cf-closed (accessed on 8 May 2025).
[8] Electric & Hybrid Marine Technology International. 2024. https://ehm.mydigitalpublication.com/september-2024-issue-/page-56 (accessed on 8 May 2025).
[9] Geng T, Schoen MA, Kuznetsov AV, Roberts WL. Combined numerical and experimental investigation of a 15-cm valveless pulsejet. Flow Turbulence Combust. 2006;78:17-33. https://doi.org/10.1007/s10494-006-9032-8
[10] Gieras M. Komory spalania silników turbinowych (in Polish). Warsaw University of Technology Publishing House. Warsaw 2010.
[11] Jones R, Goldmeer J, Monetti B. Adressing Gas Turbine Fuel Flexibility. GE Energy 2011.
[12] Lefebvre AH, Ballal DR. Gas Turbine Combustion. CRC Press 2010. https://doi.org/10.1201/9781420086058
[13] Merkisz J, Markowski J, Pielecha J, Mikutel T, Kozłowski R. Emisja spalin z silników lotniczych [Exhaust emissions from aircraft engines] (in Polish). Zeszyty Naukowe Akademii Marynarki Wojennej. 2013;54(1):89-104.
[14] New Zealand Adopts Wrightspeed Jet And Battery Power For Buses. https://www.forbes.com/sites/samabuelsamid/2016/04/22/new-zealand-adopts-wrightspeed-jet-and-battery-power-for-buses/ (accessed on 13 May 2025).
[15] Pasalkar SM, Shaikh MS, Pipulyawala MM, Jasdanwalla H. Design and CFD analysis of combustion chamber of jet engine to reduce formation of NOx. International Research Journal of Engineering and Technology. 2020;7(6):5172-5180. www.irjet.net
[16] Pukalskas S, Kriaučiūnas D, Rimkus A, Przybyła G, Droździel P, Barta D. Effect of hydrogen addition on the energetic and ecologic parameters of an SI engine fueled by biogas. Appl Sci. 2021;11:742. https://doi.org/10.3390/app11020742
[17] Rolls-Royce Ltd. The jet engine. Rolls-Royce 2005.
[18] Sayres JR, Scott J. Computational fluid dynamics for pulsejets and pulsejet related technologies. Master's thesis, North Carolina State University 2011.
[19] Serbin S, Radchenko M, Pavlenko A, Burunsuz K, Radchenko A, Chen D. Improving ecological efficiency of gas turbine power system by combusting hydrogen and hydrogen-natural gas mixtures. Energies. 2023;16(9):3618. https://doi.org/10.3390/en16093618
[20] Sher AA, Ahmad N, Sattar M, Phelan P, Lin A. Computational analysis of multi-fuel micro-gas turbine annular combustion chamber. J Therm Anal Calorim. 2024;149:3317-3329. https://doi.org/10.1007/s10973-024-12924-z
[21] Skobiej K. A review of hydrogen combustion and its impact on engine performance and emissions. Combustion Engines 2025;200(1):64-70. https://doi.org/10.19206/CE-195470
[22] Suchocki T. Performance and emission characteristics of a small gas turbine engine using hexanol as a biomass-derived fuel. Materials. 2024;17:6011. https://doi.org/10.3390/ma17236011
[23] Trzeciak A. Badania procesu pulsacyjnego spalania. Doctoral Thesis. Warsaw University of Technology. Warsaw 2023.
[24] Turbosprężarka Garrett 880693-5002S G30-770 (super core) | TOMSON Motorsport. https://tomson.com.pl/product-pol-7305-Turbosprezarka-Garrett-880693-5002S-G30-770-super-core.html (accessed on 14 May 2025).
[25] Wtryskiwacz Swirl Burst umożliwia ultra czyste spalanie biopaliw (in Polish). https://karlobag.eu/pl/ekologia/wtryskiwacz-swirl-burst-umozliwia-ultraczyste-spalanie-biopaliw-rewolucyjne-rozwiazanie-w-zakresie-redukcji-emisji-i-zrownowazonego-rozwoju-sektora-energetycznego-vxdjo?utm_source=chatgpt.com (accessed on 8 May 2025).
[26] Zheng F. Computational investigation of high speed pulsejets. Doctoral Thesis. NC State 2009. http://www.lib.ncsu.edu/resolver/1840.16/5968

Marcin Dopieralski, MSc. – Faculty of Mechanical Engineering, Military University of Technology, Warsaw, Poland.
e-mail: *marcin.dopieralski@student.wat.edu.pl*

Filip Polak, DEng. – Faculty of Mechanical Engineering, Military University of Technology, Warsaw, Poland.
e-mail: *filip.polak@wat.edu.pl*

Article citation info:
Brzozowski M, Cieślar K, Nowakowski J. Numerically effective 10 degrees of freedom model in autonomous vehicle motion planning. Combustion Engines. 2026;204(1):13-19. https://doi.org/10.19206/CE-208521

Michał BRZOZOWSKI
Kacper CIEŚLAR
Jacek NOWAKOWSKI

Combustion Engines
Polish Scientific Society of Combustion Engines

Numerically effective 10 degrees of freedom model in autonomous vehicle motion planning

ARTICLE INFO

Received: 2 June 2025
Revised: 17 July 2025
Accepted: 22 July 2025
Available online: 15 September 2025

Simplified vehicle models dominate the literature on autonomous driving, with the 3 degrees of freedom (3 DoF). The model is the most frequently used due to its high computational efficiency. However, such models have significant limitations, particularly in their inability to account for detailed tire–road interactions.
This study proposes an extended model with ten degrees of freedom (10 DoF), developed using the Newton–Euler formalism. Analytical derivation of the mass matrix and the vector of right-hand sides enables a significant reduction in computation time by eliminating matrix operations. For comparison, another 10 DoF model based on the homogeneous and joint coordinate transformation method is also considered. The aim is to assess how the choice of modeling formalism affects both computational efficiency and the fidelity of real-world motion representation.
All three models (3 DoF and both 10 DoF variants) were tested in simulations of an overtaking maneuver under varying weather conditions. The analysis focused on differences in steering angle trajectories and tracking errors. Additional evaluations included a lane-change maneuver and a 736-meter driving scenario.
Results show that extended models provide improved accuracy and better capture of dynamic vehicle behavior. In particular, the Newton–Euler-based 10 DoF model offers significant computational advantages. The maximum observed difference in steering angle between models reached 2 degrees, attributed to the 3 DoF model's simplified treatment of tire forces and lack of friction coefficient consideration. The proposed models show strong potential for implementation in motion planning for autonomous vehicles.

Key words: *autonomous vehicle, vehicle modelling, vehicle dynamics, steering algorithm, path fallowing*

1. Introduction

Two major contemporary research areas related to vehicles focus on pollutant emissions and the broadly defined domain of autonomous driving [20, 26]. The present work addresses the application of vehicle dynamic models in the context of motion planning for autonomous vehicles. Autonomous vehicle motion planning consists few stages, among them we can distinguish: route planning, path planning, path following, trajectory realization (Fig. 1).

Fig. 1. Scheme of planning the motion of an autonomous vehicle

Vehicle dynamics models are frequently used in the path following task. The 3 degrees of freedom models dominate in the literature; they may also be called bicycle models [9, 24, 25]. Figure 2 presents a classic model of a vehicle with 3 degrees of freedom. The rotational motion of wheels is not taken into consideration.

This model takes into account the flat motion only, i.e., displacement in the xy plane and yaw angle ψ around the z' axis of the local system {C}', parallel to the z axis of the roadway system {O}. The generalized coordinates vector has the form:

$$\mathbf{q} = \begin{bmatrix} V'_x \\ V'_y \\ \psi \end{bmatrix} \tag{1}$$

where: V'_x, V'_y – are components of the vehicle speed vector in vehicle's body coordinate system {C}', ψ – is the vehicle's body yaw angle marked in the Fig. 2 as the angle of the vehicle's longitudinal axis x' to the axis x of the roadway system {O}.

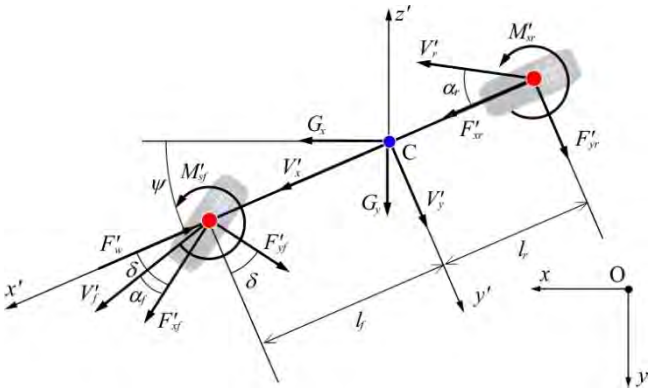

Fig. 2. Classic bicycle-type model [4]

In some cases, the bicycle model can be understood as a model with 2 degrees of freedom rather than 3 degrees of freedom [15, 23]. Model of a vehicle with 3 DoF can also be formulated in the roadway system [5], then vector of generalized coordinates is:

$$\mathbf{q} = \begin{bmatrix} x_c \\ y_c \\ \psi \end{bmatrix} \tag{2}$$

where x_c and y_c are coordinates of the vehicle's center of mass in the roadway system.

In the paper [21], a 3 degrees of freedom model was compared with a 9 degrees of freedom model. The authors have proved that the classic model with 3 degrees of freedom can be successfully used in a path following task, assuming that lateral acceleration fulfils the condition $a'_y < 0.5\,g$. This assumption has practical significance because it confirms the possibility of using a simple vehicle model while at the same time defining specific conditions for its application.

From the analysis of the literature, it is seen that the 3 degrees of freedom model is the most commonly used in the issues of motion planning and in autonomous vehicle control. However, its application is limited to modeling motion with small lateral accelerations [21]. Attempts are being made to circumvent this limitation. Paper [1] presents a model and a controlling algorithm ensuring the implementation of the trajectory of motion in the condition of slip. In the study [7], a 3 degrees of freedom model was implemented to model a vehicle's motion in a muddy terrain, which required the development of a model of the contact of the road wheel (tire model) with soft ground. In the study [12], the use of a 3 degrees of freedom model in the execution of the control with additional consideration of a simplified model of the steering system and differential mechanism was discussed. The authors of [2] present an application of the bicycle model enhanced with the ability to account for the tire-road friction coefficient. They implement it for a route with varying curvature. In studies [3, 14], the bicycle model is used in a path-tracking task in combination with a model predictive control (MPC) approach.

In contrast, in study [13], this model is applied to vehicle control during parking maneuvers. Meanwhile, in [28], the bicycle model is used to address the control problem of a vehicle driving on a highway. In summary, the bicycle model is applicable to vehicle control across a wide range of driving speeds.

Models with a higher complexity can be met rather seldom in the literature on autonomous vehicles. Paper [7] presents a flat (2D) model with 5 degrees of freedom. Except from three degrees of freedom present in the bicycle model, rotation angles of the front and rear wheels were also additionally taken into consideration (connecting suitably two road wheels and presenting them as one), what has enabled introduction of driving and braking torques into the considerations and simulations, as well as adoption of tire model. Model with 7 degrees of freedom, considering flat motion (V'_x, V'_y, ψ) and rotation angles of road wheels $\gamma^{(1)}, \gamma^{(2)}, \gamma^{(3)}, \gamma^{(4)}$ was presented in the papers [16, 17, 27].

In the present paper, a vehicle dynamic model with 3 DoF, defined in the roadway system, and hence with a vector of generalized coordinates defined in [2], and two models with 10 DoF differing in formalism used in the course of their formulation are presented.

2. Vehicle model with 10 DoF

Vehicle model presented below (Fig. 3) take into account motion of vehicle's body as a rigid element (together with attached masses of suspensions) with 6 degrees of freedom, motion of which is described by components of the vector:

$$\mathbf{q}_b = \begin{bmatrix} \mathbf{r}_c \\ \boldsymbol{\phi} \end{bmatrix} \tag{3}$$

where: $\mathbf{r}_c = \begin{bmatrix} x_c \\ y_c \\ z_c \end{bmatrix}$ – denotes position vector of the center of mass, $\boldsymbol{\phi} = \begin{bmatrix} \psi \\ \theta \\ \varphi \end{bmatrix}$ – is the vector defining orientation, i.e., the Euler angles ZYX: ψ, θ, φ.

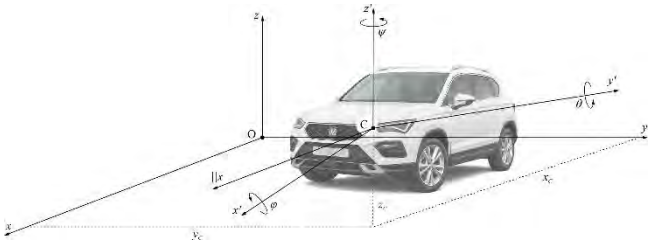

Fig. 3. Scheme of a vehicle model with 10 degrees of freedom

Transformation of the coordinates from the vehicle's body system $\{C\}'$ to system connected with the road $\{O\}$ is performed according to the dependency:

$$\mathbf{r} = \mathbf{r}_c + \mathbf{R}\mathbf{r}' \tag{4}$$

where: $\mathbf{r}_c = [x_c \quad y_c \quad z_c]^T$ – determines location of the local system origin $\{C\}'$ in the roadway system $\{O\}$, $\mathbf{r}$ – coordinate vector in the roadway system $\{O\}$, $\mathbf{r}'$ – coordinate vector in the local system $\{C\}'$,

$$\mathbf{R} = \begin{bmatrix} \cos\psi & -\sin\psi & 0 \\ \sin\psi & \cos\psi & 0 \\ 0 & 0 & 1 \end{bmatrix} \begin{bmatrix} \cos\theta & 0 & \sin\theta \\ 0 & 1 & 0 \\ -\sin\theta & 0 & \cos\theta \end{bmatrix} \begin{bmatrix} 1 & 0 & 0 \\ 0 & \cos\varphi & -\sin\varphi \\ 0 & \sin\varphi & \cos\varphi \end{bmatrix}.$$

To perform transformation of the coordinate between the $\{C\}'$ and $\{O\}$ systems, therefore two operations on the vectors are needed (multiplying the vector by the matrix and adding the vectors). When homogeneous coordinates are used (extension of the vectors describing displacements by the fourth coordinate equal to 1), the transformation is performed by means of a single operation of multiplying the matrix by the vector:

$$\mathbf{r} = \mathbf{B}\mathbf{r}' \tag{5}$$

where: $\mathbf{r} = \begin{bmatrix} x \\ y \\ z \\ 1 \end{bmatrix}$ – coordinates vector in the roadway system $\{\}$, $\mathbf{r}' = \begin{bmatrix} x' \\ y' \\ z' \\ 1 \end{bmatrix}$ – coordinates vector in the local system $\{C\}'$, $\mathbf{B} = \mathbf{B}(\mathbf{q}_b) = \begin{bmatrix} \mathbf{R} & \mathbf{r}_c \\ \mathbf{0} & 1 \end{bmatrix}$ – matrix of homogeneous transformations.

Motion of the wheels relative to the vehicle's body is described by: steering angle δ_i and rotation angles γ_i, $i = 1, 2, 3, 4$ (Fig. 4a).

Coordinates from the wheel system $\{i\}_u^{\wedge}$ to the system $\{C\}'$ are transformed according to the dependency:

$$\mathbf{r}_i' = \left(\mathbf{r}_s' + \boldsymbol{\Omega}^{(i)}\hat{\mathbf{r}}_u^{(i)}\right) \tag{6}$$

where: $\mathbf{r}_{s'} = \begin{bmatrix} x_s'^{(i)} & y_s'^{(i)} & z_s'^{(i)} \end{bmatrix}^T$, $\hat{\mathbf{r}}_u^{(i)}$ – coordinate vector of a point in the system $\{i\}_u^{\wedge}$, $\boldsymbol{\Omega}^{(i)} = \begin{bmatrix} c\delta^{(i)} & -s\delta^{(i)} & 0 \\ s\delta^{(i)} & c\delta^{(i)} & 0 \\ 0 & 0 & 1 \end{bmatrix}$,

a)

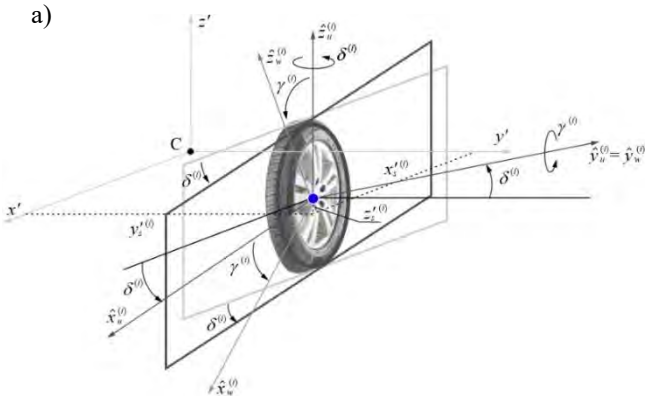

b)

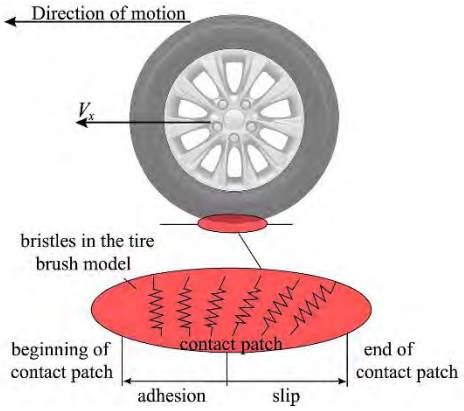

Fig. 4. Forces acting on the wheel a) coordinate systems, b) brush tire model

when the homogeneous transformations are not used, and according to the formula:

$$\mathbf{r}_i' = \mathbf{D}_i\mathbf{W}_i\mathbf{r}'_{w,i} \tag{7}$$

where: $\mathbf{D}_i = \begin{bmatrix} \boldsymbol{\Omega}_i & \mathbf{r}'_s \\ \mathbf{0} & 1 \end{bmatrix}$, $\boldsymbol{\Omega}_i = \begin{bmatrix} \cos\delta_i & -\sin\delta_i & 0 \\ \sin\delta_i & \cos\delta_i & 0 \\ 0 & 0 & 1 \end{bmatrix}$, $\mathbf{W}_i = \begin{bmatrix} \boldsymbol{\Lambda}_i & 0 \\ \mathbf{0} & 1 \end{bmatrix}$, $\boldsymbol{\Lambda}_i = \begin{bmatrix} \cos\varphi_i & 0 & \sin\varphi_i \\ 0 & 1 & 0 \\ -\sin\varphi_i & 0 & \cos\varphi_i \end{bmatrix}$, when homogeneous transformations are used.

In the present study it was assumed that the angles δ_i are known function of time:

$$\delta^{(1)} = \delta^{(2)} = \delta(t), \tag{8}$$

$$\delta^{(3)} = \delta^{(4)} = 0, \tag{9}$$

where: $\delta(t)$ – average steering angle of the front wheels.

The consequence of such assumption is that $\boldsymbol{\Omega}^{(i)} = \boldsymbol{\Omega}^{(i)}\left(\delta(t)\right)$ and the same $\mathbf{D}_i = \mathbf{D}_i(t)$. Generalized coordinates vector of the vehicle has therefore 10 components and it can be represented in the following form:

$$\mathbf{q} = \begin{bmatrix} \mathbf{q}_b \\ \mathbf{q}_\gamma \end{bmatrix} \tag{10}$$

where: $\mathbf{q}_b$ was specified in (3), while vector of the steering angles takes the form of:

$$\mathbf{q}_\gamma = \begin{bmatrix} \gamma_1 \\ \gamma_2 \\ \gamma_3 \\ \gamma_4 \end{bmatrix} \tag{11}$$

In case of known normal forces $F_{Kz}^{(i)}$ (Fig. 4a), forces of the roadway's surface acting on the road wheels lying in the roadway's plane and the stabilizing torque $F_{Kx}^{(i)}, F_{Ky}^{(i)}, M_s^{(i)}$ have been determined with use of brush tire model of the tire according to [18] with modifications according to [23] (Fig. 4b). This is analytical model that allows for determination of reaction of road surface on vehicle wheels with taking into account large drift angles. The forces $F_{Kz}^{(i)}$ were determined analysing deflection of tires in contact points of the wheel with the road, modifying stiffness coefficients in such way to take into account the flexibility of the suspensions.

Equations of the motion are written in form:

$$\mathbf{M}(\mathbf{q})\ddot{\mathbf{q}} = \mathbf{f}\left(\mathbf{q}, \dot{\mathbf{q}}, \delta(t)\right) \tag{12}$$

where: $\mathbf{M}$ – interia matrix, $\mathbf{q}$ – vector of generalized coordinates.

Equations of the motion have been integrated using the Runge-Kutta method of the 4th order with a constant integration step. Initial conditions were determined by solving the appropriate equation of static equilibrium of the vehicle.

The main differences between the models formulated in this study, concern not only the form of formulas transforming the coordinates. The M10/1 model, which uses homogeneous transformations (vectors with 4 coordinates – formulas (5), (7) was formulated using the second-order Lagrange equations. This model is described in detail in the work [10]. The M10/2 model is based on vectors having three components – formulas (4), (6) from the Newton-Euler formulas. A detailed description of this model is presented in the paper [4]. The most important differences between these models are listed in Table 1.

Table 1. Characteristics of the M10/1 and M10/2 models

Feature	M10/1	M10/2
Formalism in deriving equations	Lagrange equations of II kind	Newton-Euler equations
Vector of generalized coordinates	$\mathbf{q} = \begin{bmatrix} \mathbf{q}_b \\ \mathbf{q}_\gamma \end{bmatrix}$	
Structure of the inertia matrix	$\begin{bmatrix} Mbb & Mbg \\ Mgb & Mgg \end{bmatrix}$	$\begin{bmatrix} Mbb & 0 \\ 0 & Mgg \end{bmatrix}$
Model of the tire	Sharp-Pacejka	
Taking into account the influence of wheel rotation on vehicle's body	yes	no
Analytic equations for elements of Mbb matrix	no	yes

In general, it can be said that the M10/1 model describes vehicle motion more precisely. Its disadvantage is the greater demand for computing power of the processor performing

calculations. This is due to the necessity to generate a large number of transformation matrices and their derivatives, as well as due to the form of the inertia matrix **M**.

Verifications and validations of the models are presented in the studies: M10/1 (7), M10/2 and 3 DoF in the study [4]. Acceptable consistence with the CarSim software package and with results of real experiments reported in the literature was achieved [6, 11] – the error did not exceed 1%.

3. Results and discussion

As mentioned in the introduction chapter, planning of motion of the autonomous vehicle requires defining the route (maneuver to be performed). In general, the route is defined in a discrete way, providing points near which the center of mass of the vehicle should be located. Implementation of geometric algorithms for the determination of the steering angle requires presentation of the route in a continuous manner. Therefore, it is necessary to perform an approximation of the route (discrete one) to the path (continuous one). In the present study, the B_5 spline functions were used [8]. This method has proved to be very effective. The approximation error for the route longer than 700 m does not exceed 20 cm. In addition, the applied method has allowed obtaining the path with a smooth curvature. This has a positive effect on the operation of the control algorithms.

The maneuver of lane change belongs to one of the most frequently simulated maneuvers, included in the ISO 3888-1standard. The task of the vehicle is to overcome a specific track. The scheme of this maneuver is shown in the Fig. 5.

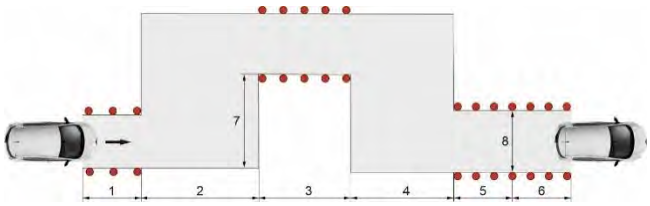

Fig. 5. Scheme of the track according to the ISO standard was elaborated basing on (ISO 3888-1, 2018)

Within the framework of this study the both models with 10 degrees of freedom, and a simple 3 degrees of freedom model, were tested in the task of executing the path, which simulates the maneuver of changing lanes. In the first test, a simulation was performed for the adhesion coefficient having a value of 0.85, which corresponds to a dry road surface. The run of the steering angle of the wheels was presented in Fig. 6.

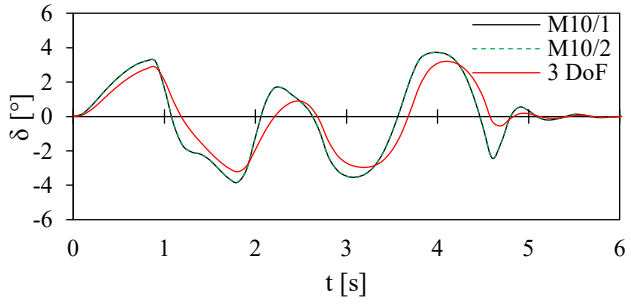

Fig. 6. Steering angle for lane change maneuver, μ = 0.85

To evaluate it, the B3M algorithm described in the study [4] was used. This algorithm determines the steering angle of the wheel based on equations of the model with 3 degrees of freedom, and using information which was read from the path. The same (common) steering angle was taken for both front road wheels of the vehicle. The speed of the vehicle amounted to 65 km/h. Parameters of the vehicle were taken according to the Carsim software – "Class A" hatchback.

Presented runs indicate a very high compliance of both models with 10 degrees of freedom. The obtained trajectories are shown in Fig. 7.

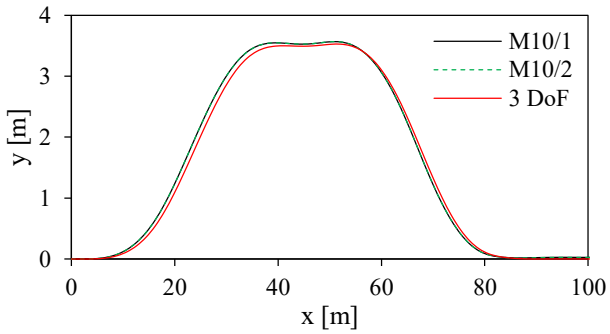

Fig. 7. Trajectory for lane change maneuver, μ = 0.85

The diagram of the trajectory shown in the Fig. 7 indicates that differences between the M10/1 and M10/2 models are negligible. The differences between the models with 10 DoF and 3 DoF are noticeable. Even greater differences between the 10 DoF and 3 DoF models can be seen in the case of a reduced adhesion coefficient. In the second simulation, one assumed μ = 0.5. The results are presented in the Fig. 8 and 9.

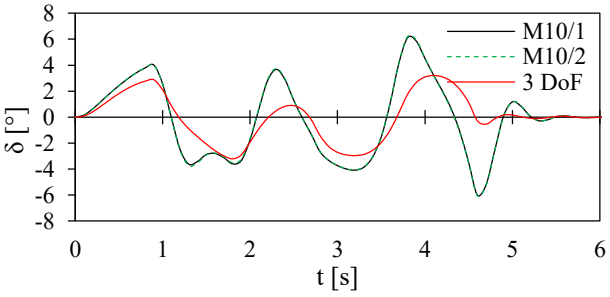

Fig. 8. Steering angle for lane change maneuver, μ = 0.5

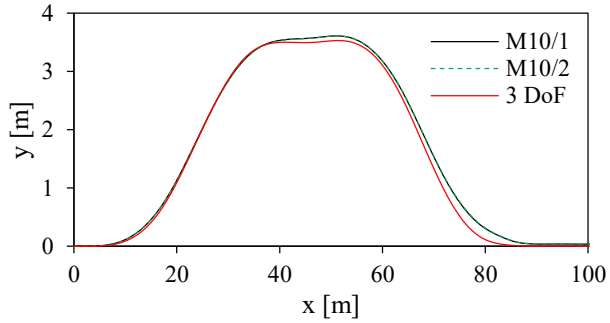

Fig. 9. Trajectory for lane change maneuver, μ = 0.5

A change in the adhesion coefficient significantly affected the steering angles and trajectories determined by the models. The bicycle model does not take into account the adhesion coefficient, and therefore does not makes possible to correctly represent this maneuver with assumed parameters of the vehicle and the speed. The difference in the designated steering angle is up to 2 degrees. The differences caused by simplifications of the 3 DoF model are now more visible. The steering angle determined using 3 DoF model (Fig. 8) distinctly differs from the models with 10 DoF. Such differences are shown in Table 2, where ε_{MAX} [m] denotes the difference between the coordinates of the path and the trajectory of the center of mass.

Table 2. Maximal mapping error of the route for lane change maneuver, ε_{MAX} [m]

–	μ = 0.5		μ = 0.85	
3 DoF	M10/1	M10/2	M10/1	M10/2
0.001	0.235	0.246	0.170	0.171

Attention should be paid to the fact that a very small error for the 3 DoF model means that the vehicle was driving almost on the preset path. In reality, the steering angle determined using a 3 DoF model cannot be executed. This model, unlike spatial models containing models of tire, does not take into account large angles of drift and slip. The calculations with the use of expanded models show that the ideal execution of such a maneuver is not possible at a preset speed, although the mapping error of the route of 0.246 m can be considered as acceptable.

Calculation time is a significant parameter during the planning of the motion of the autonomous vehicle. In the Table 3. is shown calculation time for the presented maneuver.

Table 3. Calculation time [s] for maneuver of change of the lane during 6 s

3 DoF	M10/1	M10/2
0.32	2.74	0.88

Since the difference in mapping error of the trajectory between the M10/1 and M10/2 models is negligible, and the proposed M10/2 model based on the Newton–Euler equations is three times faster, the remaining part of this paper was restricted to calculations using this model.

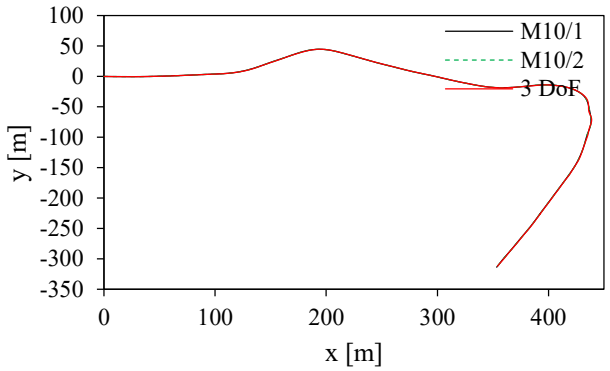

Fig. 10. Trajectory for route "Hałcnów"

The second simulation concerned the implementation of a more extensive route of driving. Within the framework of the test, one simulated motion of the vehicle along the Matylda Linnert street in Bielsko-Biała city. The trajectory is shown in Fig. 10. The constant speed of 36 km/h was assumed.

Although the model with 3 degrees of freedom ultimately achieved higher mapping accuracy than spatial models (Table 4), the steering angle of the road wheels (Fig. 11) points to a certain instability of the calculations. This results from the fact that the vehicle is then taking a turn (approximately 50 s). Lateral acceleration is then > 0.5 g, and the condition for the use of the 3 degrees of freedom models assumed in [22] is not fulfilled.

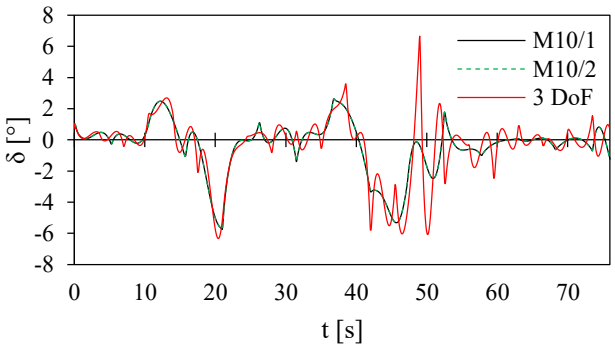

Fig. 11. Steering angle for route "Hałcnów"

The resulting steering angle trajectory indicates a certain instability in the calculations when using a simplified vehicle model (3 DoF). At the 50th second, a large oscillation in the angle occurs. This is due to the fact that when attempting to execute any trajectory, the simplified model is unable to accurately reproduce the complex maneuver. Calculations using 10 DoF models allowed for the determination of the steering angle trajectory that could be realistically executed. Oscillations are smaller, and the trajectory is smoother. Both 10-DoF models yield nearly identical results in terms of steering angle profiles.

Table 4 shows the mapping errors of the driving route. The results obtained for the 10 DoF models are identical. Calculations using the 3 DoF model generate a similar mapping error as the more complex models.

Table 4. Maximal mapping error of the route "Hałcnów", ε_{MAX} [m]

3 DoF	M10/1	M10/2
0.209	0.276	0.276

4. Conclusions

The considerations presented in this paper indicate that both 10 degrees of freedom models can be used for modeling the dynamics of autonomous vehicles. They accurately replicate real-world driving conditions. A comparison with the simplified 3 degrees of freedom model proves that simplified models have significant limitations. The lack of consideration for the rotational motion of the wheels in the 3 degrees of freedom model means that the assumption of small slip angles must be made. The conducted simulation studies confirm the condition presented in the referenced

work [22]. However, a comparison of the calculation times clearly shows that more complex models are numerically inefficient. Even though the 10 degrees of freedom model presented in this paper, formulated using Newton–Euler equations (M10/2), is more than four times faster than the model formulated using Lagrange equations. It is worth noticing that the difference in the quality of reality reproduction between these two models is negligible. The main conclusions drawn from the presented analyses and simulations are outlined below.

– In the literature, simplified models prevail. This is due to their high numerical efficiency, which is considered the leading criterion.
– There is a need to develop dynamic models to increase their numerical efficiency.
– The comparison presented in this paper enables a comparison of two 10 degrees of freedom models formulated in different ways.
– The analytical formulas for the elements of the matrix M and the vector h in the 10 degrees of freedom model (M10/2) allow for eliminating matrix operations. The proposed solution directly affects the calculation time.
– Calculations using the 3 degrees of freedom model indicate a very small trajectory reproduction error. This is due to the simplifications made in the model, and it should be noted that achieving such results in reality is impossible.
– Calculations using the 10 degrees of freedom models prove the correctness of both models. The trajectory reproduction error is nearly identical.
– The difference in the calculated steering angle (for a lane change maneuver) is even 2 degrees. This is because the 3 degrees of freedom model does not account for the friction coefficient.

Future work is planned to extend the simulation studies to include heavy-duty and multi-articulated vehicles.

Bibliography

[1] Ajanović Z, Regolin E, Shyrokau B, Ćatić H, Horn M, Ferrara A. Search-based task and motion planning for hybrid systems: agile autonomous vehicles. Eng Appl Artif Intel. 2023;121:105893. https://doi.org/10.1016/j.engappai.2023.105893

[2] Atoui H, Sename O, Alcala E, Puig V. Parameter varying approach for a combined (kinematic + dynamic) model of autonomous vehicles. IFAC-PapersOnLine. 2020;53(2): 15071-150716. https://doi.org/10.1016/j.ifacol.2020.12.2028

[3] Brown M, Funke J, Erlien S, Gerdes JC. Safe driving envelopes for path tracking in autonomous vehicles. Control Eng Pract. 2017;61:307-316. https://doi.org/10.1016/j.conengprac.2016.04.013

[4] Brzozowski M. Planowanie ruchu samochodu autonomicznego z zastosowaniem modeli dynamiki (dissertation in Polish). University of Bielsko-Biala, Faculty of Mechanical Engineering and Computer Science. Bielsko-Biala 2025.

[5] Brzozowski M, Drąg Ł. Application of dynamic optimization for autonomous vehicle motion control. Transport Problems. 2023;18(2):209-222. https://doi.org/10.20858/tp.2023.18.2.18

[6] Chebly A, Talj R, Charara A. Coupled longitudinal/lateral controllers for autonomous vehicles navigation, with experimental validation. Control Eng Pract. 2019;88:79-96. https://doi.org/10.1016/j.conengprac.2019.05.001

[7] Dallas J, Jain K, Dong Z, Sapronov L, Cole M, Jayakumar P et al. Online terrain estimation for autonomous vehicles on deformable terrains. J Terramechanics. 2020;91:11-22. https://doi.org/10.1016/j.jterra.2020.03.001

[8] Diachuk M, Easa SM. Motion planning for autonomous vehicles based on sequential optimization. Vehicles. 2022;4: 344-374. https://doi.org/10.3390/vehicles4020021

[9] Gillespie TD. Fundamentals of vehicle dynamics. SAE International. Warrendale 1992.

[10] Grzegożek W, Adamiec-Wójcik I, Wojciech S. Komputerowe modelowanie dynamiki pojazdów samochodowych (in Polish). Cracow University of Technology. Cracow 2003.

[11] Guo H, Cao D, Chen H, Sun Z, Hu Y. Model predictive path following control for autonomous cars considering a measurable disturbance: implementation, testing, and verification. Mech Syst Signal Pr. 2019;118:41-60. https://doi.org/10.1016/j.ymssp.2018.08.028

[12] Hu C, Qin Y, Cao H, Song X, Jiang K, Rath J et al. Lane keeping of autonomous vehicles based on differential steering with adaptive multivariable super-twisting control. Mech Syst Signal Pr. 2019;125:330-346. https://doi.org/10.1016/j.ymssp.2018.09.011

[13] Joševski M, Katriniok A, Riek A, Abel D. Disturbance estimation for longitudinal vehicle dynamics control at low speeds. IFAC-PapersOnLine. 2017;50(1):987-993. https://doi.org/10.1016/j.ifacol.2017.08.204

[14] Li X, Sun Z, Cao D, Liu D, He H. Development of a new integrated local trajectory planning and tracking control framework for autonomous ground vehicles. Mech Syst Signal Pr. 2017;87:118-137. https://doi.org/10.1016/j.ymssp.2015.10.021

[15] Lozia Z. Examples of authorial models for simulation of motor vehicle motion and dynamics. Zeszyty Naukowe Instytutu Pojazdów Politechniki Warszawskiej. 2015;104:9-27.

[16] Lozia Z. Model symulacyjny ruchu i dynamiki samochodu dwuosiowego, wykorzystywany w symulatorze (in Polish). Zeszyty Naukowe Instytutu Pojazdów PW. 1999;4(34):37-51.

[17] Lozia Z. Symulatory jazdy samochodem (in Polish). Wydawnictwo Komunikacji i Łączności. Warszawa 2008.

[18] Pacejka HB, Sharp RS. Shear force development by pneumatic tyres in steady state conditions, a review of modeling aspects. Veh Syst Dyn. 1991;20(3-4):121-175. https://doi.org/10.1080/00423119108968983

[19] Paden B, Čáp M, Yong SZ, Yershov D, Frazzoli E. A survey of motion planning and control techniques for self-driving urban vehicles. IEEE Trans Intell Veh. 2016;1(1):33-55. https://doi.org/10.1109/TIV.2016.2578706

[20] Pielecha J, Kurtyka K, Skobiej K. The impact of vehicle dynamic parameters on the exhaust emissions in RDE tests. Combustion Engines. 2018;175(4):26-34. https://doi.org/10.19206/CE-2018-404

[21] Polack P, Altché F, Novel B, de La Fortelle A. The kinematic bicycle model: a consistent model for planning feasible trajectories for autonomous vehicles? 2017 IEEE Intelligent Vehicles Symposium. 2017:812-818. https://doi.org/10.1109/IVS.2017.7995816

[22] Polack P. Consistency and stability of hierarchical planning and control systems for autonomous driving. Paris: Université Paris Sciences et Lettres; 2018. Available from: https://hal.science/tel-02096788/

[23] Rajamani R. Vehicle dynamics and control. 2nd ed. Springer. New York 2012. https://doi.org/10.1007/978-1-4614-1433-9

[24] Ribeiro AM, Koyama MF, Moutinho A, de Paiva EC, Fioravanti AR. A comprehensive experimental validation of a scaled car-like vehicle: lateral dynamics identification, stability analysis, and control application. Control Eng Pract. 2021;116:104924. https://doi.org/10.1016/j.conengprac.2021.104924

[25] Vial P, Puig V. Kinematic/dynamic SLAM for autonomous vehicles using the linear parameter varying approach. Sensors. 2022;22(21):8211. https://doi.org/10.3390/s22218211

[26] Wróbel RS, Sroka Z, Sierzputowski G, Dimitrov R, Mihaylov V, Ivanov D. Driving protocols: the possibility of using routing protocols in autonomous transport. Combustion Engines. 2024;196(1):3-9. https://doi.org/10.19206/CE-170418

[27] Zhang F, Gonzales J, Li SE, Borrelli F, Li K. Drift control for cornering maneuver of autonomous vehicles. Mechatronics. 2018;54:167-174. https://doi.org/10.1016/j.mechatronics.2018.05.009

[28] Zhou S, Wang Y, Zheng M, Tomizuka M. A hierarchical planning and control framework for structured highway driving. IFAC-PapersOnLine. 2017;50(1):9101-9107. https://doi.org/10.1016/j.ifacol.2017.08.1705

Michał Brzozowski, DEng. – Faculty of Mechanical Engineering and Computer Science, University of Bielsko-Biała, Poland.
e-mail: *mbrzozowski@ath.bielsko.pl*

Kacper Cieślar, MEng. – Faculty of Mechanical Engineering and Computer Science, University of Bielsko-Biała, Poland.
e-mail: *kcieslar@ubb.edu.pl*

Prof. Jacek Nowakowski, DSc., DEng. – Faculty of Mechanical Engineering and Computer Science, University of Bielsko-Biała, Poland.
e-mail: *jnowakowski@ubb.edu.pl*

Article citation info:
Sawczuk W, Kołodziejski S, Bartkowiak A, Kubacki Ł. Microfiltration of oils in combustion engines in drive and hydraulic systems – research and review of solutions. Combustion Engines. 2026;204(1):20-26. https://doi.org/10.19206/CE-208770

Wojciech SAWCZUK
Sławomir KOŁODZIEJSKI
Agnieszka BARTKOWIAK
Łukasz KUBACKI

Combustion Engines
Polish Scientific Society of Combustion Engines

Microfiltration of oils in combustion engines in drive and hydraulic systems – research and review of solutions

ARTICLE INFO

Received: 8 June 2025
Revised: 23 July 2025
Accepted: 29 July 2025
Available online: 11 September 2025

The article presents the issue of the cleanliness of oils and fuels used in combustion engines of automotive and rail vehicles. In the article, after a review of the membrane separation field, attention was drawn to the possibility of using additional oil and fuel filtering systems to increase the cleanliness class. For this purpose, a methodology for testing the condition of oil and fuels in a portable laboratory in accordance with the requirements of SAE AS 4059, ISO 4406:99, and NAS 1638 standards was presented. Solutions for portable devices for microfiltration of oils and fuels by Kleenoil were presented. Additionally, the results of tests of sample new engine, gear, and hydraulic oils were presented, which, according to the cited standards, are out-of-class oils and require additional microfiltration. The novelty of the article is the presentation of a simple method for examining the condition of oil in combination with microfiltration. Both the oil condition analyzer and the microfiltration machine are portable stations for field and laboratory applications.

Key words: *microfiltration, engine, gear and hydraulic oils, oil testing, metallic contamination, water in oil*

1. Introduction

Membrane separation process (MSP) is an operation of separating mixtures. In this process, the membrane acts as a filter, creating a permeable or semi-permeable barrier that partially or completely restricts the flow of some components in the flowing liquid stream [21]. The fluid flowing through the membrane is driven by the pressure difference. In this process, the solution is separated into a concentrate remaining on the membrane and a purified liquid (permeate) [20]. The concentrate contains components (contaminants) with particles larger than the membrane pores, and the liquid stream behind the membrane has components smaller than the membrane pore size. Figure 1 shows a diagram of membrane separation with the solution flow parallel to the membrane, i.e. tangential flow [3, 22].

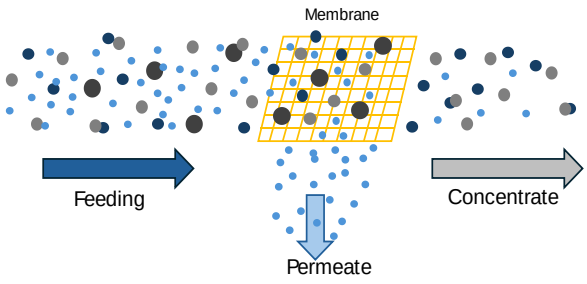

Fig. 1. The idea of tangential (cross) membrane separation [5]

Membrane separation processes are classified according to the size of the membrane pores and the particles that are retained in them, and the pressure in the system during filtration, which is included in Table 1.

Over time, the membrane can become more resistant to filtration, reducing the flow rate and separation efficiency (microfiltration). This is due to the accumulation of solid particles on the membrane surface or in the pores, which causes its clogging. The first way to improve membrane filtration in the long term is to use a serial (cascade) filtration system. In such a system, the MF microfiltration membrane performs the initial cleaning, and the UF ultrafiltration membrane performs the fine cleaning [6, 14]. Initial cleaning ensures that larger particles do not block the UF membrane channels. The MF pre-membrane does not block or change the flow. In the work [25], it was shown that the hybrid MF/UF system proved to be very effective in providing the purified fluid flow below the permissible limit.

Table 1. Classification of membranes according to their porosity [5, 23]

No.	Membrane	Pore diameter	Pressure
1	Microfiltration (MF)	0.1–10 µm (10^{-7}–10^{-5} m)	from 0.1 to 2 bars
2	Ultrafiltration (UF)	1–100 nm (10^{-9}–10^{-7} m)	from 1 to 7 bars
3	Nanofiltration (NF)	0.5–1 nm ($5\cdot10^{-10}$–10^{-9} m)	from 5 to 25 bars
4	Reverse Osmosis (RO)	0.1–0.5 nm (10^{-10}–$5\cdot10^{-10}$ m)	from 15 to 80 bars
5	Gas Separation (GS)	< 0.1 nm (10^{-10} m)	from 60 to 80 bars

The second way to increase the flow through filtration membranes and thus improve membrane stability is to incorporate nanoparticles and modify the membrane surface. This has led to the development of membranes capable of withstanding very high pressures [4, 19]. For highly polluted wastewater containing dissolved salts, polar and non-polar organic compounds, oils, and surfactants, more complex hybrid filtration systems of MF and UF series filtration are used. In such a case, according to the work [1, 18], a combined process of electrocoagulation EC, microfiltration MF and membrane distillation MD is used. Electrocoagulation and then microfiltration is the initial treatment of e.g. wastewater before the main membrane distillation [24].

Membranes can be made of polymer, ceramic, metal, or carbon materials. Polymer membranes are widely used in industry, made of materials such as polyamide, cellulose acetate, and cellulose triacetate [9]. The membrane consists of a polymer material, the chains of which are relaxed at atmospheric pressure, and the application of pressure promotes the densification of the polymer chains [16, 27]. Carbon membranes are made of sintered carbon, while ceramic membranes are manufactured as multi-channel tubular ones. Apart from the mechanical industry, another important application of filtration membranes is the chemical and food industry, especially in the processing of liquid food. When using conventional separation methods, many volatile food aromas tend to be separated. However, in membrane processes, these flavor components are retained in the food [10, 25]. Membrane ultrafiltration (UF) is a basic technology in the treatment of oily wastewater [7, 16]. Microfiltration, in addition to its basic purpose of purifying various liquid substances from contaminants, also has a reverse application. An example of this is the extraction of microalgae, i.e., autotrophic microorganisms, from fresh and seawater. The most commonly extracted microalgae is the green marine microalga Nannochloropsis oculata [14].

2. Microfiltration in industry and automotive

The microfiltration technique dates back to the 1970s, when there was a conflict in the Middle East between Israel and the Arabs. At that time, American troops reported problems with military vehicles in terms of lubrication of hydraulic systems due to the desert climate. Additional external filters were then installed in military vehicles. In the 1980s, the technique entered civilian use in the United States, and in the 1990s, it became common in Europe. In Poland, around 2000, it began to be noticed by companies servicing hydraulic systems in construction vehicles, agricultural vehicles, municipal equipment, and in power hydraulics. In automotive and industrial applications, microfiltration is a method of removing water, solids, and other components from oil mixtures in the form of colloidal systems or suspensions using filters from 1 to 4 μm. Microfiltration takes place under a small overpressure of up to 6 bar. The holes (pores in the membrane) of 1 to 4 μm are small enough to retain bacteria found in oils or fuels [11]. Microfiltration is performed on portable stations, as shown in Fig. 2, in a bypass manner. Oil filtration in the tank is performed during the operation of the hydraulic system. This minimizes the downtime of the device, financial outlays, and the amount of used oil, related to its more frequent replacement.

In industrial applications, microfiltration of hydraulic oil is already very common. It is observed when cleaning filter systems in construction and road machines, tractors, and agricultural machines, as well as in production machines with hydraulic systems.

Figure 3 shows the application of the Kleenoil MS2+MM5 microfiltration station during oil cleaning in a Libher 566 wheel loader and in a Billion H3500/550 injection molding machine. These are examples of the use of a filtration machine with simultaneous examination of the condition of hydraulic oil by the authors of the article. In automotive applications, microfiltration is used for engine fuels, engine oils, and transmission oils. Kleenoil by-pass filter systems have already been used to remove contaminants and wear products from rolling bearings, sliding bearings, gear wheels, or the interaction of the engine piston with rings with the cylinder liner. The problem of engine oil contamination has already been analyzed in [13, 28]. Figure 4 shows the diagram of the operation of the additional filter system in the lubrication system of the combustion engine and an example of the use of the system on a city bus.

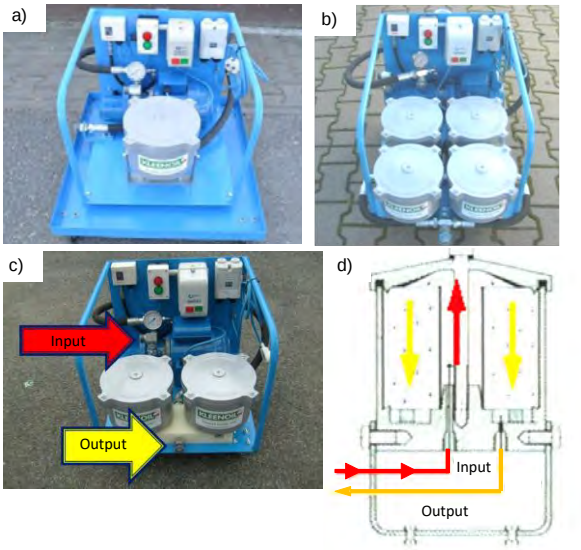

Fig. 2. View of a portable hydraulic oil filter unit with: a) one filter element, b) four filter elements, c) two filter elements, d) oil flow diagram through the filter element

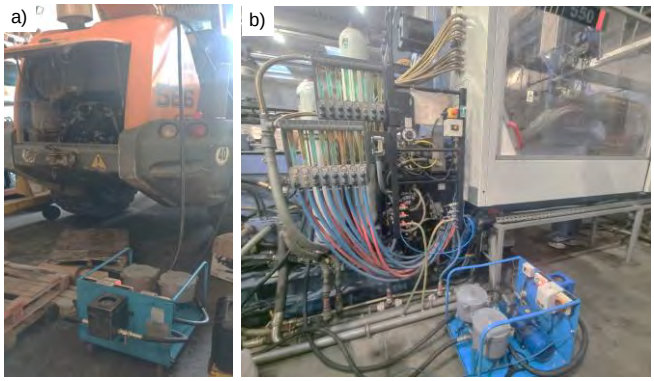

Fig. 3. View of the machine's use during microfiltration of hydraulic oil in: a) Liebher 566 wheel loader, b) Billion H3500/550 injection molding machine [fot. S. Kołodziejski]

Research conducted by Kleenoil on city buses in Lublin showed that adding an additional engine oil microfiltration system working in parallel with the combustion engine lubrication system extended the oil life to the next change by 4 times. During the engine oil filtration period, the oil was periodically tested for changes in kinematic viscosity during the use of buses.

Kleenoil has also conducted research into fuel purity by installing an additional diesel fuel microfiltration system on a vehicle and at fuel stations. Figure 5 shows a view of a vehicle with an additional KleenFuel filter in the fuel system. Figure 6 shows a view of the use of the MS4+MM5 microfiltration machine at a fuel station in a transport company.

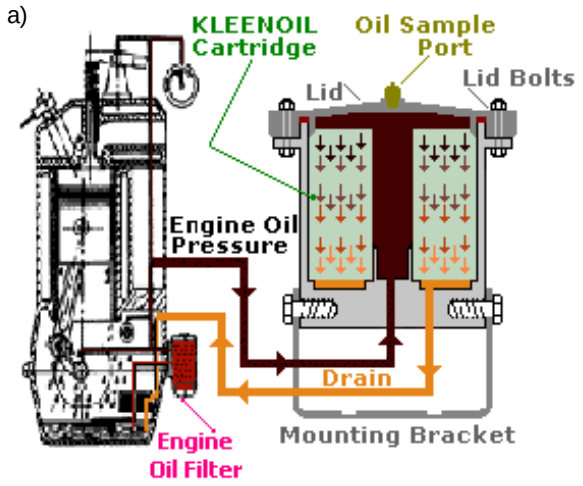

Fig. 4. a) Diagram of the filter system in the combustion engine lubrication system, b) View of the additional engine oil microfiltration system mounting in a city bus [fot. Ł. Kubacki]

Fig. 5. View of the additional tank with a fuel microfiltration insert on the truck b) view of the tank with the KleenFuel insert with fuel lines [fot. Ł. Kubacki]

Both during the adaptation of the device for microfiltration of engine oil and fuel, kleenoil and kleenfuel filter inserts with a hole diameter of 1 μm were used. This allows for the removal of organic impurities such as oxidation or thermal combustion products, inorganic impurities such as metal particles, and the removal of water by 99.95% [12]. The advantage of microfiltration devices is the possibility of replacing filter inserts without the need to drain the oil. The filter containers are located above the oil tank. The microfiltration application examples in Fig. 4–6 were an attempt to implement large-scale oil and fuel separation in motor vehicles and at gas stations. Despite successful testing, these solutions were not implemented in everyday operation.

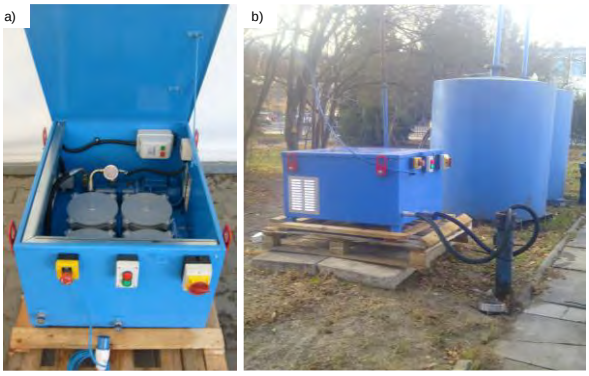

Fig. 6. a) View of the enclosed fuel microfiltration machine at the petrol station with four tanks b) view of the microfiltration device with fuel tanks [fot. Ł. Kubacki]

3. Oil purity class standards

In terms of regulations governing the purity of hydraulic and lubricating oils, the following standards should be indicated:

- ISO 4406
- SAE AS 4059
- NAS 1638
- GOST 17216.

ISO 4406:99 standard was published by Turkish Standards Institute (TSE) under the title: Hydraulic Fluid Power – Fluids – Method for Coding the Level of Particulate Contamination. SAE Aerospace standard, the full name of this standard is: SAE AS 4059 Aviation Fluids – Cleanliness Classification for Hydraulic Fluids. This standard specifies cleanliness classes for particulate contamination of hydraulic fluids and includes methods for reporting the relevant data. NAS 1638 is the American aviation standard, and GOST 17216 is the Russian standard for oil cleanliness. NAS 1638 was replaced by SAE AS 4059 in 2001. Both ISO and SAE standards refer to the number of particles recognized as contamination with a size larger than 4 μm, 6 μm, 14 μm, and 21 μm.

To assess the condition of the oil in terms of its contamination, the first 3 impurity values (4, 6, and 14 μm) found in 100 ml of the tested oil are selected. For example, hydraulic oil that received a cleanliness class result of 22/20/17 after testing (according to ISO 4406) means that it contained impurities in the number of [2]:

- from 20000 to 40000, about size above 4 μm
- from 5000 to 10000, about size above 6 μm
- from 640 to 1300, about size above 14 μm.

Cleanliness classes according to ISO 4406 standard were correlated with average cleanliness classes according to NAS 1638 standard, which is presented in Table 2. The table additionally presents requirements for various hydraulic system units in terms of oil cleanliness. In the case of finding that the cleanliness class of hydraulic oil is too high for the requirements set by the hydraulic system units and their intended use, it is possible to reduce the oil class thanks to microfiltration. According to the work [8], micro-

filtration allows for reducing the oil cleanliness by up to 6 classes. This depends on the filtration time and the number of used filter inserts.

Table 2. Hydraulic oil purity classes according to standards ISO 4406 and NAS 1638 [12]

Cleanliness class		Required oil cleanliness class			
ISO 4406	NAS 1638	Pumps and motors	Valves	Bear-ings	Drivers
23/21/18	12	Highly contaminated oil. Absolute oil change or microfiltration with system cleaning			
22/20/17	11				
21/19/16	10				
20/18/15	9	gear	return		
19/17/14	8	vane, piston	proportion, mushroom	sliding	cylinders
18/16/13	7				
17/15/12	6			roller	Hydrostatic
16/14/11	5	Aircraft applications, high-pressure systems up to 32 MPa with proportional elements and high working load			
15/13/10	4				
14/12/9	3				
13/11/9					
12/10/8	2	Highly precise hydraulic systems above 32 MPa			
10/9/8					
10/9/7	1				
10/8/6					
9/8/6	0				

4. Research methodology

4.1. Purpose and object of oil research

The aim of the study was to evaluate the ISO, SAE, and NAS cleanliness classes and the relative humidity of three selected new oils contained in a 5-liter plastic container. Achieving the study objective required conducting the study in three stages. The first stage involved testing the new oils, the second stage involved testing the oils after the first microfiltration, and the third stage involved testing the oils after the second microfiltration.

Hydraulic oil type HV46, ATF II D oil for automatic gearboxes, and 20W-50 engine oil were used for the tests. The research methodology diagram is presented in Fig. 7.

The choice of the tested oil in a plastic canister resulted from the fact that this type of packaging has the least impact on the phenomenon of evaporation and condensation of water inside during storage and transport. In contrast to metal tanks (barrels), this phenomenon is common, and it is necessary to filter the oil before pouring it into the machine or engine. Especially in a situation where metal tanks are stored without a roof and in warehouses with variable temperature, which depends on the ambient temperature.

4.2. Research method

Hydraulic oil condition tests were performed on the portable analyzer OPComII Portable Oil Lab PPCO 300-1000 by ArgoHytos. The general structure of the analyzer and its view are shown in Fig. 8.

The principle of the analyzer is to shine a laser beam through the flowing oil through a solid particle monitor. Contaminants in the oil block the beam of light falling from the source onto the detector. Then a signal is generated proportionally to the size of the particles in the oil. The electronic system signals to assign the particle size in µm and the number of particles in the oil. Table 3 shows the parameters and values measured by the oil analyzer.

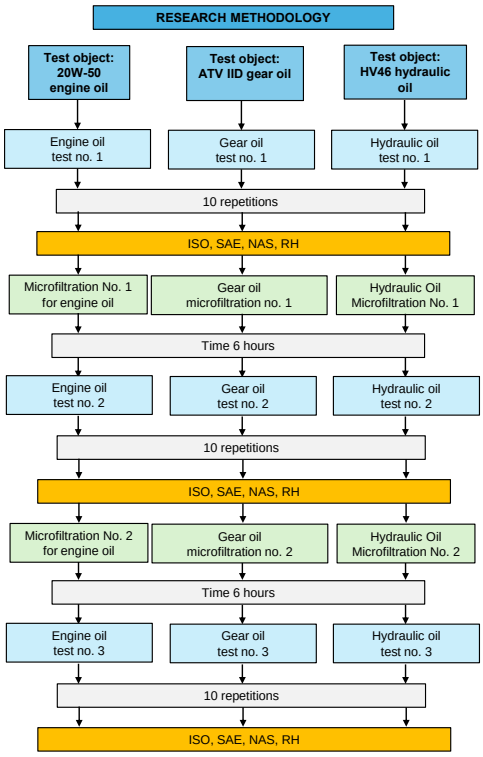

Fig. 7. Oil testing methodology diagram

Table 3. Measured parameters and values of the device OPComII Portable Oil Lab PPCO 300-1000 [2]

Parameter	Abbreviation	Unit
Temperature	T	°C/°F
Relative permittivity	P	–
Conductivity	C	pS/m
Relative oil humidity	RH	%
ISO cleanliness level	ISO	–
SAE cleanliness level	SAE	–
NAS cleanliness level	NAS	–
GOST cleanliness level	GOST	–
Concentration	Conc	p/ml
Flow rate	Findex	ml/min

The basic parameters of the device are [12]:

- Operating pressure range from 2.5 to 350 bar (35–5000 psi)
- Operating viscosity range from 1 to 300 cSt
- Operating temperature from –30°C to +80°C
- Operating temperature for oil from +5°C to +80°C
- Operating temperature for fuel from –20°C to +70°C
- Relative humidity in the range of 0% RH to 100% RH.

After basic tests of new oils from the canister, microfiltration was carried out on the Kleenoil MS2+MM5 device shown in Fig. 2c with two tanks and filter inserts.

5. Results of oil tests

The results of oil tests on a portable oil cleanliness class analyzer are presented in Table 4. The tests were conducted for compliance with ISO, SAE, and NAS standards. Each test was repeated 10 times. Due to the repetition of results within the above-mentioned oil cleanliness classes, only 3 results are presented in Table 4. The only variable value during the oil cleanliness test was relative humidity.

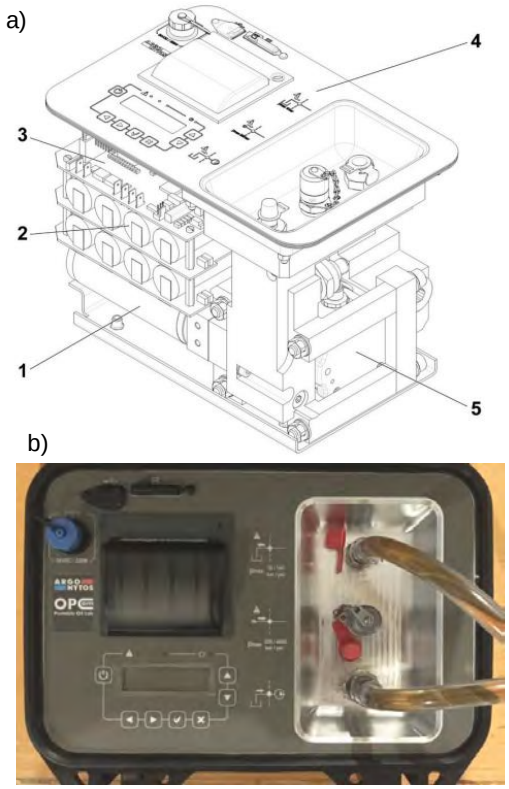

Fig. 8. a) General structure of the oil condition analyzer: 1 – engine with pump and electric gear, 2 – battery, 3 – control electronics, 4 – top side with control panel, 5 – particulate monitor, b) view of the portable oil condition analyzer OPComII Portable Oil Lab PPCO 300-1000 by Argo-Hytos

According to the work [2], relative humidity RH above 70% indicates that water contained in the oil is in a dissolved form. For oils, the permissible relative humidity of the oil is exceeded, and urgent microfiltration of the oil is recommended. The device for testing the oil condition in the generated test reports, already at relative humidity above 50% provides information about a high water level. Figure 9 presents the results of relative humidity tests for new oil (engine, gear, and hydraulic) with the average value and the spread of values from 10 measurements in the form of error bars. For tests related to the oil cleanliness class itself, subsequent repetitions do not result in significant changes. The cleanliness class in subsequent measurements is the same or changes by one class.

Table 4. Canister oil test results wg ISO, SAE and NAS

ISO 4 µm	ISO 6 µm	ISO 14 µm	SAE 4 µm	SAE 6 µm	SAE 14 µm	NAS	RH %
HV46 Hydraulic Oil							
23	21	17	12	12	11	12	52.8
23	21	17	12	12	11	12	52.7
23	21	17	12	12	11	12	52.7
ATV IID Transmission Oil							
22	19	14	12	11	8	11	37.8
22	19	14	12	11	8	11	37.2
22	19	14	12	11	8	11	36.9
20W-50 Engine Oil							
18	17	14	9	8	8	10	36.4
18	17	14	9	8	8	10	35.9
18	17	14	9	8	8	10	34.2

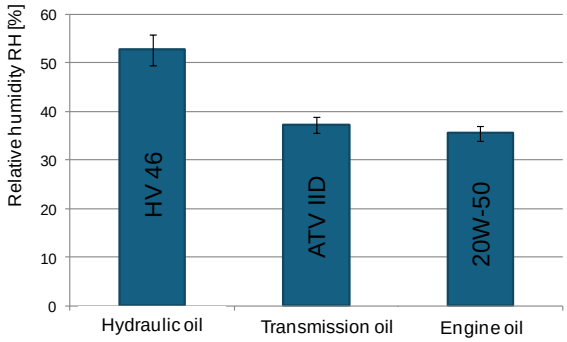

Fig. 9. Relative humidity (RH) test results of the analyzed oils before microfiltration

Based on Fig. 9, it was found that the new engine and transmission oil did not have a relative humidity above 50%, unlike the hydraulic oil. It was also found that the hydraulic oil had the largest dispersion of measurement results as a standard deviation from the mean value (3.17%), while in the case of engine and transmission oil, the standard deviation was 1.60% for 20W-50 oil and 1.62% for ATV IID oil.

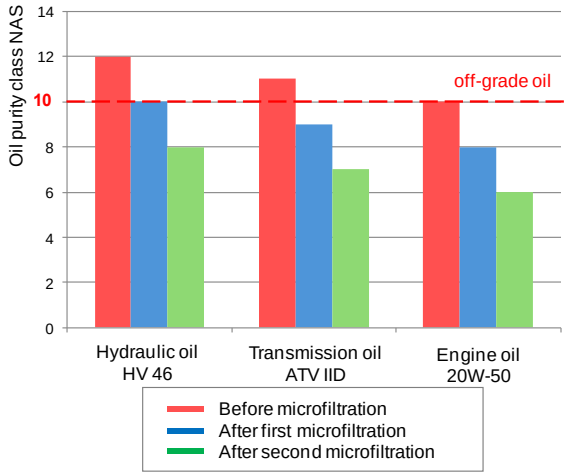

Fig. 10. Results of the NAS purity class test of the analyzed oils after two microfiltrations

After the oil was tested for cleanliness class and relative humidity, two microfiltrations lasting 6 hours were carried out. After each filtration, the cleanliness class and relative humidity were tested with the OPComII Portable Oil Lab PPCO 300-1000 oil analyzer. Figures 10 and 11 show the results of the oil tests (NAS and RH class) after two microfiltrations, the results were related to the first oil test after opening the canisters.

Analyzing the results of the tests presented in Fig. 10 and Fig. 11, it was found that after the first microfiltration lasting 6 hours, the cleanliness of the gear oil and engine oil was reduced by two NAS classes, which, according to Table 2, made the oil clean and suitable for use. In the case of hydraulic oil, the NAS class was reduced from 12 to 10 and required another microfiltration. The second microfiltration, which lasted 6 hours, allowed for a further reduction (by 2 classes) of oil cleanliness. In terms of relative humidity, each microfiltration on the portable Kleenoil MS2+MM5

device reduced the RH value with a standard error of 2.5% for hydraulic oil and about 1% for gear oil and engine oil.

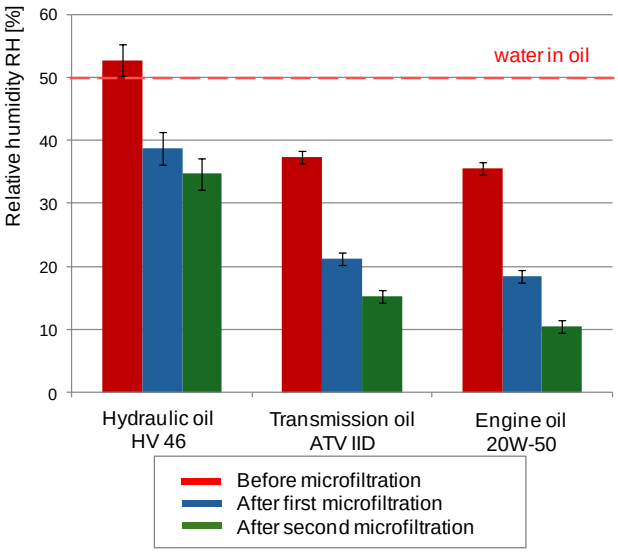

Fig. 11. The results of the relative humidity (RH) test of the analyzed oils after two microfiltrations

Analyzing the authors' research, they concluded that, in field conditions, oil microfiltration at portable stations should be conducted concurrently with oil testing for solid contaminants and water. Assessing the degree of filter contamination (filter elements) in the Kleenoil MS2+MM5 machine does not allow for classifying the oil into a given cleanliness class according to current standards. The authors believe that oil microfiltration should be conducted concurrently with oil testing.

5. Conclusions

The main advantage of using membranes in separation processes is simple operation. This is a technology that generates little waste and is more environmentally friendly compared to other separation methods. It is also economically viable due to the lower amount of energy used. The conducted literature study in the field of microfiltration and the authors' research allow for the formulation of the following conclusions:

a) The use of portable hydraulic oil condition analyzers allows for ongoing diagnostics of hydraulic oil in all conditions, especially in the field where vehicles or work machines are used.
b) The use of portable oil microfiltration devices together with an oil condition analyzer allows for the oil cleaning process to be carried out to the required cleanliness class. The microfiltration time will depend on the current cleanliness class of the oil.
c) The new oil tested was out of class (12 NAS class for HV46 oil, 11 NAS class for ATV, and 10 class for 20W-50) and requires microfiltration before flooding the hydraulic system, transmission, or combustion engine, which was confirmed by the authors.
d) New oil from manufacturers may be off-grade due to long distribution and storage periods. The purity class may rise to the level of off-grade. It is recommended to test the purity class before pouring the oil.
e) One-time microfiltration of hydraulic oil lasting about 6 hours allows for the oil cleanliness to be reduced by two NAS classes.

Acknowledgements

The investigations were carried out within the Implementation Doctorate Program of the Ministry of Education and Science, realized in the years 2022-2026.

Nomenclature

ATF	automatic transmission fluid
cSt	centistokes
EC	electrocoagulation
GOST	Gosudarstwiennyj Standard
HV	high viscosity
ISO	International Organization for Standarization
MD	membrane distillation
MF	microfiltration
NAS	National Aerospace Standard
UF	ultrafiltration
RH	Relative Humidity
SAE AS	Society of Automotive Engineers Aerospace

Bibliography

[1] Abdel-Shafy HI, Mansour MSM, El-Toony MM. Integrated treatment for oil free petroleum produced water using novel resin composite followed by microfiltration. Sep Purif Technol. 2020;234:116058. https://doi.org/10.1016/j.seppur.2019.116058
[2] ArgoHytos Fluid Management and Oil Monitoring. Technical Guide. The Way to Clean Oil. https://www.argohytos.com/fileadmin/user_upload/downloads/Polish/Technical_Handbook_PL.pdf (accessed on 08.06. 2025)
[3] Arunagiri V, Prasannan A, Udomsin J, Lai J, Wang C, Hong P et al. Facile fabrication of eco-friendly polycaprolactone (PCL)/Poly-D, L-Lactic acid (PDLLA) modified melamine sorbent for oil-spill cleaning and water/oil (W/O) emulsion separation. Sep Purif Technol. 2021;259:118081. https://doi.org/10.1016/j.seppur.2020.118081
[4] Chang Q, Zhou J, Wang Y, Liang J, Zhang X, Cerneaux S et al. Application of ceramic microfiltration membrane modified by nano-TiO_2 coating in separation of a stable oil-in-water emulsion. J Membrane Sci. 2014;456:128-133. https://doi.org/10.1016/j.memsci.2014.01.029
[5] Daneluz J, Ferreira da Silva G, Duarte J, Turossi TC, Santos V, Baldasso C et al. Characterization of microfiltration and ultrafiltration membranes for application in kombucha filtration. J Ind Eng Chem. 2023;126:264-269. https://doi.org/10.1016/j.jiec.2023.06.015
[6] Filipponi A, Masi G, Matos M, Benito JM, Gutiérrez G, Bignozzi MC. Development of metakaolin-based geopolymeric asymmetric membrane for oil-in-water emulsion microfiltration. Ceram Int. 2024;50:21107-21117. https://doi.org/10.1016/j.ceramint.2024.03.220

[7] Gao Y, Xu G, Zhao P, Liu L, Zhang E. One step co-sintering synthesis of gradient ceramic microfiltration membrane with mullite/alumina whisker bi-layer for high permeability oil-in-water emulsion treatment. Sep Purif Technol. 2023;305: 122400. https://doi.org/10.1016/j.seppur.2022.122400

[8] Garcia Lesak GV, Xavier LA, Valadares de Oliveira T, Fontana F, Santos AF, Cardoso VL et al. Enhancement of pozzolanic clay ceramic membrane properties by niobium pentoxide and titanium dioxide addition: Characterization and application in oil-in-water emulsion microfiltration. J Petrol Sci Eng. 2022;217:110892. https://doi.org/10.1016/j.petrol.2022.110892

[9] Jebur M, Chiao YH, Kupaaikekaiao T, Patra T, Cao Y, Lee K et al. Combined electrocoagulation-microfiltration-membrane distillation for treatment of hydraulic fracturing produced water. Desalination. 2021;500:114886. https://doi.org/10.1016/j.desal.2020.114886

[10] Kaźmierczak E. Testing the oil flow parameters of CLAAS ARION 610 tractor pump. Rail Vehicles. 2020;2:48-54. https://doi.org/10.53502/RAIL-138551

[11] Kim DY, Lee J, Park H, Park SJ, Lee JH. Ecofriendly hydrophilic modification of microfiltration membranes using pyrogallol/ε-polylysine. Sep Purif Technol. 2024;350:127988. https://doi.org/10.1016/j.seppur.2024.127988

[12] Kołodziejski S, Bartkowiak A, Sawczuk W. The concept of microfiltration of hydraulic oil in rail vehicles. Rail Vehicles. 2024;1-2:3-10. https://doi.org/10.53502/RAIL-192525

[13] Kozak M, Siejka P. Soot contamination of engine oil – the case of a small turbocharged spark-ignition engine. Combustion Engines. 2020;182(3):3-9. https://doi.org/10.19206/CE-2020-305

[14] Kücük S, Hejase CA, Kolesnyk IS, Chew JW, Tarabara VV. Microfiltration of saline crude oil emulsions: Effects of dispersant and salinity. J Hazard Mater. 2021;412:124747. https://doi.org/10.1016/j.jhazmat.2020.124747

[15] Li H, Zhang B, Hong X, Wu Y, Wang T. Optimizing the microstructure and properties of microfiltration carbon membranes enabled with PAN fibers for emulsified oil removal from wastewater. Chem Eng Res Des. 2022;84:566-576. https://doi.org/10.1016/j.cherd.2022.06.035

[16] Liu S, Rouquié C, Frappart M, Szymczyk A, Rabiller-Baudry M, Couallier E. Separation of lipids and proteins from clarified microalgae lysate: The effect of lipid-protein interaction on the cross-flow and shear-enhanced microfiltration performances. Sep Purif Technol. 2024;328:124985. https://doi.org/10.1016/j.seppur.2023.124985

[17] Nandi BK, Uppaluri R, Purkait MK. Microfiltration of stable oil-in-water emulsions using kaolinbased ceramic membrane and evaluation of fouling mechanism. Desalin Water Treat. 2010;1-3(22):133-145. https://doi.org/10.5004/dwt.2010.1658

[18] Poli A, Dagher G, Santos AF, Baldoni-Andrey P, Jacob M, Batiot-Dupeyrat C et al. Impact of C-CVD synthesis conditions on the hydraulic and electronic properties of SiC/CNTs nanocomposite microfiltration membranes. Diam Relat Mater. 2021;120:108611. https://doi.org/10.1016/j.diamond.2021.108611

[19] Purnima M, Paul T, Pakshirajan K, Pugazhenthi G. Onshore oilfield produced water treatment by hybrid microfiltration-biological process using kaolin based ceramic membrane and oleaginous Rhodococcus opacus. Chem Eng J. 2023;453(2): 139850. https://doi.org/10.1016/j.cej.2022.139850

[20] Rouquié C, Szymczyk A, Rabiller-Baudry M, Roberge H, Abellan P, Riaublanc A et al. NaCl precleaning of microfiltration membranes fouled with oil-in-water emulsions: Impact on fouling dislodgment. Sep Purif Technol. 2022;285: 120353. https://doi.org/10.1016/j.seppur.2021.120353

[21] Suresh K, Pugazhenthi G, Uppaluri R. Fly ash based ceramic microfiltration membranes for oil-water emulsion treatment: Parametric optimization using response surface methodology. Journal of Water Process Engineering. 2016;13:27-43. https://doi.org/10.1016/j.jwpe.2016.07.008

[22] Szymlet N, Rymaniak Ł, Kurc B. Chromatographic analysis of the chemical composition of exhaust gas samples from urban two-wheeled vehicles. Energies. 2024;17(3):709-1–709-17. https://doi.org/10.3390/en17030709

[23] Tummons EN, Tarabara VV, Chew JW, Fane AG. Behavior of oil droplets at the membrane surface during crossflow microfiltration of oil–water emulsions. J Membrane Sci. 2016;500:211-224. https://doi.org/10.1016/j.memsci.2015.11.005

[24] Wang Z. Chapter 3 – Microfiltration. Fundamentals of Membrane Separation Technology. 2014:55-124. https://doi.org/10.1016/B978-0-443-13904-8.00012-X

[25] Wu J, Meeten GH, Jones TGJ, Cagney N, Boek ES. Membrane fouling during the harvesting of microalgae using static microfiltration. Sep Purif Technol. 2025;353: 127737. https://doi.org/10.1016/j.seppur.2024.127737

[26] Xaviera LA, Garcia Lesaka GV, Valadares de Oliveira T, Eiras D, Pedersen Voll FA, Vieira RB. Ceramic membrane applied to seawater pre-treatment: effect of flocculation and temperature on microfiltration. Desalin Water Treat. 2023; 310:43-49. https://doi.org/10.5004/dwt.2023.29929

[27] Yao Y, Zhang B, Jiang M, Hong X, Wu, T. Wang Y et al. Ultra-selective microfiltration SiO_2/carbon membranes for emulsified oil-water separation. Journal of Environmental Chemical Engineering. 2022;10:107848. https://doi.org/10.1016/j.jece.2022.107848

[28] Zacharewicz M, Bogdanowicz A, Socik P. Capacitance-based assessment of water content in fuels and lubricating oils for marine engines. Combustion Engines. 2025;202(3): 81-87. https://doi.org/10.19206/CE-204692

Prof. Wojciech Sawczuk, DSc., DEng. – Faculty of Civil and Transport Engineering, Poznan University of Technology, Poland.
e-mail: *wojciech.sawczuk@put.poznan.pl*

Agnieszka Bartkowiak, MSc, MA – Faculty of Engineering Management, Doctoral School of Poznan University of Technology, Poznan, Poland.
e-mail: *agnieszka.bartkowiak@doctorate.put.poznan.pl*

Sławomir Kołodziejski, MEng. – Faculty of Civil and Transport Engineering, Doctoral School of Poznan University of Technology, Poland.
e-mail: *slawomir.kolodziejski@doctorate.put.poznan.pl*

Łukasz Kubacki, MEng. – Technical advisor, Sales and Marketing Manager in technical companies, Poznan, Poland.
e-mail: *l.kubacki18@gmail.com*

Article citation info:
Kawakami T, Liu J. Enhancing combustion characteristics in a constant volume chamber using a novel multi-injection system for liquid fuel and propane-air stratified mixtures. Combustion Engines. 2026;204(1):27-34. https://doi.org/10.19206/CE-208773

Tadashige KAWAKAMI
Jinru LIU

Combustion Engines
Polish Scientific Society of Combustion Engines

Enhancing combustion characteristics in a constant volume chamber using a novel multi-injection system for liquid fuel and propane-air stratified mixtures

ARTICLE INFO

Received: 9 June 2025
Revised: 14 July 2025
Accepted: 29 July 2025
Available online: 29 October 2025

This study proposes a novel multi-injection strategy to enhance fuel atomization and combustion in a constant volume combustion chamber. By integrating a third injector into the conventional axis-opposed spray configuration and optimizing injection timing, the strategy significantly improves fuel–air mixing and ignition reliability, particularly under cold-start conditions. Two fuels with contrasting reactivity – n-hexadecane and iso-octane – were used to investigate spray and combustion characteristics. Laser diffraction analysis showed that the proposed strategy substantially reduced the Sauter Mean Diameter compared to single or impinging injection alone. Combustion experiments demonstrated improved ignition stability, advanced heat release phasing, and increased total heat release with the multi-injection approach. These effects were more pronounced for iso-octane, where ignition failure was frequent under baseline conditions. The results confirm that the proposed multi-injection strategy effectively stabilizes combustion and enhances thermal efficiency for both high- and low-reactivity fuels.

Key words: *multi-injection, axis-opposed spray, fuel atomization, low-reactivity fuel, combustion efficiency*

1. Introduction

Direct injection (DI) systems have been widely adopted in diesel engines to promote homogeneous fuel-air mixture formation and achieve higher thermal efficiency, particularly under high compression ratio conditions. In contrast, port fuel injection (PFI) remains a common strategy in gasoline engines due to its stability and low cost. Given that internal combustion engines contribute significantly to greenhouse gas (GHG) emissions [23], increasingly stringent emission regulations have prompted the automotive industry to develop more advanced engine technologies. In response to strict emission standards issued by the U.S. Environmental Protection Agency (EPA) and the National Highway Traffic Safety Administration (NHTSA) [5], manufacturers have accelerated the adoption of gasoline direct injection (GDI) systems. GDI offers superior fuel and thermal efficiency compared to PFI, largely owing to its enhanced injection precision [4, 29]. Kalwar et al. [13] highlighted the advantages of GDI in terms of power output and efficiency, emphasizing the importance of a well-mixed fuel-air mixture for stable combustion under homogeneous conditions. In addition, GDI engines also tend to emit fewer unburned hydrocarbons and show less combustion variability, particularly under medium-to-high load operating conditions. However, GDI engines still face challenges, notably elevated particulate matter (PM) and particle number (PN) emissions. These challenges necessitate further optimization of fuel injection strategies and combustion control to comply with upcoming emission standards.

PM and PN emissions are significantly elevated under cold-start conditions, where low cylinder wall temperatures and incomplete fuel vaporization promote the formation of liquid fuel films on the piston or liner surfaces. This leads to increased unburned hydrocarbon (UHC) and soot emissions [12, 22, 24]. Studies show that GDI engines generally emit more PM and PN than PFI counterparts, primarily due to the higher elemental carbon content present in the exhaust [2, 7, 25, 27]. Among various pollutants, organic gas emissions have been found to be the most sensitive to cold-start conditions. Moreover, cold-start contributes a disproportionately large fraction of total emissions over the unified driving cycle, especially in vehicles certified to stricter emission standards [3]. To mitigate wall-film-related emissions, several strategies have been investigated. For example, Rostampour et al. [24] reported that, under cold start conditions, the fuel film formation in PFI engines can reach up to 55% of total injected fuel, severely impacting fuel distribution and emissions. To address these issues, they adopted the advanced port fuel injection (APFI), and the maximum amount of fuel film formed on the walls is reduced by about 75%. Zhang et al. [28] proposed a dual-injection strategy combining GDI and PFI, which effectively reduced soot emissions at a 65:35 GDI/PFI ratio. In GDI engines, high-pressure injection, multi-pulse strategies, and split injection have been applied to enhance fuel atomization and minimize spray-wall impingement [14, 17, 26]. Lonari et al. [21] demonstrated that three-pulse injection at 35 MPa significantly reduced HC and NO_x emissions by up to 80% during cold-start catalyst light-off compared to conventional two-pulse injection at 25 MPa. Han et al. [11] experimentally investigated multiple injection strategies in a boosted single-cylinder DISI engine and found that increasing injection events significantly reduced PN emissions and knock intensity, while improving thermal efficiency and maintaining combustion stability. They further reported that multiple injections increased knock limits while maintaining torque and combustion stability, and reduced NO_x and UHC emissions by approximately 25%. A similar trend was reported by Guo et al. [10], proposed a novel direct-start strategy using multistage and split injection and experimentally demonstrated that three-stage injection and optimized split timing significantly improve com-

bustion phasing and reduce UHC emissions under cold-start conditions. In addition, Fellner et al. [6] developed an algorithm-based calibration method for multiple injection pattern design in DISI engines, showing that optimized split strategies can prevent wall impingement and reduce particle formation while adapting to varying combustion conditions. Beyond injection strategies, further optimization has been explored by delay intake valve opening timing to enhance fuel atomization, thus achieve a 50–90% reduction in PN emissions [18], utilizing dual-fuel dual-direction injection strategy that successfully suppressed knock, improved thermal efficiency and expanded engine load [15], or employing dual spark plugs with multi-injection strategy to improve combustion stability and reduce CO emission [1], all of which have shown to improve combustion stability and reduce emissions.

Similar challenges are observed in GDI engines, diesel engines also suffer from comparable issues under certain operating conditions [8, 17, 22]. Kang et al. [16] evaluated multi-stage split injection with five injection events in a light-duty diesel engine and found that this strategy reduced fuel consumption and PM emissions by improving heat release smoothness, reducing flame penetration, and enhancing fuel-air utilization.

However, despite these advancements, the control of spray impingement and liquid fuel deposition remains a major challenge, especially under transient or low-temperature conditions. Recent studies also suggest that preheating or injection strategy adaptation can help mitigate these challenges [9]. Among various factors, fuel atomization plays a pivotal role in suppressing wall wetting and ensuring homogeneous mixture formation, which are essential for reducing PM and PN emissions. The core solution lies in enhancing fuel atomization quality, shortening the overall injection duration, and minimizing fuel impingement on the combustion chamber walls. To address these issues, our previous work proposed an impinging injection strategy, in which two injectors were installed axisymmetrically, directing sprays toward each other to induce droplet breakup through spray impingement interaction. The feasibility of this concept was demonstrated in earlier studies [19, 20], where improvements in atomization and combustion characteristics were observed. For fuels with varying viscosities, the Sauter mean diameter (SMD) of impinging injection was consistently reduced compared to conventional one-sided injection, indicating enhanced atomization performance. However, under low injection pressure conditions, the persistence of coherent liquid jets was observed in the impingement zone, leading to non-uniform droplet distribution and compromised fuel-air mixture homogeneity, ultimately hindering thermal efficiency. To overcome these limitations, the present study introduces a novel multi-injection strategy that integrates axis-opposed impinging injection with a one-sided injection. By employing three injectors and optimizing injection timing, this configuration aims to shorten the total injection duration and reduce the local SMD near the ignition zone, thereby enhancing mixture uniformity and promoting stable combustion under cold-start and low-load conditions.

In this study, a constant volume combustion chamber was employed to investigate the feasibility of a multi-injection strategy. The results showed that the proposed multi-injection strategy significantly improved atomization by reducing the Sauter Mean Diameter (SMD) compared to one-sided and conventional impinging injection. For fuel with low reactivity, the multi-injection strategy substantially enhanced ignition stability and improved combustion characteristics, particularly under pre-injection conditions. These improvements demonstrate that an appropriately timed pre-injection can promote ignition stability, faster flame propagation, and higher thermal efficiency, making it a promising strategy to improve combustion stability under cold-start and low-load conditions.

The work proceeds by introducing the experimental setup and test conditions, followed by an analysis of spray atomization and combustion characteristics using two representative fuels: n-hexadecane and iso-octane, which differ in ignition reactivity. Key combustion metrics such as maximum burning pressure, total burning time, and heat release rate are discussed. The study concludes with a summary of findings and their implications for improving engine performance under cold-start and low-load conditions.

2. Experiment apparatus and conditions

2.1. Experiment apparatus

Figure 1 shows the schematic diagram of the experimental apparatus, including a constant volume combustion

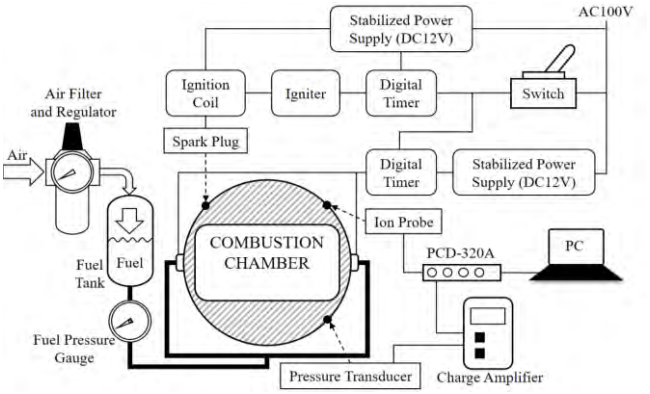

Fig. 1. Experiment apparatus

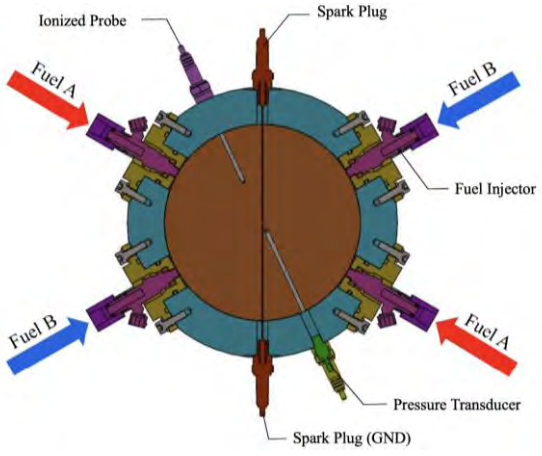

Fig. 2. Details of a constant volume combustion chamber

chamber, a propane-air mixture tank, a data sampling control system, a fuel injection system, and an ignition system. Details of the combustion chamber (volume 5600 cc, diameter 160 mm) are shown in Fig. 2. Two pairs of injectors (EAT321, 150 μm, 8 holes) were opposite and coaxially set on the chamber wall. The injection pressure was supplied by compressed air. The combustion pressure was recorded by a piezo-electric sensor (KISTLER 6041A, charge amplifier 5011B). The laser diffraction spray analyzer (LDSA-SPR1500, Microtract) and the analysis software Aerotrac ver.15 were used to observe droplet size distributions of different blend fuel types.

2.2. Experiment conditions

In this study, experiments were conducted at room temperature and atmospheric pressure. The injection pressure was 0.5 MPa. To investigate the influence of fuel properties on spray behavior and combustion, two pure fuels were used: n-hexadecane and iso-octane. These fuels differ significantly in physical properties, particularly viscosity, which directly affects the SMD of the spray. Table 1 lists the basic fuel properties. As shown in Table 1, n-hexadecane exhibits higher viscosity than iso-octane, resulting in larger SMD values.

Table 1. Fuel properties

Fuel type	n-hexadecane	iso-octane
Chemical formula	$C_{16}H_{24}$	C_8H_{16}
Density [g/ml]	0.774	0.68
Boiling point [K]	560	372
Viscosity [cP]	3.454	0.502
Cetane number	100	10
Octane number	–20	100
Low heat value [kJ/mol]	9953.3	5065.5
Vapor pressure	133.3 Pa (105°C)	5.1 kPa (20°C)

Spray characterization was performed using an LDSA. The system operated in trigger mode with a sampling window of 30 ms, and an SMD measurement range of 5–300 μm. To evaluate the atomization effect induced by spray impingement interaction, we compared the SMD of a one-sided injection, an impinging injection, and a multi-injection. Tests were carried out for both fuels under various injection durations.

For the combustion characteristics experiments, all test conditions were set to maintain the same overall equivalence ratio, Φ = 0.95. To minimize the influence of injection duration on combustion results, the same injection duration was applied for both fuel types under all operating conditions. Since n-hexadecane and iso-octane have different densities and low heat values, the equivalence ratio of the propane-air mixture was adjusted accordingly to ensure a consistent overall equivalence ratio. Figure 3 illustrates the procedure for calculating the equivalence ratio of the propane-air mixture and the corresponding fuel quantity. Table 2 lists the specific equivalence ratios of the propane-air mixture used for the two fuels under multi-injection conditions.

To investigate the effect of injection timing, two types of injection conditions were defined: pre-injection and post-injection. In the pre-injection case, spark ignition was initiated after the spray tail had reached the central region of the chamber. In the post-injection case, ignition occurred before the start of fuel injection.

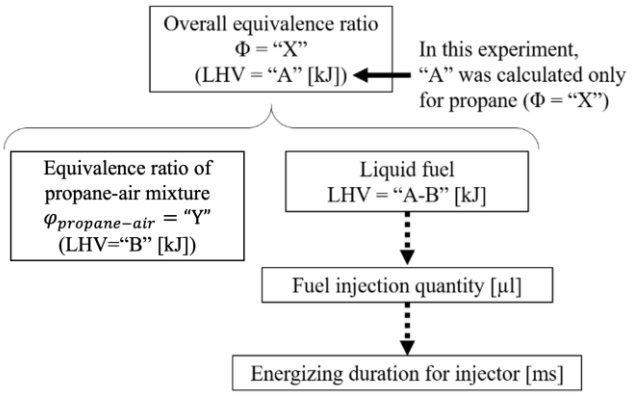

Fig. 3. Flow of calculating the equivalence ratio of propane and the liquid fuel injection quantity

Table 2. Equivalence ratio of propane-air mixture for multi-injection

Overall equivalence ratio Φ = 0.95		
Fuel type	$C_{16}H_{24}$	C_8H_{18}
Equivalence ratio of propane-air mixture	0.876	0.883

In our previous studies, a multi-impinging injection involving two injection stages was proposed. In contrast, the present study introduces a simplified multi-injection strategy with a single injection stage. Unlike conventional impinging injection or multi-impinging injection, which utilizes two axis-opposed injectors (injector BL and BR shown in Fig. 2) aimed toward each other, the multi-injection integrates a third centrally located injector (injector AR shown in Fig. 2), forming a three-spray system. This layout enables enhanced spray impingement interaction and mixture formation near the ignition zone, while simplifying the injection schedule.

This multi-injection aims to reduce SMD around the spark region, shorten the injection duration, and improve the spatial uniformity of the fuel-air mixture, thereby enhancing ignition reliability and combustion stability. For each experimental condition, ten repeated tests were conducted. The average values of combustion characteristics were calculated after excluding the maximum and minimum data points to reduce variability. In-cylinder pressure was recorded using a piezoelectric pressure sensor, and the heat release rate was calculated according to Equation (1).

$$\frac{dQ}{dt} = \frac{1}{\kappa - 1}\left(V \cdot \frac{dP}{dt}\right) \tag{1}$$

where: P = pressure of combustion chamber [Pa], t = time from ignition [s], V = combustion chamber volume [m^3], κ = 1.34 (specific heat ratio: constant value).

3. Results and discussions

3.1. Spray characteristics

As discussed in the introduction, the quality of fuel atomization has a significant effect on mixture preparation and combustion performance, particularly under cold-start or low-load conditions. In this study, the spray characteristics of different injection strategies were evaluated: one-

sided injection, in which only a single injector (BR) was activated; impinging injection, where two axis-opposed injectors (BL, BR) were simultaneously operated; and multi-injection, in which three injectors (AR, BL, and BR) were simultaneously operated. The test fuels were n-hexadecane and iso-octane. The injection durations were set to 8 ms for the multi-injection and 10 ms for the conventional impinging injection. Although the overall fuel quantity and equivalence ratio were kept constant, the multi-injection configuration utilized three injectors operating simultaneously, allowing the required fuel to be delivered within a shorter duration compared to the conventional impinging injection setup. To investigate the effect of injection duration for each injection strategy, the conventional impinging injection was also tested with an 8 ms injection duration. From Table 1, n-hexadecane has high viscosity and low volatility, which generally results in larger droplet size. In contrast, iso-octane, with lower viscosity and higher vapor pressure, tends to facilitate finer atomization. The objective was to clarify how injection strategy and fuel properties affect the temporal evolution of droplet size.

Figure 4 and Fig. 5 show the temporal variation of SMD for n-hexadecane and iso-octane, respectively, under different injection conditions. Across both fuels, the impinging injection and multi-injection consistently resulted in significantly reduced SMD values than the one-sided injection under the same injection duration condition. Specifically, the SMD of n-hexadecane decreased by 33.3%, while iso-octane exhibited a higher SMD reduction of up to 70.0%. This reduction indicates that spray impingement interaction promotes enhanced atomization by inducing secondary breakup.

As shown in Fig. 4 and Fig. 5, n-hexadecane exhibits minimal differences in SMD between the impinging injection and multi-injection strategies under an 8 ms injection duration. However, when the injection duration is extended to 10 ms, the rate of SMD reduction decreases, indicating a saturation effect in fuel atomization improvement. Since the fuel mass was kept constant for all combustion experiments, the multi-injection achieves comparable atomization within a shorter injection duration. The time-saving effect is particularly advantageous under practical engine conditions where injection timing is limited. Therefore, the superiority of multi-injection lies in its ability to enhance fuel atomization efficiency while minimizing injection duration.

For iso-octane, its lower viscosity leads to overall reduced SMD values compared to n-hexadecane. However, even for this low-viscosity fuel, the impinging injection showed limited sensitivity to injection duration, as indicated by the minimal difference in SMD between the 8 ms and 10 ms injection duration conditions.

Compared to conventional impinging injection, the multi-injection strategy achieved a 37.5% reduction in SMD within the first 3 ms, highlighting its effectiveness in promoting atomization during the initial phase. The minimum SMD observed reached the 10 µm range, indicating highly effective atomization under this condition. This suggests that multi-injection is effective not only for high-viscosity fuels but also enhances atomization efficiency in favorable conditions, by accelerating droplet breakup and shortening the spray injection duration.

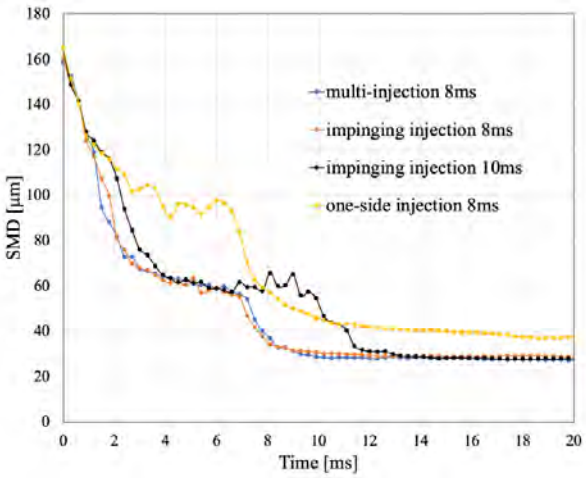

Fig. 4. SMD of n-hexadecane under different injection strategies

The enhanced atomization achieved by the newly proposed multi-injection method is expected to promote more homogeneous fuel-air mixture formation and enhance combustion stability, especially under challenging ignition conditions. The impact of this improved spray behavior on combustion characteristics is discussed in the following sections.

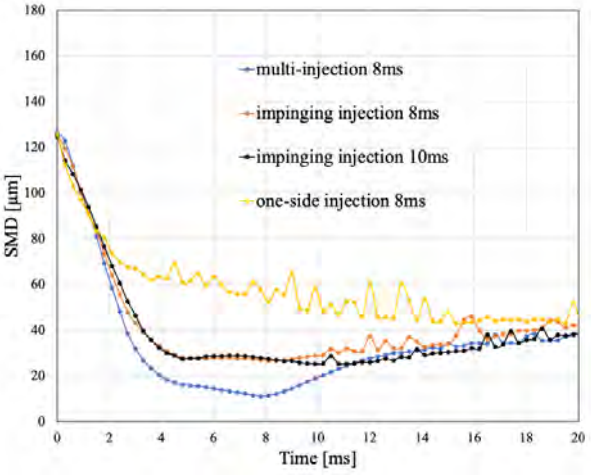

Fig. 5. SMD of iso-octane under different injection strategies

3.2. Combustion characteristics of n-hexadecane

Figure 6 presents the comparison of maximum burning pressure (MBP) and total burning time (TBT) for n-hexadecane under various injection strategies. The propane–air case ($\Phi = 0.95$) involved no liquid fuel injection and served as the baseline reference. It has the highest MBP (0.655 MPa) owing to less latent heat loss, but TBT is longer due to slow flame propagation speed.

In our previous study, the post30 injection timing with conventional impinging injection yielded the highest MBP, among the impinging injection cases, reaching 0.595 MPa. However, with the new multi-injection strategy, which featured a shorter injection duration, the same injection timing was no longer effective. In fact, the MBP of multi-

injection with post30 injection timing is 0.577 MPa, representing a 3.0% decrease compared to conventional impinging injection with post30 injection timing. As the injection timing was advanced from post30 to post10, MBP increased to 0.601 MPa, showing an increase of 4.2% over the multi-post30 case. Notably, although pre-injection conditions were previously unsuitable for n-hexadecane with conventional impinging injection, the current results show that pre-injection is compatible with the newly proposed multi-injection strategy. The MBP reached 0.613 MPa at the multi-pre10 condition, marking a 3.0% increase relative to imp-post30.

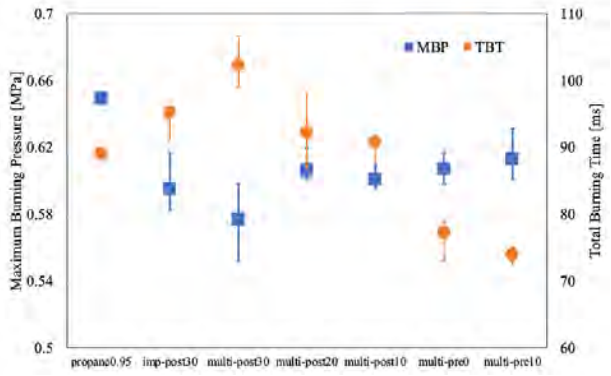

Fig. 6. Maximum burning pressure (MBP) and total burning time (TBT) under different injection strategies for n-hexadecane

Regarding combustion duration, the TBT of imp-post30 was 95.2 ms. TBT was gradually shortened as the injection timing advanced from post30 to post10. Under pre-injection conditions, TBT decreased to 74 ms at the multi-pre10 condition, which corresponds to a 22.3% reduction compared to imp-post30. Notably, multi-injection strategies with pre-injection showed reduced variability, as indicated by narrow error bars, suggesting improved combustion stability. These findings indicate that optimal injection timing is strongly dependent on the injection configurations. Multi-injection combined with pre-injection conditions enables faster flame propagation and shorter combustion durations.

Figure 7 illustrates the heat release rate (HRR) of n-hexadecane under various injection strategies. The graphs are divided into post-injection (Fig. 7a) and pre-injection (Fig. 7b) to highlight the effects of injection timing and configuration on combustion behavior.

In the post-injection conditions shown in Fig. 7a, the impinging injection post30 condition exhibits a relatively delayed and broadened HRR curve compared to the propane-air case, and it has an evident second stage combustion at the end of combustion, which indicates the heterogeneity of the fuel-air mixture. The introduction of the third injector in the multi-injection significantly altered the combustion characteristics. As the injection timing is advanced from 30 ms to 10 ms after ignition (multi-post30 → post20 → post10), the onset of heat release gradually shifts forward and the peak intensity becomes higher and more concentrated. Specifically, the maximum HRR increased from 112.9 J/ms at multi-post30 to 135.9 J/ms at multi-post10, corresponding to an increase of 20.4%. Compared to the impinging injection (112.2 J/ms), this represents an 18.9% maximum HRR increment. These results suggest that multi-injection promotes improved atomization and mixture formation near the spark location, thereby enhancing ignition quality and accelerating the flame propagation process.

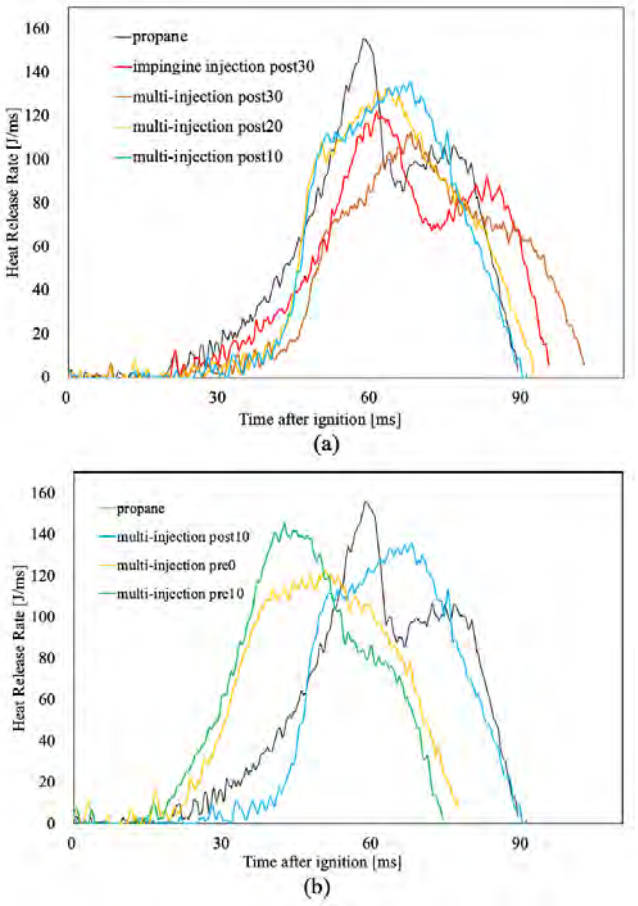

Fig. 7. Heat release rate (HRR) of n-hexadecane under different injection strategies: a) post-injection strategies (impinging and multi-injection); b) pre-injection strategies (multi-injection)

In the pre-injection conditions (Fig. 7b), this trend is even more pronounced. Both multi-pre0 and multi-pre10 demonstrate significantly earlier HRR initiation compared to post10 and propane cases. The combustion phase becomes more compact and the HRR curve steeper, indicating faster flame propagation speed and reduced ignition delay. In particular, the multi-pre10 condition achieved a maximum HRR of 145.3 J/ms, which is 28.7% higher than multi-post30 and 18.9% higher than impinging injection. These findings suggest that sufficient premixing prior to ignition plays a critical role in enhancing combustion phasing and thermal efficiency.

The mass fraction burned (MFB) is a key indicator used to characterize the combustion progress by quantifying the fraction of the total fuel mass that has been burned at a given time. Among its milestones, the time to reach 1% MFB (often termed MFB 1%) is commonly used as an approximation for ignition delay and combustion onset. A shorter MFB 1% value indicates faster ignition and finer mixture preparation near the spark plug.

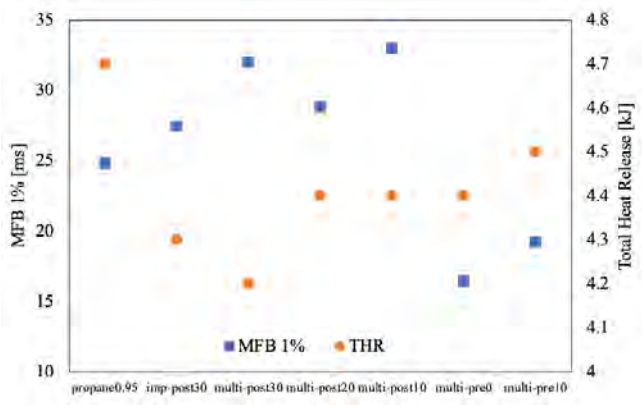

Fig. 8. Mass fraction burned duration (MFB 1%) and total heat release (THR) of n-hexadecane under various injection strategies

Figure 8 presents the combustion duration, represented by the time to reach 1% mass fraction burned (MFB 1%), and the total heat release (THR) for n-hexadecane under different injection strategies. MFB 1% duration increases significantly in the post-injection conditions. This indicates a slower combustion onset due to limited premixing time. In contrast, the pre-injection strategies result in the shortest MFB 1 value, suggesting accelerated early-stage combustion facilitated by improved mixture formation prior to spark timing. THR remains relatively stable across most conditions but shows a slight increase for the multi-pre10 case. This implies that early injection allows for more effective fuel utilization. Interestingly, even though MFB 1 is shorter for multi-pre cases, their THR does not drop, suggesting that faster initial combustion does not compromise total energy release.

Through these findings, while using n-hexadecane, the combination of pre-injection and multi-injection demonstrates a synergistic effect: it promotes more rapid and stable combustion. These findings confirm the superiority of the proposed multi-injection strategy over conventional impinging injection. The addition of a third spray source and optimized injection phasing significantly improves mixture preparation, resulting in faster combustion.

3.3. Combustion characteristics of iso-octane

Figure 9 shows the MBP and TBT of iso-octane under multi-injection with different injection timing conditions. Although iso-octane is inherently low reactivity, it still demonstrated strong combustion performance when appropriately injected. Among the tested conditions, the post10 condition resulted in the lowest MBP of 0.603 MPa, due to insufficient premixing. As the injection timing was progressively advanced into the pre-injection domain, both MBP and TBT showed substantial improvement. The multi-pre10 condition yielded the highest MBP of 0.674 MPa, representing an 11.8% increase compared to post10. Meanwhile, the TBT decreased from 89.9 ms (post10) to 73.6 ms (pre10) and further to 71.2 ms (pre20), corresponding to an 18.0% and 20.8% reduction, respectively.

Figure 10 presents the HRR of iso-octane under various injection conditions. Pre-injection strategies, particularly multi-pre10 and multi-pre20, demonstrate significantly earlier HRR onset and sharper peak shapes. The maximum HRR increased from 134.9 J/ms in the post10 case to 181.9 J/ms in pre10 and 168.7 J/ms in pre20, corresponding to an increase of 34.8 % and 25.1%, respectively. Additionally, the time to peak HRR advanced from 56.8 ms in post10 to 47.6 ms in pre10 and 42.8 ms in pre20, representing time reductions of 16.2% and 24.7%, respectively. These features reflect faster energy release and improved combustion phasing, enabled by better fuel-air mixture formation near the ignition site. The results highlight the critical role of pre-injection in promoting rapid and robust flame development under multi-injection strategies.

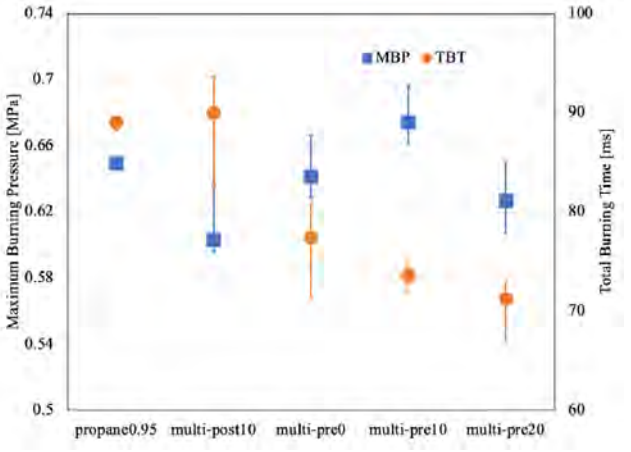

Fig. 9. Maximum burning pressure (MBP) and total burning time (TBT) of iso-octane under multi-injection with different injection timing conditions

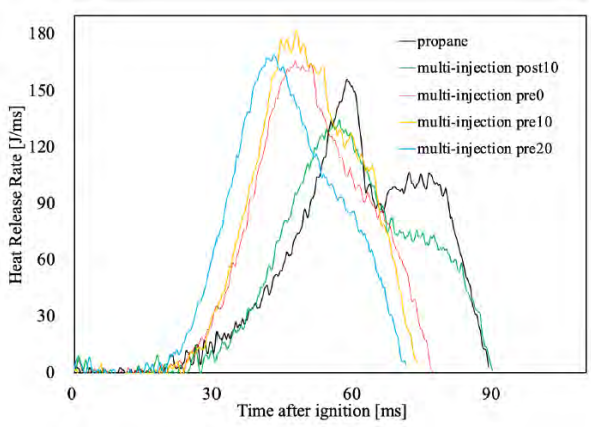

Fig. 10. Heat release rate (HRR) of iso-octane under multi-injection with different injection timing conditions

Figure 11 presents the MFB 1% duration and THR of iso-octane under various injection strategies. The shortest MFB 1% duration was observed under the multi-pre20 condition, indicating a more rapid combustion onset, which corresponds to previous results. Across all pre-injection strategies, THR values remained consistently above 4.5 kJ. Notably, the multi-pre10 case exhibited the highest THR of 4.9 kJ. The THR of the multi-pre10 condition slightly exceeds that of the propane baseline. While the total fuel-air equivalence ratio was maintained, this may be attributed to improved local fuel-air mixing near the ignition kernel, reduced wall heat loss, and more complete combustion under the multi-injection strategy.

These results highlight that the pre-injection strategy, when combined with multi-injection, is particularly effective for low-reactivity fuels. Compared to post-injection, it increased the maximum combustion pressure by up to 11.8% and reduced the total burning time by up to 20.8%, demonstrating substantial improvement in both combustion intensity and speed.

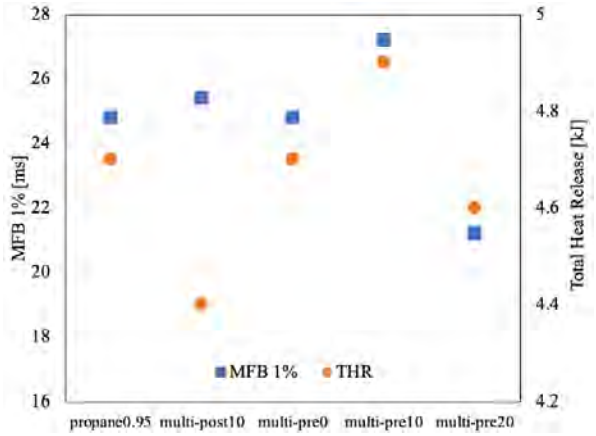

Fig. 11. Mass fraction burned duration (MFB 1%) and total heat release (THR) of iso-octane under multi-injection with different injection timing conditions

4. Conclusion

In this study, a novel multi-injection strategy was proposed and experimentally evaluated in a constant volume combustion chamber. By integrating a third, centrally located injector into a conventional impinging injection system, this approach aimed to enhance fuel atomization, improve mixture formation, and optimize combustion characteristics for fuels with varying reactivities. Two representative fuels, n-hexadecane and iso-octane, were selected to assess the effectiveness of the strategy under both high- and low-reactivity conditions. The key findings are summarized as follows:

1. Spray atomization was significantly improved with the multi-injection approach, leading to a 60.7% reduction in Sauter mean diameter (SMD) with low-viscosity fuel under identical total injection duration compared to the conventional impinging injection. In contrast, spray atomization of the high-viscosity fuel was barely affected by the multi-injection strategy. Nevertheless, when combined with optimal injection timing, a shortened total injection duration in multi-injection resulted in a shorter total burning time.
2. For high-reactivity fuel (n-hexadecane), compared to conventional impinging injection, the multi-injection strategy with pre-injection accelerated the start of combustion, as indicated by a 36% decrease in MFB 1% timing, and 18.9% increase in the maximum heat release rate. The total heat release was also increased by 4.7%, along with a 22.3% decrease in total burning time, suggesting that multi-injection with pre-injection conditions contributes to reducing the proportion of incomplete combustion and enhancing flame propagation.
3. For the low-reactivity fuel (iso-octane), the multi-injection strategy significantly improved combustion characteristics, particularly under the pre10 condition. Compared to the conventional propane case, multi-pre10 increased the maximum burning pressure by 3.9%, the maximum heat release rate by 16.8%, and the total heat release by 4.3%. In addition, the total burning time was shortened by 17.3%. These improvements suggest that pre-injection with multi-injection effectively promoted flame propagation and reduced heat losses, even for low-reactivity conditions.

Nomenclature

APFI	advanced port fuel injection
CO	carbon monoxide
DI	direct injection
DISI	direct injection spark ignition
EPA	Environmental Protection Agency
GDI	gasoline direct injection
GHG	greenhouse gas
HC	hydrocarbon
HRR	heat release rate
LDSA	laser diffraction spray analyzer
MBF	mass fraction burned
MBP	maximum burning pressure
NHTSA	National Highway Traffic Safety Administration
NOx	nitrogen oxides
PFI	port fuel injection
PM	particulate matter
PN	particle number
SMD	Sauter Mean Diameter
TBT	total burning time
THR	total heat release
UHC	unburned hydrocarbon

Bibliography

[1] Ahamad J, Kumar P, Dhar A. Influence of twin spark on performance and emissions of methanol fueled direct injection engine under multi-injection approach. J Energy Inst. 2025;120:102120. https://doi.org/10.1016/j.joei.2025.102120

[2] Bahreini R, Xue J, Johnson K, Durbin T, Quiros D, Hu S et al. Characterizing emissions and optical properties of particulate matter from PFI and GDI light-duty gasoline vehicles. J Aerosol Sci. 2015;90:144-153. https://doi.org/10.1016/j.jaerosci.2015.08.011

[3] Bielaczyc P, Szczotka A, Woodburn J. An overview of cold start emissions from direct injection spark-ignition and compression ignition engines of light duty vehicles at low ambient temperatures. Combustion Engines. 2013;154(3):96-103. https://doi.org/10.19206/CE-116992

[4] Davis SC, Williams SE, Boundy RG, Moore S. Vehicle Technologies Market Report [Internet]. Oak Ridge (TN): Oak Ridge National Laboratory; 2015 (accessed on 2017 Apr 20). http://cta.ornl.gov/vtmarketreport/pdf/2015_vtmarketreport_full_doc.pdf

[5] EPA; NHTSA. 2017 and later model year light-duty vehicle greenhouse gas emissions and corporate average fuel economy standards; final rule. Fed Regist. 2012 Oct 15. https://www.govinfo.gov/content/pkg/FR-2012-10-15/pdf/2012-21972.pdf

[6] Fellner F, Fitz P, Kraus C, Joerg C, Miyamoto A, Härtl M et al. Algorithm-calculated multiple injection patterns to meet future requirements to direct-injection spark ignited engines. SAE Technical Paper 2022-01-1068. 2022. https://doi.org/10.4271/2022-01-1068

[7] Fushimi A, Kondo Y, Kobayashi S, Fujitani Y, Saitoh K, Takami A et al. Chemical composition and source of fine and nanoparticles from recent direct injection gasoline passenger cars: effects of fuel and ambient temperature. Atmos Environ. 2016;124:77-84. https://doi.org/10.1016/j.atmosenv.2015.11.017

[8] Glassey S, Stockner A, Flinn M. HEUI – a new direction for diesel engine fuel systems. SAE Technical Paper 930270. 1993. https://doi.org/10.4271/930270

[9] Gęca MJ, Radica G. Effect of compression ignition engine preheating on its performance under cold start conditions. Combustion Engines. 2022;188(1):67-74. https://doi.org/10.19206/CE-142346

[10] Guo W, Xiao M, Zhang Z, Wang Y, Shi L, Deng K. Effects of multiple injections on the combustion and hydrocarbon emission characteristics of the start cylinder in direct-start process. Fuel. 2022;320:123851. https://doi.org/10.1016/j.fuel.2022.123851

[11] Han T, Singh R, Lavoie G, Wooldridge M, Boehman A. Multiple injection for improving knock, gaseous and particulate matter emissions in direct injection SI engines. Appl Energy. 2020;262:114578. https://doi.org/10.1016/j.apenergy.2020.114578

[12] Hashimoto J, Nouno Y. Numerical analysis on soot formation due to fuel deposits under a DI gasoline engine like condition. JSAE Rev. 2014;45(5):787-792. https://doi.org/10.11351/jsaeronbun.45.787

[13] Kalwar A, Agarwal AK. Overview, advancements and challenges in gasoline direct injection engine technology. In: Singh A, Sharma N, Agarwal R, Agarwal AK, editors. Advanced combustion techniques and engine technologies for the automotive sector. Springer. Singapore 2020. 97-115. https://doi.org/10.1007/978-981-15-0368-9_6

[14] Kaminaga T, Fujikawa T, Hara R, Youso T, Yamagawa M. Combustion technologies of high compression ratio engine using high pressure gasoline injection (first report): feasibility study of high pressure gasoline injection. Trans Jpn Soc Automot Eng. 2018;49(4):745-750. https://doi.org/10.11351/jsaeronbun.49.745

[15] Kang R, Zhou L, Hua J, Feng D, Wei H, Chen R. Experimental investigation on combustion characteristics in dual-fuel dual-injection engine. Energy Convers Manag. 2019; 181:15-25. https://doi.org/10.1016/j.enconman.2018.11.057

[16] Kang S, Lee S, Bae C. Effects of multi-stage split injection on efficiency and emissions of light-duty diesel engine. Energies. 2022;15(6):2219. https://doi.org/10.3390/en15062219

[17] Kato T, Tsujimura K, Shintani M, Minami T. Spray characteristics and combustion improvement of D.I. diesel engine with high pressure fuel injection. SAE Technical Paper 890265. 1989. https://doi.org/10.4271/890265

[18] Liu H, Liu Q, Wang C. A novel valve strategy for particulate matter reduction in a gasoline direct injection engine operated at cold conditions. Int J Engine Res. 2024;26(3): 325-338. https://doi.org/10.1177/14680874221149819

[19] Liu J, Kawakami T, Oiwa R, Suzuki T, et al. Effect of blend fuel properties on combustion improvement under heterogeneous combustion field by using multi-impinging injection system. SAE Technical Paper 2021-01-1194. 2021. https://doi.org/10.4271/2021-01-1194

[20] Liu J, Kawakami T, Oiwa R, Suzuki T, Aoki H. Experimental study of combustion improvement in heterogeneous combustion field by using new type multi-impinging injection system. SAE Technical Paper 2020-01-2105. 2020. https://doi.org/10.4271/2020-01-2105

[21] Lonari Y, Yoneya N, Miyake T, Namaizawa Y. Investigation of high fuel pressure and multiple injection to reduce engine emission during catalyst light-off. SAE Technical Paper 2023-01-0244. 2023. https://doi.org/10.4271/2023-01-0244

[22] Matsui Y, Sugihara K. Sources of hydrocarbon emissions from a small direct injection diesel engine. SAE Technical Paper 871613. 1987. https://doi.org/10.4271/871613

[23] May AA, Nguyen NT, Presto AA, Gordon TD, Lipsky EM, Karve M et al. Gas- and particle-phase primary emissions from in-use, on-road gasoline and diesel vehicles. Atmos Environ. 2014;88:247-260. https://doi.org/10.1016/j.atmosenv.2014.01.046

[24] Rostampour A, Shojaeefard MH, Molaeimanesh GR, Safaei-Arshi A. Effects of wall wetting and in-cylinder fuel distribution in an advanced turbo-charged engine. J Cent South Univ. 2022;29(7):2165-2178. https://doi.org/10.1007/s11771-022-5087-5

[25] Saliba G, Saleh R, Zhao Y, Presto AA, Lambe AT, Frodin B et al. Comparison of gasoline direct-injection (GDI) and port fuel injection (PFI) vehicle emissions: emission certification standards, cold-start, secondary organic aerosol formation potential, and potential climate impacts. Environ Sci Technol. 2017;51(11):6542-6552. https://doi.org/10.1021/acs.est.6b06509

[26] Sun Z, Cui M, Ye C, Yang S, Li X, Hung D et al. Split injection flash boiling spray for high efficiency and low emissions in a GDI engine under lean combustion condition. Proc Combust Inst. 2021;38(4):5769-5779. https://doi.org/10.1016/j.proci.2020.05.037

[27] Zhang S, McMahon W. Particulate emissions for LEV II light-duty gasoline direct injection vehicles. SAE Int J Fuels Lubr. 2012;5(2):637-646. https://doi.org/10.4271/2012-01-0442

[28] Zhang T, Yang Z, Zhao H, Li B, Qin J. Simulation study on the influence of fuel injection strategy on the soot emission of dual-injection engine. E3S Web Conf. 2022;356:03046. https://doi.org/10.1051/e3sconf/202236001023

[29] Zhao F, Lai MC, Harrington DL. Automotive spark-ignited direct-injection gasoline engines. Prog Energy Combust Sci. 1999;25(5):437-562. https://doi.org/10.1016/S0360-1285(99)00004-0

Prof. Kawakami Tadashige, DEng. – Faculty of Science and Engineering, Hosei University, Japan.
e-mail: *kawakami@hosei.ac.jp*

Liu Jinru, DEng. – Faculty of Science and Engineering, Hosei University, Japan.
e-mail: *jinru.liu.76@hosei.ac.jp*

Article citation info:
Kurzawska-Pietrowicz P, Szrama S, Jasiński R, Siedlecki M. Evaluation of jet engine performance parameters fueled with sustainable aviation fuel. Combustion Engines. 2026;204(1):35-42. https://doi.org/10.19206/CE-208774

Paula KURZAWSKA-PIETROWICZ
Slawomir SZRAMA
Remigiusz JASIŃSKI
Maciej SIEDLECKI

Combustion Engines
Polish Scientific Society of Combustion Engines

Evaluation of jet engine performance parameters fueled with sustainable aviation fuel

ARTICLE INFO

Received: 29 April 2025
Revised: 24 July 2025
Accepted: 29 July 2025
Available online: 15 September 2025

As sustainable aviation fuels are one of the mid and long term solutions for aviation emissions reduction, this article focuses on jet engine performance with different HEFA-SPK blends. Blends used in the tests were 30% and 50% of HEFA-SPK fuel, and also pure Jet A-1 as a conventional fuel. Experiments were carried out on a miniature jet engine, GTM 400, and the aim was to assess the impact of SAFs on operational parameters. Selected engine performance parameters were calculated and analyzed for the tested blends. One of the results is that the blend of HEFA-SPK led to an average improvement of thrust-specific fuel consumption by about 3%, and an increase of static thrust by 2.7–11.2%.

Key words: *GTM, miniature jet engine, SAF, HEFA, engine performance*

1. Introduction

The growing requirements of air transport have resulted in an increased need for jet fuel. Roughly 300 billion liters of jet fuel are produced annually on a global scale. The significant utilization of jet fuel results in considerable emissions of greenhouse gases, contributing to the aviation sector being accountable for 3% of the total current GHG emissions [8]. Many new technologies, initiatives, and solutions are being developed to reduce the impact of aviation on the environment, and the actions in the aviation sector can be divided into changes in the construction of aircraft and engines, to make the aircraft and engines more ecological, and to find alternative fuels that have better emission indexes than conventional aviation fuel. As sustainable aviation fuels (SAF) have been seriously developed since 2009, when the first production pathway of SAF was certified, sustainable aviation fuels are currently one of the most promising mid-term solutions to reduce greenhouse gases in the aviation sector [14]. Nowadays, more than 700 thousands of flights have been operated using SAF since 2011, and 69 airports are regularly supplied with SAF [1]. According to Fit for 55, the percentage of SAF used in air transport should be 6% by 2030, 20% by 2035, 34% by 2040, 42% by 2045 and 70% by 2050 [24].

Currently, there are 8 production pathways certified in the standard for sustainable fuels in aviation, ASTM D7566, and 3 co-processing pathways described in ASTM D1655 standard [13]. Most of this attention has been around streamlining the conversion pathways to produce a drop-in fuel, which is also achieving good emission results compared to conventional aviation fuel. Drop-in fuel is a term used to describe sustainable aviation fuels that are compatible with existing fuel infrastructure, aircraft engines, and fuel distribution networks [8]. It can be used in the aircraft engine as a blend with conventional aviation fuel in proportions specified by the standard ASTM D7566. The proportions in which SAF can be mixed with conventional fuel vary depending on the production process, from a maximum of 10% (e.g. HFS-SIP, HHC) to 50% (e.g. HEFA-SPK, ATJ-SPK). Mixing limits result from the physicochemical properties of individual fuels and their degree of mixing with conventional fuel, e.g. SIP fuel, with a blending limit of 10%, has a high viscosity value, which makes energy consumption and mass-based fuel consumption the highest among certified SAF fuels and can indicate inefficient energy conversion, often stemming from challenges associated with flow dynamics [15]. Some of the physicochemical properties of SAF fuels make them attractive for consideration as high-performance fuels, e.g. low aromatic content, high thermal stability, and high specific energy. Additionally, the energy efficiency of the engine can be affected by various other physicochemical properties of the fuel. First one is viscosity, which plays a significant role in influencing the heat transfer coefficients, which in turn dictate the amount of waste heat that is recovered by the fuel and reintroduced into the engine through the combustor, the other one is thermal stability of the fuel drives numerous overarching design choices concerning the thermal regulation of an engine and mainly depends of chemical composition and physical conditions of fuel. Another parameter that has an impact on the energy efficiency is the hydrogen-to-carbon ratio, which affects the composition of exhaust gases in the combustor, leading to a slight influence on the ratio of heat capacities and the temperature at the combustor exit. Energy density directly influences volumetric flow rates, which in turn affect heat transfer coefficients. Also, the specific heat directly affects the temperature increase in the fuel per unit of absorbed heat energy, potentially impacting the rate of coking [6]. Volatility impacts the fuel's vaporization and is one of the most desired fuel qualities for ignition [12]. According to Kroyan et al. [15], among certified sustainable aviation fuels, FT-SPK/A (Fischer-Tropsch Synthetic Paraffinic Kerosene with Aromatics) stands out with the highest carbon content, the highest volumetric lower heating value, and very high density. Studies show that the aromatic content in sustainable aviation fuels plays a crucial role, as it significantly influences both the fuel properties and the performance of jet

engines, and too low aromatic content may affect fuel leakage problems [12]. The fuel properties of FT-SPK/A closely resemble those of conventional aviation fuel Jet-A1, primarily due to its aromatic content, and the end-use performance of FT-SPK/A is also very similar to standard Jet A-1. The purely FT-SPK (Fischer-Tropsch Synthetic Paraffinic Kerosene), compared to other certified SAFs, features low density, the lowest carbon content, intermediate mass-based net calorific value, and the lowest volumetric net calorific value. According to studies [15] HEFA-SPK (Hydroprocessed Ester and Fatty Acids Synthetic Paraffinic Kerosene) and ATJ-SPK (Alcohol-to-Jet Synthetic Paraffinic Kerosene) also have low density, so the volumetric fuel consumption is higher, but both these fuels also have the lowest fuel consumption mass compared to other certified sustainable aviation fuels and conventional aviation fuel [15]. Studies made by Mazlan et al. [19] show that as the proportion of SAF fuel in the fuel mixture increases, the maximum engine thrust increases and fuel consumption decreases. The studies also show that the heat capacity has an influence on engine thrust increase and that the density of the fuel impacts the specific fuel consumption: an increase in density increases specific fuel consumption [19]. For pure CSPK (Camelina Bio-Synthetic Paraffinic Kerosene), the maximum thrust was slightly higher than for JSPK (Jatropha Bio-Synthetic Paraffinic Kerosene), although the lower heating value of JSPK is higher (44.3 MJ/kg) than that of CSPK (44.0 MJ/kg), which reveals that not only the lower heating value impacts the maximum thrust [19]. Table 1 presents selected physicochemical parameters of certified SAF fuels according to ASTM D7566 standard [25].

Table 1. Specified physicochemical parameters of selected certified production pathways of SAF [25]

	Jet A-1	FT-SPK	FT-SKA	HEFA-SPK	SIP	ATJ-SPK
Aromatics [vol %]	8–25	0.5	20/21.2	0.5	0.5	0.5
Cycloparaffins, mass [%]		15	15	15		15
Sulfur [mg/kg]	0.3	15	15	15	2	15
Final boiling point, [°C]	300	300	300	300	225	300
Distillation T90–T10 [°C]		22	22	22	5	21
Flash point [°C]	38	38	38	38	100	38
Freezing point [°C]	–40	–40	–40	–40	–60	–40
Density at 15°C [kg/dm^3]	775–840	730–770	755–800	730–770	765–780	730–770
Energy density [MJ/kg]	42.8	–	–	44.1	43.5	–
Antioxidants [mg/dm^3]	24	17–24	17–24	17–24	17–24	17–24

Sustainable aviation fuel tested in this research is HEFA-SPK (Hydroprocessed Esters and Fatty Acids Synthetic Paraffinic Kerosene). HEFA-SPK is a production pathway certified in 2011 and described in Annex 2 in ASTM D7566 standard [14]. The feedstock used in the production of HEFA-SPK is mostly used cooking oil, oily biomass like camelina or jatropha, municipal solid wastes, and other raw materials [18]. The range of raw materials used in the production of HEFA-SPK fuel is constantly expanded by producers to include more wastes and residues from different sectors of the economy.

The aim of this article is to analyze the impact of the blend ratio of HEFA-SPK and Jet A-1 on the combustion parameters and the engine's performance. The research was made on 30% of HEFA-SPK and 50% of HEFA-SPK and reference conventional fuel Jet A-1.

2. Methodology

2.1. Tested engine

The tests were carried out on the engine GTM 400. It is a microjet turbine engine which consist of the following elements: inlet duct, single stage radial compressor, annular combustion chamber with vaporizers, single stage axial turbine, exhaust duct with constant geometry, electrical starter, digital controller FADEC, geared fuel pump, engine starting solenoid valve, fuel shut-off solenoid valve, rpm optical sensor transmitter-receiver and Exhaust Gas Temperature thermocouple (EGT) mounted in the exhaust nozzle. In jet engines, variable geometry refers to adjusting the shape or size of specific components to optimize engine performance across different flight conditions. This can involve changing the area of the nozzle, the pitch of the compressor blades, or even the geometry of the inlet. "Constant geometry" refers to an engine design where the physical dimensions of key components, such as the nozzles, are fixed and do not change during operation.

The schematic view of the tested engine is presented in Fig. 1. Engine stations designations were marked by the engine manufacturer and do not comply with the aviation industry.

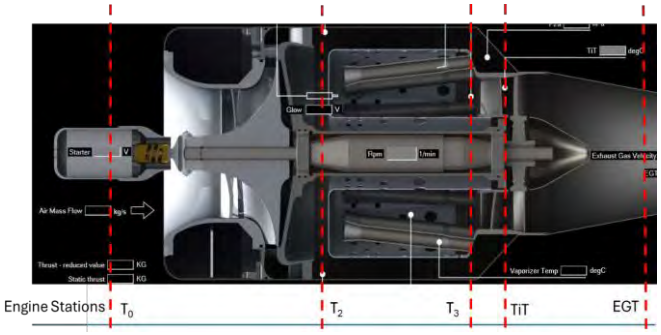

Fig. 1. Schematic view of the tested engine

Tested engine GTM 400 has a maximum thrust of 400 N and minimum thrust of 15 N. It is constructed for conventional fuel Jet A-1, with the possibility of changing the supply fuel to alternative fuels using an additional fuel distributor. The engine is lubricated with the engine fuel supply system using a mixture of JET-A1 and lubrication oil. The lubrication type for this engine is the mixture of 4% Mobil Jet Oil II and Jet-A1 fuel. Specific engine parameters are presented in Table 2.

In addition to the engine performance data, there are some other parameters recorded like engine starter voltage level [V], engine fuel pump voltage [V], engine igniter (glow) voltage signal [V], engine fuel ignition and combustion valves position [%], and engine rotation speed related to maximum rotation speed [%] [23].

In order to be able to conduct engine tests running on the sustainable aviation fuel, the engine was equipped with an additional internal fuel manifold dedicated to the alternative fuel type. This manifold construction was designed with the threaded connector at the end of the manifold, which allows for connecting a sustainable fuel line.

Table 2. Parameters of GTM 400

Parameter	Value
Maximum thrust	400 N
Minimum thrust	15 N
Max. spool rpm	85 000 rpm
Min spool rpm	27 000 rpm
Compression ratio	3.3:1
Mass air flow rate	770 g/s
Exhaust gas temperature	750°C
Fuel consumption	1200 g/min
Diameter	150 mm
Length	390 mm
Total weight	3200 g

An additional sealed access port in the engine case allows borescope inspections of the combustion liner and turbine nozzle vanes.

2.2. Measurements

The tests were carried out on the described engine GTM 400. The atmospheric conditions during measurements were an ambient temperature of 20◦C and an atmospheric pressure of 1000.9 hPa.

Tested fuels were blends of 30% volume of HEFA-SPK with Jet A-1 (HEFA30) and 50% volume of HEFA-SPK and Jet A-1 (HEFA50). The reference fuel was conventional aviation fuel Jet A-1. The feedstock used for this specific HEFA fuel production was mostly used cooking oil.

For every tested fuel, there were 12 measurement points: 7, 10, 20, 30, 40, 50, 60, 70, 80, 85, 90, and 100% Rc, so the measurement points also included the engine setup for the LTO cycle (Landing and Take-off). Every measurement point was set up for 20s, and the results were averaged. Despite changing conventional fuel to a blend with SAF, it was possible to obtain the same relative thrust and fuel flow. During experiments following parameters were recorded: static thrust [N], fuel flow [kg/h], total pressure at compressor diffuser p_2 [hPa], total temperature at combustion chamber exit T_3 [°C], total mass flow [kg/s], rpm [1/min], turbine inlet temperature TIT [°C], and exhaust gas temperature [°C]. Due to measurements of these parameters, it was possible to calculate specific engine parameters, such as specific fuel consumption, specific thrust, engine power, and engine thermal efficiency.

4. Research results

4.1. Thrust specific fuel consumption (TSFC)

Thrust-specific fuel consumption (TSFC) is one of the most important engine performance parameters. It is defined as the amount of fuel used to generate one unit of thrust over a finite period of time. This parameter tells us how efficiently engine power (thrust) is produced. TSFC is frequently given in the dimension of kg of fuel/daN of thrust/hour. In imperial units, its unit is noted as lbm fuel/lbf thrust/hours.

Thrust-specific fuel consumption – TSFC is defined as the relation of the fuel mass burnt in the combustion chamber in one hour to the thrust generated by the engine.

TSFC is the parameter that characterizes jet engine economy. TSFC reduction allows for increased aircraft flight duration and range. Since primary engine design considerations, particularly for commercial air transport, are those of low specific fuel consumption and weight, this is the reason why this parameter was used to analyze engine performance and economy based on the different aviation fuel types [22].

Mathematical expression of the TSFC is noted as a relation of the fuel mass flow provided to the engine, to the thrust generated as a result of the thermal energy produced in the combustion process:

$$\mathrm{TSFC} = \frac{\dot{m}_f}{F_c}\left[\frac{\mathrm{kg}}{\mathrm{daN}\cdot\mathrm{h}}\right] \tag{1}$$

where: TSFC – thrust specific fuel consumption, $\dot{m}_f$ – fuel mass flow provided to the combustion chamber, F_c – thrust force generated out of the combustion process.

TSFC calculated for the specific engine power levels is presented in Fig. 2.

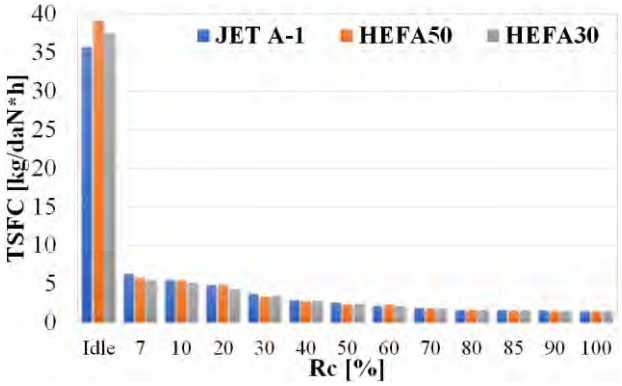

Fig. 2. Comparison of the thrust specific fuel consumption (TSFC) for the very specific engine throttle level Rc [%]

For the idle engine power level, the lowest TSFC was achieved for the clean Jet-A1 fuel, about 8% lower than HEFA50 and 3% than HEFA30. Still, it is worth noting that for such a low engine power level, it was extremely hard to set the same power level. For 7% and 10% of the engine rpm, TSFC was 8-10% higher than for HEFA50 and HEFA30. What is very important to stress is that starting from about 70% of engine rpm, TSFC was always higher than for other mixed fuels, with an average of 3.5%.

4.2. Fuel-to-air ratio

Another important engine performance parameter that is used to determine engine operation efficiency is the fuel-to-air ratio (FAR), noted as τ. Engine combustion efficiency strongly depends on two parameters. The first one is the air mass flow velocity entering the combustion chamber. The second one is the FAR. To achieve the highest combustion efficiency, the FAR for the jet engines should be between 1:60 and 1:130 of kerosene.

FAR is strongly related to the specific thrust and TSFC and might be noted as follows:

$$\tau = \mathrm{TSFC} \cdot \mathrm{F_s} \tag{2}$$

Fuel to air ration is also calculated as the fuel mass flow rate related to the air mass flow rate – eq. (3).

$$\tau = \frac{\dot{m}_f}{\dot{m}} \tag{3}$$

FAR calculated for the specific engine power levels is presented in Fig. 3.

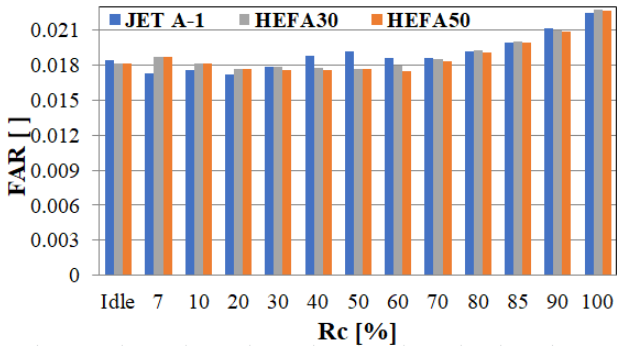

Fig. 3. Analysis of the fuel-to-air ratio for the very specific engine throttle level Rc [%]

What might be deduced from Fig. 3 is the fact that only for the low engine power levels (7–20%), FAR for Jet-A1 is lower than for other mixed fuels (average 0.05%). Starting from 30%, the engine power level was always higher, with an average of 0.1%. Only for 100% engine rpm FAR for mixed fuels was higher. The reason for this could be that the engine control panel allowed for setting 100% still with various physical rpms.

4.3. Specific thrust

Specific $\mathrm{F_s}$ thrust is one of the key engine performance parameters. It is the relation of the thrust $\mathrm{F_c}$ generated by the engine to the air mass flow through the engine $\dot{m}$ In the physical sense, specific thrust might be treated as a thrust generated out of 1 kg air mass flow through the engine in 1 s.

$$\mathrm{F_s} = \frac{\mathrm{F_c}}{\dot{m}} \left[\frac{\mathrm{m}}{\mathrm{s}}\right] \tag{4}$$

Assuming that the mass flow at the engine exhaust equals the sum of the engine inlet air mass flow plus fuel mass flow added, and assigning: $\left(\dot{m} + \dot{m}_p\right) = (1 + \tau) \cdot \dot{m}$ eq. (4) could be written as follows:

$$\mathrm{F_s} = \frac{\mathrm{F_c}}{\dot{m}} = (1 + \tau)(\mathrm{V_8} - \mathrm{V_0}) \tag{5}$$

From eq. (5) may deduce that the specific thrust depends on the velocity differences of the engine inlet and outlet airflow.

Engine-specific thrust depends on the engine compression rate, turbine inlet temperature, and compression/expansion efficiency. The higher the specific thrust, the lower the air mass flow required to generate the same level of power or thrust, which allows for the design and build of smaller and lighter aircraft engines.

Engine-specific thrust is the indicator of the engine efficiency because an engine with a higher F index generates higher thrust, for the same air mass flow. Calculating thrust to specific thrust ratio provides information on the air mass flow rate through the engine, which determines engine cross-section area and, as a result, engine dimensions.

Engine-specific thrust calculated for the specific engine power levels is presented in Fig. 4.

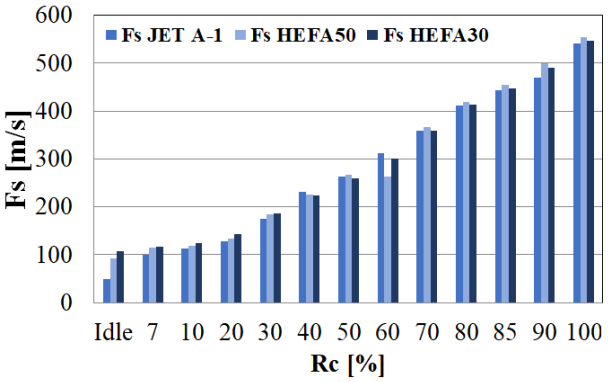

Fig. 4. Comparison of the specific thrust (Fs) for the very specific engine throttle level (Rc)

Having analyzed the comparison of the Specific Thrust at each engine power level, it might be noticed that for all engine rpm levels except 60%, the engine-specific thrust was higher for the HEFA50 mixed fuel type with a difference of 2–9%. The engine on HEFA30 was working with a similar specific thrust to Jet-A1.

4.4. Thermal efficiency

TSFC is directly related to the thermal and propulsive efficiencies and, as a result, the overall engine efficiency [9]. Since specific fuel consumption is directly related to thermal efficiency, let us explain what thermal efficiency is and how it is calculated.

The ability of an engine to convert the thermal energy inherent in the fuel (which is unleashed in a chemical reaction) to a net kinetic energy gain of the working medium is called the engine thermal efficiency, and it is noted as η_c [10]. In combustion-based engines, thermal efficiency depends on the pressure and temperature in the combustion chamber.

Thermal efficiency ($\eta_{thermal}$) is generally defined as the ratio of useful work output (or, in the case of a jet engine, the kinetic energy imparted to the flow) to the energy input (fuel energy).

Considering enthalpy flux for a jet engine, the energy balance involves:

- Fuel energy input: $\dot{m}_f \cdot \mathrm{LHV}$ (lower heating value)
- Energy carried away by the exhaust: enthalpy flux, kinetic energy, and pressure work.

The thermal efficiency, considering the enthalpy flux, can be expressed as:

$$\eta_{thermal} = \frac{\text{useful energy output}}{\text{energy input}} \tag{6}$$

Assuming steady-flow and idealized engine cycle and noting:

- Mass flow rate of air: $\dot{m}_a$
- Mass flow rate of fuel: $\dot{m}_f$

– Fuel's lower heating value: LHV
– Inlet (ambient) conditions: temperature T_0, enthalpy h_0
– Exhaust conditions: temperature T_{exit}, enthalpy h_{exit}
– Exhaust velocity: V_{exit}
– Specific heats: c_p (assumed constant)
– Air inlet enthalpy: $h_0 = c_p T_0$
– Exhaust enthalpy: $h_{exit} = c_p T_{exit}$
– Fuel energy input rate: $\dot{Q}_f = \dot{m}_f \cdot LHV$.

Let us calculate the energy balance:

The total energy flux leaving the engine per unit time (per unit mass of air) includes:

– Enthalpy flux: $\dot{m}_a h_{exit}$
– Kinetic energy flux: $\frac{1}{2}\dot{m}_a V_{exit}^2$.

The total energy input from fuel: $\dot{Q}_f = \dot{m}_f \cdot LHV$.

The thermal efficiency reflects the ratio of the useful energy imparted to the flow (enthalpy + kinetic energy) to the energy supplied by the fuel:

$$\eta_{thermal} = \frac{\text{energy increase in the airstream}}{\text{fuel energy input}} \tag{7}$$

Expressed explicitly:

$$\eta_{thermal} = \frac{\dot{m}_a\left(h_{exit} + \frac{V_{exit}^2}{2} - h_0\right)}{\dot{m}_f \cdot LHV} \tag{8}$$

This detailed form captures the essential thermodynamic parameters, including enthalpy flux $c_p(T_{exit} - T_0)$ and kinetic energy flux $\frac{V_{exit}^2}{2}$, normalized by fuel energy input per unit air mass flow, providing a comprehensive measure of jet engine thermal efficiency considering enthalpy flux.

For instance, for the very popular aviation fuel JET-A1 net calorific value LHV should be no less than 42.8 MJ/kg.

Equation (8) compares the mechanical power production in the engine to the thermal power investment in the engine [11].

Thermal efficiency is a prime factor in gas turbine performance. It is the ratio of the network produced by the engine to the chemical energy supplied in the form of fuel. The three most important factors affecting thermal efficiency are turbine inlet temperature, compression ratio, and the component efficiencies of the compressor and turbine. Other factors that affect thermal efficiency are compressor inlet temperature and combustion efficiency.

Since combustion efficiency depends on the combustion chamber construction, fuel system, and the fuel combustion process efficiency, which directly depends on the type of fuel used in the combustion, that is why it is extremely significant to compare thermal efficiencies for the different types of aviation fuels used and various mixture ratios of the JET-A1 fuel and the sustainable fuel.

A high engine thermal efficiency means low specific fuel consumption and, therefore, less fuel for a flight of a given distance at a given power. Thus, the practical importance of high thermal efficiency is one of the most desirable features in the performance of an aircraft engine.

Thermal efficiencies calculated in accordance with eq. (8) The specific engine power levels and three types of fuel were presented in Fig. 5.

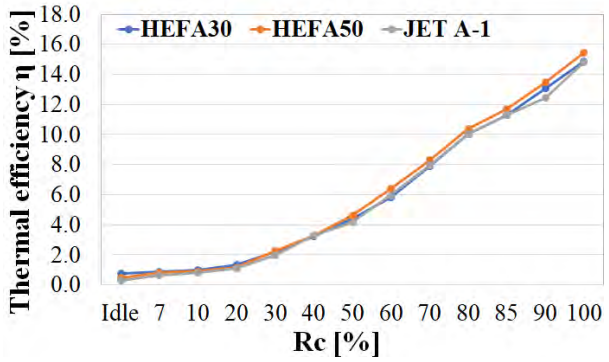

Fig. 5. Thermal efficiency η [%] for the very specific engine throttle level Rc [%]

Engine thermal efficiency for all engine power levels was higher for HEFA50 with about 0.1–0.4%. The results achieved confirm our assumptions that engine thermal efficiency will be higher for the HEFA50 fuel mixture. It is worth noticing that even though thermal efficiency is not very high, reaching about 16%, increasing thermal efficiency increases overall engine efficiency and, as a result, engine performance in return for the lower engine fuel consumption.

4.5. Temperatures

Total temperature – T_3

The results achieved in the engine test were very promising as far as the performance is concerned. However, the question is whether the achieved results resulted in higher temperatures measured in engine control points.

Let us analyze the first measured temperature T_3, which is the combustion chamber outlet. Jet engines achieve better performance when the temperatures achieved out of the combustion chamber are higher.

In Figure 6, T_3 total temperatures measured at specific engine cross-sections in relation to the engine throttle level (Rc) are presented.

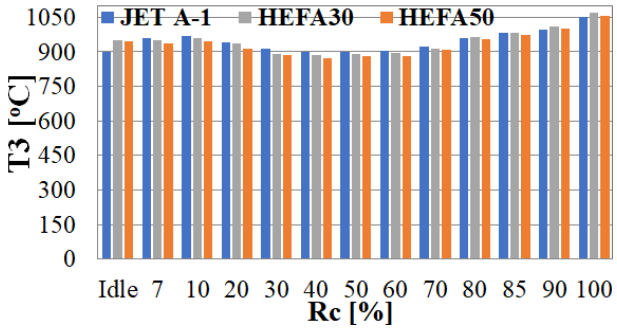

Fig. 6. Total temperature T3 for the very specific engine throttle level Rc [%]

Having analyzed achieved T_3 temperatures it might be concluded that up to 85%, T_3 temperatures generated from the Jet-A1 fuel were about 2% higher than for the sustainable fuels. For 90–100% engine power level T_3 temperatures achieved for HEFA50 and HEFA30 were 1–2% higher.

Turbine inlet temperature – TIT

Turbine inlet temperature (TIT) is one of the crucial temperatures in the jet engine for two reasons. The first one is the engine health status and endurance, while the other

one is the engine performance. From the perspective of the engine-generated thrust, the higher TIT, the higher energy generated at the turbine inlet, which is converted to the turbine work as well as engine exhaust gases acceleration.

In Figure 7, TIT measured at specific engine cross-sections in relation to the engine throttle level (Rc) is presented.

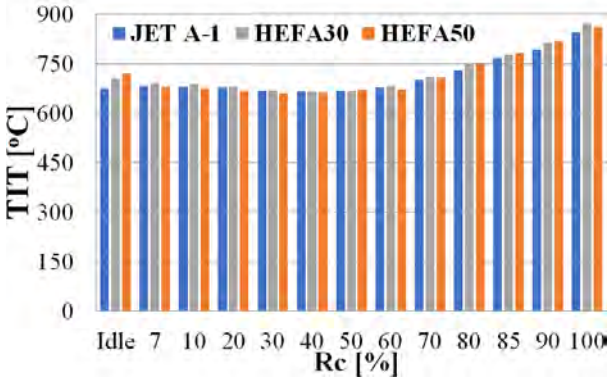

Fig. 7. Turbine inlet temperature TIT for the very specific engine throttle level Rc [%]

As for the TIT, for almost all the engine power levels, exhaust gas temperatures resulting from Jet-A1 were lower by 0–3.3% from the fuel mixtures

Exhaust gas temperature – EGT

Exhaust gas temperature (EGT) is the total temperature, which is measured at various points, depending on the engine construction. This temperature results from the TiT, engine construction, and engine capabilities of the engine conversion to the turbine work. This engine parameter must be controlled and monitored. Exceeding the allowed EGT might result in engine severe failure or even damage.

In Figure 8 exhaust gas temperature EGT measured at specific engine cross-sections concerning the engine throttle level (Rc) is presented.

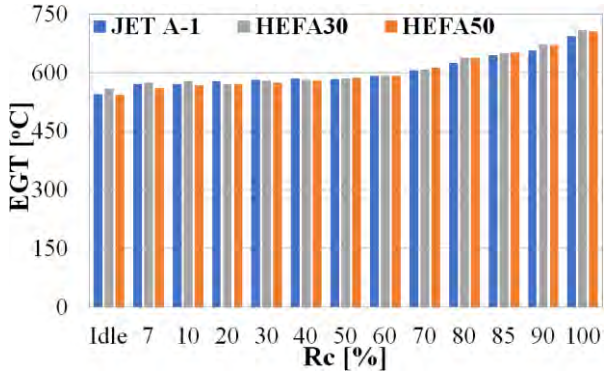

Fig. 8. Exhaust gas temperature EGT for the very specific engine throttle level Rc [%]

Up to 50% of the engine power level EGT generated from Jet-A1 is higher in comparison to HEFA50 and HEFA30 of 0.2–1.3%. Starting from 50% of rpm, the generated exhaust gas temperature is higher for sustainable fuel mixtures from 0.2–2.5%, which is a remarkable increment.

4.5. Engine static thrust – F_c

Having analyzed all the most important engine parameters, it is worth checking how fuel additives affect engine static thrust Fc in comparison to the clean Jet-A1.

Static thrust Fc of the turbojet engine can be calculated in accordance with eq. (9):

$$F_c = (\dot{m} + \dot{m}_f)V_8 + (p_8 - p_0)A \tag{9}$$

where: p_8 – exhaust gases pressure in nozzle cross-section, p_0 – atmospheric pressure, A – exhaust nozzle cross-section area.

Results were presented in Fig. 9.

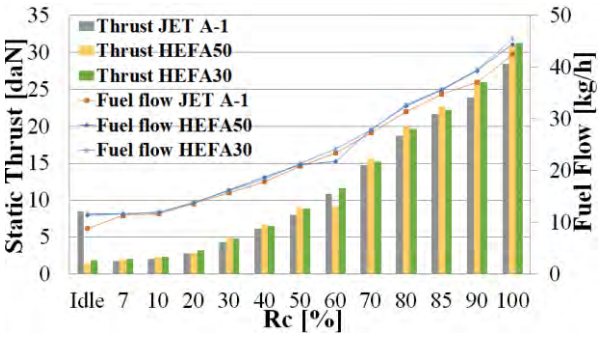

Fig. 9. Engine static thrust Fc for the very specific engine throttle level Rc [%]

As it might be deduced from Fig. 9, the fact that summarizes conducted research case studies is that sustainable aviation fuels not only affect environmental pollution, but they also allow for higher thermal efficiency and engine performance.

Analyzing engine static thrust generated from all the fuel types, it might conclude that engine static thrust Fc achieved from HEFA50 and HEFA30 is higher by about 2.7–11.2%

5. Discussion

According to the literature data, several studies indicate that blending SAFs with conventional jet fuels can lead to a reduction in TSFC. For instance, a 7% FT (Fischer-Tropsch) blend resulted in a 6.67% reduction in TSFC across all thrust settings [17]. Similarly, the use of CHJ (Catalytic Hydrothermolysis Jet) fuel blends showed lower TSFC compared to conventional fuels [16]. Different biofuel blends, such as those containing Jatropha and Camelina, have been tested and found to improve engine performance by reducing TSFC. For example, biofuels like Jatropha Bio-Synthetic Paraffinic Kerosene (JSPK) and Camelina Bio-Synthetic Paraffinic Kerosene (CSPK) showed a 1% to 3% lower TSFC compared to Jet-A fuel [7]. The impact of SAFs on TSFC is influenced by the specific properties of the fuel and the design of the engine. For instance, the lower heating value of the fuel plays a significant role in determining TSFC. Blends with appropriate fuel properties, such as a lower carbon-to-hydrogen ratio and higher combustion efficiency, tend to reduce fuel consumption [21]. The benefits of SAFs in reducing TSFC are observed across various thrust settings. For example, a 10% CHJ fuel blend provided higher thrust and lower TSFC throughout the entire range of thrust output settings

[16]. The literature confirms the obtained results for HEFA fuel. In the case of the studies presented in the article, an average reduction in TSFC of 3% was achieved for Jet A-1 and HEFA blends.

SAFs are required to meet higher thermal stability standards than conventional jet fuels, which can be leveraged to improve energy efficiency in new engine designs. Higher energy density fuels, which SAFs can provide, directly impact aircraft efficiency, with an increase in fuel specific energy (enthalpy per unit mass, LHV) leading to a 0.43% improvement in aircraft efficiency per MJ/kg increase in LHV [5].

SAFs composed of cycloalkanes and some aromatics have been found to maximize energy savings in high power engine operating conditions. This is likely due to the effects of the hydrogen-to-carbon (H/C) ratio on turbine performance, which can enhance the thermal efficiency of the engine [16]. However, at low power conditions, SAF mixtures have not yet surpassed conventional petroleum fuels in terms of energy savings [2].

Studies have shown that the use of SAFs can lead to slight improvements in engine efficiency. For instance, leveraging the high thermal stability of synthetic fuels can result in a combined efficiency savings of around 0.5%, with a significant portion attributed to the thermal properties of the fuel [6]. This efficiency gain is partly due to the ability of SAFs to maintain stable combustion at higher temperatures. The ability of SAFs to absorb heat without significant degradation is crucial for maintaining engine performance. This property ensures that the fuel can effectively manage the thermal load, prevent overheating and maintain optimal engine temperatures [3, 4]. The high thermal stability of SAFs means they can withstand higher operating temperatures without forming deposits that could impair engine performance [20]. The conducted studies showed that the thermal efficiency of the engine at all power levels was higher for HEFA50 by approximately 0.1–0.4%.

The presented literature sources indicate trends in jet engine performance parameters following the use of aviation fuels blended with SAF. The research presented in this article also confirms these trends under test conditions, as described in the conclusions of this study. From the perspective of engine performance, the use of SAF may prove beneficial, although not necessarily from an economic standpoint – a matter that, however, is beyond the scope of this paper.

6. Conclusions

The conducted research aimed to assess the impact of sustainable aviation fuel on the operational parameters of the engine. The obtained results were compared with available literature. A thorough analysis of the collected measurements allowed for the formulation of the following conclusions:

- The use of HEFA-SPK fuel resulted in an average improvement of TSFC by approximately 3% across the engine's operating range
- Specific thrust improved by 2–9%, depending on the operating point of the engine powered by the HEFA-SPK fuel blend
- The engine's thermal efficiency increased by an average of 0.4% due to the use of HEFA fuel
- Exhaust gas temperature at various engine points remained similar regardless of the type of fuel used
- Static thrust increased by 2.7%–11.2% for the engine powered by HEFA fuel.

These conclusions indicate that the use of sustainable aviation fuels is beneficial not only for environmental reasons but also for engine performance.

Nomenclature

ATJ-SPK	alcohol-to-jet synthetic paraffinic kerosene
CHJ	catalytic hydrothermolysis synthesized kerosene
CH-SK	catalytic hydrothermolysis synthesized kerosene
CO	carbon monoxide
CO_2	carbon dioxide
CSPK	camelina bio-synthetic paraffinic kerosene
EGT	exhaust gas temperature
FAR	fuel-to-air ratio
FT-SPK	Fischer-Tropsch Synthetic Paraffinic Kerosene
FT-SPK/A	Fischer-Tropsch Synthetic Paraffinic Kerosene with aromatics
GHG	greenhouse gases
HEFA-SPK	hydroprocessed ester and fatty acids synthetic paraffinic kerosene
HFS-SIP	hydroprocessed fermented sugars to synthetic isoparaffins
HHC	hydroprocessed hydrocarbons, esters and fatty acids synthetic paraffinic kerosene
JSPK	jatropha bio-synthetic paraffinic kerosene
LHV	lower heating value
LTO	landing and take off cycle
SAF	sustainable aviation fuel
SIP	hydroprocessed fermented sugars to synthetic isoparaffins
TSFC	thrust-specific fuel consumption

Bibliography

[1] Aviation Benefits Beyond Borders. Sustainable Aviation Fuel. https://aviationbenefits.org/environmental-efficiency/climate-action/sustainable-aviation-fuel (accessed on 20 November 2024)

[2] Behnke LC, Boehm RC, Heyne JS. Optimization of sustainable alternative fuel composition for improved energy consumption of jet engines. In: AIAA Science and Technology Forum and Exposition, AIAA SciTech Forum 2022. https://doi.org/10.2514/6.2022-2056

[3] Billingsley M, Keim N, Hill-Lam B, Synovec R, Freye C. Hydrocarbon fuel thermal performance modeling based on systematic measurement and comprehensive chromatographic analysis. 52nd AIAA/SAE/ASEE Joint Propulsion Conference. 2016. https://doi.org/10.2514/6.2016-4903
[4] Billingsley M, Keim N, Synovec R, Hill-Lam B, Wilhelm C. Progress toward quality assurance standards for advanced hydrocarbon fuels based on thermal performance testing and chemometric modeling. IASH 2015 – 14th International Symposium on Stability, Handling and Use of Liquid Fuels 2015.
[5] Boehm RC, Faulhaber C, Behnke L, Heyne J. The effect of theoretical SAF composition on calculated engine and aircraft efficiency. Fuel. 2024;371:132049. https://doi.org/10.1016/j.fuel.2024.132049
[6] Boehm RC, Scholla LC, Heyne JS. Sustainable alternative fuel effects on energy consumption of jet engines. Fuel. 2021;304:121378. https://doi.org/10.1016/j.fuel.2021.121378
[7] Cican G, Mirea R. An experimental insight into the use of n-butanol as a sustainable aviation fuel. Fire. 2024;7(9):313. https://doi.org/10.3390/fire7090313
[8] Detsios N, Theodoraki S, Maragoudaki L, Atsonios K, Grammelis P, Orfanoudakis NG. Recent advances on alternative aviation fuels/pathways: a critical review. Energies. 2023;16:1904. https://doi.org/10.3390/en16041904
[9] European Aviation Safety Agency (EASA) Part-66, Gas Turbine Engine, Training Material, April 2003.
[10] Farokhi S. Aircraft propulsion. 2nd ed. John Wiley&Sons Ltd 2014.
[11] Federal Aviation Administration. Aviation maintenance technician handbook – Powerplant Vol. I and II. U.S. Department of Transportation 2012.
[12] Gan C, Ma Q, Bao S, Wang X, Qiu T, Ding S. Discussion of the standards system for sustainable aviation fuels: an aero-engine safety perspective. Sustainability. 2023;15:16905. https://doi.org/10.3390/su152416905
[13] ICAO Environment, Conversion processes. https://www.icao.int/environmental-protection/GFAAF/Pages/Conversion-processes.aspx (access on 12 December 2024).
[14] Jasiński R, Kurzawska P, Przysowa R. Characterization of particle emissions from a DGEN 380 small turbofan fueled with ATJ blends. Energies. 2021;14:3368. https://doi.org/10.3390/en14123368
[15] Kroyan Y, Wojcieszyk M, Kaario O, Larmi M. Modeling the impact of sustainable aviation fuel properties on end-use performance and emissions in aircraft jet engines. Energy. 2022;255:124470. https://doi.org/10.1016/j.energy.2022.124470
[16] Liu Z, Yang XY. Engine performance and emission characteristics of cellulosic jet biofuel blends. Chin Pet Process Petrochem Technol. 2023;25(3):29-36. https://caod.oriprobe.com/articles/65965986/Engine_Performance_and_Emission_Characteristics_of.htm??
[17] Liu Z, Yu S, Yang X. Insight of effects of air quality and sustainable aviation fuel blend on energy saving and emission reduction in airport. Bioresour Bioprocess. 2024;11(1):84. https://doi.org/10.1186/s40643-024-00798-w
[18] Marszalek N, Lis T. The future of sustainable aviation fuels. Combustion Engines. 2022;191(4):29-40. https://doi.org/10.19206/CE-146696
[19] Mazlan NM, Savill M, Kipouros T. Effects of biofuels properties on aircraft engine performance. Aircraft Eng Aerosp Technol. 2015;87(5):437-442. https://doi.org/10.1108/aeat-09-2013-0166
[20] Mielczarek DC, Blakey S, Hughes KJ, Ingham DB, Pourkashanian M, Wilson CW. Experimental and theoretical investigation of pathways to deposit formation in thermally stressed aviation fuel in the presence of nitrogenous additives. 13th International Conference on Stability, Handling and Use of Liquid Fuels. 2013:230-240.
[21] Ogawa S, Hongo T, Mori K, Maeda Y, Phuong Uyen NH. Evaluation of exhaust gas from micro-jet engine using SAF made from coconut. AIAA SciTech Forum and Exposition; 2024. https://doi.org/10.2514/6.2024-0105
[22] Szrama S. Aircraft turbine propulsion. Poznan University of Technology Publishing House. Poznan 2023.
[23] Szrama S. F-16 turbofan engine monitoring system. Combustion Engines. 2019;177(1):23-35. https://doi.org/10.19206/CE-2019-205
[24] The European Parliament. Regulation of the European Parliament and of the Council on ensuring a level playing field for sustainable air transport (ReFuelEU Aviation) 2021/0205 (COD). 2023.
[25] Zhang L, Butler TL, Yang B. Recent trends, opportunities and challenges of sustainable aviation fuel. Green energy to sustainability: strategies for global industries. 1st ed. 2020.

Paula Kurzawska-Pietrowicz, MEng. – Faculty of Civil and Transport Engineering, Poznan University of Technology, Poland.
e-mail: *paula.kurzawska@put.poznan.pl*

Remigiusz Jasiński, DSc., DEng. – Faculty of Civil and Transport Engineering, Poznan University of Technology, Poland.
e-mail: *remigiusz.jasinski@put.poznan.pl*

Sławomir Szrama, DEng. – Faculty of Civil and Transport Engineering, Poznan University of Technology, Poland.
e-mail: *slawomir.szrama@put.poznan.pl*

Maciej Siedlecki, DEng. – Faculty of Civil and Transport Engineering, Poznan University of Technology, Poland.
e-mail: *maciej.siedlecki@put.poznan.pl*

Article citation info:
Wojs M, Laskowski P, Zimakowska-Laskowska M. Numerical investigation of intake flow dynamics in hydrogen-fueled engines. Combustion Engines. 2026;204(1):43-50. https://doi.org/10.19206/CE-208775

Marcin WOJS
Piotr LASKOWSKI
Magdalena ZIMAKOWSKA-LASKOWSKA

Combustion Engines
Polish Scientific Society of Combustion Engines

Numerical investigation of intake flow dynamics in hydrogen-fueled engines

ARTICLE INFO

Received: 13 June 2025
Revised: 15 July 2025
Accepted: 29 July 2025
Available online: 12 September 2025

This paper presents a computational fluid dynamics (CFD) study of hydrogen injection in a modified intake system of a small industrial internal combustion engine. Two injector positions (8 mm and 12 mm from the valve stem axis) and two injection profiles were evaluated for their impact on in-cylinder mixture formation. The results indicate that injector placement significantly affects hydrogen jet penetration and turbulence interaction. A more gradual injection profile produced better mixture homogeneity. The 8 mm configuration with Profile B demonstrated the most uniform distribution, which is favorable for combustion stability and NO_x emission reduction. These findings support the need for integrated optimization of intake geometry and fuel delivery strategies in hydrogen engines.

Key words: *hydrogen combustion, intake manifold, injector positioning, fuel-air mixing, piston geometry*

1. Introduction

The growing interest in hydrogen as a sustainable fuel for internal combustion engines has intensified the need to understand the complex dynamics of fuel-air mixture formation and in-cylinder flow behavior [43, 50]. Hydrogen internal combustion engines (H2-ICEs) are increasingly regarded as a promising pathway to decarbonize the transport sector. These engines utilize hydrogen fuel in a conventional combustion process, offering near-zero carbon dioxide emissions and significantly lower levels of particulates and unburned hydrocarbons. When combined with direct injection (DI) and advanced ignition systems, H2-ICEs can achieve peak thermal efficiencies of up to 50% and average driving cycle efficiencies above 35%, especially in hybrid vehicle configurations [3, 7, 9].

Applications of H2-ICEs range from heavy-duty trucks and city buses to retrofitted power units in hybrid drivetrains. Positive ignition (PI) concepts with DI and jet ignition (JI) provide high power density and efficient lean-burn operation. However, port fuel injection (PFI) systems – although easier to retrofit – require careful control to avoid backfire and pre-ignition events [10, 24, 51]. Similarly, Yang et al. [49] showed that in Reactivity Controlled Compression Ignition (RCCI) engines, split-injection parameters have a key influence on multi-stage heat release and engine efficiency, emphasizing the need for precise tuning of the injection strategy.

Despite these advantages, H2-ICEs face several technical challenges. Key among them are elevated NO_x emissions due to high combustion temperatures, material degradation from hydrogen exposure, and the need for redesigned thermal systems to handle hydrogen-specific intake air and heat transfer characteristics [4, 32]. Recent studies also demonstrate that water injection can significantly reduce NO_x formation and improve torque and combustion stability at high loads [33].

Therefore, adequate air-fuel mixing, injection strategy, and combustion chamber geometry management are critical to ensure stable operation and emission compliance. These aspects are particularly relevant to developing small-displacement engines, where compact design constraints amplify the effects of mixture formation on overall performance.

Hydrogen's unique properties – including high diffusivity and flame speed – make it attractive but pose challenges such as backfire risk and mixture stratification [5].

Achieving a homogeneous hydrogen-air mixture is one of the most critical aspects of ensuring efficient and stable combustion in H2-ICEs. Mixture stratification can lead to local hot spots, increased NO_x formation, and incomplete combustion. As a result, understanding the dynamics of fuel-air mixing is essential for developing low-emission hydrogen engines. As emphasized by Vasudev et al. [45], accurate modelling of fuel-air stratification remains a critical challenge in low-temperature combustion strategies, which justifies the use of detailed Computational Fluid Dynamics (CFD) analyses even before ignition.

Recent studies show that injection timing strongly influences mixture quality, with early injection events (e.g., –120°CA aTDC) promoting better distribution across the combustion chamber [27]. Dual injection strategies and in-cylinder flow patterns, especially tumble and swirl, have also enhanced mixture homogeneity [34]. Although high injection pressures can accelerate mixing, their effect is often less significant than proper timing and piston geometry [2, 47, 52].

CFD simulations and optical diagnostics, such as tracer-based laser-induced fluorescence (TLIF), have enabled detailed characterization of hydrogen jet penetration and flow structures [8]. These methods reveal that injector positioning, nozzle design, and in-cylinder motion must be considered jointly to achieve optimal fuel-air distribution.

Therefore, proper control of injection parameters and combustion chamber dynamics is decisive in determining engine performance, NO_x emissions, and operational stability.

In addition to stratification, hydrogen engines are especially prone to abnormal combustion events such as backfire and pre-ignition. These issues are caused by hydrogen's low ignition energy and high flame speed and are often triggered by hot residual gases, improper injection timing,

or elevated wall temperatures [17, 41]. Controlling these phenomena is essential for ensuring safe and stable operation.

Furthermore, hydrogen combustion at high temperatures promotes NO_x formation. While ultra-lean mixtures can suppress NO_x, they may also reduce power output and increase cycle-to-cycle variability [1, 20]. Thus, effective mitigation strategies – such as water injection, cooled EGR, optimized injection, and valve timing – are needed to balance performance and emissions [12, 39].

Computational Fluid Dynamics has become a crucial tool for analyzing hydrogen combustion due to the complexity of flame propagation, pollutant formation, and flow interactions. CFD models, ranging from Reynolds-Averaged Navier–Stokes (RANS) to Large Eddy Simulations (LES), have been validated against experimental data and allow for detailed investigation of in-cylinder processes [15, 37]. These simulations are beneficial for assessing the effects of geometry, injection strategies, and turbulent mixing in hydrogen-fueled engines.

3D-CFD simulations, in particular, provide superior accuracy in predicting heat release rates and flame development compared to simplified 2D or 0D models [16, 36].

This study uses computational fluid dynamics (CFD) simulations to investigate the behavior of air–hydrogen mixtures flowing through the intake valve system and interacting with various piston crown geometries. The primary objective is to assess how piston design influences turbulence intensity, mixing quality, and combustion efficiency – factors critical for stable, efficient hydrogen combustion [29, 43].

Previous studies have emphasized the importance of optimizing charge motion – particularly swirl and tumble flows – for enhancing combustion in engines fueled with alternative gases such as sewage gas or hydrogen-enriched blends [3]. Modifications to intake and combustion chamber geometry have proven effective in improving swirl characteristics and reducing NO_x emissions.

For instance, [25] demonstrated that geometric adjustments near the inlet valve seats can enhance charge motion and combustion quality while meeting emission constraints. Similarly, swirl-stabilized flame studies indicate that adding hydrogen increases NO_x formation, but this can be mitigated by raising excess air levels or swirl intensity, thereby improving mixture homogeneity and reducing peak temperatures [22].

These findings underscore the necessity of carefully designing the intake system and piston geometry to optimize in-cylinder flow and minimize emissions in hydrogen-fueled internal combustion engines.

The role of intake geometry – including plenum volume, port shape, and runner length – cannot be overstated in this context. Optimized intake configurations can improve air-fuel mixing, reduce dead zones, and enhance tumble or swirl motion, leading to better combustion efficiency and lower emissions [2, 23]. Variable intake systems offer flexibility across engine speeds, further optimizing torque and fuel economy. Injection strategy – including timing, duration, and split/single injection schemes – strongly influences mixture formation and combustion characteristics. Delayed injection in DI engines improves efficiency and reduces pre-ignition risk, while split injection may enhance mixing but requires careful calibration to avoid NO_x spikes [28, 30].

Injection strategies must also be tailored to engine type. For example, rotary engines benefit from early injection, while dual-fuel setups require precise pilot injection control [14, 44]. These parameters are key to leveraging hydrogen's combustion potential across diverse engine architectures.

Additionally, the intake design affects engine response and thermal behavior, making it a critical factor in performance and durability [6, 40].

2. Related work

2.1. Hydrogen combustion characteristics in ICEs

Hydrogen's broad flammability limits, minimal ignition energy, and rapid diffusion support lean-burn combustion. Yet, these same traits heighten the risk of backfire, pre-ignition, and elevated NO_x levels due to increased combustion temperatures [46]. Huang et al. [2] pointed out that consistent mixture formation and effective control of in-cylinder air motion are key to mitigating these issues.

Thanks to its combustion properties – such as fast flame speed and low ignition threshold – hydrogen enables efficient lean-burn operation. Nevertheless, these characteristics also introduce challenges like knock, spontaneous ignition, and greater NO_x emissions under high-temperature conditions. Research [13, 35] indicates that quick combustion enhances thermal efficiency, though it can reduce power output under stoichiometric conditions. To stabilize combustion and curb NO_x formation, strategies like direct injection and targeted mixture preparation near the ignition site are essential [30, 48].

2.2. Importance of in-cylinder flow and swirl motion

Proper in-cylinder airflow plays a key role in ensuring thorough air-fuel mixing and maintaining stable combustion. Swirl and tumble flows, induced by the design of intake ports and valve geometry, enhance turbulence and speed up flame development [18, 21]. Increased swirl in hydrogen-fueled engines enables lower emissions while maintaining high volumetric efficiency, as shown, among others, in studies using Particle Image Velocimetry (PIV) and CFD simulations [26, 38].

Studies by [25] on alternative fuel engines showed that optimizing the intake system—especially the regions near the inlet valves – can significantly improve swirl intensity. Their results, validated through flow-bench and combustion tests, revealed that geometric changes could yield better combustion characteristics and lower NO_x emissions.

Swirl and tumble motions are fundamental in direct-injection hydrogen engines to avoid stratification and ensure reliable ignition. Through CFD, Liu et al. [29] demonstrated that piston crown shape directly influences large-scale vortex formation, affecting mixing efficiency and flame propagation dynamics.

2.3. CFD simulation as a tool for flow characterization

CFD methods are vital for examining the unsteady and intricate flow behavior within combustion chambers. Traversari et al. [43] employed high-fidelity CFD simulations

to analyze turbulence generated by interactions between valves and the piston. Their research underlined the significance of fine mesh resolution and the selection of appropriate turbulence models, such as k–ε or LES, for accurate prediction of in-cylinder processes.

In hydrogen-air mixture studies, CFD modelling – using approaches like k–ε or LES – enables simulation of vortex structures and the influence of moving components such as valves and pistons [19, 23]. Furthermore, CFD tools are valuable beyond engine analysis. For example, Czyż et al. [11] used them to assess the aerodynamic influence of individual vehicle elements, quantifying drag contributions in an ultra-efficient electric vehicle. Their analysis highlighted how body shape affects flow detachment and turbulence formation – insights that are also critical in optimizing intake system performance.

Combining CFD with machine learning methods allows for optimization of injection parameters and significantly accelerates the design of H_2 fuel systems [23].

Mattarelli et al. [31] further validated that advanced piston profiles could enhance turbulence, speed up flame propagation, and reduce cycle-to-cycle variability. This supports the view that piston geometry is not merely a mechanical component but a functional element in combustion optimization.

2.4. Hydrogen-methane blends and swirl stabilization

Recent research on swirl-stabilized combustion in hydrogen-enriched methane flames [25] has revealed a trade-off between enhanced mixing and increased NO_x emissions. Their results suggest that increasing swirl can homogenize the mixture and lower peak flame temperatures, thus reducing NO_x emissions. However, excessive swirl may lead to incomplete combustion or flame quenching.

These studies underline the necessity for a balanced intake strategy, where geometric configurations of valves, intake ducts, and piston crowns work synergistically to manage in-cylinder dynamics without incurring performance penalties.

3. Methods

3.1. Research object

The combustion engine on which the geometry of the intake and crank-piston system was based was the Yamaha EH65 engine. It is an industrial, two-cylinder, V-shaped, air-cooled engine with a capacity of 653 cm^3. The basic technical data of the unit are presented in Table 1.

Table 1. Technical data of the Yamaha EH65

Parameter	Unit	Value
Engine type	–	Air-cooled, OHV, V2, with horizontal shaft
Cylinder bore × stroke	mm	80 × 65
Displacement	cm^3	653
Maximum power	kW	15 at 3600 rpm
Maximum torque	Nm	45.6 at 2600 rpm
Compression ratio	–	8.3
Fuel	–	Unleaded petrol
Ignition system	–	TCI ignition
Service weight	kg	49.5
Dimensions (length × width × height)	mm	463 × 499 × 476

Figure 1 shows the Yamaha EH65 internal combustion engine.

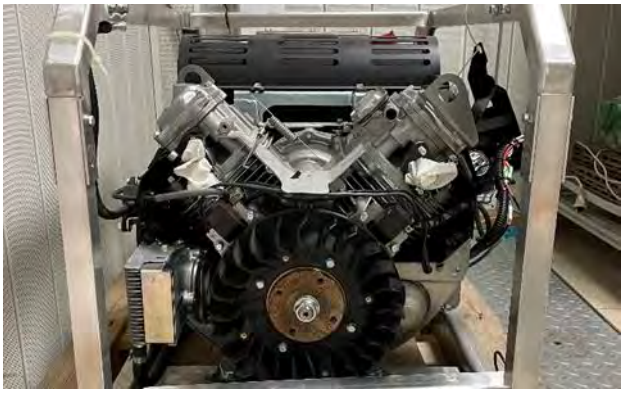

Fig. 1. Yamaha EH65 internal combustion engine

The combustion engine has an indirect injection system with two injectors, one for each cylinder. This forced the modification of the intake system to install additional injectors supporting LPG, CNG, and hydrogen HANA H2001 Gold. Figure 2 shows the model of the intake manifold with additional sockets for gas injectors.

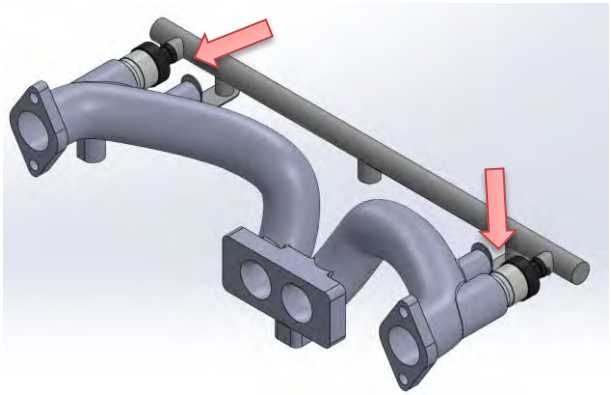

Fig. 2. Yamaha EH65 engine modified intake system model. Arrows indicate the location of the additional gas injector ports

3.2. Simulation parameters

The conducted research is preliminary in nature. It aims to understand the behavior of injected hydrogen in the intake manifold of an internal combustion engine. Additionally, it aims to determine the optimal injector nozzle position relative to the intake valve stem diameter. Furthermore, the authors attempted to modify the hydrogen injection length characteristics. For this reason, many elements of the simulation model were simplified. The model does not simulate the combustion process, focusing solely on the process of filling the combustion chamber with hydrogen. The CFD flow analysis was performed in SolidWorks Flow Simulation. The engine geometry was mapped using reverse engineering techniques. The software uses the k–ε (k–epsilon) turbulent model – or more precisely, a modified version of the k–ε model adapted to CFD engineering applications. Similar simplifications in CFD setup were employed in external aerodynamics studies of UAVs, where mesh density and CAD model fidelity were adjusted to balance computational cost and simulation accuracy [42]. The mesh was

based on cubes and consisted of 8037 cells and 4585 fluid cells that bordered the solid material. The basic mesh had the size Nx = 10, Ny = 14, Nz = 12. The critical locations of the mesh were automatically densified to increase the accuracy of the calculations. The authors are aware of the small number of cells, but this is a preliminary study aimed at investigating the problem. In the future, simulation studies will be conducted with a much more refined mesh, and the results will be compared. Figure 3 shows a basic mesh model of the Yamaha EH65 engine.

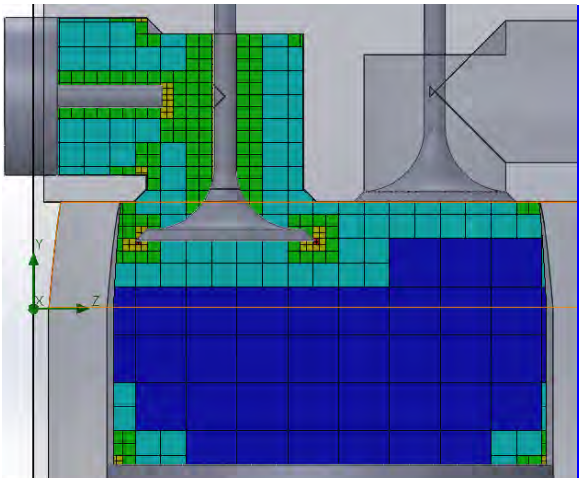

Fig. 3. Yamaha EH65 engine basic mesh model

The initial/boundary conditions of the working medium parameters in the intake manifold were assumed in accordance with the measurements of the actual engine running on standard Pb 95 gasoline. The test scenario assumed two different locations for mounting the injector tip. The first is 8 mm from the intake valve stem axis, and the second is 12 mm from the exact location. The location of the injector tip in the intake manifold lumen is consistent with the location of the additional gas injector sockets shown in Fig. 2. The injector nozzle distance depends on the factory HANA H2001 Gold injector fuel channel extensions. Two lengths are available to approximate the dimensions specified. Figure 4 shows the location of the injection tip at a distance of 8 mm from the valve stem axis.

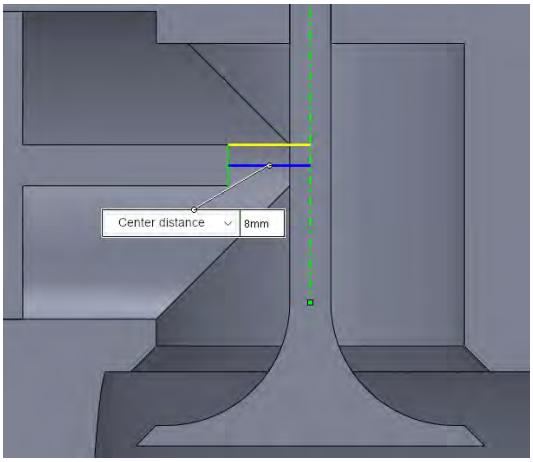

Fig. 4. The location of the injection tip at a distance of 8 mm from the valve stem axis

Another parameter that was changed during the tests was the hydrogen injection profile. The calculated hydrogen injection of 0.15 kg/s for one work cycle completely replaces the energy dose of gasoline necessary to operate the engine at a rotational speed of 3000 rpm. The injection dose and rotational speed parameters were selected in accordance with the actual operating parameters of the engine, which is the driving element of the mobile generator. Injection profile A, shown in Fig. 5, introduces a dose of hydrogen at one peak at 4 milliseconds.

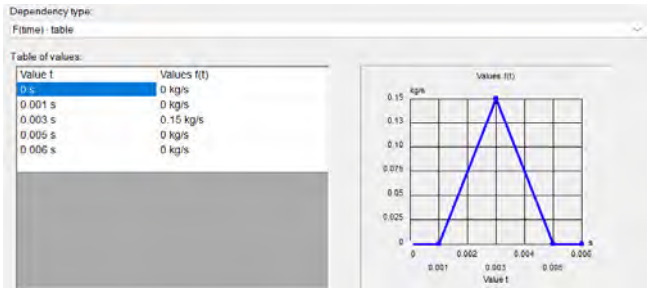

Fig. 5. Injection profile A

Injection profile B, shown in Fig. 6, on the other hand, spreads the fuel dose, reducing the dose peak by half while maintaining the injection time.

Fig. 6. Injection profile B

The results were presented in time windows, which were chosen to show the hydrogen injection process optimally. The selected windows are 0.001, 0.0011, 0.0012, 0.0014, 0.0016, 0.0018, 0.002, 0.0022, 0.0028, 0.004, 0.005 seconds.

3.3. Justification for the selection of parameters and simulation methods

The main assumptions of the CFD model result from the need to analyze the mechanisms of hydrogen mixing with air in the intake valve area and the initial phase of cylinder filling. The literature [2, 27] emphasizes that intake geometry, injection timing, and H_2 stream parameters significantly impact the homogeneity of the mixture and the formation of depleted or enriched zones. The selection of two injection profiles (pulsed – A and distributed – B) and two injector tip locations (8 mm and 12 mm from the valve stem axis) reflects typical strategies used in experiments and CFD analyses [47]. Studies [34] have shown that a shorter injector tip distance promotes vorticity intensification and improves mixing. In turn, the B-profile, extended in time,

limits local excess hydrogen concentration, reducing the risk of pre-ignition or knocking [8, 13].

The simulations were performed without considering the combustion reaction, allowing the focus to be only on the mixing and flow phases. This approach is commonly used in preliminary work on H2-ICE engines and is confirmed in the literature [16, 47].

Additionally, the adopted mesh size and local densities in critical regions (e.g., injector area) ensure adequate accuracy of the flow analysis without excessive increases in computational costs.

4. Results

4.1. Effect of injector location

The simulation results include a spatial-temporal analysis of hydrogen distribution in the intake system for different injector location variants (8 mm and 12 mm) and two injection time profiles (A and B). The simulations were performed in the time range from 0.001 s to 0.005 s.

The numerical simulations detailed the hydrogen flow patterns under varying injector positions and injection profiles. Figures 3–5 and the accompanying data snapshots illustrate transient behavior in the intake manifold at critical time frames (0.001 s to 0.005 s).

When the injector was positioned closer to the intake valve stem (8 mm), the resulting hydrogen jet exhibited higher penetration velocity and more direct alignment with intake airflow. This configuration enhanced local turbulence intensity, promoting better initial mixing with ambient air.

In contrast, positioning the injector further away (12 mm) led to a wider dispersion pattern but slower penetration, suggesting increased residence time for mixture formation but potentially less directional control.

For the configuration with the injector placed 8 mm from the intake valve, faster spray penetration, and a more dispersed hydrogen distribution are observed in the initial injection phases (t = 0.001–0.002 s). In the 12 mm configuration, the spray has a more directed character, and the high-concentration region remains longer near the injector. These differences are apparent in the isosurfaces shown in Fig. 7 (columns 1 and 3). For t = 0.005 s, hydrogen spreads towards the intake valve in both cases, but the 8 mm configuration shows a more uniform distribution.

4.2. Effect of injection profile

Injection Profile A (sharp 4 ms pulse) caused a strong, concentrated fuel jet. While this led to rapid mixture generation, it also increased the risk of localized stratification.

Injection Profile B, which delivered hydrogen over the same period with lower peak flow, produced a more homogeneous distribution and better integration with the in-cylinder swirl.

Profile A (shorter pulse) generates a more focused stream with a transparent hydrogen concentration gradient along the injection axis. Profile B (extended injection time) results in a broader gas distribution in the manifold space. For the same injector position (e.g., 8 mm), Fig. 7 (columns 1 and 2) simultaneously shows apparent differences in the stream geometry and isosurface range. For profile B, the stream reaches a greater lateral range, which may affect the mixing conditions at the intake valve.

4.3. Combined effects

The best mixing performance – assessed visually by spatial uniformity and flow symmetry – is observed for the 8 mm injector distance using Injection Profile B. This configuration showed early-stage uniform fuel-air mixing with minimal backflow or stagnation zones.

The most uniform hydrogen distribution in the collector volume was obtained for the configuration with the injector placed 8 mm from the intake valve and time profile B. In this configuration, the hydrogen concentration isosurfaces show the most excellent coverage of space, which may indicate favorable conditions for mixture homogeneity. The distribution details are shown in Fig. 7 in the bottom row.

5. Discussion

The simulations demonstrate that piston crown geometry and intake conditions must be designed with an injection strategy to optimize hydrogen fuel delivery in ICEs.

The closer injector location (8 mm) benefits from the kinetic energy of the intake stream, enabling better entrainment and momentum coupling. Although less aggressive, Profile B avoids sharp flow transitions, reducing swirl destabilization.

These results align with findings from [4] and [5], emphasizing the critical interplay between injection dynamics and in-cylinder turbulence for hydrogen engines.

5.1. Implications for combustion

Optimized mixture formation not only supports more complete combustion but also addresses typical issues in hydrogen-fueled ICEs:

- Backfire and pre-ignition mitigation via smoother concentration gradients.
- NO_x control through stratification avoidance and lower local temperatures.

The studies [13] showed that the homogeneity of the mixture directly affects the reduction of knock combustion zones and local overheating, which correlates with the efficiency of the B injection profile observed in this work. Therefore, the 8 mm + B configuration can reduce cycle variability and improve ignition stability, which is crucial in ignition systems with many starts [20].

5.2. Simulation limitations

The simulations use simplified geometry and mesh resolution, which may not fully capture fine-scale turbulence or heat exchange effects.

The lack of combustion phase modeling restricts conclusions to pre-ignition flow behavior.

The limitation of the flow phase, without modeling of chemical reactions, is typical for preliminary analyses in H2-ICE projects [16]. Failure to consider thermal losses and material properties (e.g., thermal conductivity of the piston crown) may lead to an underestimation of the influence of local temperature gradients on spontaneous ignition. In the following steps, it is worth considering including combustion submodels (e.g., Zeldovich for NO_x) and validation using optical methods (e.g., TLIF) [8]. According to Vasudev et al. [45], a validated integration of mixing models with thermo-kinetic combustion submodels enables accurate ignition timing and pollutant formation prediction.

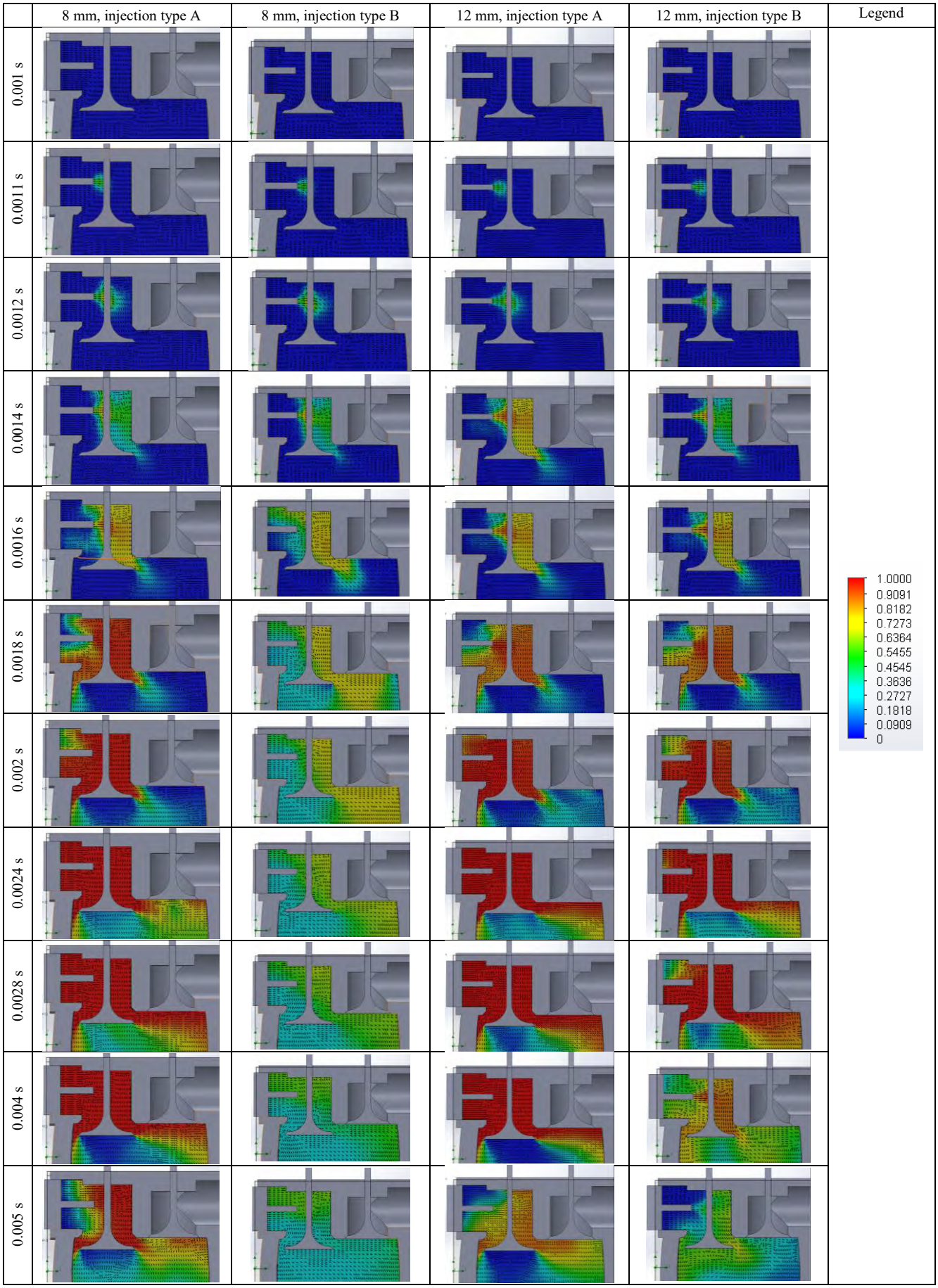

Fig. 7. The data snapshots illustrate transient behaviour in the intake manifold at critical time frames (0.001 s to 0.005 s)

This highlights the importance of extending CFD simulations beyond the intake phase in future work.

Despite these constraints, the study provides a valuable parametric baseline for future experimental validation and full-cycle combustion modeling.

6. Conclusion

The conducted CFD simulations have confirmed that the hydrogen injection strategy – specifically injector location and temporal profile – has a decisive impact on mixture homogeneity and spatial fuel distribution within the intake manifold.

Key conclusions are as follows:

- Injector placement 8 mm from the intake valve results in higher flow penetration velocity and better mixing due to the synergy with intake air momentum
- With a temporally extended hydrogen dose, Injection Profile B reduces concentration gradients and mitigates local stratification zones
- Combining 8 mm positioning with Profile B yields the most favorable conditions for air–hydrogen mixing, suggesting benefits in terms of combustion stability and NO_x mitigation.

Despite being combustion-free, the simulation approach offers valuable insights into pre-ignition mixture dynamics and supports further experimental work.

These findings reinforce the importance of coordinated optimization of the intake geometry, injector configuration, and injection parameters in developing hydrogen-powered ICEs.

In the next stage of the work, the following is planned:

- Implement full-cycle simulations that take into account the modeling of the combustion process, including the mechanisms of nitrogen oxide formation (e.g., Zeldowicz model)
- Experimental validation of results using advanced optical diagnostics, such as laser-induced fluorescence (TLIF) or Schlieren imaging
- Extension of analyses to multi-cylinder configurations and assessment of the impact of variable load conditions on mixing efficiency and engine stability.

Acknowledgments

This work was supported by the Dean of the Faculty of Automotive and Construction Machinery Engineering, Warsaw University of Technology.

Bibliography

[1] Aljabri H, Silva M, Houidi MB, Liu X, Allehaibi M, Almatrafi F et al. Comparative study of spark-ignited and prechamber hydrogen-fueled engine: a computational approach. Energies. 2022;15(23):8951. https://doi.org/10.3390/en15238951

[2] Anaclerio G, Capurso T, Torresi M, Camporeale SM. Numerical characterization of hydrogen under-expanded jets with a focus on internal combustion engines applications. Int J Engine Res. 2023;24(8):3342-3358. https://doi.org/10.1177/14680874221148789

[3] Arsie I, Battistoni M, Brancaleoni PP, Cipollone R, Corti E, Di Battista D et al. A new generation of hydrogen-fueled hybrid propulsion systems for the urban mobility of the future. Energies. 2023;17(1):34. https://doi.org/10.3390/en17010034

[4] Azeem N, Beatrice C, Vassallo A, Pesce F, Rossi R, Khalid A. Review and evaluation of metals and alloy's compatibility with hydrogen-fueled internal combustion engines. Int J Engine Res. 2023;24(9):4204-4225. https://doi.org/10.1177/14680874231184981

[5] Bednarski M, Gis M, Wojs M.K. Global transport challenges in reducing harmful emissions: selected examples for Polish Part of Trans-European Road Network (TERN). In: Pokojski J, Gil M, Newnes L, Stjepandić J, Wognum N (eds). Advances in Transdisciplinary Engineering. IOS Press 2020. https://doi.org/10.3233/ATDE200132

[6] Bera P, Drzewosz A. A novel formula for calculating the dynamic torque of an engine based on its geometric parameters and static measurements. Energies. 2024;17(20):5036. https://doi.org/10.3390/en17205036

[7] Biswas S, Naik AK, Kashyap K. A review of hydrogen storage system (HSS) and hydrogen internal combustion engine (H2-ICE) for the potential H2-ICE vehicle. SAE Technical Paper 2024-28-0129. 2024. https://doi.org/10.4271/2024-28-0129

[8] Blotevogel T, Hartmann M, Rottengruber H, Leipertz A. Tracer-based laser-induced fluorescence measurement technique for quantitative fuel/air-ratio measurements in a hydrogen internal combustion engine. Appl Opt. 2008;47(35): 6488. https://doi.org/10.1364/AO.47.006488

[9] Boretti A. Hydrogen internal combustion engines to 2030. Int J Hydrogen Energ. 2020;45(43):23692-23703. https://doi.org/10.1016/j.ijhydene.2020.06.022

[10] Buzzi L, Biasin V, Galante A, Gessaroli D, Pesce F, Tartarini D et al. Experimental investigation of hydrogen combustion in a single cylinder PFI engine. Int J Engine Res. 2024;25(2):358-372. https://doi.org/10.1177/14680874231199641

[11] Czyż Z, Karpiński P, Koçak S. Numerical analysis of the influence of particular parts of the high efficient electric vehicle on the aerodynamic forces. Adv Sci Technol Res J. 2019;13(4):1-7. https://doi.org/10.12913/22998624/112835

[12] Dhyani V, Subramanian KA. Control of backfire and NO_x emission reduction in a hydrogen fueled multi-cylinder spark ignition engine using cooled EGR and water injection strategies. Int J Hydrogen Energ. 2019;44(12):6287-6298. https://doi.org/10.1016/j.ijhydene.2019.01.129

[13] Falfari S, Cazzoli G, Mariani V, Bianchi G. Hydrogen application as a fuel in internal combustion engines. Energies. 2023;16(6):2545. https://doi.org/10.3390/en16062545

[14] Fan B, Pan J, Liu Y, Zhu Y, Pan Z, Chen W et al. Effect of hydrogen injection strategies on mixture formation and combustion process in a hydrogen direct injection plus natural gas port injection rotary engine. Energ Convers Manage. 2018;160:150-164. https://doi.org/10.1016/j.enconman.2018.01.034

[15] Gal T, Schmelcher R, Vacca A, Cupo F, Chiodi M, Casal Kulzer A. Modeling of hydrogen combustion from a 0D/1D analysis to complete 3D-CFD engine simulations. Energies. 2024;17(22):5543. https://doi.org/10.3390/en17225543

[16] Gammaidoni T, Miliozzi A, Zembi J, Battistoni M. Hydrogen mixing and combustion in an SI internal combustion engine: CFD evaluation of premixed and DI strategies. Case Studies in Thermal Engineering. 2024;55: 104072. https://doi.org/10.1016/j.csite.2024.104072

[17] Gao J, Wang X, Song P, Tian G, Ma C. Review of the backfire occurrences and control strategies for port hydrogen injection internal combustion engines. Fuel. 2022;307:121553. https://doi.org/10.1016/j.fuel.2021.121553

[18] Gargouri A, Jemni MA, Kchaou H. Guide swirl and tumble systems effect on the aerodynamic flow of the cylinder in an SI engine using a hydrogen-enriched blend. Arab J Sci Eng. 2024;50:9405-9429. https://doi.org/10.1007/s13369-024-09461-0

[19] Höhne T, Mamedov T. CFD simulation of aeration and mixing processes in a full-scale oxidation ditch. Energies. 2020;13(7):1633. https://doi.org/10.3390/en13071633

[20] Huang H, Xue X, Liu Y, Zhao J, Tian M, Niu Y. Numerical studies of a water-cooled premixed burner for low NO_x combustion of natural gas. J Energy Inst. 2024;114:101647. https://doi.org/10.1016/j.joei.2024.101647

[21] Huang RF, Huang CW, Chang SB, Yang HS, Lin TW, Hsu WY. Topological flow evolutions in cylinder of a motored engine during intake and compression strokes. J Fluid Struct. 2005;20(1):105-127. https://doi.org/10.1016/j.jfluidstructs.2004.09.002

[22] Huang Z, Liu B, Zeng K, Huang Y, Jiang D, Wang X et al. Experimental study on engine performance and emissions for an engine fueled with natural gas−hydrogen mixtures. Energy Fuels. 2006;20(5):2131-2136. https://doi.org/10.1021/ef0600309

[23] Jose A, Probst D, Biware M. A machine learning approach for hydrogen internal combustion (H2ICE) mixture preparation. SAE Technical Paper 2024-26-0254. 2024. https://doi.org/10.4271/2024-26-0254

[24] Khalid AH, Muhamad Said MF, Veza I, Abas MA, Roslan MF, Abubakar S et al. Hydrogen port fuel injection: review of fuel injection control strategies to mitigate backfire in internal combustion engine fuelled with hydrogen. Int J Hydrogen Energ. 2024;66:571-581. https://doi.org/10.1016/j.ijhydene.2024.04.087

[25] Konstantinoff L, Möltner L, Pillei M, Steiner T, Dornauer T, Herdin G et al. Optimization of the charge motion in internal combustion engines driven by sewage gas for combined heat and power units. J Eng Gas Turb Power. 2018;140(10): 102805. https://doi.org/10.1115/1.4039756

[26] Lee K, Bae C, Kang K. The Effects of Tumble and Swirl Flows on Flame Propagation in a Four-Valve S.I. engine. Appl Therm Eng. 2007;27(11-12):2122-2130. https://doi.org/10.1016/j.applthermaleng.2006.11.011

[27] Li Y, Gao W, Zhang P, Ye Y, Wei Z. Effects study of injection strategies on hydrogen-air formation and performance of hydrogen direct injection internal combustion engine. Int J Hydrogen Energ. 2019;44(47): 26000-26011. https://doi.org/10.1016/j.ijhydene.2019.08.055

[28] Liang M, Su J, Liu RW, Lam JSL. AISClean: AIS data-driven vessel trajectory reconstruction under uncertain conditions. Ocean Eng. 2024;306:117987. https://doi.org/10.1016/j.oceaneng.2024.117987

[29] Liu H, Ma J, Tong L, Ma G, Zheng Z, Yao M. Investigation on the potential of high efficiency for internal combustion engines. Energies. 2018;11(3):513. https://doi.org/10.3390/en11030513

[30] Lu C, Chen W, Zuo Q, Kou C, Wang H, Xiao G et al. numerical investigation on gaseous fuel injection strategies on combustion characteristics and NO emission performance in a pure hydrogen engine. Fuel. 2024;363:130911. https://doi.org/10.1016/j.fuel.2024.130911

[31] Mattarelli E, Fontanesi S, Rinaldini C, Valentino G, Iannuzzi S, Severi E et al. Combustion optimization of a marine DI diesel engine. SAE Technical Paper 2013-24-0020. 2013. https://doi.org/10.4271/2013-24-0020

[32] Menariya PG, Shinde V. Exploring the impacts of hydrogen internal combustion engine (H2 ICE) technology on vehicle thermal systems (radiator and charge air cooler): a review. SAE Technical Paper 2024-28-0051. 2024. https://doi.org/10.4271/2024-28-0051

[33] Mohamed M, Biswal A, Wang X, Zhao H, Harington A, Hall J et al. Exploring the benefits of hydrogen-water injection technology in internal combustion engines: a rigorous experimental study. Int J Engine Res. 2025;26(5):724-740. https://doi.org/10.1177/14680874241288624

[34] Mota Ferreira J, Oung R, Foucher F. Effect of in-cylinder flow motion on fuel-air mixture formation in a medium-duty DI-SI H2 engine: an experimentally supported CFD study. SAE Technical Paper 2024-01-2117. 2024. https://doi.org/10.4271/2024-01-2117

[35] Nieminen J, D'Souza N, Dincer I. Comparative combustion characteristics of gasoline and hydrogen fuelled ICEs. Int J Hydrogen Energ. 2010;35(10):5114-5123. https://doi.org/10.1016/j.ijhydene.2009.08.098

[36] Pashchenko D. Comparative analysis of hydrogen/air combustion CFD-modeling for 3D and 2D computational domain of micro-cylindrical combustor. Int J Hydrogen Energ. 2017;42(49):29545-29556. https://doi.org/10.1016/j.ijhydene.2017.10.070

[37] Pashchenko D. Hydrogen-rich fuel combustion in a swirling flame: CFD-modeling with experimental verification. Int J Hydrogen Energ. 2020;45(38):19996-20003. https://doi.org/10.1016/j.ijhydene.2020.05.113

[38] Rabault J, Vernet JA, Lindgren B, Alfredsson PH. A study using PIV of the intake flow in a diesel engine cylinder. Int J Heat Fluid Fl. 2016;62:56-67. https://doi.org/10.1016/j.ijheatfluidflow.2016.06.020

[39] Salvi BL, Subramanian KA. Experimental investigation on effects of compression ratio and exhaust gas recirculation on backfire, performance and emission characteristics in a hydrogen fuelled spark ignition engine. Int J Hydrogen Energ. 2016;41(13):5842-5855. https://doi.org/10.1016/j.ijhydene.2016.02.026

[40] Srivastava A, Ramesh CS. Study on structural stability and thermal analysis of intake manifold valve through numerical analysis. SAE Technical Paper 2023-01-0989. 2023. https://doi.org/10.4271/2023-01-0989

[41] Stępień Z. A comprehensive overview of hydrogen-fueled internal combustion engines: achievements and future challenges. Energies. 2021;14(20):6504. https://doi.org/10.3390/en14206504

[42] Szczepaniak R, Czyż Z, Bąbel R, Mańka A, Zahorski T, Omen Ł et al. Analysis of the basic aerodynamic characteristics of an unmanned combat aerial vehicle based on a CAD model. Adv Sci Technol Res J. 2025;19(6):235-247. https://doi.org/10.12913/22998624/201434

[43] Traversari R, Rossi A, Faretra M. Virtual prototyping technique applied to the design of a process reciprocating compressor. ASME 2011 World Conference on Innovative Virtual Reality. Milan, ASMEDC 2011:243-252. https://doi.org/10.1115/WINVR2011-5550

[44] Tripathi G, Sharma P, Dhar A, Sadiki A. Computational investigation of diesel injection strategies in hydrogen-diesel dual fuel engine. Sustainable Energy Technologies and Assessments. 2019;36:100543. https://doi.org/10.1016/j.seta.2019.100543

[45] Vasudev A, Mikulski M, Balakrishnan PR, Storm X, Hunicz J. Thermo-kinetic multi-zone modelling of low temperature combustion engines. Prog Energ Combust. 2022;91:100998. https://doi.org/10.1016/j.pecs.2022.100998

[46] Verhelst S, Wallner T. Hydrogen-fueled internal combustion engines. Prog Energ Combust. 2009;35(6):490-527. https://doi.org/10.1016/j.pecs.2009.08.001

[47] Wang Y, Scarcelli R, Bestel D, Demir S, Srna A. Multi-dimensional modeling of mixture formation in a hydrogen-fueled heavy-duty optical engine with direct injection. ASME 2024 ICE Forward Conference. San Antonio, Texas. 2024. V001T06A004. https://doi.org/10.1115/ICEF2024-140413

[48] Winklhofer E, Jocham B, Philipp H, Kapus P, Leitner D, Heindl R et al. Hydrogen ICE combustion challenges. SAE Technical Paper 2023-24-0077. 2023. https://doi.org/10.4271/2023-24-0077

[49] Yang L, Ji S, Niu W, Zare A, Hunicz J, Brown RJ. Effect of split injection strategy of diesel fuel on multi-stage heat release and performance of a RCCI engine fueled with diesel and natural gas. Fuel. 2024;362:130930. https://doi.org/10.1016/j.fuel.2024.130930

[50] Zimakowska-Laskowska M, Laskowski P, Orliński P, Wiśniowski P, Wojs MK. The use of hydrogen as a fuel in road transport on the polish path to climate neutrality – a literature review. Environmental Protection and Natural Resources. 2023;34(4):11-20. https://doi.org/10.2478/oszn-2023-0013

[51] Zimakowska-Laskowska M, Kozłowski E, Laskowski P, Wiśniowski P, Świderski A, Orynycz O. Vehicle exhaust emissions in the light of modern research tools: synergy of chassis dynamometers and computational models. Combustion Engines. 2025;200(1):145-154. https://doi.org/10.19206/CE-201224

[52] Żmudka Z, Postrzednik S, Przybyła G. Throttleless control of SI engine load by fully flexible inlet valve actuation system. Combustion Engines. 2016;164(1):44-48. https://doi.org/10.19206/CE-116488

Marcin Wojs, DEng. – Faculty of Automotive and Construction Machinery Engineering, Warsaw University of Technology, Poland.
e-mail: *marcin.wojs@pw.edu.pl*

Piotr Laskowski, DEng. – Faculty of Automotive and Construction Machinery Engineering, Warsaw University of Technology, Poland.
e-mail: *piotr.laskowski@pw.edu.pl*

Magdalena Zimakowska-Laskowska, DEng. – Environment Protection Centre, Motor Transport Institute, Poland.
e-mail:
magdalena.zimakowska-laskowska@its.waw.pl

Article citation info:
Rymaniak Ł, Pielecha J, Ziółkowski M, Sobczak J, Szymlet N. Comparison of pollutant emissions per passenger for public and individual transport. Combustion Engines. 2026;204(1):52-57. https://doi.org/10.19206/CE-210469

Łukasz RYMANIAK
Jacek PIELECHA
Maciej ZIÓŁKOWSKI
Jakub SOBCZAK
Natalia SZYMLET

Combustion Engines
Polish Scientific Society of Combustion Engines

Comparison of pollutant emissions per passenger for public and individual transport

ARTICLE INFO

Received: 7 August 2025
Revised: 5 September 2025
Accepted: 8 September 2025
Available online: 25 September 2025

The current policy of the European Union aims to reduce the negative impact of the transport sector on the emission of pollutants generated by combustion engines into the atmosphere. One of the key trends in this expansion is to increase the share of public transport. The article presents a scenario of passenger travel in an urban agglomeration, using a passenger car and a bus. The input data were obtained from tests carried out under real operating conditions using PEMS (Portable Emissions Measurement Systems) equipment. Both objects tested met the same emission standard – Euro 5/V. The obtained pollutant emission values were converted into emissions generated by passengers. The results show that travelling by bus has a much lower impact on the environment, but the journey time is longer and requires the bus schedule to be adjusted to the travel plan.

Key words: *city bus, exhaust emission, passenger car, passenger travel, PEMS*

1. Introduction

The European Union's sustainable development policy is important in the context of protecting the environment, which must be safeguarded for future generations [3]. This issue is significant in the context of civilisational development, which is often associated with the use of natural resources or the degradation of the planet. One of the most serious consequences is the creation of pollution, which intensifies smog, acid rain, and the greenhouse effect, and has a destructive impact on human health [15]. Transport plays an important role here, as it is primarily based on the combustion of fossil fuels – combustion engines and the production of electricity for electric vehicles. The latter source is characterised by different indicators for different regions of Europe and the world [12].

The introduction of emission standards for powertrains, clean transport zones, and other restrictions in the field of transport has a positive impact on environmental protection [1]. Vehicle manufacturers and scientists are constantly working to introduce innovative solutions to improve the ecological parameters of means of transport, including those related to weight, powertrain systems, and travel planning [4, 8, 17]. Current European Union policy and industry activities focus on the use of hydrogen in fuel cells, which is the most promising direction for the automotive industry [5, 9]. However, work is ongoing to assess pollutant emissions as one of the main problems of engine drives [2, 10]. However, it is necessary to continuously educate people about caring for natural resources. In order to ensure good education, it is necessary to provide scientific evidence that will convince people to make efforts to care for the environment, as in the publication [13]. This is the origin of this article, which presents research conducted in real operating conditions on a passenger car equipped with a compression ignition engine and a city bus in order to quantify which means of transport is more environmentally friendly. The results are supplemented by a reference to the pollutant emissions per passenger.

2. Selection of research objects

Based on data from the Central Register of Vehicles and Drivers, at the end of 2023, there were approximately 27 million vehicles in the register, with approximately 7 million being unused vehicles with various histories of termination or long-term interruption of operation [7, 11]. When analysing the average age of passenger cars in Poland, a significant problem can be observed. According to data from the 2022/2023 automotive report, the average age of a passenger car in Poland exceeds 15 years [19]. The exact result is influenced by the determination of the share of the aforementioned unused vehicles. However, the average age indicates that the solutions used in many passenger cars in Poland are outdated, which may also mean increased pollutant emissions. Referring to Central Statistical Office reports, it can be concluded that newer vehicles are used in larger agglomerations. This is particularly evident in the capital, where significant rates of new registrations are achieved. However, it should be remembered that this applies to company vehicles associated with businesses operating or registered in Warsaw.

According to a report by the European Automobile Manufacturers' Association (ACEA) [21], the average age of buses operating in our country is 16 years. For city buses, the rates are highly varied depending on the area of use. In large agglomerations, younger fleets are used. This is due to ongoing investments, a high level of subsidies, and European Union requirements in this regard. On the other hand, older fleets are used on suburban lines and in small towns, often several decades old, with millions of kilometres on the clock.

Based on the data presented on vehicle age and the objective of the article, two research objects were selected. The first was a passenger car with a conventional drive system using a compression ignition engine, referred to in the article as a passenger car (Fig. 1). The manufacturer's declaration ensures compliance with the Euro 5 standard. In terms of internal and external exhaust gas treatment sys-

tems, the following were used: EGR (Exhaust Gas Recirculation), DOC (Diesel Oxidation Catalyst), and DPF (Diesel Particulate Filter). Table 1 presents the basic data on the research object. The maximum torque of 250 Nm is achieved in the range from 1500 to 2500 rpm, thanks to the use of turbocharging. The maximum engine power is 81 kW at 4200 rpm.

Fig. 1. View of the tested passenger car with measuring equipment

Table 1. Characteristics of the research object – passenger car

Parameter	Unit	Value
Year of manufacture	–	2011
Vehicle weight	kg	1266
Layout, number of cylinders, valves	–	In-line, 4, 16
Displacement	dm^3	1.968
Power at rotational speed	kW at rpm	81 at 4200
Torque at rotational speed	Nm at rpm	250 at 1500–2500
Compression ratio	–	16.5:1
Turbocharging	–	turbocharger
Exhaust gas treatment systems	–	EGR, DOC, DPF
Exhaust emission standard	–	Euro 5

The second research object was an 18-metre-long city bus, also with a conventional internal compression ignition engine, referred to in the article as a city bus (Fig. 2). It complied with the EURO V – EEV standard. Table 2 presents the characteristic data of the research object. The maximum torque produced by the engine occurs at a crankshaft speed of 1100 rpm, which indicates its adaptation to urban traffic conditions, where frequent stops and starts are common – particularly important in the case of city buses.

Fig. 2. View of the tested city bus

Table 2. Characteristics of the research object – city bus

Parameter	Unit	Value
Year of manufacture	–	2009
Vehicle weight	kg	16 000
Layout, number of cylinders, valves	–	In-line, 6, 24
Displacement	dm^3	9.186
Power at rotational speed	kW at rpm	228 at 2200
Torque at rotational speed	Nm at rpm	1275 at 1100–1700
Compression ratio	–	17.4:1
Turbocharging	–	turbocharger
Exhaust gas treatment systems	–	EGR, DOC, DPF
Exhaust emission standard	–	EURO V

3. Research methodology

3.1. Measurement equipment

Portable Emissions Measurement Systems (PEMS) were used to test the vehicles, measuring toxic compound concentrations under real operating conditions [6, 16]. The environmental assessment of the passenger car was carried out using the Axion R/S+ device. This analyser enables the measurement of both gaseous compounds and particulate matter concentrations. Non-dispersive infrared analysers were used to measure the concentrations of carbon monoxide, carbon dioxide, and hydrocarbons, which determine the absorbed radiation in a narrow wavelength band characteristic of a given substance. The result obtained is compared with the radiation absorbed by the reference gas [14]. For nitrogen oxides and oxygen concentrations, an electrochemical method is used, based on the conversion of an electrical signal. The exhaust gas flow is calculated using parameters read by the OBD system or information from sensors (rotational speed, temperature, and pressure in the intake system) [20].

The city bus was tested using a Semtech DS device. The device measures hydrocarbon concentrations using a FID (Flame Ionisation Detector) analyser, while carbon monoxide and carbon dioxide concentrations are determined using a non-dispersive infrared analyser, as in the Axion R/S+. The concentration of nitrogen oxides is determined in a non-dispersive analyser using ultraviolet light. A mass exhaust gas flow meter is required to determine the concentrations of harmful compounds [20].

Both instruments were calibrated and prepared for operation in accordance with their instructions before measurements were taken [20, 21]. GPS positioning systems were also used in the study to obtain data on vehicle movement parameters. All calibrated measuring elements acquired data at a frequency of 1 Hz.

Due to the specific nature of real-world operating conditions, especially in urban areas, it is impossible to obtain identical journeys on a given route. The paper presents the results of individual journeys in which uninterrupted, continuous measurements of pollutant emissions and vehicle operating parameters were performed. This is an advantage of road tests over tests in repeatable conditions (e.g. chassis dynamometer, engine dynamometer), as it allows the impact of various factors on the results obtained during road tests to be assessed. In accordance with the accepted and applied standards, the measuring instruments used can be successfully used in tests during actual operation, as they

have the appropriate certificates (including EU 2016/427 compliance). Their data are presented in Table 3.

Table 3. Technical specifications of the portable exhaust emission analyzers: Axion R/S+ and Semtech DS [18, 20]

Axion R/S+		
Parameter	Measurement method	Accuracy
Component concentration:		
CO	NDIR, 0–10%	±3%
HC	NDIR, 0–4 000 ppm	±3%
NO	electrochemical, 0–5000 ppm	±3%
CO_2	NDIR, 0–20%	±3%
O_2	electrochemical, 0–25%	±1%
Semtech DS		
Parameter	Measurement method	Accuracy
Component concentration:		
CO	NDIR, 0–10%	±3%
HC	FID, 0–10 000 ppm	±2.5%
NO_x	NDUV, 0–3000 ppm	±3%
CO_2	NDIR, 0–21%	±3%
O_2	electrochemical, 0–21%	±1%
Exhaust gas flow	mass flow rate	±2.5%
	T_{max} to 700°C	±1%

3.2. Research route

Research on pollutant emissions from research objects was conducted under real operating conditions in the Poznań agglomeration. The research route covered a transport line operated by a local transport company. It ran through the city centre, with the end points being the Dębina and Sobieskiego housing estates in Poznań (Fig. 3). This choice of test route made it possible to compare the results obtained for a passenger car with the emission tests for a city bus. The measurements were carried out on a weekday, around midday. The total length of the test route was 17.2 km. It consisted of sections with varying speed limits (from 30 km/h to 50 km/h).

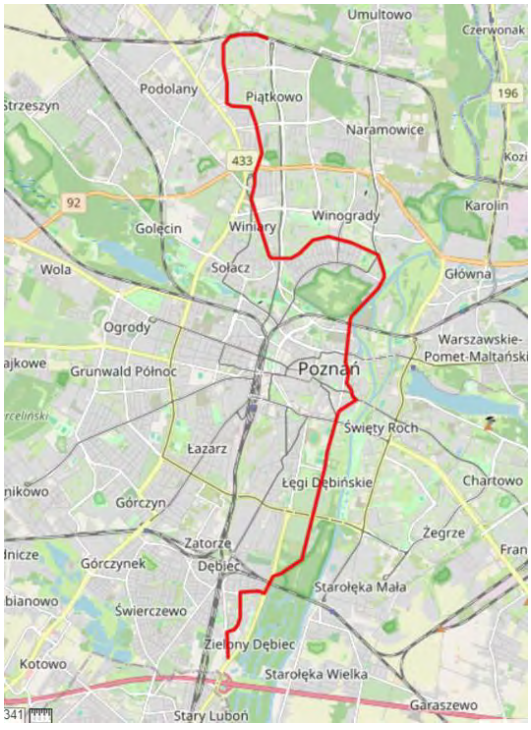

Fig. 3. Research route [19]

4. Analysis of operating conditions of research objects

The bus under test was operating according to the scheduled service on a route operated by the local transport company. To achieve the objective of the study, the passenger car was operated on the same route, but without stopping at bus stops. The characteristics of the speeds achieved by the research objects are presented in Fig. 4. In both measurement cycles, the vehicles achieved similar maximum instantaneous speeds (approximately 50 km/h), which was due to the characteristics of the traffic arteries and the restrictions applied in the agglomeration. The average speeds were 22.6 km/h for passenger car and 15.7 km/h for bus. The city bus achieved a lower average result, which was due to the need to serve passenger stops.

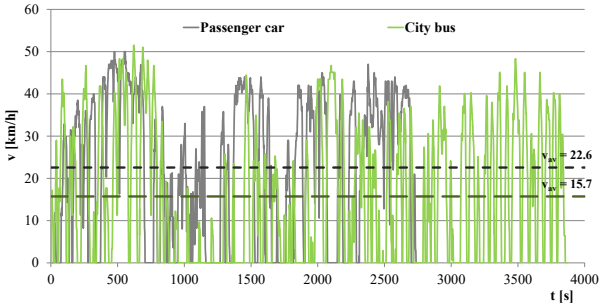

Fig. 4. Velocity characteristics of the research objects

The data collected during measurements in urban traffic conditions concerning vehicle speeds throughout the test and corresponding accelerations are presented as a function of time density. Figure 5 shows the characteristics of vehicle operation during test runs.

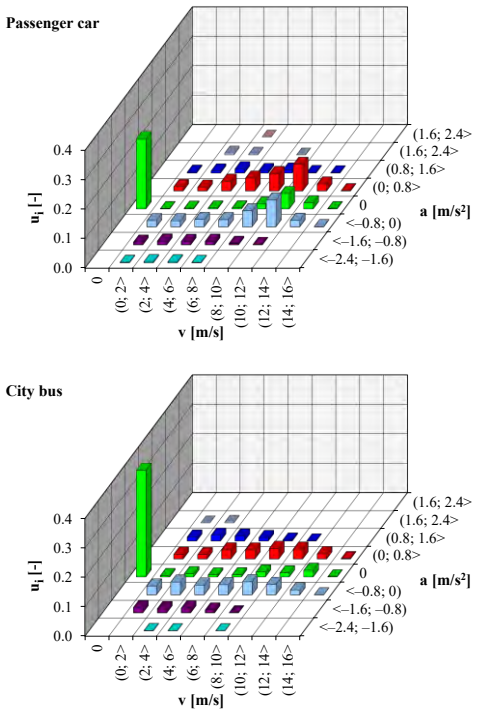

Fig. 5. Shares of vehicles operating time in speed and acceleration compartments during road tests

In both tests, the largest share of operating time was recorded for stops, respectively: 24% for passenger cars and 36% for city buses. The data presented shows that neither vehicle moved for almost a quarter of the test journey, which was due to the traffic conditions in the city centre. The greater share of operating time spent by city buses at stops was due to serving bus stops. The values for the extreme intervals are the lowest, which indicates that sudden braking or acceleration occurred very rarely. For both vehicles, accelerations above 0.8 m/s^2 accounted for up to 7% of the test time, and decelerations below –0.8 m/s^2 accounted for up to 6% of the test time. In total, therefore, acceleration values exceeded the ±0.8 m/s^2 range for approximately 13% of the test time. Referring to the traffic results at a constant speed, where a = 0 m/s^2, 10% and 8% of the test time were obtained for the objects, respectively. Apart from the aforementioned ranges at zero acceleration, the passages were dominated by conditions in the range of accelerations from –0.8 m/s^2 to 0.8 m/s^2.

5. Comparison of environmental indicators for vehicles

Based on the data recorded by the analysers and auxiliary devices, the road emissions of the research objects during the tests were determined (Fig.6). Based on the results obtained, it can be concluded that the city bus achieved approximately three times higher CO_2 road emissions (1230 g/km). This harmful compound is directly dependent on fuel consumption, which was undoubtedly influenced by the weight of the tested objects.

Road emissions of CO and HC were several times higher for the passenger car, which achieved 9.84 g/km (approximately 4 times more than the bus) and 1.88 g/km (approximately 3 times more than the bus), respectively. The design of the drive systems had a significant impact on these differences in results. The combustion engine of a city bus, together with the gearbox, is designed for the characteristic operating conditions on city routes – frequent stops and accelerations. The crankshaft speed range is limited, and the rated torque parameters are already present from 1100 rpm. A passenger car's drive system must be more versatile, i.e. it is designed for use not only in urban conditions, but also in non-urban conditions and on motorways. The combustion engine used operates in a much wider range of crankshaft speeds. During the tests, the passenger car did not simulate stop operations. Frequent stops related to urban infrastructure had a direct impact on the occurrence of unstable operating conditions of the combustion engine. This confirms that the road emission results obtained indicate a significant contribution of incomplete and partial combustion to the processes occurring inside the combustion engine.

NO_x emissions in internal combustion processes are directly related to engine load and thus to the temperatures occurring at the flame front. For a passenger car, the specified value of the aforementioned relationship reached 1.08 g/km. This was approximately 10 times lower than for a bus (9.87 g/km). It should be noted that in a passenger car, the EGR system was primarily responsible for limiting NO_x emissions. In contrast, in the city bus, in addition to EGR, an SCR (Selective Catalytic Reduction) system was used. However, it should be noted that its operation is not continuous and depends on the parameters of the exhaust gas flow (temperature, mass flow).

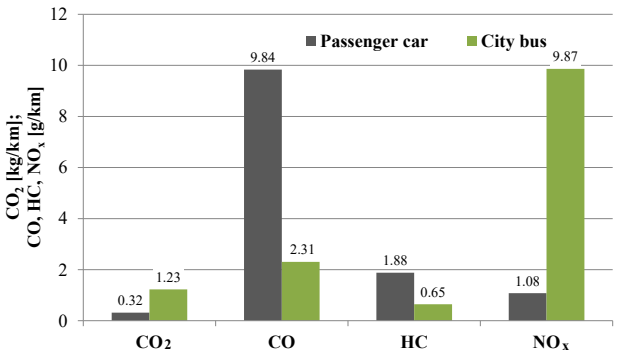

Fig. 6. Road emission of toxic compounds for research objects

The relationship between road emissions and the number of passengers is shown in Fig. 7. For a passenger car, the maximum number of passengers could be 5. However, during testing under real operating conditions, there were 2 people in the vehicle: the driver and the equipment operator. The entire set of apparatus, including electrical energy storage devices, weighs approximately 60 kg. The pollutant emission results obtained were divided by 3, thus taking into account the weight of the measuring equipment. In the case of a city bus, the vehicle configuration allowed for 40 seats and 135 standing places. The bus load was assumed to be 50% of capacity due to the high passenger traffic on this route, so the road emission value obtained was divided by 88. This value was adopted based on passenger exchange on the bus during testing, and the guidelines contained in EU Regulation 582/2011 were also taken into account.

Based on the determined relationships, it was concluded that public transport is significantly more environmentally friendly than individual transport, such as the passenger car analysed. The CO_2 emissions balance would be equal between the two vehicles if 10 people travelled on the bus. For NO_x, similar values would be achieved when transporting 25 people in a city bus. City buses are public transport vehicles used for the mass transport of people over short distances in urban traffic conditions. Passenger cars have far fewer seats and are not designed exclusively for use in urban traffic.

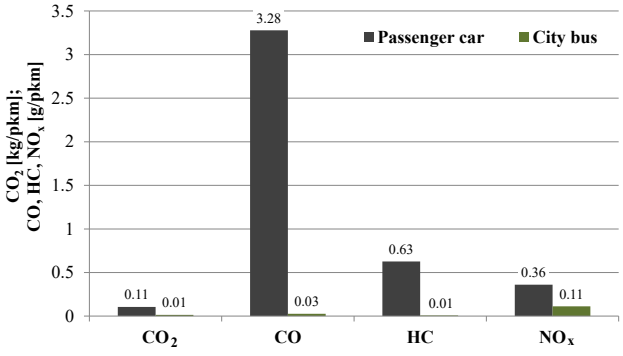

Fig. 7. Summary of road emissions per passenger during tests

6. Emissions from vehicles in urban areas

Passenger cars remain an important element of the transport system in urban areas, accounting for a significant proportion of daily passenger transport. Considering the key role of passenger cars in cities and their average age in Poland, it can be assumed that a significant percentage of vehicles in use are less technically efficient, which may result in higher levels of pollutant emissions. In addition, the long-term use of conventionally powered passenger cars exclusively for short journeys (e.g. commuting to work, service premises, etc.) is disadvantageous both in terms of pollutant emissions and vehicle operation. Such use hinders the effective operation of exhaust gas treatment systems and may also result in increased fuel and engine oil consumption, as well as accelerated mechanical wear of engine components.

The emission results for passenger cars and city buses per passenger clearly show that public transport is more advantageous. This is due to the significantly greater capacity of such vehicles. Another important aspect is that, regardless of the traveller's choice of transport, public transport vehicles will continue to run their routes because they operate according to a pre-determined timetable. In this respect, when analysing pollutant emissions, it was found that pollutant emissions from city buses will occur anyway (in amounts depending on the number of passengers), while pollutant emissions from passenger cars are an additional burden on the environment. For this reason, public transport should be used, as increasing the number of passengers also reduces the rate of harmful emissions per passenger.

However, it is not always possible to use public transport exclusively. In this case, it is environmentally beneficial to travel by car with a larger number of passengers. Therefore, in order to reduce harmful emissions into the atmosphere, solutions such as carpooling should be promoted. This is a form of travel that involves sharing a car journey with several people (at least two) travelling on the same or a similar route. This is not a form of commercial activity – the driver does not make a profit from the journey, but only receives compensation for the costs incurred. Thanks to this solution, it is possible to use the space in vehicles more efficiently, reduce the number of vehicles on the road, and limit the amount of pollution per passenger.

7. Summary

The research conducted revealed differences in the operational characteristics of passenger cars and city buses. Despite similar maximum speeds achieved in urban traffic, the average speed of a passenger car was higher (22.6 km/h) than that of a bus (15.7 km/h), which was due to the need for public transport vehicles to serve stops. An analysis of the distribution of accelerations and decelerations showed that both vehicles were stationary for a significant part of the time (24% for cars and 36% for buses), which is characteristic of congested urban infrastructure.

The research revealed significant differences between the vehicles analysed. Due to its greater weight and fuel consumption, the city bus generated approximately three times more CO_2 emissions (1230 g/km) than the passenger car (320 g/km), but had significantly lower CO and HC emissions thanks to the adaptation of the drive system to urban conditions. On the other hand, NO_x emissions were significantly higher for buses (9.87 g/km) than for passenger cars (1.08 g/km), which was due to different exhaust gas reduction systems and drive unit loads. However, when emissions were related to the number of passengers, public transport clearly had the advantage – even when the public transport vehicle was only partially full, the unit emissions per passenger were significantly lower. This means that, from an environmental perspective, the development and promotion of public transport is a key element in reducing emissions in urban areas.

Passenger cars, despite their important role in everyday urban transport, generate a significant environmental burden, especially due to their high average age and unfavourable operating conditions on short journeys. Inefficient exhaust gas treatment systems and intensive mechanical wear increase pollutant emissions, which, when calculated per passenger, make individual transport less efficient than public transport. City buses, which operate on fixed routes regardless of the number of passengers, have a more favourable emissions balance per person. Therefore, in order to reduce the negative impact of transport, it is necessary to promote alternative solutions, such as public transport or carpooling, which, through more efficient use of vehicles, can reduce the number of cars on the roads and the level of emissions in cities.

Acknowledgements

The study presented in this article was performed within statutory research (No. 0415/SBAD/0362).

Nomenclature

a	acceleration
CI	compression ignition
DOC	diesel oxidation catalyst
DPF	diesel particulate filter
EGR	exhaust gas recirculation
PEMS	portable emissions measurement systems
SCR	selective catalytic reduction
t	time
u_i	share of working time
v	velocity

Bibliography

[1] Glazener A, Khreis H. Transforming our cities: best practices towards clean air and active transportation. Current Environmental Health Reports. 2019;6(1):22-37. https://doi.org/10.1007/s40572-019-0228-1

[2] Kadyrov A, Warguła Ł, Kukesheva A, Dyssenbaev Y, Kaczmarzyk P, Klapsa W et al. Optimization of vertical ultrasonic attenuator parameters for reducing exhaust gas smoke of compression-ignition engines: efficient selection of emit-

ter power, number, and spacing. Appl Sci. 2025;15(14): 7870. https://doi.org/10.3390/app15147870
[3] Kenig-Witkowska MM. The concept of sustainable development in the European Union policy and law. JCULP. 2017;1:64.
[4] Kowalczyk J, Matysiak W, Sawczuk W, Wieczorek D, Sędłak K, Nowak M. Quality tests of hybrid joint – clinching and adhesive – case study. Appl Sci. 2022;12(22):11782. https://doi.org/10.3390/app122211782
[5] Kurc B, Gross X, Szymlet N, Rymaniak Ł, Woźniak K, Pigłowska M. Hydrogen-powered vehicles: a paradigm shift in sustainable transportation. Energies. 2024;17(19):4768. https://doi.org/10.3390/en17194768
[6] Merkisz J, Gallas D, Siedlecki M, Szymlet N, Sokolnicka B. Exhaust emissions of an LPG powered vehicle in real operating conditions. EDP Sciences. 2019:00053. https://doi.org/10.1051/e3sconf/201910000053
[7] Piątek P. Ile jest w Polsce samochodów? Mamy nowe dane o liczbie i wieku pojazdów (in Polish). motofakty.pl. 2024. https://motofakty.pl/ile-jest-w-polsce-samochodow-mamy-nowe-dane-o-liczbie-i-wieku-pojazdow/ar/c4-18400955 (accessed on 06.2025).
[8] Pielecha I, Sidorowicz M. Effects of mixture formation strategies on combustion in dual-fuel engines – a review. Combustion Engines. 2021;60(1):30-40. https://doi.org/10.19206/CE-134237
[9] Pielecha I, Szwajca F. Experimental study and modeling of an air-cooled proton exchange membrane fuel cell stack in the static and dynamic performance. Eksploat Niezawodn. 2024;26(2). https://doi.org/10.17531/ein/184232
[10] Pielecha J, Kurtyka K. Exhaust emissions from Euro 6 vehicles in WLTC and RDE – part 1: methodology and similarity conditions studies. Energies. 2023;16(22):7465. https://doi.org/10.3390/en16227465
[11] Pryciński P, Pielecha J, Korzeb J, Jachimowski R, Pielecha P. Impact of vehicle aging and mileage on air pollution emissions. Energies. 2025;18(4):939. https://doi.org/10.3390/en18040939
[12] Scarlat N, Prussi M, Padella M. Quantification of the carbon intensity of electricity produced and used in Europe. Appl Energy. 2022;305:117901. https://doi.org/10.1016/j.apenergy.2021.117901
[13] Siedlecki M, Ziółkowski A, Ratajczak K, Bednarek M, Jagielski A, Igielska-Kalwat J. Analysis of the impact of the comfort systems in sport utility vehicles on the exhaust emissions measured under worldwide harmonized light vehicles test cycles conditions. Journal of Ecological Engineering. 2024;25(12). https://doi.org/10.12911/22998993/193754
[14] Szymlet N. Emisja związków toksycznych z miejskich pojazdów jednośladowych w rzeczywistych warunkach eksploatacji (in Polish). Doctoral Thesis. Poznana Univeristy of Technology. Poznan 2022.
[15] Wojtal R. Zanieczyszczenie powietrza w miastach w aspekcie ruchu samochodowego (in Polish). Transport miejski i regionalny. 2018.
[16] Woźniak K, Szymlet N, Sobczak J, Rymaniak Ł, Pielecha P. The method for ecological assessment of a diesel-electric multiple unit. Journal of Ecological Engineering. 2025; 26(9):229-238. https://doi.org/10.12911/22998993/204172
[17] Wróbel R, Sroka Z, Sierzputowski G, Dimitrov R, Mihaylov V, Ivanov D. Driving protocols: the possibility of using routing protocols in autonomous transport. Combustion Engines. 2024;63(1):3-9. https://doi.org/10.19206/CE-170418
[18] Axion R/S+ PEMS. https://www.globalmrv.com/axion-rs-2/ (accessed on 06.2025).
[19] GPS Visualizer. https://www.gpsvisualizer.com (accessed on 06.2025).
[20] SEMTECH-DS. On board, In-use emissions analyzer. https://d3pcsg2wjq9izr.cloudfront.net/files/28865/download/302428/1.SEMTECH-DS-GaseousPortableEmissionsMeasurementSystem–Brochure.pdf (accessed on 06.2025).
[21] Vehicles on European Roads. https://www.acea.auto/files/ACEA-Report-Vehicles-on-European-roads-.pdf (accessed on 06.2025).

Prof. Łukasz Rymaniak, DSc., DEng. – Faculty of Civil and Transport Engineering, Poznan University of Technology, Poland.
e-mail: *lukasz.rymaniak@put.poznan.pl*

Maciej Ziółkowski, Eng. – Faculty of Civil and Transport Engineering, Poznan University of Technology, Poland.
e-mail: *maciej.ziolkowski.2001@gmail.com*

Prof. Jacek Pielecha, DSc., DEng. – Faculty of Civil and Transport Engineering, Poznan University of Technology, Poland.
e-mail: *jacek.pielecha@put.poznan.pl*

Jakub Sobczak, MEng. – Faculty of Civil and Transport Engineering, Poznan University of Technology, Poland.
e-mail: *jakub.sobczak@doctorate.put.poznan.pl*

Natalia Szymlet, DEng. – Faculty of Civil and Transport Engineering, Poznan University of Technology, Poland.
e-mail: *Natalia.szymlet@put.poznan.pl*

Article citation info:
Lew K, Wojewoda P, Lubas J. The analysis of the impact of the storage period of engine and transmission oil on operational properties. Combustion Engines. 2026;204(1):58-65. https://doi.org/10.19206/CE-209702

Krzysztof LEW
Paweł WOJEWODA
Janusz LUBAS

Combustion Engines
Polish Scientific Society of Combustion Engines

The analysis of the impact of the storage period of engine and transmission oil on operational properties

ARTICLE INFO

Received: 13 June 2025
Revised: 5 August 2025
Accepted: 19 August 2025
Available online: 3 October 2025

The purpose of the research presented in this article was to determine the impact of the storage period of engine and transmission oils on their operational properties. The prolonged storage of oils leads to a series of physicochemical changes that can significantly affect their lubrication efficiency. Changes such as reduced viscosity, changes in density, and deterioration in lubricity can lead to increased wear of the engine, transmission, and other mechanical components. The study included samples of new and five-year-old engine and transmission oils, as well as engine oil after the break-in period (with a mileage of approximately 800 km). The SAE 10W40 oil after use in an internal combustion engine shows a significant reduction in scuffing resistance (approximately one-third lower scuffing load compared to new and old oil). Long-term five-year storage also slightly reduces its scuffing resistance at higher temperatures. In contrast, long-term storage of SAE 30 oil significantly decreases its scuffing resistance across both tested temperature ranges (by about 20%). Storage time did not significantly alter the viscosity index of SAE 10W40, whereas old SAE 30 oil showed a slightly better index than new oil.

Key words: *oil samples, lubricity, viscosity, density, aging process*

1. Introduction

Engine oils play a crucial role in ensuring the proper functioning and durability of internal combustion engines, particularly modern units that operate under increasingly demanding conditions. Their primary function is to lubricate moving mechanical components, protect against wear, corrosion, and overheating, with precisely adjusted viscosity being one of the key parameters determining the effectiveness of lubrication [7–9, 13, 14, 16].

Studies, such as the analysis of Marinol RG 1240 oil in the Cegielski-Sulzer 3AL25/30 engine, demonstrate that lubricating properties undergo dynamic changes, initially improving with ageing (even a threefold increase in anti-scuffing load capacity). However, this beneficial effect gradually decreases with the accumulation of contaminants [11]. Oil degradation is a multistage process that accelerates under harsh operating conditions, such as high temperatures, intense loads, or fuel dilution [12, 17, 18]. However, changes in oil properties occur not only during operation but also during long-term storage, posing an additional challenge for supply chains and end users [6, 11, 13, 14, 16].

A comprehensive assessment of the condition of the oil requires considering both the initial benefits of oil maturation and the negative effects of contaminant accumulation. Monitoring parameters such as viscosity, base number (TBN), acid number (TAN), and thermal stability are essential [1, 3, 5, 16]. Excessively low viscosity increases oil consumption and harmful emissions, while excessively high viscosity complicates cold starts and increases fuel consumption. However, viscosity alone is insufficient for a full assessment of oil condition: advanced analytical methods such as FTIR spectroscopy or TAN / TNB balance analysis are necessary [1, 5, 16].

The results of long-term storage studies (up to 5 years) of engine and gear oils revealed significant changes in their operational properties, including, for example, a 30% decrease in anti-scuffing resistance in SAE 10W40 oil used at 40°C [2–5, 13, 16]. These observations confirm that optimal oil management requires customised selection and replacement strategies, taking into account both operating and storage conditions. Insufficient monitoring or excessively long oil change intervals can lead to faster engine wear, failures, and reduced lifespan [7, 10, 12, 15].

This article combines an analysis of oil ageing processes under engine operation with an evaluation of the impact of long-term storage on oil properties, providing practical recommendations for the automotive industry in the context of increasing efficiency and environmental requirements. An important part of this work is the analysis of changes in the anti-seizure properties of engine oils after working in sliding pairs of combustion engine and long-term storage. The results obtained in the study provide an important suggestion regarding possible changes to the composition of oil during storage time, which can often be a long time from the production of oil to its use.

2. Measuring equipment and test methodology

2.1. Measuring equipment

The determination of the density, viscosity and lubricity of the oils selected for the tests was performed using research equipment that is part of the facilities of the Laboratory of Operational Materials at the Department of Motor Vehicles and Transport Engineering.

The density measurement of the oils was conducted using the DMA 4500 M apparatus (Fig. 1), which has the following parameters:

- Measurement range: density from 0 to 3 g/cm³, temperature from 0 to 90°C
- Accuracy: 5×10^{-5} g/cm³, 0.03°C
- Sample volume: min. 1 ml.

To measure the kinematic viscosity of the selected oils, the automatic Herzog HVU 482 apparatus was used, based

on the Ubbelohde viscometer (Fig. 2). This device is characterised by the following key parameters:

- Temperature range for measurements: from –40 to +100°C
- Measurement range: depending on the capillary used, 1 to 50 000 mm²/s
- Thermostatic system: external, with a temperature regulation range of –80 to +20°C
- Temperature stabilisation accuracy: ±0.01°C.

This apparatus allows measurements to be performed in accordance with the following standards: PN-EN ISO 3104, ASTM D445, ASTM D2270, and DIN 51562.

Fig. 1. DMA 4500 M apparatus for density determination

Fig. 2. HVU 482 apparatus for determining kinematic viscosity

To evaluate the lubricity of the tested oils, a four-ball T-02U apparatus was used (Fig. 3), which consists of a testing machine and a measurement control system. The mechanical part of the apparatus is composed of a housing, a drive unit, a load unit for the friction assembly, a ball holding unit, and a base.

The friction assembly consists of three stationary lower balls clamped in a holder and an upper ball mounted in a rotating spindle (500 rpm). The test elements are standardised bearing balls with a nominal diameter of 1/2", made of bearing steel ŁH15 with a hardness of 60–65 HRC. The mechanical system enables a linear increase in the load on the friction assembly during the test (loading rate: 408.8 N/s).

Fig. 3. View of the test stand for lubricity evaluation with the T-02U four-ball apparatus

2.2. Test methodology

Basic parameters tests, that is, density, viscosity, and lubricity, were carried out for five oil samples (Fig. 4). The specifications of the oils tested are given in Table 1. One of them was a sample of "new" semi-synthetic SAE 10W40 engine oil, and for comparison, a sample of 5-year-old oil of the same grade, both unused and used during the break-in period of a 1.3 dm³ naturally aspirated spark ignition (SI) engine (mileage approx. 800 km). The next two samples were mineral SAE 30 oils, one new and the other after five years of storage. Both oils were unused. The selected oils are commonly used in older and newer generations of combustion engines, which allows for determining the area of application of these oils in selected engine designs and evaluating their impact on the operation and wear processes of lubricated friction pair elements.

Tests of selected anti-scuffing oil parameters (scuffing load) and (pressure of seizure) were performed using the T-02U four-ball apparatus at oil temperatures of 40 and 100°C (standard practice for calculating viscosity index from kinematic viscosity at 40°C and 100°C – international standard D2270-24) (Fig. 3). The recorded test curves allowed for the determination of (Scuffing load) and (Pressure of seizure) according to the methodology provided by the equipment manufacturer (parameter determination scheme shown in Fig. 6) [11].

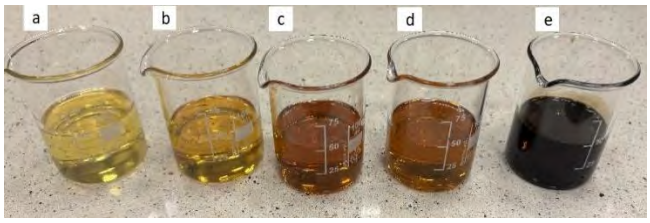

Fig. 4. Tested oil samples: a) SAE 30 old, b) SAE 30 new, c) SAE 10W40 old, d) SAE 10W40 new, e) SAE 10W40 used

The viscosity measurement device was controlled using dedicated HLIS 32 computer software (Fig. 5), with measurements performed using an NIR-type capillary (in accordance with the ASTM D 2162 standard).

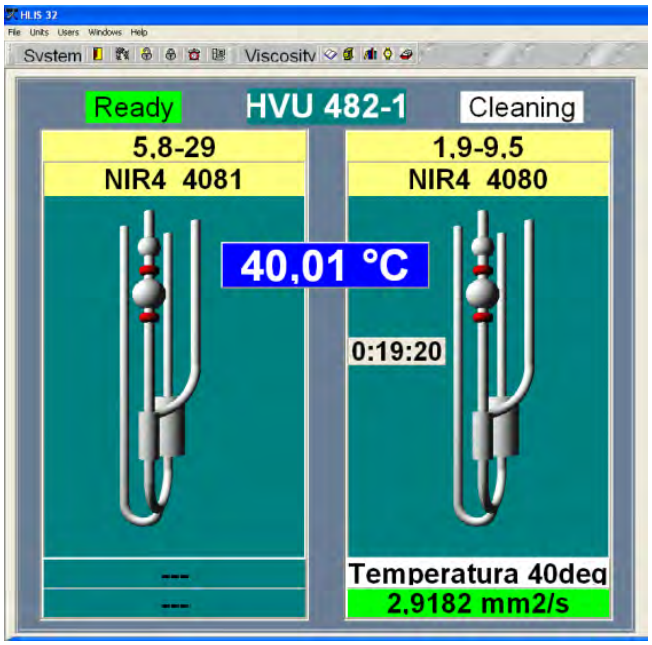

Fig. 5. HLIS 32 software windows with capillary identification and device status

Table 1. Characteristics of oil [19–21]

Lubricant	SAE 10W40	SAE 30
Parameter	Value	Value
Kinematic viscosity at 40°C [mm^2/s]	102.5	No data
Kinematic viscosity at 100°C [mm^2/s]	15	10.9
Viscosity index	153	91
	High performance Technosynthese® lubricant specially designed for cars powered by gasoline or diesel engines, naturally aspirated or turbocharged, indirect or direct injection. Standards: ACEA A3/B4, API SERVICE SN/CF	Mineral engine oil without additives (may contain depressants to lower the pour point). Application: in devices that do not require refined oil. Standards: PN-73/C-96085, API: SA, SAE: 30

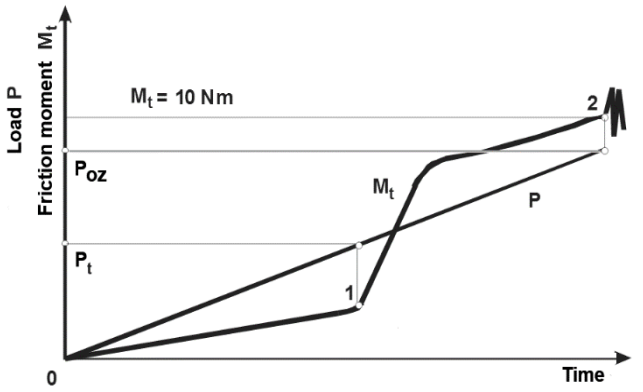

Fig. 6. Method for determining the scuffing load (P_t) and the seizure limit load (P_{oz}) [11]: 1 – point corresponding to the scuffing initiation, 2 – point corresponding to the seizure

3. Results and discussion

Oil tests revealed significant changes in anti-seizure properties, characterised by scuffing load (Fig. 7) and pressure of seizure (Fig. 8 and Table 2).

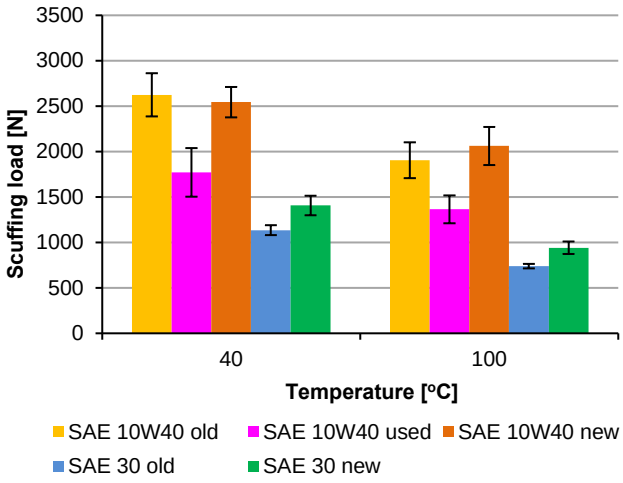

Fig. 7. Scuffing load of oil at temperatures of 40 and 100°C

The scuffing load values of the tested oils are significantly influenced by the temperature and the state of their wear. SAE 10W40 oil tests reveal substantial differences depending on the wear condition: for oil used in an internal combustion engine, a significant decrease in scuffing load (by approximately one-third compared to old and new oil) was observed at 40°C (Fig. 7). On the contrary, the comparison between old and new oil shows only a 3% difference in scuffing load, with higher values for old oil.

At 100°C, the scuffing load decreases by approximately 30% for old oil, 25% for used oil, and 20% for new oil. In particular, at this temperature, the new SAE 10W40 oil exhibits the highest resistance to the onset of scuffing initiation (~8% higher than the old oil), while the lowest resistance (at 40°C) was observed for engine-used oil (~34% lower than the new oil). For SAE 30 oil, new samples showed ~20% higher resistance to scuffing initiation than old samples at both 40°C and 100°C. Comparative analysis indicates nearly twice better anti-scuffing properties for SAE 10W40 versus SAE 30 oil (Fig. 7).

The pressure of seizure p_{oz} was calculated from the seizure limit load determined from the friction torque curves under increasing load at 40°C and 100°C (Table 3). Calculations demonstrate favourable tribological properties of the used SAE 10W40 oil, which exhibits nearly double the anti-seizure resistance of old/new oils at both temperatures (Fig. 8). New and old SAE 10W40 oils show comparable seizure load values. For SAE 30 oil, new samples had ~10% higher seizure load than old samples at 40°C, with marginal differences at 100 °C. The higher temperature reduced the seizure load by ~8% (old) and 18% (new).

In particular, SAE 30 oil showed ~30% lower seizure resistance than SAE 10W40 for both new and old states (Fig. 8).

Table 2. Pressure of seizure p_{oz}

Pressure of seizure p_{oz} [N/mm^2]						
Temperature	40 °C			100 °C		
Sample number	1	2	3	1	2	3
SAE 10W40 old	238.20	264.42	240.10	252.46	244.80	266.77
	Ø	247.57		Ø	254.68	
	σ	14.62		σ	11.15	
SAE 10W40 used	543.32	484.28	494.67	449.73	434.08	464.36
	Ø	507.42		Ø	449.39	
	σ	31.52		σ	15.14	
SAE 10W40 new	242.36	252.09	261.15	253.32	256.58	273.02
	Ø	251.87		Ø	260.97	
	σ	9.40		σ	10.56	
SAE 30 old	180.16	189.42	192.65	157.82	174.44	182.34
	Ø	187.41		Ø	171.54	
	σ	6.48		σ	12.52	
SAE 30 new	195.26	196.06	226.41	158.66	182.44	164.00
	Ø	205.91		Ø	168.37	
	σ	17.76		σ	12.48	

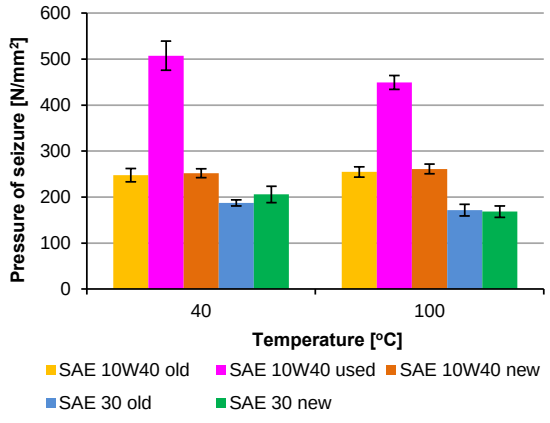

Fig. 8. Pressure of seizure of oil at temperatures of 40 and 100°C

The important key parameters for characterizing oil useful properties are kinematic viscosity and viscosity index (Fig. 9 and 10). At 40°C, the highest kinematic viscosity was measured for the new SAE 30 oil at approximately 100.5 mm²/s, while the lowest value was recorded for the old SAE 30 oil of the same grade, showing a 30% difference between these two oil conditions (Fig. 9).

For SAE 10W40 oil, the highest kinematic viscosity values were obtained for new oil (93.9 mm²/s), followed by old oil (87.8 mm²/s), and engine-used oil (72 mm²/s). At 100°C, the highest kinematic viscosities were measured for SAE 10W40 oil at 13.2, 12.1, and 13.9 mm²/s for old, used, and new oil, respectively. In comparison, SAE 30 oil showed lower values of 8.9 and 10.7 mm²/s for old and new oil.

Comparison of measured kinematic viscosity values with those specified in the oil data sheets revealed that for SAE 10W40 oil, viscosity was lower by 8.7 mm²/s at 100°C and 1.1 mm²/s at 40°C, while for SAE 30 oil, it was lower by 0.2 mm²/s at 100°C (Table 3).

Table 3. Kinematic viscosity

Temp. [°C]	SAE 10W40 old	SAE 10W40 used	SAE 10W40 new	SAE 30 old	SAE 30 new
	Kinematic viscosity [mm^2/s]				
40	87.8	72.0	93.9	69.5	100.5
100	13.2	12.1	13.9	8.9	10.7

Table 4. Viscosity index

SAE 10W40 old	SAE 10W40 used	SAE 10W40 new	SAE 30 old	SAE 30 new
Viscosity index				
151	166	152	102	89

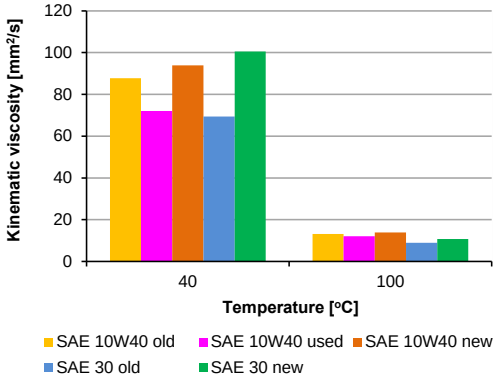

Fig. 9. Kinematic viscosity of oil at temperatures of 40 and 100°C

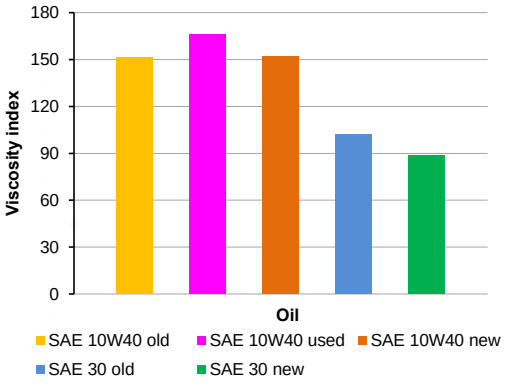

Fig. 10. Viscosity index of oil

Due to the minimal values of measurement uncertainties on the order of tenths of a unit, the error bars are not visible on the graphs in the adopted scale (Fig. 9 and 10).

The viscosity index calculations revealed the highest value for used SAE 10W40 oil (166), followed by lower and similar values for new and old oils of the same grade (152 and 151 respectively) (Fig. 10). For new SAE 30 oil, the viscosity index was 41% lower compared to new SAE 10W40 oil and 32% lower for old oils. The difference between new and old SAE 30 oils was approximately 13%.

Comparison of measured viscosity index values with those specified in the oil technical data sheets showed comparable results, with the SAE 10W40 being 1 unit lower and the SAE 30 being 2 units lower (Table 4).

The influence of temperature on the density of engine oils constitutes a crucial factor in evaluating their suitability for use in kinematic friction components of internal combustion engines operating under variable thermal conditions. Analysis of the graph (Fig. 11) showing density variations as a function of temperature for different SAE oil grades (SAE 10W40: new, used, old; and SAE 30: new, old) revealed a clear decreasing density trend with increasing temperature, characteristic of liquids.

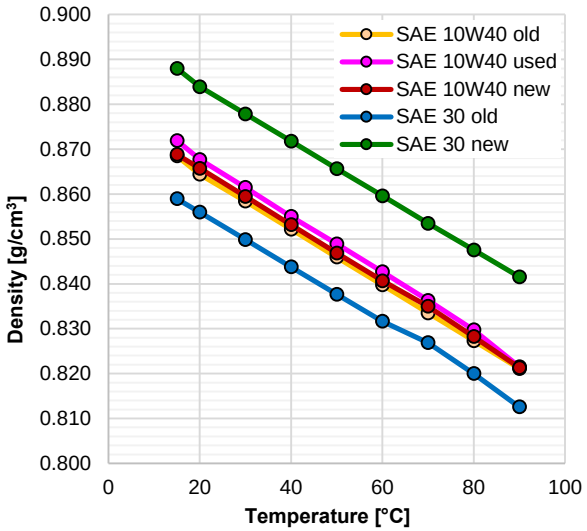

Fig. 11. Engine oil density [g/cm³]

SAE 30 new oil is characterised by the highest density (from 0.888 g/cm³ at 15°C to 0.842 g/cm³ at 90°C). The new and old SAE 10W40 oil achieve similar values throughout the range, from 0.869 g/cm³ (15°C) to 0.821 g/cm³ (90°C), while its used version ranges from 0.872 to 0.821 g/cm³, slightly higher than previous versions. The lowest density is exhibited by old SAE 30 oil, whose density drops from 0.859 to 0.812 g/cm³.

Analysis of density changes in SAE 30 and SAE 10W40 engine oils as a function of temperature and their technical condition revealed noticeable differences for the oils tested. In the case of SAE 30, a decrease in density was observed in the old oil compared to the new one, ranging from 3.11% to 3.44% in the temperature range of 15 to 90°C, clearly indicating oil degradation due to ageing. The greatest differences were observed at higher temperatures, which may suggest a deterioration in the lubricating properties of the oil during engine operation under high temperature conditions.

For SAE 10W40 oil, the differences between the new, old, and used states were much smaller, ranging from 0.02% to 0.17%, which may indicate its higher density stability during use.

Actual trends in the changes in friction moment for the tested oils as a function of increasing continuous load on the friction pair (Fig. 12 and 13). The analysis of the friction moment trends showed that for the selected oils, seizure of the friction pair occurs at a load of 10 Nm [11] (according to the ITeE Standard). This applies to SAE 10W40 old oil (40°C, Fig. 12a), SAE 30 old and new oils at 40°C and 100°C (Fig. 12d, e and Fig. 13d, e).

However, in the case of SAE 10W40 old oil at 100°C (Fig. 13a) and SAE 10W40 used and new oils at 40°C and 100°C (Fig. 12b, c and Fig. 13b, c), the seizure of the friction pair occurred below 10 Nm [11].

The tests conducted demonstrated the need for careful lubricant selection. SAE 10W40 oil used in an internal combustion engine changed its operating properties, including due to fuel and exhaust gases entering the combustion chamber from the oil pan through piston ring leaks, the accumulation of contaminants resulting from the action of detergent-dispersant additives, and wear products of the engine friction pairs. These changes can reduce the scuffing load of used SAE 10W40 oil, as new SAE 10W40 oil enables the formation of a more durable boundary layer that protects the friction pair components from the beginning of the scuffing process (Fig. 7). The reverse relationship occurs in the case of scuffing resistance tests. The calculated values of the pressure of seizure are higher when the friction pair is lubricated with used SAE 10W40 oil (Fig. 8). Additives in engine oil, including anti-wear and anti-seize additives are activated during operation in an internal combustion engine as a result of chemical reactions occurring in the oil as a result of tribochemical processes, which may explain the increase in the pressure of seizure of used oil compared to new oil; additionally, oxidation processes occurring during the operation of the oil in the engine generate surface-active organic impurities, forming a boundary layer on the metal surface, improving the lubricating properties of the engine oil [2–5, 13, 16]. Storage factors affect the properties of engine oil and can lead to oil degradation, resulting in a deterioration of its lubricating, protective, and operational properties. Temperature, humidity, and air access are among the most important factors affecting changes in oil properties during long-term storage. These factors can cause oil oxidation and viscosity degradation or reduced corrosion protection, deposit formation, and additive precipitation, as well as reduced oil film durability [14].

4. Conclusions

Long-term storage of oils (5 years) leads to significant changes in their physicochemical properties, including viscosity, density, and scuffing resistance, although the degree of degradation depends on the type of oil.

Based on the test results of the engine oils, the following conclusions can be drawn:

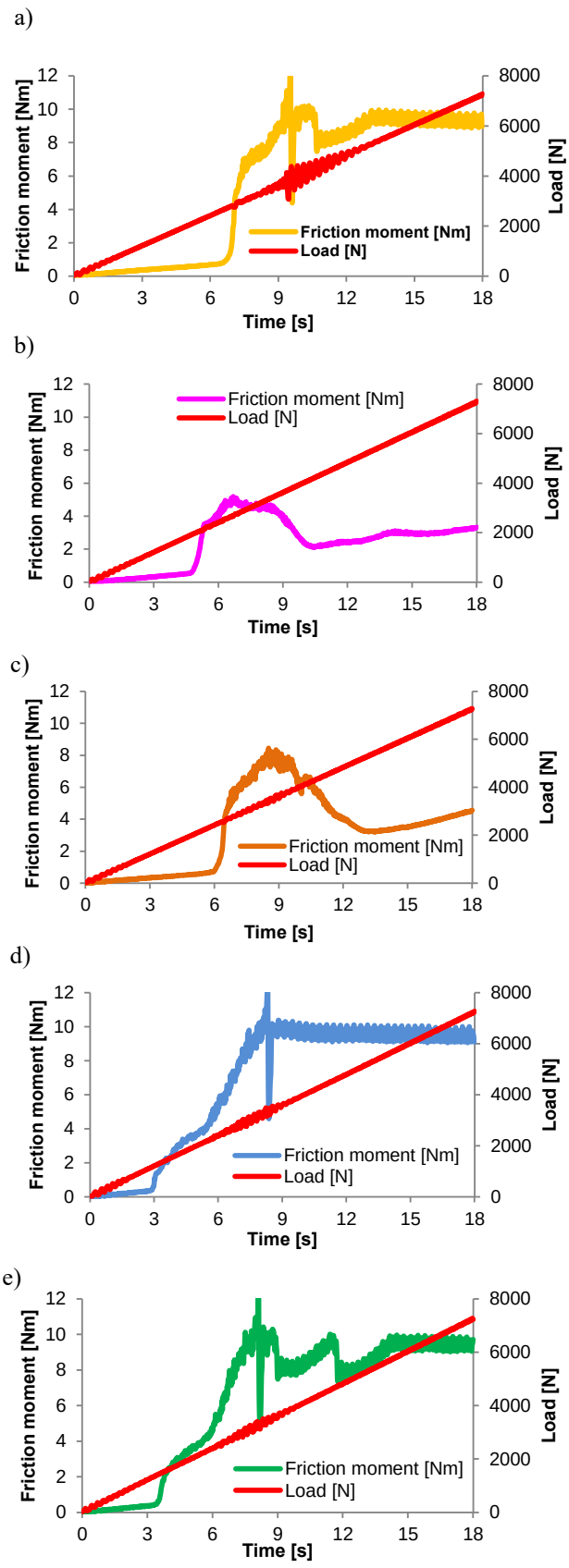

Fig. 12. Friction moment curve obtained under continuous load conditions of oil at temperatures of 40 °C: a) SAE 10W40 old, b) SAE 10W40 used, c) SAE 10W40 new, d) SAE 30 old, e) SAE 30 new

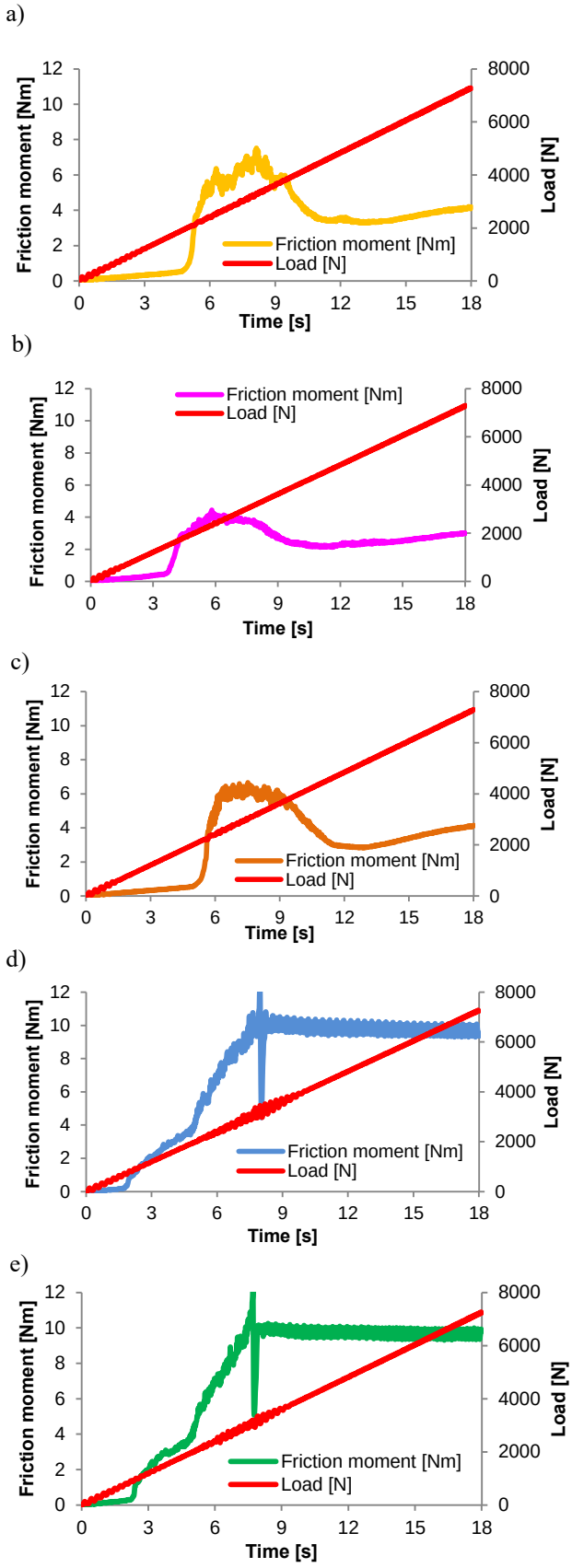

Fig. 13. Friction moment curve obtained under continuous load conditions of oil at temperatures of 100 °C: a) SAE 10W40 old, b) SAE 10W40 used, c) SAE 10W40 new, d) SAE 30 old, e) SAE 30 new

1. SAE 10W40 oil after use in an internal combustion engine shows a significant reduction in scuffing resistance (approximately one-third lower scuffing load compared to new and old oil). Long-term five-year storage also slightly reduces its scuffing resistance at higher temperatures. In contrast, long-term storage of SAE 30 oil significantly decreases its scuffing resistance across both tested temperature ranges (by about 20%).
2. Lubricating the friction zone with used SAE 10W40 oil increases scuffing resistance by nearly 50% compared to the new and old oil (particularly at lower temperatures). However, storage time has no significant effect on seizure pressure (this applies to both tested temperatures).
3. Kinematic viscosity measurements revealed notable changes at 40°C, where the new SAE 30 oil has the highest viscosity among all oils tested, while prolonged storage caused it to exhibit the lowest viscosity. For SAE 10W40 oil, the highest viscosity was measured in new oil, with a significantly lower value in engine-used oil and a slightly lower value after 5 years of storage.
4. SAE 10W40 oil has the most favourable viscosity index, while the new SAE 30 oil has the lowest. Storage time did not significantly alter the viscosity index of SAE 10W40, whereas old SAE 30 oil showed a slightly better index than new oil.

It would be advisable to modify the composition of SAE 30 oils (e.g., by adding anti-oxidant and anti-wear additives) to enhance their storage durability.

Further research on the impact of short-term use (break-in period) on oil properties would be beneficial, as it could optimise oil change intervals. The development of oil condition monitoring systems (e.g., real-time quality sensors) could help more accurately determine the optimal oil replacement time, especially for oils prone to ageing.

The study confirms that storage time and operating conditions significantly affect oil properties, with SAE 10W40 being more resistant to degradation than SAE 30. The findings have important industrial implications, highlighting the need for proper oil selection and monitoring of condition. Future research should focus on optimising oil formulations and developing methods for quality assessment during storage and operation.

Bibliography

[1] Akpoveta OV, Opuyor S, Ekwe CO, Umudi Q, Arogbotimi P, Alajiki HM. Evaluation of physicochemical characterization and elemental composition of used, recycled, and fresh lubricating engine oils of total quartz and hardex brands. J Appl Sci Environ Manag. 2024;28(12):4057-4065. https://doi.org/10.4314/jasem.v28i12.15

[2] Chmielewski Z. Badania oleju silnikowego jako źródła informacji o stanie technicznym silnika spalinowego o ZS (in Polish). Logistyka. 2010;2. bwmeta1.element.baztech-article-BPL8-0019-0008

[3] Chmielewski Z. Pokładowe systemy diagnostyki oleju silnikowego – historia i przyszłość (in Polish). Logistyka. 2011;3. bwmeta1.element.baztech-article-BPL1-0003-0042

[4] Chmielewski Z. Assessment of the kinetics of changes in selected physicochemical indicators of engine oil in operation. Combustion Engines. 2022;188(1):24-29. https://doi.org/10.19206/CE-141337

[5] Gołębiowski W, Zając G, Sejkorová M, Wolak A. Assessment of oil change intervals in urban buses based on the selected physicochemical properties of used engine oils. Combustion Engines. 2024;196(1):15-23. https://doi.org/10.19206/CE-169807

[6] Hadło K, Lubas J, Szczypinski-Sala W, Tomala A, Konieczny D. Tribological properties of a sliding joint with an a-C:H:W coating under lubrication conditions with PAO8 oil and the addition of 2% MoS2 nanoparticles. Materials. 2024;17(4):870. https://doi.org/10.3390/ma17040870

[7] Idzior M. Aging of engine oils and their influence on the wear of an internal combustion engine. Combustion Engines. 2021;185(2):15-20. https://doi.org/10.19206/CE-138033

[8] Idzior M, Wichtowska K. Badanie wpływu przebiegu pojazdów na zmiany właściwości olejów silnikowych (in Polish). Autobusy: technika, eksploatacja, systemy transportowe. 2016;17(6):900-904. https://bibliotekanauki.pl/articles/317004.pdf

[9] Jakóbiec J, Budzik G. Czynniki majce wpływ na stopień degradacji oleju silnikowego w okresie eksploatacji (in Polish). Archiwum Motoryzacji. 2007;3:209-216. http://yadda.icm.edu.pl/baztech/element/bwmeta1.element.baztech-article-BGPK-1839-6954

[10] Jankowski A, Kowalski M, Kulczycki A, Dzięgielewski W, Kałużny J, Merkisz J. The influence of molecular clusters on lubricating film formation. Proceedings of the IRF2018: 6th International Conference Integrity-Reliability-Failure; 22-26 July 2018; Lisbon, Portugal. INEGI/FEUP. 2018;927-238. https://paginas.fe.up.pt/~irf/Proceedings_IRF2018/data/papers/7154.pdf

[11] Malinowska M, Zera D. Analiza zmian smarności oleju silnikowego stosowanego w silniku Cegielski-Sulzer 3AL25/30 (in Polish). Zeszyty Naukowe Akademii Morskiej w Gdyni. 2016;96:93-104. bwmeta1.element.baztech-65bcb498-e0d4-4901-8dc8-b42d656692bb

[12] Rostek E, Babiak M. Thermogravimetric analysis in the synthetic engine oil 5W-30. Combustion Engines. 2017; 170(3):188-192. https://doi.org/10.19206/CE-2017-332

[13] Sala R, Węglarz K, Suchecki A. Analysis of lubricating oil degradation and its influence on brake specific fuel consumption of a light-duty compression-ignition engine running a durability cycle on a test stand. Combustion Engines. 2023;195(4):109-115. https://doi.org/10.19206/CE-169488

[14] Sejkorová M, Hurtová I, Jilek P, Novák M, Voltr O. Study of the effect of physicochemical degradation and contamination of motor oils on their lubricity. Coatings. 2021;11(1): 60. https://doi.org/10.3390/coatings11010060

[15] Sharma BC, Gandhi OP. Performance evaluation and analysis of lubricating oil using parameter profile approach. Ind Lubr Tribol. 2008;60(3):131-137. https://doi.org/10.1108/00368790810871057

[16] Urzędowska W, Stępień Z. Wybrane zagadnienia dotyczące zmian właściwości silnikowego oleju smarowego w eksploatacji (in Polish). Nafta-Gaz. 2012;68(12):1102-10. bwmeta1.element.baztech-1c19b8bc-750e-431a-a786-2833e244640d

[17] Wolak A, Zając G, Żółty M. Changes of properties of engine oils diluted with diesel oil under real operating conditions. Combustion Engines. 2018;173(2):34-40. https://doi.org/10.19206/CE-2018-206
[18] Wolak A, Zając G. The kinetics of changes in kinematic viscosity of engine oils under similar operating conditions. Eksploat Niezawodn. 2017;19(2):260-267. https://doi.org/10.17531/ein.2017.2.14
[19] SAE International Recommended Practice, Engine Oil Viscosity Classification, SAE Standard J300_202405, Revised May 2024, Issued June 1911. https://doi.org/10.4271/J300_202405
[20] Oil specification according to Technical Data Sheet 10W-40.
[21] ASTM D-7042. Standard Test Method for Dynamic Viscosity and Density of Liquids by Stabinger Viscometer (and the Calculation of Kinematic Viscosity); ASTM International: West Conshohocken, PA, USA, 2004. https://store.astm.org/d7042-21a.html

Krzysztof Lew, DEng. – Faculty of Mechanical Engineering and Aeronautics at Rzeszow University of Technology, Poland.
e-mail: *klew@prz.edu.pl*

Paweł Wojewoda, DEng. – Faculty of Mechanical Engineering and Aeronautics at Rzeszow University of Technology, Poland.
e-mail: *pwojewod@prz.edu.pl*

Janusz Lubas, DSc., DEng. – Faculty of Mechanical Engineering and Aeronautics at Rzeszow University of Technology, Poland.
e-mail: *lubasj@prz.edu.pl*

Article citation info:
Noga M, Moskal T. Conversion to hydrogen fueling of a range extender SI engine of a 48 V hybrid electric vehicle. Combustion Engines. 2026;204(1):66-71. https://doi.org/10.19206/CE-209908

Marcin NOGA
Tomasz MOSKAL

Combustion Engines
Polish Scientific Society of Combustion Engines

Conversion to hydrogen fueling of a range extender SI engine of a 48 V hybrid electric vehicle

ARTICLE INFO

Received: 19 June 2025
Revised: 9 August 2025
Accepted: 25 August 2025
Available online: 18 September 2025

The purpose of the article is to present further development stages of the range extender designed for a 48 V electric vehicle. The initial design of the system consisted of a 160 cm³ single-cylinder carbureted gasoline engine coupled to a synchronous 3-phase AC generator. The conversion of the engine included an adaptation of a port hydrogen injection with a stand-alone engine management system. The research was focused on engine calibration first of all, in order to achieve its stable operation, avoiding abnormal combustion when running on hydrogen. In addition to the basic engine performance indicators, the composition of exhaust gases emitted by the engine was also measured. Initial tests proved the conversion to be stable, and the range extender reaches efficiency slightly higher than achieved when the engine was fueled by gasoline.

Key words: *hydrogen, range extender, electric vehicle, spark-ignition engine, decarbonization*

1. Introduction

In the decarbonization phase of road transport, new technologies are being sought to further facilitate the adoption of battery electric vehicles [5]. One such technology is the use of a range-extender device, which significantly enhances the autonomy of a BEV and allows for both stricter control and relocation of toxic exhaust gas emissions [3, 18]. Range extenders are, in essence, onboard electricity generators, the vast majority of which are fueled by liquid fuels [13]. These generators can be powered by classic combustion engines [2], rotary engines [21], opposed-piston engines [19], or even fuel cells [15]. The emission of toxic exhaust gases can be controlled by selecting the most efficient power source, as well as by using hydrogen as fuel [8, 16, 20].

Research on hydrogen being used as a fuel for combustion engines has been conducted worldwide in numerous institutes, including Poland [10, 14]. One of the well-experienced institutions in this field is Cracow University of Technology, where the first successful attempts with hydrogen-running engines were made at the beginning of the 1980s [7].

In recent years, the development of hydrogen engines has also included special types of engines, advanced methods of variability of engine design parameters, and their specific applications [1]. In the paper of C. Zhang et al, a rotary engine has been used in combination with hydrogen fuel for electricity generation with a peak efficiency of 30% [22]. Research conducted by Seungjae et al. shows that by varying the compression ratio of a single cylinder hydrogen piston engine, peak efficiency can reach as high as 42.3% [6]. The research conducted by Dingel et al. shows a rising potential of applying a range-extender device for battery-powered commercial vehicles operating in urban areas, e.g. garbage collection vehicles [4].

An example of a range-extender device has been developed at Cracow University of Technology [11]. This article describes further development steps for the range-extender device, including electronic hydrogen injection, replacing carbureted gasoline fueling.

The range extender in the current development phase has been prepared for further research concerning the hydrogen combustion control with the use of the indicated pressure readout.

The next chapters of the article describe the test stand used for this research, its development stages, and the methodology used for calculations. Next, results are presented with a focus on engine setpoint parameters, engine load, and exhaust gas composition.

2. Research problem

2.1. Subject of research

The range-extender previously developed at the Cracow University of Technology has been used to conduct the research described in this paper. It has been built for a 48 V light commercial battery electric vehicle and consists of a single cylinder spark ignition engine and a belt-driven three-phase AC synchronous generator with electromagnetic excitation. The generator itself is an adaptation of a commercial vehicle alternator to enable 48 V generation.

In its primary stage, the 163-cc engine was fueled by a float carburetor, and its ignition system was set to a constant ignition advance angle. The carburetor throttle was adjusted by a centrifugal governor.

In further stages, the range extender was equipped with an exhaust aftertreatment system consisting of a three-way catalytic converter and an excess air ratio (λ) control system, which, by adding additional air to the rich mixture, was able to keep the mixture stoichiometric. The range extender performance parameters are listed in Table 1.

The research carried out on the range extender at that stage proved its peak efficiency to be at around 19%. Considering the type of generator and simplicity of the power unit, the result can be evaluated as high.

Table 1. Range-extender technical data before H_2 modifications

Engine model	WEIMA 168FA (Honda GX160-class)
Engine type	four-stroke, SI, single cylinder
Engine displacement	163 cm^3
Engine maximum power	3.8 kW at 3600 rpm
Ignition timing	fixed, 27°CA BTDC
Generator type	Synchronous 3-phase AC
Nominal voltage	48 V
Continuous output power	2200 W
Peak overall efficiency	18.8 %

2.2. Further development of the range extender

In the current stage, the range extender has been adapted for hydrogen fueling. Due to highly specific characteristics of this gas in a combustion engine application [12], it has been decided to tune the engine with the use of an integrated electronic engine management system. Its basic functionality is to control the ignition setpoint and the gas injection timing to the engine intake with excess air ratio closed loop control based on a wide-band oxygen sensor in the exhaust gases.

Such an approach allows for safe and effective operation of a hydrogen-fueled engine. The engine management system used is an ECUmaster Black, which also features a live combustion control interface, making real-time corrections feasible. The adoption of this system required the engine to be equipped with specific actuators (ignition coil, hydrogen injector), as well as a variety of sensors sending the crankshaft position, knock, and temperature sensors. The fitment of camshaft and crankshaft position sensors posed a tremendous challenge, as it required precise mechanical changes in the engine to fit them in a confined space.

Figure 1 illustrates the first part of the main actuators and sensors used in the revised range extender.

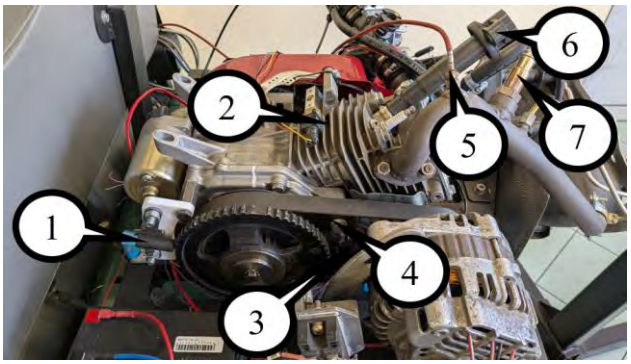

Fig. 1. Range extender equipment: 1 – crankshaft position sensor; 2 – engine temperature sensor; 3 – camshaft position sensor; 4 – knock sensor; 5 – EGT sensor; 6 – ignition coil (active); 7 – wideband oxygen sensor

In Figure 2, the next group of sensors and actuators is shown. The engine has been equipped with a complete set of sensors, which is needed for future research, although the knock sensor was not used in this research, as its efficient use when the engine is running on hydrogen requires fine-tuning of the settings of the ECU with the use of an in-cylinder pressure sensor.

One of the crucial additions to the sensor set was a Bosch LSU 4.9 wideband exhaust oxygen sensor. With the constant feedback signal to the Engine Management Unit, it is feasible to hold stable combustion conditions up to an excess air ratio of 2.

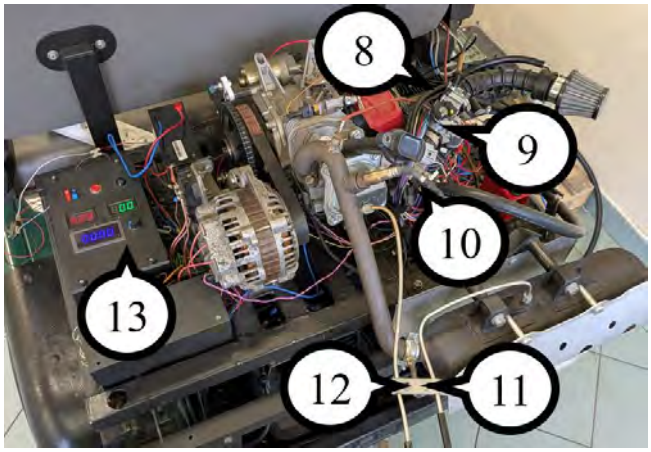

Fig. 2. Range extender equipment, continued: 8 – engine management unit; 9 – throttle body w/ TPS and idle actuator; 10 – H_2 injector; 11 – exhaust gas port after TWC; 12 – exhaust gas port before TWC; 13 – battery charge controller w/ RPM, charge current & voltage readout

The throttle has been fitted with a linear DC actuator, acting on a cable to be able to precisely set the throttle opening.

Hydrogen supply is carried out with a two-stage BRC Zenith CNG reducer with an output pressure of 2 bar. The reducer is equipped with an intake pipe pressure compensation. The elements are illustrated in Fig. 3.

Fig. 3. Range extender equipment, continued: 14 – gas reducer; 15 – combi pressure/temperature sensor for H_2 consumption calculation

The throttle body assembly was adapted with a Bosch NGI-2-K injector (Bosch P/N: 0 280 158 839), dedicated to the application of natural gas. The coil resistance of this injector is 8.9 Ω, and its inductance is 18 mH. When powered directly from a 12 V electrical system, this injector does not require peak and hold control. Instead, it is satisfied with simple saturated control. With this control method, the maximum value of the coil current does not exceed 1.6 A, which is a value far lower than the permissible value of 5 A/output for the used ECU. At the stage of preliminary tests, it was determined that at a supply pressure of 2.0 bar, the injector output is 12 g/min of hydrogen (134.8 SLPM). During the subsequent tests of the hydrogen-powered engine, the injection time of the fuel at high engine load was on average 6–8 ms, depending on the engine speed. This confirms that the injector was selected correctly for this

application. The view of the NGI-2-K injector with the fuel supply adapter installed is shown in Fig. 4.

Fig. 4. Injector nozzle view

2.3. Test stand

The mass of consumed hydrogen was calculated based on the gas pressure and temperature readout from a Bosch PST-F 2 sensor, mounted on a CNG reducer inlet attached to a 50 dm^3 high-pressure cylinder. To ensure the most accurate measurement of the hydrogen temperature on the high-pressure side of the cylinder, the sensor is equipped with a heat shield. The sensor parameters are described in Table 2.

Table 2. Pressure/temperature sensor characteristics

Sensor model	Bosch PST-F 2 280 bar
Pressure sensor type	Steel diaphragm
Pressure sensitivity	14.3 mV/bar
Temperature sensor type	NTC thermistor, 10 kΩ @ 25°C

Exhaust gas composition was measured with the use of a Capelec 3201 exhaust gas analyzer.

Exhaust gas temperature was measured with the use of a metal PT100 resistor with its dedicated processor.

Electrical parameters of the generated electrical energy have been recorded with a Racelogic datalogger. The data was acquired at a 10 Hz frequency.

The engine load consists of a synchronous 3-phase AC generator, charging the vehicle's primary energy source – LiFePO4 batteries. The generator is externally excited with a regulated power supply. To avoid an overload of the battery, a 48 V to single-phase 230 VAC inverter is connected to the vehicle's 48 V system, to which a switchable 1/2 kW fan heater is attached.

Figure 5 illustrates the dependencies and energy flow in the revised range extender.

In Figure 6, the entire test stand can be observed, consisting of the light commercial vehicle equipped with the updated range extender, the 50 dm^3 hydrogen tank with reducer, a power supply, a portable computer for data logging, and the exhaust gas analyzer.

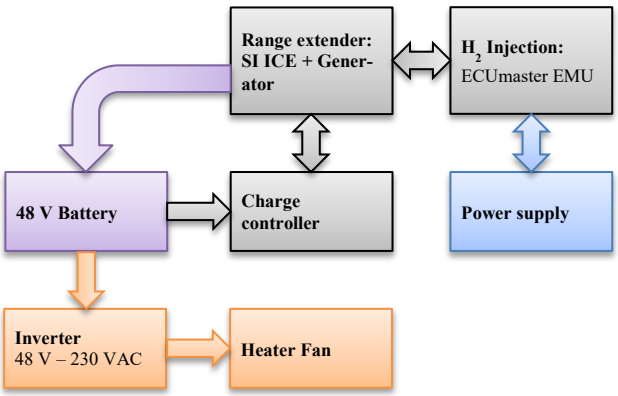

Fig. 5. Test stand diagram

Fig. 6. Range extender test stand

3. Results

The tests were carried out at 5 measurement points, for different values of engine speed and load. The value of the ignition advance angle was reduced to 16°CA BTDC (compared to 27°CA BTDC on the carburetor) due to the specific nature of hydrogen combustion in a piston engine application. After initial testing, the value was set permanently after reaching engine stability in the desired operating range.

The injector opening angle was firmly set to 340°CA BTDC. Estimating the injection time no longer than 10 ms, which results from the parameters of the selected injector and hydrogen pressure, allows for the fuel injection sequence to happen entirely during the opening of the engine intake valve. The engine control algorithm had a lower limit of excess air ratio set to $\lambda = 1.75$. Using a richer mixture when feeding with port hydrogen injection may cause improper engine operation (abnormal combustion, spontaneous ignition of the mixture in the intake system).

In Figure 7, the setpoint data can be observed, with both the throttle position values and manifold absolute pressure values. The setpoint duration was set to maintain a similar level of hydrogen consumption across all test runs.

The operating points were selected in such a way as to indicate high engine load in all cases. This is evidenced by high average absolute pressure values in the intake duct, close to atmospheric pressure, which was 99 kPa during the tests. This allows the engine to achieve high thermal efficiency in these operating conditions.

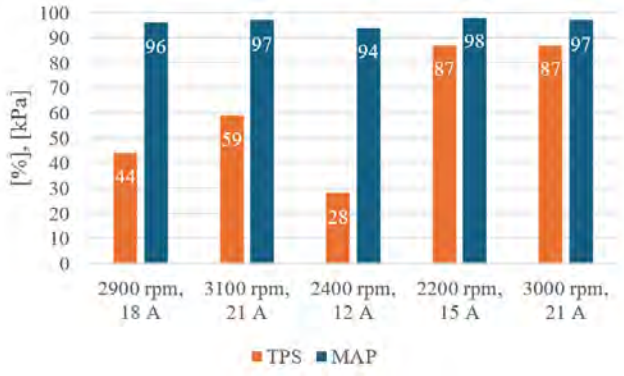

Fig. 7. Range extender setpoint data

Figure 8 shows the excess air ratio across all the set-points. The richest mixture was recorded in the third set-point.

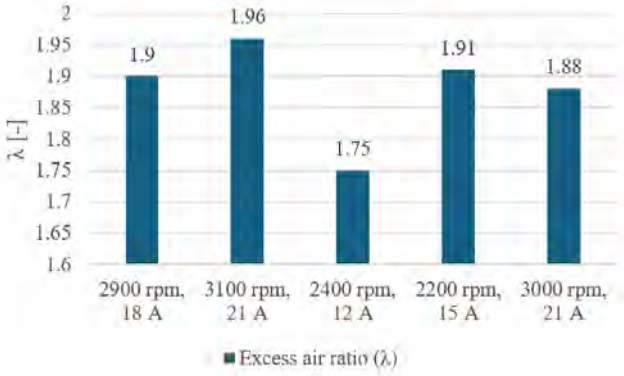

Fig. 8. Range extender excess air ratio (λ)

In the following Table 3, the range extender efficiency is presented. Hydrogen consumption was calculated based on pressure and temperature sensor readouts together with an algorithm developed by Lemmon et al., considering the compressibility factor of hydrogen in relation to temperature and pressure [9].

Table 3. Total RE efficiency on hydrogen fuel

Test run	Electric energy [kJ]	Hydrogen consumption [g]	Hydrogen combustion energy [kJ]	η
2900 rpm, 18 A	292.03	12.94	1552.41	0.188
3100 rpm, 21 A	312.59	13.50	1619.80	0.193
2400 rpm, 12 A	232.82	11.68	1401.78	0.166
2200 rpm, 15 A	305.00	12.61	1513.71	0.201
3000 rpm, 21 A	270.72	11.04	1324.44	0.204

Electrical energy generated by the RE was calculated based on battery voltage and charging current readouts logged by the Racelogic data logger. To calculate the H_2 combustion energy, hydrogen parameters from [17] have been used.

In addition, Fig. 9 shows the calculated specific fuel consumption for hydrogen. The highest value of SFC can be observed for the third run, where the least amount of electrical energy was generated.

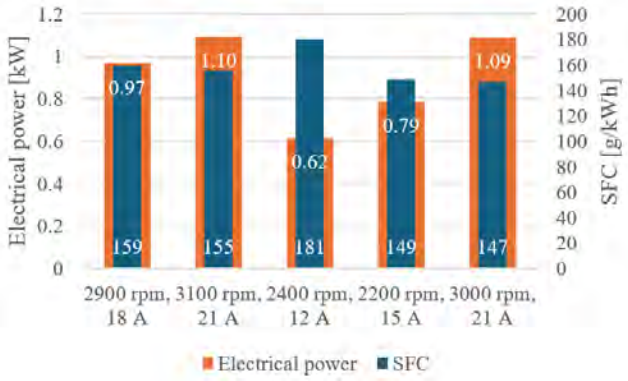

Fig. 9. Range extender performance

The values of the obtained overall genset efficiency are generally relatively high, which can be explained by the engine working with a relatively high load and with a mixture composition favorable due to the efficiency of the engine working on hydrogen. Only for the third point does the efficiency obtained by the range extender have a lower value. On the one hand, this results from the parameters of the engine itself (lower load and richer mixture for this point) and on the other hand from the parameters of the generator (the lowest output power and therefore lower efficiency too) and the ribbed belt transmission (a larger share of parasitic losses at its low load). The specific fuel consumption when powered by hydrogen is significantly lower than when powered by other fuels, which is due to the almost three times higher calorific value of hydrogen in relation to e.g. gasoline.

Table 4. Exhaust gas emission analysis on hydrogen fuel

Test run	NO_x before TWC [ppm vol]	NO_x after TWC [ppm vol]	O_2 before TWC [%vol]	O_2 after TWC [%vol]
2900 rpm, 18 A	67	86	11.8	12.1
3100 rpm, 21 A	19	37	11.9	12
2400 rpm, 12 A	186	218	10.6	10.9
2200 rpm, 15 A	33	58	11.8	11.8
3000 rpm, 21 A	34	49	11.7	11.6

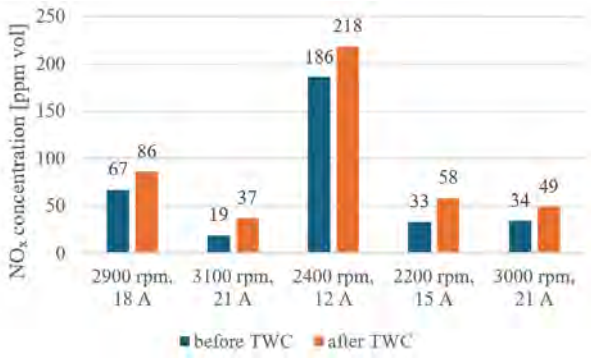

Fig. 10. NO_x concentration in exhaust gases of the hydrogen fueled RE

Table 4 consolidates the results of exhaust gas composition analysis. When it comes to the CO and CO_2, the analyzer readouts equaled in every case 0, and for HCs never exceeded 5 ppm, being just at the threshold sensitivity of the device. Due to this reason, they were skipped in the analysis. Only NO_x emission and O_2 concentration are presented, also visually in Fig. 10 and 11 respectively.

The NO_x concentration values are generally very low, which results from several factors. Primarily from the lean hydrogen-air mixture and the specifics of hydrogen combustion, which occurs significantly faster than gasoline, so the exposure of the cylinder working medium to high temperature is shortened. In addition, it should be remembered that the ignition timing was not set too aggressively, but rather conservatively in the preliminary stage of the engine management unit calibration. Another important observation is the noticeable increase in NO_x concentration in the exhaust system outlet, which results from the process of combining nitrogen with oxygen still present in the exhaust gases (lean mixture) in the hot catalyst integrated in a muffler of the engine. Certainly, the process of oxidation of NO to NO_2 also takes place in TWC.

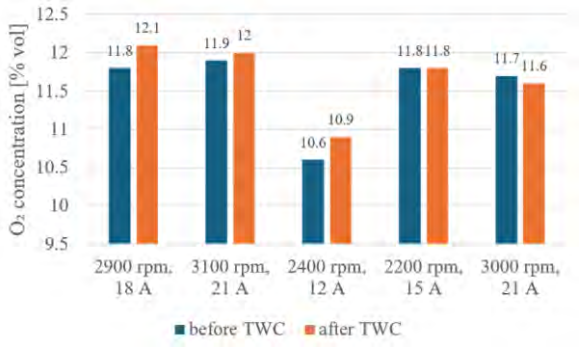

Fig. 11. Range extender O_2 concentration in exhaust gases

The oxygen concentration is high, directly proportional to the adjusted excess air ratio. Small increases in the oxygen concentration measured before and after the TWC may be the result of a certain change in the thermodynamic parameters of the exhaust gases and the specificity of the exhaust gas analyzer used, and to a lesser extent, changes in their composition (see observed NO_x increase).

Values of the temperature of exhaust gases measured upstream of the TWC are presented in Fig. 12.

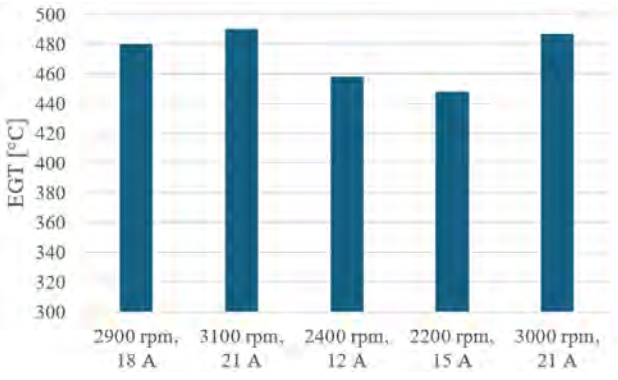

Fig. 12. Exhaust gas temperature of RE fueled by hydrogen

The exhaust gas temperature reaches relatively low values, which was expected in the case of hydrogen fueling and high excess air ratio values. The values for individual points are proportional to the power generated by the range extender engine.

4. Discussion

Compared to the results of previous tests of the range-extender powered by gasoline [11], it is easy to notice a significant reduction in power when powered by hydrogen. This is due to the low calorific value of the hydrogen-air mixture, which in turn is caused by the combustion of a lean mixture ($\lambda = 1.8$) and a reduction in volumetric efficiency, because hydrogen, a gas with very low density, takes up several times more volume in the mixture than gasoline vapors. On the other hand, operation with a lean mixture and a large throttle opening needed to achieve the appropriate power allowed for a noticeably higher (over 1 percentage point) value of the maximum overall efficiency of the range extender. It is expected that more accurate engine calibration will allow for slightly higher range extender power and even better efficiency results. Achieving stable, long-term operation of the hydrogen-powered range extender should certainly be considered a success. This is even more important because the engine used for the tests is a very simple design.

The main goal of using hydrogen as a fuel for the combustion engine is to eliminate any carbon compound emissions. In the case in question, this was fully achieved. The concentration of CO and CO_2 was at a level that was not measurable by the analyzer used. The HC concentration oscillated around the analyzer's sensitivity threshold (5 ppm vol.). In the case of gasoline fueling, these values were approximately ~0.6% CO, ~14.3% CO_2, and ~180 ppm HC in raw exhaust gases. The remaining emissions of the range-extender engine fueled with hydrogen, however, were very low values, usually below 100 ppm, compared to about 3000 ppm when fueling with gasoline.

5. Conclusions

The results of this preliminary research are promising, proving that the stability of such a small piston engine serving the purpose of a range extender can be achieved.

It must be considered that only a few optimization steps have been performed during the construction of the H_2-RE, serving as a small impulse for further research on the matter.

Looking at the exhaust gas analysis data, the benefits of using hydrogen as a fuel can be clearly visible, with CO_2, CO, and HC emissions at a level below the analyzer sensitivity. It can be determined that hydrogen fuel holds a tremendous advantage in lowering carbon emissions further into the atmosphere.

What must be observed is the low NO_x emission, but also the poor performance of the H_2-RE in terms of NO_x aftertreatment. The reason for this fact is that the TWC is unsuitable for lean mixtures required due to the method of hydrogen supply used. For efficient NO_x emission decrease, another aftertreatment method, like Selective Catalytic Reduction, should be considered. Hydrogen, recognized as an effective reductive agent, could be used in this method.

Nomenclature

BEV	battery electric vehicle
BTDC	before top dead center
CNG	compressed natural gas
ECU	engine control unit
H_2-RE	hydrogen range-extender
SI	spark ignition
SLPM	standard cubic decimetre per minute
TPS	throttle opening
TWC	three-way catalytic converter
λ	excess air ratio

Bibliography

[1] Antila M, Galimova T, Breyer C, Norouzi S, Repo S, Pihlatie M et al. Future energy technology for nonroad mobile machines. Adv. Energy Sustainability Res. 2025;6:2400257. https://doi.org/10.1002/aesr.202400257

[2] Borghi M, Mattarelli E, Muscoloni J, Rinaldini CA, Savioli T, Zardin B. Design and experimental development of a compact and efficient range extender engine. Appl Energ. 2017;202:507-526. https://doi.org/10.1016/j.apenergy.2017.05.126

[3] Brito FP, Martins J, Lopes F, Castro C, Martins L, Moreira ALN. Development and assessment of an over-expanded engine to be used as an efficiency-oriented range extender for electric vehicles. Energies. 2020;13(2):430. https://doi.org/10.3390/en13020430

[4] Dingel O, Mayrock M, Peteranderl C. CNG Range extender for an electrically driven garbage collection vehicle. ATZ Heavy Duty worldwide. 2021;14(1):20-5. https://doi.org/10.1007/s41321-021-0406-6

[5] Kęska A, Dziubek M, Michalik D. The economic aspects of vehicle operation in the context of electromobility strategies. Combustion Engines. 2024;196(1):146-152. https://doi.org/10.19206/CE-172821

[6] Kim S, Lee J, Lee S, Lee S, Kim K, Min K. Effects of various compression ratios on a direct injection spark ignition hydrogen-fueled engine in a single-cylinder engine. Int J Automot Technol. 2024;25(5):1159-72. https://doi.org/10.1007/s12239-024-00096-6

[7] Kordzinski C, Papuga T, Rudkowski M. Electronically controlled fuel supply system of hydrogen spark ignition engines. Advances in Hydrogen Energy. V Proceedings of the 5th World Hydrogen Energy Conference, Toronto, 15-20 July 1984. 4:1649-1654.

[8] Lei J, Niu J, Tian G, Xin G, Yang X, Shi C. Advances in hydrogen as a zero-carbon fuel for rotary engines: a review. Fuel. 2025;381:133681. https://doi.org/10.1016/j.fuel.2024.133681

[9] Lemmon EW, Huber ML, Leachman JW. Revised standardized equation for hydrogen gas densities for fuel consumption applications. J Res Natl Inst Stand Technol. 2008;113(6):341. https://doi.org/10.6028/jres.113.028

[10] Leroux C, Böwing R, Hochfilzer B, Zuschnig A, Behr M. Hydrogen in the gas network – challenges and solutions for high performance engines for power generation. In: Heintzel A. Heavy-Duty-, on- und Off-Highway-Motoren 2022 Stand der Energiewende im Heavy-Duty-Bereich. Springer Vieweg. 2023:143-157. https://doi.org/10.1007/978-3-658-41477-1_11

[11] Noga M, Gorczyca P, Hebda R. The effects of use of the range extender in a small commercial electric vehicle. AE. 2020;4(1):5-19. https://doi.org/10.31603/AE.4137

[12] Noga M, Moskal T. Hydrogen and ethanol co-combustion in a SI engine for CO_2 emission reduction. Proceedings of 28th International Scientific Conference. Transport Means. 2024;1:981-986. https://doi.org/10.5755/e01.2351-7034.2024.P981-986

[13] Pielecha I. Control algorithms for a range extender vehicle with an combustion engine. Combustion Engines. 2020;183(4):3-10. https://doi.org/10.19206/CE-2020-401

[14] Ruíz-Domínguez JJ, Trejo-Valdez MD, Grave-Capistrán MA, Torres-SanMiguel CR. Experimental assessment of hydrogen combustion cells in a four-stroke engine. In: Carbone G, Quaglia G. Proceedings of I4SDG Workshop 2025 - IFToMM for Sustainable Development Goals Volume 2. Springer; 2025.559-568. https://doi.org/10.1007/978-3-031-91179-8_58

[15] Skarlis S, Molos T, Ayfantopoulou G, Nikiforiadis A, Bakouros L. Light commercial electric vehicles with hydrogen fuel-cell range extender: refueling strategy evaluation. Research in Transportation Business & Management. 2023;50:101040. https://doi.org/10.1016/j.rtbm.2023.101040

[16] Sutkowski M, Mareczek M. Operational experience and new developments for industrial gas engines fuelled with hydrogen fuels. Combustion Engines. 2024;197(2):146-151. https://doi.org/10.19206/CE-183185

[17] Szwaja S. Combustion pressure fluctuations study in the hydrogen fueled internal combustion engine (in Polish). Częstochowa University of Technology Publishing House. Częstochowa 2010.

[18] Tran M, Bhatti A, Vrolyk R, Wong D, Panchal S, Fowler M et al. A review of range extenders in battery electric vehicles: current progress and future perspectives. WEVJ. 2021;12(2):54. https://doi.org/10.3390/wevj12020054

[19] Wu L, Feng H, Zhang Z, Jia B, Wang J, Yang F et al. Experimental analysis on the operation process of opposed-piston free piston engine generator. Fuel. 2022;325:124722. https://doi.org/10.1016/j.fuel.2022.124722

[20] Wu Z, Han Z, Shi Y, Liu W, Zhang J, Huang Y et al. Combustion optimization for fuel economy improvement of a dedicated range-extender engine. P I Mech Eng D-J Aut. 2021;235(9):2525-39. https://doi.org/10.1177/0954407021993620

[21] Zambalov SD, Yakovlev IA, Maznoy AS. Effect of multiple fuel injection strategies on mixture formation and combustion in a hydrogen-fueled rotary range extender for battery electric vehicles. Energ Convers Manage. 2020;220:113097. https://doi.org/10.1016/j.enconman.2020.113097

[22] Zhang C, Xu Z, Wang Y, Liu L. Development of a hydrogen free-piston engine generator for range extenders. Sustainable Energy Technologies and Assessments. 2024;65:103788. https://doi.org/10.1016/j.seta.2024.103788

Marcin Noga, DSc., DEng. – Faculty of Mechanical Engineering, Cracow University of Technology, Poland.
e-mail: *noga@pk.edu.pl*

Tomasz Moskal, MEng. – Faculty of Mechanical Engineering, Cracow University of Technology, Poland.
e-mail: *tomasz.andrzej.moskal@gmail.com*

Article citation info:
Kravchenko S, Obodets D, Kuzmenko A. Improving the energy efficiency of a two-stroke engine with crankcase scavenging for UAVs by implementing an electronic fuel injection system. Combustion Engines. 2026;204(1):72-80. https://doi.org/10.19206/CE-213457

Serhii KRAVCHENKO
Dmytro OBODETS
Anatolii KUZMENKO

Combustion Engines
Polish Scientific Society of Combustion Engines

Improving the energy efficiency of a two-stroke engine with crankcase scavenging for UAVs by implementing an electronic fuel injection system

ARTICLE INFO

Received: 19 August 2025
Revised: 30 September 2025
Accepted: 21 October 2025
Available online: 22 November 2025

The article considers the use of an electronic fuel injection system as a way to increase the energy efficiency of a two-stroke piston engine with crank-chamber purge for UAVs. An analysis of publications reveals the advantages of injection over carburetor power systems, particularly increased power, reduced fuel consumption, and lower emissions of harmful substances. An electronic fuel injection system, based on a microcontroller electronic control unit with sensors (MAP, TPS, ECT, IAT, CKP) and actuators, has been developed. EFI Studio software has been implemented for system calibration and monitoring. The control algorithm is based on the Alpha-N method taking into account dead time and injection phase shift. A hardware implementation is presented that provides dosing accuracy and flexible control of engine operating modes. The results confirm the practical significance of the technology for increasing the efficiency and environmental friendliness of small UAV engines.

Key words: *UAV engine, two-stroke engine, electronic fuel injection, electronic control unit, energy efficiency*

1. Introduction

Recently, unmanned aerial vehicle (UAV) technologies have been rapidly advancing alongside the swift development of microelectronics and communication technologies. Compared to manned aircraft, UAVs typically have significantly smaller dimensions, lower weight, and are less demanding in terms of runway characteristics. They are also characterized by relatively low production and operational costs. As a result, UAVs are widely used in the military, geographic services, satellite operations, navigation, medicine, and other fields [10].

A key component of any UAV is its powerplant, which provides propulsion and supplies energy to onboard systems. Reciprocating engines are the most common type of propulsion for UAVs. These engines have several types, among which the two-stroke engines are the most common ones [15].

Two-stroke piston engines with crankcase-scavenged loop charging and spark-ignition of the air-fuel mixture are characterized by high specific power output and mechanical simplicity. These features have contributed to their widespread adoption in small- and medium-sized unmanned aerial vehicles (UAVs) [13, 15]. Numerous companies – such as 3W, Gobler Hirth, and Limbach in Germany; Wilksch in the United Kingdom; Zanzottera in Italy; and XRDi and DeltaHawk in the United States, as well as DLA in China – currently specialize in the production of this class of engines [17].

Flight endurance has increasingly been regarded as one of the most important technical parameters in evaluating UAV performance. Given the limited onboard fuel capacity of UAVs, their endurance is directly influenced by the thermodynamic efficiency of the propulsion system, i.e., the fuel consumption of the aircraft engine.

Unlike conventional four-stroke engines, which are equipped with complex valvetrain mechanisms, gas exchange in two-stroke engines is typically achieved by the movement of the piston itself. While this simplified scavenging mechanism facilitates engine design and manufacturing, it also results in lower volumetric efficiency and a substantial loss of the fresh charge from the cylinder during the scavenging process [4, 9, 19, 20, 24].

Thus, optimizing the working cycle of these engines remains a relevant engineering challenge. Improving engine performance necessitates the implementation of advanced technologies that enable effective control of combustion processes and, as a result, the realization of the engine's full potential. The integration of modern electronic fuel injection systems offers a promising approach to enhancing the operational characteristics of two-stroke engines. The replacement of traditional carburetion systems with electronic fuel injection (EFI) has become a focus of research for both academic institutions and engineering firms. While carburetors offer certain advantages, detailed analyses of their performance have revealed several limitations. These include high sensitivity to ambient environmental conditions, a tendency to flood, dependence on the physical properties of gasoline, and the risk of carburetor icing. For example, 3W International offers engine models equipped with either carburetor or EFI systems, emphasizing the advantages of EFI [1]. These include reduced fuel consumption, improved air-fuel mixture formation, enhanced power output, and more stable performance across varying engine orientations and environmental conditions. Moreover, EFI systems significantly reduce the dependency on the physical and chemical properties of gasoline (such as volatility), sensitivity to ambient conditions, and the risk of fuel condensation or intake manifold icing. This marks a substantial improvement over carbureted systems, which are more susceptible to these limitations.

Fuel injection serves as an alternative to carburetion for preparing the air-fuel mixture suitable for proper functioning of spark-ignition (SI) engines. Injection systems operate based on physical principles distinct from those of carbure-

tors, both in terms of fuel metering and atomization within the air mass. Specifically, these systems meter fuel in proportion to the engine's air intake flow, relying not on the intake vacuum generated by the engine but on increased fuel pressure provided by a pump. Moreover, whereas in a carburetor fuel atomization is driven by the higher velocity of the intake air stream that entrains and breaks the fuel into progressively finer droplets. In an injection system, fuel is delivered at high velocity through a nozzle, producing a fine spray via kinetic atomization.

2. Literature review

The efficiency of the engine combustion process can be enhanced, and the flight endurance of UAVs can be extended, through the implementation of optimal fuel delivery control technologies. Consequently, an increasing number of researchers and engineers have turned their attention to the development and refinement of fuel supply systems for UAV engines [3, 6, 7, 12, 21, 22].

There is a general trend toward the adoption of electronic fuel injection (EFI) systems in two-stroke spark-ignition engines [12, 22]. Although fuel injection into the intake manifold of two-stroke engines does not eliminate fuel–air mixture losses during scavenging, it can improve overall engine performance due to more precise control of the air–fuel ratio. In general, EFI systems allow the engine to operate with leaner mixtures compared to carbureted systems. Another notable advantage is that fuel injection can provide up to 20% higher output power relative to a carbureted version. Moreover, hydrocarbon (HC) emissions are significantly lower across the full throttle range when using injection systems. For instance, in [12], which investigates the application of such an injection system in a two-stroke engine, an increase in power from 3.6 kW to 4.2 kW was observed, accompanied by a reduction in HC emissions from 2310 ppm to 1200 ppm. In [22], additional studies were conducted to improve the efficiency of UAV powerplants by employing intake manifold fuel injection. A fuel delivery strategy based on controlling the excess air coefficient (λ) was proposed, and a control algorithm using a PID regulator was implemented to mitigate deviations in λ under all engine operating conditions. As a result, the thermal efficiency of the cycle was improved by 5–25%. Other reported benefits of such systems include improved cold start behavior and enhanced engine controllability [3].

One method of reducing fuel loss through the exhaust ports is the use of resonant exhaust systems, as presented in [18]. However, due to UAV design constraints, integrating specific exhaust system geometries is not always feasible. Therefore, one promising approach to reducing, or potentially eliminating fuel losses during scavenging and minimizing hydrocarbon emissions in the exhaust gases involves the use of direct fuel injection into the engine cylinders [4, 7, 11, 13]. Nonetheless, due to the unique operating characteristics of two-stroke engines, implementing such a system significantly complicates the lubrication system. Perhaps the most representative contributions reflecting the current state of the art are those presented in [11, 13]. These studies employed high-pressure fuel injection systems similar to those used in diesel engines. While peak engine power was found to be nearly unaffected by the application of direct injection, there was a notable reduction in brake-specific fuel consumption (BSFC), reaching 300 g/kWh, compared to 370 g/kWh for the carbureted version. A similar pattern was observed for emissions: hydrocarbon emissions were reduced by 53%, and carbon monoxide (CO) emissions by 40% when using injection systems as compared to carburetors [13]. The effectiveness of direct fuel injection was further confirmed in [11] with the use of compressed natural gas, where the maximum brake thermal efficiency was increased by 9.1%, while unburned HC emissions were reduced by 79.3% and CO emissions by 94.5% compared to the carbureted engine.

The aim of this study is to implement measures aimed at improving the energy efficiency of a two-stroke engine with crankcase scavenging through the integration of an electronic fuel injection system.

3. Principle of fuel quantity calculation

Spark-ignition engines operate by combusting a premixed fuel–air charge. Accordingly, the primary function of the fuel supply system is to meter the appropriate amount of fuel required to achieve an optimal air–fuel ratio (AFR) in accordance with the engine's operating conditions. In principle, the optimal AFR for spark-ignition engines depends to some extent on the specific operating conditions. That is, it is defined as the ratio that ensures the required output power with the lowest possible fuel consumption, while maintaining uninterrupted and reliable engine operation.

Combustion of the fuel–air mixture in the cylinder of an internal combustion engine with spark ignition occurs only within a certain range of AFR, typically from 8.0 to 25.5. The stoichiometric ratio is approximately 14.7. Lean mixtures generally improve fuel economy, whereas rich mixtures tend to increase engine torque output. Enrichment of the air–fuel mixture can also be employed as a strategy to reduce combustion temperatures and prevent thermal overload during high-load operating modes (see Fig. 1).

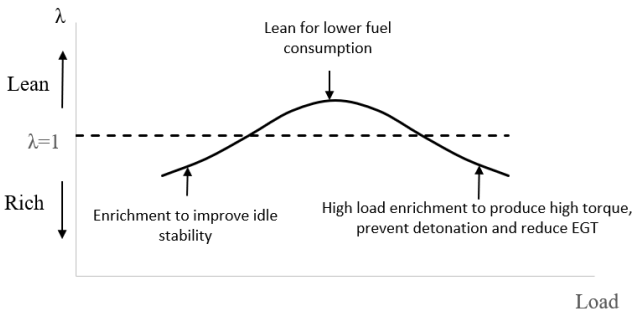

Fig. 1. Influence of the air–fuel mixture composition on engine operating modes

Therefore, depending on the specific operating conditions, it is necessary to find a compromise between competing requirements by selecting the value of the air–fuel equivalence ratio, λ, that yields the most favorable results. This implies that, for each point within the engine's operating range, it is possible to define, based on different performance requirements, the most appropriate value of λ, which the fuel supply system should aim to maintain.

Moreover, λ is defined as the ratio of the actual amount of air participating in the combustion process to the theoretical amount of air required for the complete combustion of the given quantity of fuel. It can be expressed as follows:

$$\lambda = \frac{m_{air}}{l_0 \cdot m_{fuel}} \quad (1)$$

where m_{air} is the mass of air that participates in the combustion of m_{fuel} kilograms of fuel.

The mass airflow rate in the intake manifold passing through the throttle valve is given by:

$$m_{air} = \frac{n \cdot V_h \cdot \rho_{air} \cdot \eta_v}{60} \quad (2)$$

where ρ_{air} is the air density in the intake manifold, n is the engine speed, V_h is the engine displacement volume, and η_v is the volumetric efficiency.

Since air density can be expressed as $\rho_{air} = P_{air}/(RT_{air})$, where P_{air} and T_{air} represent the pressure and temperature of the air in the intake manifold, and R is the specific gas constant, the equation can also be written as:

$$m_{air} = \frac{n \cdot V_h \cdot P_{air} \cdot \eta_v}{60 \cdot R \cdot T_{air}} \quad (3)$$

When the injector opens, fuel is delivered under high pressure, generating a fuel flow. The following equation can describe the fuel flow rate:

$$m_{fuel} = \mu S_{inj} \sqrt{2 \cdot g \cdot \rho_f (P_{fuel} - P_m) \cdot PW} \quad (4)$$

where $\dot{m}_{fuel}$ denotes the mass flow rate of fuel during a single injection event, μ is the injector discharge coefficient, S_{inj} represents the total area of the injector orifices, ρ_f is the fuel density, P_{fuel} is the fuel pressure, P_m is the intake manifold pressure, and PW is the fuel injection pulse width per engine cycle.

The following section considers the characteristics of well-known algorithms used to calculate the required amount of fuel based on input parameters received by the engine control unit (ECU).

MAF

According to this algorithm, the amount of injected fuel is calculated directly based on the input from the Mass Air Flow (MAF) sensor and the desired air-fuel ratio. Fuel injection systems employing this approach interpret the MAF sensor output as a direct representation of the engine's current air intake flow. This method enables a straightforward and intuitive calculation of the required fuel quantity and does not require specific calibration for each engine or its sensors. In this case, the engine load (volumetric efficiency) can be instantly determined as:

$$m_{air} = \frac{MAF}{V_h \cdot \rho_{air} \cdot n} \quad (5)$$

The required fuel mass flow rate can be determined using the following expression:

$$m_{fuel} = \frac{m_{air}}{AFR_{target}} \quad (6)$$

where AFR_{target} is the desired air-fuel ratio.

Speed Density

An alternative to direct measurement of the intake air flow is the estimation of air mass based on signals from other sensors, such as those measuring intake manifold pressure and air temperature. This fuel injection control strategy is referred to as the Speed-Density method [14] (Fig. 2). In this approach, the intake air flow rate is not measured directly. Instead, the mass of air entering the engine is calculated based on intake air temperature, manifold absolute pressure (MAP), and engine speed, using a reference volumetric efficiency (VE) table.

The volumetric efficiency of the engine is a parameter influenced by both operating conditions (such as crankshaft rotational speed and manifold pressure) and engine design characteristics (such as displacement volume, intake manifold geometry, and compression ratio). The primary VE table is typically defined as a two-dimensional function of manifold absolute pressure (MAP) and engine speed (RPM).

Based on the selected VE value, along with the measured MAP and intake air temperature, the engine control unit calculates the air mass entering the engine.

For a warmed-up engine, the air mass per cylinder per cycle ma is calculated using the following expression:

$$m_{air} = \eta_v(N) \cdot \rho_{air}(T, P) \cdot V_h = \frac{\eta_v \cdot V_h \cdot P_{air}}{R \cdot T_{air}} \quad (7)$$

After calculating the mass air flow entering the engine, the corresponding fuel mass flow rate can be determined. The primary limitation of this method lies in the necessity to develop or calibrate the VE table individually for each engine type. This requirement arises because the airflow velocity may exhibit similar values under different engine speeds and MAP sensor operating conditions. Therefore, it becomes essential to determine the steady-state values of the volumetric efficiency η_v across all regions of the VE table with sufficient accuracy.

Alpha-N

In the Alpha-N strategy, the air mass is calculated using an empirical map and is defined as follows:

$$m_{air} = VE(\alpha, N) \cdot V_h \cdot \rho_a(T, p) \quad (8)$$

In other words, the injector opening duration is calculated based on empirical correlations between the engine crankshaft speed and the throttle valve opening angle (Fig. 3). To improve accuracy, ambient air pressure and temperature are also taken into account.

For each of these primary algorithms, additional strategies for adjusting the injector opening duration may be implemented depending on the engine's operational model:

Percent Baro (Speed-Density + Atmospheric Pressure)

This strategy adjusts the volumetric efficiency based on an additional ambient atmospheric pressure sensor. Its application is particularly relevant for UAVs operating above 1000 meters, where air–fuel mixture correction becomes necessary.

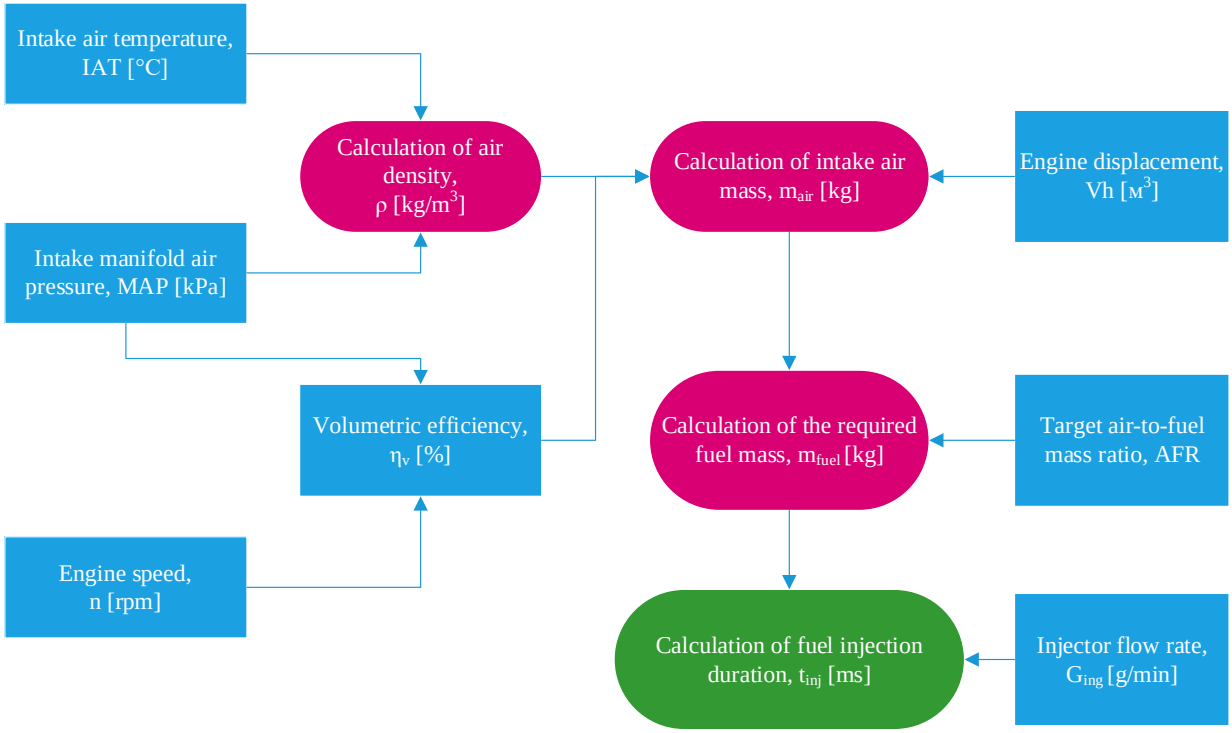

Fig. 2. Speed Density algorithm for calculating the required fuel quantity

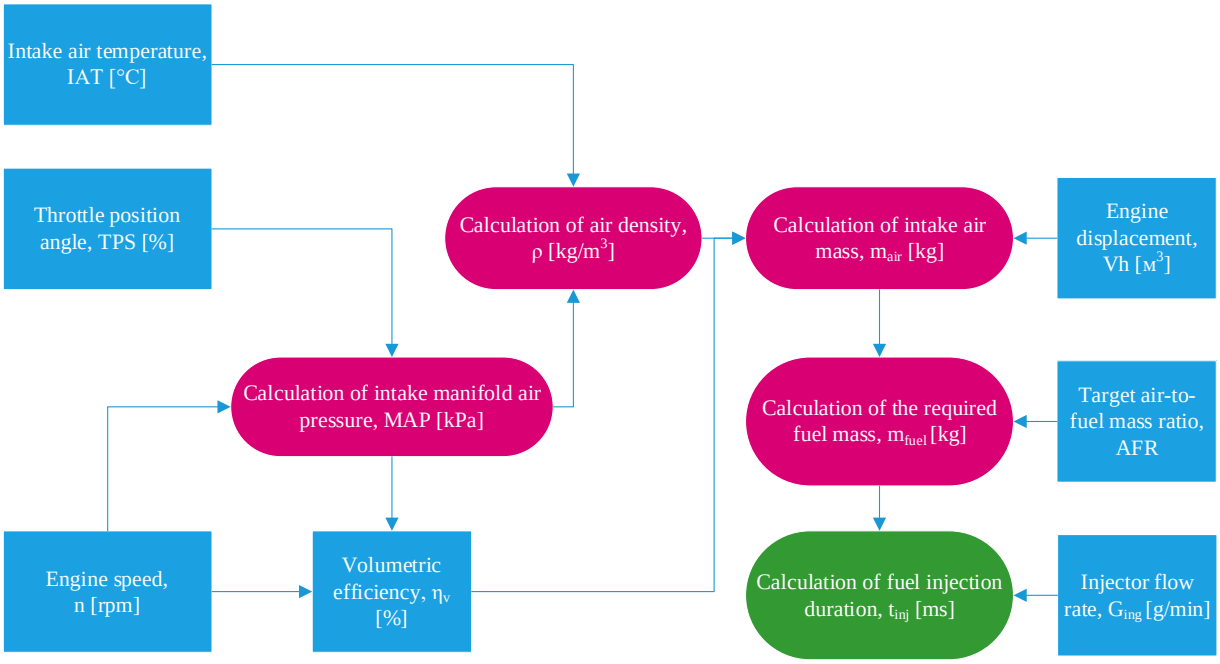

Fig. 3. Alpha-N algorithm for calculating the required fuel quantity

Lambda Feedback (Closed-Loop Control)

This method monitors the composition of the exhaust gases to fine-tune fuel injection in real time, ensuring the air–fuel ratio (AFR) remains close to the target value.

Transient Fuel Compensation

This adjustment controls fuel delivery during rapid throttle changes. It includes fuel enrichment during acceleration and fuel cut-off during deceleration.

Cold Start Enrichment

This strategy compensates for poor fuel vaporization at low temperatures by enriching the mixture during cold engine starts.

4. Implementation of the fuel injection system for a two-stroke UAV engine with crankcase scavenging

The fuel injection system must be capable of detecting changes in parameters that influence the optimal air–fuel

ratio required by the engine and transmitting this information to the Electronic Control Unit (ECU). The ECU integrates the individual signals received from sensors and calculates the required amount of fuel m_{fuel} to be injected for a given engine operating mode.

Thus, in the fuel injection system, the primary control parameters that must be continuously monitored for accurate dosing are:

- Intake air flow rate, which serves as the fundamental input for calculating the mass of fuel to be injected
- Ambient air temperature and pressure, which influence air density and mixture formation
- Crankshaft rotational speed, which determines the injection frequency and the amount of fuel required per cycle
- Pressure differential Δp is maintained across the injector nozzle, which affects fuel atomization and delivery
- Throttle valve position, representing the engine load index which, in conjunction with crankshaft speed, allows the ECU to identify the appropriate value on predefined maps stored in memory
- Engine temperature is used for fuel delivery correction. During cold starts, increased injection duration is required. During engine warm-up, a temporary enrichment of the mixture is applied, depending on the engine temperature.

The developed electronic fuel injection unit is a microcontroller-based system that reads sensor data from the engine and generates an actuation signal for the injector, which is installed in the engine's intake manifold. The required pulse width for injector opening duration is computed based on lookup tables and constants stored in the microcontroller's memory.

A block diagram of the fuel injection control unit is shown in Fig. 4. Functionally, the system consists of a fuel injection control unit, a set of sensors (including the throttle position sensor (TPS), engine temperature sensor (CHT), manifold absolute pressure (MAP) sensor, intake air temperature (IAT) sensor, and crankshaft position sensor), and actuators (a fuel pump with a pressure regulator and injectors).

Figure 5 presents the schematic diagram of the fuel injection control unit. The control unit comprises the following components: an 8-bit microcontroller (ATmega328P) with digital input/output ports and a 10-bit analog-to-digital converter (ADC); an interface IC for actuator control (MC33812); a CAN bus module for bidirectional data exchange; and signal conditioning and input protection circuitry for the microcontroller.

The design of the printed circuit board (Fig. 6) is based on the use of the MC33812 integrated circuit [16], which was specifically developed by NXP for control units in 2-stroke and 4-stroke engine applications. This chip integrates a voltage regulator and actuator drivers, and includes diagnostic functionality to detect faults such as open or short circuits in the actuators.

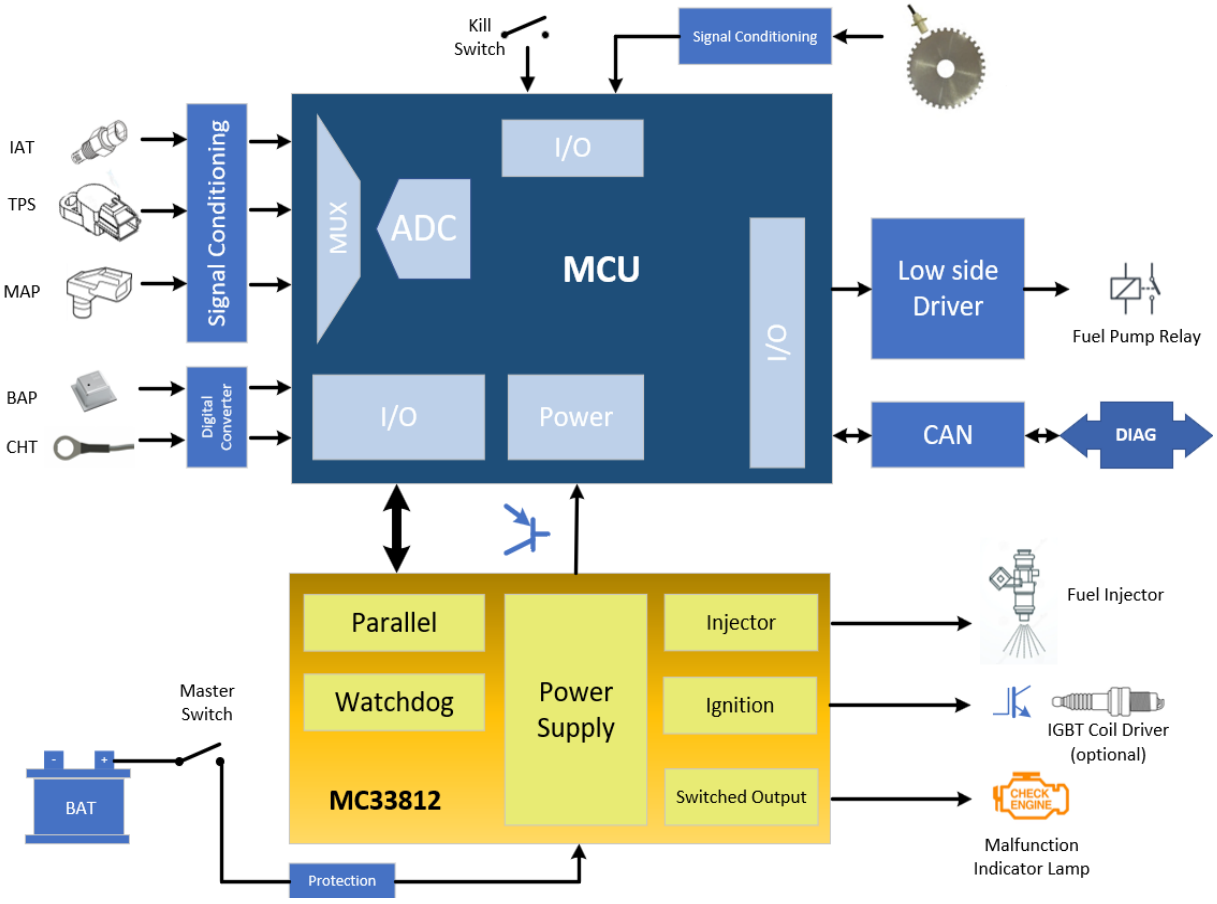

Fig. 4. Block diagram of the electronic fuel injection control system

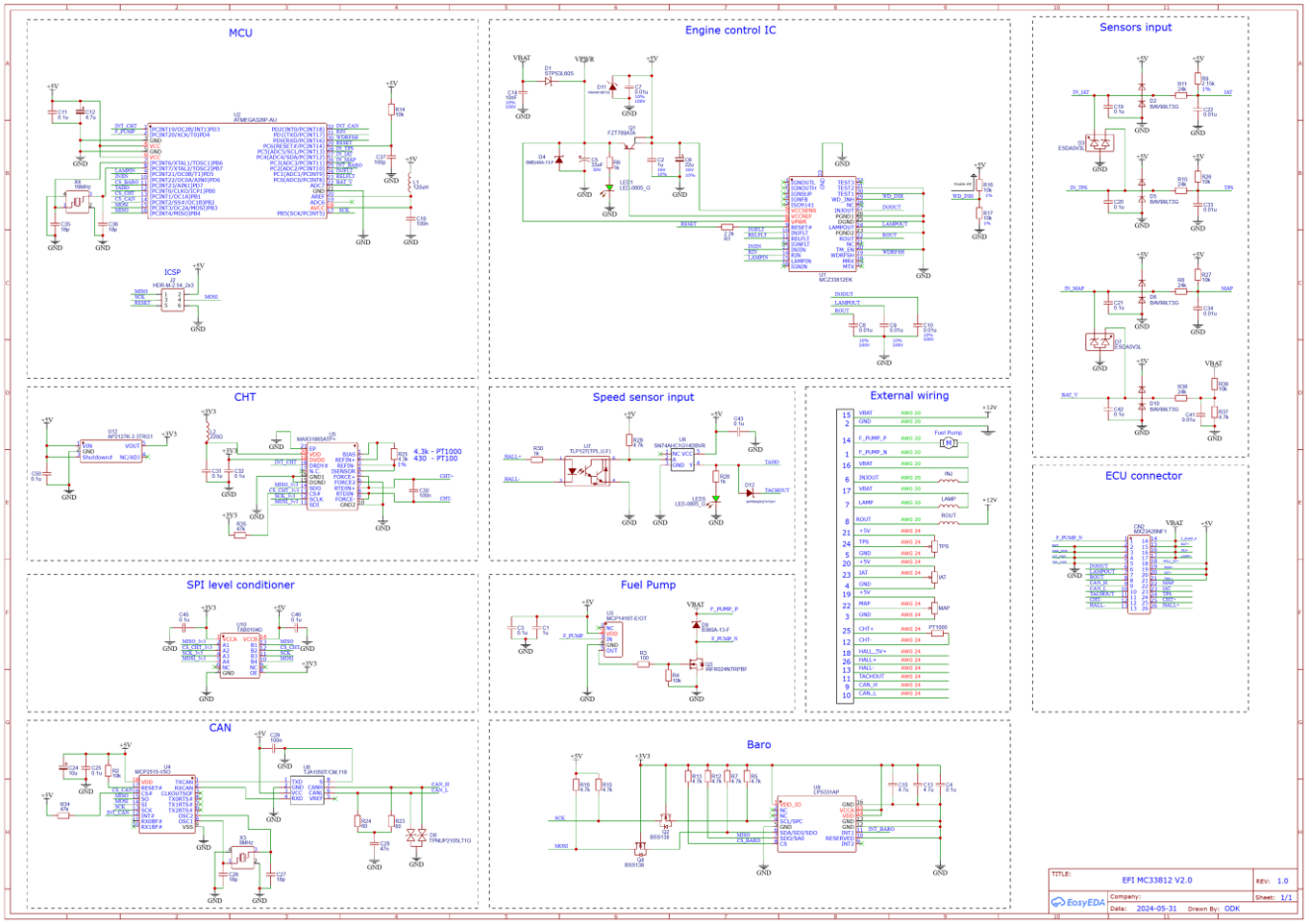

Fig. 5. Schematic diagram of the electronic fuel injection control unit

A platinum PT100 sensor is used as the engine cylinder temperature sensor (CHT). Its characteristics enable high-accuracy temperature measurements across a wide operating range from –50°C to +400°C. The MAX31865 [2] resistance-to-digital converter is employed for signal conditioning. In addition to high-precision resistance measurements, this chip supports diagnostics for sensor disconnection and short circuits. It includes a DRDY (Data Ready) output to indicate the completion of conversion and readiness of data for reading.

The fuel injection control unit is equipped with a barometric pressure sensor for altitude-based correction of fuel delivery. This sensor is implemented using the LPS331AP integrated circuit. It interfaces with the main microcontroller via SPI and includes a dedicated INT1 interrupt output to signal data readiness.

Since the ATmega328P microcontroller does not include a built-in CAN interface, this functionality is provided by two external components: the MCP2515 CAN controller and the TJA1050T transceiver. By utilizing the SPI interface and structuring data as 1–4 byte packets per variable (including floating-point types), high data transfer speeds are achieved, minimizing delays in the main program during data transmission or reception.

The microcontroller's crankshaft position sensor (CKP) input is galvanically isolated via an optocoupler and further equipped with a Schmitt-trigger buffer to suppress electromagnetic interference.

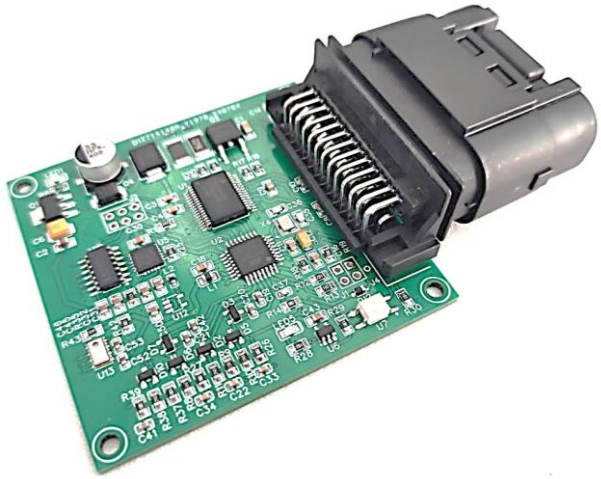

Fig. 6. External view of the developed printed circuit board design for the fuel injection control unit

To configure the parameters of the fuel injection control unit, the EFI Studio software was developed within the LabVIEW environment. The software interface is shown in Fig. 7. This software enables diagnostics of the control unit, sensor calibration, real-time monitoring of parameters, and, most importantly, modification of the settings of tables and constants necessary for calculating the fuel injection duration, including:

– Engine displacement, cm³
– Injector flow rate, g/min
– VE table (n, TPS) – volumetric efficiency coefficient depending on engine speed and throttle position
– AFR table (n, TPS) – required air-fuel ratio depending on engine speed and throttle opening angle
– Correction coefficient tables: cor_IAT(IAT), cor_CHT(CHT), cor_Baro(Baro) – correction factors for intake air temperature, cylinder head temperature, and barometric pressure, respectively
– mult_start table (N_cycle) – enrichment coefficient during cold start
– DT = f(V_bat) table – injection duration correction map accounting for power supply voltage drop.

The algorithm for calculating the engine crankshaft speed utilizes the microcontroller's hardware features. For this purpose, the 16-bit timer/counter is configured in input capture mode. The filtered signal is fed to the microcontroller's ICP1 (Input Capture Pin). When a rising edge is detected, the current timer value is latched and copied into the ICR1 register, triggering an interrupt. During the first interrupt call, the ICR1 register value is stored; during the second call, the difference between the current and previous timer values is calculated. Since the timer continues running and is not reset, an overflow interrupt is used to count the number of full timer cycles. This overflow count is taken into account in the RPM calculation.

The primary advantage of this method is its high measurement accuracy, as signal capture occurs immediately upon detection, independent of the main program's execution.

The required fuel amount is calculated using the Alpha-N method described above. This method was selected based on the operating characteristics of the UAV engine, which runs mostly at throttle openings close to maximum during flight. Therefore, the Alpha-N strategy offers an advantage due to its simple implementation and good response to acceleration and deceleration.

Upon powering the EFI control unit, the fuel pump is briefly activated to pressurize the fuel rail. When the first crankshaft position sensor (CKP) pulse is received, a priming fuel injection occurs. The amount of fuel injected is determined from a table based on the engine cylinder temperature.

To generate the injector control signal, two timers are used. One timer controls the injection duration, while the other manages the injection phase shift relative to the CKP signal.

The core of the control program is a state machine, which coordinates and manages the operating modes of the electronic control unit. Its main task is to ensure a consistent transition between modes such as "normal operation", "startup mode," and "programming/debugging mode".

Figure 8 shows an oscilloscope trace of current and voltage at the injector terminals. From this waveform, it can be concluded that when controlling fuel injectors, it is necessary to consider the so-called dead time – the delay between the application of the electrical pulse and the actual start of fuel injection. This delay depends on supply voltage and the physical characteristics of the injector, and it significantly affects fuel metering accuracy. Neglecting this delay can lead to enrichment or enleanment of the air-fuel mixture, especially in operating modes with short injection durations. Since the dead time is independent of the injection duration and is a function of the injector's electrical characteristics (under constant fuel pressure), it should be treated as an additive constant, which is added on top of the other multiplicative factors [23].

5. Conclusions

1. The use of two-stroke engines as the powerplant for UAVs is considered the most promising due to their simple design and high specific power characteristics.

2. The efficiency of the engine combustion process can be improved, and the UAV flight duration extended, through the use of electronic fuel injection (EFI) systems.

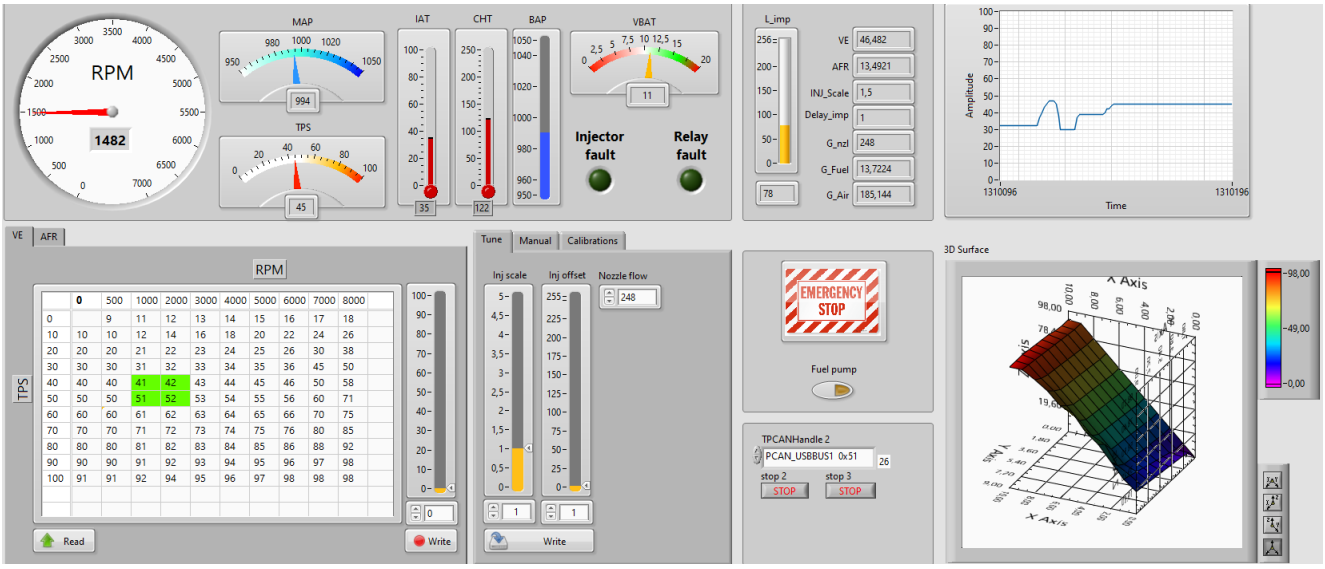

Fig. 7. Interface of the developed EFI Studio software

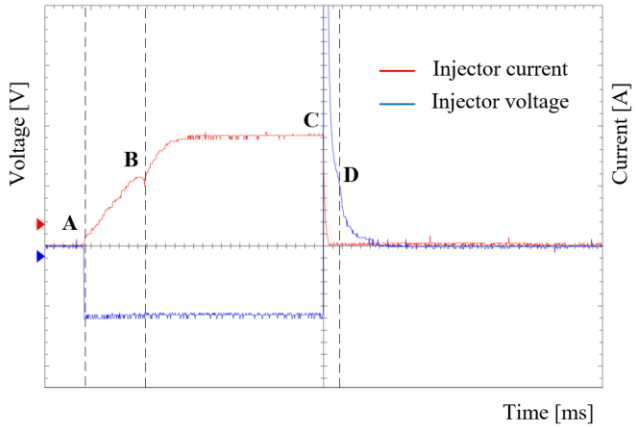

Fig. 8. Oscillogram of the injector control signal; AB – injector opening, BC – fully open nozzle, CD – injector closing, AC – EFI control pulse

3. One of the most effective methods for reducing or even eliminating fuel losses through the exhaust port during scavenging, as well as for decreasing hydrocarbon emissions in two-stroke engines, is the implementation of direct fuel injection into the cylinders. However, given the operating specifics of a two-stroke engine, such an approach significantly complicates the lubrication system.

4. Within the framework of this study, an electronic fuel injection control unit was developed for a two-stroke engine with crankcase scavenging. The unit includes an 8-bit ATmega328P microcontroller, an MC33812 interface IC for actuator control, a CAN bus module for bidirectional data exchange, signal conditioning circuits, and input protection for the microcontroller.

5. Since the UAV engine operates mostly at wide open throttle during flight, the Alpha-N algorithm was selected for fuel quantity calculation.

6. Dedicated software called EFI Studio was developed in the LabView environment to configure the parameters of the EFI control unit.

7. A current and voltage oscilloscope trace at the injector terminals was obtained for one of the operating modes, confirming the functionality of the developed electronic control unit.

8. The next stage of research will focus on testing the developed injection system directly on a two-stroke internal combustion engine, with an assessment of the efficiency and environmental characteristics of the fuel-injected engine in comparison to the carbureted version.

Acknowledgements

The research was carried out with the grant support of the National Research Foundation of Ukraine within the framework of the project 2023.04/0124 "Improving the tactical and technical characteristics of domestic UAVs by developing an aircraft engine with promising specific power indicators".

Nomenclature

AFR	air-fuel ratio
BSFC	brake-specific fuel consumption
CKP	crankshaft position
CO	carbon monoxide
ECU	engine control unit
EFI	electronic fuel injection
HC	hydrocarbon
IAT	intake air temperature
MAF	mass Air Flow
MAP	manifold absolute pressure
SI	spark ignition
TPS	throttle position sensor
UAV	unmanned aerial vehicles
VE	volumetric efficiency

Bibliography

[1] 3W-International's performance partner sky power releases new injection and ignition system. UAS Weekly; 2018 Apr 6. https://uasweekly.com/2018/04/06/3w-internationals-performance-partner-sky-power-release-new-injection-and-ignition-system/ (accessed on 2025.09.24)

[2] Analog Devices. MAX31865 RTD-to-digital converter. Data sheet. https://www.analog.com/media/en/technical-documentation/data-sheets/max31865.pdf

[3] Archer M, Bell G. Advanced electronic fuel injection systems – an emissions solution for both 2- and 4-stroke small vehicle engines. SAE Technical Paper 2001-26-0010. 2001. https://doi.org/10.4271/2001-26-0010

[4] Blair G. Design and simulation of two-stroke engines. SAE International 1996:623.

[5] Blyenburg & Co. UAS Yearbook: Unmanned aircraft systems – the global perspective 2010/2011. Paris 2010:214. http://www.dcabr.org.br/download/cursos-eventos/eventos/eventos-realizados/2010/seminario-vant-27-10-2010/cd-uvs-yearbook/

[6] Darwin RB, Purwoko AT, Sopiyan. Design and experiment of a prototype electronic control unit direct injection fuel system arduino-based for 2-stroke spark ignition engine. Automotive Experiences. 2022;5(1):49-56. https://doi.org/10.31603/ae.5472

[7] Darzi M, Johnson D, Ulishney C, Clark N. Low pressure direct injection strategies effect on a small SI natural gas two-stroke engine's energy distribution and emissions. Appl Energy. 2018;230:1585-1602. https://doi.org/10.1016/j.apenergy.2018.09.091

[8] Hassanalian M, Rice D, Abdelkef A. Evolution of space drones for planetary exploration: a review. Prog Aerosp Sci. 2017;97:61-105. https://doi.org/10.1016/j.paerosci.2018.01.003

[9] Heywood JB. Internal combustion engine fundamentals. New York: McGraw-Hill 1988.

[10] Kolisnyk K, Kartashov V, Tomashevskyi R, Kolisnyk V, Koval S, Zamiatin P. The use of drones to improve the efficiency of using telemedicine systems in emergencies. 2022 IEEE 3rd KhPI Week on Advanced Technology (KhPIWeek); 2022 Kharkiv. https://doi.org/10.1109/KhPIWeek57572.2022.9916362

[11] Kumarappa S, Prabhukumar GP. Improving the performance of two stroke spark ignition engine by direct electronic CNG

injection. Jordan Journal of Mechanical and Industrial Engineering. 2008;2:169-174.
[12] Loganathan M, Manivannan PV, Ramesh A. Investigations on performance and emissions of a two-stroke SI engine fitted with a manifold injection system. Indian Journal of Engineering & Materials Sciences. 2006;13:95-102.
[13] Marouf M, Mursaleen M, Saad P. Investigations on two stroke cycle spark ignition engine using gasoline direct injection. Energy and Power. 2012;2(7):116-122.
[14] Meng L, Luo J, Yang X, Zeng C. Intake air mass observer design based on extended Kalman filter for air-fuel ratio control on SI engine. Energies. 2019; 12(18):3444. https://doi.org/10.3390/en12183444
[15] Newcome LR. Unmanned aviation: a brief history of unmanned aerial vehicles. Reston (VA): AIAA 2004.
[16] NXP Semiconductors. Multifunctional ignition and injector driver 33812. Data sheet. https://www.nxp.com/docs/en/data-sheet/MC33812.pdf
[17] Obodets DK. Modern trends in the development of unmanned aerial vehicle engines. Aviation and Space Technology. 2024;5(199):27-38.
[18] Obodeh O, Otunuya AD. Improving the performance of two-stroke motorcycle with tuned adjustable exhaust pipe. Research Journal of Applied Sciences. Engineering and Technology. 2009;1(2):59-65.
[19] Sapate KD, Tikekar AN. Pollution aspects of emissions from small two-stroke automobile engines. Nat Env Poll Tech. 2008;7(1):33-38.
[20] Volckens J, Olson DA, Hays MD. Carbonaceous species emitted from handheld two-stroke engines. Atmos Environ. 2008;42(6);1239-1248.
[21] Wang Y, Shi Y, Cai M, Xu W, Zhang J, Zhong W. Optimization of fuel injection control system of two-stroke aeroengine of UAV. Complexity. 2020;8921320. https://doi.org/10.1155/2020/8921320
[22] Wang Y, Shi Y, Cai M, Xu W, Yu Q. Efficiency optimized fuel supply strategy of aircraft engine based on air-fuel ratio control. Chinese Journal of Aeronautics. 2019;32(2):489-498. https://doi.org/10.1016/j.cja.2018.10.002
[23] Więcławski K, Mączak J, Szczurowski K. Electric current characteristics of the injector generating fuel doses. Diagnostyka. 2018;19(4):59-64. https://doi.org/10.29354/diag/97225
[24] Wróblewski P, Bratkowski P, Borcuch D, Kiszkowiak Ł. Prototype station dedicated to aircraft engine propeller profiles and advanced materials testing. Combustion Engines. 2025;201(2):165-175. https://doi.org/10.19206/CE-204319

Serhii Kravchenko, DEng. – Department of Engines and Hybrid Power Plants, National Technical University "Kharkiv Polytechnic Institute", Kharkiv, Ukraine.
e-mail: *serhii.kravchenko@khpi.edu.ua*

Anatolii Kuzmenko, DEng. – Internal Combustion Engine, Kharkiv National Automobile and Highway University, Ukraine.
e-mail: *kuzmatolja@gmail.com*

Dmytro Obodets, MEng. – Department of Engines and Hybrid Power Plants, National Technical University "Kharkiv Polytechnic Institute", Kharkiv, Ukraine.
e-mail: *dmytro.obodets@ieee.khpi.edu.ua*

Article citation info:
Samoilenko D, Lasocki J, Bednarski M, Cho HM. The influence of biogas injector location on air-biogas mixture homogeneity in a dual-fuel compression-ignition engine. Combustion Engines. 2026;204(1):81-87. https://doi.org/10.19206/CE-211070

Dmytro SAMOILENKO
Jakub LASOCKI
Mateusz BEDNARSKI
Haeng Muk CHO

Combustion Engines
Polish Scientific Society of Combustion Engines

The influence of biogas injector location on air-biogas mixture homogeneity in a dual-fuel compression-ignition engine

ARTICLE INFO

Received: 17 June 2025
Revised: 10 September 2025
Accepted: 18 September 2025
Available online: 24 September 2025

This paper deals with the dual-fuel supply of a compression-ignition engine fuelled with diesel oil and biogas. The aim was to investigate the influence of the location of biogas injectors in the engine intake manifold on the selected characteristics of the air-biogas mixture introduced into the cylinders. A 3D scanning of geometrically complex elements was used as part of the development of a detailed 3D model of the engine intake system. A simulation of the fluid flow was performed for several variants of biogas injector location. The boundary conditions for the simulation were determined experimentally in the engine dynamometer test cell. The obtained results were analysed in terms of the homogeneity of the air-biogas mixture formed in the intake manifold. Finally, the optimal location of the injector was identified. The conclusions from the study provide guidance for the implementation of biogas injection solutions in compression-ignition engines operating in dual-fuel mode.

Key words: *dual-fuel engine, biogas, flow simulation, fuel injection, mixture homogeneity*

1. Introduction

The use of internal combustion engines (ICEs) has been a subject of fierce debate in recent decades. The prevailing trend is to gradually phase out the use of ICEs in both mobile and stationary applications. The reason behind it is mainly the negative impact of engines on environmental aspects, such as the emission of pollutants that endanger the health of living organisms and cause the global climate to be unstable [9]. Furthermore, the large-scale use of non-renewable natural resources for the production of petrol and diesel oil has become a growing issue [18]. In response to the above threats, various proposals have emerged to address the shortcomings of ICEs powered by conventional fuels.

In transportation, the solution has been sought in the widespread use of electric drives, which offer numerous advantages, including energy efficiency, lower maintenance requirements, ease of control, and reliability [7]. However, practical experience has proved that the rapid implementation of such a concept on a large scale is not feasible. Limited energy storage in batteries and the lack of developed infrastructure remain challenges [22]. While efforts to electrify vehicle and machine drive systems have not been abandoned and are still being continued, there is a trend of returning to the well-known and proven methods of energy conversion offered by ICEs, although with a certain change in the approach to fuels used.

Currently, many car manufacturers assume that the continued use of ICEs requires switching to alternative fuels [22]. Among the numerous possible options, biofuels, hydrogen, and synthetic fuel are most often considered. Their use allows for maintaining the performance of ICEs at a similar level to current ones based on fossil fuels, but with significantly reduced environmental impact.

This paper focuses on biogas application in dual-fuel compression-ignition engines. This kind of alternative fuel has some favorable properties. Above all, biogas is renewable and can be produced from biomass of various origins, including waste [2]. The use of biogas reduces greenhouse gas emissions [16]. It is also a cost-effective solution, especially in rural areas, where it allows for the management of agricultural waste and the production of clean energy. On the other hand, raw biogas is not suitable for direct powering of combustion engines as it naturally contains only 40–60% of methane (CH_4), the only energy source, and the remaining substances, among others hydrogen sulfide (H_2S), water, siloxanes (silicon and oxygen compounds) and carbon dioxide (CO_2), are not combustible [8]. Purifying biogas to biomethane quality is a well-established technology [6], but it is associated with high energy expenditure, especially in terms of CO_2 removal. This prompts the search for areas of application of 'pre-purified' biogas, containing only CH_4 and CO_2. Although this solution has been successfully used for years in stationary engines of electricity generators operated in biogas plants, it raises certain technical challenges in relation to vehicle applications.

Another technical issue is the combustion system of biogas-powered ICEs. It has gained significant attention in scientific literature, particularly in practical publications. [23]. The most convenient way is to apply biogas to a spark-ignition ICE, which is the dominant method in stationary electric generating units [17]. Biogas application in a compression-ignition ICE is more challenging. Such an engine can operate in two modes: single-fuel or dual-fuel. In single-fuel mode, it uses only biogas, while in dual-fuel mode, it utilizes both diesel and biogas. Operating in single-fuel mode requires specific modifications to the engine, such as lowering the compression ratio and incorporating an ignition system similar to that of spark-ignition engines [5]. For simpler engines, these modifications are relatively easy to implement and do not significantly increase costs [19]. Conversely, compression-ignition engines operating in dual-fuel mode use diesel oil to initiate combustion through auto-ignition, which subsequently ignites the biogas-air mixture. In this case, it is necessary to add a separate biogas supply system and change the engine control algorithms [15].

Numerous research works have been carried out to investigate the performance of dual-fuel compression-ignition ICEs under all possible operating conditions, static and dynamic.

Matuszewska et al. [14] examined the emissions of exhaust gas components from a compression-ignition ICE that was converted for dual-fuel operation using diesel oil and biogas composed mainly of CO_2 and CH_4 with various proportions. The engine originated from an agricultural tractor, featuring four cylinders and an original diesel oil supply system with a distributor injection pump. The dual-fuel biogas conversion was accomplished without the need for complicated construction or regulatory adjustments. The dynamometer test results showed that compared to running solely on diesel oil, the dual-fuel system resulted in higher concentrations of hydrocarbons (HC) and carbon oxide (CO) and lower concentrations of particulate matter (PM) in exhaust gases. The level of emission of particular components depended on the biogas composition used. Jagadish and Gumtapure [11] studied a compression-ignition ICE fueled by dual-fuel diesel oil and biogas with increased methane content (88%). It was a single-cylinder, four-stroke engine with direct diesel oil injection into the cylinder and indirect biogas injection into the intake manifold. Selected operating parameters and pollutant emissions were compared between a dual-fuel engine (taking into account various doses of biogas) and an engine operating in single-fuel mode (powered by diesel oil only). While there were differences between the individual mixture variants with different biogas shares, some general trends could be identified when compared to a single-fuel diesel system. A reduction in emissions of nitrogen oxides (NO_x) and PM was observed, as well as an increase in emissions of CO and HC. More examples and generalization of research results can be found in the comprehensive review papers [8, 9].

Some researchers direct their efforts to investigate the phenomena related to biogas or biomethane injection and its optimization to improve ICE operating parameters.

Barik and Murugan [3] investigated the performance and emission characteristics of a compression-ignition engine operating in dual fuel mode with diesel oil injected directly into the cylinder and biogas inducted at varying flow rates to the intake manifold. Based on experimental findings, among the four biogas flow rates considered, a flow rate of 0.9 kg/h yielded the best engine performance along with the lowest emissions. In comparison to diesel-only operation, the dual fuel system demonstrated the highest peak cylinder pressure and a longer ignition delay. Notably, the dual fuel mode significantly reduced PM and nitric oxide (NO) emissions by about 49% and 39%, respectively.

Chandekar and Debnath [7] focused on the influence of ICE intake geometry on the mixing of methane-enriched biogas (90% CH_4) with air. They considered four intake systems with different injector configurations to optimize mixture homogeneity. The research was based on CFD simulation in ANSYS Fluent. The following quantities were compared between the considered configurations: pressure, velocity, turbulence kinetic energy, helicity, and mass fraction of CH_4. Particular attention was paid to determining the optimal ratio of the radius of the curvature of the manifold to the diameter of the manifold (R/D). The simulations showed that the best design was one with an R/D ratio of 1.75 and 2.

Adithya et al. [1] also conducted research on the optimization of the intake system of a dual-fuel compression ignition ICE, fueled with diesel oil and biogas. In contrast to the previously discussed paper [7], here the experiments were empirical, performed on a laboratory stand. The aim was to improve the volumetric efficiency of the ICE and to check the effect of the dual-fuel concept on pollutant emissions. Modification of the intake system, designed based on the Chrysler ram theory and Helmholtz resonator theory, allowed for increased ICE performance in single- and dual-fuel mode as well as reduced pollutant emissions.

Regarding the technical aspects of biogas-air mixture preparation, Bembenek et al. [2] noted that there is a lack of research on biogas injectors and decided to fill this gap. They selected five injectors available on the market and empirically tested their properties, such as contingent productivity, the linearity of operation, the injector response time, the resistance of the injector coil, the ability to maintain factory parameters, and the service life. On this basis, the researchers recommended the best injectors for use in both spark-ignition and compression-ignition ICEs.

A review of the scientific literature shows that numerous research results have been published on ICEs fueled with biogas, bio-CNG, and other biogas-based fuels. They mainly concern the basic operating parameters of the ICE, i.e. power, torque, fuel consumption, and pollutant emissions. However, there are disproportionately few papers devoted to the phenomena of biogas injection, which is a decisive factor for the formation of the fuel-air mixture and hence has a significant impact on the operating parameters of the ICE. Therefore, the aim of this paper was to investigate the influence of the location of biogas injectors in the ICE intake system on the selected characteristics of the air-biogas mixture introduced into the cylinders.

2. Experimental setup

The intake manifold considered in this study (Fig. 1) is a component of the intake system of the JCB 444 TA4i-81 I1 engine. Basic technical specification of the engine is given in Table 1. It was adapted to operate in a dual-fuel

Fig. 1. Intake manifold of JCB 444 TA4i-81 I1 engine

system, with diesel oil as the primary fuel and biogas additionally fed to the air supplying the cylinders. The biogas injectors were initially located in the intake system, between the turbocharger and the intercooler. In this study, a new location of the injectors was proposed, i.e. in the intake manifold, closer to the engine cylinders.

Table 1. Main technical specifications of JCB 444 TA4i-81 I1 engine

Parameter	Data
Manufacturer	JCB
Type	444 TA4i-81 I1
General features	4-stroke, DOHC, compression ignition, turbocharged with intercooler
Emission compliance	US-EPA Tier 4i, EU Stage IIIB
Number and configuration of cylinders	4, in-line
Compression ratio	16.7
Bore/stroke [mm]	103/132
Displacement [cm^3]	4399
Rated power [kW@rpm]	81@200
Maximum torque [Nm@rpm]	516@ 1500
Fuel system	Direct injection, Common Rail
Cooling system	Liquid-cooled

3. Three-dimensional model of the intake manifold

In order to accurately reproduce the geometry of the internal spaces of the intake manifold, casting was made using molding silicone (Fig. 2). Due to the complex shape of the channels, the intake manifold was cut to remove the silicone castings. Silicon elements were scanned using the Micron3D Green Stereo scanner (Fig. 3), manufactured by SMARTTECH Ltd. [23]. Based on the obtained data, a 3D model of the intake manifold was developed (Fig. 4).

Fig. 2. Intake manifold filled with molding silicone

Fig. 3. Scanning of intake manifold castings with the SMARTTECH Micron3D Green Stereo scanner

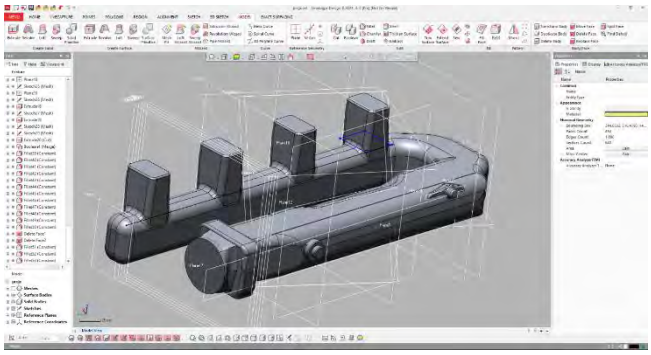

Fig. 4. 3D model of the interior of the intake manifold developed based on scanned data

4. Methodology of the research

The aim of CFD analysis was to find an optimal location for biogas injectors in the inlet manifold of a dual-fuel compression ignition engine. Additionally, one and four biogas injector concepts were studied. In the current research, ANSYS Fluent software was used for the simulations, which is a CFD solver of ANSYS Workbench 19.2 solution. At the beginning, the previously developed 3D model of the intake manifold was imported into the Design Modeler module of ANSYS Workbench 19.2 software. After some geometrical corrections, 3 models were developed for the needs of flow analysis. They are shown in Fig. 5–7. Numbers in red correspond to the cylinder numbers. Model 1 shown in Fig. 5 has only 1 biogas inlet (1 injector concept) located at the entrance to the manifold. Model 2 (Fig. 6) and model 3 (Fig. 7) have four biogas inlets (4-injector concept) gathered in series and located at various distances from the manifold's outlet. According to preliminary assumptions, a four-injector solution would allow for an increase in the air-biogas homogeneity formation rate compared to the 1-injector case.

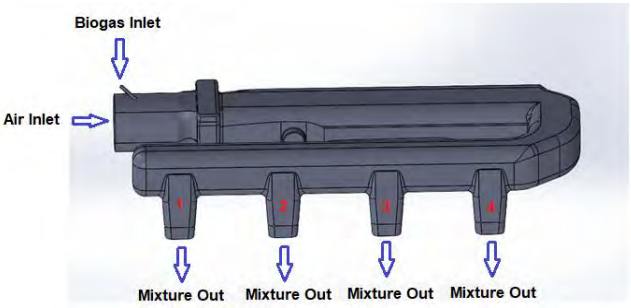

Fig. 5. 3D model of intake manifold with one biogas inlet (model 1)

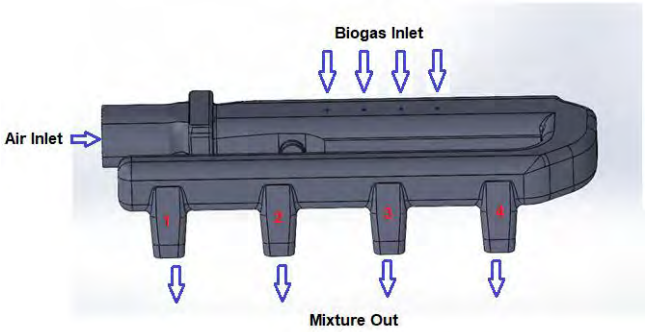

Fig. 6. 3D model of intake manifold with 4 biogas inlet (model 2)

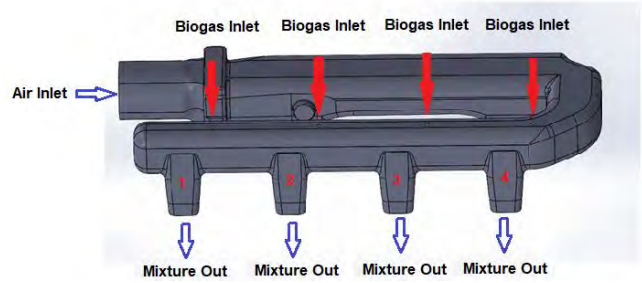

Fig. 7. 3D model of intake manifold with 4 biogas inlet (model 3)

To discretize the models, ANSYS Mesher was used. Meshed models are shown in Fig. 8 to Fig. 10. Meshing was done with the standard 5-layer inflation. There were 1553795 elements and 297199 nodes generated for model 1, 1567226 elements and 298941 nodes for model 2, and 1590822 elements and 303268 nodes for model 3. Other common characteristic dimensions of the mesh are as follows: target skewness 0.9 (default), medium smoothing, inflation with smooth transition, and transition ratio 0.272, growth rate 1.2; mesh sizing with capture curvature.

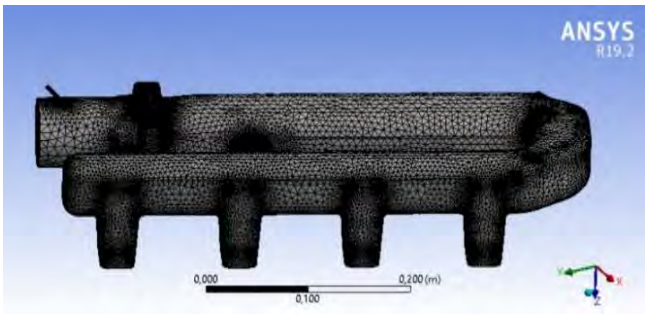

Fig. 8. Meshed model of intake manifold with one biogas inlet (model 1)

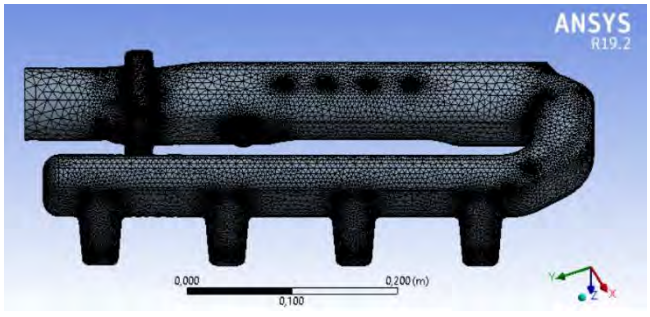

Fig. 9. Meshed model of intake manifold with 4 biogas inlets (model 2)

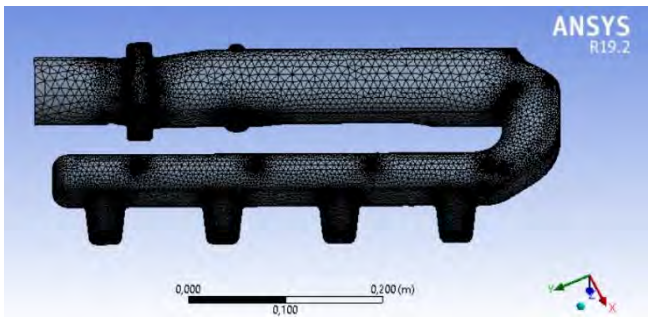

Fig. 10. Meshed model of intake manifold with 4 biogas inlets (model 3)

The Navier–Stokes equations and the species transport equation were applied for flow simulations. The energy equation was also used. RNG k−ε viscous model with enhanced wall treatment was applied to solve the flow problems.

Boundary conditions for the simulations were determined experimentally in the engine dynamometer test cell. Engine operation mode with power output 83.3 kW and crankshaft rotation speed 1600 rpm was chosen for the current simulation research. Key parameters used as boundary conditions in the simulation study are shown in Table 1. For all 3 models, the same conditions were used that allowed for the comparison of mixing characteristics and the study of the flow behaviour of the air and biogas mixture in the models.

Table 2. Boundary conditions

BC name	Type	Temperature, K	Mass flow rate, kg/s	Species
Air inlet	mass-flow inlet	300	0.1	
Biogas inlet (1 injector)	mass-flow inlet	300	0.0014	CH_4 and CO_2
Biogas inlet (4 injectors)	mass-flow inlet	300	4x0.00035	CH_4 and CO_2
Mixture out	outflow	–	–	–
Inlet Manifold	wall	–	–	–
Biogas injector	wall	–	–	–

In the current study 30% of the diesel fuel was substituted with biogas. The concept of "pre-purified" biogas was implemented with 60% methane and 40% CO_2 content.

5. Results and discussions

The analysis of the simulation results was done in the CFD post-processing module of the ANSYS software. The following parameters were analysed: 3D velocity and 3D CH_4 mass fraction (gradient) distribution in the inlet manifold, surface velocity distribution at the manifold outlets. Separately, obtained results related to 3D CH_4 mass fraction (gradient) distribution was analysed in terms of the homogeneity of the air-biogas mixture formed in the intake manifold. Here, CH_4 was chosen because it is the only combustible component of the mixture. Finally, the optimal location of the injector was offered.

Visualizations of CFD calculation results of flow velocity and CH_4 mass fraction (gradient) distribution in the inlet manifold for 3 different locations of fuel injector/injectors are shown in Fig. 11 to Fig. 13 and Fig. 17 to Fig. 19.

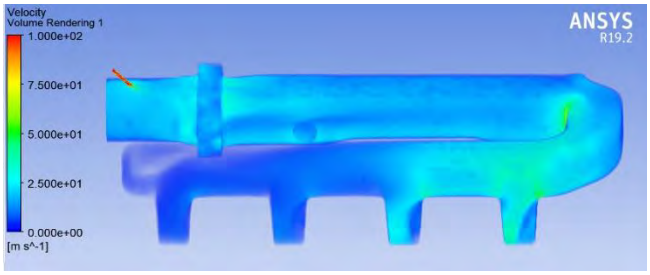

Fig. 11. 3D velocity distribution in the intake manifold (model 1)

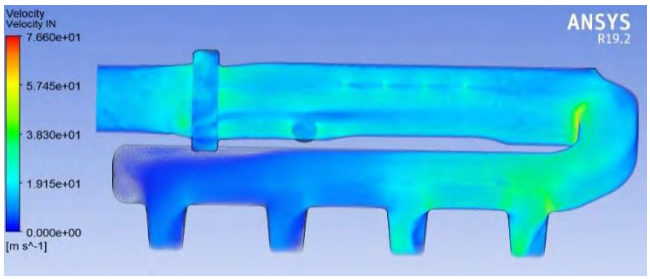

Fig. 12. 3D velocity distribution in the intake manifold (model 2)

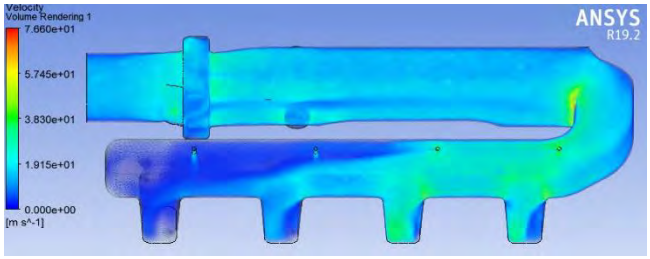

Fig. 13. 3D velocity distribution in the intake manifold (model 3)

As can be seen from Fig. 11 to Fig. 13, regardless of injector locations, there is an uneven velocity distribution in the regions corresponding to manifold outlets. Higher flow velocities were observed at the outlets 4.3 and lower at 2.1. To complement 3D velocity research, a surface velocity distribution at the manifold outlets analysis was conducted. Results are shown in Fig. 14 to Fig. 16.

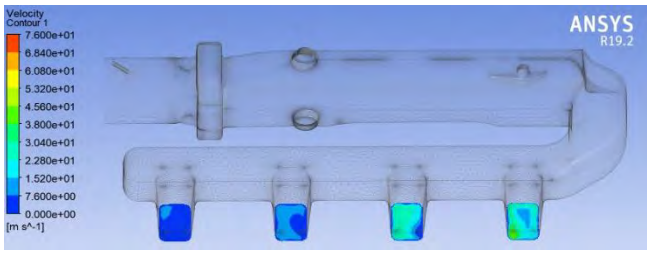

Fig. 14. Velocity contours at the outlets from the manifold (model 1)

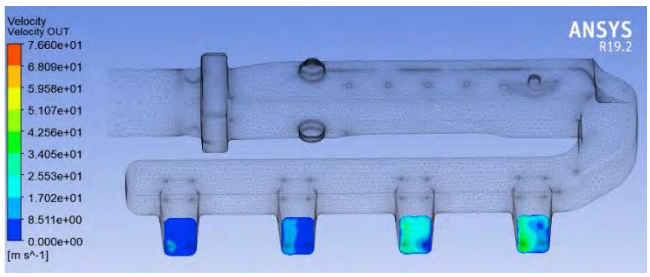

Fig. 15. Velocity contours at the outlets from the manifold (model 2)

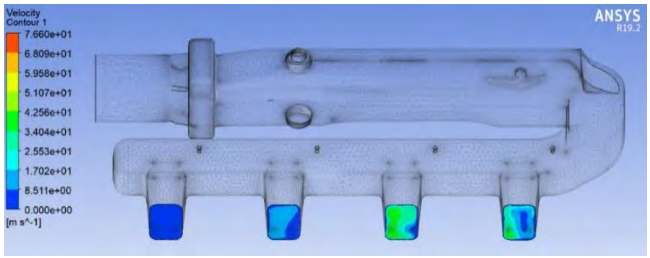

Fig. 16. Velocity contours at the outlets from the manifold (model 3)

It can be concluded from Fig. 14 to Fig. 16 that the highest velocity fluctuations could be established for the outlets 4 and 3, which will result in a higher flow turbulence rate for these outlets. Additionally, the air-biogas mixture average velocities at the manifold's outlet were defined. Results are shown in Table 3.

Table 3. Mixture average velocities at the outlet from the manifold, m/s

Model	Mixture Out 1	Mixture Out 2	Mixture Out 3	Mixture Out 4
Model 1	13.8	13.62	15.24	20.17
Model 2	13.91	13.85	17.23	20.21
Model 3	15.22	14.27	16.92	19.45

It could be concluded that in order to make the velocity distribution at the outlets more uniform, it is recommended to redesign the inlet manifold and make it more straight than curved.

At the final stage of the simulation analysis, a 3D mass fraction (gradient) distribution for CH_4 was studied. Results are shown in Fig. 17 to Fig. 19. Here, for the studied models, a characteristic zone where homogeneity of the air-biogas mixture is formed (or weakly formed) could be established.

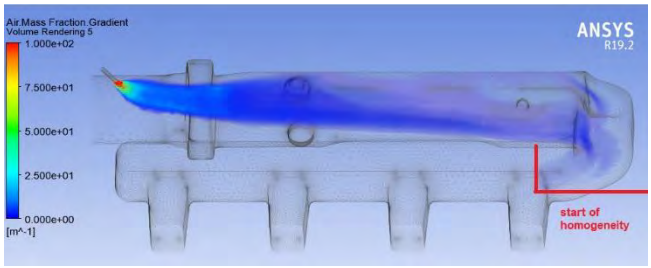

Fig. 17. CH_4 mass fraction (gradient) distribution in the inlet manifold – model 1

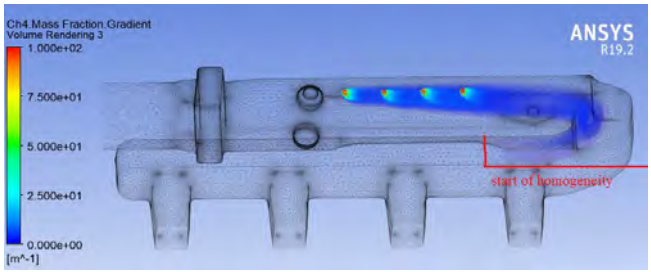

Fig. 18. CH_4 mass fraction (gradient) distribution in the inlet manifold – model 2

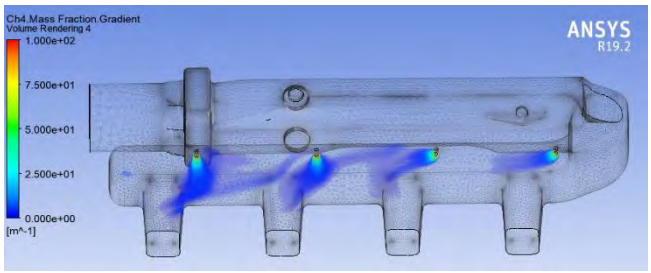

Fig. 19. CH_4 mass fraction (gradient) distribution in the inlet manifold – model 3

As it can be seen from Fig. 17–19, there is a risk of air-biogas non-homogeneity at the inlet to the engine cylinders for the model 3 (Fig. 19). At the same time model 1 and model 2 characterized by the minimum risk for inhomogeneous air-biogas mixture delivering inside the engine's cylinders, but model 2 gives more uniform cloud structure of biogas in stratified mixture. Thus, the optimal location of the injectors is related to the model 2.

6. Conclusions

1. Sources analysis showed that there are disproportionately few papers devoted to the phenomena of biogas injection location , which is a decisive factor for the formation of the fuel-air mixture and has a significant impact on the operating parameters of the ICE. Therefore, in this paper the influence of the location of biogas injectors in the compression ignition ICE intake system on the selected characteristics of the air-biogas mixture introduced into the cylinders was investigated.
2. The reverse engineering technique was applied to reproduce the geometry of the commercial intake manifold. The 3D model obtained was used for further CFD analysis.
3. Simulations were conducted for 3 models; in the first model, there was only 1 biogas inlet (1 injector concept) located at the entrance to the manifold; the second and third models had 4 biogas inlets (4-injector concept) gathered in series and located at various distances from the manifold's outlet.
4. The main results of the CFD analysis are as follows:

– regardless of injector/injectors locations, there is uneven velocity distribution in the regions corresponding to commercial manifold outlets; higher flow velocities were observed at the outlets 4,3, and lower in 2,1; to make the velocity distribution more uniform, it is recommended to redesign the inlet manifold and make it more straight.
– there is a risk of air-biogas non-homogeneity at the inlet to the engine cylinders observed in model 3, where 4 injectors were located close to the manifold's outlets; model 1 (with one injector) and model 2 (4 injectors) were characterized by the minimum risk of inhomogeneity for air-biogas mixture delivered inside the engine's cylinder, at the same time model 2 gives more uniform cloud of biogas located in stratified mixture, that's why biogas injectors location from model 2 is considered as optimal in this study.

Acknowledgements

Research was funded by Warsaw University of Technology within the Excellence Initiative: Research University (IDUB) programme.

We would like to express our sincere gratitude to SMARTTECH Ltd., in particular Paweł Aksamit, for the digital scanning of the intake manifold castings. Furthermore, we appreciate the technical assistance provided by Cezary Korab and Igor Kotłowski, who were engaged in 3D modeling of the engine intake system components.

Nomenclature

CFD computational fluid dynamics
CNG compressed natural gas
ICEs internal combustion engines
PM particulate matter
RNG renewable natural gas

Bibliography

[1] Adithya K, Ahmed F, Padmanathan P, Mohan CG, Prakash R. Design optimization of intake manifold of dual fuel engine. Mater Today: Proc. 2021;45(2):646-651. https://doi.org/10.1016/j.matpr.2020.02.726

[2] Archana K, Visckram A, Kumar P, Manikandan S, Saravanan A, Natrayan L. A review on recent technological breakthroughs in anaerobic digestion of organic biowaste for biogas generation: challenges towards sustainable development goals. Fuel. 2024;358:130298. https://doi.org/10.1016/j.fuel.2023.130298

[3] Barik D, Murugan S. Investigation on combustion performance and emission characteristics of a DI (direct injection) diesel engine fueled with biogas–diesel in dual fuel mode. Energy. 2014;72:760-771. https://doi.org/10.1016/j.energy.2014.05.106

[4] Bembenek M, Melnyk V, Karwat B, Rokita T, Hnyp M, Mosora Y et al. Study of the technical and operational parameters of injectors using biogas fuel. Energies. 2024; 17(21):5445. https://doi.org/10.3390/en17215445

[5] Bieniek A, Mamala J, Graba M, Prażnowski K, Śmieja M, Wereszczyński D. Application of biogas to supply the high compression ratio engine. Combustion Engines. 2019;179(4): 40-6. https://doi.org/10.19206/CE-2019-406

[6] Castellanos-Sánchez JE, Aguilar-Aguilar FA, Hernández-Altamirano R, Venegas Venegas JA, Raj Aryal D. Biogas purification processes: review and prospects. Biofuels. 2023; 15(2):215-227. https://doi.org/10.1080/17597269.2023.2223801

[7] Chandekar AC, Debnath BK. Effect of intake manifold design on the mixing of air and bio-CNG in a port-injected dual fuel diesel engine. J Therm Anal Calorim. 2020;141:2295-2309. https://doi.org/10.1007/s10973-020-09591-1

[8] Deheri C, Acharya SK, Thatoi DN, Mohanty AP. A review on performance of biogas and hydrogen on diesel engine in dual fuel mode. Fuel. 2020;260:116337. https://doi.org/10.1016/j.fuel.2019.116337

[9] Feroskhan M, Ismail S, Natarajan G, Manavalla S, Khan TMY, Khadar SDA et al. A comprehensive study of the effects of various operating parameters on a biogas-diesel dual fuel engine. Sustainability. 2023;15(2):1232. https://doi.org/10.3390/su15021232

[10] Guzek M, Jackowski J, Jurecki RS, Szumska EM, Zdanowicz P, Żmuda M. Electric vehicles – an overview of current issues – part 1 – environmental impact, source of energy, recycling, and second life of battery. Energies. 2024;17(1):249. https://doi.org/10.3390/en17010249

[11] Jagadish C, Gumtapure V. Experimental investigation of methane-enriched biogas in a single cylinder diesel engine by the dual fuel mode. Energy Sources, Part A. 2019;44(1):1898-1911. https://doi.org/10.1080/15567036.2019.1647314
[12] Jameel MK, Mustafa MA, Ahmed HS, Mohammed AJ, Ghazy H, Shakir MN et al. Biogas: production, properties, applications, economic and challenges: a review. Results Chem. 2024;7:101549. https://doi.org/10.1016/j.rechem.2024.101549
[13] Kalghatgi G. Is it the end of combustion and engine combustion research? Should it be? Transp Eng. 2022;10: 100142. https://doi.org/10.1016/j.treng.2022.100142
[14] Matuszewska A, Owczuk M, Zamojska-Jaroszewicz A, Jakubiak-Lasocka J, Lasocki J, Orliński P. Evaluation of the biological methane potential of various feedstock for the production of biogas to supply agricultural tractors. Energy Convers Manag. 2016;125:309-319. https://doi.org/10.1016/j.enconman.2016.02.072
[15] Rahman MM, Hassan M, Islam MN, Mahmud S, Islam MR. Recent advances in ZnO-based photocatalysts for water purification: A review. Int J Hydrogen Energy. 2024;49(14): 6618-6640. https://doi.org/10.1016/j.ijhydene.2023.12.086
[16] Samson-Bręk I, Matuszewska A, Rogulska M, Lasocki J. Emission of greenhouse gases (except for water vapor) in well-to-wheel cycle of methane fuels. Przemysł Chemiczny. 2020;99(8):1131-1137. https://doi.org/10.15199/62.2020.8.3
[17] Semikow J, Sumera J. Some aspects of long-term testing of cogeneration set fueled with biogas. Combustion Engines. 2019;179(4):136-141. https://doi.org/10.19206/CE-2019-422
[18] Singh PP, Ambika, Verma M. Recent advances in alternative sources of energy. In: Singh P, Singh S, Kumar G, Baweja P (eds). Energy. 1st ed. Wiley. 2021:55-71. https://doi.org/10.1002/9781119741503.ch3
[19] Siripornakarachai S, Sucharitakul T. Modification and tuning of multi-valve diesel bus engine to run on biogas for electricity production. Int J Renewable Energy. 2018;3(2):1-13. https://doi.org/10.14456/iire.2008.10
[20] Subaru Corporation, Toyota Motor Corporation, Mazda Motor Corporation. Press release 28.05.2024. https://global.toyota/en/newsroom/corporate/40850156.htm
[21] Smarttech3D. Kopia Micron3D Green Stereo. https://www.smarttech3d.com/kopia-micron3d-green-stereo
[22] Tuffour JP, Ewing R. Can battery electric vehicles meet sustainable energy demands? Systematically reviewing emissions, grid impacts, and coupling to renewable energy. Energy Res Soc Sci. 2024;114:103625. https://doi.org/10.1016/j.erss.2024.103625
[23] Vasan V, Sridharan NV, Feroskhan M, Vaithiyanathan S, Subramanian B, Tsai PC et al. Biogas production and its utilization in internal combustion engines – a review. Process Saf Environ Prot. 2024;186:518-539. https://doi.org/10.1016/j.psep.2024.04.014

Prof. Dmytro Samoilenko, DSc., DEng. – Faculty of Automotive and Construction Machinery Engineering, Warsaw University of Technology, Poland.
e-mail: *dmytro.samoilenko@pw.edu.pl*

Mateusz Bednarski, MEng. – Faculty of Automotive and Construction Machinery Engineering, Warsaw University of Technology, Poland.
e-mail: *mateusz.bednarski@pw.edu.pl*

Jakub Lasocki, DEng. – Faculty of Automotive and Construction Machinery Engineering, Warsaw University of Technology, Poland.
e-mail: *jakub.lasocki@pw.edu.pl*

Haeng Muk Cho, MEng. – Mechanical System Engineering, Kongju National University, Korea (South).
e-mail: *hmcho@kongju.ac.kr*

Article citation info:
Sordyl A, Adamiak B, Merkisz J. Comparison of nitrogen oxide emission with two PEMS measurement methods. Combustion Engines. 2026;204(1):88-95. https://doi.org/10.19206/CE-209991

Adam SORDYL
Borys ADAMIAK
Jerzy MERKISZ

Combustion Engines
Polish Scientific Society of Combustion Engines

Comparison of nitrogen oxide emission with two PEMS measurement methods

ARTICLE INFO

Received: 20 June 2025
Revised: 7 July 2025
Accepted: 27 August 2025
Available online: 7 October 2025

Mobile emission measurement systems (PEMS), according to current legal acts, can measure nitrogen oxide emission intensity using two different methods, one of which uses the chemiluminescence method and the other the ultraviolet light method. Stationary (laboratory) systems, according to the regulation, use only the chemiluminescence method. The following article analyses the results of tests obtained during WLTC tests from laboratory analysers (chemiluminescence method) with the results from two mobile analysers using nitrogen oxide analysers operating on the basis of two different methods. As a result of this analysis, the differences in the results of nitrogen oxide emissions from mobile systems compared to measurements from stationary systems in the WLTC test on a chassis dynamometer were described. The research was performed at the BOSMAL Institute of Automotive Research and Development using a passenger car equipped with a spark-ignition engine. The analysis showed differences in the results of nitrogen oxide emissions between mobile analysers for measuring nitrogen oxide emission intensity using the NDUV method and mobile analysers CLD. Measurements with mobile analysers also differ noticeably from the results obtained from stationary (laboratory) analysers. However, the greatest influence on the difference in the obtained results is the applied measurement method.

Key words: *emission, analyzer, accuracy, PEMS, RDE, WLTC*

1. Introduction

In recent years, environmental protection has become a priority for the whole world, which has also affected means of transport. In order to take care of the environment, the European Union is introducing increasingly stringent exhaust emission standards. Vehicle tests are no longer carried out only on roller stands and engine dynamometers, but since September 2019, a mandatory test is the measurement of exhaust emissions in real driving conditions – RDE performed using mobile PEMS exhaust gas analyzers. Currently, the Euro 6e-bis standard is in force in the EU, which is to be an introduction to the Euro 7 standard. The implementation of the Euro 6 standard and the need to measure emissions of harmful substances in exhaust gases forced manufacturers of measuring equipment to create portable PEMS exhaust gas analyzers. These analyzers should be reliable, and their accuracy and repeatability should be similar to those of stationary analyzers. Over the years, comparisons of these analyzers have been carried out against stationary systems, which confirm their correct operation and correct results [1, 2, 9, 12, 19]. One of the two components covered by RDE limits is nitrogen oxides. They are measured by analyzers using the chemiluminescence method (CLD) and the method using ultraviolet light (NDUV). In stationary systems, in accordance with the regulation, nitrogen oxide emission intensity must be measured using the chemiluminescence method, while mobile analyzers can measure it in two different ways [7]. Analyzers using the NDUV measurement method are cheaper than CLD analyzers and are easier to maintain, which is why many manufacturers use them in mobile systems.

2. Description and construction of stationary measurement systems

BOSMAL's emissions testing laboratories are advanced, ambient (Emission Laboratory No. 1) and climate controlled (Emission Laboratory No. 2) facilities for performing emissions, fuel consumption and performance tests over a range of driving cycles and a broad range of ambient conditions. Exhaust emissions testing itself is carried out with the aid of sampling bags (legislative tests), diluted and raw modal analysis (development tests) for use with CI, SI, and hybrid vehicles.

Table 1. Measurement range and accuracy of nitrogen oxide analyzer systems for stationary systems

System – Lab 1			
Measured range	Bag measurement / continuous measurement		Measurement accuracy
	lowest	highest	
NO_x (CLD)	0–5 ppm	0–1000 ppm	±2% at the measuring point ±1% on the scale

System – Lab 2					
Measured range	Bag measurement		continuous measurement		Measurement accuracy
	lowest	highest	lowest	highest	
NO_x low (CLD)	0–1 ppm	0–50 ppm	0–10 ppm	0–500 ppm	±2% at the measuring point ±5% on the scale
NO_x high (CLD)	0–100 ppm	0–1000 ppm	0–1000 ppm	0–10000 ppm	

These facilities permit the execution of a wide range of legislative and development emissions tests, including:
- CVS bag diluted emissions testing to international standards [6, 8]
- CO_2 emissions and fuel consumption measurement according to EU standards [17, 18]
- gravimetric and numerical quantification of particulate matter emission according to [10, 11]

– measurement of battery current balance according to [8]
– measurement of compounds which are unregulated in the EU, such as N_2O, NH_3, using additional analyzers
– measurement of soot and particulate matter from raw exhaust gases using additional devices
– checks of vehicles according to Conformity of Production (COP) requirements [8, 17]
– maximum power measurement on the wheels of the vehicle [18]
– electric consumption energy and electric vehicles range [6, 8].

3. Description of measurement methods for NO_x

3.1. Analyzer CLD

The analyzer for measuring the concentration of nitrogen oxide and nitrogen dioxide uses the CLD measurement method. The oxidation of nitrogen oxide with ozone O_3 produces light in the wavelength range of about 600 nm to 3200 nm, with a maximum radiation intensity at about 1200 nm. This is chemiluminescent radiation, which is proportional to the concentration of nitrogen oxide. In the case of excess ozone, it is captured by the detector and converted into an electrical signal. In order to determine the concentration of nitrogen oxides and nitrogen dioxide, the oxides contained in the gas are previously reduced to nitrogen oxide in a convector.

The chemiluminescence measurement is based on the following chemical reactions:

$$NO + O_3 \rightarrow NO_2^* + O_2 \quad (1)$$

$$NO + O_3 \rightarrow NO_2 + O_2 \quad (2)$$

After a partial reaction (1), a certain amount of excited nitrogen dioxide is formed, which changes to the ground state (3) and emits light (electromagnetic radiation):

$$NO_2^* \rightarrow NO_2 + h \cdot \nu \quad (3)$$

where: $h \cdot \nu$ – radiation energy at a specific wavelength:

$$NO_2^* + M \rightarrow NO_2 + M \quad (4)$$

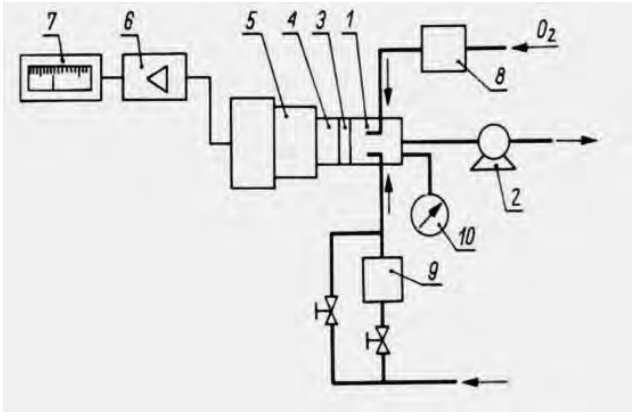

Fig. 1. Analyzer operation diagram CLD [13]: 1 – reactor, 2 – pump, 3 – quartz window, 4 – optical filter, 5 – converter, 6 – amplifier, 7 – meter, 8 – ozone generator, 9 – thermal converter, 10 – manometer

The greater part of the excited nitrogen dioxide releases its energy in the form of kinetic energy to the M molecules according to reaction (4). The ratio of released radiant energy (3) to nonradiative energy (4) depends on the reaction pressure and the type of reaction partners. The lower the reaction pressure, the greater the probability that the excited nitrogen dioxide molecule will release its energy in the form of light (Fig. 1) [3, 5, 14–16].

3.2. Analyzer NDUV

The analyzer for measuring the concentration of nitrogen oxides used in mobile systems is most often an NDUV analyzer (Non-Dispersive Ultraviolet). The UV analyzer is characterized by the following features:

– its measurement capabilities are very sensitive and stable with respect to NO
– the concentrations of nitrogen oxide and nitrogen dioxide are measured directly
– it is characterized by a high level of selectivity in relation to the accompanying components contained in the gas sample (exhaust gas) and has no effect on carbon dioxide and water in particular [4].

The UV analyzer is a multi-component UV photometer with high zero and endpoint stability. Its measurement operation is based on the properties of gases (such as NO and NO_2), which create discrete vibration absorption bands and absorb radiation in the wavelength range from 200 nm to 500 nm. The main element of the analyzer is a UV radiation source, an electrodeless discharge lamp ELD (Electrodeless Discharge Lamp), which, induced by high frequency, emits, among others, radiation specific for nitrogen oxide in an electromagnetic field:

$$N_2 + O_2 \rightarrow NO_2^* \rightarrow NO + h\nu \quad (5)$$

$$2NO \rightarrow N_2 + O_2 \quad (6)$$

This measurement method is therefore a resonance method and is referred to as DUV resonance absorption spectroscopy. Other UV-absorbed gases, such as nitrogen dioxide and sulfur dioxide, are determined by interference filter correlation as a non-dispersive UV method (Fig. 2) [4].

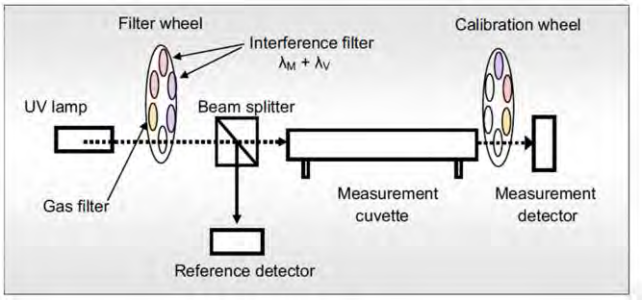

Fig. 2. Analyzer operation diagram NDUV [4]

The radiation emitted by the UV radiation source is modulated by means of a filter wheel and divided into a measuring beam and a reference beam in a semi-transparent divider. During one measurement, a total of four signals were recorded for two positions of the interference filter via the measuring beam and the reference beam, and calculated by forming double quotients. This four-beam method is the basis for the high measurement stability achieved in the measurement of nitrogen oxide concentration. Thanks to this, the analyzer is largely independent of

any contamination in the measuring cuvette or aging of the radiation source (Fig. 3) [4].

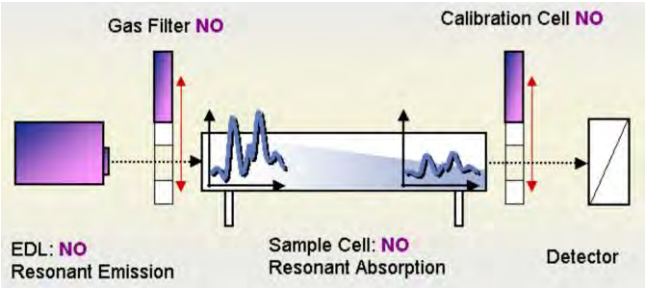

Fig. 3. Absorption measurement NO [19]

The required specific signal is determined in two stages:
- at the beginning, in the measurement phase, the full absorption measurement is recorded
- in the next reference phase, the gas filter filled with nitrogen oxide is set
- in the appropriate position and only those parts of the spectrum that are not absorbed by nitrogen oxide reach the detector through the measuring cuvette [4].

4. Research object

The aim of the research was to measure and analyse the nitrogen oxide emission intensity exhaust emissions results of a passenger car, with measurement carried out over the WLTC test on two stationary laboratories equipped with CLD analysers, with simultaneous measurement from two different PEMS systems, of which the first was equipped with an NDUV analyser and the second with a CLD analyser to measure NO_x. The test objects were PEMS systems, the data for which are shown in Table 2.

Table 2. Parameters of the mobile emissions measurement system

Method and measurement range of mobile analyzers		
Measured component	Continuous measurement of undiluted exhaust gases	Measurement accuracy
System A		
NO_2 (NDUV)	0–2500 ppm	±2% or ≤ 5 ppm
System B		
NO_x (CLD)	0–3000 ppm	±2% in the point ±0.3 on the scale

A brand new passenger car equipped with gasoline direct injection and fulfilling the Euro 6 norm was used for the measurements. Table 3 shows the data on the vehicle.

Table 3. Data of the test vehicle

Parameter	Value
Fuel type	Gasoline
Fuel delivery strategy	GDI
Vehicle mass [kg]	1008
Swept volume [cm^3]	1000
Power [kW]	51
Gearbox	Manual (5-speed)
Mileage [km]	170
Emission standard	Euro 6d

The speed profile of the WLTC test, consisting of four phases: low, middle, high, and extra-high, is the legislative test for EU type approval testing of vehicles with a total weight not exceeding 3.5 t, introduced in September 2018 for all newly manufactured vehicles (Fig. 4; detailed data on test characteristics are presented in Table 4).

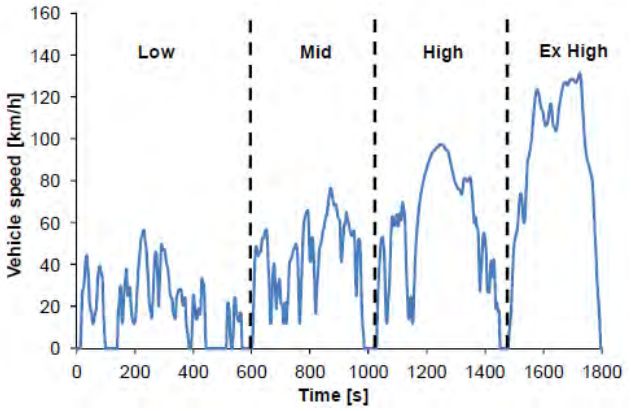

Fig. 4. The speed trace for the WLTC class 3b test cycle

Table 4. WLTC test data

Parameter	Unit	Value
Distance	km	23.266
Duration	s	1800
Number of pull-away events	–	8
Pull-away events per km	km^{-1}	0.34
Length of initial idling (before first pull-away event)	s	11
Total idling time	s	234
Idling time (proportion)	%	13
Maximum speed	km/h	131.3
Mean speed (all phases, including idling)	km/h	46.50
Time at which the mean speed is first exceeded	s	217
Maximum acceleration	m/s^2	1.67
Maximum value of v·a	m^2/s^3	20.57
Proportion of time for which speed > 100 km/h	%	10.11
Engine temperature before test start	°C	23±3

5. Research results

Currently, in order to allow a new vehicle type be sold for use on public roads, it is necessary to thoroughly check the exhaust emissions. For this purpose, exhaust gas analyzers – both stationary and mobile – are used. The results presented below show the difference between the results of nitrogen oxide from the stationary and mobile analyzers. Each of the WLTC tests was performed by the same experienced driver, to minimize driver-dependent variables (and their influence on the results) as directly as possible. In addition, the test vehicle performed each test in the same selectable driving mode with the same chassis dynamometer settings. In order to eliminate additional measurement irregularities, prior to each test, the vehicle was stored in a climatic chamber under constant atmospheric conditions. After each test, the vehicle was conditioned for at least 12 hours so that the temperature of operating fluids stabilized in the range of 22–24°C. The results of the three measures of nitrogen oxide emissions were averaged and then analyzed and presented in the graphs below. Tests were con-

ducted with the Start&Stop system turned off, and the results are presented without RCB and S&D corrections.

Below are presented the results of specific distance emissions of nitrogen oxides in laboratory No. 1 and in laboratory No. 2, respectively. The results have been divided into the results from tests at 14 and 23°C and from cold and warm engine start-up.

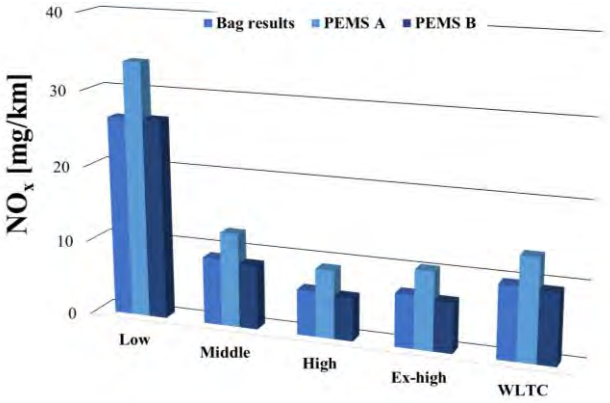

Fig. 5. NO_x specific distance emission in WLTC test in 14°C from cold start engine in laboratory 1

The highest measured specific distance emission level of nitrogen oxides from the WLTC test conducted with a cold engine start at a temperature of 14°C occurred in the low phase and was about 25 mg/km in the case of measurement made using the laboratory system and the PEMS B system (Fig. 5). The specific distance emission level determined using the PEMS A system was about 35 mg/km. The lowest specific distance emission was recorded in the high phase and did not exceed 7 mg/km for the measurement using the laboratory system and PEMS B, while for the measurement using the PEMS A system it was at the level of 9 mg/km. Both in the entire test and in each phase, the results using the PEMS A system differ from those using the other systems (they are higher).

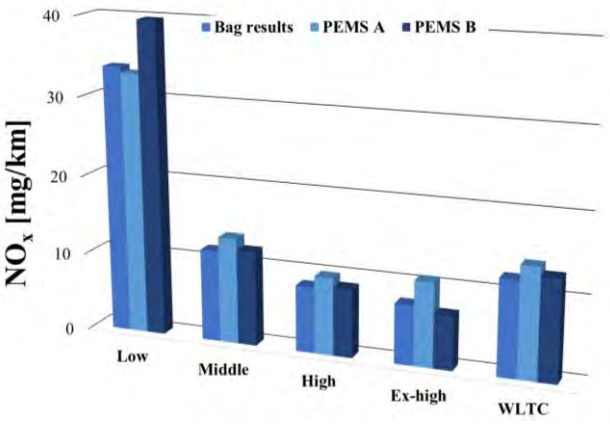

Fig. 6. NO_x specific distance emission in WLTC test in 14°C from hot start engine in laboratory 1

The highest specific distance emission of nitrogen oxides from the WLTC test performed at a temperature of 14°C for a warm engine start was recorded in the first phase, and the lowest in the fourth (Fig. 6). In the first phase, it was found that the PEMS B system determined the specific distance emission value of nitrogen oxides to be about 5 mg/km higher than the other systems, while in the remaining three phases the specific distance emission measurement is higher in the case of the measurement performed using the PEMS A system. In the entire test, the highest determined specific distance emission was recorded by the PEMS A system.

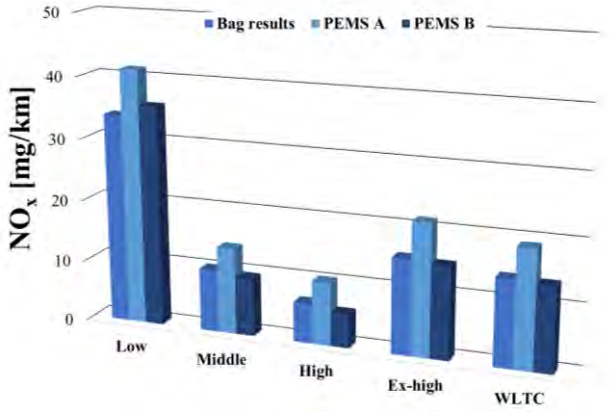

Fig. 7. NO_x specific distance emission in WLTC test in 23°C from cold start engine in laboratory 1

The highest level of specific distance emissions of nitrogen oxides from the WLTC test for a cold engine start at a temperature of 23°C was recorded in the first phase (Fig. 7), while its value for the entire test is about 15 mg/km. Both in the entire test and in its individual phases, the emission measurement results from the PEMS A system differ from those from the rest of the systems and are clearly higher. For the entire test, this difference is about 5 mg/km.

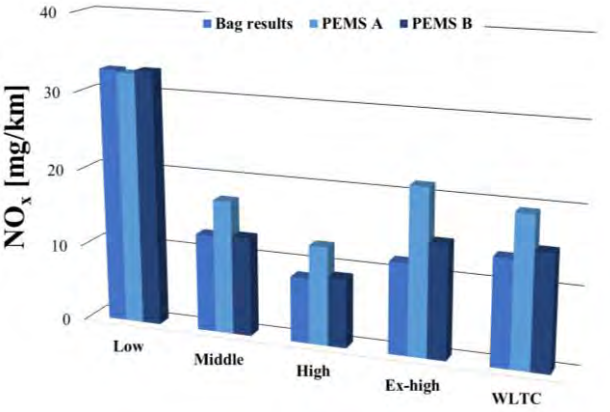

Fig. 8. NO_x specific distance emission in WLTC test in 23°C from the hot start engine in laboratory 1

The highest nitrogen oxide emissions from the WLTC test conducted at a temperature of 23°C with a warm engine start were recorded in the first phase of the test (Fig. 8). In the next three phases, the emission volume is higher for the PEMS A system. In the entire test, the emission measured using the PEMS A system is higher by about 5 mg/km compared to the other systems.

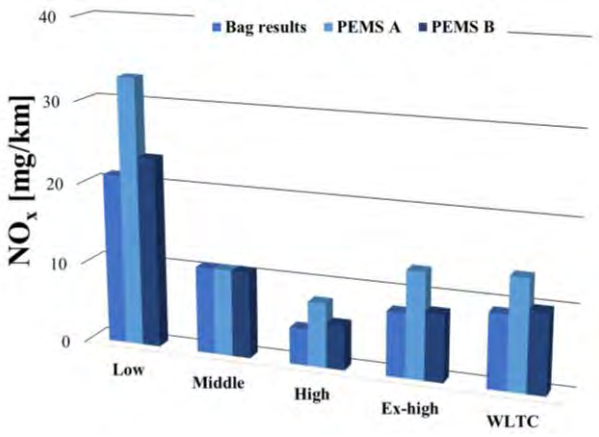

Fig. 9. NO_x specific distance emission in WLTC test in 14°C from cold start engine in laboratory 2

The maximum specific distance emission of nitrogen oxides from the WLTC test conducted at a temperature of 14°C with a cold engine start was measured in the first phase (PEMS A system, Fig. 9). In the second phase, the results obtained from both mobile systems are similar to those obtained using the laboratory system, while in the remaining analyzed phases – the results measured using the PEMS A system are higher than the others. The total measurement results take analogous values in the case of analyses using the laboratory system and PEMS B, while those obtained from the PEMS A system are significantly higher (by about 5 mg/km).

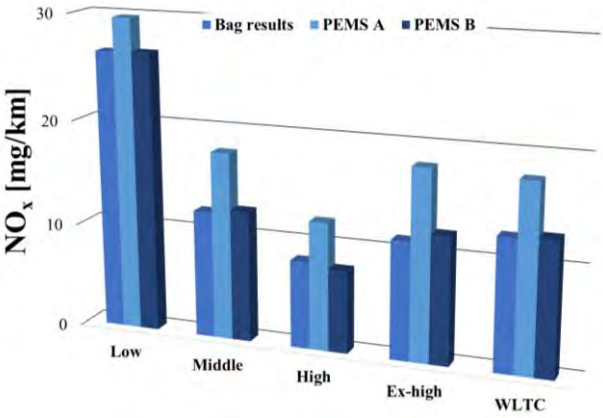

Fig. 10. NO_x specific distance emission in WLTC test at 14°C from the hot start engine in laboratory 2

For the WLTC test, conducted at a temperature of 14°C with a warm engine start, the highest specific distance emission of nitrogen oxides was recorded in the first phase (Fig. 10), and the maximum differences in measurements were characteristic of the PEMS A system (significantly higher specific distance emission levels compared to the other analyzed systems). In the entire test, the emission measured using the PEMS A system was higher by about 5 mg/km compared to the other systems.

The highest specific distance emission of nitrogen oxides from the WLTC test, performed at a temperature of 23°C with a cold engine start, was recorded in the first phase, and the maximum – for the PEMS A system (more by about 6 mg/km than the other systems, Fig. 11). In the subsequent phases, the results obtained using the PEMS A system are also significantly higher compared to the others. In the perspective of the entire test, comparable measurement results were obtained for the laboratory systems and the PEMS B system, while the results obtained as a result of measurements with the PEMS A system were characterized by significantly higher results.

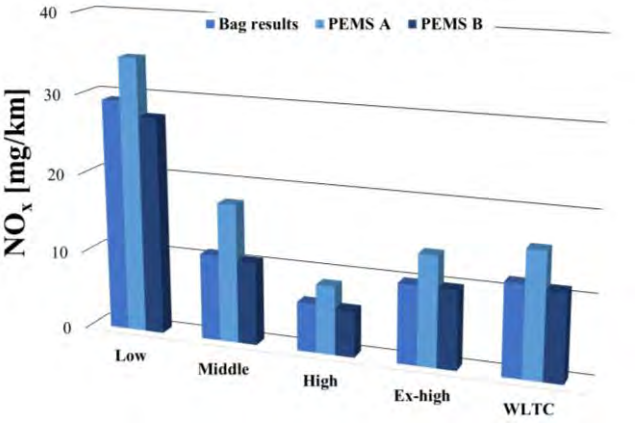

Fig. 11. NO_x specific distance emission in WLTC test in 23°C from cold start engine in laboratory 2

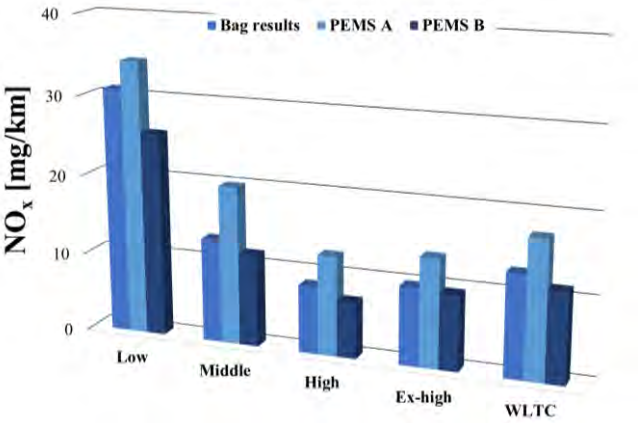

Fig. 12. NO_x specific distance emission in WLTC test in 23°C from hot start engine in laboratory 2

The maximum specific distance emission of nitrogen oxides from the WLTC test, carried out at a temperature of 23°C, with a warm engine start, was recorded in the first phase, and the greatest differences in the measurement were characteristic of the PEMS A system (Fig. 12). The results obtained as a result of its use were higher than the others in all the phases considered, and in the perspective of the entire test – higher in total by about 5 mg/km.

Based on the collected results of specific distance emissions of nitrogen oxides, the obtained results were compared with each other and presented graphically in the charts below, showing relative differences for temperatures of 14 and 23°C from a cold and warm engine start, respectively.

The largest difference between the results of specific distance emissions of nitrogen oxides using mobile systems and measurements using measuring bags was noted in the

high phase for the measurement using PEMS A system, compared to the results obtained in laboratory No. 2, and it amounted to 78%, which translated to 3.5 mg/km of absolute difference (Fig. 13). The smallest difference was noted in the middle phase for the measurement using both PEMS A and B systems, compared to the results obtained in laboratory No. 2, and it was below 0.2%. In the perspective of the entire test, the largest difference was noted for PEMS A system in relation to the measurements carried out using laboratory system No. 2, and it amounted to about 50% (4.5 mg/km of absolute value), while the smallest – for PEMS B system in comparison to laboratory system No. 1, and it was at the level of about 3% (0.3 mg/km of absolute value).

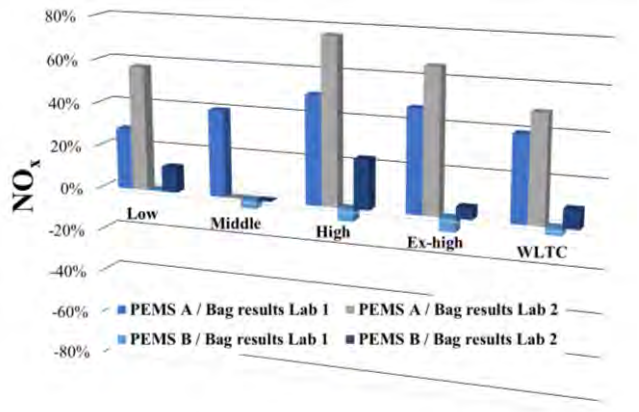

Fig. 13. Relative difference of specific distance emission measurements of nitrogen oxides for WLTC test at 14°C from a cold start engine

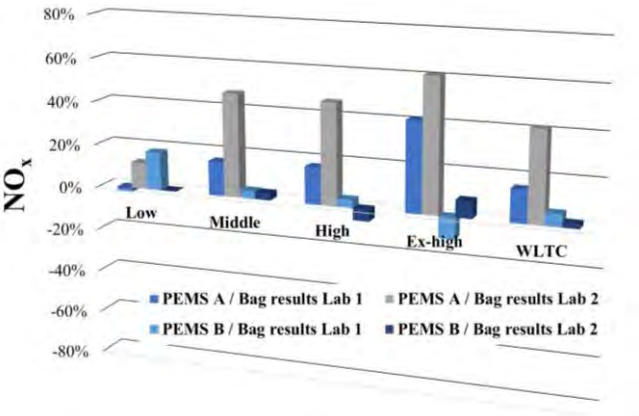

Fig. 14. Relative difference of specific distance emission measurements of nitrogen oxides for WLTC test at 14°C from a hot start engine

The maximum relative difference between specific distance emissions of nitrogen oxides using mobile systems and measurements using measuring bags, for tests conducted at a temperature of 14°C with a warm engine start, was recorded in the extra high phase for measurements using the PEMS A system compared to the results obtained in laboratory No. 2 and amounted to –61%, which translated to 7 mg/km of absolute difference (Fig. 14). The smallest relative difference characterized the low phase and took place with the use of the PEMS B system in relation to the results obtained in laboratory No. 2 and amounted to less than 0.5% (0.1 mg/km of absolute difference). For the entire test, the maximum difference was observed for the PEMS A system compared to the measurements carried out using laboratory system No. 2 and it amounted to approximately 42% (5 mg/km absolute difference), while the smallest – for the PEMS B system compared to laboratory system No. 2 and it took the value of approximately 2% (0.3 mg/km absolute difference).

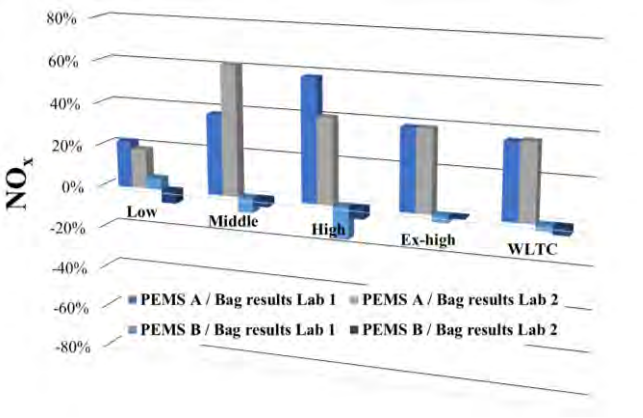

Fig. 15. Relative difference of specific distance emission measurements of nitrogen oxides for WLTC test in 23°C from cold start engine

The maximum relative difference between specific distance emissions of nitrogen oxides using mobile systems and measurements using measuring bags, for tests conducted at a temperature of 23°C with a cold engine start, was observed in the middle phase using the PEMS A system, in relation to the results obtained in laboratory No. 2, and it amounted to 61%, which translated to less than 7 mg/km of absolute difference (Fig. 15). The smallest relative difference was characteristic of the extra high phase using the PEMS B system, in comparison to the results obtained in laboratory No. 2, and it amounted to about –1% (0.1 mg/km of absolute difference). For the entire test, the largest difference was observed for the PEMS A system, in relation to the measurements performed using laboratory system No. 2, and it amounted to approximately 37% (4 mg/km of absolute value), while the smallest – for the PEMS B system in comparison to laboratory system No. 1, and it was at the level of approximately –3%, 0.4 mg/km of absolute value.

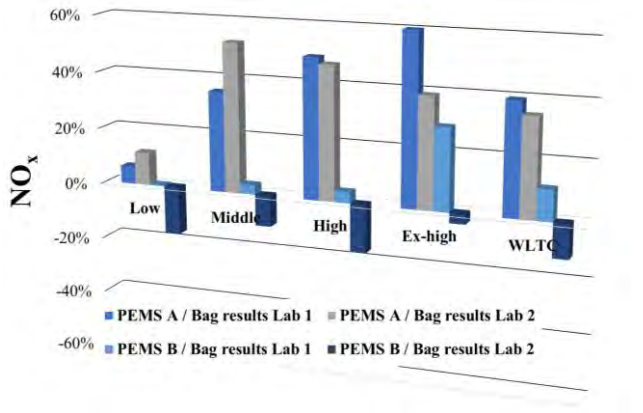

Fig. 16. Relative difference of specific distance emission measurements of nitrogen oxides for WLTC test in 23°C from hot start engine

For specific distance emissions of nitrogen oxides using mobile systems and measuring bags, for tests conducted at a temperature of 23°C with warm engine start-up, the largest relative difference between measurements was noted in the extra high phase for the PEMS A system compared to the results obtained in laboratory No. 1 and amounted to 66%, which translated to 9 mg/km of absolute difference (Fig. 16). The smallest difference was noted in the low phase for the PEMS B system compared to the results obtained in laboratory No. 1 and amounted to about 0.5% (0.1 mg/km of absolute difference). In the perspective of the entire test, the largest difference was noted for the PEMS A system in relation to laboratory system No. 1 and amounted to about 40% (5.5 mg/km of absolute value), while the smallest – for the PEMS B system in relation to laboratory system No. 1 and it was at the level of about 11% (1.5 mg/km of absolute value).

6. Conclusion

Based on the obtained results, it can be stated that mobile analyzers using the NDUV measurement method for measuring nitrogen oxide emissions are characterized by lower measurement accuracy, and the results differ by several dozen percent compared to the others.

A detailed comparison of the results for distance emissions of nitrogen oxides is provided below:

- For tests conducted at 14°C from a cold engine start, the largest relative difference is at the level of about 49% for the specific distance emission value of nitrogen oxides for the mobile PEMS A system compared to Laboratory 2, while the smallest is –3% for the mobile PEMS B system compared to the laboratory system 1, which translated into a relative value of 4.5 mg/km and –0.3 mg/km, respectively.
- At a temperature of 14°C from a warm engine start, where the specific distance emission of nitrogen oxides was at a similar level to the emission of nitrogen oxides from a cold engine start, the largest difference was also recorded for the measurement with the PEMS A system compared to the measurement from the Stationary Laboratory No. 2 I, it amounted to 41%, which gave about 5 mg/km of absolute difference. On the other hand, the smallest relative difference was recorded for the measurement results from the mobile PEMS B system compared to the measurement from the Stationary Laboratory No. 2 I, which amounted to 2%, giving 0.2 mg/km of absolute difference.
- In tests at an ambient temperature of 23°C, the largest differences at cold engine start were recorded for the mobile PEMS A system compared to the measurement from the laboratory system 2 and amounted to 32%, while the smallest relative difference was –2.6% for the measurement from the mobile PEMS B system compared to the measurement from laboratory No. 1. The absolute values were approximately 4 and –0.3 mg/km, respectively.
- Tests with warm engine start at a temperature of 23°C showed that the largest difference in measurements is for the measurement from the mobile PEMS A system compared to the measurement from the stationary laboratory No. 1, and is 39%, which gives approximately 6 mg/km of absolute difference. The smallest difference is for the measurement from the mobile PEMS B system compared to the measurement from the laboratory system No. 1, and is 11%, which gives approximately 2 mg/km of difference.

Thanks to the obtained results, although the differences in the measurement of nitrogen oxides using the NDUV analyzer amounted to even several dozen percent, in reality, these values were at the level of a few mg/km, so we can state that NDUV analyzers installed in mobile systems are reliable.

Nomenclature

CLD	chemiluminescence detector
NDUV	nondispersive ultra violet spectroscopy
PEMS	portable emissions measurement system
RDE	real driving emissions
WLTC	Worldwide Harmonized Light Vehicles Test Cycles

Bibliography

[1] Adamiak B, Andrych-Zalewska M, Merkisz J, Chłopek Z. The uniqueness of pollutant emission and fuel consumption test results for road vehicles tested on a chassis dynamometer. Eksploat Niezawodn. 2024;27(1). https://doi.org/10.17531/ein/195747

[2] Adamiak B, Szczotka A, Woodburn J, Merkisz J. Comparison of exhaust emission results obtained from Portable Emissions Measurement System (PEMS) and a laboratory system. Combustion Engines. 2023;195(4):128-135. https://doi.org/10.19206/CE-172818

[3] AVL AMA I60 Device Description of the Emission Bench. June 2016 AT2519E, Rev. 12.

[4] AVL Gas PEMS and AVL Gas PEMS iX Product Guide.

[5] Bielaczyc P, Szczotka A, Klimkiewicz D. Wpływ analizatorów spalin na wyniki emisji oraz analiza możliwości zwiększenia dokładności pomiarów emisji gazo-wych związków szkodliwych spalin przez zastosowanie nowoczesnych analizatorów pod kątem badania, samochodów o bardzo niskiej emisji (in Polish). TTS Technika Transportu Szynowego. 2015.

[6] Commission Regulation (EU) 2017/1151 of 1 June 2017 supplementing Regulation (EC) No 715/2007 of the European Parliament and of the Council on type-approval of motor vehicles with respect to emissions from light passenger and commercial vehicles (Euro 5 and Euro 6) and on access to vehicle repair and maintenance information, amending Directive 2007/46/EC of the European Parliament and of the Council, Commission Regulation (EC) No 692/2008 and Commission Regulation (EU) No 1230/2012 and repealing Commission Regulation (EC) No 692/2008. Official Journal of the European Union, L 175, 1-643, 7.7.2017. https://eur-lex.europa.eu/eli/reg/2017/1151/oj/eng

[7] Commission Regulation (EU) 2023/443 of 8 February 2023 amending Regulation (EU) 2017/1151 as regards the emission type approval procedures for light passenger and commercial vehicles (Text with EEA relevance). http://data.europa.eu/eli/ reg/2023/443/oj
[8] Commission Regulation (EC) No 692/2008 of 18 July 2008 implementing and amending Regulation (EC) No 715/2007 of the European Parliament and of the Council on type approval of motor vehicles with respect to emissions from light passenger and commercial vehicles (Euro 5 and Euro 6) and on access to vehicle repair and maintenance information. Official Journal of the European Union, L199, 1136, 28.7.2008.
[9] European Commission. Joint Research Centre. Real Driving Emissions (RDE): 2020 assessment of Portable Emissions Measurement Systems (PEMS) measurement uncertainty. LU: Publications Office. 2021. https://data.europa.eu/doi/10.2760/440720
[10] Giechaskiel B, Lahde T, Suarez-Bertoa R, Clairotte M, Grigoratos T, Zardini A et al. Particle number measurements in the European legislation and future JRC activities. Combustion Engines. 2018;174(3):3-16. https://doi.org/10.19206/CE-2018-301
[11] Global technical regulation No. 15, Global technical regulation on Worldwide harmonized Light vehicles Test Procedures (WLTP), Amendment 3, Established in the Global Registry on 15 November 2017.
[12] Kasab JJ, Strzelec A. Automotive emissions regulations and exhaust aftertreatment systems. R-477. SAE International 2020.
[13] Klingenberg H. Automobile exhaust emission testing – measurement of regulated and unregulated exhaust gas components, exhaust emission tests. Springer-Verlag, Berlin-Heidelberg 1996. https://doi.org/10.1007/978-3-642-80243-0
[14] MEXA 7xxx • Basic Training from 21. until 25.04.2008.
[15] NO/NO_x Analyzer CLA-750A HORIBA.
[16] NO/NO_x Analyzer CLA-750LE HORIBA.
[17] Regulation No 101 of the Economic Commission for Europe of the United Nations (UN/ECE) – Uniform provisions concerning the approval of passenger cars powered by an internal combustion engine only, or powered by a hybrid electric power train with regard to the measurement of the emission of carbon dioxide and fuel consumption and/or the measurement of electric energy consumption and electric range, and of categories M1and N1vehicles powered by an electric power train only with regard to the measurement of electric energy consumption and electric range. Supplement 7 to the original version of the Regulation – Date of entry into force: 18 June 2007. https://eur-lex.europa.eu/eli/reg/2012/101(2)/oj/eng
[18] Regulation No 115 of the Economic Commission for Europe of the United Nations (UN/ECE) Uniform provisions concerning the approval of: I. specific LPG (liquefied petroleum gases) retrofit systems to be installed in motor vehicles for the use of LPG in their propulsion system; II. specific CNG (compressed natural gas) retrofit systems to be installed in motor vehicles for the use of CNG in their propulsion system, Supplement 6 to the original version of the Regulation. https://eur-lex.europa.eu/eli/reg/2014/115/oj/eng
[19] Valverde V, Kondo Y, Otsuki Y, Krenz T, Melas A, Suarez-Bertoa R et al. Measurement of gaseous exhaust emissions of light-duty vehicles in preparation for Euro 7: a comparison of portable and laboratory instrumentation. Energies. 2023;16:2561. https://doi.org/10.3390/en16062561

Adam Sordyl, MEng. – Engine Research Department, BOSMAL Automotive Research & Development Institute Ltd. in Bielsko-Biała, Poland.
e-mail: *adam.sordyl@bosmal.com.pl*

Borys Adamiak, DEng. – Engine Research Department, BOSMAL Automotive Research & Development Institute Ltd. in Bielsko-Biała, Poland.
e-mail: *borys.adamiak@bosmal.com.pl*

Prof. Jerzy Merkisz, DSc., DEng. – Faculty of Civil and Transport Engineering, Poznan University of Technology, Poland.
e-mail: *jerzy.merkisz@put.poznan.pl*

Article citation info:
Szkoda M, Romowicz B. Effectiveness evaluation of a high-power diesel locomotive using a twin-engine propulsion system. Combustion Engines. 2026;204(1):96-103. https://doi.org/10.19206/CE-210986

Maciej SZKODA
Bartłomiej ROMOWICZ

Combustion Engines
Polish Scientific Society of Combustion Engines

Effectiveness evaluation of a high-power diesel locomotive using a twin-engine propulsion system

ARTICLE INFO

Received: 6 June 2025
Revised: 5 August 2025
Accepted: 16 September 2025
Available online: 25 September 2025

One of the methods of reducing the operating costs of high-power diesel locomotives, and especially the costs of fuel consumption, is the use of a drive system with two engines. The paper presents the characteristics of selected designs of multi-engine locomotives used in Poland and around the world and assesses the efficiency of a high-power six-axle locomotive in two variants of the drive system configuration: single and double-engine using a main engine with a power of 3000 kW and an auxiliary engine with a power of 400 kW. The comparative analysis took into account: the costs of maintaining the drive system, fuel consumption costs, AdBlue consumption costs and environmental costs. The analyses carried out showed that the double-engine variant ensures compliance with the exhaust emission requirements according to the Stage V standard as well as optimal adaptation of the locomotive to operation with a significant share of idle time.

Key words: *multi-engine locomotives, diesel traction efficiency, emission in rail transport, LCC assessment*

1. Introduction and literature analysis

With the growing demands for climate protection and the need to increase energy efficiency, rail transportation plays a crucial role in the European Union's sustainable development strategy. Particular attention is paid to the need to reduce the operating costs of internal combustion traction vehicles and bring them into compliance with current emission standards [14]. The literature emphasizes the importance of field studies on the actual emissions of pollutants generated by rail vehicles [16, 24], as well as the need to implement technical solutions, such as engine or injection system modifications [17, 19]. As stated in the paper [14], decarbonizing the rail sector requires both technological and systemic changes. A more holistic approach is proposed by Fonseca-Soares and co-authors [9], highlighting the need to incorporate Life Cycle Analysis and integrate rail with other forms of transportation, among other considerations, into emissions analyses.

In parallel, measures are being developed to enhance energy efficiency and reduce locomotive operating costs. The modernization of older types of vehicles, such as the SM42-series locomotives, significantly reduces fuel consumption, as confirmed in studies [26]. Similar conclusions are presented by Andrzejewski et al. in [1], highlighting the crucial importance of fuel consumption and drive train energy intensity in the operational evaluation of different locomotive types.

In the context of power supply system development, the forecasts presented in [12] suggest that despite the intensification of electrification processes in the rail network, the demand for liquid fuels in the rail sector will remain high at least until 2040, especially in sections without electric traction. In response to these challenges, new design solutions are emerging, including vehicles with hybrid drivetrain that combine internal combustion with battery-powered electric propulsion. As the authors [3] point out, the use of this type of locomotive, tested in real-world conditions, brings tangible benefits in terms of reduced fuel consumption and lower emissions.

CO_2 regulations are also becoming increasingly important. As described in more detail in Section 2 of the paper, EU Regulation 2016/1628 establishing Stage V emission standards [7], Directive 97/68/EC [4], and the tenets of the EU's "Fit for 55" package [8] remain the key documents in this regard. A very valuable review of current legal and technical requirements in the context of propulsion systems was made by the authors of the publication [18]. Conclusions from previous studies indicate the need to implement modern design solutions in diesel rolling stock, in line with current environmental and operational requirements. One such solution is the use of multi-engine propulsion systems, which allow for the optimization of engine operation depending on the operating conditions, such as idling or tractive operation [20, 28].

The paper presents a comparative evaluation of the efficiency of a high-power diesel locomotive in two variants of the drivetrain configuration: single-engine and twin-engine, utilizing a 3000 kW main engine and a 400 kW auxiliary engine.

2. Environmental emission requirements for diesel locomotives

The emission standards applicable to new and retrofitted diesel locomotives align with the European Commission's current policy, as outlined in the European Union's Green Deal [6]. It outlines goals for the European Union to address climate and environmental problems. The formulated goals refer to a resource-efficient and competitive economy that aims to achieve zero greenhouse gas emissions by 2050. European emission standards for non-road vehicles were first announced in 1997 and implemented in two stages: Stage I in 1999 and Stage II between 2001 and 2004. Stage I/II standards did not cover engines used in railroad locomotives. It was not until the introduction of Stage IIIA and IIIB standards between 2006 and 2013 that strict limits

were introduced for locomotive engines. The Stage IV emissions standard was introduced in 2014 and applies to two categories of engines, ranging from 56 kW to 560 kW. Compliance with this standard requires the use of exhaust after-treatment systems, such as selective catalytic reduction (SCR) or diesel particulate filter (DPF). Stage V, the latest emissions standard, covers RLL engines used in locomotives and RLR engines in railroad cars. The standards take effect in 2019 for engines with a power rating below 56 kW and above 130 kW, and in 2020 for engines with a power rating between 56 kW and 130 kW [25].

Regarding national requirements, Poland has a Decree of the Minister of Economy dated April 30, 2014, which outlines detailed requirements for the emission of gaseous and particulate pollutants by internal combustion engines, including those used in railroad vehicles [22]. The regulation implements selected provisions of EU law into the national legal order and includes, among other things, emission limits for specific engine categories.

Regulation (EU) 2016/1628 of the European Parliament and of the Council of 14 September 2016 on requirements for emission limits for gaseous and particulate pollutants and type approval for internal combustion engines intended for non-road mobile machinery, amending Regulations (EU) No. 1024/2012 and (EU) No. 167/2013 and amending and repealing Directive 97/68/EC (OJ. EU. L 252/53, 16.9.2016) as amended by Regulation (EU) 2022/992, regulating the requirements for permissible toxic components contained in exhaust gases, is currently in force for railroad vehicles in Europe. Article 4 of Regulation 2016/1628 divides engines into categories, of which the RLL category includes engines for use exclusively in, for propulsion of, or intended for propulsion of locomotives. According to Article 4, Section 1, point 7 of Regulation 2016/1628, the RLL category for engines used for propulsion in locomotives is defined in two subcategories (Table 1).

Table 1. Subcategories of the RLL category railroad engines [7]

Category	Ignition type	Speed operation	Power range [kW]	Subcategory	Reference power
RLL	all	variable	P > 0	RLL-v-1	Maximum net engine
		constant	P > 0	RLL-c-1	Rated net power

Regulation 2016/1628 introduced Stage V, which has stringent limits for the content of particulate matter (PM), carbon monoxide (CO), hydrocarbons (HC), and nitrogen oxides (NO_x) in the exhaust gases. Stage V introduced a new particulate number emission limit, PN, which requires particulate filters on all engine types. Before that, there had been harmonization of EU regulations with US Tier standards. However, harmonization was largely lost at Stage V.

Table 2. Stage V emission limits for RLL category engines [7]

Engine sub-category	Power range [kW]	CO [g/kWh]	HC [g/kWh]	NO_x [g/kWh]	PM [g/kWh]	A
RLL-c-1 RLL-v-1	P > 0	3.50	($HC + NO_x$ ≤ 4.00)		0.025	6.00

Stage V emission limits for RLL category railroad engines as defined in Article 4, Section. 1, point 7 of Regulation 2016/1628 is shown in Table 2.

3. Examples of solutions for multi-engine systems in locomotives

Multi-engine locomotives are railroad vehicles equipped with multiple drive units that can be started and stopped as needed to meet current traction requirements. With this design, higher operational flexibility is achieved, along with optimized fuel consumption and reduced emissions. Multi-engine locomotives offer several significant operational and environmental advantages over traditional designs with a single large diesel engine. The most important advantages of such solutions include:

a) Possibility of working at partial power

Locomotives equipped with several drive units allow flexible management of available power. In the case of smaller loads, for example, during shunting, driving with light formations, or during prolonged stops, the operation of all engines is not required. In such situations, it is possible to turn off some units and leave only the necessary units active. This approach reduces fuel consumption and unnecessary wear and tear on mechanical components, resulting in greater durability and increased overall operating efficiency of the locomotive.

b) Optimization of fuel consumption

Adapting the number of running units to actual traction demand enables a significant reduction in average fuel consumption. In traditional locomotives, the large internal combustion engine often operates in a suboptimal load range, resulting in increased fuel burn. In multi-aggregate designs, each engine can operate closer to its optimum characteristics, and it is possible to quickly start additional drive units if necessary.

c) Reduction of CO_2 and NO_x emissions

Reduced fuel consumption directly translates into reduced carbon dioxide (CO_2) emissions, the main greenhouse gas responsible for climate change. In addition, emissions of nitrogen oxides (NO_x) and particulate matter (PM) are also reduced, thanks to the use of modern aggregates that meet current emission standards (such as EPA Tier 4 or Stage V). This aspect is particularly important in the context of tightening environmental regulations in the rail transportation sector.

d) Higher reliability

Multi-engine locomotives are characterized by greater resistance to failure compared to single-engine designs. In the event of damage or failure of one unit, the remaining units can continue operating, allowing them to complete manoeuvres or reach the nearest service station. Such a solution increases the operational reliability of the locomotive and minimizes the risk of downtime in railroad traffic [11].

To illustrate the variety of existing solutions for multi-engine systems, the following table summarizes selected types of multi-engine locomotives, along with their basic technical information and performance characteristics.

Table 3. Examples of multi-engine locomotives [13, 15, 27, 29]

Locomotive type	 **Traxx DE ME**	 **6Dk**	 **6Dl (SU4210 series)**	 **Class Dr19**
Manufacturer	Bombardier	PESA	NEWAG	STADLER
Year of manufacturing	2013	2014	2013	2023
Engine configuration	4 × Caterpillar C18	2 × Caterpillar C15	2 × Caterpillar C18	2 × Caterpillar C32
Total power	4 × 563 kW (2252 kW)	2 × 403 kW (806 kW)	2 × 563 kW (1126 kW)	2 × 950 kW (1900 kW)
Maximum speed	160 km/h	80 km/h	95 km/h	120 km/h
Scope of application	Passenger and freight trains	Shunting work, light freight	Freight trains and shunting work	Freight trains and shunting work

4. Characteristics of the analyzed variants of propulsion systems

In this paper, two variants of a high-powered diesel locomotive's drive train are analyzed in a comparative study:

1. Single-engine standard propulsion system with Caterpillar Type C175 3000 kW, Stage V engine
2. A twin-engine propulsion system using a 3000 kW C175 main engine and a 430 kW Caterpillar C13B auxiliary engine, Stage V. The auxiliary engine acts as a power unit to support the locomotive when stationary at stations and passing stations, and performing loose shunting work.

Table 4. Summary of the basic parameters of the engines in the analyzed drive systems

Specification	Main engine	Auxiliary engine
Manufacturer	Caterpillar	Caterpillar
Type:	C175	C13B
Power:	3000 kW	430 kW
Torque	16852 Nm	2648 Nm
Capacity:	85.7 dm^3	12.5 dm^3
Exhaust emission standard	Stage V	Stage V
Cylinder arrangement	V16	R6
Rotational speed	1800 rpm	1800 rpm
Exhaust gas treatment module	SCR technology, AdBlue	AdBlue

a)

Fig. 1. CAT C175-16 engine with 3000 kW [5]

b)

Fig 2. CAT C13B engine with 430 kW [10]

The C175 type main engine is a popular drive unit in modern high-powered diesel locomotives. The engine is used, among other applications, in the EURO 4001 series of locomotives featuring the Co'Co' axle system, offered by Stadler, for both freight and passenger services at speeds of up to 160 km/h. The engine meets the latest emission regulations (EU Stage V). In addition, they are adapted to the use of HVO fuel, supporting the decarbonization of the transportation sector. EURO 4001 locomotives are operated in freight transport in France by Captrain France, among others, as well as by carriers outside Europe (South America, New Zealand).

5. Efficiency evaluation of the single- and twin-engine variants

5.1. Performance and cost analysis of propulsion system variants under different operating scenarios

Based on the actual costs of diesel fuel, AdBlue solution, and maintenance and repair costs for internal combustion engines, an evaluation of the efficiency of the single- and twin-engine variants of the propulsion system configuration was conducted. The comparative analysis included:

- the cost of maintaining the propulsion system
- fuel consumption costs
- AdBlue consumption costs
- environmental costs.

The comparative analysis of the propulsion system includes a comparison of a single-engine variant with a Caterpillar Type C175 engine with a twin-engine variant that uses a Caterpillar Type C175 primary engine and a Caterpillar Type C13B auxiliary engine. In the analysis for the twin-engine variant, three operating scenarios were considered, which differ in the share of main engine C175 and auxiliary engine C13B operating time in total locomotive operating time:

1. Scenario 1: 60% of the work is done by the C13B engine and 40% by the C175 engine
2. Scenario 2: 50% of the work is done by the C13B engine and 50% by the C175 engine
3. Scenario 3: 40% of the work is done by the C13B engine and 60% by the C175 engine.

5.2. Maintenance cost comparison

The measure of the interval for performing inspections and periodic repairs of internal combustion engines is the actual operating time expressed in engine hours. Reducing the operating time of the main engine of the C175 by elimi-

nating idling has a significant impact on extending the duration of periodic engine maintenance and repairs.

The calculations take into account the locomotive's actual operating profile at the rail carrier, which varies depending on the engine load. In addition, the following assumptions were made:

– engine load at locomotive idling within 300–400 kW
– the engine obtains power (except for idling) at 1800 rpm
– average operating time of the locomotive: 6400 [hours/year]
– the operating time of the engine: 32,000 hours.

The analysis of engine maintenance costs included material and labor costs. The analysis required obtaining source data from Caterpillar Inc., the internal combustion engine manufacturer, regarding the detailed scope of activities resulting from the maintenance plan for the C13B auxiliary engine and the C175 main engine, from 500 hours to 12,000 hours. Due to the confidentiality of the data provided, unit cost information for individual inspections and repairs is not included in this paper.

A comparison of total maintenance costs and unit costs for the single-engine variant with a Caterpillar type C175 engine and the twin-engine variant (C175 + C13B) for all three operating scenarios considered is shown in Table 5 and Fig. 3. The analysis covered an operating time of 32,000 hours (approximately 5 years), and the interval for primary repair of the C175 engine was assumed to be extended to 24,000 hours, as per the manufacturer's instructions.

Table 5. Comparison of maintenance costs of the single-engine variant (CAT C175) and the twin-engine variant (C175 + C13B) for three operating scenarios

Specification	Single-engine variant	Two-engine variant Scenario 1	Two-engine variant Scenario 2	Two-engine variant Scenario 3
Total cost of engine maintenance (thous. PLN)	3,700.9	1,136.1	1,399.1	3,133.6
Unit cost of engine maintenance (PLN/hour)	115.7	35.5	43.7	97.9

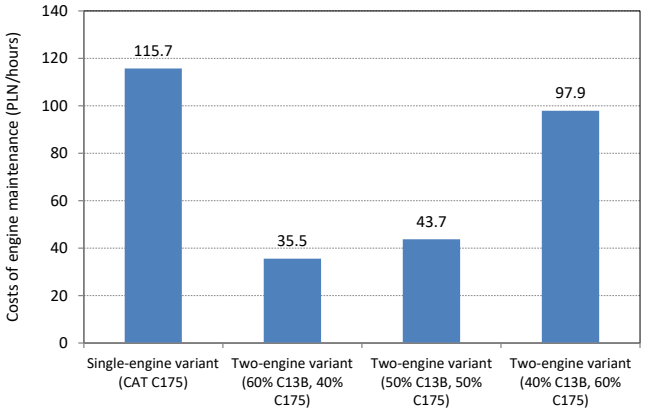

Fig 3. Comparison of unit costs of engine maintenance (PLN/hours) for the single-engine variant (CAT C175) and the two-engine variant (C13B and C175 engine) for three operating scenarios

The analysis shows that for the twin-engine variant, reducing the idling time of the C175 main engine can result in unit costs [PLN/hour] being reduced by as much as 69.3% compared to 15.4%. Annual savings range from PLN 113,920.00 to PLN 513,280.00 over a period of 32,000 hours of locomotive operation (5 years of operation).

5.3. Comparison of fuel consumption costs

Figures 4 and 5 show graphs of power (in kW) and fuel consumption (in g/kWh) for CAT C175 and CAT C13B engines. The charts indicate a power range of 300–400 kW, which corresponds to the locomotive's idle power requirements. From Figure 4, it can be observed that within this range, the C13B engine operates within the optimal range of specific fuel consumption characteristics: 199.3–200.6 g/kWh, in contrast to the C175 engine, for which consumption ranges from 240.7 to 245.2 g/kWh.

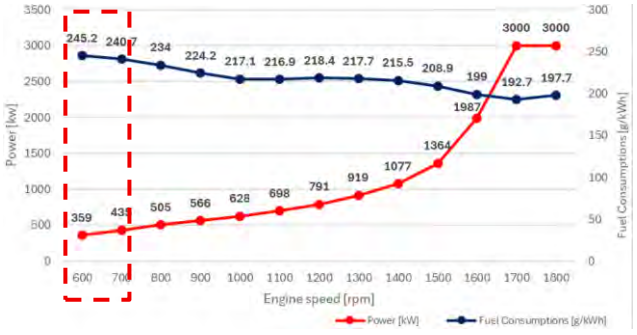

Fig. 4. Power and specific fuel consumption of the CAT C175 3000 kW engine as a function of speed

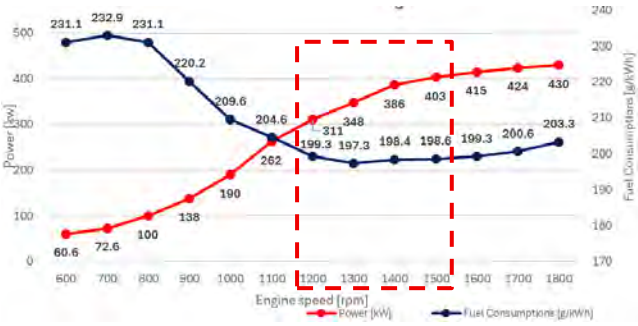

Fig. 5. Power and specific fuel consumption of the CAT C13B 430 kW engine as a function of speed

Tables 6 and 7 summarize the detailed calculations for the single- and two-engine variants, comparing idle fuel consumption. The calculations took into account the locomotive's actual operating profile at the carrier and:

– the required engine load when the locomotive is idling: 300–400 kW
– average operating time of the locomotive: 6400 [hours/year]
– the cost of diesel fuel: PLN 4.90 net/liter.

The analysis was conducted for three operating scenarios, which differ in the proportion of locomotive idling time to total operating time: 40%, 50%, and 60%.

Table 6. Consumption costs of fuel at idle in a single-engine variant (C175 engine)

Specification	Scenario 1	Scenario 2	Scenario 3
Idling time [hr]	60% – 3840	50% – 3200	40% – 2560
Average fuel consumption at idle [dm^3/hr]	113.5	113.5	113.5
Average fuel consumption at idle [dm^3/year]	435,648.0	363,040.0	290,432.0
Fuel cost [thous. PLN/year]	2134.7	1778.9	1423.1

Table 7. Fuel consumption costs at idle in the two-aggregate variant (C175 engine + C13B engine)

Specification	Scenario 1	Scenario 2	Scenario 3
Idling time [hr]	60% – 3840	50% – 3200	40% – 2560
Average fuel consumption at idle [dm^3/hr]	93.8	93.8	93.8
Average fuel consumption at idle [dm^3/year]	360,192.0	300,160.0	240,128.0
Fuel cost [thous. PLN/year]	1764.9	1470.8	1176.6

The analysis shows that the fuel consumption of the two-aggregate variant, in which only the auxiliary engine C13B runs at idle with a power demand of 400 kW, can be reduced by 17.3%. During train operation, a high-powered basic unit (CAT C175) is used, and fuel consumption for both variants is identical.

Figure 6 shows a comparison of idling fuel consumption costs for a single-engine variant (CAT C175) and a two-engine variant (CAT C13B and C175) as a function of idling time. In the two-aggregate variant, thanks to the reduction of the C175 main engine's operating time, the savings range from PLN 246,489.60 to PLN 369,734.40 in one year of locomotive operation.

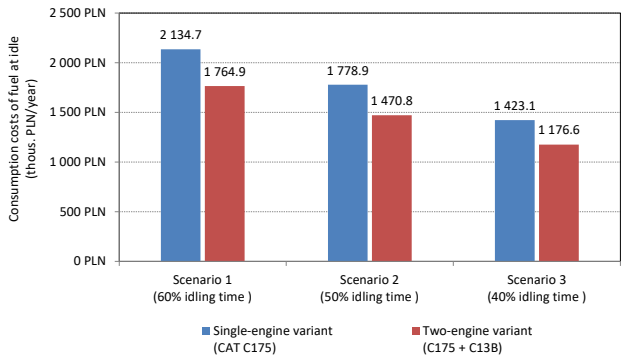

Fig. 6. Comparison of annual fuel consumption costs at idle for single-engine and two-engine variants depending on the operating scenario

5.4. Cost comparison of AdBlue consumption

The consumption of AdBlue solution is directly proportional to diesel fuel consumption, and, according to the manufacturer's declaration, it ranges from 3% to 8%, depending on the type of engine [2, 21]. The use of two engines not only reduces fuel consumption at idle but also significantly reduces the frequency of hydrocarbon neutralization in the exhaust gas aftertreatment system of the C175 engine, as it does not operate under low loads. According to the manufacturer, the C175 engine's AdBlue urea consumption accounts for 7.8% of the fuel consumption.

Tables 8 and 9 summarize the detailed calculations for the single- and two-engine variants, comparing AdBlue consumption. The calculations took into account the actual operating profile of the locomotive and the cost of AdBlue at a net price of PLN 2.25 per liter. The analysis was conducted for three assumed operating scenarios.

Table 8. Costs of AdBlue consumption at idle in a single-engine variant (C175 engine)

Specification	Scenario 1	Scenario 2	Scenario 3
Idling time [hr]	60% – 3840	50% – 3200	40% – 2560
Average fuel consumption at idle [dm^3/year]	435,648.0	363,040.0	290,432.0
Average AdBlue consumption [dm^3/year]	33,980.54	28,317.12	22,653.70
AdBlue cost [PLN/year]	76,456.22	63,713.52	50,970.82

Table 9. Costs of AdBlue consumption at idle in the two-aggregate variant (C175 engine + C13B engine)

Specification	Scenario 1	Scenario 2	Scenario 3
Idling time [hr]	60% – 3840	50% – 3200	40% – 2560
Average fuel consumption at idle [dm^3/year]	360,192.0	300,160.0	240,128.0
Average AdBlue consumption [dm^3/year]	28,094.98	23,412.48	18,729.98
AdBlue cost [PLN/year]	63,213.70	52,678.08	42,142.46

Figure 7 shows a comparison of AdBlue consumption at idle for a single-engine variant (CAT C175) and a two-engine variant (CAT C13B and C175) as a function of idling time. In the two-aggregate variant, thanks to the reduction in the running time of the C175 main engine, the savings in AdBlue consumption are estimated to range from PLN 8828.35 to PLN 13,242.53 in one year of locomotive operation.

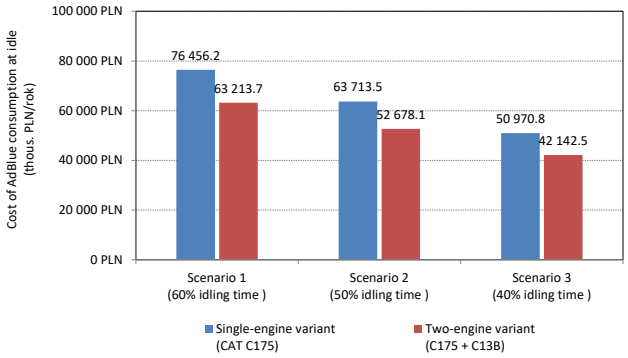

Fig. 7. Comparison of the annual cost of AdBlue consumption at idle for the single-engine variant and the two-engine variant depending on the operating scenario

5.5. Environmental cost comparison

The EU ETS (Emissions Trading System) is part of the Fit for 55 legislative package. According to the amendment to the ETS reform adopted by the European Parliament in April 2023, the obligation to purchase emission allowances will be extended to the automobile, air, and water transport sectors, starting in 2027 (it was initially scheduled for 2024). The EU ETS reform was supported by the Community of European Railway and Infrastructure Companies

(CER). In the next phase of regulatory changes, it is expected that diesel traction in rail transportation will also be subject to these additional costs.

Given these requirements, it is necessary to compare the environmental impact, particularly the carbon dioxide (CO_2) and other pollutants emitted by the single- and two-engine variants.

Table 10 shows the unit emission values for the single- and two-engine variants of the locomotive under idling conditions, while Tables 11 and 12 show the annualized values in kg/year for the three operating scenarios subject to analysis.

Table 10. Specific emission values under locomotive idling conditions

No.	Specification	Single-engine variant (C175 engine)	Two-engine variant (C175 engine + C13B engine)
1	NO_x [g/h]	935	26
2	CO [g/h]	1206	34
3	HC [g/h]	27	5
4	CO_2 [kg/h]	318	208

Table 11. Emission value at idle in the single-engine variant (C175 engine)

Specification	Scenario 1	Scenario 2	Scenario 3
Idling time [hr]	60% – 3840	50% – 3200	40% – 2560
NO_x [kg/year]	3590.4	2992.0	2393.6
CO [kg/year]	4631.0	3859.2	3087.4
HC [kg/year]	103.7	86.4	69.1
CO_2 [kg/year]	1221.1	1017.6	814.1

Table 12. Idle emission value of the two-aggregate variant (C175 engine + C13B engine)

Specification	Scenario 1	Scenario 2	Scenario 3
Idling time [hr]	60% – 3840	50% – 3200	40% – 2560
NO_x [kg/year]	99.8	83.2	66.6
CO [kg/year]	130.6	108.8	87.0
HC [kg/year]	19.2	16.0	12.8
CO_2 [kg/year]	798.7	665.6	532.5

The unit costs of carbon dioxide and other pollutants were adopted by Annex No. 2 to Prime Minister's Order No. 559 of May 10, 2011, on mandatory bid evaluation criteria other than price for certain types of public procurement (Journal of Laws 11.96.559 of 10.5.2011) – Table 13.

Table 13. Unit costs of carbon dioxide and pollution emissions [23]

Carbon dioxide CO_2	Nitric oxide NO_x	Hydrocarbons HC	Particulate matter PM
0.115–0.154 [PLN/kg]	0.0169 [PLN/g]	0.00384 [PLN/g]	0.334 [PLN/g]

The chart compares the annual cost of CO_2 emissions and other pollutants contained in the exhaust at idle for the single- and two-engine variants. The analysis indicates that the savings in environmental expenses for the two-engine variant are estimated at up to 49.9%, i.e., from PLN 82,909.64 to PLN 124,364.47 depending on the scenario, over the course of one year of locomotive operation.

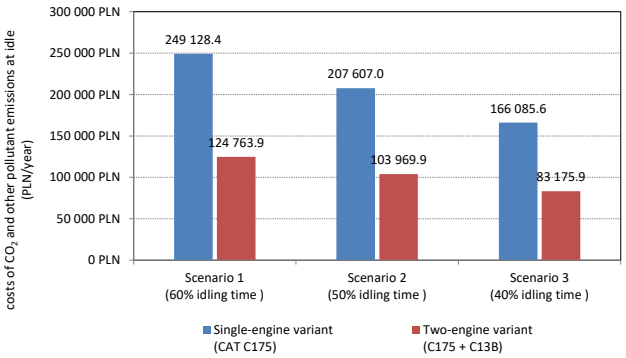

Fig 8. Comparison of the annual costs of CO_2 and other pollutant emissions at idle for the single-engine and twin-engine variants, depending on the operating scenario

5.6. Summary of the effectiveness of the single- and two-engine variants

Table 14 summarizes the efficiency of the single- and two-engine variants in terms of the drive system configuration for three operating scenarios that differ in the share of the locomotive idling time in the total operating time:

1. Scenario 1: 60% idling time
2. Scenario 2: 50% idling time
3. Scenario 3: 40% idling time.

Table 14. Summary of single- and two-engine variant efficiencies for three scenarios

Specification	Two-engine variant [thous. PLN/year]	Single-engine variant [thous. PLN/year]	Savings [thous. PLN/year]
Scenario 1	2180.1	3200.4	1020.3
Scenario 2	1907.2	2790.4	883.2
Scenario 3	1928.7	2380.4	451.7

In all scenarios analyzed, the two-engine variant proves more economical than the single-engine variant. The largest savings were achieved in Scenario 1, where the idle time share was as much as 60%. In this case, the annual operating costs for the two-engine system amounted to PLN 2180.1 thousand, while for the single-engine system it was as much as PLN 3200.4 thousand. This translates to savings of approximately PLN 1020.3 thousand per year. As the idle time share decreases, the difference in costs between the variants decreases. In Scenario 2 (50% idle time), the savings amount to PLN 883.2 thousand, while in Scenario 3 (40% idle time), they are only PLN 451.7 thousand. PLN. This trend indicates that the advantage of the two-engine variant is particularly visible in conditions of frequent idling of the locomotive, while in scenarios with a lower share of this mode, the economic difference gradually decreases.

6. Conclusions

The comparative analysis demonstrated clear advantages of the two-engine drive system for high-power diesel locomotives, especially in idling conditions. The use of a smaller auxiliary engine reduces wear on the main unit, contributing to lower maintenance costs and improved energy efficiency.

In addition to the economic aspects, the dual-engine solution proved to deliver significant environmental benefits. Reduced fuel consumption and lower CO_2 and NO_x emissions make this configuration more compatible with tightening EU regulations and climate policy targets.

Another advantage of the two-engine configuration is increased operational flexibility and system reliability. Adjusting power output to real traction needs allows for better adaptation to varying operational scenarios and reduces the risk of failures.

Although the investment costs of the dual-engine variant are higher, the estimated payback period of 3–5 years makes this solution attractive in the long term. Considering the nominal service life of locomotives, this approach provides strong justification for further development.

Future work should include a broader range of operating scenarios and experimental validation of the simulation results, as well as an assessment of the life-cycle environmental impact of multi-engine locomotives. Comparative studies with hybrid and alternative-fuel solutions could also provide valuable insights into sustainable strategies for non-electrified railway lines.

Similar comparative analyses of locomotive drive systems have been undertaken by other researchers, but the scope has so far been limited, mainly focusing on fuel consumption and emissions. The present study extends this perspective by combining technical, economic, and environmental aspects, highlighting the potential of dual-engine locomotives as a competitive solution for the future.

Bibliography

[1] Andrzejewski M, Świechowicz R, Merkisz J, Stawecki W, Daszkiewicz P. Assessment of the energy intensity of diesel locomotive drive systems. Autobusy. 2019;6:134-138. https://doi.org/10.24136/atest.2019.139

[2] C175-16 Locomotive Engine. EU Stage V Locomotive 3000 bkW/4023 bhp @1800 rpm. Caterpillar 2019.

[3] Cipek M, Pavković D, Kljaić Z, Mlinarić TJ. Assessment of battery-hybrid diesel-electric locomotive fuel savings and emission reduction potentials based on a realistic mountainous rail route. Energy. 2019;(173):1154-1171. https://doi.org/10.1016/j.energy.2019.02.144

[4] Directive 97/68/EC on the approximation of the laws of the Member States relating to measures against the emission of gaseous and particulate pollutants from internal combustion engines. OJ L 059, 27.2.1998.

[5] Eneria. CAT. 2025. Available from: https://eneria.pl/product/2001-2550-bkw/

[6] European Commission. Communication from the Commission of 11 December 2019 to the European Parliament, the European Council, the Council, the European Economic and Social Committee and the Committee of the Regions.

[7] European Parliament and Council Regulation (EU) 2016/1628 of 14 September 2016 on requirements relating to gaseous and particulate pollutant emission limits and type-approval for internal combustion engines for non-road mobile machinery. OJ L 252, 16.9.2016.

[8] European Union Agency for Railways. Fit for 55 – Implications for the rail sector. 2024. https://www.era.europa.eu/system/files/2024-07/20242052_PDF_TR0924239ENN_002.pdf (accessed on 1.06.2025)

[9] da Fonseca-Soares D, Eliziário SA, Galvincio JD, Ramos-Ridao AF. Greenhouse gas emissions in railways: systematic review of research progress. Buildings. 2024;539(14). https://doi.org/10.3390/buildings14020539

[10] Industrial Diesel Engines. C13B. 2025. Available from: https://www.cat.com/en_US/products/new/power-systems/industrial/industrial-diesel-engines/89679639553.html (accessed on 1.06.2025)

[11] Kaźmierczak AR. Research on the wear of novel sets of piston rings in a diesel locomotive engine. Combustion Engines. 2023;195(4):56-62. https://doi.org/10.19206/CE-168518

[12] Klemba S. Forecast of liquid fuel consumption in rail transport until 2040. Transport Miejski i Regionalny. 2022;06:17-26.

[13] Loco 6Dk. 2025. Available from: https://www.mainlinediesels.net/index.php?lang=en&nav=1001175 (accessed on 1.06.2025)

[14] Majewski J. Decarbonization of rail transport as an element of climate policy. 2021;12:16-21.

[15] Majszyk K. Koniec piekielnych podróży na Hel. Oto nowe lokomotywy PKP Intercity (in Polish). 2025. Available from: https://forsal.pl/transport/aktualnosci/galeria/7612582,koniec-piekielnych-podrozy-na-hel-oto-nowe-lokomotywy-pkp-intercity-zdjecia.html (accessed on 1.06.2025)

[16] Marciniak Z, Pielecha I. Impact of combustion engines of traction vehicles operated in Poland on the environment – tests, research and guidelines for emission reduction. Rail Vehicles/Pojazdy Szynowe. 2009;1:34-43. https://doi.org/10.53502/RAIL-139749

[17] Marciniak Z, Stawecki W, Merkisz J, Pielecha I, Pielecha J. Possibilities of modifying diesel rolling stock to reduce pollutant emissions. Technika. 2011;3:43-48.

[18] Merkisz J, Pielecha I, Daszkiewicz P, Andrzejewski M. Legal conditions in the aspect of pollutant emissions from exhaust systems of rail vehicle engines. Journal of KONES Powertrain and Transport. 2018;25(1):257-264. https://doi.org/10.5604/01.3001.0012.2475

[19] Merkisz-Guranowska A, Pielecha I, Gallas D, Andrzejewski M, Daszkiewicz P. Ways of reducing the pollutant emissions in freight railway transport. Rail Vehicles/Pojazdy Szynowe. 2015;4:11-17. https://doi.org/10.53502/RAIL-138821

[20] Michalak P, Urbański P, Jakuszko W, Gallas D, Stobnicki P, Tarnawski P. Technical aspects of the selection of an engine-generator set for a dual-drive locomotive. Combustion Engines. 2024;197(2):97-105. https://doi.org/10.19206/CE-176799

[21] Performance Data (EM240) C175-16 Locomotive Engine, Caterpillar, October 12, 2020.

[22] Regulation of the Minister of Economy of 30 April 2014 on detailed requirements for internal combustion engines regarding the limitation of gaseous and particulate pollutant emissions. Dz.U. 2014 poz. 588.

[23] Regulation of the Prime Minister of 10 May 2011 on non-price mandatory criteria for evaluating tenders in some types of public procurement. Dz.U. 2011 nr 96 poz. 559.

[24] Rymaniak Ł, Sobczak J, Szymlet N, Pielecha P, Wiśniewski S. Emission testing of diesel multiple units complying with different emission standards during real operating conditions. Rail Vehicles/Pojazdy Szynowe. 2024;3-4:44-53. https://doi.org/10.53502/RAIL-202044

[25] Sobczak J, Kamińska M, Ziółkowski A, Rymaniak Ł, Szymlet N. Analysis of pollutant emissions of a railbus based on real train emissions measurements. Combustion Engines 2025;201(2):22-33. https://doi.org/10.19206/CE-201217
[26] Szkoda M. Assessment of the modernization effectiveness of the SM42 diesel locomotive based on LCC analysis. Rail Vehicles/Pojazdy Szynowe. 2012;1:35-39. https://doi.org/10.53502/RAIL-139421
[27] TRAXX DE Multi Engine. 2025. Available from: https://www.mainlinediesels.net/index.php?nav=1000930&lang=en (accessed on 1.06.2025)
[28] Tułecki A, Szkoda M. Ecology, energy efficiency and resource efficiency as the objectives of rail vehicles renewal. Transportation Research Procedia. 2017;(25):386-406. https://doi.org/10.1016/j.trpro.2017.05.416
[29] VR FleetCare chosen to maintain VR Group's newest diesel locomotive. 2025. Available from: https://www.vrfleetcare.com/en/vr-fleetcare/news/vr-fleetcare-chosen-to-maintain-vr-groups-newest-diesel-locomotive-021220211340/ (accessed on 1.06.2025)

Prof. Maciej Szkoda, DSc., DEng. – Faculty of Mechanical Engineering, Cracow University of Technology, Department of Rail Vehicles and Transport, Cracow, Poland.
e-mail: *maciej.szkoda@pk.edu.pl*

Bartłomiej Romowicz, MEng. – Faculty of Mechanical Engineering, Cracow University of Technology, Department of Rail Vehicles and Transport, Cracow, Poland.
e-mail: *bartlomiej.romowicz@pk.edu.pl*

Article citation info:
Sufe G. Advancements in hybrid nanofluids for diesel engine thermal management: a comparative review. Combustion Engines. 2026;204(1):104-118. https://doi.org/10.19206/CE-207153

Gadisa SUFE

Combustion Engines
Polish Scientific Society of Combustion Engines

Advancements in hybrid nanofluids for diesel engine thermal management: a comparative review

ARTICLE INFO

Received: 9 April 2025
Revised: 12 June 2025
Accepted: 14 June 2025
Available online: 16 September 2025

Hybrid nanofluids show considerable promise for improving thermal management in diesel engines – outperforming both single-nanoparticle fluids and standard coolants. When it comes to performance, we rigorously evaluated multiple hybrid formulations against four key metrics: thermal conductivity, viscosity, long-term stability, and corrosion resistance. Blending specific nanoparticle types, namely alumina (Al_2O_3), silica (SiO_2), and titania (TiO_2), with carefully chosen surfactant agents. This combination directly boosted how effectively these fluids transfer thermal energy. The research demonstrates that hybrid nanofluids substantially boost thermal conductivity, increasing it by 30% to 50% compared to conventional coolants. In particular, the Al_2O_3-SiO_2-TiO_2 combination showed exceptional effectiveness, surpassing other nanofluid mixtures by roughly 20–30%. Surfactants significantly enhanced the dispersion of nanoparticles, reduced their aggregation, and decreased viscosity by around 10–15%, which subsequently reduced the energy required for pumping. These advancements increased the durability and reliability of hybrid nanofluids, thereby broadening their potential applications. The study emphasized the importance of surfactants in maintaining effective nanoparticle suspension and preventing sedimentation, ensuring sustained stability. Among all the compounds analyzed, the surfactant-modified Al_2O_3-SiO_2-TiO_2 nanocomposite blend showed superior outcomes, striking a balance between enhanced thermal conductivity, stability, and controllable viscosity. Hybrid nanofluids present a promising method for improving diesel engine cooling; however, significant obstacles such as cost, scalability, and durability remain. This study tackles these barriers and contributes valuable perspectives for advancing thermal management technologies. The paper amalgamates experimental and theoretical findings from 82 peer-reviewed studies, providing a comparative analysis without introducing new experimental data.

Keywords: *hybrid nanofluids, diesel engine cooling, thermal management, heat transfer, stability, viscosity reduction*

1. Introduction

Efficient thermal management is at the heart of achieving diesel engine performance, reliability, and durability. Excessive heat production during the operation of engines could lead to thermal stress, reduced fuel efficiency, increased emissions, and increased wear of sensitive components. Excessive build-up of heat, if not properly released, could lead to a compromise in engine performance, resulting in early failure and increased maintenance costs. To mitigate these challenges, cooling systems have been used to maintain engine temperature and achieve optimum operation [49]. Diesel engines have conventionally relied on conventional coolant systems that utilize a mix of water and ethylene glycol as a working fluid. Such coolants utilize convective heat transfer as a predominant mechanism, dissipating excess heat generated in the engine and conveying it through radiators and cooling passages. These cooling fluids have been predominant due to ease of use and compatibility with common engine components, as well as affordability and ease of implementation. However, as engines have been developed to accommodate increased power output and stringent emissions regulations, weaknesses of conventional coolants have been revealed, and superior thermal management technologies have been sought [23, 45].

One of the serious drawbacks of traditional coolant systems is that they have a comparatively low thermal conductivity that barely enables them to reject heat under high-load operation effectively [3, 41]. Although water is a very popular base fluid in cooling systems due to its excellent heat capacity, it is still found wanting when it comes to thermal conductivity and thus compromises the overall performance of a cooling system. Ethylene glycol, often combined with water to inhibit freezing and corrosion, intensifies this drawback by reducing the coolant's thermal conductivity. Moreover, conventional coolants experience more significant degradation over time as a result of thermal cycling, chemical instability, and exposure to contaminants [8]. This degradation results in reduced heat transfer efficiency, increased likelihood of corrosion, and deposit formation within the cooling system, which can hinder flow channels and make cooling operations more challenging. These drawbacks are particularly prominent in high-performance and heavy-duty diesel engines, where the increased thermal demands necessitate more efficient heat dissipation techniques to avoid overheating and ensure long-term reliability [37, 38].

Nanofluids are next-generation heat transfer fluids consisting of nanoparticles in conventional base fluids such as water, ethylene glycol (EG), or oil. The thermal conductivity, heat transfer coefficient, and fluid stability are improved significantly by these nanoparticles, and thus, nanofluids are quite suitable in engine cooling systems. Among numerous different formulations, surfactant-stabilized metal oxide or hybrid particle-based water-based nanofluids are the most effective in engine coolant applications [79]. According to the kind of nanoparticle used, nanofluids are single nanofluids (a single type of nanoparticle) or hybrid nanofluids (two or multiple different nanoparticles), and are divided according to these characteristics. In both cases,

suspension stability is a leading aspect that determines them due to the tendency of nanoparticles to agglomerate as a result of van der Waals forces. In order to address this, surfactants are often utilized as they go a long way towards enhancing dispersibility, reducing sedimentation, and increasing the heat transfer coefficient in nanofluids [40].

The exploration of nanofluids as a substitute for conventional coolants has been a focal point for researchers aiming to overcome current obstacles. Nanofluids are meticulously crafted mixtures of nanoparticles suspended in a base fluid, intended to enhance the heat transfer capabilities of standard cooling systems. Nonetheless, the practical application of single-component nanofluids is often restricted by certain limitations, inhibiting their extensive adoption in diesel engines. Specifically, these constraints restrict the integration of single-component nanofluids into diesel engine systems. The inclusion of thermally conductive nanoparticles, such as aluminum oxide (Al_2O_3), copper oxide (CuO), silicon dioxide (SiO_2), and titanium dioxide (TiO_2), has shown substantial improvement in the heat transfer capabilities of base fluids by enhancing thermal conductivity and convection heat transfer rates. Nevertheless, nanofluids created through conventional methods often suffer from instability, resulting in rapid sedimentation that diminishes their effectiveness in heat transfer. Nanoparticles, due to their small size, interact more effectively with fluids, thereby reducing thermal resistance and improving the efficiency of heat dissipation [34, 66]. At present, a significant hurdle in the application of nanofluid technology is resolving issues such as particle sedimentation, heightened viscosity, extended instability, and potential material incompatibility. Tackling these essential challenges is vital for the adoption of nanofluids as viable alternatives to traditional cooling fluids in practical scenarios.

Hybrid nanofluids have emerged as a new approach to solving the single-component nanofluid problems inherent in diesel engine heat transfer. While single-component nanofluids do not perform all of these functions sufficiently, hybrid nanofluids have been found to use a base fluid with two or more types of nanoparticle-allowing researchers to make full use complementarity between different materials and thus enhance thermal performance [30]. Hybrid nanofluids with different nanoparticle compositions can have better thermal conductivity, dispersant additional stability, and the compatibility of viscosity and composite technology with bombarding particles. For example, use a combination of metallic and metallic oxide nanoparticles; this not only increases the heat transfer of the original fluid but also reduces aggregate sediment at the same time. Furthermore, by using surfactant modifiers and new dispersion technology, the long-term stability of hybrid nanofluids has gone up, making them more feasible for practical cooling applications [5, 82]. As a result, hybrid nanofluids boast high potential in surpassing traditional coolants. They also effectively address what single-component nanofluids lack.

With the increasing complexity of modern diesel engines today, coupled with the ever-growing need for energy efficiency and environmental protection, advanced cooling solutions have been thrown into sharp relief. As engine power output continues to climb, traditional systems are struggling to cope with ever-increasing heat loads, demanding more innovative and effective methods for thermal management [11, 33]. Using water as the base fluid, hybrid nanofluids have demonstrated significant potential, providing an efficient approach to boost convective heat transfer while remaining stable and compatible with the components of current cooling systems. The integration of hybrid nanofluids into diesel engine cooling systems has the potential to reduce engine operating temperatures, improve fuel efficiency, minimize wear and tear, and lower emissions, making them an attractive research focus for both academia and industry [6].

Despite their significantly enhanced thermal conductivity, ionic liquids continue to present a concern due to their corrosive nature. Some ionic liquids have been found to accelerate corrosion in aluminum and copper components; corrosion inhibitors or protective coatings must be used to avoid this situation entirely. For example, [56] NG SAIC has shown that in hybrid nanofluids containing ionic liquids, a further 58 certainly can reduce the corrosion speed by 40%.

Although hybrid nanofluids appear quite promising, their application in diesel engines remains restricted. The main challenges involve achieving cost-effectiveness, scalability, and reliable performance under diverse conditions. While extensive research has been done on nanofluids for thermal management, comprehensive comparative analyses of different hybrid nanofluid formulations specifically for cooling diesel engines are lacking. This review aims to bridge this gap by thoroughly evaluating different hybrid nanofluids, focusing on crucial performance metrics such as thermal conductivity, viscosity, dispersion stability, corrosion resistance, and cost-effectiveness. This review combines insights from previous research and theoretical perspectives to offer a thorough evaluation of the practicality and effectiveness of hybrid nanofluid cooling systems. It places special emphasis on the crucial role of surfactants in optimizing nanoparticle dispersion and enhancing thermophysical properties. Additionally, it scrutinizes the potential for large-scale implementation, cost limitations, and regulatory hurdles. The primary aim is to aid the future design of thermal management strategies by pinpointing the most efficient hybrid nanofluid formulations and resolving barriers to their application, thus fostering the development of more efficient, durable, and eco-friendly cooling systems for diesel engines. It should be noted that this review relies exclusively on previously published literature, unless indicated differently. All figures, tables, and quantitative data are taken from the literature with appropriate references, and any original visual content is specified. This work does not include any new experimental investigations. Primarily synthesizing existing research, this review also identifies key research gaps, particularly regarding long-term operational stability and large-scale applications, and proposes directions for future research in this dynamic field.

2. Nanofluids as an emerging solution

In recent years, nanofluids have emerged as a revolutionary innovation in thermal management systems, particularly for cooling engines. By incorporating nanoparticles into typical base fluids such as water, ethylene glycol, or oil,

these nanofluids offer considerably enhanced heat transfer properties due to the nanoparticles' high thermal conductivity [15]. This enhanced thermal efficiency leads to better temperature regulation, decreased thermal resistance, and improved cooling performance. Unlike traditional cooling fluids, nanofluids deliver greater stability, lower viscosity, and better convective heat transfer, making them ideal for high-performance engines, power plants, and a variety of industrial applications [9].

Nanofluids play a crucial role in boosting energy efficiency and promoting environmental sustainability. They manage this by enabling more efficient heat dispersal, reducing the overheating risk, and thereby extending the engine's operational life. Incorporating nanoparticles like aluminum oxide (Al_2O_3), copper oxide (CuO), and carbon-based compounds such as graphene enhances the coolant's thermal and flow properties. Despite persistent challenges related to nanoparticle dispersion, stability, and potential corrosion, ongoing advancements in nanotechnology are persistently addressing these concerns [28, 29]. As a result, nanofluids are being increasingly acknowledged as transformative components set to innovate cooling solutions in automotive and industrial contexts.

3. Composition of single and hybrid nanofluids with surfactants

3.1. Single nanoparticle-based nanofluids

To improve heat transfer characteristics, nanofluids consisting of a single type of nanoparticle are formulated by uniformly distributing these nanoparticles within a base fluid. Diverse research investigations have explored the efficacy of various nanoparticles, including metal oxides, pure metals, and carbon-based materials, for cooling applications (see Fig. 1). Nanofluids that combine metal oxides like alumina oxide-water (Al_2O_3-water) and copper oxide-water (CuO-water) exhibit significant enhancements in thermal conductivity, stability, and material compatibility, making them highly valuable for cooling engines [56]. Metal oxide nanoparticles including aluminum oxide (Al_2O_3), titanium dioxide (TiO_2), zinc oxide (ZnO), copper oxide (CuO), and iron oxide (Fe_3O_4) are widely utilized due to their remarkable stability, effective dispersion in water, and moderate rise in thermal conductivity. In contrast, pure metal nanoparticles like copper (Cu), silver (Ag), and gold (Au) offer outstanding thermal conductivity but tend to oxidize, which requires the application of surface treatments or surfactants to ensure stable dispersions. On the other hand, carbon-based nanoparticles, including carbon nanotubes (CNTs), graphene nanoplatelets (GNPs), and fullerenes, are noted for their outstanding thermal attributes due to high surface area and exceptional phonon transport, though their dispersion in polar solvents such as water presents a significant challenge [22, 24].

In single-component nanofluids, the typical nanoparticle concentration ranges from 0.1% to 5% by volume. Increasing this concentration can adversely affect viscosity, potentially increasing the need for pumping power and reducing coolant circulation efficiency. Thus, selecting nanoparticles demands an evaluation of the specific application requirements, the desired thermal performance, and their compatibility with existing cooling systems.

3.2. Hybrid nanoparticle-based nanofluids

Hybrid nanofluids utilize a combination of two or more distinct nanoparticles to synergistically improve thermal conductivity, stability, and viscosity management, thereby addressing the limitations of nanofluids based on a single type of nanoparticle [12]. These constraints encompass challenges such as sedimentation, heightened viscosity, and only moderate improvements in heat transfer. Commonly studied hybrid nanoparticle types include metal-metal oxide combinations (like Cu-Al_2O_3, Ag-TiO_2, CuO-ZnO), metal-

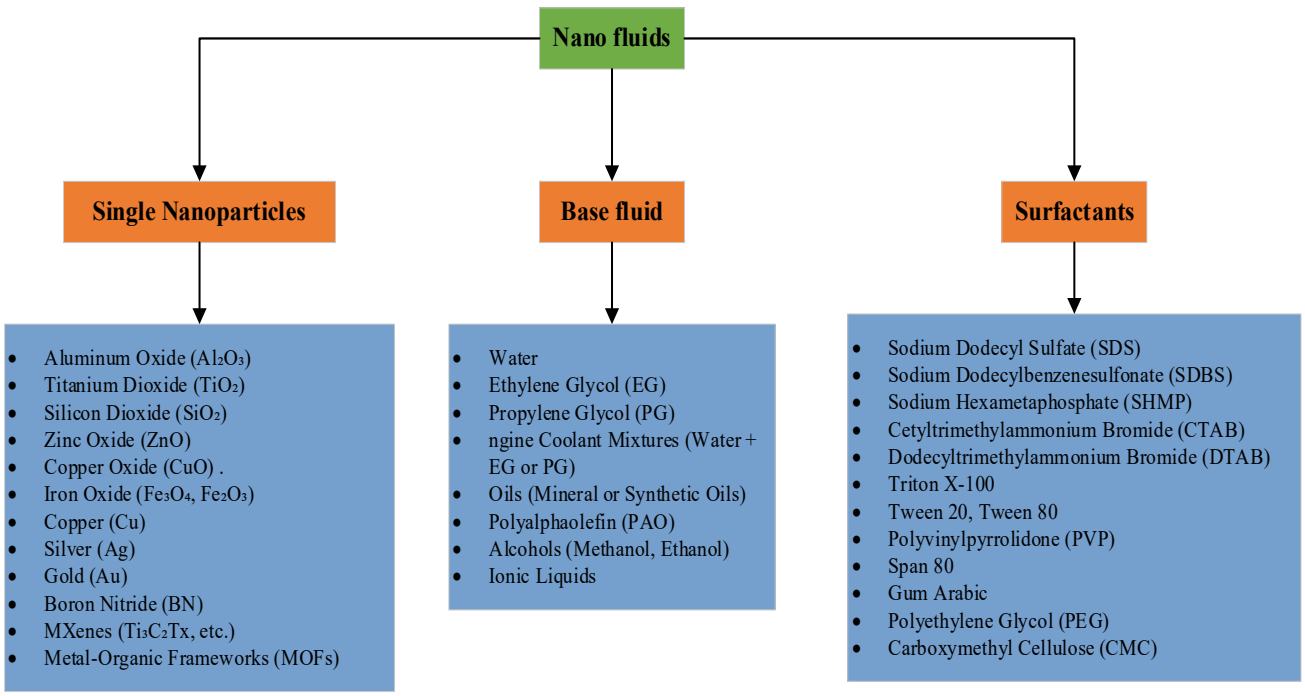

Fig. 1. Single nanoparticle-based nanofluids

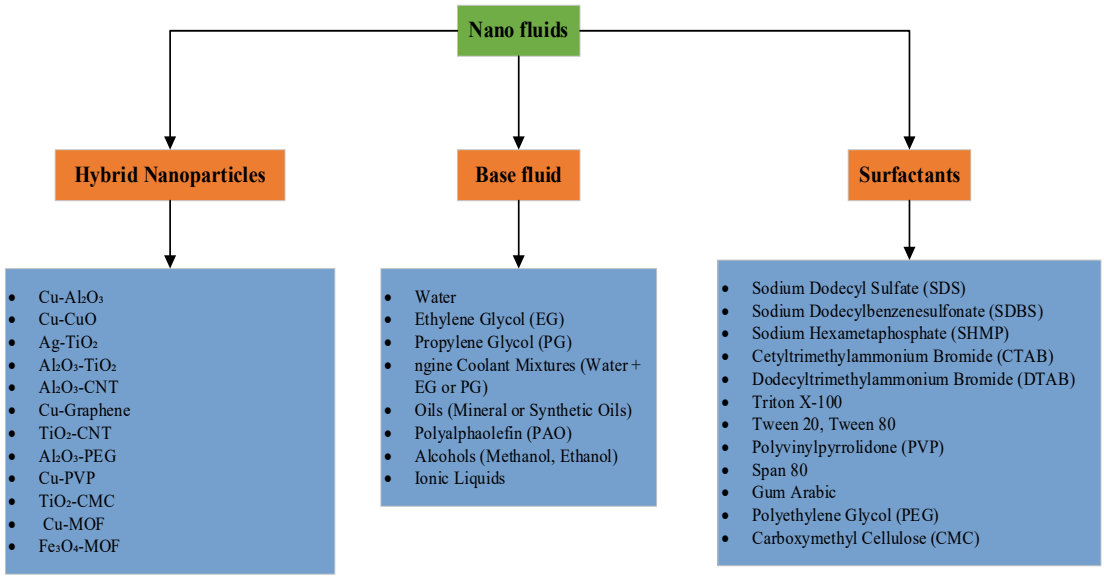

Fig. 2. Hybrid nanoparticle-based nanofluids. Studies have demonstrated that hybrid nanofluids exhibit higher thermal conductivity, improved stability, and reduced viscosity compared to single nanofluids. The enhanced properties result from the combination of high-conductivity materials with nanoparticles that provide improved dispersion and stability in the base fluid. However, the formulation of hybrid nanofluids requires precise control over nanoparticle ratios, dispersion techniques, and long-term stability considerations

carbon mixtures (such as Al_2O_3-CNT, Cu-Graphene, TiO_2-GNP), and metal-polymer blends (such as Al_2O_3-PEG, Cu-PVP) (Fig. 2) [18, 19]. Among these, hybrid nanofluids such as Al_2O_3-CuO and TiO_2-CNT show outstanding potential for engine cooling applications, thanks to their superior thermal conductivity, enhanced stability, and optimized viscosity [58]. Choosing nanoparticles suitable for hybrid nanofluids involves a careful assessment of thermal efficiency, fluid stability, and viscosity management.

3.3. Role of surfactants in nanofluid stability

One of the main challenges in manufacturing nanofluids is ensuring that nanoparticles remain uniformly distributed in the base liquid for prolonged durations. Nanoparticles often have a tendency to cluster because of attractive van der Waals forces, which can result in the formation of sediment, potential obstructions, and reduced thermal efficiency [42]. To address these challenges, surfactants – also known as dispersants or stabilizers – are used to alter the surface properties of nanoparticles, thus enhancing their interaction with the base fluid. Nonionic surfactants like polyvinylpyrrolidone (PVP) and Triton X-100 are especially effective in engine coolant applications. Notable characteristics include superior dispersion abilities, robust chemical resistance, and a minimal impact on the fluid's viscosity [71].

Surfactants can be grouped into four categories according to their charge: anionic, cationic, nonionic, and polymeric. Anionic surfactants, like sodium dodecyl sulfate (SDS), sodium dodecylbenzene sulfonate (SDBS), and sodium hexametaphosphate (SHMP), are notably efficient at stabilizing metal oxide nanoparticles such as Al_2O_3, TiO_2, and CuO in water-based solutions. In contrast, cationic surfactants like cetyltrimethylammonium bromide (CTAB) and dodecyl trimethylammonium bromide (DTAB) are used to stabilize carbon-based and metallic nanoparticles in nonpolar solvents. Nonionic surfactants like Triton X-100, Tween 20, Tween 80, PVP, and Span 80 are preferred because of their broad compatibility and limited interaction with coolant additives [17]. Moreover, polymeric dispersants like polyethylene glycol (PEG), carboxymethyl cellulose (CMC), and gum arabic significantly improve the long-term stability of nanoparticles by effectively inhibiting their agglomeration and sedimentation [26, 31].

To effectively stabilize nanoparticles while preventing significant fluid viscosity increases or thermal conductivity decreases, it is vital to maintain optimal surfactant concentrations, preferably ranging from 0.1 to 2% by weight. However, an excess of surfactants can lead to foaming, increased flow resistance, and compatibility issues with cooling system materials. Therefore, careful selection and adjustment of surfactant types and concentrations are necessary to guarantee the performance and reliability of nanofluids.

3.4. Optimization of nanofluid composition

The effectiveness of nanofluids is significantly influenced by the precise mix of nanoparticles, base fluid, and surfactants [32, 76]. To create efficient nanofluids suitable for engine cooling, it is crucial to enhance thermal conductivity, preserve stability, control viscosity, and verify compatibility with cooling systems. Research indicates that water-based nanofluids containing Al_2O_3, CuO, or hybrid combinations like Al_2O_3-CuO, stabilized with non-ionic surfactants such as PVP, are particularly well-suited for automotive engine use. These formulations exhibit excellent heat transfer performance, maintain stability over time, and have a negligible impact on viscosity [73]. Materials with high thermal conductivity, like copper (Cu), silver (Ag), and graphene, can greatly boost heat transfer but often require specific stabilization methods to prevent oxidation or clumping. The selection of suitable surfactants is essential for ensuring uniform dispersion and lasting stability. On the other hand, a high nanoparticle concentration or the choice of inappropriate surfactants may result in an

increase in viscosity, negatively impacting coolant flow and heat transfer effectiveness [59].

Recent studies indicate that well-optimized hybrid nanofluids, when combined with the right surfactants, can enhance thermal conductivity by 30% to 50% over traditional coolants, making them very appealing for modern engine cooling systems [39, 45]. Ongoing research is investigating functionalized nanoparticles, new dispersion techniques, and innovative surfactant formulations, which are anticipated to further advance nanofluid technology, providing effective and sustainable options for future automotive and industrial cooling applications.

4. Performance metrics and evaluation criteria

4.1. Effects of single nanofluid usage in engine cooling

The effectiveness of using both single and hybrid nanofluids to cool diesel engines is contingent on factors such as thermal conductivity, viscosity, stability, and compatibility with materials. Viscosity is crucial for defining the required pumping power and the flow characteristics of the nanofluids. While higher viscosity formulations might improve thermal conductivity, they typically lead to greater energy consumption. Hence, it is essential to maintain a balanced relationship among these factors. This review assesses nanofluid formulations according to five primary criteria: (1) enhancements in thermal conductivity, (2) impact on viscosity, (3) long-term stability, (4) potential for corrosion, and (5) economic feasibility. The improvement in thermal conductivity significantly boosts heat dissipation, resulting in a 30% to 50% increase over traditional coolants [60]. Hybrid nanofluids often outperform single-component formulations by striking an ideal balance between thermal efficiency and stability. Despite the advantages of higher thermal conductivity, controlling viscosity is essential to prevent unnecessary energy consumption. Increased viscosity demands more pumping power, which could undermine the advantages of enhanced thermal conductivity.

Optimal nanoparticle concentrations, generally between 0.1% and 1%, have been found to effectively balance heat transfer performance and fluid flow efficiency [73]. Moreover, stability is essential to avoid issues such as sedimentation and particle clumping. Nanoparticles like SiO_2 and TiO_2 show outstanding dispersion characteristics, and employing surfactants can further enhance uniformity. Instability can cause system blockages and inconsistent heat transfer, reducing cooling efficiency. The compatibility of materials is critical because nanoparticles such as CuO can significantly increase corrosion rates [50, 78]. Furthermore, nanoparticles such as CuO and Fe_3O_4 may exhibit corrosive behaviors, which could impact the long-term durability of engine components. While surfactants like sodium dodecyl sulfate (SDS) have the potential to form protective coatings that minimize corrosion, additional research is necessary to understand their prolonged effects on metals like copper and aluminum. Future investigations should implement standardized corrosion testing protocols utilizing copper and silver plates. Non-corrosive options like Al_2O_3 and SiO_2, together with protective coatings and passivation strategies, can reduce corrosion risks and maintain system integrity. Ensuring chemical stability is crucial for the ongoing use of both single and hybrid nanofluids in diesel engines.

Considerable attention has been focused on the use of various nanofluids in engine cooling systems, as they can enhance thermal management and increase engine performance. Figure 3 illustrates that integrating nanofluids into these systems can improve heat transfer, lower operational temperatures, and offer enhanced thermal stability. However, the efficacy of nanofluids is heavily contingent on the nanoparticle type utilized, as presented in Table 1. Nanoparticles like Al_2O_3 and TiO_2 are prized for their outstanding stability and resistance to corrosion, making them ideal for prolonged use in cooling systems [56]. Nanoparticles like CuO and Fe_3O_4 demonstrate impressive thermal conductivity, yet they also pose challenges such as increased viscosity and a greater risk of corrosion, which could damage engine components. On the other hand, carbon-based nanoparticles, including Multi-Walled Carbon Nanotubes (MWCNTs) and Graphene Nanoplatelets, are well-noted for their excellent thermal conductivity and have the potential to significantly boost cooling efficiency.

Despite this, practical application is hindered by challenges such as increased viscosity, instability, high costs, and the tendency of particles to agglomerate and settle, causing blockages and reducing cooling efficiency [2, 13, 46]. These challenges highlight the importance of meticulously choosing nanoparticles to meet distinct cooling demands. In engine cooling systems, economic considerations greatly influence the choice of nanoparticles. SiO_2 and ZnO nanoparticles present a cost-efficient blend of thermal performance, stability, and corrosion resistance, making them suitable for budget-conscious scenarios requiring dependable solutions.

Conversely, the financial burden and technical challenges associated with MWCNTs and Graphene Nanoplatelets limit their application in extensive industrial environments [13, 27]. Achieving an optimal equilibrium between cost and performance is essential for the advancement of effective nanofluid-based cooling systems.

Although promising, single nanofluids grapple with major adoption barriers due to a crucial compromise between thermal conductivity and viscosity. High viscosity linked with nanoparticles like MWCNTs and Graphene Nanoplatelets demands greater pumping power, which negatively affects fluid dynamics and overall system performance [16]. Stability presents another major issue, as nanoparticles such as CuO and Fe_3O_4 are prone to agglomeration and sedimentation, reducing the system's effectiveness over an extended period. Although Al_2O_3 and TiO_2 nanoparticles offer improved stability, their thermal conductivity is insufficient for optimal cooling performance. Moreover, addressing nanoparticle-induced corrosion requires either using corrosion inhibitors or opting for alternative nanoparticle materials [75]. Ensuring the longevity and functional effectiveness of nanofluid cooling systems necessitates systematic solutions to stability and corrosion problems. If not addressed, these challenges can compromise thermal efficiency and the longevity of engine components. In addition to these technical concerns, economic factors also pose a barrier to broad implementation. As detailed in Table 1, the steep price of advanced nanoparticles – like MWCNTs

and graphene nano-platelets – makes them untenable for widespread industrial deployment, especially in sectors sensitive to costs [1, 68]. High expenses also hinder the adoption of single nanofluids. The prohibitive costs of carbon-based nanoparticles, coupled with the moderate performance of cheaper alternatives like SiO_2 and ZnO, highlight the need for cost-effective solutions. Future studies should focus on improving the techniques for synthesizing and manufacturing nanoparticles to increase efficiency and maintain cost-effectiveness [7, 74].

While single-component nanofluids offer substantial promise for improving engine cooling, their real-world application is currently limited due to issues such as elevated viscosity, long-term instability, corrosion hazards, and costly materials. To achieve the ideal balance between thermal efficiency and system integration, it is essential to pursue novel approaches like developing hybrid nanofluids or implementing surface modification techniques. Future research should prioritize evaluating the longevity and effectiveness of nanofluids in real-world conditions to maintain reliability and material integrity. In Figure 1, the illustration and Table 1, the summary highlights the importance of carefully choosing and combining nanoparticles to maintain a balance between improved thermal capabilities and usability. Addressing these technical and economic hurdles is vital to fully unlocking the potential of nanofluid technology for modern engine cooling systems.

Table 1. Summary of single nanofluid effects (original synthesis based on data from [49, 43, 34, 66])

Nanoparticle	Thermal conductivity (W/m·K)	Viscosity effect	Stability	Corrosion effect	Density (kg/m³)	Cost	Overall rank	Author reference
Al_2O_3 (aluminum oxide)	✓ low (~30)	✓✓ Low	✓✓✓ Excellent	✓✓✓ Low	3970	✓✓✓ Cheap	☆☆☆ (3.6/5)	[43, 49]
CuO (copper oxide)	✓✓✓ High (~70)	✗ High	✓✓ Moderate	✗ Can corrode	6310	✗ Expensive	☆☆☆ (3.1/5)	[34, 66, 82]
TiO_2 (titanium dioxide)	✓ Moderate (~11)	✓✓ Low	✓✓✓ Excellent	✓✓✓ Very Low	4230	✓✓ Cheap	☆☆☆ (3.5/5)	[31, 60]
SiO_2 (silicon dioxide)	✓ Moderate (~1.4)	✓ Low	✓✓✓ Excellent	✓✓ Low	2650	✓✓✓ Very Cheap	☆☆☆ (3.7/5)	[36, 39, 57]
ZnO (zinc oxide)	✓✓ Moderate (~23)	✓✓ Low	✓✓✓ Good	✓✓ Low	5610	✓✓ Affordable	☆☆☆ (3.3/5)	[3, 72]
Fe_3O_4 (magnetite iron oxide)	✓✓ High (~80)	✗ High	✓ Moderate	✗ Corrosive	5180	✗ Expensive	☆☆☆ (3.1/5)	[35, 67]
MWCNT (multi-walled carbon nanotubes)	✓✓✓ Very High (~3000)	✗✗ Very High	✗ Poor	✓✓ Low	~1400	✗✗ Very Expensive	☆☆☆ (3.9/5)	[12, 13, 67]
Graphene nano-platelets	✓✓✓ Very High (~5000)	✗ High	✓✓ Moderate	✓ Low	~2200	✗ Expensive	☆☆☆☆ (4/5)	[9, 64]

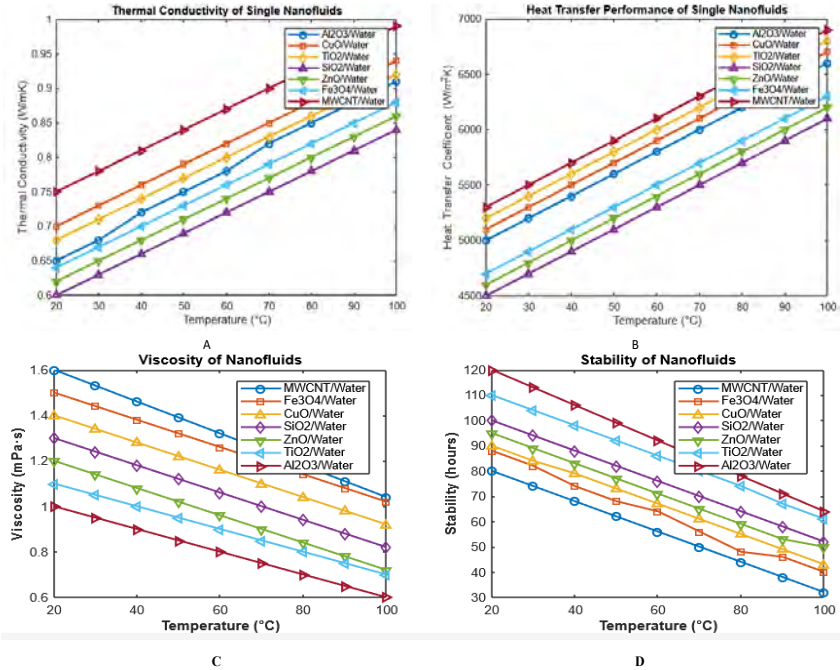

Fig. 3. Effects of single nanofluid usage (adapted with permission from [49]; experimental data from [43]

4.2. Effects of hybrid nanofluid usage in engine cooling

Hybrid nanofluids have recently captured attention for their exceptional ability to improve thermal management and enhance engine cooling system efficiency. Figure 4 demonstrates that these nanofluids possess superior heat transfer capabilities compared to conventional coolants, resulting in reduced operating temperatures and enhanced thermal stability [44, 48]. Table 2 illustrates that the effectiveness of these fluids greatly depends on the specific nanoparticle combinations used. As a result, selecting suitable hybrid formulations is crucial for improving cooling performance while maintaining a balance between efficiency, stability, and cost-effectiveness.

Hybrid nanofluids, specifically combinations of metals and metal oxides like Cu-Al_2O_3/water and Cu-TiO_2/water, show notable improvements in thermal conductivity from 30% to 40%, thereby enhancing heat transfer capability. Nonetheless, their moderate stability and increased viscosity may limit their feasibility for sustained application in engine cooling systems. Carbon-based hybrid nanofluids such as CNT-Al_2O_3/water and graphene-TiO_2/water provide significant enhancements in thermal conductivity, achieving improvements between 40% to 50%, and exhibit excellent heat transfer properties. However, their augmented viscosity and high production expenses restrict their widespread application [14, 51].

Hybrid nanofluids, despite their excellent thermal properties, still encounter practical challenges. For instance, metal-carbon hybrid nanofluids like Cu-CNT/water and Al_2O_3-graphene/water exhibit marked improvements in thermal conductivity (approximately 35% to 45%) and demonstrate remarkable stability with minimal corrosion risk, making them ideal for engine cooling systems. Despite these advantages, nanofluids often face issues such as moderate viscosity hikes and increased production costs compared to metal-metal oxide solutions [25, 53]. In contrast, metal-polymer hybrid nanofluids such as Al_2O_3-PVP/water and CuO-PVP/water generally show moderate enhancements in thermal conductivity, typically between 20% and 30%. These combinations are particularly efficient in providing stability, managing viscosity, and resisting corrosion. Their strong economic feasibility and durability make them particularly appealing for applications where it is essential to sustain cost-effectiveness and long-lasting functionality.

To select appropriate hybrid nanofluids for engine cooling, one must consider both their effectiveness and costs. Hybrid nanofluids incorporating rare-earth elements, such as CeO_2-TiO_2/water and CeO_2-CuO/water, provide a moderate boost in thermal conductivity, ranging from 20% to 30%, and show excellent stability. However, their high price and relatively limited heat transfer efficiency, particularly when contrasted with carbon-based or metal-carbon nanofluids, hinder their extensive application [51]. Thus, achieving a balance between thermal performance and economic feasibility is vital. While nanofluids based on carbon and metal-carbon hybrids offer exceptionally high thermal conductivity, they also increase viscosity, require more pumping power, and reduce flow efficiency, complicating their use in high-performance engine cooling systems. It is essential to develop innovative methods to lower viscosity without compromising thermal characteristics. Moreover, stability challenges pose considerable difficulties, particularly for carbon-based nanofluids that have a tendency to aggregate and settle, which can result in blockages and decrease the effectiveness of cooling systems. While metal-polymer and rare-earth metal nanofluids offer improved stability, corrosion issues continue to be a significant concern for both metal-metal oxide and carbon-based nanofluids, potentially damaging engine components over an extended period [4, 55]. Employing corrosion inhibitors or substituting materials can mitigate these issues, although these measures might increase costs and complicate implementation.

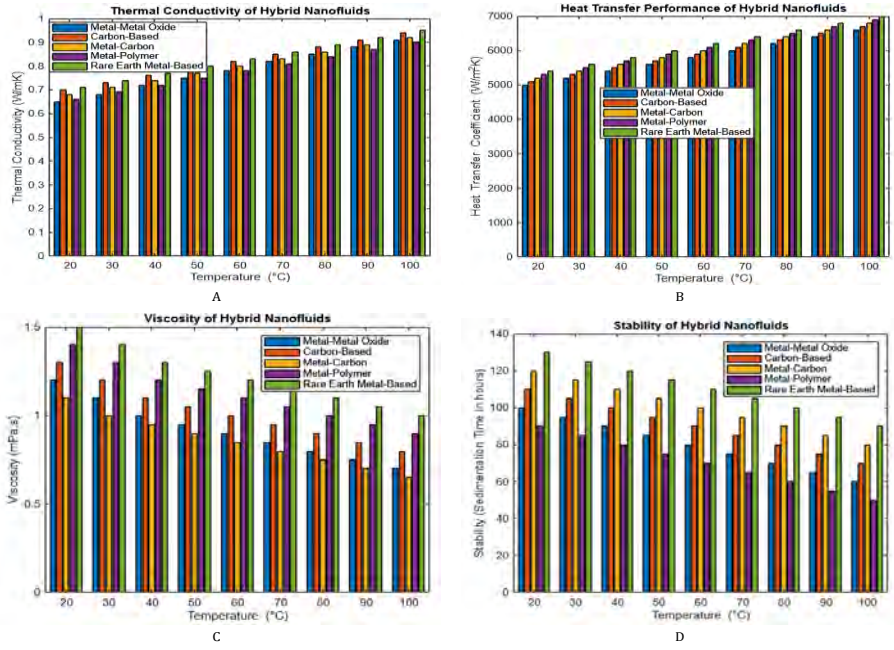

Fig. 4. Hybrid nanofluid performance (original visualization based on [21, 31, 47])

Table 2. Hybrid nanofluid effects [24, 68, 69]

Type	Composition	Thermal conductivity enhancement	Heat transfer performance	Stability	Viscosity increase	Corrosion effects	Cost	Overall rank	Reference
Metal-metal oxide	Cu-Al_2O_3/Water, Cu-TiO_2/Water	✔✔✔ High (30–40%)	✔✔ very good	✔ Moderate	✔ Moderate	✔✔ Low-Moderate	✔✔ Affordable	☆☆☆ (3.5/5)	[24, 32, 49]
Carbon-based	CNT-Al_2O_3/Water, Graphene-TiO_2/Water	✔✔✔ Very High (40–50%)	✔✔✔ Superior	✔✔ Low-Moderate	✕ High	✔✔ Moderate	✕ Expensive	☆☆☆☆ (4/5)	[12, 83]
Metal-carbon	Cu-CNT/Water, Al_2O_3-Graphene/Water	✔✔✔ High (35–45%)	✔✔✔ Excellent	✔✔✔ Excellent	✔ Moderate	✔✔✔ Low	✔✔ Affordable	☆☆☆☆ (4.2/5)	[24, 70, 72]
Metal-polymer	Al_2O_3-PVP/Water, CuO-PVP/Water	✔✔ Moderate (20–30%)	✔ Good	✔✔✔ Excellent	✔✔ Low	✔✔✔ Low	✔✔✔ Cheap	☆☆☆☆ (4/5)	[5, 68]
Rare earth metal-based	CeO_2-TiO_2/Water, CeO_2-CuO/Water	✔✔ Moderate (20–30%)	✔ Good	✔✔✔ Excellent	✔✔ Low	✔✔✔ Very Low	✕ Expensive	☆☆☆ (3.2/5)	[44, 75, 81]

The expense significantly hinders the broad adoption of hybrid nanofluids for engine cooling purposes. As shown in Table 2, although carbon-based and rare-earth metal-based hybrid nanofluids exhibit exceptional thermal properties, their high production costs severely restrict their commercial scalability. Conversely, metal-metal oxide and metal-polymer hybrid nanofluids offer a cheaper alternative. However, their relatively moderate thermal conductivity might restrict their efficiency in demanding cooling scenarios [35, 61]. This highlights the urgent need for innovative, cost-efficient formulations that provide enhanced thermal conductivity while ensuring long-term stability and affordability.

In essence, while hybrid nanofluids present significant potential to enhance the effectiveness of engine cooling systems, their real-world application is hindered by factors such as increased viscosity, difficulties maintaining dispersion stability, corrosion concerns, and substantial costs. Figure 2 illustrates, and Table 2 elaborates, that the deliberate selection and formulation of hybrid nanofluids play a pivotal role in aligning thermal performance with practical application. Upcoming research endeavors should prioritize creating novel hybrid nanofluids that heighten thermal conductivity, improve dispersion stability, and reduce viscosity, all at an economical cost. Achieving this equilibrium is crucial for the broad adoption of hybrid nanofluids in engine cooling, promoting advancements in efficient, long-lasting, and reliable thermal management systems within the automotive sector.

4.3. The effect of hybrid nanofluids with surfactants for engine cooling systems

Integrating surfactants into hybrid nanofluids holds substantial promise for improving their efficiency in engine cooling applications. As illustrated in Fig. 5, surfactants like Sodium Dodecyl Sulfate (SDS) play a crucial role in improving the dispersion and stability of nanoparticles, thereby enhancing both their thermal and fluid dynamic properties [20, 64]. Table 3 compares hybrid nanofluids, distinguishing between those incorporating surfactants and those without, and underscores the notable benefits linked to surfactant usage. Hybrid nanofluids without surfactants generally demonstrate high thermal conductivity; however, they often face issues with particle agglomeration, which diminishes their overall effectiveness [57, 62]. In contrast, the addition of 1% SDS surfactant enhances thermal conductivity by roughly 2–5% due to better nanoparticle dispersion and minimized agglomeration. Although the improvement is moderate, it significantly boosts heat transfer efficiency in engine cooling applications.

One significant advantage of employing surfactants lies in their ability to decrease viscosity, which is crucial for evaluating engine cooling performance. Typically, in the absence of surfactants, hybrid nanofluids present higher viscosity, leading to increased demands for pump power and reduced fluid flow effectiveness. Nevertheless, adding 1% SDS surfactant can reduce viscosity by about 10–15% by promoting particle dispersion and decreasing interparticle friction [63]. A reduction in viscosity translates to lower energy requirements for pumping and enhanced fluid dynamics, leading to more streamlined flow conditions and a pressure drop reduction of about 5–10%, thereby enhancing the cooling system's performance [47].

The addition of surfactants significantly increases the duration of stability in hybrid nanofluids. In the absence of surfactants, these nanofluids are prone to settling over time, potentially leading to blockages and decreased thermal effectiveness. Table 3 shows that incorporating 1% SDS surfactant plays a crucial role in sustaining long-term dispersion stability, thus avoiding particle clustering and settling. Enhancing stability is crucial for engine cooling systems as it ensures reliable and steady performance over extended durations. Moreover, surfactants like SDS can help reduce corrosion by creating protective coatings on metal surfaces, thereby curbing oxidation and extending the life of engine components.

Surfactants provide notable advantages when used in hybrid nanofluids; however, they also introduce some challenges. These agents can lead to extra chemical interactions that might influence the fluid's long-term performance. Therefore, it is crucial to regulate surfactant concentrations carefully, as excessive amounts can cause issues such as

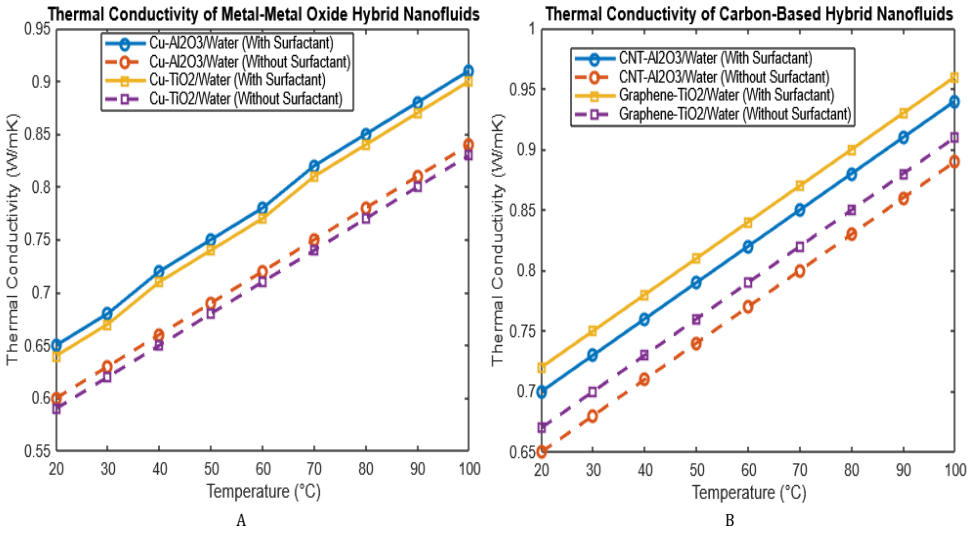

Fig. 5. The effect of hybrid nanofluids with and without surfactants for engine cooling systems [35, 47, 62]

Table 3. Summery the effect of hybrid nanofluids with and without surfactants for engine cooling systems [38, 48, 68, 71]

Property	Effect without surfactant	Effect with 1% sds surfactant	Reference
Thermal Conductivity	High, but particle agglomeration may reduce performance.	Slightly improved (~2-5%) due to better dispersion.	[38, 71]
Viscosity	High, causing higher pump power consumption.	Reduced (~10-15%) due to better particle spacing.	[48, 68]
Stability	Moderate risk of sedimentation over time.	Highly stable (long-term dispersion).	[54, 59]
Corrosion Risk	Low	Even lower, as SDS prevents oxidation.	[22, 59]
Pressure Drop	Slightly high due to viscosity.	Reduced (~5-10%) due to smoother flow.	[24, 69]

foaming. Despite these concerns, surfactants are vital for improving thermal conductivity, lowering viscosity, increasing stability, and reducing corrosion risks, demonstrating their effectiveness in hybrid nanofluids for engine cooling [36, 67].The integration of surfactants into hybrid nanofluids enhances thermal performance, fluid dynamics, and stability, as demonstrated in Figure 5 and Table 3. Surfactants like SDS are vital in addressing the key challenges tied to hybrid nanofluids, enhancing their efficiency in engine cooling applications. Future studies should focus on fine-tuning surfactant concentrations and investigating different surfactant varieties to bolster the performance and reliability of hybrid nanofluids in real-world cooling situations.

4.4. Improvements with surfactant addition in hybrid nanofluids

Hybrid nanofluids, formed by dispersing distinct nanoparticles into a base fluid, provide promising advancements for improving heat transfer in numerous applications, especially in heavy-duty diesel engines. Studies highlighted in [52, 69] involving truck engines demonstrated that CuO-Al_2O_3 hybrid nanofluids could reduce operating temperatures by approximately 7–10°C. The main factor behind this reduction is CuO's superior thermal conductivity, which enables rapid heat release, thereby decreasing fuel consumption and emissions. While this is advantageous, CuO nanoparticles pose a corrosion risk that necessitates the use of anti-corrosion additives, thereby adding to the complexity and expense of maintenance. Moreover, achieving long-term stability presents a challenge; however, surfactants mitigate this by lowering the surface tension between the nanoparticles and the base fluid, promoting even distribution and preserving consistent thermal properties over time. Hence, selecting appropriate nanoparticles and surfactants is critical for maximizing heat transfer efficiency, improving system compatibility, and ensuring ongoing stability [70].

The automotive sector is not just focusing on the applications of heavy-duty engines but is also investigating the use of hybrid nanofluids to improve thermal management in high-performance and electric vehicles. Ensuring ideal thermal conditions is crucial for the lifespan of batteries and the system's overall efficiency in electric vehicles. Studies reveal that hybrid nanofluids effectively reduce battery temperatures, thereby decreasing the risk of thermal runaway and boosting energy efficiency [21, 72]. For high-performance internal combustion engines, improved heat dissipation enhances both efficiency and durability. Car manufacturers are extensively testing hybrid nanofluids; however, their broad adoption is limited due to cost and scalability issues [77, 80]. Currently, the complex and costly processes involved in producing and distributing nanoparticles impede their accessibility in the mass market. Furthermore, challenges related to standardization and regulatory compliance also impede their large-scale commercial application.

An evaluation of the compositions of hybrid nanofluids, as depicted in Fig. 6 and Table 4, highlights the interaction among thermal conductivity, viscosity, stability, corrosion, and cost factors. For example, a mixture consisting of Al_2O_3, SiO_2, TiO_2, and SDS in water showcases both superior stability and controllable viscosity, with a considerable increase in thermal conductivity ranging from 20% to 30%

[77, 81]. SDS is crucial for ensuring stability by preventing particles from clumping together. In contrast, although incorporating MWCNTs with Al_2O_3 boosts thermal conductivity by 35–50%, this combination leads to notable downsides, including extremely high viscosity and insufficient stability due to poor dispersion. Similarly, CuO-based nanofluids provide excellent thermal conductivity but carry a moderate corrosion risk. The cost variability across formulations, notably the higher expense of MWCNT-based fluids, underscores the need for comprehensive design strategies that integrate performance, cost, and reliability, including surfactant use for stability. Although hybrid nanofluids show considerable promise for experimental and practical applications in engine cooling, their widespread adoption is hindered by challenges related to economic feasibility, scalability, and stability [26, 58]. Future research should aim to reduce nanoparticle production costs, enhance stabilization methods, and conduct thorough evaluations of long-term durability. Advancements in nanotechnology, manufacturing processes, and regulatory frameworks can enhance the adoption of hybrid nanofluids for engine cooling, thereby improving efficiency, reducing emissions, and extending engine life [15, 49].

Figure 6c demonstrates the impact of different formulations on viscosity properties, based on experimental findings. The displayed values relate to the dynamic viscosity, an important factor in evaluating water-based nanofluids for use in engine cooling systems. These viscosity changes highlight relative differences under laboratory settings, using the viscosity of water at 25°C as a reference point. It is crucial to note that this study does not take into account the variations in water viscosity across temperatures between 20°C and 80°C. Subsequent research should include these temperature-induced changes to facilitate more precise analyses of viscosity variations with temperature. While the rise in viscosity might seem significant, it is relatively modest when compared to the much higher viscosities of standard engine or transmission oils, which far exceed that of water. Therefore, the findings have been characterized as indicating a "moderate increase in viscosity."

Figure 6 and Table 4 highlight the essential importance of surfactants in enhancing the performance of hybrid nanofluids. Surfactants are essential in improving nanoparticle dispersion and stability, resulting in enhanced thermal conductivity and more efficient heat transfer. Therefore, they are crucial for the optimal performance of hybrid nanofluids in engine cooling systems. Among the evaluated formulations, the Al_2O_3 + SiO_2 + TiO_2 hybrid nanofluid stands out for its well-rounded performance, demonstrating exceptional stability, moderate viscosity, and significant enhancements in thermal conductivity. In contrast, while CuO-based hybrid nanofluids exhibit outstanding heat transfer capabilities, they often have higher viscosity and a tendency to cause corrosion, which might limit their practical applications. These findings emphasize the necessity of careful nanoparticle selection to maximize benefits while minimizing drawbacks.

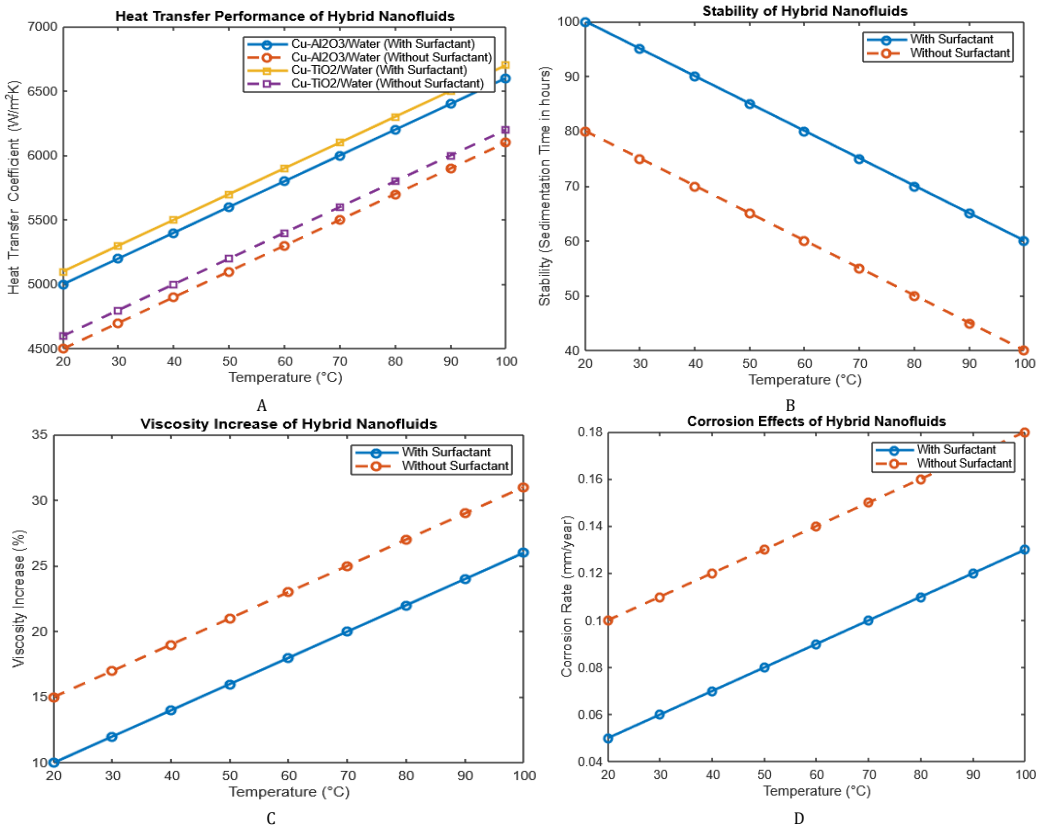

Fig. 6. Viscosity increase (%) of hybrid nanofluids relative to water at 25°C (dynamic viscosity; ASTM D445). Heat transfer coefficient and stability data are derived from [59, 62, 68]. Water's viscosity trend (dotted line) is included for reference (data from [60]). Note: Viscosity values represent percentage change based on literature-reported experimental data. Under general physical principles, viscosity typically decreases with temperature; the values shown reflect formulation-specific behaviors

Table 4. Summary improvements with surfactant addition in hybrid nanofluids

Nanoparticle composition	Base fluid	Fraction [%]	Thermal conductivity [W/m·K]	TC improvement [%]	Viscosity effect	Stability	Corrosion effect	Cost	Overall rank
Al_2O_3 + SiO_2 + TiO_2 + SDS	Water	49.5% Al_2O_3 + 29.7% SiO_2 + 19.8% TiO_2 + 1% SDS	0.7–1.2	~20–30%	⚠ Medium	☑ Excellent	☑ Low	§§	1st 🏆
CuO + Al_2O_3 + TiO_2 + SDS	Water	40% Al_2O_3 + 30% TiO_2 + 29% CuO + 1% SDS	1.2–2.0	~30–40%	✕ High	⚠ Medium	⚠ Medium (CuO may accelerate corrosion)	§§§	2nd 🥈
Al_2O_3 + SiO_2 + CuO + SDS	Water	40% Al_2O_3 + 30% SiO_2 + 29% CuO + 1% SDS	1.0–1.8	~25–35%	⚠ Medium	☑ Good	⚠ Medium	§§	3rd 🥉
MWCNT + Al_2O_3 + SDS	Water	50% MWCNT + 49% Al_2O_3 + 1% SDS	2.0–3.5	~35–50%	✕ Very high (causes flow issues)	✕ Low (difficult to disperse)	⚠ Medium	§§§§§	5th
TiO_2 + SiO_2 + SDS	Water	50% TiO_2 + 49% SiO_2 + 1% SDS	0.6–1.1	~15–25%	☑ Low	☑ Excellent	☑ Low	§	4th

Critical factors for the widespread implementation of hybrid nanofluids in industry include cost-effectiveness, meeting regulatory requirements, and their practicality in real-world settings. Despite being currently cost-effective for certain niche applications, the broader use of high-performance hybrid nanofluids relies on developing synthesis methods that are both affordable and scalable. Assessing the long-term environmental effects of nanoparticle-based coolants is essential to meet the ever-tightening regulatory standards. Despite certain challenges, initial tests by automotive manufacturers, especially in high-performance and electric vehicles, highlight the practical advantages and viability of hybrid nanofluids. These experiments provide vital insights that can guide future development and integration strategies. By tackling both practical and regulatory challenges, hybrid nanofluids hold the potential to greatly enhance advanced thermal management technologies, boost engine efficiency, and support more sustainable automotive solutions.

5. Challenges and future research directions

5.1. Economic feasibility

Although hybrid nanofluids present significant benefits compared to traditional coolants, they still face numerous technical, economic, and practical hurdles. To enhance the adoption of hybrid nanofluids in cooling systems for diesel engines, these challenges need to be addressed. Key issues involve cost-effectiveness, scaling for large applications, and sustained reliability, all of which are vital for moving these advanced coolants from research environments to industrial and commercial use.

The significant cost poses a primary barrier to the extensive commercial use of hybrid nanofluids. The processes required for producing, distributing, and stabilizing nanoparticles involve sophisticated techniques, which render these fluids substantially more expensive than traditional coolants. Moreover, the cost is increased due to the elevated prices of raw materials such as copper oxide (CuO), multi-walled carbon nanotubes (MWCNTs), and graphene-based nanoparticles. Also, using methods like ultrasonication, surfactants, or chemical treatments to ensure stable nanoparticle dispersions further escalates the processing costs. While hybrid nanofluids offer superior thermal efficiency, their high price limits market attractiveness, particularly in cost-sensitive sectors like the commercial automotive industry. Subsequent research should aim to develop cost-effective synthesis strategies and scalable production methods, which maintain high performance levels while minimizing overall expenses.

5.2. Large-scale implementation challenges

The shift of hybrid nanofluids from initial research phases to extensive application in industrial and automotive fields faces considerable challenges. Key concerns include maintaining uniformity in production processes and optimizing supply chain logistics, especially for the large-scale manufacturing and distribution of nanoparticles. Additionally, ensuring compatibility with current cooling systems makes broad adoption difficult, as it is essential to thoroughly assess how hybrid nanofluids interact with cooling system components like radiators, hoses, pumps, and engine materials to avoid potential system damage. Furthermore, the lack of standardized testing methods and industry regulations hinders commercial uptake. To address these implementation hurdles, establishing detailed regulatory frameworks and industry-standard compliance guidelines will be crucial.

5.3. Long-term reliability and stability

To ensure effective practical uses, the long-term reliability and stability of hybrid nanofluids must be preserved. Challenges like sedimentation and phase separation are critical since nanoparticles may settle over time, reducing the efficiency of the coolant. Additionally, nanoparticles such as CuO and Fe_3O_4 can cause corrosion and degradation in cooling system components, thereby shortening their lifespan. It is also vital to assess thermal and chemical stability thoroughly, including tests under various temperature cycles, extensive usage, and potential contaminant exposure. Addressing these issues requires future research to concentrate on advanced stabilizers and surfactants that enhance nanoparticle dispersion and reduce sedimentation. Corrosion-resistant formulas need to be developed and rigorously tested in the field and in collaboration with industry to ensure their durability and suitability for maintenance in practical scenarios.

5.4. Future research directions

Hybrid nanofluids hold great potential for improving cooling in diesel engines, as they offer advancements in thermal conductivity, stability, and heat transfer characteristics. Comparative analyses indicate that hybrid mixes such as Al_2O_3 + SiO_2 + TiO_2 achieve a well-rounded performance, whereas CuO-based hybrids excel in thermal conductivity but also present greater challenges with viscosity and corrosion concerns. Therefore, hybrid nanofluids are acknowledged as innovative solutions for reducing engine temperatures, enhancing fuel economy, and minimizing environmental effects. However, their successful implementation requires addressing substantial challenges related to cost, scalability, and maintaining consistent reliability. Future investigations ought to focus on devising cost-effective production methods, undertaking extensive field research, and formulating regulatory frameworks to support market entry. Technological advancements coupled with targeted research are expected to enable hybrid nanofluids to improve thermal management systems within the automotive and industrial fields, leading to more efficient, durable, and environmentally friendly cooling solutions.

6. Conclusion

Hybrid nanofluids mark a notable advancement in enhancing the thermal performance of diesel engines, providing improved heat transfer, heightened stability, and ideal viscosity compared to both conventional coolants and single-component nanofluids. By meticulously combining different nanoparticles, hybrid mixtures enhance thermal conductivity, addressing issues like nanoparticle sedimentation, excessive viscosity, and material incompatibility. Surfactants are crucial, aiding in nanoparticle dispersion, minimizing agglomeration, and decreasing viscosity for better performance and lasting stability. This review highlights:

- Enhanced heat transfer compared to standard fluids
- Boosted dispersion stability by using nanoparticle combinations and surfactants
- Optimized viscosity reduces pumping demands and energy usage
- Effective corrosion prevention through proper nanoparticle and surfactant selection
- Environmental and fuel efficiency improvements due to effective cooling and minimized emissions
- The critical role of surfactants like Sodium Dodecyl Sulfate (SDS) in improving nanofluid attributes
- The continuous challenges faced in introducing products to the market include manufacturing costs, industry certification, and adherence to regulatory requirements
- Suggested future research focuses on cost reduction, durability tests, and the integration of advanced cooling technologies.

Although there are considerable benefits, challenges regarding economic feasibility, scale of implementation, and reliability remain, demanding more research into nanoparticle synthesis, better dispersion techniques, and rigorous durability testing. Moreover, it is crucial to examine regulatory factors and industrial tactics to transform laboratory accomplishments into viable, marketable innovations. Recent advancements indicate that hybrid nanofluids could significantly transform thermal management in a range of applications, including diesel engines.

Bibliography

[1] Abidi A, Sajadi SM. Numerical assessment of hydraulic behavior and thermal efficiency of multiphase hybrid nanofluid in a shell-and-tube heat exchanger with inclined baffles. Eng Anal Bound Elem. 2023;156:114-125. https://doi.org/10.1016/j.enganabound.2023.08.002

[2] Al-Hotmani OMA, Al-Obaidi MA, John YM, Patel R, Manenti F, Mujtaba IM. Minimisation of energy consumption via optimisation of a simple hybrid system of multi effect distillation and permeate reprocessing reverse osmosis processes for seawater desalination. Comput Chem Eng. 2021;148:107261. https://doi.org/10.1016/j.compchemeng.2021.107261

[3] Ali M, El-Leathy AM, Al-Sofyany Z. The effect of nanofluid concentration on the cooling system of vehicles radiator. Adv Mech Eng. 2014;2014:1-13. https://doi.org/10.1155/2014/962510

[4] Alklaibi AM, Sundar LS, Chandra Mouli KVV. Experimental investigation on the performance of hybrid Fe_3O_4 coated MWCNT/water nanofluid as a coolant of a plate heat exchanger. Int J Therm Sci. 2022;171:107249. https://doi.org/10.1016/j.ijthermalsci.2021.107249

[5] Allahyar HR, Hormozi F, Zarenezhad B. Experimental investigation on the thermal performance of a coiled heat exchanger using a new hybrid nanofluid. Exp Therm Fluid Sci. 2016;76:324-329. https://doi.org/10.1016/j.expthermflusci.2016.03.027

[6] Al-Obaidi MA, Rashid FL, Rasheed MK, Aljibori HSS, Mohammed HI, Mahdi AJ et al. Recent achievements in heat transfer enhancement with hybrid nanofluid in heat exchangers: a comprehensive review. Int J Thermophys. 2024;45:133. https://doi.org/10.1007/s10765-024-03428-x

[7] Alqarni MM, Ibrahim M, Assiri TA, Saeed T, Mousa AAA, Ali V. Two-phase simulation of a shell and tube heat exchanger filled with hybrid nanofluid. Eng Anal Bound Elem. 2023;146:80-88. https://doi.org/10.1016/j.enganabound.2022.10.001

[8] Amira N, Waini I, Safwa N, Rahman A, Kasim M, Naganthran K et al. Stagnation point hybrid nanofluid flow past a stretching/shrinking sheet driven by Arrhenius kinetics and radiation effect. Alexandria Engineering Journal. 2023;68:29-38. https://doi.org/10.1016/j.aej.2023.01.005

[9] Anitha S, Pichumani M. Numerical analysis on heat transfer performance of industrial double-tube heat exchanger using CNT: Newtonian/non-Newtonian hybrid nanofluids. J Therm Anal Calorim. 2022;147:9603-9624. https://doi.org/10.1007/s10973-022-11249-z

[10] Anoh KOO, Mapoka TT, Abd-Alhameed RAA, Ochonogor O, Jones SMR. On the Application of Raised-Cosine Wavelets for Multicarrier Systems Design. International Journal on Communications Antenna and Propagation (IRECAP) [Internet]. 2014 Aug 31;4(4):143. https://doi.org/10.15866/irecap.v4i4.2455

[11] Arasu CPAV. Effect of dispersing single and hybrid nanoparticles on tribological, thermo physical, and stability characteristics of lubricants: a review. J Therm Anal Calorim. 2021;143:1773-1809. https://doi.org/10.1007/s10973-020-09837-y

[12] Asokan N, Gunnasegaran P, Vicki V. Experimental investigation on the thermal performance of compact heat exchanger and the rheological properties of low concentration mono and hybrid nanofluids containing Al_2O_3 and CuO nanoparticles. Thermal Science and Engineering Progress. 2020;20:100727. https://doi.org/10.1016/j.tsep.2020.100727

[13] Bahiraei M, Kok Foong L, Hosseini S, Mazaheri N. Neural network combined with nature-inspired algorithms to estimate overall heat transfer coefficient of a ribbed triple-tube heat exchanger operating with a hybrid nanofluid. Measurement. 2021;174:108967. https://doi.org/10.1016/j.measurement.2021.108967

[14] Basem A, Alhuyi Nazari M, Mehrabi A, Ahmadi MH, Atamurotov F. Effect of applying serpentine channels and hybrid nanofluid for thermal management of photovoltaic cell: numerical simulation, ANN and sensitivity analysis. Renew Energy. 2024;232:121077. https://doi.org/10.1016/j.renene.2024.121077

[15] Basha JS, Al Balushi M, Soudagar MEM, Safaei MR, Mujtaba MA, Khan TMY et al. Applications of nano-additives in internal combustion engines: a critical review. J Therm Anal Calorim 2022;147:9383-9403. https://doi.org/10.1007/s10973-022-11199-6

[16] Basir H, Hosseini SA, Nasrollahnezhad S, Jahangiri A, Rosen MA. Investigation of engine's thermal management based on the characteristics of a map-controlled thermostat. Int Commun Heat Mass. 2022;135:106156. https://doi.org/10.1016/j.icheatmasstransfer.2022.106156

[17] Bhattad A, Atgur V, Rao BN, Banapurmath NR, Khan TMY, Vadlamudi C et al. Review on mono and hybrid nanofluids: preparation, properties, investigation, and applications in IC Engines and heat transfer. Energies. 2023;16(7):3189. https://doi.org/10.3390/en16073189

[18] Çetin I, Sezici E, Karabulut M. A comprehensive review of battery thermal management systems for electric vehicles. P I Mech Eng E-J Pro. 2023;237:989-1004. https://doi.org/10.1177/09544089221123975

[19] Daungthongsuk W, Wongwises S. A critical review of convective heat transfer of nanofluids. Renew Sust Energ Rev. 2007;11:797-817. https://doi.org/10.1016/j.rser.2005.06.005

[20] Dilbaz F, Selimefendigil F, Öztop HF. Comparisons of different cooling systems for thermal management of lithium-ion battery packs: phase change material, nano-enhanced channel cooling and hybrid method. J Energy Storage. 2024;90:111865. https://doi.org/10.1016/j.est.2024.111865

[21] Dinarvand S, Abbasi A, Gharsi S. A review of the applications of nano fluids and related hybrid variants in flat tube car radiators. Fluid Dyn Mater Proc. 2025;21(1):37-60. https://doi.org/10.32604/fdmp.2024.057545

[22] Eastman JA, Choi SUS, Li S, Yu W, Thompson LJ. Anomalously increased effective thermal conductivities of ethylene glycol-based nanofluids containing copper nanoparticles. Appl Phys Lett. 2001;78:718-720. https://doi.org/10.1063/1.1341218

[23] Eftekhar M, Keshavarz A, Ghasemian A, Mahdavinia J. The impact of nano-fluid concentration used as an engine coolant on the warm-up timing. Automotive Science and Engineering. 2013;3(1):356-367. https://sid.ir/paper/321754/en

[24] Elahi M, Soudagar M, Nik-ghazali N, Kalam A, Badruddin IA, Banapurmath NR et al. The effect of nano-additives in diesel-biodiesel fuel blends: A comprehensive review on stability, engine performance and emission characteristics. Energy Convers Manage. 2018;178:146-177. https://doi.org/10.1016/j.enconman.2018.10.019

[25] Elsaid AM, El-Said EMS, Abdelaziz GB, Sharshir SW, El-Tahan HR, Raboo MFA. Performance and exergy analysis of different perforated rib designs of triple tubes heat exchanger employing hybrid nanofluids. Int J Therm Sci. 2021;168:107006. https://doi.org/10.1016/j.ijthermalsci.2021.107006

[26] Ettefaghi E, Ahmadi H, Rashidi A, Nouralishahi A, Saeid S. Preparation and thermal properties of oil-based nano fl uid from multi-walled carbon nanotubes and engine oil as nano-lubricant. Int Commun Heat Mass. 2013;46:142-147. https://doi.org/10.1016/j.icheatmasstransfer.2013.05.003

[27] Fazeli I, Sarmasti Emami MR, Rashidi A. Investigation and optimization of the behavior of heat transfer and flow of MWCNT-CuO hybrid nanofluid in a brazed plate heat exchanger using response surface methodology. Int Commun Heat Mass. 2021;122:105175. https://doi.org/10.1016/j.icheatmasstransfer.2021.105175

[28] Girhe N, Botewad S, Pawar P, Kadam A. Development of water-based CuO/GO/MWCNT ternary nanofluid and comparative study of thermal conductivity and viscosity with CuO, GO, MWCNTs mono nanofluids. Indian J Phys. 2023;97:1137-1145. https://doi.org/10.1007/s12648-022-02487-w

[29] Hajatzadeh A, Aghakhani S, Afrand M, Mahmoudi B. An updated review on application of nano fluids in heat exchangers for saving energy. Energy Convers Manag. 2019;198:111886. https://doi.org/10.1016/j.enconman.2019.111886

[30] Hamza NFA, Aljabair S. Heliyon Evaluation of thermal performance factor by hybrid nanofluid and twisted tape inserts in heat exchanger. Heliyon. 2022;8:e11950. https://doi.org/10.1016/j.heliyon.2022.e11950

[31] Hashemi SM. An empirical study on heat transfer and pressure drop characteristics of CuO – base oil nano fluid flow in a horizontal helically coiled tube under constant heat flux. Int Commun Heat Mass. 2012;39:144-151. https://doi.org/10.1016/j.icheatmasstransfer.2011.09.002

[32] Huang D, Wu Z, Sunden B. Effects of hybrid nanofluid mixture in plate heat exchangers. Exp Therm Fluid Sci. 2016;72:190-196. https://doi.org/10.1016/j.expthermflusci.2015.11.009

[33] Huang Y, Li H, Hu J, Xu C, Wang X. Study on enhanced heat transfer and stability characteristics of Al_2O_3–SiO_2/water hybrid nanofluids. Int J Thermophys. 2023;44:156. https://doi.org/10.1007/s10765-023-03262-7

[34] Irshad K, Islam N, Zahir H, Ali A. Case studies in thermal engineering thermal performance investigation of therminol55/MWCNT + CuO nanofluid flow in a heat exchanger from an exergy and entropy approach. Case Studies in Thermal Engineering. 2022;34:102010. https://doi.org/10.1016/j.csite.2022.102010

[35] Islam MR, Shabani B, Rosengarten G, Andrews J. The potential of using nanofluids in PEM fuel cell cooling systems: a review. Renew Sust Energ Rev. 2015;48:523-539. https://doi.org/10.1016/j.rser.2015.04.018

[36] Kandhal M. Jadeja RB, Chavda N. Nanofluid as a coolant in internal combustion engine – a review. International Journal of Ambient Energy. 2023;44:363-380. https://doi.org/10.1080/01430750.2022.2127891

[37] Keblinski P, Eastman JA, Cahill DG. Nanofluids for thermal transport. Mater Today. 2005;8:36-44. https://doi.org/10.1016/S1369-7021(05)70936-6

[38] Khedkar RS, Kiran AS, Sonawane SS, Wasewar K, Umre SS. Thermo physical characterization of paraffin based Fe_3O_4 nanofluids. Procedia Eng. 2013;51:342-346. https://doi.org/10.1016/j.proeng.2013.01.047

[39] Khoshvaght-Aliabadi M, Hormozi F, Zamzamian A. Experimental analysis of thermal – hydraulic performance of copper – water nanofluid flow in different plate-fin channels. Exp Therm Fluid Sci. 2014;52:248-258. https://doi.org/10.1016/j.expthermflusci.2013.09.018

[40] Kshirsagar DP, Venkatesh MA. A review on hybrid nanofluids for engineering applications. Mater Today Proc. 2021; 44(1):744-755. https://doi.org/10.1016/j.matpr.2020.10.637

[41] Kumar V, Sahoo RR. 4E's (Energy, Exergy, Economic, Environmental) performance analysis of air heat exchanger equipped with various twisted turbulator inserts utilizing ternary hybrid nanofluids. Alexandria Engineering Journal. 2022;61:5033-5050. https://doi.org/10.1016/j.aej.2021.09.037

[42] Li Z, Rostami S. Numerical assessment on the hydrothermal behavior and irreversibility of MgO-Ag/water hybrid nanofluid flow through a sinusoidal hairpin heat-exchanger. Int Commun Heat Mass. 2020;115:104628. https://doi.org/10.1016/j.icheatmasstransfer.2020.104628

[43] Machines T, Brayn L. Numerical Simulation of Nanofluid Cooling in a Single-Cylinder Diesel Engine. 2023;(June).

[44] Madheswaran DK, Vengatesan S, Varuvel EG, Praveenkumar T, Jegadheeswaran S, Pugazhendhi A et al. Nanofluids as a coolant for polymer electrolyte membrane fuel cells: recent trends, challenges, and future perspectives. J Clean Prod. 2023;424:138763. https://doi.org/10.1016/j.jclepro.2023.138763

[45] Madiwal S, Naduvinamani NB. Heat and mass transformation of casson hybrid nanofluid (MoS_2 + ZnO) based on engine oil over a stretched wall with chemical reaction and thermo-diffusion effect. Lubricants. 2024;12(6):221. https://doi.org/10.3390/lubricants12060221

[46] Malika M, Bhad R, Sonawane SS. ANSYS simulation study of a low volume fraction CuO–ZnO/water hybrid nanofluid in a shell and tube heat exchanger. J Indian Chem Soc. 2021; 98:100200. https://doi.org/10.1016/j.jics.2021.100200

[47] Meng Y, Su F, Chen Y. Supercritical fluid synthesis and tribological applications of silver nanoparticle-decorated graphene in engine oil nanofluid. Sci Rep. 2016:6:31246. https://doi.org/10.1038/srep31246

[48] Miansari M, Jafari SS, Alizadeh A, Fazilati MA. Hydrothermal behavior of different hybrid nanofluids in a dimpled tube heat exchanger. Eng Anal Bound Elem. 2023;157:21-33. https://doi.org/10.1016/j.enganabound.2023.08.035

[49] Micali F, Milanese M, Colangelo G, de Risi A. Experimental investigation on 4-strokes biodiesel engine cooling system based on nanofluid. Renew Energy. 2018;125:319-326. https://doi.org/10.1016/j.renene.2018.02.110

[50] Nilpueng K, Wongwises S. Experimental study of single-phase heat transfer and pressure drop inside a plate heat exchanger with a rough surface. Exp Therm Fluid Sci. 2015; 68:268-275. https://doi.org/10.1016/j.expthermflusci.2015.04.009

[51] Okonkwo EC, Wole-Osho I, Almanassra IW, Abdullatif YM, Al-Ansari T. An updated review of nanofluids in various heat transfer devices. J Therm Anal Calorim. 2021;145: 2817-2872. https://doi.org/10.1007/s10973-020-09760-2

[52] Patel P, Pathak R. Experimental analysis and comparison of thermophysical properties of the three different hybrid nanocatalyst blended diesel fuels. Australian Journal of Mechanical Engineering. 2024;1-16. https://doi.org/10.1080/14484846.2024.2383041

[53] Ponangi BR, Krishna V, Seetharamu KN. Performance of compact heat exchanger in the presence of novel hybrid graphene nanofluids. Int J Therm Sci. 2021;165:106925. https://doi.org/10.1016/j.ijthermalsci.2021.106925

[54] Qiu Y, He Y, Wang W, Du B, Wang K, Qiu Y et al. An experimental study on the heat transfer performance of a prototype molten-salt rod baffle heat exchanger for concentrated solar power. Energy. 2018;156:63-72. https://doi.org/10.1016/j.energy.2018.05.040

[55] Rabiei M, Gharehghani A, Andwari AM. Enhancement of battery thermal management system using a novel structure of hybrid liquid cold plate. Appl Therm Eng. 2023;232: 121051. https://doi.org/10.1016/j.applthermaleng.2023.121051

[56] Rahmati B, Sarhan AAD, Sayuti M. Morphology of surface generated by end milling AL6061-T6 using molybdenum disulfide (MoS_2) nanolubrication in end milling machining. J Clean Prod. 2014;66:685-691. https://doi.org/10.1016/j.jclepro.2013.10.048

[57] Rao MS, Rao CS, Kumari AS. Synthesis, stability, and emission analysis of magnetite nanoparticle based biofuels. J Eng Appl Sci. 2022:69:79. https://doi.org/10.1186/s44147-022-00127-y

[58] Rashid FL, Al-Obaidi MA, Dulaimi A, Bahlol HY, Hasan A. Recent advances, development, and impact of using phase change materials as thermal energy storage in different solar energy systems: a review. Designs. 2023;7(3):66. https://doi.org/10.3390/designs7030066

[59] Rashid FL, Al-Obaidi MA, Dulaimi A, Bernardo A, Ali Z, Redha A et al. Recent advances on the applications of phase change materials in cold thermal energy storage : a critical review. J Compos Sci. 2023;7(8):338. https://doi.org/10.3390/jcs7080338

[60] Rashin MN, Hemalatha J. Viscosity studies on novel copper oxide – coconut oil nanofluid. Exp Therm Fluid Sci. 2013; 48:67-72. https://doi.org/10.1016/j.expthermflusci.2013.02.009

[61] Shaban WM, Kabeel AE, Attia MEH, Talaat FM. Optimizing photovoltaic thermal solar systems efficiency through advanced artificial intelligence driven thermal management techniques. Appl Therm Eng. 2024;247:123029. https://doi.org/10.1016/j.applthermaleng.2024.123029

[62] Singh SK, Sarkar J. Hydrothermal performance comparison of modified twisted tapes and wire coils in tubular heat exchanger using hybrid nanofluid. Int J Therm Sci. 2021;166: 106990. https://doi.org/10.1016/j.ijthermalsci.2021.106990

[63] Singh SK, Sarkar J. Improving hydrothermal performance of hybrid nanofluid in double tube heat exchanger using tapered wire coil turbulator. Adv Powder Technol. 2020;31(5): 2092-2100. https://doi.org/10.1016/j.apt.2020.03.002

[64] Sokhal SG, Dhindsa GS, Jakhar A, Malhi GS, Tonk R. Role of hybrid nanofluids on the performance of the plate heat exchanger: experimental study. Mater Today Proc. 2022; 68(4):962967. https://doi.org/10.1016/j.matpr.2022.07.376

[65] Sroka ZJ, Gadisa S, Kejela E. Improving heat transfer in an air-cooled engine by redesigning the fins. Combustion Engines. https://doi.org/10.19206/CE-195440

[66] Sundar LS. Synthesis and characterization of hybrid nanofluids and their usage in different heat exchangers for an improved heat transfer rates: a critical review. Engineering Science and Technology, an International Journal 2023; 44:101468. https://doi.org/10.1016/j.jestch.2023.101468

[67] Sundar LS, Singh MK, Sousa ACM. Investigation of thermal conductivity and viscosity of Fe_3O_4 nanofluid for heat transfer applications. Int Commun Heat Mass. 2013;44:7-14. https://doi.org/10.1016/j.icheatmasstransfer.2013.02.014

[68] Tavakoli M, Soufivand MR. Performance evaluation criteria and entropy generation of hybrid nanofluid in a shell-and-tube heat exchanger with two different types of cross-sectional baffles. Eng Anal Bound Elem. 2023;150:272-284. https://doi.org/10.1016/j.enganabound.2023.01.024

[69] Tiwari AK, Ghosh P, Sarkar J. Heat transfer and pressure drop characteristics of CeO_2/water nanofluid in plate heat exchanger. Appl Therm Eng. 2013;57:24-32. https://doi.org/10.1016/j.applthermaleng.2013.03.047

[70] Torregrosa AJ, Broatch A, Olmeda P. Assessment of the improvement of internal combustion engines cooling system using nanofluids and nanoencapsulated phase change materials. Int J Engine Res. 2021;22:1939-1957. https://doi.org/10.1177/1468087420917494

[71] Venkatesh S, Kumar A, Bhattacharya A, Pramanik S. Ionic wind review-2020: advancement and application in thermal management. Sādhanā. 2021;46(165). https://doi.org/10.1007/s12046-021-01687-0

[72] Vermahmoudi Y, Peyghambarzadeh SM, Hashemabadi SH, Naraki M. Experimental investigation on heat transfer performance of Fe_2O_3/water nanofluid in an air-finned heat exchanger. Eur J Mech B-Fluids. 2014;44:32-41. https://doi.org/10.1016/j.euromechflu.2013.10.002

[73] Wajs J, Mikielewicz D. Influence of metallic porous microlayer on pressure drop and heat transfer of stainless steel plate heat exchanger. Appl Therm Eng. 2016;93:1337-1346. https://doi.org/10.1016/j.applthermaleng.2015.08.101

[74] Wang D, Ali MA, Sharma K, Almojil SF, Alizadeh A, Alali AF et al. Multiphase numerical simulation of exergy loss and thermo-hydraulic behavior with environmental cosiderations of a hybrid nanofluid in a shell-and-tube heat exchanger with twisted tape. Eng Anal Bound Elem. 2023;147:1-10. https://doi.org/10.1016/j.enganabound.2022.11.024

[75] Waqas H, Farooq U, Liu D, Abid M, Imran M, Muhammad T. Heat transfer analysis of hybrid nanofluid flow with thermal radiation through a stretching sheet: A comparative study. Int Commun Heat Mass. 2022;138:106303. https://doi.org/10.1016/j.icheatmasstransfer.2022.106303

[76] Wei H, Azwadi N, Sidik C, Saidur R. Hybrid nanocoolant for enhanced heat transfer performance in vehicle cooling system. Int Commun Heat Mass. 2022;133:105922. https://doi.org/10.1016/j.icheatmasstransfer.2022.105922

[77] Yang Y, Zhang ZG, Grulke EA, Anderson WB, Wu G. Heat transfer properties of nanoparticle-in-fluid dispersions (nanofluids) in laminar flow. Int J Heat Mass Tran. 2005;48: 1107-1116. https://doi.org/10.1016/j.ijheatmasstransfer.2004.09.038

[78] Yaw CT, Koh SP, Sandhya M, Kadirgama K, Tiong SK, Ramasamy D et al. Heat transfer enhancement by hybrid nano additives – graphene nanoplatelets/cellulose nanocrystal for the automobile cooling system (radiator). Nanomaterials. 2023;13(5):808. https://doi.org/10.3390/nano13050808

[79] Yeneneh K, Sufe G. Enhancing diesel engine performance and emissions using alumina nanoparticle-blended waste plastic oil biodiesel: an experimental and predictive approach. Ind Eng Chem Res. 2025 18;64(24):11681-11694. https://doi.org/10.1021/acs.iecr.5c01296

[80] Yu W, Xie H, Chen L, Li Y. Enhancement of thermal conductivity of kerosene-based Fe_3O_4 nanofluids prepared via phase-transfer method. Colloids Surfaces A. 2010;355:109-13. https://doi.org/10.1016/j.colsurfa.2009.11.044

[81] Zafarani-Moattar MT, Majdan-Cegincara R. Fluid phase equilibria investigation on stability and rheological properties of nanofluid of ZnO nanoparticles dispersed in poly (ethylene glycol). Fluid Phase Equilib. 2013;354:102-108. https://doi.org/10.1016/j.fluid.2013.06.030

[82] Zoynal M. Recent development of combined heat transfer performance for engine systems: a comprehensive review. Results in Surfaces and Interfaces. 2024;15:100212. https://doi.org/10.1016/j.rsurfi.2024.100212

Gadisa Sufe, MSc. – PhD Student, Doctoral School, Faculty of Mechanical Engineering, Wrocław University of Science and Technology, Poland.
e-mail: *gadisa.sufe@pwr.edu.pl*

Article citation info:
Wróblewski P, Bratkowski P, Kachel S. Investigation of the influence of propeller blade profile and angle of attack on the performance parameters of an aircraft piston engine. Combustion Engines. 2026;204(1):119-131. https://doi.org/10.19206/CE-208772

Piotr WRÓBLEWSKI
Przemysław BRATKOWSKI
Stanisław KACHEL

Combustion Engines
Polish Scientific Society of Combustion Engines

Investigation of the influence of propeller blade profile and angle of attack on the performance parameters of an aircraft piston engine

ARTICLE INFO

Received: 3 April 2025
Revised: 23 July 2025
Accepted: 29 July 2025
Available online: 22 September 2025

This article presents the results of experimental research concerning the influence of propeller blade profile and angle of attack on the performance parameters of the 3W 275 XI B2 CS aircraft piston engine. A specialised test stand was utilised, enabling real-time measurement of thrust, cylinder head temperature, and crankshaft rotational speed. The research was conducted with various propeller configurations (2- and 3-bladed) and at differing rotational speeds, which allowed for an assessment of the impact of propeller geometry on engine operational efficiency. The findings demonstrated that appropriate selection of the angle of attack, blade profile, and number of blades significantly affects the achieved parameters – particularly thrust and temperature distribution, which is of critical importance for the safety and durability of the powertrain components. The developed test stand facilitates further research into propeller selection for light aircraft piston combustion engines.

A novel aspect of this work is the utilisation of a new type of test stand that permits the determination of changes in thrust values obtained during tests across wide ranges of engine crankshaft rotational speeds. The selection of propellers, considering the number of blades and their profile, is very difficult to predict and should always be undertaken individually for each engine following testing. Such a tailored blade profile and number of propeller blades allow for high engine operational flexibility and good propeller thrust depending on the crankshaft's rotational speed.

Key words: *propeller blade profile, angle of attack, thrust, bench tests, two-stroke aircraft engine*

1. Introduction

Contemporary ultralight aviation and the unmanned aerial vehicle (UAV) sector are undergoing rapid development. This, in turn, translates into an increasing market demand for economical and highly reliable piston combustion engines. This is particularly pertinent in the domain of two-stroke engines, which, owing to their design and low inherent mass, are gaining popularity among light aircraft designers. From the perspective of enhancing thrust and reducing fuel consumption, a critical factor influencing the development of these engines is the appropriate selection of propeller geometry. This primarily involves the selection of the blade profile and angle of attack. The interaction between the propeller design and the piston combustion engine significantly impacts the thrust generated, the efficiency of the propulsion system, and the engine's thermal and mechanical parameters. The correct selection of blade shape and angle of attack can lead not only to increased thrust and fuel savings but also to improved cooling and more uniform load distribution. From the standpoint of flight safety and the durability of the piston combustion engine, several factors are of particular importance: cooling the engine cylinder heads, ensuring adequate lubrication at high temperatures, and defining the engine's cooling range for selected propeller parameters. It is important to note that two-stroke engines designed to power small aircraft are cooled exclusively by ambient air. An additional cooling airflow is generated by the propeller's thrust, as it is typically positioned directly adjacent to the engine. This arrangement ensures the appropriate shaping of the air stream, which is dependent on both the propeller geometry and the aircraft's cruising speed. Furthermore, it must also be considered that the direct coupling of the propeller to the engine's crankshaft imposes additional stresses on the engine's primary mechanical components, in the form of complex vibrations transmitted to the engine block.

In the case of small aircraft – both manned and unmanned aerial vehicles (UAVs) – the propeller remains a key element of the propulsion system [15]. It is responsible for the amount of thrust generated, which is why its design and its matching to a specific engine, most often a piston type, have a significant impact on performance, fuel consumption, and the overall reliability of the drive system [15]. Low-power piston engines – in the range of a few to several dozen horsepower – are widely used in unmanned aerial vehicles, models, and manned light aviation [7]. They typically work in conjunction with two- or three-bladed propellers made from wood, metal, or composites [7]. A conceptual design for the construction of an unmanned aerial vehicle was also presented in [9], which primarily described the design assumptions and concepts for the propulsion system [9].

The propeller, as a rotor with a precisely defined geometry, converts the torque transmitted by the engine shaft into thrust, which is generated due to the pressure difference on either side of the blade [10]. Pitch, diameter, rotational speed, and blade shape are the main parameters influencing the propeller's operational efficiency and its compatibility with the engine's characteristics [7]. When designing a propulsion system for small aircraft, requirements concerning range, climb performance, ceiling, and flight endurance must be taken into account [15]. Propeller-specific coefficients, such as the thrust coefficient and power coefficient, which describe the relationship between the

power absorbed by the propeller and the thrust produced, are helpful in this regard [10].

A study concerning the AOS H2 motor glider described an instance where a propeller with a blade angle of 15°, a diameter of 0.53 m, and a rotational speed of 2300 rpm generated a static thrust of approximately 26 N [10]. The calculations were performed using a simulation method. The appropriate selection of a propeller involves achieving a trade-off between efficiency and energy consumption, whilst considering design constraints such as system mass, available engine rpm, and operating conditions [12]. In an analysis of a quadcopter, it was noted that too small a distance between the propeller disc and the fuselage leads to flow disturbances, which worsen the thrust and efficiency of the system [12]. This phenomenon was investigated using CFD simulations in ANSYS Fluent [12].

Changing the propeller itself – without any modification to the engine – affects the operating characteristics of the entire propulsion system, including the shaft's rotational speed, power requirements, and the amount of thrust generated [15]. In amateur circles, as well as in experimental aviation, tests on propellers and propulsion systems are conducted, providing a valuable source of data for academic projects and applications in general aviation [4].

Modern propellers in unmanned aerial vehicles and light aviation are most commonly made from fibre-reinforced plastics – primarily carbon fibre and nylon [16]. Research indicates that carbon fibre is characterised by greater stiffness, lower deformation, and better thermal resistance at crankshaft rotational speeds of around 6000 rpm [16]. Concurrently, nylon exhibits better resistance to impact loads, making it suitable for simpler, commercial unmanned aerial vehicles [16]. The application of various composites in aircraft, including in the construction of propulsion system components, is presented in [2]. This work lists many advantages of using such solutions: high resistance to impacts and cracking, low specific density/low mass, non-susceptibility to corrosion, low thermal expansion, non-conductivity of electricity, low relative permittivity, and vibration damping [2]. Unfortunately, these materials also have disadvantages, such as low compressive strength, difficulty in machining and processing, hygroscopicity, and high cost [2]. The use of composite materials eliminates problems associated with corrosion effects [18]. In multi-rotor aircraft such as quadcopters, the mass and stiffness of the propellers are crucial for stability, flight time, and energy consumption [5]. In most small aircraft, an important aspect is the energy consumed to generate adequate thrust, as well as flight duration or distance covered. Any additional energy loss necessitates storing more energy on board the aircraft, whether from fuel or rechargeable batteries. This, in turn, translates to an increase in the aircraft's total mass. Therefore, selecting the appropriate propeller geometry can contribute not only to increased thrust but also to an improvement in the efficiency of the entire aircraft propulsion system.

In multi-rotor aircraft such as quadcopters, the mass and stiffness of the propellers are crucial for stability, flight time, and energy consumption [5]. In most small aircraft, an important aspect is the energy consumed to generate adequate thrust, as well as flight duration or distance covered. Any additional energy loss necessitates storing more energy on board the aircraft, whether from fuel or rechargeable batteries. This, in turn, translates to an increase in the aircraft's total mass. Therefore, selecting the appropriate propeller geometry can contribute not only to increased thrust but also to an improvement in the efficiency of the entire aircraft propulsion system.

The IS-2 documentation emphasises that despite the use of a turbine propulsion system, the geometry of the tail rotor is of immense importance for performance and proper torque transfer [14]. Literature recommends verifying design assumptions through experimental measurements of torque and thrust [8]. In UAV projects, increasing emphasis is being placed on the use of advanced CAD and CAE tools for modelling propellers and optimising their shape in terms of aerodynamics [6].

Although most studies pertain to turbine engines, some conclusions are also applicable to piston-driven systems – particularly in the context of mechanical stresses in the engine-propeller assembly [1]. Monitoring operational parameters in such drive systems is becoming increasingly common, especially for early diagnostics and maintenance planning [11]. The selection and design of a propeller for a small piston engine is a task requiring a comprehensive approach. Aerodynamic and structural analysis is necessary, as is consideration of the engine's operating characteristics and the conditions under which the entire system will be operated. Modern simulation tools significantly facilitate this process, allowing for preliminary design optimisation even before physical trials commence. Materials, blade geometry, and their number are of key importance here – each of these factors directly influences the aircraft's performance. During the design phase, it is worthwhile to consider both the mechanical and thermal properties of the materials used, as well as how the propeller interacts with the rest of the structure in terms of airflow.

This research is being conducted on a 3W 275 XI B2 CS engine, which is a two-stroke engine with a displacement of 273 cm³. Although a number of publications are available on the market concerning the improvement of propeller parameters in the context of low-power engines, the majority of these works focus on theoretical analyses. Such analyses often do not correspond to real-world conditions, necessitating individual research for each specific engine. The thrust measurement results presented in this article are based on the use of a new test stand, which permits the precise and multifaceted measurement of key engine operating parameters and the thrust generated by the propeller at various angles of attack and blade profiles. The application of a load cell for thrust measurement, telemetric temperature monitoring systems, and precise rotational speed recording systems allows for the assessment of the mechanical and thermal processes occurring within the engine.

Owing to the capability for rapid exchange and adjustment of propeller blade profiles and angles of attack, this work encompasses a broad spectrum of configurations. Such a defined scope of tests allows for the identification of optimal solutions for both ultralight aircraft and unmanned

aerial vehicles of various sizes. Detailed monitoring of cylinder head temperatures, correlated with thrust data, enables the investigation of the links between propeller aerodynamics and achieved engine parameters. Consequently, it is possible to identify design and operational solutions that improve both the performance and durability of the combustion engine used. The test stand has been designed in such a way as to facilitate not only future changes to propeller shape and angle of attack but also modifications to the engine itself (e.g., testing anti-wear or thermal barrier coatings). Such versatility in shaping research conditions constitutes a significant advantage for further development work.

Thanks to these features, the presented concept combines elements of classical aerodynamic studies with advanced thermomechanical analysis of the engine. This allows for capturing the multidimensional aspect of a two-stroke aero engine's operation. There is a significant gap in research of this type utilising combustion engines. The results and methodology presented in this work can be utilised by engine and propeller manufacturers, as well as by research teams specialising in the development of modern propulsion systems for aviation applications. As such, this work makes a significant contribution to the development of engineering methods and tools for establishing methodologies for selecting propeller configurations for piston aero engines; furthermore, it fills a gap concerning practical, comprehensive analyses of the influence of propeller geometry on the operational parameters of small combustion engines.

2. Materials and methods

2.1. Construction of a test rig for propeller evaluation

The test rig was constructed to facilitate the testing of two-stroke piston engines utilised in light aviation and unmanned aerial vehicles (UAVs) (Fig. 1). Further technical details on the construction of the test stand are provided in reference [17]. The entire structure of the test rig is based on a steel frame, protected by a layer of zinc and a powder coating offering increased resistance to atmospheric conditions. The frame is equipped with four adjustable feet featuring an M16 thread, enabling precise levelling of the rig with the aid of a laser level. Mounted within the frame is a steel engine mount, adapted for the installation of two engine models: the DLE170 (a twin-cylinder, two-stroke engine with a 170 cm³ capacity) and the 3W 275 XI B2 CS (a twin-cylinder, two-stroke engine with a 273 cm³ capacity). The mount allows for the adjustment of the crankshaft axis inclination angle within a range of ±15°, which permits the engine's position to be altered relative to the force sensor [17]. Fastening is accomplished using class 12.9 bolts and spring washers, which prevent the connections from loosening during engine operation.

The supply system provides independent regulation of fuel and air flow. The fuel system comprises a 500 ml capacity tank, fuel filters, petrol-resistant silicone tubing, and a non-return valve. The fuel-oil mixture ratio is 40:1 in test mode and 30:1 during the running-in of new engine components. The oil used is Castrol Power1 A747 Racing 2T. The oil-fuel mixture can be freely selected depending on the tests being conducted and the anticipated maximum loads on the engine's main mechanical components.

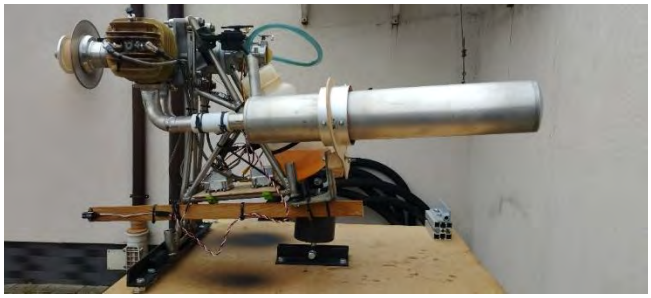

Fig. 1. Test rig construction

Cooling is provided by the thrust generated by the propeller, which is positioned close to the cylinder heads. Additionally, cooling fans can be mounted on the rig, their speed being automatically regulated according to the engine cylinder head temperature. However, for rig-based tests, it is more advantageous to conduct evaluations without utilising fans. This is because it allows for an assessment of how the thrust generated by the propeller and its geometric parameters affect the temperature change of the cylinder heads in relation to the engine crankshaft's rotational speed. The measurement system includes a CL14-type force sensor with a measurement range of up to 5 kN, a sensitivity of 1 mV/V, and linearity of ≤ 0.5%. The sensor's strain gauge bridge has an input resistance of 410 Ω and an output resistance of 350 Ω [17]. The sensor is coupled with a CL 450 data logger, enabling data recording with 24-bit resolution and a speed of up to 29,000 samples per second [17]. The recorder is equipped with an OLED screen and USB 2.0 communication capability (Fig. 2).

Fig. 2. Data logger construction

To measure the temperature, a type 1 type K-type thermocouple is used (accuracy of ± 1.5°C or 0.4% read), mounted directly in the engine block at the spark plug sockets, along with additional SBS-01T sensors.

The latter communicate via the S.BUS2 bus with a Futaba T18SZ RC transmitter and permit real-time temperature readings in the range of –20°C to +200°C (Fig. 3) [17]. Additional measurement equipment includes: an optical propeller rotational speed sensor with a resolution of 1 pulse per revolution, a Hall effect throttle position sensor, and a digital shaft rotational speed sensor integrated with the ignition

module. The engine is started using an ignition module, powered by a regulated voltage source of either 6.0 V (NiCd) or 7.4 V (LiPo) [17]. The spark plugs used are NGK CM6, and the ignition timing advance is automatically adjusted depending on the engine's operating temperature.

Fig. 3. Futaba RC Measurement and Control System

For testing purposes, the engine manufacturer recommends using propellers in various configurations: two-blade 36×12 and 36×14, as well as three-blade 32×12 and 34×12. This allows for the modelling of various dynamic load conditions on the powertrain. The rig facilitates continuous tests (up to 30 minutes of operation under steady conditions) and cyclical load changes. The collected data enable real-time analysis of engine operating parameters, including thrust, cylinder head temperatures, rotational speed, and throttle position. This facilitates the evaluation of the effectiveness of applied tribological coatings and thermal barriers on the primary mechanical components, such as the piston, piston rings, and cylinder.

2.2. Propellers utilised during rig tests

The test rig facilitates the mounting of propellers with various profiles and numbers of blades. Propeller mounting is carried out using bolts with special securing adapters. All propellers are tightened to the appropriate torque, depending on the material from which they are made (Fig. 4). The mounting assembly comprises 1 central bolt and 5 circumferentially arranged bolts. It is also important to remember that over-tightening the mounting bolts can cause excessive stress and damage to the propeller. Such an eventuality is particularly dangerous if personnel conducting measurements are located in the vicinity of the rig.

Six types of propellers were used for the rig tests. An illustrative example of mounted 2- and 3-blade propellers is shown in Fig. 5 and Fig. 6.

Fig. 4. Propeller mounting assembly

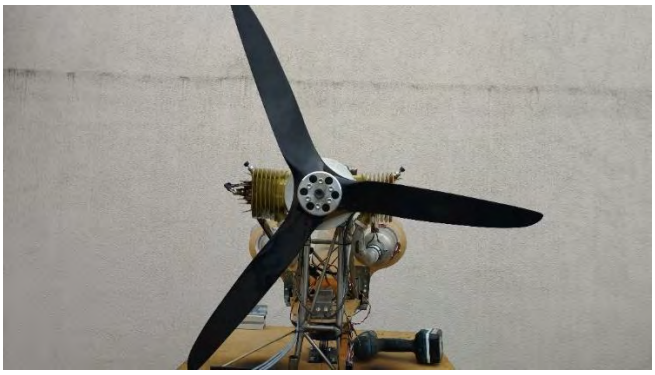

Fig. 5. 3-blade propeller made of carbon fibre

2.3. Test conditions for investigating thrust as a function of propeller geometry

To determine the weight of the individual propellers selected for testing, their weight was measured using a WLC 30/F1/K precision balance. The readability of the balance is 0.5 g, with a linearity of ±1.5 g. The balance provides readings via a display.

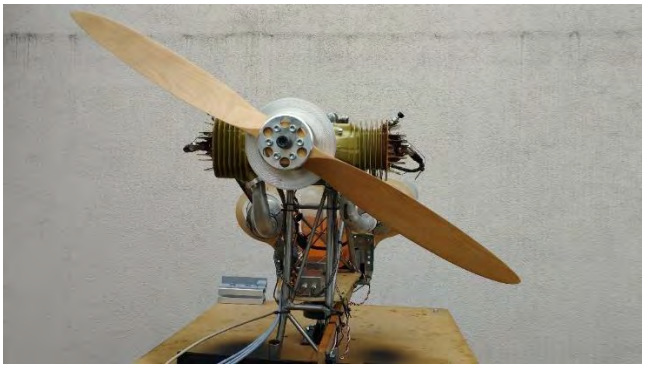

Fig. 6. 2-blade propeller made of wood

Tests utilising the test rig were conducted at an ambient temperature of approximately 10°C and a humidity of approximately 35–40%. The rotational speed range extended from idle speed to the maximum engine rotational speed. The maximum engine rotational speed is dependent on the propeller profile and geometry used. All measurements were conducted under similar ambient conditions; the influence of these conditions on the measurement results was negligible. A steady crosswind with an average speed of 16 km/h was present, and the ambient temperature during the measurements was approximately 13–14°C.

3. Results and discussion

3.1. Characteristics of propellers used in rig tests

For the rig tests, six propeller models with varying numbers of blades and dimensions were utilised.

- Fiala 2-blade propeller 30/18 (Fig. 7 and 8)
- Fiala 2-blade propeller 32/16 (Fig. 9 and 10)
- Fiala 2-blade propeller 32/18 (Fig. 11 and 12)
- Biela 3-blade propeller 32/14 (Fig. 13 and 14)
- Biela 3-blade propeller 32/12 (Fig. 15 and 16)
- Falcon 3-blade propeller 32/13 (Fig. 17 and 18).

Prior to conducting tests for thrust, cylinder head temperature, and the aero engine's crankshaft rotational speed,

preliminary measurements of the mass of all propellers were performed (Fig. 19). Readings were obtained after placing each propeller on the metal platform of the balance. This measurement provides a realistic indication of the influence of weight on the engine's operational parameters obtained, in relation to the number of blades and the propeller profile geometry. The Fiala propellers are made of wood; the Biela 32/14 propeller is constructed from a carbon and glass fibre composite using a high-strength resin. The Falcon 32/13 and Biela 32/12 propellers are made entirely of carbon fibre.

Fig. 7. Fiala 30/18 2-blade propeller – view

Fig. 8. Fiala 30/18 2-blade propeller – geometry designation

Fig. 9. Fiala 32/16 2-blade propeller – view

Fig. 10. Fiala 32/16 2-blade propeller – propeller geometry designation

Fig. 11. Fiala 32/18 2-blade propeller – view

Fig. 12. Fiala 32/18 2-blade propeller – propeller geometry designation

Fig. 13. Biela 32/14 3-blade propeller – view

Fig. 14. Biela 32/14 3-blade propeller – propeller geometry designation

Fig. 15. Biela 32/12 3-blade propeller – view

Fig. 16. Biela 32/12 3-blade propeller – propeller geometry designation

Fig. 17. Falcon 32/13 3-blade propeller – view

Fig. 18. Falcon 32/13 3-blade propeller – propeller geometry designation

3.2. Measurement of the mass of propellers used in the tests

The choice between a two-blade and a three-blade propeller is contingent upon numerous factors, such as torque requirements, crankshaft rotational speed, and the specific operational conditions of the aircraft. Differences in mass can influence the dynamic balance and energy efficiency of the entire system. There is no definitive answer as to which propeller constitutes the optimal solution for a given engine. This cannot be predicted at the assembly stage based on geometric and mass parameters. Only bench tests allow for the determination of which propeller can achieve the maximum thrust value, the thrust characteristic curve, the thermal loading on the engine heads, and the maximum attainable engine rotational speed. To a significant extent, speed and thrust determine the correct selection of the propeller profile and number of blades for a particular type of aircraft piston combustion engine. The self-mass of the propeller is influenced not only by its geometry and the number of its blades but also by the type of materials utilised. This is particularly observable in the considerably lower mass of the Falcon 32/13 propeller compared to its three-blade counterparts from Biela, models 32/12 and 32/14. The Falcon propeller is approximately 31.3% lighter than the Biela 32/14 model and about 26.5% lighter than the Biela 32/12 model. An exemplary measurement of a propeller's self-mass is depicted in Fig. 19.

A compilation of all propeller weight measurements taken during the bench tests is provided in Table 1.

Table 1. Self-mass of propellers used in the tests

Propeller name	Self-mass m [g]
Fiala 2-blade propeller 30/18	273.0
Fiala 2-blade propeller 32/16	302.0
Fiala 2-blade propeller 32/18	299.5
Biela 3-blade propeller 32/14	586.0
Biela 3-blade propeller 32/12	547.5
Falcon 3-blade propeller 32/13	402.5

Data for calculating measuring uncertainty:

- Own weight of propellers – values from Table 1: 273.0–586.0 g
- Laboratory scale WLC 30/F1/K – Read plot d = 0.5 g, linearity ±1.5 g (manufacturer specification)
- Five measurements were carried out for each propeller and the same reading on the measuring weight was obtained.

Type A uncertainty (repeatability)

$$u_a = \frac{s}{\sqrt{n}} \tag{1}$$

where: s = 0, s – standard deviation of the mass measurements series (here s = 0, s = 0 g, because all readings were identical), n – number of measurement repetitions (here n = 5).

Type B uncertainty (characteristic of the device)

Display resolution:

$$D = 0.5\ \text{g} \rightarrow u_d = \frac{d}{2\sqrt{3}} = 0.144\ \text{g} \tag{2}$$

Nonliney of the weight:

$$\pm 1.5\ \text{g} \rightarrow u_{lin} = \frac{1,5}{\sqrt{3}} = 0.866\ \text{g} \tag{3}$$

The total standard uncertainty is:

$$u_c = \sqrt{u_d^2 + u_{lin}^2} = \sqrt{0.144^2 + 0.866^2} = 0.878\ \text{g} \tag{4}$$

Extended (trust level 95 %, k = 2k = 2):

$$U = 2u_c = 1.756\ \text{g} \tag{5}$$

where: d – reading plot (readability) of weight; the mass difference corresponding to the change by one display, U – extended uncertainty, u_c – total standard uncertainty, u_d – a component of standard uncertainty caused by the completed display resolution, u_{lin} – a component of standard uncertainty associated with weight non-linearity.

The measurement-uncertainty results for the propeller masses are presented in Table 2.

Table 2. Self-mass of propellers used in the tests

Propeller Name	Self-mass [g]	Expanded uncertainty U (95%) [g]	Relative uncertainty U/m [%]
Fiala 2-blade propeller 30/18	273.0	1.756	0.643
Fiala 2-blade propeller 32/16	302.0	1.756	0.581
Fiala 2-blade propeller 32/18	299.5	1.756	0.586
Biela 3-blade propeller 32/14	586.0	1.756	0.300
Biela 3-blade propeller 32/12	547.5	1.756	0.321
Falcon 3-blade propeller 32/13	402.5	1.756	0.436

Zero deviations of the series confirm the good repetition of the weight, but does not remove the main restriction – non-linearity ±1.5 g. A relative uncertainty below 1% – even for the lightest propeller - is sufficiently small for analysing the forces and energy of the propulsion system; periodic calibration of the balance to verify its non-linearity parameter is more important than performing additional weighing.

Fig. 19. Exemplary measurement of propeller mass using WLC 30/F1/K scales – result 273.0 g

3.3. Study of the relationship between thrust, shaft rotational speed, and head temperatures

All propellers tested demonstrate a direct relationship between thrust and crankshaft rotational speed – as the rotational speed increases, so does the thrust. However, the thrust characteristics vary depending on the specific model and type of propeller. To determine the propeller-generated thrust of the propulsion system accurately, the correction coefficient k_G must be established. It depends on the distances A and B. In this case, A equals 0.4245 m and B equals 0.3329 m. This value should be verified experimentally, not just geometrically. If a different engine is installed in the frame, the coefficient k_G may change, so the corresponding geometric measurements and mass-load verification must be repeated.

In the tested dynamometer, the track power measurement is not performed in the drive axis, but on a strainometric sensor attached to the back of the frame. There is a lever system (Fig. 20) between the propeller axis and the sensor) with two arms.

From a condition of the moments for static load:

$$F_S B = F_T A \tag{6}$$

$$F_T = F_S \frac{B}{A} \rightarrow k_G = \frac{A}{B}, F_T = \frac{F_S}{k_G} \tag{7}$$

$$k_G \approx 1.27516 \tag{8}$$

where: A – distance from the axis of the propeller to the front bed (engine mounting point to the frame), B – distance from the axis of the propeller to the axis of the force sensor, F_S – the force recorded by the strain-gauge sensor mounted at the rear of the frame [N], F_T – the actual static propeller thrust along the drive axis [N], k_G – the factor calculated by the geometric method.

To accurately verify the calculated value of the correction coefficient, precise experimental measurements are performed. In such a case, a line is mounted exactly on the propeller axis, set to be perfectly parallel with the axis, the alignment of which is verified using a spirit level. At the end of the line, there is a wheel attached to a post opposite the test stand. A weight of an appropriate mass is suspended from the end of the line. In this instance, calibration of the read values was performed for masses of 10 kg and 20 kg. The value from the sensor was read and then corrected against the actual load suspended on the line. This value is accurate and serves as an additional verification of the conversion coefficient.

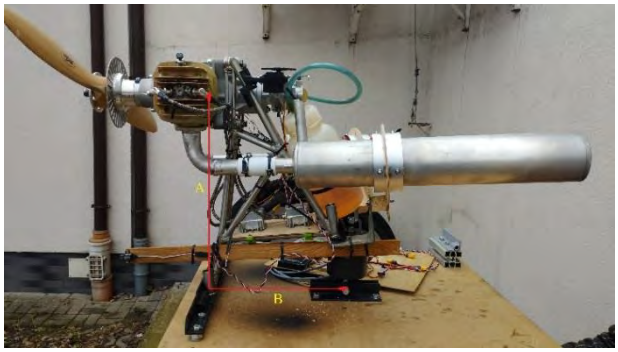

Fig. 20. Calculating the correction coefficient value

To verify the correctness of the calculated k_G, an independent calibration test with a known applied load is performed. To confirm the correctness of the calculated k_g (geometrically determined from a distance A = 0.4245 m and B = 0.3329 m → $k_G \approx 1.27516$) an independent standard examination is performed by strength load.

Verification of the parallelism of the rope from the axis is done using a 0.1° accuracy level. The verification test uses a 2 mm steel rope, with its stretchiness 0.2% for 1 kN. A block with ball bearings with an efficiency of about 0.995 was also used, which minimizes friction losses. The rope is attached concentrically to a spacer sleeve bolted in place of the propeller hub.

The wire runs parallel to the engine axis. A deviation of less than 0.5 mm over a distance of 1 meter is checked with a spirit level. A pulley is installed on the opposite post. The free end of the wire hangs vertically, 1.0 meter above the ground.

The test uses 10 kg and 20 kg M1 class weights, providing a tolerance of ±5 g. The CL14 force sensor has a nonlinearity of ≤ 0.5%. The value of g was taken as 9.80665 m/s² for Warsaw.

For a mass of 10 kg, the reference force (F_{Tw}= mg) is 98.066 N, and for a mass of 20 kg, the reference force is 196.133 N. For the 10 kg mass, the sensor output was 125.2 N, and for the 20 kg mass, the sensor output was 249.7 N.

The value of the coefficient determined experimentally using reference masses k_{exp} can be calculated from the following formula:

$$k_{exp} = \frac{F_S}{F_{Tw}} \tag{9}$$

Accordingly k_{exp} for the 10 kg mass is 1.2767, and for the 20 kg mass it is 1.2731. After calculating the mean value from the reference measurements k_{exp} = 1.2749.

The difference between the coefficients k_{exp} and k_G is:

$$k_{exp} - k_G = 0.00026\ (0.02\%) \tag{10}$$

The uncertainty calculation for determining the coefficient k includes the following components:

- Force sensor nonlinearity, limit ±0.5F, rectangular distribution, standard deviation u_i = 0.289% and relative standard deviation u_i/k = 0.00289
- Pulley friction, limit ±0.5 F, rectangular distribution, standard deviation u_i = 0.289% and relative standard deviation u_i/k = 0.00289
- Mass of the weights, limit ±5 g, rectangular distribution, standard deviation u_i = 0.029% and relative standard deviation u_i/k = 0.00029
- Acceleration due to gravity (g), limit $\pm 5\times10^{-5}$, rectangular distribution, standard deviation u_i = 0.003 % and relative standard deviation u_i/k = 0.00003
- Wire alignment (0.2°), limit ±cosθ, normal distribution, standard deviation u_i = 0.006% and relative standard deviation u_i/k = 0.00006
- Sensor thermal drift, limit ±0.05%/°C, ΔT=5°C, rectangular distribution, standard deviation u_i = 0.029% and relative standard deviation u_i/k = 0.00029. The value of

0.029% applies when the temperature changes by no more than ~1°C during a short weight test.

Accordingly, the combined standard uncertainty u_k is:

$$u_k = \sqrt{\sum u_i^2} = 0.409\% \tag{11}$$

The expanded uncertainty (95%) U_k is:

$$U_k = 2u_k = 0.82\% \tag{12}$$

The accuracy of the performed calculations—the difference of 0.02% between k_{exp} and k_G is 40 times smaller than the calculated expanded uncertainty of 0.82%. The experimental method confirms the geometric value k_G with a large margin of confidence. Therefore, it can be stated that the value 1.275, adopted for correcting the force readings from the sensor, is very accurate. The largest contributions to the uncertainty budget (45% each) come from the sensor nonlinearity and pulley friction. Improving either of these components will reduce U_k below 0.6%.

The value of U_{FS}/F_S comes from the following specification for the CL14 sensor:

- Force sensor nonlinearity, limit ±0.5 F, rectangular distribution, standard deviation $u_i/F_S = 0.289\%$
- Repeatability (noise), limit ±0.15 (1σ), normal distribution, standard deviation $u_i/F_S = 0.150\%$
- Sensor thermal drift, limit ±0.25%, rectangular distribution, standard deviation $u_i/F_S = 0.144\%$
- A/D converter resolution (24 bit, 5 kN range), limit ±0.04% $F_S \rightarrow \leq 0.02\%$ of reading, rectangular distribution, $u_i/F_S = 0.02\% / \sqrt{3} = 0.012\%$.

Total standard uncertainty of the sensor:

$$\frac{u_{FS}}{F_S} = \sqrt{\sum u_i^2} \approx 0.332\% \tag{13}$$

Expanded uncertainty (coverage factor k = 2):

$$\frac{U_{FS}}{F_S} = \frac{2u_{FS}}{F_S} \approx 0.664\% \tag{14}$$

In engineering reports, it is often assumed that the final uncertainty should be rounded up to the first significant digit. 0.664% → 0.7% is already a rounding, but increasing it to 1% provides an additional margin for potential sources that are difficult to quantify (such as frame microvibrations, humidity changes, minor power supply drifts in the bridge circuit).

Accordingly, the contribution to the total thrust uncertainty can be calculated using the following formula:

$$F_T = \frac{F_S}{k} \tag{15}$$

$$\frac{U_{FT}}{F_T} = \sqrt{\left(\frac{U_{FS}}{F_S}\right)^2 + \left(\frac{U_k}{k}\right)^2} \approx$$

$$\approx \sqrt{(1.0\%)^2 + (0.82\%)^2} \approx 1.3\% \tag{16}$$

Thus, thanks to the verification of k, the total measurement uncertainty of thrust does not exceed 1.3%, which is a very good result for this type of experimental research.

The method of verifying the coefficient and determining its value is effective and easily repeatable. It should be performed after each change in the position of the engine or sensor, as well as periodically (e.g., every 50 hours of test bench operation).

In the case of temperatures recorded by sensors, the main components of uncertainty and standard deviation are: u_{TC} – type K thermocouple tolerance, class 1, limit ± max {1.5°C; 0.4% T}, rectangular distribution, standard deviation $u_i = 0.866$°C, u_{CJC} – cold junction compensation error (CL450), tolerance ±0.5°C, rectangular distribution, standard deviation $u_i = 0.289$°C, u_{res} – display resolution, tolerance ±0.5°C, rectangular distribution, standard deviation $u_i = 0.289$°C, u_{rep} – repeatability, noise, interferences, normal distribution, standard deviation $u_i = 0.200$°C, u_{inst} – contact with the pipe (thermal paste + clamp pressure), tolerance ±2.0°C, rectangular distribution, standard deviation $u_i = 1.155$°C.

The total standard uncertainty for temperature measurement is:

$$u_c = \sqrt{u_{TC}^2 + u_{CJC}^2 + u_{res}^2 + u_{rep}^2 + u_{inst}^2} \approx$$

$$\sqrt{0.866^2 + 0.289^2 + 0.289^2 + 0.200^2 + 1.115^2}$$

$$\approx 1.514\text{°C} \tag{17}$$

Extended uncertainty (95 %, K = 2) is:

$$U = 2u_c = 3.03\text{°C} \tag{18}$$

Relative uncertainty for an example value t = 60°C

$$\frac{U}{T} = \frac{3.03}{60} \approx 5.0\% \tag{19}$$

The thermal contact of the sensors has become the dominant component affecting the uncertainty of the measurement (59% of the total balance). The accuracy can be improved using: stronger mechanical pressing of the sensor, a thinner layer of paste with a higher conductivity or increase the measurement time to stabilize the temperature for a given engine mode.

Based on the analysis of measurement data concerning three models of Fiala 2-blade propellers – 30/18, 32/16, and 32/18 – a number of significant conclusions can be drawn regarding their operating characteristics, efficiency, and impact on the engine's thermal conditions. For all propeller variants, the obtained values for thrust and temperature were approximated using a power function.

The Fiala 30/18 propeller exhibits a linear, yet moderate, increase in thrust in the low and medium crankshaft rotational speed ranges; however, at values above 5200 rpm, thrust increases more significantly. The maximum thrust value is approximately 460 N (Fig. 21). Nevertheless, this propeller achieves its best thrust parameters only above 5700 rpm. The average temperature recorded by sensors is about 50°C. It increases as the crankshaft rotational speed increases. Nonetheless, this temperature (or its increase) is slight, which is due to the short duration of the test conducted under very stable engine operating conditions. At maximum thrust, this temperature is approximately 48–49°C (Fig. 22). This indicates that maximum engine power is achieved with this propeller. A small increase in the temperature recorded by sensors can also be observed in the range from 3300 to 4600 rpm. In the case of both sensors,

the temperature remained at a similar level, depending on the crankshaft rotational speed.

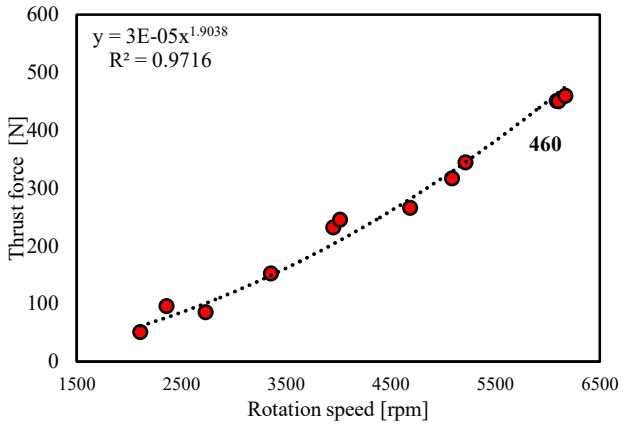

Fig. 21. Corrected thrust obtained for the Fiala 30/18 propeller as a function of crankshaft rotational speed

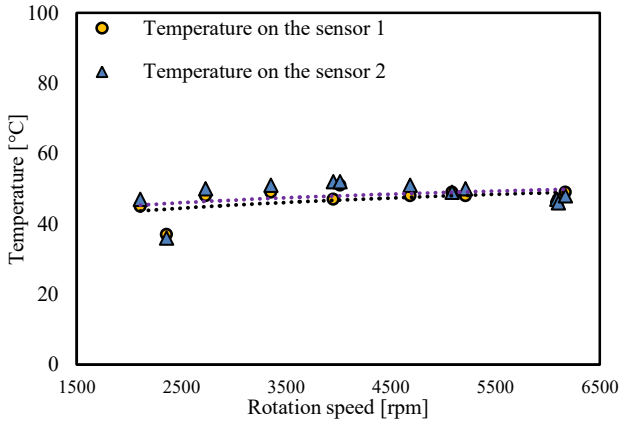

Fig. 22. Measured engine head temperature during tests of the Fiala 30/18 propeller for given engine rotational speeds.

The Fiala 32/16 model, in comparison to the previous one, achieves higher maximum thrust values – up to approximately 498 N – at a lower rotational speed (approx. 5853 rpm) (Fig. 23). This represents an increase in thrust of approximately 8.26% compared to the previous propeller. In the lower range of the crankshaft speed (up to about 3800 rpm) the engine operates at higher temperatures in part of the head, reaching about 64°C; However, as the shaft speed increases and a greater string, the temperature is recovered by the sensors – ultimately to even 41°C. This indicates that this propeller is designed for operation at high shaft rotational speeds, and its geometry allows for more effective utilisation of the engine's power output in the upper shaft rotational speed range. Higher shaft speeds with this type of propeller allow better cooling, as you can observe in Fig. 24. It shows a systematic decrease in temperature as air flow increases, resulting from the increase in speed and draft. This propeller is characterised by a gradual increase in thrust relative to the increase in shaft rotational speed. The most effective operating parameters for the power unit with this propeller are achieved in the 5500 rpm to 5850 rpm range.

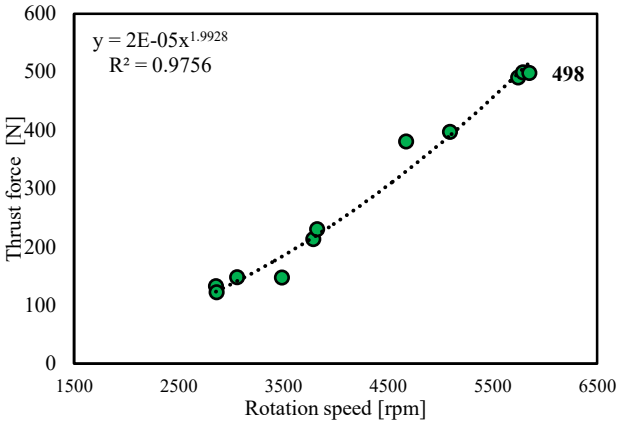

Fig. 23. Corrected thrust obtained for the Fiala 32/16 propeller as a function of crankshaft rotational speed

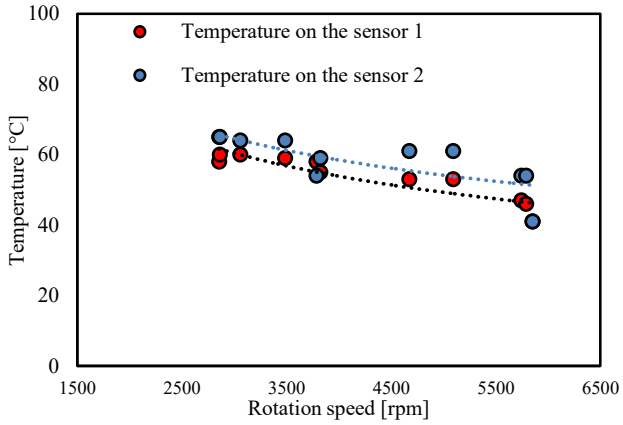

Fig. 24. Measured engine head temperature during tests of the Fiala 32/16 propeller for given engine rotational speeds.

The Fiala 32/18 propeller, in turn, is characterised by a relatively high thrust value even in the low shaft rotational speed range – for example, at just 3500 rpm, it generates approximately 200 N, which, compared to other models, makes it exceptionally effective in the low shaft speed range (Fig. 25). The temperatures recorded by the sensors are much higher, on average about 70°C, which may indicate a higher engine load compared to the previous variants of the propeller (Fig. 26). The temperature in the scope of both engine heads is the highest in the lower and upper ranges of the engine shaft speed. This is certainly related to achieving a good engine torque distribution in this range. The maximum thrust value obtained is 476 N, at a rotational speed of 5610 rpm. Based on the data, it can be observed that this propeller allows the lowest crankshaft rotational speed to be achieved. Despite this decrease in rotational speed, a high thrust value can be achieved. At maximum thrust, an increase in head temperature is visible. Nevertheless, a decrease in head temperature is noted in the 5000 rpm to 5500 rpm range. However, it should be generally assumed that the temperature remains almost constant at different rotational speeds of the engine shaft.

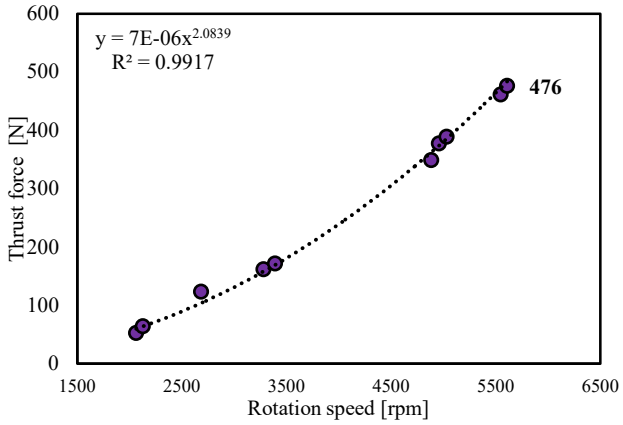

Fig. 25. Corrected thrust obtained for the Fiala 32/18 propeller as a function of crankshaft rotational speed

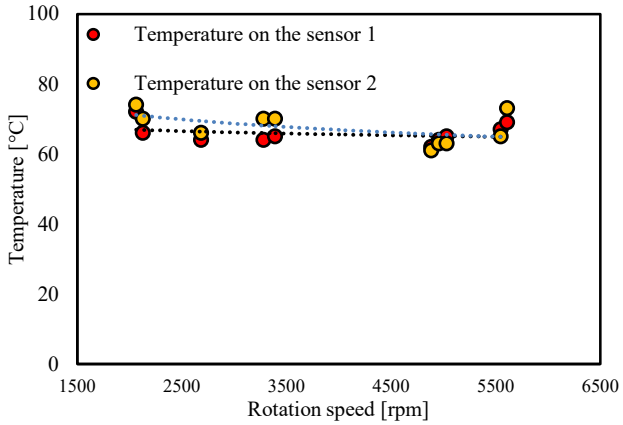

Fig. 26. Measured engine head temperature during tests of the Fiala 32/18 propeller for given engine rotational speeds

In the case of the Biela 32/14 3-blade propeller, an increase in thrust is observed in the shaft rotational speed range of 3700 rpm to 3800 rpm; whereas in the higher crankshaft speed range, this increase levels off. At a rotational speed of approximately 4936 rpm, a maximum thrust value of close to 529 N was achieved (Fig. 27). Such a thrust characteristic curve may indicate that the propeller achieves its highest aerodynamic efficiency in the mid-range of rotational speeds. The influence of shaft rotational speed on temperature distribution is significant. Figure 28 shows a decrease in temperature as the shaft speed increases, which undoubtedly promotes better cooling due to air flow. Even after reaching the maximum speed and shaft, the temperature is low, from 46 to 48°C. In this case, as the propeller's speed increases, the temperature decreases slightly, indicating better cooling than in the case of 2-blade propellers. The same applies to the generated thrust.

According to the data in Fig. 29 for the Biela 32/12 3-blade propeller, a sudden and dynamic increase in the thrust value can be observed starting from a shaft rotational speed of approximately 4000 rpm. With this propeller, relatively high thrust values can be obtained at a reduced shaft rotational speed in the range of 4484 to 5392 rpm. In this case, the temperature is stable in the entire range of shaft speed, between 55 and 60°C (Fig. 30). At the average speed of the shaft, a small decrease in the temperature recorded by the sensors can be observed. This is due to a lower engine load and improved airflow in this rotational speed range, as a result of its thrust characteristics. This propeller generates a maximum thrust of 524 N, which is a similar value to that of the previous 3-blade propeller variant. However, in this instance, this thrust is achieved only in the higher shaft rotational speed range. In this case, an increase in the maximum shaft rotational speed of over 400 rpm can also be observed. This indicates that this propeller imposes a lower load on the engine.

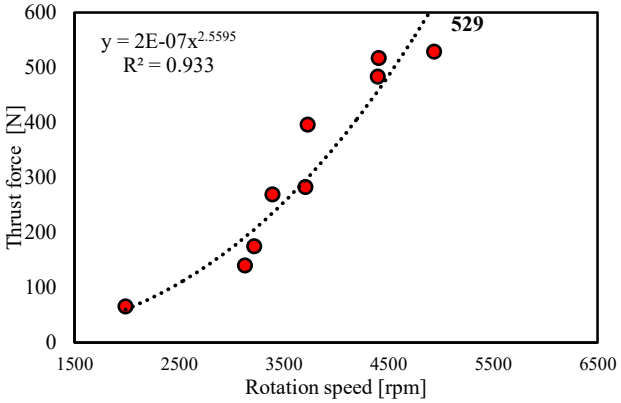

Fig. 27. Corrected thrust obtained for the Biela 32/14 propeller as a function of crankshaft rotational speed

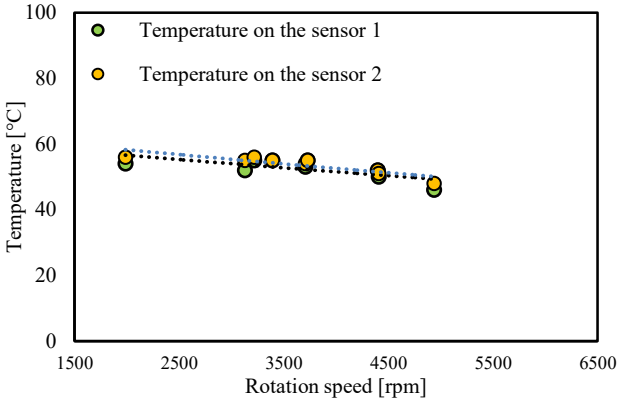

Fig. 28. Measured engine head temperature during tests of the Biela 32/14 propeller for given engine rotational speeds

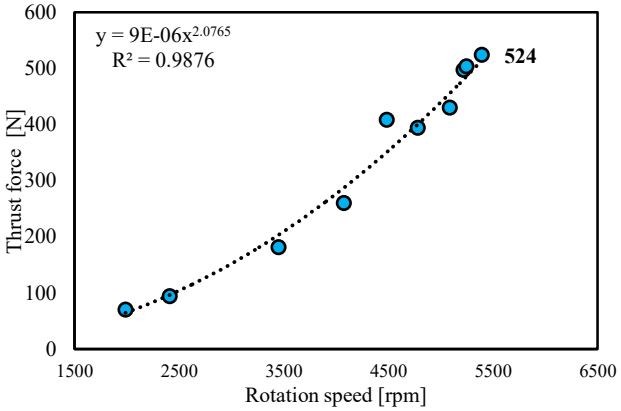

Fig. 29. Corrected thrust obtained for the Biela 32/12 propeller as a function of crankshaft rotational speed

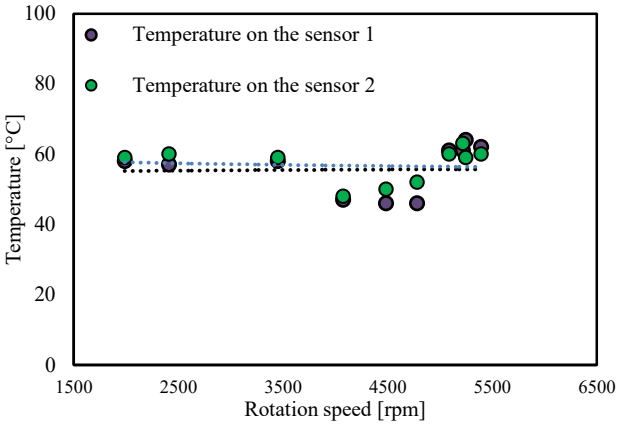

Fig. 30. Measured engine head temperature during tests of the Biela 32/12 propeller for given engine rotational speeds

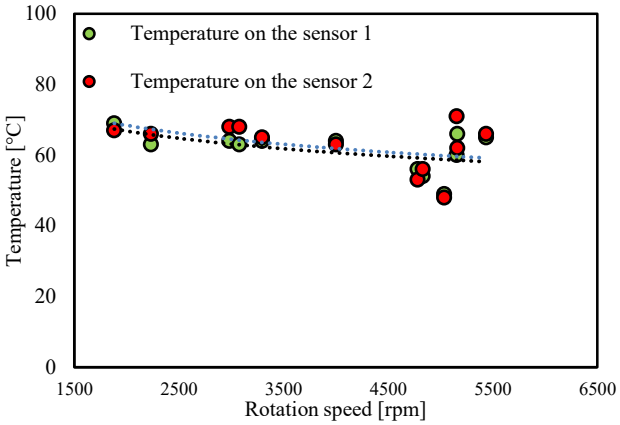

Fig. 32. Measured engine head temperature during tests of the Falcon 32/13 propeller for given engine rotational speeds

According to the results in Fig. 31, the Falcon 32/13 propeller generates the highest thrust of all the variants. The maximum thrust recorded is 569 N at 5162 rpm. According to its thrust characteristic, a linear progression of thrust with respect to shaft rotational speed can be observed. At higher shaft rotational speeds, the thrust decreases slightly. The progression of the obtained thrust is very stable from a speed of approximately 4700 rpm onwards, as can be observed in Fig. 31. This propeller also enables good cooling of the engine heads. The average temperature in the entire speed of the shaft speed is about 62°C, with the temperature decreasing as the thrust increases. It can be considered that this propeller is the best variant overall. Additionally, its relatively low self-mass for a 3-blade category propeller indicates a low load on the engine. This (its low mass) is well-balanced with the achieved thrust and the engine's operating temperature.

The lightest wooden biplane propellers by Fiala (273–302 g) generate thrust ranging from 460 N (model 30/18) to 498 N (32/16) at very high shaft rotational speeds – specifically, 6171 rpm and 5853 rpm, respectively. Their efficiency index T/m exceeds 1600 N kg^{-1}, which makes them unrivaled when the thrust-to-mass ratio is the key criterion. Unfortunately, this is associated with drawbacks such as higher noise levels and increased fuel consumption resulting from the high shaft speeds.

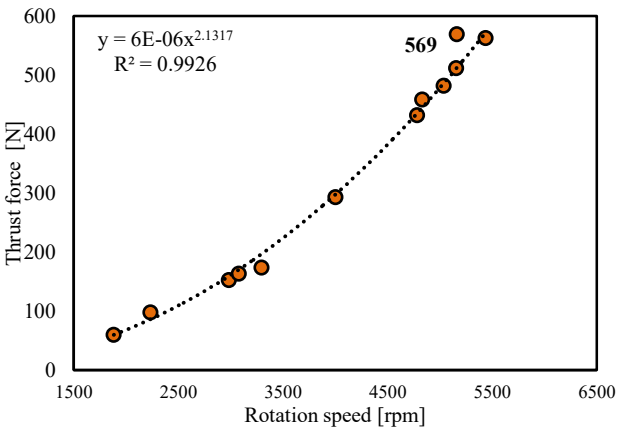

Fig. 31. Corrected thrust obtained for the Falcon 32/13 propeller as a function of crankshaft rotational speed

The Falcon 32/13 three-blade propeller, made entirely of carbon fiber, weighs 402 g about one third less than the composite Biela 32/14 propeller and one quarter less than the Biela 32/12. Thanks to the high stiffness of carbon fiber, the Falcon 32/13 propeller achieves the highest thrust value (569 N) already at moderate rotational speeds of 5162 rpm, maintaining an efficiency index T/m of 1414 N kg^{-1}. In comparison, the composite propellers from Biela are heavier (547–586 g), and their maximum thrust (524–529 N) is developed at even lower shaft speeds of 4936–5392 rpm. In this case, however, the higher mass reduces their efficiency to 903–958 N kg^{-1}. The advantage of the thicker carbon-glass laminate in the Biela 32/14 is the best cylinder head cooling – the lower rpm and greater inertia of the airflow reduce cylinder temperatures by about 8°C compared to the wooden Fiala propellers.

The data comparison clearly shows that mass determines the specific efficiency (T/m), while the material and blade stiffness dictate the required shaft rotational speeds and the engine's thermal load. Wooden propellers are an excellent choice when minimum weight is essential and high shaft speeds are acceptable. The Falcon carbon fiber propeller offers the best compromise between maximum thrust, mass, and a moderate rpm range. The heavier Biela composite propellers are recommended when reducing noise and cylinder head temperatures is the priority, even at the expense of a lower T/m index. The quantitative comparison introduced here fills a gap by demonstrating a clear relationship between geometry, material, mass, and the actual performance of each tested propeller.

The diameter of the Falcon propeller is 0.813 m, so the disk area is 0.519 m². Using the momentum equation:

$$v = \sqrt{\frac{T}{2\rho A}} \tag{20}$$

At ρ = 1.2 kg m^{-3}, the jet velocity is 21.4 m s^{-1}. The ideal power $P_i = \frac{1}{2}Tv$ is 6.1 kW. With typical data for three-blade propellers of this size – static efficiency 0.55 ±0.05 – the required shaft power is 11.1 ±1.0 kW. According to the manufacturer, the 3W 275 XI engine delivers 20–22 kW at 7000 rpm; therefore, at the rotational speed of 5162 rpm corresponding to a thrust of 569 N, there remains a 45% power reserve.

A number of factors explain why the Fiala 30/18 propeller requires as much as 6171 rpm, while the Biela 32/14 propeller needs only 4936 rpm. This is mainly related to the number of blades: each additional blade increases induced and mass drag, so the three-blade Falcon and Biela propellers reach their target thrust at around 5100 rpm, whereas the lighter two-blade Fiala propellers require higher rotational speeds to generate the same thrust. The total pitch also influences these parameters. The Biela 32/14 has a pitch of 14″, greater than the 13″ of the Falcon and the 12″ of the Biela 32/12; therefore, at the same engine torque, its shaft speed is significantly lower. Another factor is material stiffness. The wooden blades of the Fiala propellers flex under heavy load, reducing the angle of attack, which necessitates higher shaft speeds, while the Falcon carbon fiber propeller maintains its angle at lower shaft speeds. Another significant factor is inertia. The heaviest propeller, the Biela 32/14 (586 g), exhibits the highest moment of inertia, which stabilizes the shaft rotational speed at a lower level.

3.4. Limitations of the test stand and research methodology

The test stand has certain limitations concerning the results obtained, which must always be precisely defined during various tests. These primarily stem from the engine's thermal inertia during tests and changes in external conditions. Rapid changes in the temperature of the heads and the main engine mechanism after conducting a test run make it difficult to maintain stable measurement conditions. Establishing initial test conditions, namely temperature and humidity, is essential for drawing correct conclusions. Another limitation is the very movement of the frame's moving parts along with the engine. As a result of small clearances, this error is relatively minor, but it exists, and attention must always be paid to these initial test conditions. Therefore, it is always worthwhile to perform an experimental verification of the correction coefficient for each engine mounted. The measurement error is also significantly influenced by the head temperature, which constitutes a thermal load on the main mechanism. However, in this instance, the propeller profile and airflow determine the temperature achieved. Consequently, thrust results should always be checked against head temperatures, and conclusions subsequently drawn.

4. Conclusion

The research carried out confirmed that the angle of attack and profile of the blades, as well as the number of propeller blades, have a significant impact on the performance parameters achieved by the 3W 275 XI B2 CS two-stroke aero engine. Changes in propeller geometry translate directly into the thrust generated, crankshaft rotational speed, and also the engine's thermal conditions. It was also observed that the mass and structural rigidity of the propeller can determine the operational dynamics of the power unit throughout its full rotational speed range.

– The highest thrust value (569 N) was recorded using the Falcon 32/13 3-blade propeller (with a mass of 402.5 g), simultaneously achieving a shaft rotational speed of approximately 5436 rpm. This indicates the high aerodynamic efficiency of this variant and favourable head cooling conditions in the higher shaft rotational speed range of the piston aero engine.
– The 2-blade propellers (Fiala 30/18, 32/16, 32/18) achieved maximum thrust values ranging from 460 N to 498 N, depending on configuration and rotational speed (up to approx. 6000 rpm). Conversely, the 3-blade propellers (Biela 32/12, 32/14, Falcon 32/13) achieved higher thrust values – even exceeding 569 N – but in some cases, this required greater drive torque and resulted in an unfavourable temperature distribution.
– The greatest thermal load on the engine was observed during the initial phase of operation with the Fiala 32/18 propeller at medium rotational speeds (3000–4000 rpm), when the engine had to overcome significant aerodynamic drag from the propeller with an insufficiently strong cooling airflow.
– The mass of individual propellers ranged from 273 g (Fiala 30/18) to 586 g (Biela 32/14), representing a difference of as much as 30%–40% between individual 3-blade models. Self-mass primarily affects the system's inertia and the dynamic loads on the engine. Lighter propellers (e.g., Falcon 32/13) enabled faster attainment of higher shaft rotational speeds and thrust values with relatively low engine head temperatures.
– The tests demonstrated that there is no universal propeller that provides maximum thrust with simultaneously low thermal load for every small piston combustion engine. The selection of propeller configuration (profile, angle of attack, number of blades) must be verified each time through bench tests. Differences in rotational speed (even 300–500 rpm) or propeller mass (even 200 g) can determine the operational efficiency of the entire power unit and engine durability.

The presented results indicate that engine bench tests with varying propeller configurations enable the identification of a compromise between the thrust obtained, thermal load, and the engine shaft's rotational speed characteristics. This allows the power unit parameters to be appropriately adapted to operational assumptions – e.g., for aircraft flights at high speeds and the potential to achieve a higher aircraft operational ceiling. In the long term, the results of this research are significant for the safety and reliability of light aircraft, particularly in the context of extending engine service life through correct cooling conditions and optimal operation within selected shaft rotational speed ranges. An appropriately selected and relatively high thrust achieved by the power unit, and its appropriate distribution relative to shaft rotational speeds, allows for high flight dynamics. This is particularly important in combat or aerobatic flights of small aircraft. It should be remembered that the results for maximum thrust and temperature values may vary slightly between individual tests; this is mainly related to the test execution procedure. This primarily concerns the timing of the measurement: whether it is taken after the engine has warmed up or during its initial operational phase. Therefore, measurements should always be carried out under the same conditions for each propeller variant.

Acknowledgements

The paper was elaborated based on data obtained during the research carried out as part of the following project: A multi-sensor platform for imaging and detecting threats occurring in areas with high dynamics of changes in environmental conditions – DOB-SZAFIR/01/ B/038/04/2021 – funded by the National Centre for Research and Development, which was implemented at the Military University of Technology. Special thanks go to the staff of the Laboratory of Air Professions, Mr J. Milczarczyk, Mr D. Czekaj, and Mr D. Borcuch, for their technical support.

Bibliography

[1] Balicki W. Potrzeby i sposoby diagnozowania lotniczych silników turbinowych (in Polish). Prace Instytutu Lotnictwa. 2009;4(199):109-116. https://yadda.icm.edu.pl/baztech/element/bwmeta1.element.baztech-article-BSW4-0089-0014/c/Balicki_potrzeby_PIL_199_2009.pdf

[2] Błachnio J, Chalimoniuk M, Nidzgorska A. Selected applications of composites in the military. J Konbin. 2023;53(4):191-210. https://doi.org/10.5604/01.3001.0054.1761

[3] Bonisławski A, Juchniewicz M, Piotrowski R. Projekt techniczny i budowa platformy latającej typu quadrocopter (in Polish). Pomiary Automatyka Robotyka. 2014;91-97.

[4] Dunna MH, Tinetti AF, Nark DM. Open rotor noise prediction using the time-domain formulations of Farassat. Aeroacoustics. 2015;14(1-2);51-86.

[5] El-Sayed AF. Piston engines and propellers. El-Sayed AF, (ed.). Fundamentals of aircraft and rocket propulsion. Springer. London 2016. https://doi.org/10.1007/978-1-4471-6796-9_4

[6] Federal Aviation Administration. Helicopter flying handbook. Chapter 4. Washington (DC): U.S. Department of Transportation; 2023. Available from: https://www.faa.gov/sites/faa.gov/files/regulations_policies/handbooks_manuals/aviation/helicopter_flying_handbook/hfh_ch04.pdf

[7] Garner WB. Model airplane propellers. Air-Propeller Research 2009.

[8] Gosiewski Z, Ołdziej D, Słowik M. Identyfikacja modelu dynamicznego napędu dla śmigłowca czterowirnikowego (in Polish). Prace Instytutu Lotnictwa. 2009;7(202):36-50. https://yadda.icm.edu.pl/baztech/element/bwmeta1.element.baztech-article-BSW4-0092-0005/c/Gosiewski_identyfikacja_PIL_202_2009.pdf

[9] Kachel S, Okoń T, Frant M, Majcher M. Project for a reconnaissance unmanned aerial vehicle. J Konbin. 2022;52(3):187-200. https://doi.org/10.2478/jok-2022-0032

[10] Kuźniar M. Wielokryterialna ocena doboru napędów lotniczych nowej generacji z wykorzystaniem metod energetycznych [doctoral dissertation]. Rzeszów University of Technology. Rzeszow 2020.

[11] Miloudi M, Medles K, Tilmatine A, Brahami M, Dascalescu L. Modeling and optimization of a propeller-type tribocharger for granular materials. J Electrostat. 2011;69(6).

[12] Pawełczyk M, Bibik P. Wykorzystanie nowoczesnych narzędzi inżynierskich w projektowaniu bezzałogowego wiropłata czterowirnikowego (in Polish). Prace Instytutu Lotnictwa. 2013;3-4(230-231):103-110.

[13] Piłat M, Kaznowska A. Wielopłatowe, bezprzegubowe śmigło ogonowe do śmigłowca klasy lekkiej (in Polish). Prace Instytutu Lotnictwa. 2009;201:111-120.

[14] Roman K. Śmigłowcowe eksperymentalne – latające laboratoria na bazie śmigłowca IS-2 (in Polish). Prace Instytutu Lotnictwa. 2008;3-4:194-195.

[15] Sabak R. Zespoły napędowe bezzałogowych statków powietrznych (in Polish). Prace Instytutu Lotnictwa. 2011;213:185-188.

[16] Tiruvenkadam N, Shankar SG, Kumar PM, Gowtham S. Investigation of structural and thermal analysis of drone propeller materials. J Phys Conf Ser. 2024;2925(1):012002. https://doi.org/10.1088/1742-6596/2925/1/012002

[17] Wróblewski P, Bratkowski P, Borcuch D, Kiszkowiak Ł. Prototype test stand for an aircraft piston engine for testing propeller profiles and advanced materials. Combustion Engines. 2025;201(2):165-175. https://doi.org/10.19206/CE-204319

[18] Żmudziński Z. Kompozyty i inne materiały stosowane w konstrukcjach lotniczych (in Polish). Sprawozdanie ITWL 5134/50. Instytut Techniczny Wojsk Lotniczych. Warsaw 2009.

Prof. Piotr Wróblewski, DSc., DEng. – Faculty of Engineering, University of Technology and Economics H. Chodkowska in Warsaw; Faculty of Mechatronics, Armament and Aerospace, Military University of Technology, Poland.
e-mail: *piotr.wroblewski@uth.edu.pl*

Przemysław Bratkowski, MSc., Eng. – Faculty of Engineering, University of Technology and Economics H. Chodkowska in Warsaw; Faculty of Mechatronics, Armament and Aerospace, Military University of Technology, Poland.
e-mail: *przemyslaw.bratkowski@uth.edu.pl*

Prof. Stanisław Kachel, DSc., DEng. – Faculty of Mechatronics, Armament and Aerospace, Military University of Technology, Poland.
e-mail: *stanislaw.kachel@wat.edu.pl*

Article citation info:
Chojnowski J, Polak F. Potential for the use of SAF in internal combustion piston engines. Combustion Engines. 2026;204(1):132-143. https://doi.org/10.19206/CE-210466

Janusz CHOJNOWSKI
Filip POLAK

Combustion Engines
Polish Scientific Society of Combustion Engines

Potential for the use of SAF in internal combustion piston engines

ARTICLE INFO

Received: 11 June 2025
Revised: 5 September 2025
Accepted: 8 September 2025
Available online: 24 September 2025

This review examines the feasibility of using Sustainable Aviation Fuels (SAFs) in internal combustion piston engines. It analyzes major SAF types and pathways, combustion and emission characteristics, material compatibility, certification frameworks, and economic considerations. The findings confirm that paraffinic SAFs (e.g. HEFA, FT) are suitable drop-in fuels for compression-ignition engines, offering lower emissions and compatibility with existing systems. Spark-ignition engines remain limited by octane requirements. The review concludes that SAF can significantly reduce environmental impact in piston-engine applications, though full deployment is constrained by cost, certification, and fuel availability.

Key words: *SAF, piston engines, HEFA, fuel compatibility, emissions*

1. Introduction

Sustainable Aviation Fuel (SAF) refers to non-petroleum-derived jet fuel components that can be blended with conventional jet fuel (Jet A/A-1) to reduce life-cycle carbon emissions [37]. While SAF has been developed primarily for turbine engines in aviation, there is growing interest in its applicability to internal combustion piston engines across aviation, automotive, and marine sectors. The main question is whether and how these renewable fuels can replace or supplement conventional gasoline, diesel, and avgas in piston engines without compromising performance or safety. This review addresses the feasibility of using SAF in piston engines, examining combustion characteristics, material compatibility, emissions, regulatory standards, and current developments. The goal is to summarize current knowledge and identify the pros and cons of SAF utilization in various piston-engine applications. In this review, we extend the SAF concept to include analogous renewable fuels for piston engines (such as renewable diesel and high-octane biofuels), recognizing that "SAF" in the strict sense usually refers to turbine fuel. The scope covers all internal combustion piston engines – spark-ignition (gasoline/avgas) and compression-ignition (diesel/jet fuel).

2. Overview of sustainable aviation fuels (SAF)

2.1. Definition and scope

SAF is defined by the aviation industry as a "drop-in" replacement for fossil jet fuel that meets the same technical specifications (after blending) but is produced from sustainable feedstocks [37]. SAF is chemically similar to kerosene (containing the same hydrocarbon range) so that, once blended and certified under standards like ASTM D1655 [3], it can be used in existing fuel systems and engines without modification. Importantly, to be recognized under ICAO's CORSIA program, SAF must also meet sustainability criteria (e.g. at least 10% life-cycle carbon intensity reduction and sustainable feedstock sourcing) [21].

Multiple production pathways for SAF have been approved or are under development, each yielding a fuel composed mainly of paraffinic hydrocarbons (alkanes) with properties akin to jet fuel [20, 40]. Table 1 summarizes the major pathways.

Table 1. Certified SAF pathways under ASTM D7566 (Annexes A1–A7) and their blend limits [5]

SAF type	Description
HEFA-SPK [1] Hydroprocessed Esters & Fatty Acids Synthetic Paraffinic Kerosene	Produced by hydrotreating vegetable oils, used cooking oil, animal fats, and other lipids to yield straight-chain and isoparaffinic hydrocarbons. Approved in 2011 with up to 50% blend limit [33]. HEFA is the most mature and widely used SAF pathway, chemically similar to hydrotreated vegetable oil (HVO) diesel.
FT-SPK [17] Fischer–Tropsch Synthetic Paraffinic Kerosene	Gasification of biomass or solid waste to syngas, followed by Fischer–Tropsch synthesis to produce hydrocarbons. Approved in 2009, 50% blend limit. FT-SPK contains zero aromatics and sulfur. An FT variant with added aromatics (FT-SPK/A) was approved in 2015 (50% limit) to provide aromatics for seal compatibility.
ATJ-SPK [24] Alcohol-to-Jet Synthetic Paraffinic Kerosene	Converts alcohols (such as isobutanol or ethanol from biomass fermentation) into jet-range hydrocarbons via dehydration, oligomerization, and hydrogenation. Approved in 2016 (isobutanol-derived) and 2018 (ethanol-derived) with up to 50% blend.
HFS-SIP [24] Synthetic Iso-Paraffins from Fermented Sugars	Produces a specific hydrocarbon (farnesane) from sugar via microbial fermentation and hydrogenation. Approved 2014 with a 10% blend limit.
CHJ (CH-SK) [36] Catalytic Hydrothermolysis Jet	Uses catalytic hydrothermolysis of fats/oils (a process akin to hydrothermal liquefaction) to produce jet fuel. Approved 2020, 50% blend limit.
HC-HEFA [17] Hydrocarbon-Hydroprocessed EFA from algae	A pathway using algal oils (e.g. Botryococcus braunii) to produce hydrocarbons. Approved 2020 with a 10% blend limit.

In addition to these neat blending components, ASTM allows limited co-processing of biogenic oils in petroleum refineries (up to 5% biogenic content in jet or diesel fuel) as an early route to introduce sustainable content.

2.2. Production technologies, feedstocks, distribution

SAF feedstocks range from lipid materials (e.g. waste cooking oil, tallow, camelina, or jatropha oil) for HEFA, to cellulosic biomass and municipal solid waste for gasification-to-FT pathways, to sugars or alcohols from corn, sugarcane, or lignocellulosic biomass for ATJ routes. Emerging routes also include Power-to-Liquid fuels using CO_2 and renewable hydrogen [24]. The flexibility of feedstocks and processes is a key advantage of SAF – it allows production of fuel from various waste streams or renewable resources, potentially offering 50–85% net greenhouse gas reduction compared to fossil jet fuel. However, different pathways yield fuels with different chemical compositions (e.g. all-paraffinic vs some cyclic content), which influences their compatibility and performance in engines. It should be noted that the "drop-in" requirement currently means SAF is used in blends (up to 50%) with conventional fuel to meet all specifications; neat 100% SAF is not yet certified for routine use in aviation due to certain properties discussed later [5] (Fig. 1).

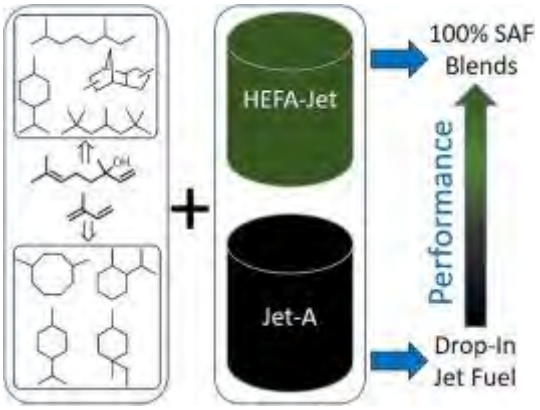

Fig. 1. Logistic path for SAF [29]

Prior to utilization in aviation applications, SAF must be blended with conventional Jet A fuel in accordance with ASTM D1655 certification standards [5]. In the case of co-processing within existing petroleum refineries, the resultant fuel can be seamlessly integrated into the current fuel supply chain, allowing for distribution via established infrastructure such as pipelines, fuel terminals, and road transport to end-user facilities, including airports. Similarly, SAF produced at standalone biorefineries is expected to be blended with Jet A at downstream fuel terminals before being conveyed to airports through traditional logistics channels, such as pipelines, tanker trucks, or barges (Fig. 2). Blending may occur either in proximity to or at a significant distance from the point of final use, depending on logistical efficiency. Importantly, fuel handling operations at airports remain unaffected, as only pre-certified, blended fuel is delivered through conventional means, thereby avoiding the need for on-site blending infrastructure, which would incur additional operational, personnel, and insurance costs. Consequently, upstream certification remains the industry-preferred approach to ensure compliance with stringent quality specifications [29].

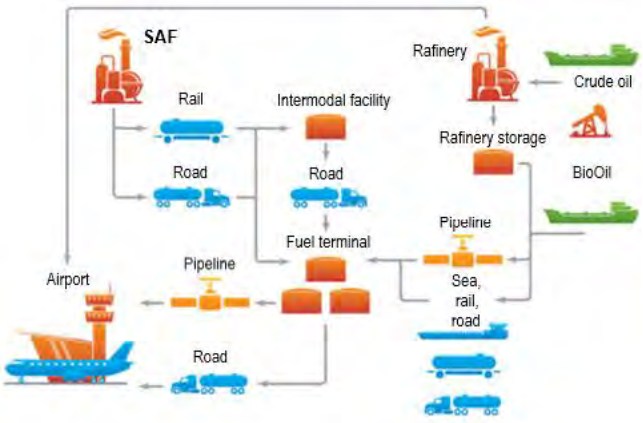

Fig. 2. Logistic path for SAF [29]

In land-based applications – particularly within the transport and defense sectors – comparable logistical frameworks can be implemented. Alternative fuels analogous to SAF, such as Hydrotreated Vegetable Oil (HVO), may be integrated into the existing diesel distribution infrastructure, including bulk storage facilities, fueling stations, and fleet refueling points, with only minimal modifications required [25]. Nonetheless, large-scale deployment remains dependent on regional regulatory approvals, the compatibility of storage tank materials, and the establishment of reliable fuel traceability systems to uphold certification standards. As in the aviation sector, centralized upstream blending and certification prior to distribution is considered the most effective strategy to facilitate supply chain integration and reduce implementation costs.

2.3. Current usage and trends

SAF usage in aviation, while still limited in volume, has been steadily increasing. Over 360,000 commercial flights have used SAF blends since 2021, at dozens of airports worldwide. Typical blend ratios are 30% or below in current airline trials, although the maximum allowed is generally 50%. Several national and industry initiatives (such as the U.S. SAF Grand Challenge and EU ReFuelEU mandate) aim to scale up SAF production to billions of gallons per year in the 2030–2050 timeframe (Fig. 3) [33].

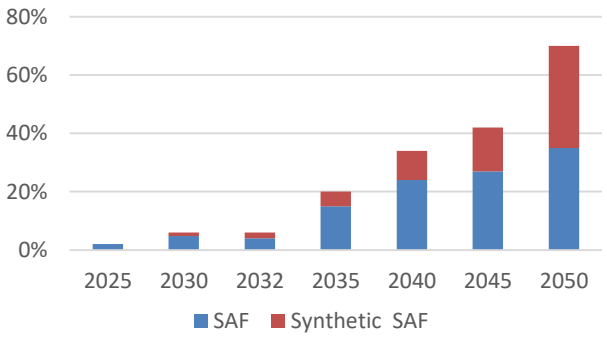

Fig. 3. Regulatory trajectory of minimum SAF blend mandates to support EU net-zero emissions target by 2050 [33]

For piston engines in aviation, the term "SAF" has not been applied in the same way – small aircraft mostly use avgas (a high-octane gasoline with lead) or, in some cases, jet fuel for diesel piston engines. Unleaded avgas formulations are being developed to eliminate lead, but these are typically petroleum-based and do not meet the sustainability criteria of SAF. Similarly, in road transport, "renewable diesel" (Hydrotreated Vegetable Oil – HVO) and other biofuels are being used as drop-in fuels for diesel engines, achieving significant CO_2 reduction. These renewable fuels are analogous to SAF and often come from the same production plants (e.g. a HEFA refinery can produce jet fuel and diesel cuts from the same process) [20]. In summary, SAF in the broad sense (renewable drop-in fuel) is already in use for diesel piston engines in some regions, and the technology and supply chains developed for aviation SAF can potentially benefit ground and marine fuels as well.

The projected fuel consumption and associated CO_2 emissions for international aviation between 2005 and 2050, as presented by ICAO, incorporate anticipated improvements in aircraft technology and air traffic management (ATM), as well as the potential deployment of sustainable aviation fuels (SAFs). These projections are illustrated in Fig. 4.

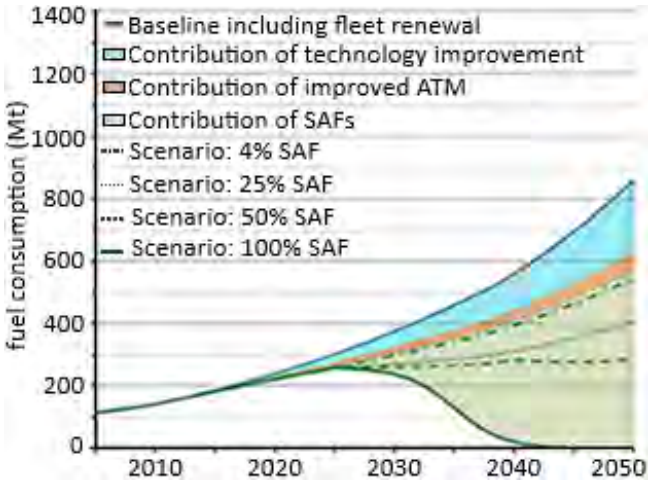

Fig. 4. Projected fuel use for international aviation according to the ICAO [9, 38]

2.4. Fuel standards and certification

2.4.1. Aviation fuel standards

The use of any fuel in certified aircraft engines is tightly governed by specifications and regulations. Jet fuel for turbines (and Diesel cycle piston aircraft) must meet DEF STAN 91-091 standard in Europe or ASTM D1655 (for Jet A/A-1) standard in the USA. SAF components are certified, which is effectively a supplement standard – once a SAF component is blended within allowed limits and meets needed requirements, it is re-identified as Jet A/A-1 fuel [20]. There are currently seven certified SAF pathways as described earlier, most with a 50% maximum blend limit. The ASTM committee is continuously reviewing data to potentially allow higher blends or new pathways; for instance, the ATJ blend limit was initially 30% and later raised to 50% after further testing. A major focus now is approving 100% SAF for future use – this will likely entail either a new ASTM specification or further annexes that include synthetic aromatic fractions to ensure a fully drop-in formulation [40]. Regulators like FAA, EASA, and ICAO are closely involved in this process through initiatives such as CAAFI (Commercial Aviation Alternative Fuels Initiative) and various demonstration programs.

For aviation spark-ignition piston engines, the relevant standard is ASTM D910 (the spec for 100LL leaded avgas) and ASTM D7547 (spec for unleaded avgas grades like UL91/UL94) [4, 6]. So far, no bio-derived avgas is certified under these standards. The unleaded avgas that is emerging (e.g., G100UL developed by GAMI, and Shell's proposed UL100) is still synthesized from petroleum in order to meet the strict volatility and high-octane requirements. These fuels aim to eliminate lead but are not necessarily lower-carbon. It's conceivable that in the future, an ASTM D7547 fuel could be formulated with some synthetic components (e.g. isopentane or ethanol-derived high-octane compounds) to be partially renewable. Such a fuel would need to go through engine testing and certification via FAA/EASA processes (e.g. Supplemental Type Certificates for each engine model, as G100UL is doing). The FAA has a broad initiative called EAGLE (Eliminate Aviation Gasoline Lead Emissions), targeting leaded avgas replacement by 2030 [16], which includes streamlining the testing of candidate unleaded fuels. While EAGLE's primary goal is lead removal, not directly carbon reduction, it could open the door to innovative fuel formulations, potentially including bio-based components.

2.4.2. Ground transport fuel standards

In the automotive world, standards are more accommodating to renewable drop-in fuels as long as they meet chemical property requirements. For diesel fuel, many countries allow a certain volume of biodiesel (FAME) blending (e.g. up to 7% in Europe's EN590 diesel). Paraffinic renewable diesel (HVO) is actually covered under a separate standard EN 15940 in Europe, which sets specifications for synthesized or hydrotreated paraffinic diesel fuels that contain essentially no aromatics [11].

Table 2. Key property ranges of EN 15940, EN 590, and ASTM D975 compliant fuel [11]

Parameter	EN 15940	EN 590:2013	ASTM D975
Cetane number	≥ 70.0	≥ 51.0	≥ 40
Density at 15°C [kg/m³]	765–800	820–845	–
Viscosity at 40°C [mm²/s]	2.00–4.50	2.00–4.50	1.9–4.1
Hydrocarbons (% m/m)	–	–	≤ 35
Polyaromatic	–	≤ 8	–
Aromatic	≤ 1.0	–	–
Olefin	≤ 0.1	–	–
Sulfur content [mg/kg]	≤ 5.0	≤ 10.0	≤ 15
Flash point [°C]	≥ 55	≥ 55	≥ 52
Lubricity HFRR at 60°C [µm]	≤ 460*	≤ 460	≤ 520
95% by volume distils at [°C]	≤ 360	≤ 360	282–338
CFPP [°C]	≤ –34	≤ –34	–
Ash content [% m/m]	≤ 0.01	≤ 0.01	≤ 0.01
Total impurity content [mg/kg]	≤ 24	≤ 24	–

* Including lubricating additives for use in vehicles approved for driving on the fuel according to the standard. CFPP: cold filter plugging point; HFRR: high frequency reciprocating rig.

EN15940 fuels (which include HVO and GTL) can be used in vehicles approved for them; notably, several major truck manufacturers (Volvo, Scania, Daimler) have endorsed HVO fuel for their engines with no changes required. In the US, ASTM D975 (diesel spec) doesn't distinguish HVO – if the fuel meets D975 properties, it can be used. Renewable diesel is fungible with fossil diesel, so it often just goes into the general diesel pool. Gasoline (EN228 or ASTM D4814) currently allows up to 10% ethanol; high-level ethanol or other high-octane components require special tuning but could be considered "alternative fuel" rather than drop-in.

2.4.3. Marine fuel standards

Marine fuels are governed by ISO 8217, which primarily covers heavy fuel oil and marine distillates [22]. There is no widely adopted standard for biofuels in marine use yet, but ISO 8217:2017 includes a mention that up to 7% FAME biodiesel may be blended into marine distillate (DMA) as long as it meets the requirements (similar to on-road diesel). Trials are being conducted with HVO in marine engines (replacing marine gas oil) as discussed in Section 8. For now, any high percentage of biofuel for marine use is handled case-by-case with engine manufacturer guidance. The International Maritime Organization (IMO) has set targets for GHG reduction in shipping, which is encouraging experimentation with drop-in biofuels as well as novel fuels like methanol, ammonia, etc. Within that, HVO is attractive for its plug-and-play nature (no sulfur, cleaner burn, usable in existing diesel ship engines), but availability and cost are limiting factors [30].

2.4.4. Certification and regulatory approvals

Whether in air, road, or sea, introducing a new fuel requires ensuring safety and compatibility. In aviation, this is formalized through fuel approval (ASTM specs) and, in many cases, additional certification by the airframe/engine manufacturer and regulators. For example, when SAF blends were first used on commercial flights, OEMs like Boeing and Airbus had issued technical approvals and worked with airlines on demonstration flights [8]. Now, any engine certified for Jet A can use SAF blends up to the approved limit without further modifications or approvals [40], since the fuel is considered Jet A once it meets D1655. For piston aircraft using Jet-A (diesel) engines, the same logic applies – those engines can run on SAF blends as long as the fuel meets Jet A specs. In contrast, if someone wanted to use an unleaded automotive gasoline in an aircraft piston engine, they need an STC (Supplemental Type Certificate) because it's a different spec fuel (this has been done for many smaller aircraft to use automotive gasoline). Similarly, using a fuel outside of spec in any certified engine typically violates warranty or regulations unless explicit approval is given.

Regulatory bodies are actively supporting SAF: ICAO has incorporated SAF into its policies for reducing aviation emissions (CORSIA framework for accounting emissions reductions from SAF). FAA and EASA fund research and test programs – for instance, FAA's CLEEN program and ASCENT Center have projects on alternative fuels, and EASA has participated in tests of unleaded avgas and SAF sustainability assessments. The close collaboration between standards organizations (ASTM), industry, and regulators aims to ensure that, as SAF use expands, it does so safely. In ground transport, regulations tend to be fuel-neutral as long as emission standards are met, so introducing renewable fuels is more about meeting fuel specs and sometimes incentives (e.g. renewable fuel standards, CO_2 fleet averaging credits for automakers, etc.) [21].

Standards like ASTM D7566 (for SAF jet fuel) and EN15940 (for renewable diesel) provide frameworks to certify and use these fuels in piston engines where applicable. The certification process ensures that engines using SAF perform equivalently to those using conventional fuels. Ongoing regulatory efforts (FAA EAGLE, CORSIA, EU mandates) are creating an environment that encourages the adoption of SAF and even demands it in some cases (e.g. EU will require increasing SAF use in aviation over time. For widespread use in piston engines, especially in aviation, updated standards for a high-octane renewable avgas may be needed in the future [24].

3. Performance in piston engines

3.1. CI and SI combustion

The feasibility of using SAF in piston engines depends on the combustion characteristics of the fuel relative to conventional fuels (gasoline, diesel, or avgas). Key considerations include ignition quality (cetane or octane rating), energy content, and how the fuel behaves across operating conditions e.g. cold start, altitude, resistance to aging processes etc.

Compression-Ignition (Diesel Cycle) piston engines – whether in aircraft or ground vehicles – are generally more compatible with SAF because SAF blends are formulated to mimic kerosene/diesel fuel. SAF like HEFA-SPK consists almost entirely of normal- and iso-paraffins, giving it a very high cetane number (typically 70 – cetane for neat HEFA, versus ~45–55 for fossil diesel) [12, 20]. This high cetane means SAF ignites readily in compression ignition, often leading to smoother combustion and potentially a shorter ignition delay. Studies in diesel engines have shown that pure HVO (a fuel equivalent to HEFA) can actually slightly increase or maintain engine power output relative to conventional diesel. For example, one experimental study found that a tractor engine running on 100% HVO delivered about the same or slightly higher peak torque and power than on fossil diesel [34]. Another engine test reported HVO yielding a small (~5%) decrease in power in a specific case, but that engine also saw significant emissions reductions (e.g. NO_x down ~12%, CO down ~14%) when using HVO [34]. Generally, because HVO/HEFA fuels have slightly lower density (≈ 6–7% lower than diesel) but similar energy per mass, an engine's volumetric fuel flow might need to increase by a few percent to deliver equal power. Modern fuel injection systems can often accommodate this automatically via longer injection duration if operating on a volumetric basis. In terms of operability, paraffinic SAF fuels have excellent low-temperature performance (high cetane and low freeze point), which is beneficial for high-altitude operation. In fact, a study on an aviation diesel (heavy-fuel) piston engine found that at

5,500 m altitude, the power loss was marginally less with SAF than with normal diesel – power drop of ~22.1% on SAF vs 23.4% on diesel (relative to sea level performance) [39]. This suggests SAF may have slightly better high-altitude combustion characteristics, possibly due to its very low aromatics improving fuel evaporation and mixing at low air densities. Overall, SAF and RP-3 fuels show comparable combustion trends to conventional diesel, with minor deviations in peak pressure and pressure rise timing that become more evident at lower engine loads. This suggests good compatibility of SAF for compression ignition engines across a range of operating conditions, as shown in Fig. 5.

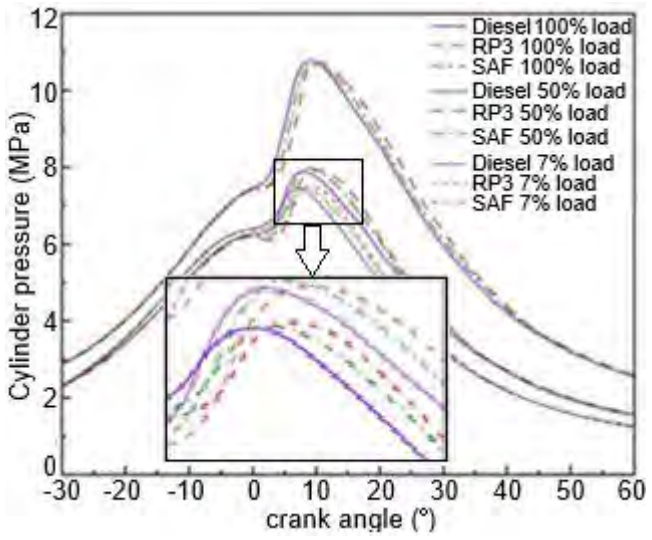

Fig. 5. In-cylinder pressure profiles for diesel, RP-3, and SAF fuels at varying engine loads [39]

For Spark-Ignition Engines (Otto Cycle) that require gasoline or avgas (typically small aircraft and most automobiles), the use of SAF presents a different challenge. Neat SAF as produced today is mostly a kerosene-type fuel with high cetane but low octane – not suitable for spark-ignition, which needs high octane to avoid knock. Aviation gasoline (100LL) has an octane rating over 100 (MON), whereas kerosene's octane rating would be far below that (roughly 20–30 octane if measured as gasoline). Therefore, direct use of SAF (as kerosene) in a gasoline engine is not feasible without engine modifications (e.g. to a compression-ignition conversion or spark-assisted diesel cycle). However, there are efforts to create high-octane sustainable fuels. One approach is to produce synthetic gasoline or bio-avgas via processes like Fischer–Tropsch (which can output gasoline-range hydrocarbons) or other bio-refineries. These fuels are not yet commonly called "SAF" but rather "renewable gasoline." For example, there are demonstration fuels such as isopentane or iso-octane made from bio-feedstocks that could serve in high-compression engines. Another approach for aviation is to modify piston aircraft engines to use existing SAF (jet fuel): this is already done in the form of diesel aircraft engines (e.g. Austro Engine AE300, Continental CD-155), which are certified to run on Jet A fuel. Those engines could likely run on SAF-blend Jet A just as turbine engines do, since from the engine's perspective, the fuel meets the same ASTM D1655 spec. Indeed, any piston engine certified for Jet A can use blended SAF without issues [37]. For legacy spark-ignition aircraft engines that rely on leaded avgas for octane, the transition to a sustainable fuel is more complex. Unleaded avgas alternatives (UL91, UL94) are petroleum-derived and only meet lower-octane requirements, suitable for ~70% of the fleet but not the highest-performance engines [14]. A truly sustainable high-octane avgas would require new fuel formulations (e.g. bio-derived aromatics or high-octane components). This is an area of active research, but no "bio-100LL" has been certified yet. In concept, alcohols like ethanol or isobutanol provide high octane and are renewable, but their other properties (low energy density, high vapor pressure, or freezing point) make them problematic for aircraft use. Thus, in spark engines, SAF use today mostly means using ethanol blends in cars (up to E10/E85, though ethanol is not a drop-in fuel) or using renewable gasoline components as they become available. Another angle is using methane or biogas in piston engines – not "SAF" per se, but sustainable fuel. However, this falls outside the drop-in hydrocarbon focus of SAF and has its own infrastructure needs.

In summary, SAF in piston engines is most straightforward for diesel/jet-fueled engines, where the combustion characteristics of paraffinic SAF (high cetane, clean combustion) are largely beneficial. For spark-ignition applications, significant fuel re-formulation (to increase octane or create new high-octane synthetic components) is required, or alternately, engine technology must shift (e.g. towards compression ignition engines that can use kerosene-type fuels).

3.2. Material compatibility and engine durability

Any alternative fuel must be compatible with the materials (metals, elastomers, plastics) used in fuel systems to avoid leaks, corrosion, or degradation. A critical difference between today's SAF and conventional fuels is the lack of aromatic hydrocarbons in SAF. Conventional gasoline, diesel, and kerosene contain aromatic compounds, which tend to swell certain rubber seals and O-rings (Fig. 6). These seals were often selected assuming the presence of aromatics. Aromatics in fuel are needed to maintain seal swell; without aromatics, some elastomers shrink and harden, leading to fuel leaks or component failures [19]. This is a well-documented issue in aviation: when synthetic paraffinic fuels (FT, HEFA, etc.) were introduced, it was found that O-rings and gaskets in older aircraft could shrink due to the fuel's low aromatic content. For this reason, ASTM D7566 initially limited SAF blending to 50% max – ensuring the final blend still has ~8% or more aromatics (since typical Jet A has ~16–18% aromatics). It was a conservative measure to guarantee seal compatibility. Modern aircraft and engine manufacturers are now addressing this by testing seals in low-aromatic fuel and, where necessary, using fuel-resistant elastomers. Some newer engines and airframes already use materials (like fluoropolymers, fluorosilicone, etc.) that do not depend on aromatics for swelling. Going forward, to enable 100% SAF use, either the fuel will need to include synthetic aromatics or the sealing materials must be qualified to tolerate all-paraffinic

fuels. There are research programs looking at bio-derived aromatics (for example, from lignin or other sources) to add to SAF so that it truly becomes a drop-in replacement even at 100% [7].

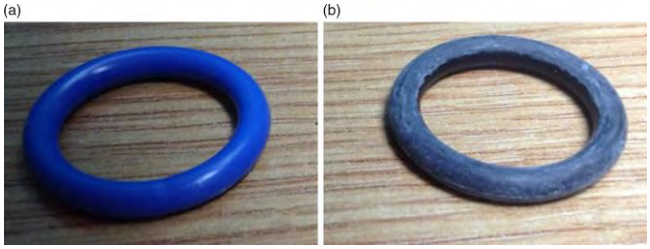

Fig. 6. Swelling and shrinkage behavior of elastomeric O-rings depending on fuel aromatic content: (a) O-ring exposed to conventional fuel containing aromatics (swollen), (b) O-ring exposed to SAF with low aromatic content (shrunken and hardened) [2]

Apart from seal swell, other material issues include lubricity and corrosivity. Ultra-low-sulfur, aromatic-free fuels like neat SAF have lower lubricity – the fuel's ability to lubricate fuel pumps and injectors. In conventional diesel, trace sulfur and aromatics provide natural lubricity; in Jet A, additives are not commonly used for lubricity, so the fuel itself must suffice. It has been noted that no dedicated lubricity additives are currently allowed in jet fuel, so the blend limit of 50% SAF also helps ensure the mix has adequate lubricity [32]. In practice, neat HEFA or FT fuels have to be treated or blended because running 100% could cause excessive wear in fuel pumps due to poor lubricity. For on-road diesel usage, this is mitigated by standards like EN 15940 (paraffinic diesel fuel), which requires a lubricity spec – HVO diesel is added to meet wear scar requirements. Similarly, any future 100% SAF for aviation may require an approved lubricity additive or a small fraction of synthetic aromatic content to protect pumps.

Metal corrosion is generally less of an issue with SAF than with biodiesel or alcohol fuels. SAF is hydrocarbon-based and contains no oxygenates, so it doesn't tend to absorb water or form acidic byproducts that corrode metals. In fact, HEFA and FT fuels are very clean (no sulfur, no olefins), which can reduce corrosive tendencies and deposit formation. Turbine engine tests on SAF have not revealed significant corrosion issues; we expect the same for piston engines – if anything, SAF may burn cleaner and leave fewer deposits that could cause hot corrosion or spark plug fouling. For example, unleaded fuel eliminates lead deposits on spark plugs and valves in aircraft engines, which should reduce maintenance needs (one motivation for unleaded avgas).

Engine wear can be affected by fuel via lubricating properties, deposit formation, and combustion temperature/pressure changes. With SAF, a positive finding is that combustion is generally cleaner, leading to fewer carbon deposits and particulate matter that can contaminate oil or cause abrasion. A study of heavy-fuel (jet-fueled) aircraft piston engines running on 100% HEFA showed dramatically lower particulate output, which implies less soot getting into the oil and less soot loading on cylinder walls [38]. Lower soot and a lack of sulfur also mean the engine oil will remain cleaner and less acidic over time, potentially extending oil life and reducing wear on rings and bearings. On the other hand, if lubricity is not managed, certain high-pressure fuel system components could wear faster with neat SAF. To address this, manufacturers like Bosch, Continental, etc., are testing pumps with SAF. So far, industry reports indicate that a 50% blend of SAF poses no problems – for instance, no hardware changes or accelerated wear have been observed when operating diesel engines or turbines on approved SAF blends. Cummins Inc. has approved its diesel generator engines to run on 100% HVO (renewable diesel) with no modifications, maintaining warranty, after validating performance and durability in testing. This suggests that, at least for compression-ignition designs, the base engine durability is not compromised by the fuel, provided it meets the spec for lubricity and such. In spark-ignition engines, using a fuel that meets the required octane will be critical to prevent knock damage. (For example, using a lower-octane fuel than required can cause pinging and eventually piston damage – a risk if someone tried to fuel a high-performance avgas engine with a kerosene-type SAF improperly.

In summary, material compatibility is a central concern for SAF use in any engine. The primary issue is the absence of aromatics in the current SAF, which impacts seal swelling and lubricity. Solutions under development include new additive packages and updated material standards. Engine durability on SAF appears promising, especially given the cleaner-burning nature of these fuels, but it requires careful attention to ensure fuel systems are appropriately conditioned for low-aromatic content.

3.3. Emission characteristics and environmental impact on the engine

One of the motivations for SAF (and related renewable fuels) is the potential to reduce harmful emissions. There are two facets to consider: regulated engine emissions (CO, HC, NOx, particulates) and life-cycle greenhouse gas emissions. We also consider how those emissions relate to engine health (deposits, wear). Figure 7 below shows the chosen pollutant emissions of HF-APE, RP3 (aviation kerosene surrogate fuel, Jet-A1 fuel substitute on the Chinese market), and Diesel fuel under specific load conditions and typed fuels are shown.

Empirical studies consistently show that paraffinic SAF fuels burn cleaner in terms of particulate matter and carbon monoxide/unburnt hydrocarbon emissions. The absence of aromatics (which tend to produce soot) and the high cetane of SAF lead to more complete combustion. For instance, tests on a heavy-fuel aircraft piston engine running 100% HEFA SAF found marked reductions in CO (Fig. 7a) and unburned HC emissions compared to RP3 jet fuel. Particulate emissions were significantly lower as well – the study reported a ~43% reduction in non-volatile particulate number and ~65% reduction in particulate mass compared to diesel fuel at the same operating condition [38].

These are substantial improvements, indicating a much cleaner exhaust. Similarly, in diesel truck engines, pure HVO has been shown to cut soot (black carbon) emissions by over 60%, with hydrocarbon and CO emissions roughly 40% lower than with petroleum diesel [26]. A comprehensive study by McCaffery et al. (2022) on an off-road engine

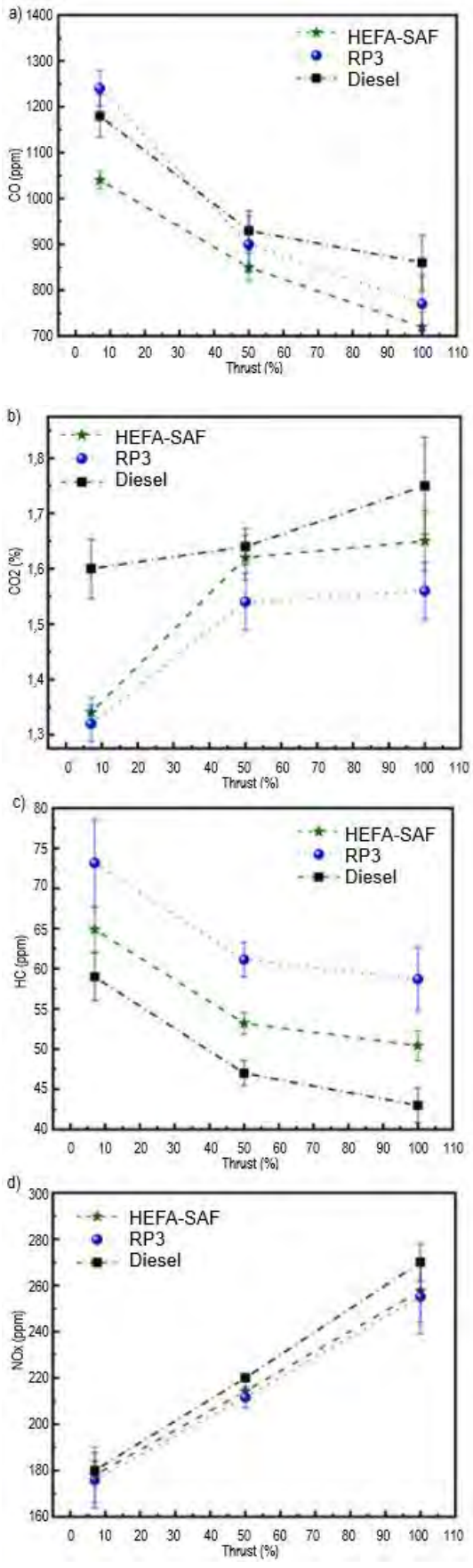

Fig. 7. Emission characteristics of different aviation fuels (HEFA-SAF, RP-3, and Diesel) at various engine thrust levels: (a) carbon monoxide, (b) carbon dioxide, (c) hydrocarbons, and (d) nitrogen oxides [38]

noted statistically significant reductions in NO_x as well (contrary to some earlier concerns that biodiesel can raise NO_x): in their tests, switching to 100% HVO decreased NO_x emissions, whereas blending biodiesel increased NO_x (Fig. 7d). They also observed fewer polycyclic aromatic hydrocarbons (PAHs) in the exhaust and lower toxicity of the particulate matter with HVO. These trends are very positive from an air quality standpoint – less smoke, less CO, and potentially lower NO_x [27].

For spark-ignition engines, if a high-octane sustainable fuel were used, emissions would likely also improve compared to gasoline, because renewable components could be formulated to avoid benzene and other aromatic toxins present in gasoline. One example: ethanol, a bio-fuel, when used in high blends (E85) drastically lowers tailpipe PM and reduces CO (owing to oxygenated fuel and high octane allowing optimized combustion), though it can raise evaporative HC emissions. A fully synthetic high-octane fuel might resemble iso-octane or other clean components, which would burn very cleanly. However, data in this area are sparse until such fuels are tested.

It's worth noting that modern automotive engines have aftertreatment (catalytic converters, particulate filters) that mitigate emissions regardless of fuel. Still, lower engine-out emissions with SAF mean the aftertreatment has less work to do and can be more effective (for example, less soot means diesel particulate filters regenerate less frequently and have longer life).

Tailpipe CO_2 emissions from SAF are similar to fossil fuels on a per-energy basis (because burning a hydrocarbon always produces CO_2). The real climate benefit of SAF comes from the renewable sourcing: the CO_2 released was previously absorbed by the biomass or was waste carbon, so the net life-cycle CO_2 is lower (Fig. 7b). Depending on feedstock and process, SAF can achieve anywhere from ~60% to 85% reduction in net GHG emissions [31]. Some pathways, like ATJ ethanol to jet, can claim up to 94% reduction in ideal cases [14]. These figures assume sustainable practices (e.g. used cooking oil feedstock has very high savings; a crop-based oil might have lower savings if land-use change is accounted). Using SAF in piston engines would confer the same life-cycle CO_2 benefits. For example, a diesel truck fleet running on HVO from waste oils can cut CO_2 emissions by ~80% compared to petro-diesel – this is already being realized in parts of Europe [34]. The environmental benefit for aviation piston engines (most of which currently use fossil avgas or Jet A) would be similarly significant in terms of carbon footprint.

Cleaner combustion with SAF generally means less soot and acidic byproducts, which is beneficial for engine longevity. Lower sulfur in fuel yields virtually zero SO_x emissions, preventing sulfuric acid formation in oil and exhaust. Also, fewer particulate emissions translate to less soot accumulation in oil, which can slow the degradation of oil and reduce engine wear due to abrasive particles. Some studies correlate the use of neat HVO with reduced engine deposits in combustion chambers and fuel injectors (because HVO has no heavy components or ash). That said, one must ensure that the fuel's lubricity is sufficient – if not, fuel pump wear could offset some benefits. In practice, adding a lu-

bricity improver or blending with a few percent of conventional fuel is enough to protect components.

In summary, SAF and related renewable fuels offer a clear emissions advantage: significantly lower local pollutants (PM, CO, HC, and, depending on conditions, NO_x reduction or at least no increase) and a large net reduction in CO_2 emissions when considering the full fuel production cycle. Additionally, by eliminating lead in avgas and sulfur in diesel, they remove two major toxic emissions (lead aerosols and SO_2) that affect health and the environment. For engine health, the cleaner burn of SAF can mean fewer deposits and potentially longer engine life, provided material compatibility issues are managed.

4. Economic and environmental considerations

4.1. Cost and availability

A major barrier to SAF adoption in any sector today is cost. SAF is currently significantly more expensive to produce than fossil fuels – roughly 2–5 times the price of Jet A on a per-gallon basis, depending on feedstock and region. This is due to the smaller scale of production, the cost of feedstocks, and processing costs. As of the mid-2020s, global SAF production is only a tiny fraction of total jet fuel use (on the order of < 1% of aviation fuel). Similar renewable diesel production is also limited relative to global diesel demand, though it's growing with many new plants under construction. There are policy measures (subsidies, tax credits, carbon pricing) that aim to bridge the price gap. For example, the United States' SAF Grand Challenge not only sets volume targets but also seeks to reduce the cost to $3 per gallon by 2030 through R&D and scaling. In road transport, some countries have mandates or incentives for renewable fuel blending (e.g. California's Low Carbon Fuel Standard credits have made renewable diesel economically attractive in that market).

For piston-engine aviation (general aviation aircraft), the market is much smaller and fragmented compared to airlines, so expecting a dedicated SAF for avgas might be economically challenging. The unleaded avgas solutions being rolled out are mostly drop-in from existing refineries. If a fully renewable avgas were developed, it would likely cost even more per liter than SAF for jets due to more complex processing (creating high-octane components efficiently is hard). Thus, in the near term, it is more practical that piston aviation decarbonizes via fleet changes (e.g. more Jet-A diesel engines that can use SAF, or electrification for short-range aircraft) rather than via a unique SAF for spark-ignition engines.

For automotive and marine, renewable fuels can piggyback on the supply being made for aviation. Indeed, refiners often produce a mix of products; for instance, a HEFA plant might output some renewable diesel and some SAF. If policies drive aviation SAF use, that could increase supply and eventually lower costs for all sectors. Conversely, if a lot of renewable diesel is pulled into trucking and shipping, it might compete with SAF for feedstock. There is a feedstock limitation: fats, oils, and greases are in finite supply, so to scale to large volumes, cellulosic and waste feedstocks via FT or ATJ must come online, which is technologically more complex.

From the consumer perspective, unless subsidized, fuel users are cost-sensitive. Airlines can perhaps pass on a small ticket surcharge for using SAF (and justify it by sustainability commitments). Private pilots or trucking companies might be less willing to pay a premium for green fuel unless required or incentivized. Thus, a combination of mandates (like blending requirements) and incentives (credits, lower taxes for SAF) is considered necessary to drive initial adoption.

Comparison of market prices for conventional Jet A-1 and various sustainable aviation fuel production pathways, including FT, AtJ, and E-jet, is shown in Fig. 8. While Jet A-1 maintains relatively stable and lower prices, alternative fuels—particularly electrofuels—show higher and more variable cost trends, reflecting technological maturity, feedstock availability, and scale-up challenges.

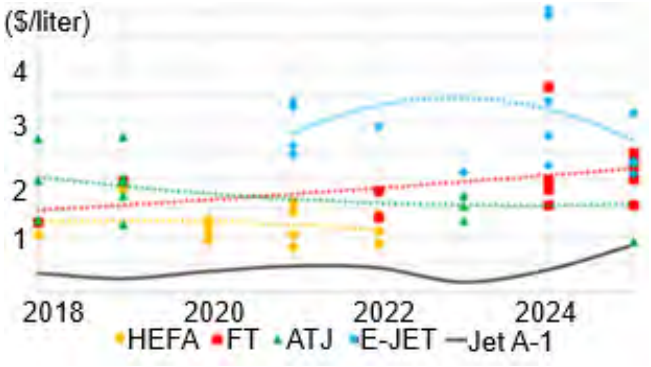

Fig. 8. Historical jet fuel prices (2018–2025) for conventional and alternative aviation fuels [23]

4.2. Environmental and sustainability aspects

The core reason for SAF is to reduce net carbon emissions and mitigate climate impact, but there are other environmental factors: resource use, land use, and air quality. If SAF is made from waste materials, it has a strong sustainability argument (avoiding landfill, utilizing residues). If made from purpose-grown crops, it raises questions about land use change, food vs fuel, etc. Regulatory criteria (like those in CORSIA or EU RED II) attempt to ensure sustainability by excluding high-deforestation risk feedstocks and encouraging advanced (non-food) feedstocks. In an optimistic scenario, SAF could provide up to 65% of the aviation sector's needed CO_2 reduction by 2050 according to industry roadmaps [36] – but only if production is scaled up massively and sustainably. For other sectors, renewable fuels are seen as a bridge or complement to electrification. For example, cars may mostly go electric, but heavy trucks, ships, and planes – sectors hard to electrify – might rely on biofuels/SAF to cut carbon. Using SAF in existing piston engines offers a way to decarbonize the existing fleet. Every piston aircraft or diesel truck that can run on a drop-in biofuel means we reduce emissions without waiting for fleet turnover or expensive modifications. This is a big environmental win in the near to medium term, as new technologies (like electric aircraft or hydrogen fuel cells) will take time to mature and replace legacy engines.

However, one must also consider non-CO_2 emissions and effects. In jet aviation, SAF's reduction in soot may also reduce contrail formation and its climate impact, an

often-cited co-benefit. In piston aviation, contrails are not an issue, but local air quality around airports (particularly piston aircraft emit lead and unburned hydrocarbons) would improve with cleaner fuels. Using unleaded, low-sulfur, low-aromatic fuels in ground vehicles improves urban air quality by cutting pollutants and air toxics (important until the vehicle fleet is fully zero-emission). Another consideration is that SAF often has slightly different density/energy content, which can affect range. Neat paraffinic SAF is a bit less dense (e.g. HEFA jet fuel might have ~3–4% lower energy per liter than standard Jet A due to no aromatics). In aircraft, that could translate to a small range reduction if tanks are volume-limited – though if burn is more efficient, the difference is minor. In practice, at blend levels of 50% or less, the effect is negligible. For HVO in diesel cars, drivers might observe a few percent higher volumetric fuel consumption, but again, very small differences in real use.

To weigh the economic and environmental aspects: on the pro side, SAF enables the use of existing engines and infrastructure while achieving large GHG reductions and cleaner emissions – essentially a drop-in decarbonization solution. It can be implemented incrementally (blending) without waiting for new technology. On the con side, current SAF supply is limited and expensive; relying on bio-based fuels alone may face feedstock constraints, and without careful sustainability governance, some pathways could have negative externalities (e.g. inducing palm oil expansion, etc.). Thus, SAF is part of a broader strategy – especially vital for aviation and long-haul transport – but not a silver bullet to replace all fossil fuel usage unless coupled with massive investment and sustainable feedstock sourcing.

5. Current studies and test campaigns

5.1. Aviation piston engine

Research and demonstration projects are actively exploring SAF use in various piston engine contexts.

Diamond Aircraft Industries announced in 2023 a dedicated SAF test program for their Austro Engine line of jet-fuel piston engines (turbocharged compression-ignition engines used in aircraft like the DA62) [13]. They installed a specialized engine test bench to run the engines on various SAF blends and measure real-time cylinder pressure and emissions (CO, NO_x, HC, CO_2). The aim is to validate and eventually approve 100% SAF (or high blends) for use in those aircraft. As of early 2023, Diamond noted they were awaiting sufficient quantities of certified SAF to conduct extensive tests, since the availability of the seven ASTM-approved SAF types was limited. In the meantime, they experimented with "regenerative fuels certified for road application" – likely HVO diesel – as an analogue. This indicates that engine manufacturers are proactively working toward SAF compatibility. We can expect results from such programs to demonstrate whether any adjustments are needed for fuel systems, and to quantify performance differences. Early indications (from informal reports and the heavy-fuel engine studies cited earlier) suggest the engines will run well on SAF, with improvements in emissions.

5.2. Heavy-fuel engine research

A team at Beihang University (China) has published studies on a heavy-fuel aviation piston engine (a compression-ignition aero-engine) running on 100% HEFA SAF. They examined both performance and emissions. One paper reported that using SAF slightly improved high-altitude engine performance (as mentioned, marginally less power loss at altitude) and met all operability requirements [38, 39]. Another paper from the same group focused on emissions and found drastically lower particulate output and reduced CO/HC with neat SAF [39]. These are among the first peer-reviewed results confirming that a piston aircraft engine can run on neat SAF and actually benefit emissions-wise. Such data is crucial for regulators considering allowing 100% SAF in general aviation in the future.

5.3. Unleaded Avgas development

In the realm of spark-ignition aviation, current test campaigns are mostly around unleaded (petroleum-based) fuels. The FAA's Piston Aviation Fuels Initiative (PAFI) had tested candidate unleaded avgas formulations over the last decade, though none met all criteria to fully replace 100LL at that time [28]. Now GAMI 's G100UL fuel has an FAA approval via STC, and another contender, Swift Fuel's UL102, is in development. These are not SAF in the strict sense, but they solve the lead problem and could serve as a bridge – if their components could be synthesized from sustainable sources in the future, that would effectively create a SAF for piston GA. One could envision, for example, synthetic isoparaffins and aromatics combined to meet a 100 octane spec. Research is needed in this area; so far, no large-scale projects are publicly known, likely because the priority has been on turbine SAF.

5.4. Automotive engine trials

On the ground, there have been numerous trials of HVO and other renewable fuels in cars, trucks, and buses. For instance, cities in Scandinavia have operated bus fleets on 100% HVO diesel for years, with success in reducing pollution and no reported engine issues. Volvo Trucks and Scania officially support HVO in their engines, and field data show performance is on par with diesel. A recent demonstration by Porsche and partners has been the production of synthetic gasoline (from CO_2 and renewable electricity) – this "e-fuel" was tested in Porsche sports cars and even in motorsport to prove that a renewable gasoline could meet demanding engine requirements. This e-fuel (made via FT synthesis to produce a gasoline-range product) essentially functioned identically to premium gasoline in high-performance engines. Such demonstrations underline that, given the right fuel composition, piston engines don't "care" about the carbon origin of the fuel. The challenges are mainly economic and scaling ones.

5.5. Marine trials

The marine sector is also testing SAF-equivalent fuels (renewable diesel/HVO) in ship engines. The UK's National Oceanography Centre, for example, conducted trials in 2024 using 100% HVO in their research ships RRS *James Cook* and *Discovery*, which normally run on marine gas oil [30]. They found HVO to be a viable drop-in with no modifications, and it was attractive for its stability and perfor-

mance in cold climates (Arctic) as well as warm regions. The trials noted that HVO's cost and limited availability were the main hurdles, not technical performance. Other marine trials include harbor tugs in Singapore and Brazil running on HVO blends, and the British Antarctic Survey testing HVO in the polar research vessel *Sir David Attenborough* to reduce its carbon footprint [10, 18]. These pilot programs are important to build confidence that renewable fuels can meet the heavy-duty requirements of marine engines over long durations.

5.6. Military and multi-fuel engine tests

The military has been interested in "single battlefield fuel" capability – using a common fuel (typically JP-8, a kerosene) in all equipment, including piston engines. This has indirectly fostered research into how different fuels perform in diesel engines. Some NATO trials have used FT synthetic fuels in armored vehicle engines, etc. The results generally found that engines run fine on these fuels, with maybe minor adjustments. Now, militaries are also exploring SAF as part of energy resilience and emissions goals. In 2018, the U.S. Navy tested ships and aircraft on biofuels (the "Great Green Fleet" demonstration), using a 50/50 blend of HEFA in naval diesel engines and jet turbines. This showed that even warship engines (some of which are essentially marine diesel engines) could use SAF blends seamlessly [10, 18, 41].

6. Conclusions and future outlook

Based on the technical evidence reviewed, SAF can be used in piston engines. For compression-ignition (diesel-cycle) piston engines, SAF in the form of synthetic paraffinic fuels (HEFA, FT, etc.) is essentially a drop-in replacement for conventional diesel or jet fuel. These fuels can power diesel engines in aircraft, vehicles, and ships with equal or better performance, providing cleaner combustion and dramatic emissions benefits (lower soot, CO, HC, and zero sulfur). Test programs by engine manufacturers (Diamond/Austro, Cummins, Volvo, etc.) have demonstrated operation on neat SAF or HVO with no modifications needed, confirming compatibility when the fuel meets appropriate standards. Thus, the primary hurdles for diesel engines are not technical but rather fuel availability, certification, and cost. As SAF production grows and standards evolve to allow 100% use, diesel engines are ready to leverage the full potential of SAF. For spark-ignition engines, the situation is more complex. Current SAF molecules do not meet the high-octane requirements, so direct use in existing gasoline engines is not feasible. However, this is spurring research into high-octane renewable fuels. In the near term, unleaded avgas initiatives will remove lead from aviation gasoline – a big environmental win – but remain fossil-derived. The long-term vision could involve synthesizing gasoline-like fuels from sustainable sources, essentially creating a "SAF for pistons" that is high-octane. This will likely lag behind the diesel side in timeline. In the interim, a practical approach for aviation piston fleet is the growing use of CI engines (many new small aircraft models offer Jet-A piston options), which can directly use SAF. Automobiles will likely see increasing blends of bio-components (ethanol, renewable gasoline fractions) as part of climate policies until electrification predominates.

Pros of SAF in piston engines:

1. Greenhouse gas reduction – SAF offers life-cycle CO_2 reductions of 50–80%+, helping decarbonize legacy fleets.
2. Air quality improvement – lower particulate matter, NOx, CO, and absolutely no lead or sulfur emissions. This has positive health impacts, especially in urban areas and around airports.
3. Drop-in convenience – in many cases, the existing distribution infrastructure and engines can be used, avoiding the need for costly new engine technologies or fuel systems. For sectors like aviation and marine, where electrification is extremely challenging, SAF provides one of the few viable paths to significant emissions cuts.
4. Energy security and flexibility – SAF can be made from diverse feedstocks available domestically in many countries, reducing reliance on petroleum and enhancing fuel supply resilience.

Cons and challenges of SAF in piston engines:

1. High cost and limited supply – currently, SAF is scarce and expensive, which limits adoption. Policy support is crucial to scale up production and drive down costs.
2. Feedstock sustainability – ensuring that feedstock sourcing (e.g. bio-oils, waste, CO_2) truly yields environmental benefits without adverse side effects (deforestation, food competition) is a constant concern. Strong sustainability criteria and perhaps next-generation feedstocks (algae, municipal waste, etc.) are needed.
3. Compatibility issues – while largely manageable, issues like seal swell and lubricity require careful qualification. Older equipment might need retrofits (e.g. swapping out a rubber seal for a fluoropolymer) if running high SAF content.
4. Regulatory and certification hurdles – the certification of new fuels, especially for aircraft, is a lengthy and rigorous process. A collaborative industry effort is needed to test and approve fuels in all the different engine models and to update standards accordingly
5. Competing solutions – in the long run, other technologies (electric, hydrogen) will also come into play, potentially limiting the window for SAF in some applications. For example, by the time SAF is cheap and abundant enough for cars, many cars might be electric. Nonetheless, for heavy-duty and aviation, SAF looks indispensable for the foreseeable future.

In conclusion, SAF has strong potential to be used in internal combustion piston engines and to make them more sustainable. In the diesel domain, the transition is already happening [41]: fleets and even aircraft engines are slowly adopting SAF blends. In the gasoline domain, more innovation is needed, but not impossible – it represents the next frontier for sustainable fuels. Achieving broad use of SAF in piston engines will require continued research, targeted investment, and supportive policy frameworks. When used appropriately, SAF can extend the useful life of existing

engine technology into a low-carbon future, buying time for new technologies to mature and ensuring that even legacy engines become part of the solution to climate change rather than just part of the problem. The journey to scale up SAF is underway, and its successful integration into piston engines across sectors will be a critical component of global decarbonization efforts.

Acknowledgements
This work was financed by the Military University of Technology under the research project UGBWIM/22012 025/15.

Nomenclature

ASTM	American Society for Testing and Materials
ATJ	alcohol-to-jet synthetic paraffinic kerosene
AVGAS	aviation gasoline
CI	compression ignition
CORSIA	Carbon Offsetting and Reduction Scheme for International Aviation
FT	Fischer-Tropsch
GHG	greenhouse gas
HEFA	hydroprocessed esters and fatty acids
IATA	International Air Transport Association
ICAO	International Civil Aviation Organization
IRENA	International Renewable Energy Agency
LCA	life cycle assessment
PtL	power-to-liquid
SAF	sustainable aviation fuel
SI	spark ignition
SIP	synthesized iso-paraffins
TEL	tetraethyl lead
UCO	used cooking oil

Bibliography

[1] Aburto J, Martínez-Hernández E, Castillo-Landero A. Is sustainable aviation fuel production through hydroprocessing of esters and fatty acids (HEFA) and alcohol-to-jet (ATJ) technologies feasible in Mexico? Sustainability. 2025; 17(4):1584. https://doi.org/10.3390/su17041584
[2] Anuar A, Undavalli VK, Khandelwal B, Blakey S. Effect of fuels, aromatics and preparation methods on seal swell. Aeronaut J. 2021;125(1291):1542-1565. https://doi.org/10.1017/aer.2021.25
[3] ASTM D1655-22a. https://store.astm.org/d1655-22a.html
[4] ASTM D7547-23: Unleaded Aviation Gasoline Specification. https://store.astm.org/d7547-23
[5] ASTM Presentation – ICAO LTAG Stocktaking Event. https://www.icao.int/Meetings/LTAGStocktaking2024/Documents/1_ASTM%20Presentation%20-%20ICAO%20LTAG%20Stocktaking%20Event%20-%20Alyson%20Fick.pdf
[6] Abderrahmane A, Qasem NAA, Mourad A, Said Z, Younis O, Guedri K et al. A recent review of aviation fuels and sustainable aviation fuels. J Therm Anal Calorim. 2024; 149(10):4287-4312. https://doi.org/10.1007/s10973-024-13027-5
[7] Bio-Based Aromatics and SAF. https://aviationweek.com/business-aviation/aircraft-propulsion/viewpoint-bio-based-aromatics-point-way-burning-100-saf
[8] Boeing and Airbus SAF Initiatives. https://www.carbonclick.com/news-views/boeing-and-airbus-sustainable-aviation-fuel-initiatives
[9] Bringezu S, Schütz H, Arnold K, Merten F, Kabasci S, Borelbach P et al. Global implications of biomass and biofuel use in Germany – recent trends and future scenarios for domestic and foreign agricultural land use and resulting GHG emissions. J Clean Prod. 2009;17:57-68. https://doi.org/10.1016/j.jclepro.200.03.007
[10] British Antarctic Survey HVO Trial. https://www.bas.ac.uk/media-post/trial-of-hvo-fuel-sda/
[11] Crown Oil – BS EN 15940. https://www.crownoil.co.uk/fuel-specifications/bs-en-15940
[12] Cummins on HVO. https://www.cummins.com/news/2022/07/01/hydrotreated-vegetable-oil-hvo-explained
[13] Diamond Aircraft – SAF Research. https://www.diamondaircraft.com/en/about-diamond/newsroom/news/article/diamond-aircraft-is-working-on-the-use-of-sustainable-aviation-fuels/
[14] EASA SIB No: 2011-01R2 – UL 91. https://www.easa.europa.eu/downloads/24036/en
[15] Eswaran S, Subramaniam S, Geleynse S, Brandt K, Wolcott M, Zhang X. Dataset for techno-economic analysis of catalytic hydrothermolysis pathway for jet fuel production. Data Brief. 2021;39:107514. https://doi.org/10.1016/j.dib.2021.107514
[16] FAA on Unleaded Avgas. https://www.faa.gov/unleaded
[17] Flayyih AH, Al Magdamy BA. Phytoremediation of petroleum hydrwikipeocarbon by micro green algae: a review. J Biotechnol Res Cent. 2025;18(2):134-144. https://doi.org/10.24126/jobrc.2024.18.2.805
[18] GoodFuels on HVO for Shipping. https://www.goodfuels.com/hvo-coastal-inland-shipping
[19] GreenAir News Article. https://www.greenairnews.com/?p=2460
[20] HEFA/HVO Fact Sheet – F3 Centre. https://f3centre.se/en/fact-sheets/hefa-hvo-hydroprocessed-esters-and-fatty-acids/
[21] ICAO CORSIA Resolution A41-22. https://www.icao.int/environmental-protection/CORSIA/Documents/Resolution_A41-22_CORSIA.pdf
[22] ISO 8217 Fuel Standard. https://www.world-kinect.com/sites/default/files/d7/documents/sites/default/files/ISO-8217-2017-Tables-1-and-2-1-1.pdf
[23] Jet fuel prieces – Statista. https://www.statista.com/chart/32710/kerosene-price-development/
[24] Lin X, He QS, Yang J. Conversion technologies for green aviation fuels. In: Aslam M, Mishra S, Aburto Anell JA (eds). Sustainable Aviation Fuels. Cham: Springer Nature Switzerland; 2025:125-147. https://doi.org/10.1007/978-3-031-83721-0_5
[25] Macedo De Araujo Azeredo F, Moll Hüther C, Barbosa Werlang J, Panizio R. Hydrotreated Vegetable Oil (HVO): A Review on Production, Properties, Environmental Impact, and

Future Perspectives. In: Brito PS, Galvão JR, Rijo B, Pedrero C, Neves F, Almeida H et al. (eds). Insights into Energy Trends. Cham: Springer Nature Switzerland. 2025:99-109. https://doi.org/10.1007/978-3-031-83811-8_10

[26] Mancarella A, Marello O. Effect of coolant temperature on performance and emissions of a compression ignition engine running on conventional diesel and hydrotreated vegetable oil (HVO). Energies. 2022;16(1):144. https://doi.org/10.3390/en16010144

[27] McCaffery C, Zhu H, Sabbir Ahmed CM, Canchola A, Chen JY, Li C et al. Effects off hydrogenated vegetable oil (HVO) and HVO/biodiesel blends on the physicochemical and toxicological properties of emissions from an off-road heavy-duty diesel engine. Fuel. 2022;323:124283. https://doi.org/10.1016/j.fuel.2022.124283

[28] Meurer A, Kern J. Fischer–Tropsch synthesis as the key for decentralized sustainable kerosene production. Energies. 2021;14(7):1836. https://doi.org/10.3390/en14071836

[29] Moriarty K, McCormick R. Sustainable Aviation Fuel Blending and Logistics. 2024. https://www.osti.gov/servlets/purl/2440801/

[30] Royal Research Ships Trial HVO. https://rina.org.uk/publications/ship-and-boat-international/royal-research-ships-trial-hydrogenated-vegetable-oil/

[31] SAF 101 – World Energy. https://worldenergy.net/resource/saf-101-an-intro/

[32] SAF 201 – Stillwater Associates. https://stillwaterassociates.com/saf-201-digging-a-bit-deeper-into-sustainable-aviation-fuel/

[33] SAF Policy Actions – EASA. https://www.easa.europa.eu/en/domains/environment/eaer/sustainable-aviation-fuels/saf-policy-actions#refueleu-aviation

[34] Smigins R, Sondors K, Pirs V, Dukulis I, Birzietis G. Studies of engine performance and emissions at full-load mode using HVO, diesel fuel, and HVO5. Energies. 2023;16(12):4785. https://doi.org/10.3390/en16124785

[35] Sondors K, Birkavs A, Dukulis I, Pirs V, Jesko Z. Investigation in tractor Claas Ares 557ATX operating parameters using hydrotreated vegetable oil fuel. Proceedings of the 13th International Scientific Conference "Engineering for Rural Development"; Jelgava, Latvia. 2024 May 29-30. https://doi.org/10.3390/en16124785

[36] The Energy Transition – ExxonMobil. https://corporate.exxonmobil.com/news/newsroom/news-releases/2023/0727_exxonmobils-work-to-drive-emission-reductions

[37] Unleaded Avgas: The SAF for Pistons. https://www.4air.aero/whitepapers/unleaded-avgas-the-saf-for-pistons

[38] Xu Z, Fan Y, Zheng Y, Ding S, Zhu M, Li G et al. Emission reduction characteristics of heavy-fuel aircraft piston engine fueled with 100% HEFA sustainable aviation fuel. Environ Pollut. 2025;368:125661. https://doi.org/10.1016/j.envpol.2025.125661

[39] Xu Z, Shi W, Wang M, Zhong S, Zhou Y, Pei J et al. Performance and combustion characteristics of heavy-fuel aircraft piston engines at high altitudes: comparison between conventional fuels and HEFA sustainable aviation fuel. Sustain Energy Technol Assess. 2025;75:104210. https://doi.org/10.1016/j.seta.2025.104210

[40] Zero-emission aviation and SAF [Internet]. Available from: https://www.aerospacemanufacturinganddesign.com/article/100-saf/

[41] Zimakowska-Laskowska M, Laskowski P. Comparison of pollutant emissions from various types of vehicles. Combustion Engines. 2024;197(2):139-145. https://doi.org/10.19206/CE-181193

Janusz Chojnowski, DEng. – Faculty of Mechanical Engineering, Military University of Technology in Warsaw, Poland.
e-mail: *janusz.chojnowski@wat.edu.pl*

Filip Polak, DEng. – Faculty of Mechanical Engineering, Military University of Technology, Poland.
e-mail: *filip.polak@wat.edu.pl*

Article citation info:
Maciorowski D, Głowacki PJ, Chachurski R. The future of leaded aviation fuel: navigating the challenges of transition. Combustion Engines. 2026;204(1):144-152. https://doi.org/10.19206/CE-210465

Damian MACIOROWSKI
Paweł Jan GŁOWACKI
Ryszard CHACHURSKI

Combustion Engines
Polish Scientific Society of Combustion Engines

The future of leaded aviation fuel: navigating the challenges of transition

ARTICLE INFO

Received: 25 May 2025
Revised: 1 July 2025
Accepted: 8 September 2025
Available online: 10 October 2025

The improvement of unleaded fuels in general aviation represents a significant milestone in the pursuit of establishing a greener and more sustainable air transportation system. Conventional aviation fuels, such as AVGAS 100LL, have TEL (Tetraethyl Lead) in their composition, which is used to increase the octane rating of fuel and improve the efficiency of piston engines used in aviation. However, these substances are considered toxic, and their emissions into the atmosphere have negative effects on the environment and human health. Therefore, very strict air quality standards have been established by the European Union and member states. Years of research and cooperation throughout the aviation sector have contributed to the elimination of lead-containing fuels from most aircraft used in general aviation operations. Most engines have already been certified for the usage of unleaded gasoline, and so are all new engines. Nevertheless, one-third of the engines currently in use in the EU are not certified to burn unleaded fuel. Besides the lead, other toxic compounds are also being emitted with exhaust gases like CO2, NOx, and UHC. In this article, the discussion is about the profits of pursuing a zero-lead policy within General Aviation and the risks associated with introducing a leaded avgas prohibition without a valid alternative.

Key words: *emission dispersion, aviation emissions, lead, nitrogen oxides, carbon monoxides*

1. Introduction

In an era characterized by the chase of environmentally friendly technologies, every sector is actively seeking for a way to reduce its emissions. According to the ICAO, in 2022, the aviation industry accounted for 3.8–4% of total EU GHG emissions and 13.9% of all transport related emissions [21]. In addition, ICAO forecasted that by 2050, international aviation emissions could be tripled [23] due to the faster growth in comparison to other transportation methods. This motivates aviation companies to introduce modernization to their products and to conduct research to minimize the aviation industry's negative impact on air quality. Modern airframes are characterized by significantly better aerodynamic properties. New engine designs for commercial airplanes introduced plenty of features that significantly reduce fuel consumption. Geared Turbofan design enabled Low Pressure Turbines to operate at optimal rotational speed [14]. Improvement of combustion chamber of modern engines, such as Rolls-Royce Phase 5 design or General Electric TAPS II (Twin Annular Premixing Swirler) combustor, introduced a significant reduction in toxic particle emissions [3, 5, 9].

General Aviation is an isolated case. The majority of the GA propulsion systems are piston engines. Transition to unleaded gasoline was not as successful as it was in the case of the automotive industry. However, when in 2000 the leaded petrol was entirely withdrawn from the EU market, the number of cars was more than 193 million. Today, the number of general aviation aircraft in the EU is around 36.8 thousand. Going further, only one-third of them have no alternative to using leaded gasoline. Nevertheless, the general aviation sector – like the automotive industry in the past – has made efforts to identify and implement lead-free alternatives to traditional lead-containing fuels. The elimination of tetraethyl lead (TEL) from automotive gasoline began in earnest in the 1970s, driven primarily by public health concerns and the need to protect catalytic converters, which are highly sensitive to lead. Governments worldwide introduced phased regulations to limit and eventually ban TEL in road fuels. This process was supported by major advancements in fuel refining (e.g., catalytic reforming and hydrocracking), allowing the production of high-octane, unleaded fuels. Additionally, engine technologies evolved to accommodate these fuels, such as hardened valve seats to resist wear in the absence of lead lubricity. Motor Octane Number is critical in aviation. Aircraft operate under sustained high load and variable altitude, which increases knock sensitivity. The Motor Octane Number of regular automotive gasoline is in the range of 81–85. Premium automotive gasoline reaches the MON up to 90. The UL94 gasoline, very popular among lower-compression aviation engines, reaches the MON of 94. However, there is still a significant percentage of aircraft powered by high-load engines, i.e., Cessna T206 powered by Lycoming TIO540 AJ1A, which are only certified to use AVGAS 100LL, which reaches the MON of 100.

2. Aviation engine issues

Piston engines represent the majority of propulsion systems within general aviation. Due to their higher efficiency, lower cost of purchase and operation (in the range 70–370 kW), they are being used to supply small aircraft. Understanding the mechanics of these engines and the impact of their operations on emission levels is crucial for environmental management and aviation safety. Especially considering the risk associated with using non-approved fuels.

The operation and maintenance of piston engines significantly affect the levels of emitted pollutants. Key factors include fuel type, engine tuning, maintenance practices, and the condition of emission control systems. The type of fuel used in piston engines is a primary determinant of emissions. Traditionally, aviation gasoline contained tetraethyl

lead (TEL), which has been used to enhance fuel performance by increasing octane rating, to prevent engine knocking, and improve efficiency. On the other side, leaded avgas is a source of lead emissions, which can pose a significant threat to human life when its concentration in the air is elevated.

To ensure optimal combustion efficiency, a proper tuning and calibration of the engine (and its components) should be provided. Non-optimal fuel-air mixtures together with incorrect ignition timing can increase emissions of CO, NO_x, and UHC. Regular maintenance and use of diagnostic tools to fine-tune the engine are essential to minimize these emissions. Worn-off spark plugs can be a cause of incomplete combustion, which increases CO and UHC emissions. Thus, regular inspection and replacement of spark plugs is recommended. Air filters should be cleaned and replaced since clogged air filters reduce airflow, causing a low air-to-fuel ratio that increases CO and particulate emissions.

It is also preferable to make sure the exhaust system is in good condition to reduce harmful emissions. Some piston engines are equipped with advanced emission control systems such as catalytic converters and exhaust gas recirculation (EGR) systems to help reduce NO_x emissions. The effectiveness of these systems depends on regular maintenance and the quality of the fuel used.

A recent regulatory change in the European Union to restrict the distribution of leaded gasoline, and in particular avgas from TEL, has raised concerns about the potential use of unapproved fuels. The use of such fuels in reciprocating engines that are not certified for them can lead to several problems, like detonation and knock combustion. Unleaded fuels often have a lower octane number compared to leaded fuels. Using them in engines designed for high-octane leaded fuels can cause detonation, leading to knock combustion – a condition in which the fuel burns unevenly. This can result in serious engine damage, including piston and cylinder wear. Lead in fuel acts as a lubricant, protecting engine components such as valve seats. The lack of lead in unleaded fuels can cause increased wear and recession of valve seats, leading to loss of engine compression and performance. Some unleaded fuels contain ethanol, which can absorb water and cause corrosion of the fuel system and engine components that were not designed to handle alcohol-based fuels. Engines equipped with catalytic converters can be damaged if unapproved fuels clog or poison the catalytic converter, reducing the effectiveness of the system and increasing emissions.

The leaded gasoline restriction creates a scenario where pilots and operators may resort to using unapproved fuels due to availability issues, especially in critical situations such as crop dusting or emergency services. This introduces significant human factor risks. The use of unapproved fuels can compromise aircraft safety, causing unpredictable engine performance and potential failure. Operating aircraft with unapproved fuels can result in non-compliance with aviation regulations, leading to legal consequences and insurance cancellation. Increased emissions from the use of unsuitable fuels can have broader environmental and public health impacts, undermining efforts to reduce aviation's environmental footprint.

3. Pollutants' adverse influence

3.1. Air pollutants from general aviation piston engines

Piston engines, which are prevalent among smaller general aviation aircraft, can emit a variety of air pollutants that contribute to environmental concerns and air quality issues. They produce carbon monoxide as a byproduct of incomplete combustion. CO is a colorless and odorless gas that can be harmful to human health when inhaled in high concentrations. Usually, its concentration in the atmosphere is less than 0.001%. Naturally, those concentrations are higher in big cities that suffer from high traffic congestion. Carbon monoxide is mostly exhaled from the lungs as unchanged gas. Less than 1% of it is oxidized to carbon dioxide. Ten to fifteen percent is bound to proteins. It competes with oxygen for binding with hemoglobin and, as a result, leads to hypoxia. [7] It can be dangerous during engine start-ups in enclosed and non-ventilated areas.

Nitrogen oxides are produced when nitrogen in the air reacts with oxygen at high temperatures during combustion. Nitrogen oxides react further with oxygen and within a few hours, Nitrogen dioxide marks its peak in a range of dispersion. In the third step, the level of NO_2 declines and the concentration of ground-level ozone increases, which is a key component of smog, and can also contribute to acid rain. Ozone compounds damage plants and their fruits and irritate the human respiratory system. [19] Figure 1 shows the pattern of how the ground-level ozone concentration increases during the day [13].

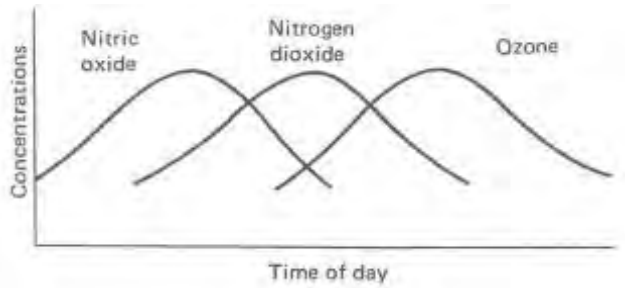

Fig. 1. Graphic describing the nitrogen oxides and ground-level ozone concentrations [19]

Hydrocarbons are unburned fuel molecules that are released into the atmosphere when combustion is not complete. In the sunlight, they react with nitrogen oxides and can contribute to the formation of ground-level ozone and have adverse effects on air quality [13]. In the literature, direct measurements of general aviation aircraft emission under various loads are presented [16].

Combustion engines emit particulate matter, tiny airborne particles that can have adverse health effects when inhaled. These particles can include soot, metal particles, and other combustion byproducts. In the upper atmosphere, it modifies Earth's radiation characteristics, impacts the formation of clouds, and catalyzes secondary pollutant formation. In the lower atmosphere, it affects atmospheric visibility and has a negative impact on human health, such as congenital heart defects, ischemic heart disease, respira-

tory and circulatory mortality, preterm birth risk, or abnormal fetal growth [17, 22].

Volatile organic compounds (VOCs) are a diverse group of carbon-based chemicals that readily evaporate at room temperature, contributing significantly to air pollution and posing various health risks. Among them, 1,3-butadiene, toluene, and benzene deserve special attention due to their widespread presence and harmful effects. 1,3-butadiene, a colorless gas with a mild gasoline odor, plays a key role in the production of synthetic rubber, essential for tires, auto parts and various industrial products. However, 1,3-butadiene is also a known carcinogen, and exposure to it is associated with an increased risk of leukemia and other cancers. Its reactivity in the atmosphere further contributes to the formation of ground-level ozone and secondary organic aerosols, worsening air quality. Butadiene has many environmental sources, in addition to those previously mentioned; it is worth adding car exhaust and tobacco smoke, pointing out that 78.8% of its emissions are caused by the combustion of fuels in a reciprocating engine, and another 19.6% by other combustion processes (such as cooking) [6].

Toluene and benzene, significant components of fossil fuel emissions, pose serious health risks, especially to gas station workers. Toluene, a clear liquid with a sweet, pungent odor, is widely used as a solvent in paints, thinners, adhesives, and chemical intermediates. Exposure to toluene, whether by inhalation, ingestion, or skin contact, can cause dizziness, headaches, and respiratory problems in the short term, while long-term exposure can lead to severe neurological damage, liver and kidney dysfunction, and developmental damage in fetuses. Benzene, a colorless or light yellow liquid with a sweet odor, is a natural component of petroleum and a byproduct of combustion processes, including automobile emissions and industrial activities. Benzene is highly carcinogenic, and long-term exposure to it is strongly associated with leukemia and other blood disorders. Even low concentrations can affect the bone marrow, leading to anemia and a weakened immune system. The combustion of fossil fuels, especially in piston engines used in general aviation, contributes significantly to the release of these volatile organic compounds. Piston engines, commonly used in small aircraft, rely on the combustion of aviation gasoline, which contains high levels of toluene and benzene. This not only poses a risk to pilots and ground personnel but also contributes to broader environmental pollution. Emissions from these engines include significant amounts of volatile organic compounds, which worsen air quality and threaten the health of surrounding communities.

Joint statement of the world's largest organizations within general aviation, one-third of piston engines in the EU used in general aviation have no alternative to leaded gasoline, such as avgas 100LL [10]. As a result, lead emissions are a serious problem, as lead is a potent neurotoxin that can harm both the environment and human health [20, 25].

Although general aviation emits these pollutants, quantitatively these emissions are much lower than those of commercial aviation, not to mention the automotive, energy or heavy industry. Nevertheless, the cumulative impact of general aviation on air quality and the environment can still be significant. Especially near the most popular airports.

3.2. International regulations

In the European Union, the air quality standards are defined in Directive 2008/50/EC of the European Parliament and of the Council of 21 May 2008 on ambient air quality and cleaner air for Europe. In the US the Environmental Protection Agency (EPA) releases National Ambient Air Quality Standards (NAAQS). Those standards are presented in the Table 1.

Table 1. EU and USA air quality standards

Pollutant	Measurement averaging time	UE Standard [μg/m^3]	USA Standard [μg/m^3]
Carbon monoxide	1 hour	N/A	40750
	8 hours	10000	10480
Lead	Rolling three months average	N/A	0.15
	1 year	0.5	N/A
Nitrogen dioxide	1 hour	200	188
	1 year	40	100
Ozone	1 hour	240*	N/A
	8 hours	N/A	137
Particulate matter (PM_{10})	24 hour	50	150
Sulfur dioxide	1 hour	350	
	24 hours	125	200
*Alert level			

4. Modeling approach

4.1. Modeling and management of aviation emissions

Emission dispersion modeling plays an important role in managing the environmental impact of the aviation industry. Precise information on the number of harmful pollutants emitted and their spatial distribution allows us to better understand what the final environmental impact of planned activities within the airport will be. Thus, it can be used to effectively manage traffic at the airport to reduce environmental impact. Emission dispersion modeling is a useful method that helps airport operations meet regulatory requirements for protecting public health and the environment. Dispersion modeling should also be used to support measurement units. A dense grid of measurement points would be very expensive to implement, however, a hybrid approach where a limited number of measurement points are supported by dispersion models seems to be an appropriate approach. Analysis of different flight routes, taxiing procedures and fuel-saving measures can lead to significant reductions in emissions. These optimizations improve air quality and increase the efficiency of flight operations. In the context of global climate change, emissions dispersion modeling is expanding to quantify emissions of greenhouse gases, such as carbon dioxide (CO_2), from aviation operations. Such comprehensive emissions inventories help evaluate strategies to reduce the aviation sector's carbon footprint.

4.2. Emission calculations

The Aviation Environmental Design Tools (AEDT) program was used to modelling emissions and dispersion of aircraft engines. AEDT uses the Emission and Dispersion Modeling System (EMDS) algorithm for emission and

dispersion calculations. The aircraft engine's emissions are calculated including their landside and airside operations among which the EDMS defines four modes: Taxi/Idle, Takeoff, Climb out and Approach. Aircraft operates in each mode for specific amount of time (TIM – Time in Mode). In Table 2 the default TIM for various aircraft is presented.

Table 2. Default time-in-mode for various aircraft categories [24]

Aircraft category	Taxi/idle	Takeoff	Climb out	Approach
Commercial				
Jet-airliner	26	0.7	2.2	4
Turbo-prop	26	0.5	2.5	4.5
Transport/piston	13	0.6	5	4.6
General Aviation				
Business jet	13	0.4	0.5	1.6
Turbo-prop	26	0.5	2.5	4.5
Piston	16	0.3	5	6
Helicopter	7	–	6.5	5.6

The emission sources of the specific airframe are its Engines, Auxiliary Power Units (APU), and Ground Support Equipment (GSE). The engine emissions are calculated using equation 1.

$$E_{ij} = \sum(TIM_{jk}) \cdot \left(\frac{FF_{jk}}{1000}\right) \cdot (EI_{ijk}) \cdot (NE_j) \quad (1)$$

where: E_{ij} – total emission of pollutant I, in pounds, produced by aircraft type j for one LTO cycle, TIM_{jk} – time in mode for mode k, in minutes, for aircraft type j, FF_{jk} – fuel flow for mode k, in pounds per minute, for each engine used on the aircraft type j, EI_{ijk} – emission index for pollutant I, in pounds of pollutants per one thousand pounds of fuel, in mode k for aircraft type k, NE_j – number of engines used on aircraft type j.

Emission index for various pollutants and engine types are sourced from the International Civil Aviation Organization (ICAO) Engine Emissions Databank and other databases. These factors are specified for different phases of flight, such as idle, takeoff, climb, cruise, and descent. During the LTO Cycle, those Emission indices are fixed. For mission calculations that go beyond the LTO cycle, various scaling methods like Boeing Fuel Flow Method 2 can be used.

GSE emission factors contained in the EDMS database are derived from the document "Technical Data To Support FAA's Advisory Circular On Reducing Emissions From Commercial Aviation" [1, 24]. Those factors are based on brake horsepower, load factor, fuel type, and coolant type. In EDMS GSE emission factors are given in kilograms per hour. With an operation time per LTO cycle given in minutes, the calculation for emissions generated per LTO cycle is the product of the emission factor and operation time.

4.3. Emission dispersion modelling in AEDT

Once emissions are quantified, AEDT employs advanced dispersion modeling techniques to predict the distribution and concentration of pollutants in the atmosphere. The dispersion modeling is based on principles of atmospheric physics and chemistry, involving complex equations that describe the transport, diffusion, and chemical transformation of pollutants.

A primary approach used in AEDT for near-field dispersion (close to the emission source) is the Gaussian Plume Model. This model assumes that pollutants disperse in the atmosphere following a Gaussian distribution, influenced by wind speed, atmospheric stability, and other meteorological conditions. The general form of the Gaussian plume equation for a continuous point source is:

$$C(x,y,z) = \frac{Q}{2\pi\sigma_y\sigma_z u}\exp\left(-\frac{y^2}{2\sigma_y^2}\right) \cdot \left[\exp\left(-\left(\frac{(z-H)^2}{2\sigma_z^2}\right)\right) + \exp\left(-\left(\frac{(z+H)^2}{2\sigma_z^2}\right)\right)\right] \quad (2)$$

where: $C(x,y,z)$ is the concentration of the pollutant at location (x,y,z), Q is the emission rate (grams per second), σ_y and σ_z the dispersion coefficients in the horizontal and vertical directions, respectively, u is the wind speed (meters per second), H is the effective source height (meters), which accounts for the initial plume rise.

For more comprehensive and regulatory-compliant assessments, AEDT integrates the AERMOD (American Meteorological Society/Environmental Protection Agency Regulatory Model). AERMOD is a steady-state plume model that simulates the dispersion of pollutants by considering both simple and complex terrain and a wide range of meteorological conditions. AERMOD requires detailed input data, including:

- Meteorological data: wind speed and direction, temperature, humidity, atmospheric pressure, and solar radiation
- Terrain data: elevation profiles and land use categories
- Emission data: source characteristics such as emission rates, stack heights, and exit velocities.

5. Results and discussion

The area of Warsaw-Babice Airport and its vicinity was selected for emission concentration assessment due to the relatively high number of operations and unique localization in the middle of the highly urbanized province of Warsaw. In the direct vicinity of the airport, there are multi-family houses and family allotment garden areas where people have a rest and grow food plants (Fig. 2).

Airplane Cessna T206 powered by Lycoming TIO540 AJ1A engine was selected due to its popularity and the fact that TIO540 AJ1A is not certified to use any unleaded gasoline. In Table 2, Lycoming TIO540 AJ1A emission indexes (by default implemented in the AEDT based on ICAO Aircraft Emission Data Bank) are presented.

Table 3. Lycoming TIO540 AJ1A engine emission indexes for different LTO cycle phases in grams per kilogram of fuel.

	Takeoff	Climb out	Approach	Taxiing
Carbon monoxide	1442.0	1470.9	1261.6	1293.7
Nitrogen oxide	0.362	0.235	1.388	0.387
Lead	0.7766	0.7766	0.7766	0.7766

Lead emission index was calculated using the upper lead content per liter of Avgas 100LL, which is 0.56 g/dm^3, and its density is equal to 0.7211 kg/ dm^3. Some of the lead compounds, like lead oxides, can be sintered on the exhaust

Fig. 2. Area of Warsaw-Babice Airport with the direct vicinity of family allotment gardens and multi-family houses

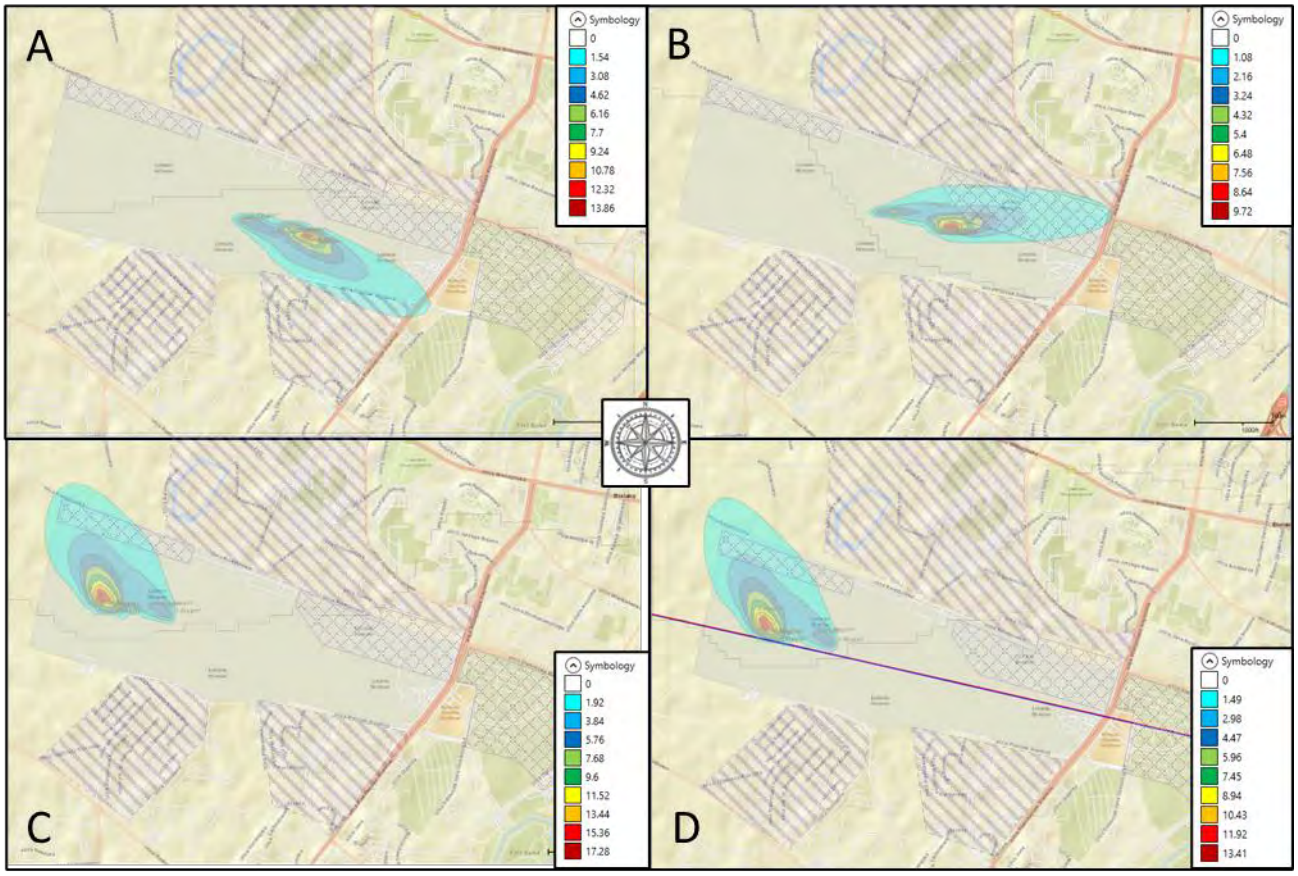

Fig. 3. Lead concentration distribution – C [ng/m^3]: A – wind: 270 deg 6 m/s, B – wind: 270 deg 12 m/s, C – wind 90 deg 3.6 m/s, D – wind 90 deg 7.2 m/s

system of the engine; however, this is negligible since the addition of ethylene dibromide in the leaded fuels significantly limits this process.

On the Warsaw-Babice, there are environmental limitations on the number of operations per hour and daily, 10 and 100 operations, respectively. Figures 3–5 show the concentration of lead, nitrogen oxides, and carbon monoxide for 4 days in June 2022 with different wind directions and/or wind speeds. Aircraft approach and departure flying in a direction opposite to the wind. For each hour of each day, 5 arrival and 5 departure operations were modelled. All presented values correspond to 1-hour averaged, tier 1 values. The meteorological data used in the modeling were obtained from the publicly available repository of the Institute of Meteorology and Water Management (IMGW).

The concentration distribution maps A and B in Fig. 3 show lead concentration for westerly winds of 6 m/s and 12 m/s, respectively. Westerly winds are particularly unfavorable for people resting in nearby allotments. However, even for that wind direction, the estimated lead concentrations resulting from the Warsaw-Babice airport's operations rank between 0 and 0.00648 ng/m^3 within the allotments area. In the case of easterly winds (maps C and D), this impact is limited to people working in the Warsaw-Babice airport area itself and people resting within allotment gardens on the north-west side of the airport. The lead concentration ranks there between 0 and 0.00384 ng/m^3. Although there is no limit to the hourly concentration of lead in the air specified in both European and US regulations, it should be remembered that 1-hour averaged values will have significantly higher values than values after annual averaging. This is due to the lack of flight operations during nighttime hours.

The NO_x concentration level presented in Fig. 4 is lower than the expected lead concentration, and this is a direct result of the lower NO_x emission index. In comparison to the emissions allowed by regulation, the resulting concentration presented in the figure below can be considered as negligible.

Compared to jet engines, the NO_x emission index of piston engines is significantly lower. This, combined with substantially lower airflows, results in considerably lower nitrogen oxide emissions from aircraft powered by piston engines. The NO_x emission index in piston engines is lower due to the fact that combustion in piston engines occurs in a confined space with a relatively short duration for NO_x formation, as the high-pressure and high-temperature conditions are transient. Jet engines have a continuous combustion process, allowing more time for NO_x formation due to prolonged exposure to high-temperature conditions in the combustion chamber. For comparison, the NOx emission index of the CFM56-7B26 engine, which is used to power Boeing 737-800 aircraft, is equal to 23.94 g/kg fuel, whereas for the Lycoming TIO540 AJ1A, it is equal only to 0.362 g/kg fuel.

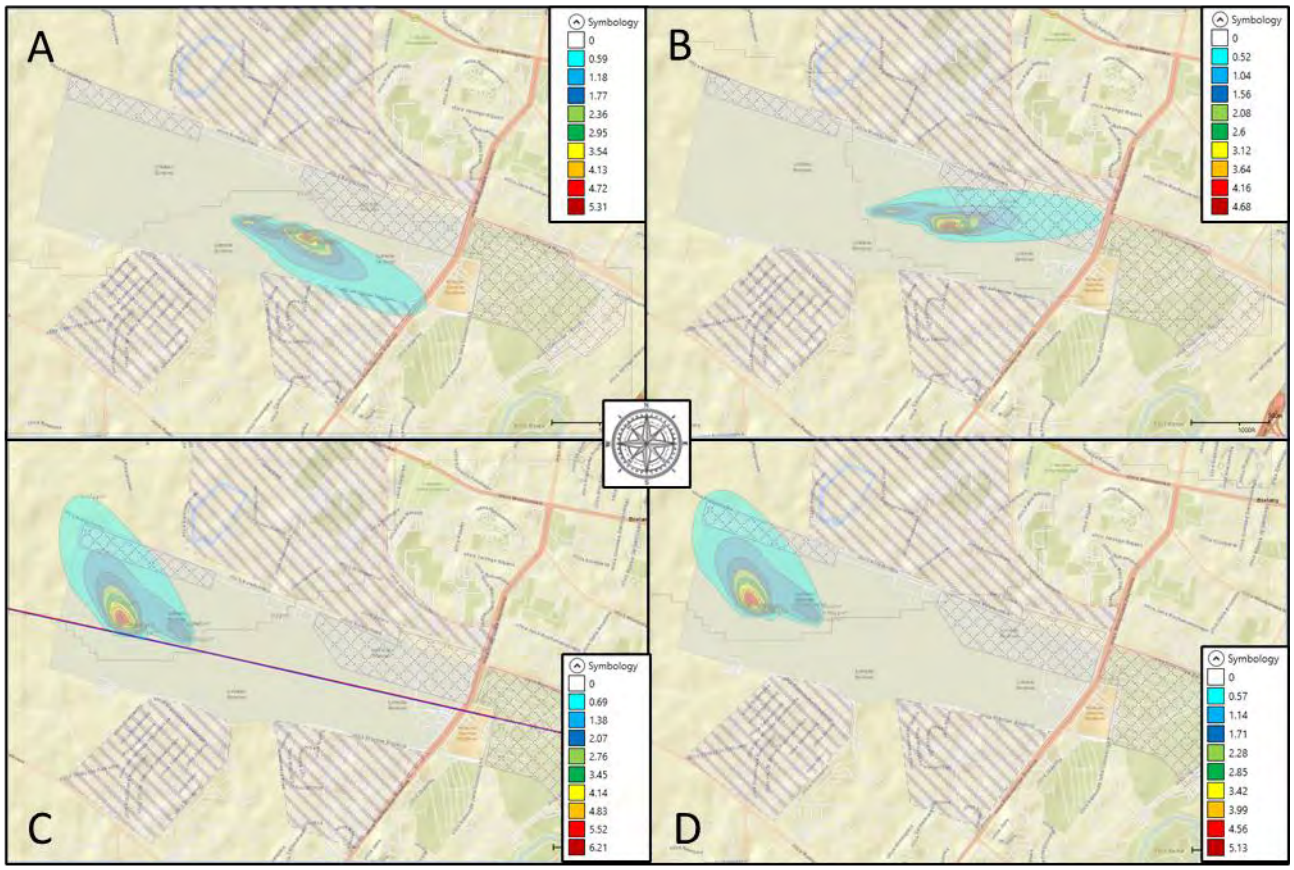

Fig. 4. Nitrogen oxides concentration distribution – C [ng/m^3]: A – wind: 270 deg 6 m/s, B – wind: 270 deg 12 m/s, C – wind 90 deg 3.6 m/s, D – wind 90 deg 7.2 m/s

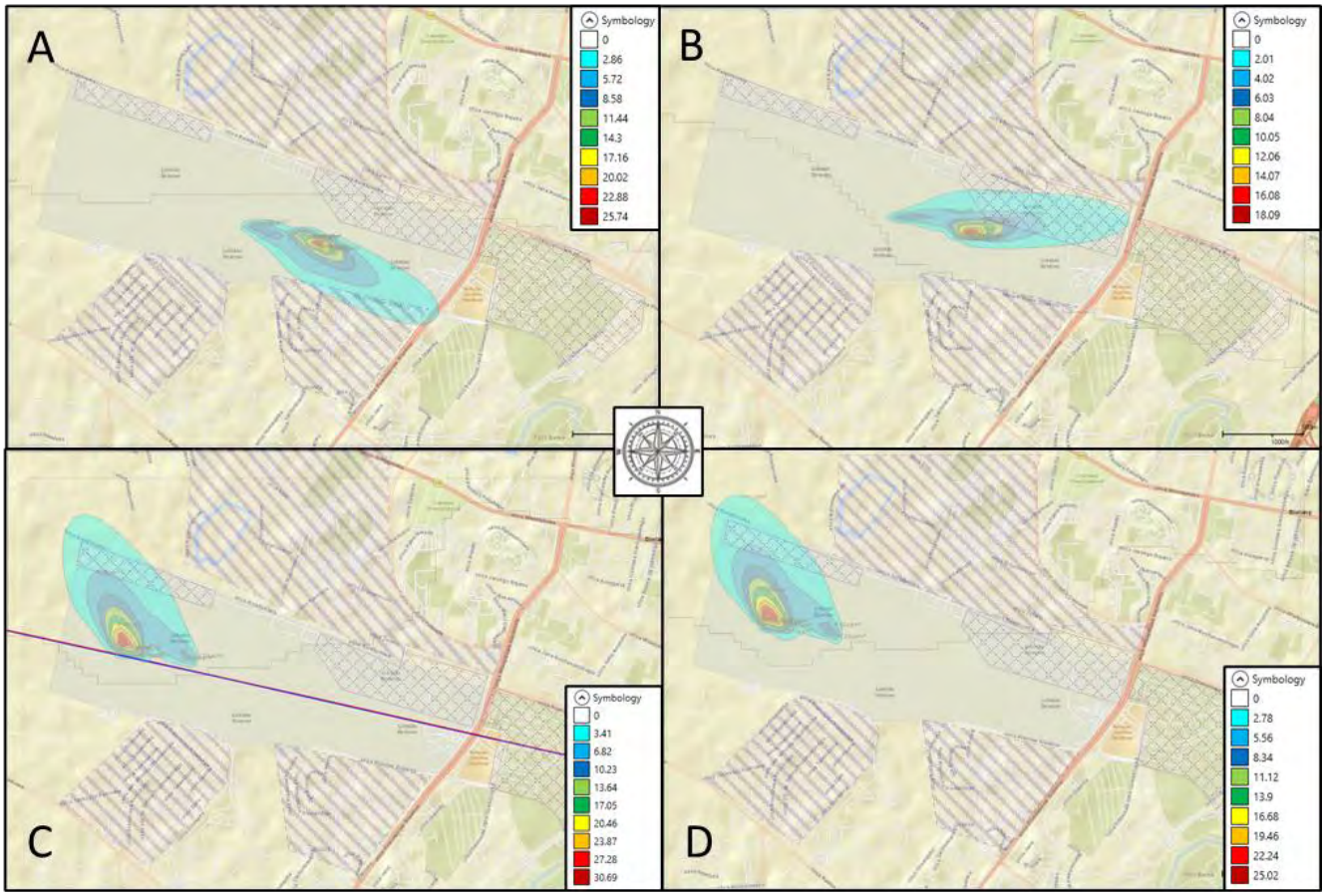

Fig. 5. Carbon Monoxide concentration distribution C [µg/m^3]: A – wind: 270 deg 6 m/s, B – wind: 270 deg 12 m/s, C – wind 90 deg 3.6 m/s, D – wind 90 deg 7.2 m/s

Figure 5 shows the CO concentration distribution. Carbon monoxide emissions result from the incomplete combustion process. In the case of jet engines, which operate with a high air-fuel ratio across most operating ranges, the majority of CO emissions and the highest concentrations are observed along taxiing routes. For piston engines, which typically operate near stoichiometric mixtures (or richer), the CO emission factor remains relatively constant across all flight phases. Richer mixtures also lead to increased CO emission factor; thus, piston engine-propelled aircraft are a significant source of that pollutant. Similar to nitrogen oxides and lead emissions, the highest concentrations of carbon monoxide are found near the end of the runway.

The global shift away from leaded gasoline in the automotive sector has resulted in an increase in the relative contribution of general aviation and stationary industrial sources. Cho highlights it in the research, indicating that roughly 50% of Pb emission comes from aviation emissions [6]. However, the high mobility of an aircraft as a source does not result in a high contribution to local lead concentration in the air. Mutlu and Lee state in their research that measurements show the highest long-term means of lead concentration in the highly industrial South Korean cities like Ulsan, Incheon, or Busan [18]. The largest annual mean Pb concentration level was recorded in 2004 in Incheon and was equal to 136 ng/m^3. Statistical analysis also showed that the highest concentration could be observed from December to May. Since General Aviation activity is the most intensive during the summer season, it might indicate that aviation is not a major contributor to the local pollution. Winter and spring seasons, however, are the times of specifically extensive energy consumption, which can be associated with increased Pb concentration. Lower lead concentration during the cold and dry winter/spring season is also reported by Feinberg on the Centennial Airport [8]. According to the FAA, roughly 1000 takeoff and landing operations are being held on the Centennial Airport, of which 89% are General Aviation operations.

Measurements within this airport show that the monthly averaged lead concentration within the airport varies from 7 to 30 ng/m^3 from month to month. In the cited research, similar tools and methodology were used. Comparison of model results to measurements showed that the approach and results presented in this research are also overestimated. Carr et al in their research from 2011 presented AERMOD model results for comparison with measurements based on the Santa Monica Municipal Airport, on which 200–300 landing and takeoff operations are held every day [4]. The results obtained in this study are similar, keeping in mind that the intensity of air traffic is almost three times higher.

6. Conclusions

The presented results of calculations indicate that the concentration of lead compounds in the air is approximately three orders of magnitude lower than the allowable threshold within the airport area. In addition, analysis shows the surroundings are not exposed to any significant lead concentration in the air. Also taking into consideration the analysis of NO_x and CO, the concentration is very limited and might only gain in importance when added up to the car traffic ingestion emissions. Nearby family allotment gardens are not exposed to the high concentrations of harmful pollutants emitted by the operations of Warsaw-Babice airport. However, the analysis does not consider concentrations resulting from traffic on Warsaw's streets. While this study focuses on airborne lead emissions due to their direct impact on human inhalation exposure, it is important to note that long-term accumulation of lead in soil near airports also poses significant environmental and health risks.

From a sociological point of view, the sudden blocking of the possibility of using traditional lead fuels can be perceived as arbitrary behavior by decision-makers who do not consider the situation of a significant number of aircraft and helicopter users. Usually, such bans are much better received when viable alternatives are pointed out at the same time.

The effects of the human factor will also be a major threat. In the absence of alternatives, some aircraft and helicopter owners will use unsuitable fuel, increasing the likelihood of failure of power units and, as a result, endangering not only the pilots but also their passengers and people/infrastructure on the ground.

Studies using a similar methodology have shown that using the AEDT model to estimate lead concentrations in the vicinity of a local airport leads to results that may be overestimated compared to actual measurements reported in the literature. This indicates that the methodology adopted may be conservative, which is an important aspect in the context of environmental risk assessment. The pollutant concentration values obtained in this research are comparable with those obtained by other researchers [4, 6, 8, 18].

However, an important limitation of the present study is the lack of consideration of emissions associated with the aircraft run-up mode, which, as Carr has shown, can significantly affect local air lead concentrations. Including this stage in future analyses could allow for a more precise assessment of the impact of aviation activities on air quality in the airport environment. Another limitation of this study is the lack of consideration for the actual durations of the individual flight phases. Current research shows significant differences between the real durations of flight phases and those defined in the LTO regulations [12, 15].

The ban on the use of fuel containing TEL will negatively affect the training of airplane and glider pilots. This should be considered in view of the growing shortage of personnel in aviation. The need to replace power units in many airplanes and helicopters will exceed the financial capacity of many aeroclubs, resulting in their demise, entailing restrictions on access to flight schools.

It seems that a good solution would be to ban the production of power units requiring leaded gasoline. There should be a transition period during which the currently used engines of this type would be taken out of service due to normal wear and tear.

In view of the rapid development of unleaded aviation fuels in recent years, the abrupt withdrawal of leaded fuels from the European market, without providing access to an alternative, is clearly premature and will have a negative impact on the owners of 16,000 aircraft. It is important to keep in mind the even larger number of European Union citizens whose business activities are based on the logistical, recreational, and sporting aspects of general aviation.

The development of G100UL fuel offered the possibility of eliminating leaded gasoline in general aviation. After more than a decade of research, it received FAA approval. It is currently the only certified lead-free substitute for high-octane fuel. There is growing interest in this fuel in the US [2, 11]. Despite this success, the problem of its availability has yet to be solved. Distributors declare that U.S. demand will not be met until 2026, which allows us to tentatively assume that G100UL will not be available in the European market before 2030. An incentive for a dynamic entry into the European market would be the interest of users in purchasing a supplemental type certificate, the possession of which authorizes the aircraft owner to use G100UL fuel.

Wind speed has a significant impact on local concentrations of harmful compounds at airports. Higher wind speeds enhance the dispersion of pollutants, leading to lower localized concentrations, while lower wind speeds contribute to the accumulation of emissions in the vicinity of their sources. This effect underscores the importance of considering meteorological conditions when assessing air quality and pollutant dispersion around airport environments.

The carbon monoxide emission index of reciprocating engines is significantly higher than that of turbine engines. This is a direct result of richer mixtures. Nevertheless, the negative effect that could result from this is significantly reduced by significantly lower mass flow rates through the cylinders.

Bibliography

[1] Anderson C, Augustine S, Embt D, Thrasher T, Plante J. Emissions and dispersion modeling system (EDMS). Reference Manual, Anderson, CSSI, Inc., Washington, DC, Technical Report.

[2] Bertorelli P. G100UL Triumphs: Now The Hard Part. www.avweb.com/insider/g100ul-triumphs-now-the-hard-part (accessed on 16.10.2024).

[3] Boies AM, Stettler MEJ, Swanson JJ, Johnson TJ, Olfert JS, Johnson M et al. Particle emission characteristics of a gas turbine with a double annular combustor. Aerosol Sci Technol. 2015;49(9):842-855. https://doi.org/10.1080/02786826.2015.1078452

[4] Carr E, Lee M, Marin K, Holder C, Hoyer M, Pedde M et al. Development and evaluation of an air quality modeling approach to assess near-field impacts of lead emissions from piston-engine aircraft operating on leaded aviation gasoline. Atmos Environ. 2011;45(32):5795-5804. https://doi.org/10.1016/j.atmosenv.2011.07.017

[5] Chen L, Cui B, Zhang C, Hu X, Wang Y, Li G et al. Impacts of fuel stage ratio on the morphological and nanostructural characteristics of soot emissions from a twin annular premixing swirler combustor. Environ Sci Technol. 2024; 58(24):10558-10566. https://doi.org/10.1021/acs.est.4c03478
[6] Chen WQ, Zhang XY. 1,3-butadiene: a ubiquitous environmental mutagen and its associations with diseases. Genes and Environ. 2022;44(3). https://doi.org/10.1186/s41021-021-00233-y
[7] Ernst A, Zibrak JD. Carbon monoxide poisoning. The New England Journal of Medicine. 1998;339(22). https://doi.org/10.1056/NEJM199811263392206
[8] Feinberg SN, Turner JR. Dispersion modeling of lead emissions from piston engine aircraft at general aviation facilities. Transp Res Rec. 2013;2325(1):34-42. https://doi.org/10.3141/2325-04
[9] Fu Z, Gao H, Zeng Z, Liu J, Zhu Q. Generation characteristics of thermal NO_x in a double-swirler annular combustor under various inlet conditions. Energy. 2020;200:117487. https://doi.org/10.1016/j.energy.2020.117487
[10] GAMA-IAOPA-EHA-EAS-ERAC-EBAA-ECOGAS-IAAPS Response to EC Consultation on Draft regulation – Ares (2021)4120146/Chemicals (REACH) regulation – amendment to the list of substances of very high concern in Annex XIV.
[11] GAMI G100UL FAQ, https://www.g100ul.com/faq (accessed on 16.10.2024).
[12] Głowacki P, Kawalec M. Aircraft emissions during various flight phases. Combustion Engines. 2015;162(3):229-240. ISSN 2300-9896.
[13] Jhun I, Coull BA, Zanobetti A, Koutrakis P. The impact of nitrogen oxides concentration decreases on ozone trends in the USA, Air Quality Atmosphere & Health. July 2014. https://doi.org/10.1007/s11869-014-0279-2
[14] Kurzke J. Fundamental differences between conventional and geared turbofans. Proceedings of the ASME Turbo Expo 2009: Power for Land, Sea, and Air. Vol. 1: Aircraft engine; ceramics; coal, biomass and alternative fuels; controls, diagnostics and instrumentation; education; electric power. Awards and Honors. Orlando, June 8–12, 2009, 145-153. ASME. https://doi.org/10.1115/GT2009-59745
[15] Maciejewska M, Kurzawska-Pietrowicz P. Adopted LTO cycle to operational conditions at polish airports. Combustion Engines. 2024;199(4):67-73. https://doi.org/10.19206/CE-187023
[16] Merkisz J, Markowski J, Pielecha J. Emission tests of the Cessna–152II aeroplane engine in stationary operating conditions. Logistyka. 2010;6.
[17] Mukherjee A, Agrawal M. World air particulate matter: sources, distribution and health effects. Environ Chem Lett. 201715:583-309. https://doi.org/10.1007/s10311-017-0611-9
[18] Mutlu A, Lee BK. Airborne lead levels in the Korean peninsula: characterization of temporal and spatial patterns and cancer risk analysis. Environ Sci Pollut Res. 2012;19:2125-2137. https://doi.org/10.1007/s11356-011-0712-0
[19] Najjar Y. Gaseous pollutants formation and their harmful effects on health and environment. Innovative Energy Policies. 2011;1:1-8. https://doi.org/10.4303/iep/E101203
[20] Navas-Acien A, Guallar E, Silbergeld E, Rothenberg S. Lead exposure and cardiovascular disease – a systematic review. Environ Health Perspect. 2006:115(3):472-482. https://doi.org/10.1289/ehp.9785
[21] Reducing emissions from aviation. https://climate.ec.europa.eu/eu-action/transport/reducing-emissions-aviation_en#aviation-emissions (accessed on 16.10.2024).
[22] Sacks J, Stanek L, Luben T, Johns D, Buckley B, Brown J et al. Review particulate matter–induced health effects: who is susceptible?, Environ Health Perspect. 2010;119(4):446-454. https://doi.org/10.1289/ehp.1002255
[23] Trends in emissions that affect climate change. https://www.icao.int/environmental-protection/Pages/ClimateChange_Trends.aspx (accessed on 16.10.2024).
[24] U.S. Department of Transportation and U.S. Environmental Protection Agency. Technical data to support FAA's advisory circular on reducing emissions from commercial aviation. Federal Aviation Administration, Washington, DC and Motor Vehicle Emissions Laboratory, Ann Arbor 1995.
[25] Wani AL, Ara A, Usmani JA. Lead toxicity: a review. Interdiscip Toxicol. 2015;8(2):55-64. https://doi.org/10.1515/intox-2015-0009

Damian Maciorowski, MEng. – Department of Aerodynamics, Lukasiewicz Research Network – Institute of Aviation, Warsaw, Poland;
Faculty of Mechatronics, Armament and Aerospace, Doctoral School, Military University of Technology, Warsaw Poland.
e-mail: *damian.maciorowski@ilot.lukasiewicz.gov.pl*

Paweł Jan Głowacki, DEng. – Department of Aircraft Propulsion, Lukasiewicz Research Network - Institute of Aviation (Retired), Warsaw, Poland.
e-mail: *p_glowacki@yahoo.pl*

Prof. Ryszard Chachurski, DSc., DEng. – Faculty of Mechatronics, Armament and Aerospace, Military University of Technology, Poland.
e-mail: *ryszard.chachurski@wat.edu.pl*

Article citation info:
Żmudka Z. Improving the uncertainty of measured and calculated data in engine problems using the equalisation calculus. Combustion Engines. 2026;204(1):153-157. https://doi.org/10.19206/CE-210987

Zbigniew ŻMUDKA

Combustion Engines
Polish Scientific Society of Combustion Engines

Improving the uncertainty of measured and calculated data in engine problems using the equalisation calculus

ARTICLE INFO

Received: 26 May 2025
Revised: 11 August 2025
Accepted: 16 September 2025
Available online: 26 September 2025

A selected example of the application of the equalization calculus to reconcile the results of experimental tests of a spark-ignition internal combustion engine is presented. The example concerns the selection of characteristic parameters of the theoretical Seiliger-Sabathe cycle in accordance with the experimentally determined real cycle. This is therefore a so-called inverse problem. The isochoric and isobaric loading parameters and the heat distribution number were reconciled. In addition, the effect of applying the reconciliation algorithm twice on the correction of measurement results with gross errors is presented.

Key words: *spark ignition engine, theoretical cycle, real cycle, measurement deviation, equalisation calculus*

1. The essence of using the equalisation calculus

The equalisation calculus is used in many fields of engineering sciences and industry where experimental research is carried out. It is a practical tool for the authentication and validation of measurement results [1, 5, 9, 11, 12].

In experimental testing of internal combustion engines, there are often situations where the number of calculated unknown quantities is less than the number of independent equations relating these quantities to the measured data. The unknowns determined directly from these equations can be calculated in a number of ways, depending on the choice of equation set. The remaining dependencies will not be fulfilled exactly, which is due to the occurrence of unavoidable measurement errors, and consequently, the same quantities will take different values. In order to avoid these differences (obtaining one parameter value) and to get the consistency of all equations, it is necessary to carry out a procedure to reconcile the equations by means of the methods of equalization calculus [8, 13]. The essence of this calculus is the correction of measurement results, after which the results of calculations of unknown quantities, determined from different sets of equations, will be the same.

The classic situation where the number of equations is greater than the number of unknowns also often occurs when carrying out measurements of the composition of exhaust gases, aimed at determining those quantities that are difficult or impossible to measure directly. The calculation algorithm then uses the balance equations of the elements involved in the combustion process. The unknowns (unit amount of air n'_a and exhaust gas n''_{ss}) can be calculated in several ways, depending on the choice of the set of balance equations. The influence of measurement errors on the deviations of the calculation results should be decisive in this respect. However, in this article, a different example will be presented, involving the application of the equalisation calculus to determine the characteristic parameters of the theoretical Seiliger-Sabathe cycle.

The subject of the article concerns primarily the problem of applying the equalization calculus in engine problems. The problem of adjusting the Seiliger-Sabathe cycle to a real cycle served only as an example of its application.

Generally, all independent equations (so-called equations of conditions) form a system of functions of the general form [8, 10]:

$$F_k = F_k\left(x_1,\ldots, x_i,\ldots, x_n, y_1,\ldots, y_j,\ldots, y_u\right), \quad k = 1\ldots r \tag{1}$$

where: x_i – measured quantity (i = 1 ... n), n – number of measured quantities, y_j – unknown quantity (j = 1 ... u), u – number of unknown quantities, r – number of equations of the conditions.

The equations of conditions forming the system (1) must satisfy the mutual independence condition and the determinability condition for the unknowns. The verification of these conditions involves examining the order of the appropriate Jacobi matrices from the partial derivatives of the function F_k according to the arguments x_i and y_j [8].

By substituting the results of the measurements and the approximate (pre-calculated) values of the unknowns into the equations of the conditions, some of them do not meet. A system of equations is obtained:

$$F_k\left(x_{1,0} \ldots x_{i,0} \ldots x_{n,0}, y_{1,0} \ldots y_{j,0} \ldots y_{u,0}\right) = -w_k \tag{2}$$

where: $x_{i,0}$ – result of measurement of the i-th quantity (i = 1 ... n), $y_{j,0}$ – approximate value of the j-th unknown (j = 1 ... u), w_k – incompatibility of the k-th equation of condition (k = 1 ... r).

Obviously, the incompatibilities w_k of the equations of the conditions used for the initial calculation of the unknowns are zero ($w_k = 0$).

In order to obtain compatibility of all the equations of the conditions, it is necessary to introduce corrections ν_i to the measurement results and corrections δ_j to the approximate values of the unknowns. These corrections are calculated from the system of equations [10]:

$$\begin{cases} \sum_{i=1}^{n} a_{ki}\, v_i + \sum_{j=1}^{u} b_{kj}\, \delta_j = w_k & (k = 1 \ldots r) \\ \dfrac{v_i}{m_i^2} = \sum_{k=1}^{r} a_{ki}\, k_k & (i = 1 \ldots n) \\ \sum_{k=1}^{r} b_{kj}\, k_k = 0 & (j = 1 \ldots u) \end{cases} \tag{3}$$

where: k_k – correlates, coefficients in determining conditional extreme, m_i – mean absolute error of the measurement result of the i-th quantity.

The coefficients a_{ki} and b_{kj} of the above system of equations are the partial derivatives of the function F_k according to the measured quantities x_i and according to the unknowns y_j, respectively, calculated at a point with coordinates:

$$\left(x_{1,0} \ldots x_{i,0} \ldots x_{n,0}\ ,\ y_{1,0} \ldots y_{j,0} \ldots y_{u,0}\right).$$

They are therefore calculated from the relationship:

$$a_{ki} = \left(\frac{\partial F_k}{\partial x_i}\right)_0 , \qquad b_{kj} = \left(\frac{\partial F_k}{\partial y_j}\right)_0 \tag{4}$$

2. Reconciling the parameters of the Seiliger-Sabathe cycle

The presented example concerns the problem of selecting the parameters of the theoretical Seiliger-Sabathe cycle (Fig. 1) according to the experimentally determined real engine cycle [2, 14]. This is therefore the so-called inverse problem.

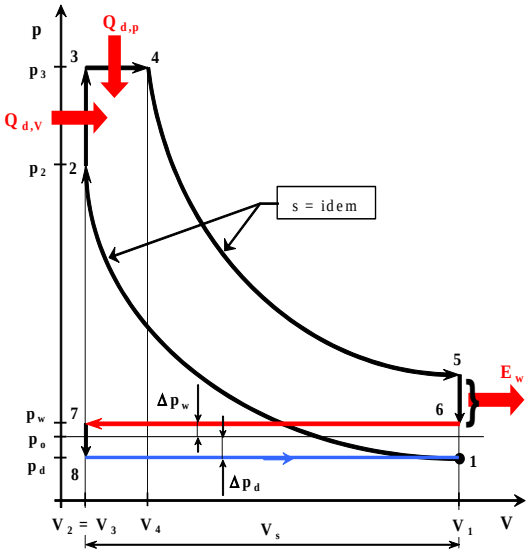

Fig. 1. Open Seiliger-Sabathe cycle

In order to unambiguously determine the course of the Seiliger-Sabathe cycle, it is necessary to determine [14]:
– isochoric load parameter (pressure increase ratio) γ:

$$\gamma = \frac{p_3}{p_2} , \qquad \gamma \geq 1 \tag{5}$$

– and isobaric load parameter (volume increase ratio) φ:

$$\varphi = \frac{V_4}{V_3} , \qquad \varphi \geq 1 \tag{6}$$

from here, the heat distribution number Ψ can be determined, defined as:

$$\Psi = \frac{Q_{d,v}}{Q_d} , \qquad 0 \leq \Psi \leq 1 \tag{7}$$

The quantities used to define the above parameters are marked in Fig. 1, which shows the Seiliger-Sabathe cycle in the p-V system. Defined parameters (5), (6) and (7) are linked together by independent formulas:

$$\gamma = 1 + \frac{E\, \Psi\, (\kappa - 1)}{\varepsilon^{(\kappa-1)}} \tag{8.1}$$

$$\varphi = 1 + \frac{(\kappa - 1)\, E\, (1 - \Psi)}{\kappa \left(E\, \Psi\, (\kappa - 1) + \varepsilon^{(\kappa-1)}\right)} \tag{8.2}$$

where: $\varepsilon = V_1/V_2$ – compression ratio, E – energy-stoichiometric parameter, defined as [7]:

$$E = \frac{Q_d}{p_1 V_1} \tag{9}$$

In the case of experimental (based on indirection) determination of approximate, preliminary values of the parameters γ_0 and φ_0, as well as knowledge of parameter E and compression ratio ε, there will be one unknown in two equations (8) – the heat distribution number Ψ. Thus, in this situation, it is possible to use the equalization calculus to obtain the reconciliation of the relations (8), which are the equations of the conditions.

The following designations have been adopted:
γ_0 – experimentally determined isochoric load parameter (preliminary value)
φ_0 – experimentally determined isobaric load parameter (preliminary value)
Ψ_0 – pre-calculated value of the heat distribution number from the formula (8.1)
v_γ – correction of the isochoric load parameter γ
v_φ – correction of the isobaric load parameter φ
δ – correction of the heat distribution number Ψ
$m_\gamma = m_\varphi = 0.1$ – mean absolute error of the measurement result γ and φ.

Taking the first of the equations of the conditions (8.1) for the initial calculation of the unknown heat distribution number Ψ, the system of equations (3) allowing the calculation of the corrections v_γ, v_φ, and δ will take the form (10):

$$-\varepsilon^{(\kappa-1)}\, v_\gamma + (\kappa - 1)\, E\, \delta = 0 \tag{10.1}$$

$$\left[\kappa\, E\, (\kappa - 1)\, \Psi_0 + \kappa\, \varepsilon^{(\kappa-1)}\right] v_\varphi + (\kappa - 1)\, E\, [(\varphi_0 - 1)\, \kappa + 1]\, \delta = w_2 \tag{10.2}$$

$$\frac{v_\gamma}{m_\gamma^2} = -\varepsilon^{(\kappa-1)}\, k_1 \tag{10.3}$$

$$\frac{\nu_\varphi}{m_\varphi^2} = \left[\kappa E (\kappa - 1)\Psi_0 + \kappa \varepsilon^{(\kappa-1)}\right] k_2 \qquad 10.4)$$

$$(\kappa - 1) E k_1 + \left[(\varphi_0 - 1)\kappa E (\kappa - 1) + (\kappa - 1) E\right] k_2 = 0 \qquad (10.5)$$

Once the corrections have been calculated, the final corrected values can be determined:
– isochoric load parameter:

$$\gamma_u = \gamma_0 + \nu_\gamma \qquad (11)$$

– isobaric load parameter:

$$\varphi_u = \varphi_0 + \nu_\varphi \qquad (12)$$

– and also, the number of heat distribution:

$$\Psi_u = \Psi_0 + \delta \qquad (13)$$

The effect of reconciliation for the analysed example is presented graphically in Fig. 2.

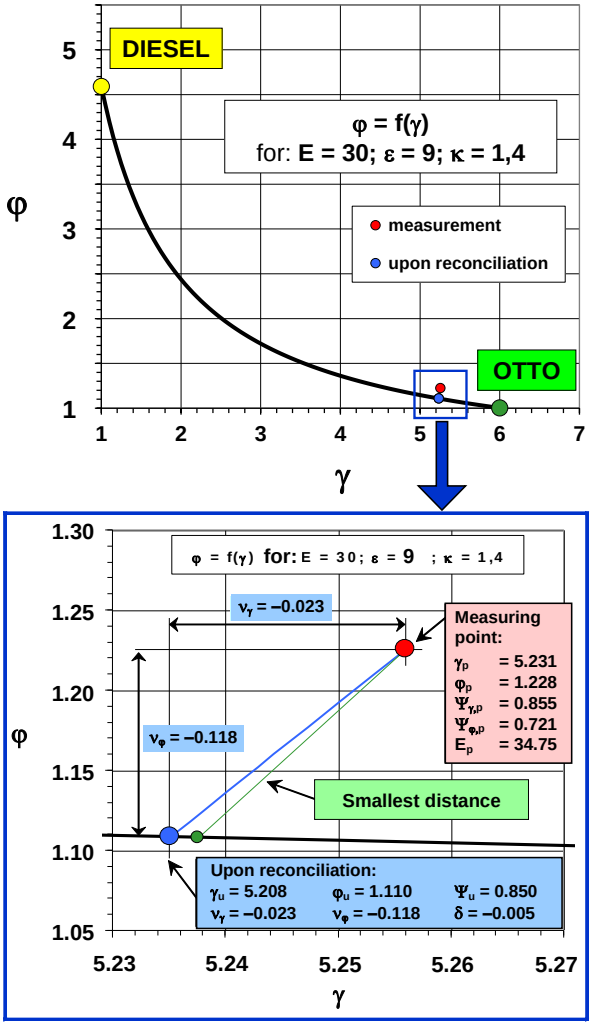

Fig. 2. Results of parameter (γ and φ) reconciliation for the Seiliger-Saba-the cycle

The experimentally determined measuring point does not lie on the characteristic showing the exact course of the relationship φ = f(γ) due to measurement errors. Also, for this reason, two different values of the unknown heat distribution number ($\Psi_{\gamma,p}$ and $\Psi_{\varphi,p}$ – Fig. 2) were obtained from the two relations (8.1) and (8.2). After applying the reconciliation procedure of the formulas (8), there was a shift of the measurement point to the line φ = f(γ), because now the relations (8) are strictly satisfied. Both formulas (8) also give the same values of the heat distribution number (marked Ψ_u in Figure 2). It is characteristic that the reconciliation algorithm does not move the measurement point to the line φ = f(γ) according to the smallest distance (Fig. 2).

The corrections ν_γ and ν_φ (Fig. 2) satisfy the condition:

$$|\nu_i| < 3|m_i| \qquad (14)$$

which satisfies the conditions for the applicability of the reconciliation method [9]. Therefore, the assumed accuracy of the measurements was maintained, and the reconciliation results can be considered satisfactory. At engine operating points where the above condition (14) is not met, the measurement results should be rejected.

Figure 3 shows, for illustration, the effect of double reconciling measurements with gross errors [4, 6]. The measuring point is located at a greater distance from the exact course of the relationship φ = f(γ). In such a situation, the reconciliation procedure does not cause this point to be shifted to the line φ = f(γ). Only the repeated application of the reconciliation algorithm shifts the point to the line of the exact function φ = f(γ). However, in this case, the values of the corrections ν_γ and ν_φ do not satisfy condition (14) for the applicability of the reconciliation algorithm.

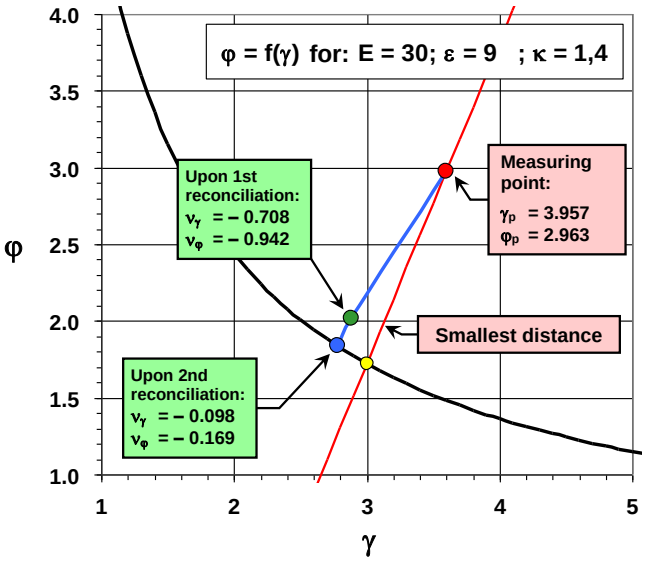

Fig. 3. Effect of double reconciliation on the correction of measurement results with gross errors

This means that the accuracy of the measurements has not been met. In this situation, the measurement results should be discarded because the errors exceed the required range. It is advisable to repeat the measurement of the parameters γ and φ for this engine operating point.

The reconciliation of measured quantities enables the determination of unambiguous and most probable values of unknowns along with an assessment of their accuracy. The

errors m_j of the unknowns y_j after reconciliation can be calculated according to the law of error transfer according to the relationship [7, 8]:

$$m_j^2 = \left(\frac{\partial y_j}{\partial x_1}\right)_0^2 m_1^2 + ... + \left(\frac{\partial y_j}{\partial x_i}\right)_0^2 m_i^2 + ... + \left(\frac{\partial y_j}{\partial x_n}\right)_0^2 m_n^2 \quad (15)$$

The presented example of the problem of selecting the parameters of the theoretical Seiliger-Sabathe cycle (load parameters γ, φ, and heat distribution number Ψ as an unknown) with the use of the equalisation calculus fully confirmed the need for its use.

Using the presented algorithm for reconciling the mentioned parameters, the example effects of selecting the theoretical cycles according to the real cycles are then presented. Example experimental tests of the real cycles were carried out on a spark-ignition engine type 170A1.046, the basic data of which are presented in Table 1. A comparison of the real engine cycles with the corresponding Seiliger-Sabathe cycles for idle and full load is illustrated in Fig. 4 and Fig. 5, respectively.

Table. 1. Technical data of the tested SI combustion engine

Engine designation	170A1.046
Engine type	spark ignition, 4-stroke, naturally aspirated
Number and arrangement of cylinders	4-cylinders in line
Piston diameter and stroke	65 × 67.7 mm
Engine displacement	0.899 dm^3
Compression ratio	9

For both tested engine operating conditions, the degree of internal excellence was also calculated, which is defined as follows [7]:

$$\xi_i = \frac{L_i}{L_o} \quad (16)$$

where: L_i – internal work (work of the real cycle), L_o – work of the theoretical cycle, and its values are presented in Table 2.

Table. 2. Degree of internal excellence for tested SI engine loads

Engine load	ξ_i
Idling (Fig. 4)	0.250
Full load, 59.6 Nm/rad (Fig. 5)	0.584

A characteristic feature of the operation of a spark-ignition engine is a much lower value of the ξ_i degree at idle speed compared to higher loads, especially full load. One of the main reasons for this situation is the quantitative method of load regulation using a throttle valve as a flow throttling element. Thus, the degree of internal excellence ξ_i characterizes the quality of thermal and flow processes occurring during engine operation. Its value, and therefore also the internal work of the engine L_i (also called indicated work, i.e. work of real cycle), is significantly influenced by many factors, in particular:

– heat exchange (engine cooling)
– charge exchange work
– incomplete combustion
– the real composition of the combustible mixture
– fuel burnout course
– working medium as a real gas
– way and the ignition point of the mixture.

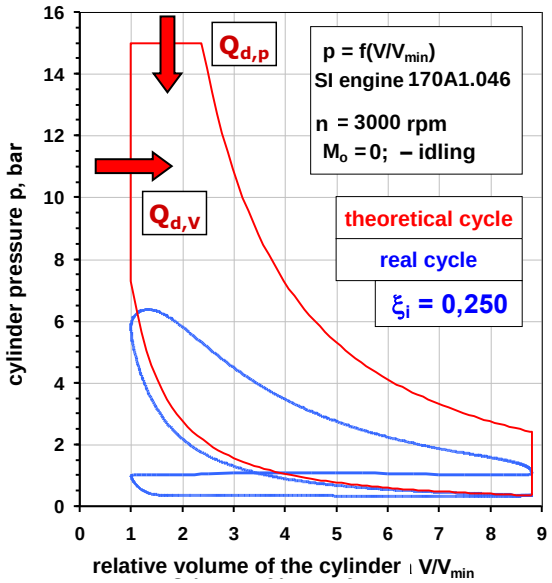

Fig. 4. Comparison of the real engine cycle with the corresponding theoretical Seiliger-Sabathe cycle for idling

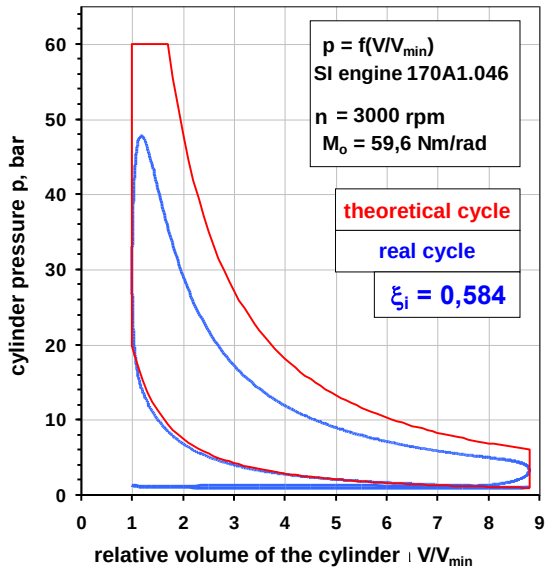

Fig. 5. Comparison of the real engine cycle with the corresponding theoretical Seiliger-Sabathe cycle for full load

The comparison of theoretical and real cycles presented in Fig. 4 and Fig. 5 additionally leads to the conclusion that the Seiliger-Sabathe cycle is also an appropriate theoretical cycle for the SI engine. Such a conclusion is justified by the fact that heat release during combustion in the spark-ignition engine also takes place at the beginning of the power stroke.

3. Conclusion

The essence, principles, and purpose of using the equalization calculus to reconcile measurement data are presented. The issue was illustrated by an example of reconciling the dependencies linking the parameters of the Seiliger-Sabathe theoretical cycle, which fully confirmed the need to use this calculus.

The reconciliation procedure is particularly useful in situations where the formulas from which the unknown quantities are calculated are particularly "sensitive" to measurement errors of experimentally determined quantities. The reconciliation algorithm provides the following advantages [3, 6, 8, 9]:

– unambiguous and most probable values of unknowns are obtained, along with an assessment of their accuracy
– probable errors of measurement results are reduced
– one obtains the ability to control whether the assumed accuracy of measurements has been met
– those measurement results whose probable error exceeded the required range can be rejected.

In addition, the equalization calculus can also be used to check the accuracy of quantities that are estimated, for example, on the basis of literature data and to control simplifying assumptions.

Acknowledgements

This research is supported by the Ministry of Education and Science (Poland) under statutory research funds of the Faculty of Energy and Environmental Engineering of Silesian University of Technology.

Nomenclature

E	energy-stoichiometric parameter
k	correlates
m	mean absolute error of the measurement result
M_o	torque
n	engine speed
p	pressure
Q	heat
s	specific entropy
V	volume
γ	isochoric load parameter (pressure increase ratio)
δ	correction of the heat distribution number
ε	compression ratio
ν_γ	correction of the isochoric load parameter
ν_φ	correction of the isobaric load parameter
φ	isobaric load parameter (volume increase ratio)
ξ_i	degree of internal excellence
Ψ	heat distribution number

Bibliography

[1] Alhaj-Dibo M, Maquin D, Ragot J. Data reconciliation: a robust approach using contaminated distribution. application in mineral processing for multicomponent products. IFAC Proceedings Volumes. 2004;37(15):155-160. https://doi.org/10.1016/S1474-6670(17)31016-9

[2] Cisek J. The influence of non-cooled exhaust gas recirculation on the indicator diagrams and heat release parameters in diesel engine cylinder. Combustion Engines 2017;171(4): 283-288. https://doi.org/10.19206/CE-2019-434

[3] Crowe CM. Data reconciliation – progress and challenges. J Process Contr. 1996;6(2-3):89-98. https://doi.org/10.1016/0959-1524(96)00012-1

[4] Di Fonzo T, Marini M. Simultaneous and two-step reconciliation of systems of time series: methodological and practical issues. J R STAT SOC C-APP. 2011;60(2):143-164.

[5] Jiang X, Liu P, Li Z. Data reconciliation and gross error detection for operational data in power plants. Energy. 2014;75;14-23. https://doi.org/10.1016/j.energy.2014.03.024

[6] Pielecha I. Control algorithms for a Range Extender vehicle with an combustion engine. Combustion Engines. 2020; 183(4):3-10. https://doi.org/10.19206/CE-2020-401

[7] Postrzednik S, Żmudka Z. Thermodynamic and ecological issues of operating internal combustion piston engines (in Polish). Publisher Silesian University of Technology, Gliwice 2007.

[8] Szargut J. Equalisation calculus in thermal technology (in Polish). Publisher PAN, Katowice 1984.

[9] Szega M. Extended applications of the advanced data validation and reconciliation method in studies of energy conversion processes. Energy. 2018;161:156-171. https://doi.org/10.1016/j.energy.2018.07.094

[10] Szega M. Methodology of advanced data validation and reconciliation application in industrial thermal processes. Energy. 2020;198. https://doi.org/10.1016/j.energy.2020.117326

[11] Yang X, Yang Q, Dong W. Aeroengine data reconciliation model based on cooperative working equations. Energy. 2019;186. https://doi.org/10.1016/j.energy.2019.115914

[12] Yu J, Han W, Chen K, Liu P, Li Z. Gross error detection in steam turbine measurements based on data reconciliation of inequality constraints. Energy. 2022;253. https://doi.org/10.1016/j.energy.2022.124009

[13] Zhanga M, Xianga M, Zhengd Z, Talebie SP, Mandic DP. A class of widely linear quaternion blind equalisation algorithms. Signal Process. 2025;230. https://doi.org/10.1016/j.sigpro.2024.109863

[14] Żmudka Z, Postrzednik S. Comparative analysis of theoretical cycles of independent valve control systems of the SI engine. Combustion Engines. 2024;197(2):15-21. https://doi.org/10.19206/CE-174321

Prof. Zbigniew Żmudka, DSc., DEng. – Faculty of Energy and Environmental Engineering, Silesian University of Technology, Poland.
e-mail: *zbigniew.zmudka@polsl.pl*

Article citation info:
Sproch M, Mamala J, Augustynowicz A, Graba M. Research on fuel and electric energy consumption in passenger cars in a mixed cycle, using the example of local road traffic in Opole. Combustion Engines. 2026;204(1):158-166. https://doi.org/10.19206/CE-209992

Maciej SPROCH
Jarosław MAMALA
Andrzej AUGUSTYNOWICZ
Mariusz GRABA

Combustion Engines
Polish Scientific Society of Combustion Engines

Research on fuel and electric energy consumption in passenger cars in a mixed cycle, using the example of local road traffic in Opole

ARTICLE INFO

Received: 19 June 2025
Revised: 11 July 2025
Accepted: 27 August 2025
Available online: 30 September 2025

This paper presents a comparative analysis of fuel and electric energy consumption by passenger cars in a mixed cycle in real road conditions, taking into account the specific nature of local traffic in the city of Opole. The research was carried out in real road conditions on a designated road cycle, in accordance with the guidelines described in the RDE (Real Driving Emissions) road cycle procedure. The designated road cycle reflects the conditions prevailing on urban, rural, and motorway roads. The results obtained from the road cycle were compared with the fuel and electric energy consumption values declared by car manufacturers in the type-approval documentation authorizing the car for use on public roads. The comparative analysis revealed discrepancies between actual and laboratory data, which for electric passenger cars are determined in relation to the WLTP cycle. In the case of combustion engine passenger cars, fuel consumption was additionally converted into energy expenditure, which enabled a comparison of the energy efficiency of different drive systems in real road conditions in the TTW (Tank-To-Wheels) system. The article highlights the challenges of developing a representative road cycle for local road conditions that complies with RDE guidelines.

Key words: *RDE, WLTP, BEV, fuel consumption, energy efficiency*

1. Introduction

In recent years, there has been a rapid development of alternative propulsion technologies, in particular electric (BEV) and hybrid (HEV/PHEV) cars, with an ongoing debate as to which propulsion system will be dominant in the future. A clear increase in the number of passenger cars equipped with electric propulsion is already being observed. According to the International Energy Agency (IEA), global sales of electric passenger cars exceeded 17 million units in 2024, accounting for more than 20% of all new passenger cars put on the road. Projections for 2025 show a further increase in sales to more than 20 million electric cars, meaning that at least a quarter of all passenger cars sold globally will be electric [16]. At the same time, the issue of reliably assessing the electric energy consumption under the actual operating conditions of an electric car is becoming increasingly important [23, 33]. Many studies have been devoted to this problem and are being carried out by various research institutions, providing databases used by car manufacturers [7, 11]. Different companies and organisations have developed tests to determine the driving range of electric vehicle with different results. Some tests have been standardised where the procedure must follow specific protocols such as NEDC, WLTP, FTP-75 and JP-08 [5]. Research procedures based on modelling, simulation, and optimization of the electric vehicle powertrain are proposed, taking into account various factors affecting the vehicle's range [2]. Driving conditions, the influence of auxiliary devices, the driving style of the driver and the braking energy recuperation strategy were considered to be the most important. The driving range of an electric vehicle is therefore not a fixed value, as it depends on many factors such as driving mode [25], road type [22], environment [17], battery aging [35], etc. Therefore, the actual value is currently different from the car manufacturer's data. The driving range depends on the capacity of the battery, provided that the above-mentioned factors remain constant, so a higher capacity results in a longer range. Nevertheless, battery capacity is not constant as it evolves with discharge rate and power demand, resulting in variable autonomy and driving range. The impact of discharge rate has been extensively studied by many authors analysing various factors that modify battery capacity due to operating conditions (uncertainty in charging decisions) [37]. In 2017, the Real Driving Emissions (RDE) cycle for combustion-powered passenger cars was introduced. It was based on real road conditions. It was introduced as part of the European Union's vehicle emissions regulations [8] to measure actual emissions during normal driving on the road and not just under laboratory conditions [24, 31]. The justification for the introduction of the cycle and its further development is confirmed by studies conducted which show significantly higher emissions during on-road measurements than those reported during chassis dynamometer tests [29, 32].

Regardless of the powertrain used in a passenger car, its type-approval documentation contains information on the fuel and/or electric energy consumption per 100 km travelled. Since September 2017, new regulations have been introduced, replacing the NEDC laboratory tests with WLTP cycles for newly manufactured cars. The driving time has been changed from 20 to 30 min., the distance covered has been increased from 11 to 23.25 km and the average cycle speed has been increased from 34 to 46.5 km, while the maximum speed has been increased from 120 to 131 km/h. This change gives a more reliable reference of the cycle to road conditions, but not the actual road conditions. A turning point in considering the reliability of fuel consumption and emission data and was the so-called 'Diesel gate scandal', which revealed the use of so-called 'defeat devices' – solutions to identify the test procedure and

the possibility of artificially underestimating emissions under laboratory conditions [10]. A study by Franco et al. showed that nitrogen oxide emissions under real-world driving conditions could exceed acceptable limits by up to 20 times, especially for modern diesel cars formally meeting Euro 5 and Euro 6 standards [13]. In response to a crisis of confidence in test procedures, the aforementioned Real Driving Emissions (RDE) procedure was developed to make measurements more transparent and representative [30]. On-road emissions of nitrogen oxides, hydrocarbons or carbon monoxide are very sensitive and variable, but carbon dioxide emissions resulting mainly from fuel burned show less sensitivity [1, 14, 20, 28, 35]. An important aspect of the test procedure is that there are a number of factors that affect fuel consumption and emissions [28]. These can be generally divided into weather-related factors (wind speed and direction, humidity and temperature), road topography (road grade, elevation, surface roughness), road environment (traffic condition, road features, travel distance), driving dynamics (speed, acceleration, deceleration, power demand) and driver behaviour (timid, aggressive) [15, 34, 36].

In view of taking the above into account, it is currently recognised that the RDE cycle procedure allows fuel consumption and carbon dioxide emissions to be determined in a realistic manner with the possibility of comparing them authentically with each other, with repeatable journeys over a given road cycle. As a result of the aforementioned several aspects of the problem under consideration, the question arises in the context of the changes in the segment of electric passenger cars produced and changes in the measurement procedure: How to reliably compare the fuel and electric energy consumption of the new types of propulsion systems – especially combustion-electric (hybrid) and electric – in the context of their consumption under conditions of everyday use. This issue becomes particularly relevant under local traffic conditions, where it is influenced by traffic volume, infrastructure, terrain or frequency of stops and accelerations, among other factors [3]. Many studies have found that local driving conditions, including the intensity of acceleration or frequency of stops, have a significant impact on the energy intensity of an electric car. EVs with different drivetrain types show different sensitivity to these factors, as confirmed by the study of Thomas et al. [30]. In the article, Mamala et al. found that the frequent braking and speed changes characteristic of urban driving contribute to efficient energy recovery in electric cars, increasing their energy efficiency [18, 19]. In contrast, for conventionally powered cars, driving in a similar style usually means an increase in fuel consumption. In this context, the findings of Fluder et al. are also relevant, as they demonstrated that the driving mode selected in a hybrid vehicle has a significant impact on the nature of energy flow and, consequently, on total fuel and energy consumption in the RDE test. Furthermore, these studies have shown that the energy efficiency of a vehicle varies depending on the drive control strategy, confirming the need for real-world measurements also for HEV/PHEV vehicles [12].

In light of the above, the analysis of fuel and electric energy consumption in the RDE cycle, set in the context of local driving conditions – on the example of mainly the Opole city area – is a justified and necessary approach for a full evaluation of the efficiency of the passenger car powertrains.

2. Research methodology and object of research, and justification for own research

2.1. Methodology of conducting own research

In view of the constant discrepancies between the declared and actual fuel and electric energy consumption at variable speed, the authors undertook their own research aimed at comparing the data from the tests approving the car for road traffic with the results obtained in local real traffic conditions. To this end, based on the RDE cycle guidelines, a mixed cycle road test was developed, with the route running mainly through the city of Opole and its immediate surroundings. The total length of the route was 92.5 km and included urban, rural, and motorway sections, covering both infrastructure characteristics and traffic intensity. Each of the declared road sections was at least 16 km long, and the proportion of individual traffic phases were determined for the road cycle developed in this way. For the road cycle prepared in such way, road tests of passenger cars were carried out using the individual case method, for which the unit energy consumption in the TTW system was determined.

The tests were conducted in a certain manner, ensuring the comparability of results between passenger cars and compliance with road test requirements. Each passenger car completed the test route with a single driver, while recording traction indicators of the speed profile and drive system indicators, with its mass in accordance with the RDE cycle requirements. The energy expenditure of the electric passenger car was recorded by measuring the energy consumption from the traction battery in terms of its current and voltage. For the combustion engine drive system, fuel consumption was measured from the fuel tank in the form of fuel mass loss over time. The obtained data allowed the determination of the energy consumption per unit distance (kWh/100 km) and the energy consumption per unit mass of the car (J/(kg·m) for both types of powertrains.

2.2. Description of research objects

Passenger cars representing different drive units in an automated drive system were used for the road tests. The first passenger car is a fourth-generation Škoda Citigo-e electric vehicle (BEV) manufactured in 2019 (Fig. 1). It is a compact car equipped with an electric drive powered by a lithium-ion battery pack with a net capacity of 32.3 kWh (total capacity: 36.8 kWh). The curb weight of this electric car is 1235 kg, of which 248 kg is accounted for by the traction battery installed in the chassis. The technical data of the EV are shown in Table 1.

The second passenger car is an internal combustion engine (ICE) car, an Audi Q5 manufactured in 2019, with a spark ignition (gasoline) engine with a displacement of 1984 cm^3. The car is equipped with an AWD (quattro) drive system (Fig. 2), an automatic transmission, and driver assistance systems typical for the mid-size SUV segment. The curb weight of the ICE car is 1789 kg. The technical data for the combustion engine vehicle is provided in Table 2.

Fig. 1. Test object no. 1 [27]

Table 1. Technical data of the BEV [27]

Technical data	Value
Gross battery capacity	36.8 kWh
Net battery capacity	32.3 kWh
Maximum speed	130 km/h
Average energy consumption WLTP	12.6 kWh/100 km
WLTP range	265 km
Engine power	61 kW
Torque	212 Nm
Curb weight	1235 kg

Fig. 2. Test object no. 2 [4]

Table 2. Technical data of the ICE vehicle

Technical data	Value
Engine capacity	1984 cm^3
WLTP CO_2 emission	187 g/km
Maximum speed	240 km/h
Average fuel consumption WLTP	8.3 dm^3/100km
Basic fuel range	843 km
Engine power	185 kW
Torque	370 Nm
Curb weight	1789 kg

The passenger cars used in the tests differ in terms of design, drive system, and traction characteristics. A car equipped with an electric drive system, taking into account the technical data, has a significantly lower curb weight and no gearbox compared to a car with a conventional drive system, and is a typical type of passenger car optimized for urban driving, providing a range suitable for everyday use with an automatic transmission. Differences in weight, movement resistance, type of drive, and intended use significantly affect energy consumption in real road conditions, which makes their comparison particularly interesting from the point of view of analysing unit energy consumption per 1 kg of car weight.

An important element of the measurements performed in the road cycle is the measurement system for traction indicators and the drive system. A GPS data recording device was used to record traction cars – speed, acceleration, distance travelled. For drive system indicators, a proprietary measurement system developed in LabView environment was used It enables the recording of drive system indicators in the time domain from the on-board data transmission network based on the CAN BUS, recording, among other things the rotational speed of the electric motor drive shaft, the intensity and current supplying the electric motor, torque, battery capacity, acceleration pedal, distance, electric motor power, and the power required to drive additional devices (Fig. 3).

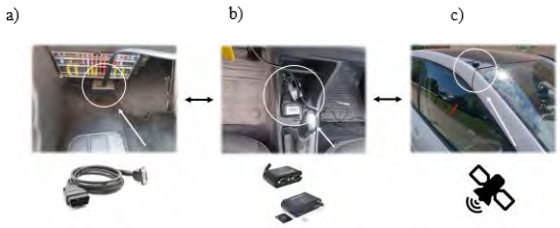

Fig. 3. Device for measuring traction indicators and the drive system: a) connection to the CAN BUS network, b) data recording device, c) GPS system recording [6]

In the case of a vehicle with a conventional internal combustion engine, fuel consumption was determined on the basis of data recorded using one of the dedicated interfaces for Volkswagen group cars (VCDS Diagnostic System). This enabled the reading and recording of the engine's operating parameters in real time. The basic parameter used in the analysis was the only signal for instantaneous fuel consumption, recorded in volume units (l/h). This data was recorded continuously during the test drive at a sampling frequency of 0.25 Hz.

In order to determine the mileage fuel consumption on a given section of the route, instantaneous fuel consumption was summed and then converted in relation to the distance travelled, which allowed for obtaining the fuel consumption unit expressed in liters per 100 km (l/100 km). The solution used is highly repeatable under comparative conditions, which makes it useful in relative analyses (e.g., comparison of routes, driving styles, or vehicles with different drive systems). The accuracy of fuel consumption measurement results from the method and algorithms applied by the vehicle's onboard computer manufacturer. The fuel measurement is based on the injector performance corrected for fuel temperature. In this case, these are Bosch injectors with a flow rate of 4 ml/s under pressure, which, with a signal sampling rate of 0.25 Hz, allows recording instantaneous fuel consumption with a dose of 1 ml.

Fuel consumption measurement for a vehicle with an internal combustion engine was an additional and comparative measurement applied in road testing. Therefore, the accuracy of fuel flow through specific injectors was not determined in relation to the gravimetric fuel consumption method. The injector calibration performed by the manufacturer, with coding specific to the engine control computer, is sufficient for road measurements based on cumulative fuel consumption and average values, while the obtained data on mileage fuel consumption should be treated as approximate.

2.3. Development of a road test in a mixed cycle

The development of a road test cycle based on the requirements of the RDE (Real Driving Emissions) procedure is a challenge when analysing the actual energy or fuel consumption in the drive system. Unlike laboratory test conditions, such as WLTP or the earlier NEDC, the RDE procedure requires measurements to be taken in real traffic conditions, taking into account variations in speed, terrain gradients, road, and weather conditions. This subsection presents the assumptions and process of developing a mixed cycle road test, which was used to compare the energy consumption of electric and combustion engine cars. The development of the test includes not only the selection of a route in accordance with RDE metrics, but also ensuring its representativeness for typical conditions of electric car use.

Table 3. Requirements for the RDE procedure compared with WLTP test conditions: a) road conditions, b) boundary conditions [9]

a)

RDE			WLTP
Test details		RDE test conditions	WLTP test conditions
Type of trip (test)		Real traffic	Laboratory test
Total trip duration		90–120 min	~30 min.
Driving area	Urban	> 16 km	Total distance: ~23.25 km
	Rural	> 16 km	
	Motorway	> 16 km	
Ratio of driving in the area to the total distance	Urban	29–44%	Specific driving phases: Low; Medium; High; Extra high
	Rural	23–43%	
	Motorway	23–43%	
Average driving speeds	Urban	15–40 km/h	Overall average: ~46.5 km/h
	Rural	60–90 km/h	
	Motorway	> 90 km/h (> 100 km/h for > 5 min)	

b)

RDE			WLTP
Parameter		RDE test conditions	WLTP test conditions
Vehicle weight		≤ 90 of max vehicle weight	Test weight – reference weight (dependent on vehicle variant)
Elevation	Moderate	0–700 m	No evaluation changes
	Extended	700–1300 m	
Altitude difference		Between start and finish of trip > 100 m	No
Cumulative altitude gain		1200 m/100 km	No hills
Ambient temperature	Moderate	0–30°C	~23°C
	Extended	(–7°C) – 0°C 30–35°C	
Percentage of stopping		6–30% during the trip in the urban area	Urban cycle simulation
Maximum speed		145 km/h (160 km/h for 3% of the driving time in the motorway area)	Up to ~131 km/h (in the 'Extra high' phase)
Dynamic boundary conditions	Max. metric	95th percentile v·a	Specific acceleration and deceleration points – no RPA
	Min. metric	RPA (Relative Positive Acceleration)	
Use of auxiliary systems		Free use without restriction as in real use	Limited

2.3.1. Detailed guidelines for RDE-compliant road cycles

To fully illustrate the difference between tests and real-world tests, a comparison of the requirements is presented in the form of Table 3 [9].

2.3.2. Detailed description of the mixed cycle in Opole

The road cycle (Fig. 4) ran mainly through the city of Opole, in accordance with the research objective. Due to the proximity of a motorway, this section of the road was integrated into the road cycle as a high-speed traffic area. The total distance of the route was in line with the RDE requirements Depending on the traffic intensity, the journey took between 90 and 120 minutes. The characteristic points of the route are shown below.

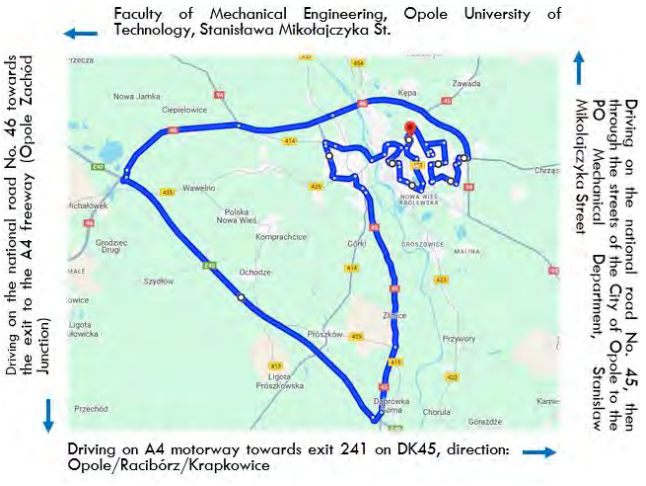

Fig. 4. Diagram of the most important points along the route

The cycle consists of five stages, including urban, rural, and motorway driving, starting and ending at the Faculty of Mechanical Engineering of the Opole University of Technology. The total distance is 92.5 km, and the estimated travel time is 1 hour and 35 minutes. The route is characterized by varied topography (143–195 m above sea level) and a speed range typical for road cycles (average 50–60 km/h, maximum 140 km/h). The most important points along the route include key transport sections around Opole, providing various traffic conditions. Taking into account the speed classification and data from the running through the city of Opole, it was possible to determine the distance for three characteristic driving areas, hence, in the urban area, the vehicle travelled 39.6 km, in the rural area 28.7 km, and 26.3 km in the motorway area, meeting the minimum distance requirement of 16 km in a given area. This route was planned to take into account real traffic conditions and topography, while meeting the RDE test requirements for distance, speed, and elevation difference.

The structure of the cycle was verified by analysing telemetry data, and the results were presented in the form of graphs and tables.

Figure 5 shows a visualization of the speed profile for the entire distance, divided into speeds that determine the area of travel: urban, rural, and motorway.

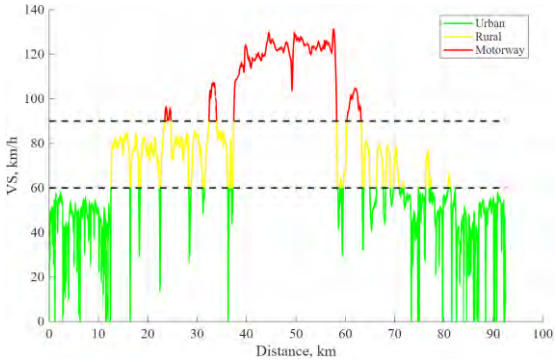

Fig. 5. Recorded speed profile for the RDE cycle in the Opole city area for a sample trip, VS – Vehicle Speed

Fig. 6. Visualisation of driving speed for a recorded road cycle

Thanks to the data recorded by the GPS system, it was possible to compile the most important kinematic parameters graphically on a map (Fig. 6) and in the form of table (Table 4), comparing them with the requirements of the RDE cycle procedure.

Table 4. Comparison of measurement data with the conditions of the RDE test procedure for cycle running through the city of Opole

Parameter	Value	RDE test conditions
Route loop area	The city of Opole and the surrounding area	Variable driving area: – urban area – rural area – motorway area
Total driving time	114 min	90–120 min
Total distance	92.5 km	> 48 km
Avg driving speed – urban areas	31.0 km/h	15–40 km/h
Avg driving speed – rural areas	74.9 km/h	60–90 km/h
Avg driving speed – motorway areas	113.2 km/h 11.5 min	> 90 km/h (> 100 km/h for 5 min)
Distance in urban areas	39.6 km	> 16 km
Distance in rural areas	28.7 km	> 16 km
Distance in motorway areas	26.3 km	> 16 km
Percentage of urban areas	42.8%	29–44%
Percentage of rural areas	31%	23–43%
Percentage of motorway areas	26.1%	23–43%
Percentage of time spent stationary in urban areas	27%	6–30%
Compliance with the RDE procedure		✓

Data from the on-board GPS receiver was also used to analyse the topography of the terrain along the entire test route. Based on the recorded geographical coordinates and altitude above sea level, it was possible to reconstruct the elevation profiles of the route (Fig. 7). The altitude values were digitally processed and then converted into a time series, which made it possible to calculate the total altitude gain in accordance with the requirements of the RDE (Real Driving Emissions) metric.

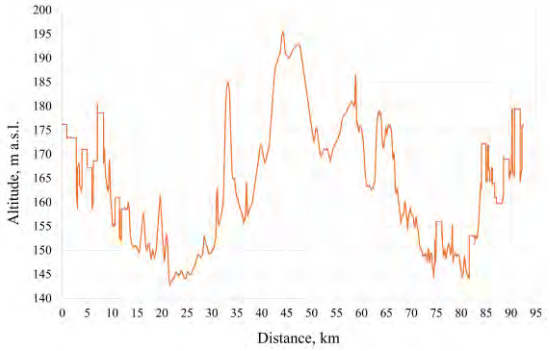

Fig. 7. Height profile and data for a registered sample measurement section

Only positive altitude changes (ascents) were used for further analysis, which made it possible to assess the actual load on the drive system resulting from the terrain. The values obtained were referenced to the total length of the route, which made it possible to verify compliance with the requirement: a maximum of 1200 m of elevation gain per 100 km (i.e. 12 m/km). In the analysed case, this value was 4.9 m/km, which means that the route was within the limits acceptable for RDE tests and can be considered representative in terms of topography. The data is summarised in the Table 5.

Table 5. Summary of terrain topography data

Parameter	Value
The main area	City of Opole
Total estimated driving time	1 h 35 min.
Total distance	92.5 km
Lowest point	143 m a.s.l.
Highest point	195 m a.s.l.
Average driving speed	50–60 km/h
Maximum driving speed	140 km/h
The greatest difference in height	52 m a.s.l.
Height difference (start – finish)	~0.3 m
Total height increase	490 m/100 km
Compliance with the RDE procedure	✓

3. Results and data analysis

3.1. Presentation of actual measurement data

Table 6 shows the discrepancy between actual and declared (homologated) electric energy consumption. In the case of a car equipped with an electric drive system, during test no. 1, with active and effective energy recuperation, the average energy consumption was 11.1 kWh/100 km, which was 12% lower than the homologation value (WLTP). A similar situation occurred in the case of a combustion engine car, where fuel consumption was 22.3% lower than the declared value. In order to verify the impact of the en-

ergy recovery level, a test with a minimum level of recuperation was carried out in test no. 2. In this case, the energy consumption was 13.2 kWh/100 km, which is only 4.8% higher than the WLTP value (12.6 kWh/100 km). Setting the control preferences in the drive system by the intensity of energy recuperation has a significant impact on the total energy consumption in the actual driving cycle.

Table 6. Comparison of actual and measured data: a) for a BEV, b) for an ICE vehicle

a)

BEV	Average EC WLTP [kWh/100 km]	Average EC RDE [kWh/100 km]
Test no. 1	12.6	11.1
Test no. 2	12.6	13.2

b)

ICE	Average FC WLTP [dm^3/100 km]	Average FC RDE [dm^3/100 km]
Test no. 3	8.3	6.8

3.2. Conversion of fuel consumption into energy expenditure

In order to compare the energy efficiency of both drive systems based on the actual road cycle, fuel consumption was converted into energy value (Wh/km), assuming the calorific value of 95-octane gasoline to be 32 MJ/dm^3 [21]. This approach allows for a direct comparison of energy values between ICE and BEV cars, also in the context of different levels of recuperation (maximum and minimum) used in electric vehicles. The results obtained are presented in a numerical summary – separately for sample drive trip.

Energy expenditure calculations for an ICE car in a TTW (Thank To Wheels) system:

$$E_c\left[\frac{Wh}{km}\right] = \frac{F_c[\frac{dm^3}{100\ km}] \cdot HV_f[\frac{MJ}{dm^3}]}{100} \quad (1)$$

where: E_c – energy consumption [Wh/km], F_c – fuel consumption [dm^3/100 km], HV_f – heating value of fuel [MJ/dm^3]

$$E_c\left[\frac{Wh}{km}\right] = \frac{6.8\left[\frac{dm^3}{100\ km}\right] \cdot 32\left[\frac{MJ}{dm^3}\right]}{100} \quad (2)$$

Energy expenditure assuming that 1 MJ = 277.78 Wh:

$$E_c\left[\frac{Wh}{km}\right] = 604.4\ [\frac{Wh}{km}] \quad (3)$$

This value is the chemical energy value of the fuel type used (Table 7).

Table 7. Summary of energy expenditure for an ICE car

ICE	Average FC RDE [dm^3/100 km]	ETTW [Wh/ km]
Test no. 3	6.8	604.4

Table 8. Summary of energy expenditure for a BEV car

BEV	Average EC RDE [kWh/100 km]	ETTW [Wh/km]
Test no. 1	11.1	111
Test no.2	13.2	132

However, the energy expenditure values for a BE vehicle in the TTW (Thank To Wheels) system can be calculated by taking into account the average energy consumption calculated on the basis of the voltage and current recordings of the vehicle's traction battery. The results are presented for two tests carried out and are shown in Table 8.

In road tests based on the RDE procedure, the energy consumption of a combustion engine (ICE) car was 604.4 Wh/km (TTW) and was calculated based on fuel consumption in a full road cycle. For an electric vehicle (BEV), varying values of electric energy consumption were recorded, amounting to 111 Wh/km for test no. 1, with maximum recuperation settings, and 132 Wh/km for test no. 2, with minimum energy recuperation. The electric car showed lower energy consumption in the TTW system compared to the ICE, more than 5 times lower, depending on the intensity of recuperation. Effective recuperation (test no. 1) additionally reduced energy consumption by approximately. 15.9% compared to test no. 2.

3.3. Energy efficiency analysis for specific driving areas

The recording of traction and drive system indicators made it possible to analyse the impact of actual road conditions on energy efficiency for specific driving areas, in accordance with the adopted RDE procedure classification, i.e., urban, rural, and motorway areas. In order to present the energy consumption of the drive system, the results were converted into kWh and kWh/100 km (Table 9). The weights for individual driving areas are also given in brackets, referring to the total energy and total distance travelled, respectively [26].

Table 9. Summary of energy expenditure for individual driving areas: a) BEV with maximum recuperation, b) BEV with minimum recuperation, c) ICE vehicle in normal operating mode [26]

a)

BEV	Driving area	ETTW [kWh]	Distance [km]	Specific EC [kWh/100 km]
Test no.1	Urban	3.4 (32.6%)	39.2 (42.4%)	8.57
	Rural	3.2 (31.3%)	30.2 (32.6%)	10.7
	Motorway	3.7 (36.1%)	23.1 (25.0%)	16.1

b)

BEV	Driving area	E_{TTW} [kWh]	Distance [km]	Specific EC [kWh/100 km]
Test no.2	Urban	3.8 (31.5%)	38.4 (41.5%)	10.0
	Rural	3.3 (31.3%)	27.7 (29.7%)	11.9
	Motorway	5.1 (41.6%)	26.4 (28.5%)	19.3

c)

ICE	Driving area	E_{TTW} [kWh]	Distance [km]	Specific EC [kWh/100 km]
Test no.3	Urban	22.6 (40.4%)	36.2 (39.1%)	62.4
	Rural	15.0 (26.8%)	29.6 (32.0%)	50.8
	Motorway	18.3 (32.7%)	26.7 (26.4%)	68.5

In accordance with the adopted classification of RDE cycle areas (urban, rural, motorway), it showed significant differences in specific energy consumption (kWh/100 km) and in the structure of the share of individual areas in total energy consumption. For a BEV car driving with maximum recuperation, the lowest energy consumption occurred in the urban area – 8.57 kWh/100 km, with a high distance share (42.4%) and a correspondingly lower energy share (32.6%). On motorways, electric energy consumption al-

most doubled to 16.1 kWh/100 km. Although motorways accounted for only 25% of the route, they consumed as much as 36.1% of the total energy, due to strong aerodynamic resistance at higher speeds.

In the case of the RDE cycle with the same car but a different energy recovery configuration (minimum electric energy recovery), the reduction in recovery resulted in an increase in unit electric energy consumption in each area, especially in urban and motorway areas: urban: 10 kWh/100 km, motorway: 19.3 kWh/100 km. In this case, the motorway area, despite accounting for 28.5% of the route, already accounted for 41.6% of total energy consumption, which further highlights its energy intensity in the absence of electric energy recovery.

RDE testing with a car with a conventional internal combustion engine (ICE) in urban areas, despite accounting for only 39.1% of the distance, accounted for as much as 40.4% of the total energy consumption, with a mileage electric energy consumption of as much as 62.4 kWh/100 km, which indicates very low efficiency in starting and braking conditions in the TTW system. The highest electric energy consumption per kilometre was recorded on the motorway – 68.5 kWh/100 km, and the share of this area in the distance was the smallest (26.4%).

3.4. Specific energy consumption

In order to carry out a physically comparable analysis of the energy efficiency of cars, a unit energy consumption indicator was used, which determines the amount of energy consumed to move a given car mass over a specific distance, regardless of the type of drive or fuel. Unlike commonly used indicators such as fuel consumption (dm^3/100 km) or electric energy consumption (Wh/km), the unit J/(kg·m) is based solely on the basic SI units (mass, distance, energy), thus ensuring full comparability of results between cars of different mass, design, and power source.

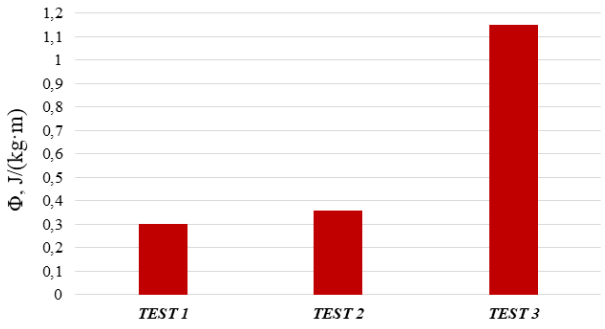

Fig. 8. Specific energy consumption for the BEV and ICE vehicle

For the calculations for the two cars tested, the masses before the road cycle test, including the driver's weight, were used. For the BEV car, this value was 1335 kg, while for the ICE car it was 1889 kg. The results are summarised in the Fig. 8.

The electric passenger car (BEV) demonstrated significantly lower specific energy consumption per unit of mass and distance travelled. During the first run, with maximum energy recovery, the specific energy consumption was 0.30 J/(kg·m), which was 74% lower in comparison to the ICE car (Φ = 1.15 J/(kg·m)). During the second run, with minimum energy recovery, the Φ value increased to 0.36 J/(kg·m), but was still 68% lower than the value obtained by a conventional car.

4. Conclusion

Analysis of actual data from the RDE cycle clearly indicates a significant advantage of electric vehicles (BEVs) over internal combustion engine vehicles (ICEs) in terms of energy efficiency – both in the TTW (Tank-to-Wheel) system and in terms of physical energy consumption [J/(kg·m)]. The lowest unit energy expenditure was achieved by the BEV car using the maximum level of energy recuperation (0.30 J/(kg·m)), while the highest was achieved by the ICE car (1.15 J/(kg·m)), which confirms the approximately four times higher unit energy consumption of a conventionally powered car. Even under conditions of limited recuperation (test no. 2), the electric car retains more than three times higher efficiency per unit of mass and distance travelled. Empirical data recorded during road tests also showed a significant impact of environmental characteristics and traffic dynamics on the distribution of energy consumption in different driving areas. In the case of BEVs, the highest energy consumption occurred in motorway conditions, while for ICEs it occurred in urban environments. This is due to differences in the traction characteristics of the car and its energy loss mechanisms, especially aerodynamic losses and rolling resistance (dominant in motorway traffic), as well as the lack of recuperation and the low efficiency of the combustion engine during frequent starting and stopping (typical of urban traffic). Currently, there is no strict standardisation of the mixed driving cycle for local conditions, which limits the possibility of objectively comparing cars in a given traffic environment. The use of averaged homologation standards (e.g. WLTP) does not take into account the characteristics of local traffic, the intensity of intersections, the length of stop phases, or the typical speed profile, which can lead to significant deviations in actual energy and emission results. Therefore, the development and validation of a local mixed driving cycle that reflects the real conditions of driving on the streets of Opole and its surroundings is an important direction for further research and may contribute to a more accurate assessment of drive technologies and the planning of future sustainable urban mobility strategies.

Nomenclature

AWD	all-wheel drive
BEV	battery electric vehicle
CAN	controller area network
CO	carbon monoxide
DK	national road
E_c	energy consumption
F_c	fuel consumption
EV	electric vehicle
HC	hydrocarbon
HEV	hybrid electric vehicle

HV_f	heating value of fuel
ICE	internal combustion engine
NEDC	New European Driving Cycle
NO_x	nitrogen oxides
PHEV	plug-in hybrid electric vehicle
RDE	real driving emissions
SUV	sport utility vehicle
TTW	thank to wheels
WLTP	Worldwide Harmonized Light Vehicle Test Procedure

Bibliography

[1] Adamiak B, Andrych-Zalewska M, Merkisz J, Chłopek Z. The uniqueness of pollutant emission and fuel consumption test results for road vehicles tested on a chassis dynamometer. Eksploat Niezawodn. 2025;27(1):195747. https://doi.org/10.17531/ein/195747

[2] Aidi A. Study of the factors affecting battery electric vehicle range. Figshare 2020. https://doi.org/10.6084/m9.figshare.12739982.v1

[3] Al-Wreikat Y, Serrano C, Sodré JR. Driving behaviour and trip condition effects on the energy consumption of an electric vehicle under real-world driving. Appl Energy. 2021; 297:117096. https://doi.org/10.1016/j.apenergy.2021.117096

[4] Audi Media Center. Even more sporty and versatile – the second generation of the Audi Q5 arrives. Warsaw: Audi Poland; (cited 2025 Aug 3). https://www.audi-mediacenter.com/en/press-releases/the-second-generation-of-the-audi-q5-arrives-10123

[5] Chen K, Zhao F, Liu X, Hao H, Liu Z. Impacts of the new Worldwide Light-Duty Test Procedure on technology effectiveness and China's passenger vehicle fuel consumption regulations. Int J Environ Res Public Health. 2021;18(6): 3199. https://doi.org/10.3390/ijerph18063199

[6] CSS Electronics. CAN bus data loggers and telematics. 2024 (cited 2025 Jun 15). https://www.csselectronics.com

[7] Edmunds tested: electric car range and consumption (cited 2025 Jun 11). https://www.edmunds.com/car-news/electric-car-range-and-consumption-epa-vs-edmunds.html#chart

[8] European Commission. Commission Regulation (EU) 2016/427 of 10 March 2016 amending Regulation (EC) No 692/2008 as regards emissions from light passenger and commercial vehicles (Euro 6). Off J Eur Union. 2016;L82:1-98.

[9] European Commission. Commission Regulation (EU) 2017/1151 of 1 June 2017 supplementing Regulation (EC) No 715/2007 of the European Parliament and of the Council on type-approval of motor vehicles with respect to emissions from light passenger and commercial vehicles (Euro 5 and Euro 6) and on access to vehicle repair and maintenance information. Off J Eur Union. 2017;L175:1-643.

[10] European Environment Agency. Exposing the true emissions of diesel cars: how effective are new EU vehicle emission standards in reducing emissions from light-duty diesel vehicles? Copenhagen: EEA 2016.

[11] EV Database. Range of full electric vehicles cheatsheet. (cited 2025 Jun 11). https://ev-database.org/cheatsheet/range-electric-car

[12] Fluder K, Pielecha I, Cieślik W. The impact of drive mode of a hybrid drive system on the energy flow indicators in the RDE test. Combustion Engines. 2018;175(4):18-25. https://doi.org/10.19206/CE-2018-403

[13] Franco V, Posada F, German J, Mock P. Real-world exhaust emissions from modern diesel cars. Washington (DC): International Council on Clean Transportation; 2014. Report. White Paper.

[14] Giechaskiel B, Valverde V, Melas A, Clairotte M, Bonnel P, Dilara P. Comparison of the real-driving emissions (RDE) of a gasoline direct injection (GDI) vehicle at different routes in Europe. Energies. 2024;17(6):1308. https://doi.org/10.3390/en17061308

[15] Guo C, Yang B, Andersen O, Jensen CS, Torp K. Ecomark 2.0: empowering eco-routing with vehicular environmental models and actual vehicle fuel consumption data. Geoinformatica. 2015;19:567-599. https://doi.org/10.1007/s10707-014-0221-7

[16] International Energy Agency. Global EV outlook 2025: catching up and pulling ahead. Paris: IEA 2025.

[17] Li J, Wu X, Xu M, Liu Y. A real-time optimization energy management of range extended electric vehicles for battery lifetime and energy consumption. J Power Sources. 2021; 498:229939. https://doi.org/10.1016/j.jpowsour.2021.229939

[18] Mamala J, Graba M, Mitrovic J, Prażnowski K, Stasiak P. Analysis of speed limit and energy consumption in electric vehicles. Combustion Engines. 2023;195(4):83-89. https://doi.org/10.19206/CE-169370

[19] Mamala J, Graba M, Stasiak P. Energy efficiency of the electric drive system of a passenger car under normal operation conditions. In: Rackov M, Miltenović A, Banić M, editors. Machine and industrial design in mechanical engineering. Mechanisms and Machine Science. 2025;174:921-932. Springer. Cham. https://doi.org/10.1007/978-3-031-80512-7_92

[20] Mei H, Wang L, Wang M, Zhu R, Wang Y, Li Y et al. Characterization of exhaust CO, HC and NO_x emissions from light-duty vehicles under real driving conditions. Atmosphere. 2021;12(9):1125. https://doi.org/10.3390/atmos12091125

[21] Minister of Climate and Environment. Regulation of 4 July 2022 on the methodology for calculating greenhouse gas emissions, determining emission factors and calorific values for individual fuels and the energy value of electricity. J Laws. 2022;1494.

[22] Mruzek M, Gajdáč I, Kučera Ľ, Barta D. Analysis of parameters influencing electric vehicle range. Procedia Eng. 2016; 134:165-174. https://doi.org/10.1016/j.proeng.2016.01.056

[23] Netherlands Organisation for Applied Scientific Research. Real-world fuel consumption and electric energy consumption of passenger cars in the Netherlands. Report No.: R10409. Delft: TNO; 2022. Available from: https://resolver.tno.nl/uuid:5d57a8

[24] Pryciński P. Selected emissivity assessment issues for electric and hybrid vehicles. Combustion Engines. 2025;202(3): 27-35. https://doi.org/10.19206/CE-205274

[25] Scurtu L, Varga BO, Mariasiu F, Buidin T, Borzan A, Moldovanu D. Numerical analysis of the SOC factor variations' influence on the autonomy of an electric vehicle. IOP Conf Ser Mater Sci Eng. 2019;568:012046. https://doi.org/10.1088/1757-899X/568/1/012046

[26] Siłka W. Teoria ruchu samochodu. WNT. Warszawa 2002.

[27] Škoda Auto. Citigoe iV – powertrain and safety. Mladá Boleslav: Škoda Auto (cited 2025 Jun 17). https://www.skodaauto.com/models/layers/layers/citigoe-iv-powertrain-and-safety

[28] Sordyl A, Chłopek Z, Merkisz J. Correlation relationships of processes in the combustion engine in the RDE test. Combustion Engines. 2024;199(4):112-125. https://doi.org/10.19206/CE-192877

[29] Suarez-Bertoa R, Valverde V, Clairotte M, Pavlovic J, Giechaskiel B, Franco V et al. On-road emissions of passenger cars beyond the boundary conditions of the real-driving emissions test. Environ Res. 2019;176:108572. https://doi.org/10.1016/j.envres.2019.108572

[30] Thomas J, Huff S, West B, Chambon P. Fuel consumption sensitivity of conventional and hybrid electric light-duty gasoline vehicles to driving style. SAE Int J Fuels Lubr. 2017;10(3):1052-1060. https://doi.org/10.4271/2017-01-9379

[31] Tietge U, Mock P, German J, Bandivadekar A, Ligterink N. From laboratory to road – a 2017 update of official and "real-world" fuel consumption and CO_2 values for passenger cars in Europe. Washington (DC): International Council on Clean Transportation; 2017. Report. White Paper.

[32] Weiss M, Bonnel P, Hummel R, Provenza A, Manfredi U. On-road emissions of light-duty vehicles in Europe. Environ Sci Technol. 2011;45(19):8575-8584. https://doi.org/10.1021/es2008424

[33] Weiss M, Winbush T, Newman A, Helmers E. Energy consumption of electric vehicles in Europe. Sustainability. 2024;16(17):7529. https://doi.org/10.3390/su16177529

[34] Xu H, Lei Y, Liu M, Ge Y, Hao L, Wang X et al. Research on the CO_2 emission characteristics of a light-vehicle real driving emission experiment based on vehicle-specific power distribution. Atmosphere. 2023;14(9):1467. https://doi.org/10.3390/atmos14091467

[35] Yao M, Zhu B, Zhang N. Adaptive real-time optimal control for energy management strategy of extended range electric vehicle. Energy Convers Manag. 2021;234:113874. https://doi.org/10.1016/j.enconman.2021.113874

[36] Zeng W, Miwa T, Morikawa T. Exploring trip fuel consumption by machine learning from GPS and CAN bus data. J East Asia Soc Transp Stud. 2015;11:906-921. https://doi.org/10.11175/easts.11.906

[37] Zhou Y, Wen R, Wang H, Cai H. Optimal battery electric vehicles range: A study considering heterogeneous travel patterns, charging behaviors, and access to charging infrastructure. Energy. 2020;197:116945. https://doi.org/10.1016/j.energy.2020.116945

Maciej Sproch, MEng. – Faculty of Mechanical Engineering, Opole University of Technology, Poland.
e-mail: *m.sproch@student.po.edu.pl*

Prof. Andrzej Augustynowicz, DSc., DEng. – Faculty of Mechanical Engineering, Opole University of Technology, Poland.
e-mail: *a.augustynowicz@po.edu.pl*

Prof. Jarosław Mamala, DSc., DEng. – Faculty of Mechanical Engineering, Opole University of Technology, Poland.
e-mail: *j.mamala@po.edu.pl*

Mariusz Graba, DEng. – Faculty of Mechanical Engineering, Opole University of Technology, Poland.
e-mail: *m.graba@po.edu.pl*

Article citation info:
Grochowalska J, Wrzask K, Kapusta Ł. Proper orthogonal decomposition analysis of an atomized fuel spray of marine diesel engine. Combustion Engines. 2026;204(1):167-175. https://doi.org/10.19206/CE-210467

Joanna GROCHOWALSKA
Klaudia WRZASK
Łukasz KAPUSTA

Combustion Engines
Polish Scientific Society of Combustion Engines

Proper orthogonal decomposition analysis of an atomized fuel spray of marine diesel engine

ARTICLE INFO

Received: 13 June 2025
Revised: 4 September 2025
Accepted: 8 September 2025
Available online: 26 September 2025

Most marine vessels are powered by diesel engines. Unfortunately, fuel combustion releases harmful toxic compounds into the atmosphere. The International Maritime Organization (IMO) regulates these emissions, making their reduction essential for engineers and scientists. The fuel combustion process in a marine diesel engine's cylinder precedes the fuel spray injection and atomization. Fuel spray's flow fluctuations and vortex structures significantly impact the combustion. This paper presents research using the Mie Scattering optical technique to analyze snapshot sequences of spray patterns recorded with a high-speed camera. These snapshots are the results of experimental research on atomized fuel sprays with a marine diesel engine injector within a constant volume chamber. The influence of different chamber backpressures on the fuel spray is studied. The Proper Orthogonal Decomposition (POD) method is promising for quantitatively analyzing spray structures and flow characteristics. This research demonstrates how different chamber conditions affect the decay of the POD singular values, which typically indicate flow characteristics like coherence and fluctuations.

Key words: *marine diesel engine, fuel sprays, Mie scattering optical technique, POD method, fuel flow characteristics*

1. Introduction

Maritime shipping is one of the most important transport sectors utilized in international trade for the transportation of goods, with most sea vessels traveling between continents. Marine vessels primarily use diesel engines for main and auxiliary propulsion. These marine diesel engines commonly burn heavy fuel oil (HFO) and marine diesel oil (MDO). Combustion of these fuels produces exhaust gases containing nitrogen oxides (NO_x), sulfur oxides (SO_x), carbon monoxide (CO), and particulate matter, significantly contributing to air pollution in marine environments [8, 19]. According to the International Maritime Organization (IMO), shipping emissions accounted for around 3% of global emissions in 2018 [9]. Despite ongoing development and introduction of alternative propulsion technologies and fuels, diesel engines continue to be the predominant equipment in vessel power plants. Diesel engines dominate maritime transport due to their reliability and established infrastructure, indicating that the shift to alternatives will be gradual. It becomes reasonable for engineers and scientists to work on improving the quality of fuel combustion in marine diesel engines. According to Deng [3], emission reduction strategies for diesel engines can be categorized into fuel optimization, pre-combustion control technologies, and exhaust after-treatment systems. The combustion process in marine diesel engine cylinders is characterized by dynamic, interdependent phenomena, with fuel atomization quality playing a critical role. Factors influencing fuel atomization include fuel injection pressure [4, 10, 17], fuel properties [16], and fuel injector nozzle geometry [22]. Furthermore, in [21], the authors show that the exhaust gas composition strongly depends on the opening pressure of the fuel injector.

When fuel is injected into the combustion chamber under high injection pressure, it is atomized, rapidly evaporates, and mixes with compressed air. The first stage of fuel jet breakup is called the primary breakup. This stage of fuel spray breakup is very important, as it determines the initial size and distribution of the resulting droplets, which directly affect the efficiency of atomization and subsequent atomization processes.

In the second stage, the disintegration of the fuel jet occurs under the influence of aerodynamic forces from the surrounding medium. Droplets formed by separation from the liquid core subsequently undergo secondary disintegration. In this context, assessing the quality of fuel atomization in internal combustion engines with direct cylinder fuel injection is crucial to achieving optimal combustion, energy efficiency, and low exhaust emissions [15]. Atomization quality is assessed based on the spray pattern and droplet distribution. It is not possible to directly measure the fuel atomization process inside the cylinder during engine operation. Therefore, specialized experimental setups equipped with constant volume chambers are typically used to investigate the fuel atomization process [6, 7, 23]. Fuel injection and atomization are rapidly changing phenomena. Optical imaging provides dynamic insights into the structural evolution of fuel sprays over time, necessitating sophisticated image processing techniques that accurately preserve structural characteristics [18]. It should also be noted that measuring droplet diameters in diesel sprays poses a challenge due to the small droplet size and high optical density, which significantly limit the range of techniques available for characterizing spray microstructure [13].

In this study, we explore the application of Proper Orthogonal Decomposition (POD) as an effective method for analyzing and quantifying the fuel atomization processes.

The POD method has been applied across various fields, including signal analysis, data compression, and image processing. In the context of fluid mechanics, POD was first introduced by Lumley [14] and was primarily used to describe turbulent flows quantitatively [1]. POD also finds

application in Computational Fluid Dynamics (CFD), particularly for dimensionality reduction [5]. This technique has become a popular and effective analysis tool in engine research. It has been successfully used to identify turbulent flows and fluctuations generated by the intake port of a direct injection spark ignition engine [11]. In [2], the authors demonstrated that POD can be applied to identify and quantify cyclic variations in intake air motion and spray structure under running engine conditions. Additionally, Weiss [20] offers a practical and intuitive tutorial on the POD method for fluid mechanics engineers, including MATLAB code examples.

This paper aims to present the application of the POD method for the preliminary analysis of the fuel injection processes inside the cylinder of a marine diesel engine. To this end, experimental results of fuel spray characteristics obtained in a constant volume chamber using a marine diesel engine injector were utilized. Integrating POD with high-speed imaging allows for decomposing complex spray behavior into low-order coherent modes and higher-order dynamics, which represent time–varying fuel flow structures and spray characteristics. In this work, the POD method was used for the preliminary assessment of the effect of changes in backpressure in a constant volume chamber on the characteristics of the fuel spray, in particular, turbulent flows and fluctuations. Through this approach, we aim to contribute to a better understanding of the fuel-air mixing and atomization process in application to design more efficient and cleaner marine combustion systems.

2. Experimental setup

This article presents laboratory research [6, 7]. The selected parameters are consistent with those typically observed in marine diesel engines. The fuel injector used in this research is part of the Sulzer Al 25/30 marine diesel engine injection system. The fuel injector system operated on the basis of a common-rail configuration. Therefore, the high-pressure fuel system (UPS – Unit Pump System) maintained a constant pressure of approximately 50 MPa. Only one hole diameter of the fuel injector was active, and the others were plugged. The nozzle diameter was 0.285 mm, and the L/D coefficient was practically 10.9, where L is the hole length and D is the hole diameter. The presented experimental tests were carried out at ambient temperature, and the fuel injection time was 0.04 s. Diesel fuel with a density of 816.1 kg/m³ at 40°C was used in this research. One of the main elements of the experimental setup was the constant volume chamber, presented in Fig. 1.

The constant volume chamber was equipped with access windows measuring 100 mm in diameter and was filled with inert gas nitrogen. Backpressures of 3.2 MPa and 4.3 MPa in the constant volume chamber were considered. These backpressures correspond to the cylinder pressures in the marine diesel engine Sulzer 3 Al 25/30 at the start of injection, 18° before top dead center, operating under low and high load conditions. The conditions of experimental research were presented in Table 1.

The mechanical injector was calibrated to fuel opening pressures of 15 MPa and 25 MPa, respectively, using a spring needle adjustment. The fuel pressure before the injector was measured with a piezoresistive pressure sensor, Kistler type 4067E [12]. The process of fuel injection into the constant volume chamber was visualized using the optical Mie scattering method with a high-speed Photron SA 1.1 camera, operating at a recording frequency of 15 kHz. The laboratory experimental setup is presented in Fig. 2. The Mie scattering optical technique requires appropriate lighting. Therefore, two halogen lamps of 500 W each were used to illuminate the fuel injection into the constant volume chamber.

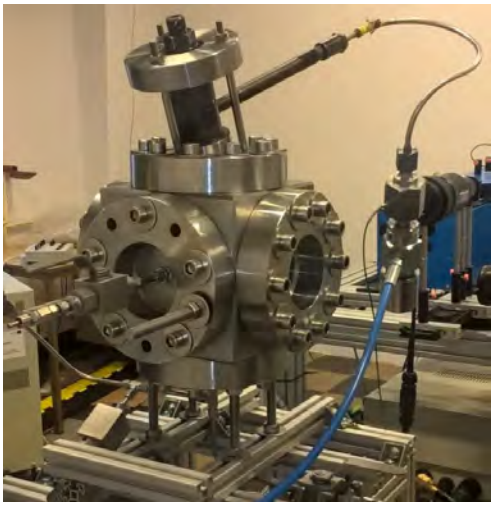

Fig. 1. The constant volume chamber

Table 1. Conditions of experimental research

Parameter	Value	Unit
Injector opening pressure	15, 25	MPa
Backpressure	3.2, 4.3	MPa
Injector opening time	0.04	s
Nozzle diameter	0.285	mm
L/D	10.9	–
Shape of the hole	cylindrical	–
Test temperature	293–298	K
Diesel oil properties		
Density (at 40°C)	816.1	kg/m^3
Viscosity	2.35	mPa·s

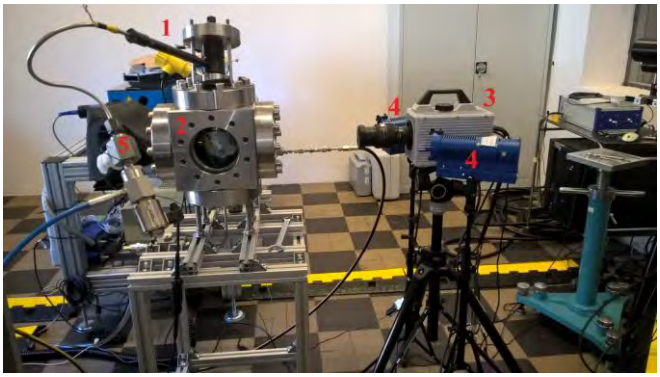

Fig. 2. The experimental set-up: 1 – marine diesel engine fuel injector, 2 – constant volume chamber, 3 – high–speed camera Photron 1.1, 4 – halogen lamps, 5 – fuel pressure sensor [6]

To assess the repeatability of the experiment, tests were conducted three times under each chamber condition. Further in the text, these tests are referred to as runs 1–3. The process of fuel injection into a constant volume chamber

was recorded from the beginning to the complete development of the spray. As a result, a series of photographs was obtained for each measurement, of which 180 images were selected for analysis. Fig. 3 presents example spray images.

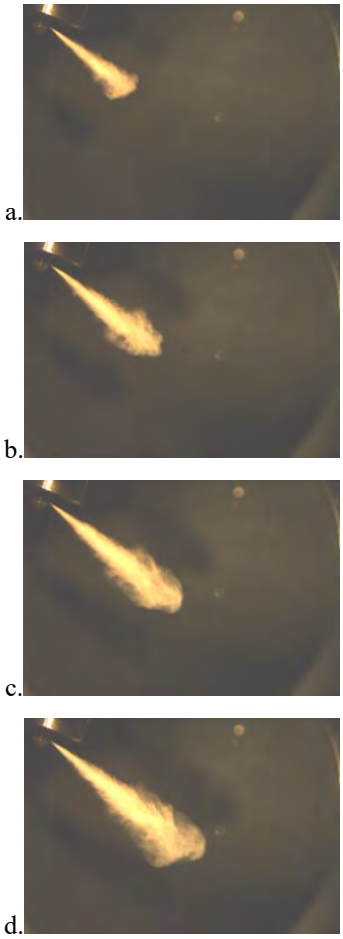

Fig. 3. Example images of fuel spray at an injector opening pressure of 25 MPa and a backpressure 3.2 MPa; time after start of fuel injection: a. 0.9 ms, b. 1.4 ms, c.1.9 ms, d. 2.4 ms

3. Data processing

To analyze the dynamic characteristics of the fuel spray, we used the POD method. POD is a technique to extract the dominant patterns from dynamically changing data, such as a sequence of spray images. It decomposes the data into spatial modes and associated time coefficients, ordered according to the most energetic structures. In this section, we explain all the steps needed to perform POD.

- Step 1: Preprocessing

For preprocessing, we first converted all images to grayscale. Then, we normalized the data within each test to eliminate differences in exposure and illumination between snapshots. Next, we ensured that the spray appeared in the same location across all snapshots and that the injection start time was consistent for all cases. This resulted in 180 snapshots per fuel spray test. Given the camera sampling rate of 15 kHz, this corresponded to 12 ms of analyzed time. The analyzed image dimensions of 464 × 710 pixels.

- Step 2: Data centering

In this step, we first calculate the mean field by averaging all the snapshots across the same test. Next, the mean field was subtracted from each snapshot, resulting in a centered dataset.

$$X' = X - \overline{X} \tag{1}$$

By performing this step, we ensure that POD will capture only the meaningful dynamics structure of the fuel spray. Further, in the POD decomposition, the average spray pattern $\overline{X}$ represents the steady-state structure and will be referred to as the zero-th mode.

- Step 3: Data organization

Additionally, we conducted image vectorization, where each 2D snapshot was transformed into a 1D vector. These vectors were then organized as columns in a data matrix $X' \in R^{m \times n}$, where m represents the number of pixels per image and n denotes the number of snapshots. In this case, it was $m = 329440$ and $n = 180$.

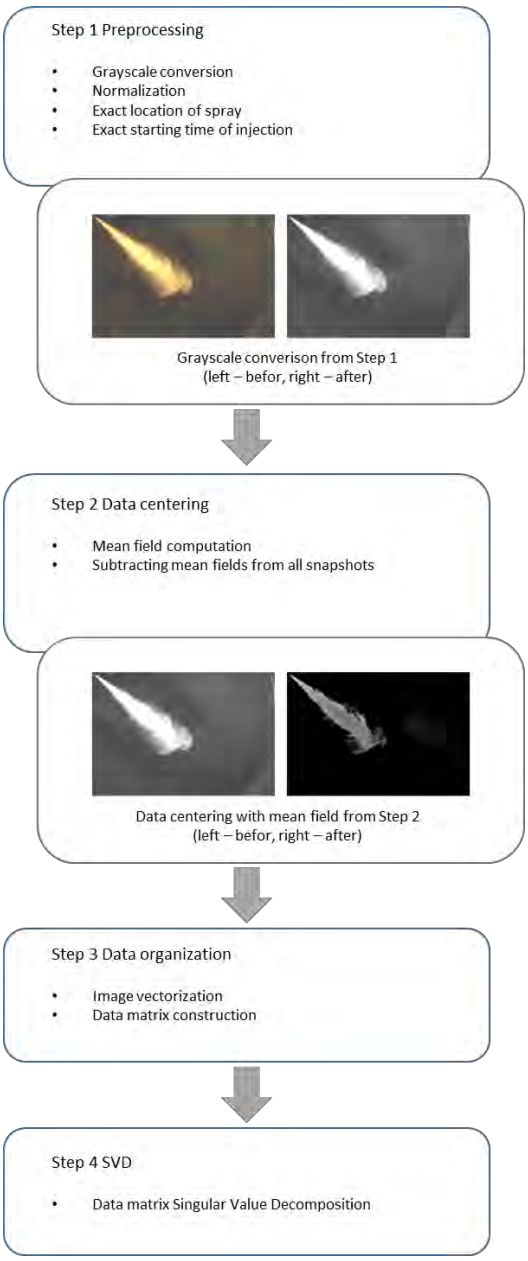

Fig. 4. Flowchart of the main steps to perform POD on a sequence of image data

- Step 4: Singular Value Decomposition (SVD)

The centered data matrix X' undergoes the Singular Value Decomposition (SVD):

$$X' = U\Sigma V^T \tag{2}$$

As a result of such data decomposition, we obtain $U \in R^{m\times n}$ – a matrix that contains the spatial modes, $\Sigma \in R^{n\times n}$ – a diagonal matrix with singular values σ_i representing each mode's energy, and $V \in R^{n\times n}$ – contains temporal coefficients showing how each mode evolves in time.

As a summary, in Fig. 4 we present a flowchart of all the steps needed to perform POD on a sequence of image data.

4. Result analysis

4.1. Singular value analysis

In this section, we present an analysis based on the POD decomposition of a sequence of snapshots – including the singular values, spatial modes, and temporal coefficients – and explain the physical interpretation of the results.

A flowchart of the possible POD analysis for spray injection dynamics, taking into account the singular values, spatial modes, and temporal coefficients, is presented in Fig. 5.

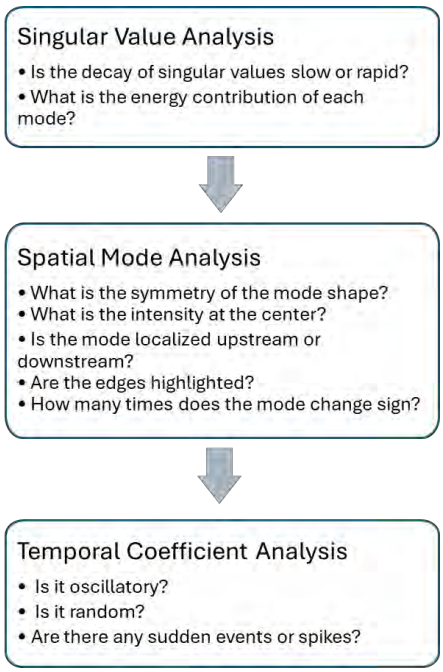

Fig. 5. Flowchart of the POD analysis

As a result of the POD decomposition on spray snapshots, we first present the singular values σ_i from the Σ matrices for each test run. The experimental trials that were conducted under the same pressure conditions are marked with the same color. In Fig. 6, the first ten singular values are presented for all experimental trials.

A rapid decay in singular values suggests that the system is dominated by a few coherent modes, which is typical in structured fluid flows. In contrast, a slow decay indicates the presence of many contributing modes and points to more complex or potentially turbulent dynamics. Further, in Fig. 7, the first 30 singular values are presented in a logarithmic scale for improved visibility. The close agreement between the singular value spectra across runs within the same pressure conditions demonstrates the reliability of the experimental setup and robust reproducibility of the flow structures captured by the POD method.

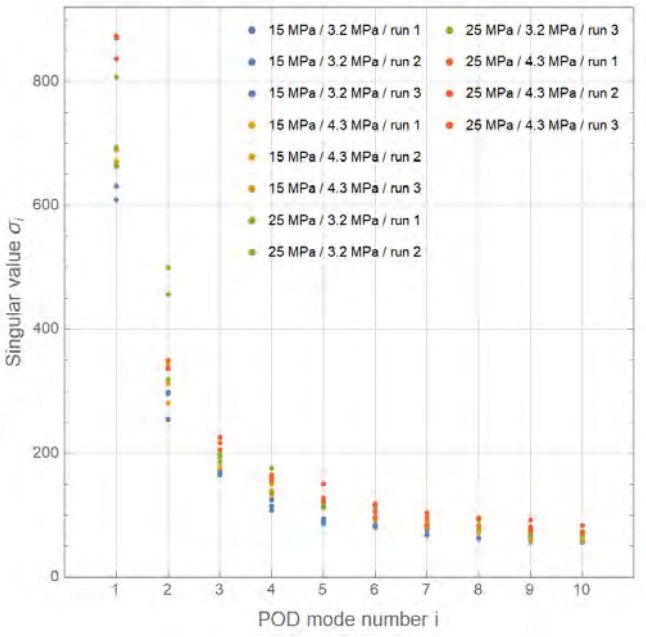

Fig. 6. Singular values, the first 10 modes for each spray run

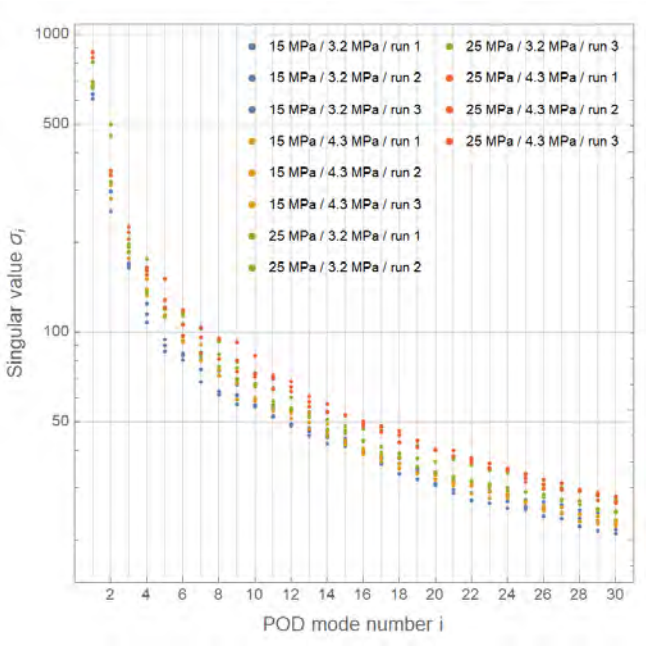

Fig. 7. Singular values, the first 30 modes for each spray run

Each singular value squared σ_i^2 represents the energy variance captured by the i-th mode. Then, the total energy in POD is defined as the sum of the singular values squared from all modes, i.e.,

$$E_{total} = \sum_{i=1}^{r} \sigma_i^2 \tag{3}$$

As a physical interpretation, the total energy corresponds to the overall variability in the spray over time, i.e., how much the spray pattern changes over time across all snapshots. In general, a higher value of energy corresponds to more dynamics. In Table 2, we show the total energy for all pressure conditions. The close agreement between the energy distributions across runs demonstrates the reliability of the experimental setup and the consistency of the POD decomposition interpretation.

From the moment fuel is injected into the combustion chamber, the jet begins to break up into droplets. The geometric parameters of the injector, such as orifice diameter, length-to-diameter ratio (L/D), and the pressure difference between the injection pressure and chamber pressure, significantly influence the primary breakup. As the fuel jet propagates further into the chamber, it undergoes secondary breakup. This secondary disintegration is driven by aerodynamic drag forces resulting from the chamber's backpressure. Based on Table 2, it was found that increasing the backpressure of gases in the constant volume chamber from 3.2 MPa to 4.3 MPa results in higher energy values, which in turn leads to enhanced spray dynamics caused by more intensive break-up of fuel spray.

Table 2. Total energy from POD decomposition

Conditions		Total energy from POD		
Opening pressure [MPa]	Back-pressure [MPa]	run 1	run 2	run 3
15	3.2	539067	604844	636939
15	4.3	658921	735052	680911
25	3.2	796846	899307	922222
25	4.3	1054458	1013955	1064898

Next, we analyze the relative energy contribution of each mode, defined as:

$$E_i = \frac{\sigma_i^2}{\sum_{j=1}^{r} \sigma_j^2} \tag{4}$$

In Fig. 8, we present the relative energy contribution of each spray injection run on a logarithmic scale. For all experimental runs, the energy contribution of mode 3 is below 10%, mode 8 is below 1%, and mode 30 is below 0.1%.

Further, in Table 3, we present the energy contributions of the first mode (E1), the first two modes (E1–E2), and the first five modes (E1–E5). The first mode captures approximately 70% of the total dynamics in most cases, indicating that the spray is coherent, though not entirely uniform. An exception is observed in two runs conducted under an opening pressure of 15 MPa and a backpressure of 3.2 MPa in the constant volume chamber, where the first mode captures only 55% of the energy. This suggests noticeable secondary dynamics – likely related to the onset of atomization and turbulence. The first two modes account for about 80–83% of the total dynamics, while the first five modes capture approximately 90–92% across all experimental spray runs. These results suggest organized, low-dimensional coherent behaviour, although minor contributions from atomisation or turbulence are still possible.

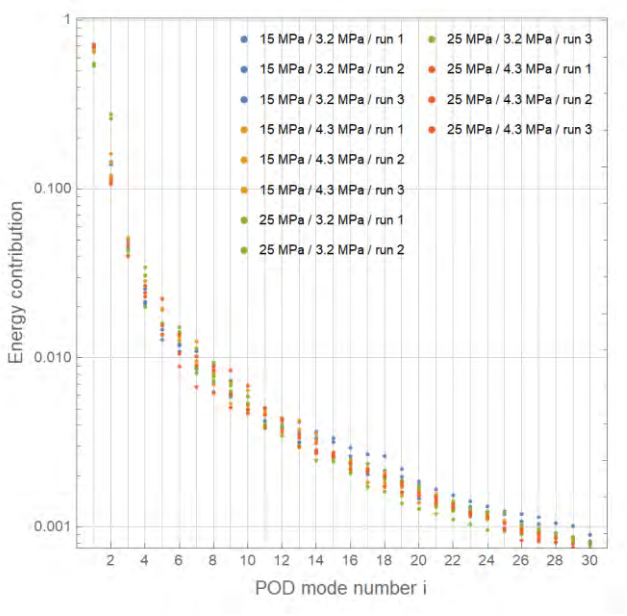

Fig. 8. Energy contribution of the first 30 modes for each spray injection run

Table 3. Energy contribution from the first mode (E1), the first two modes (E1–E2), and the first five modes (E1–E5) for each spray injection run

Energy contribution		E1 [%]			E1–E2 [%]			E1–E5 [%]		
Conditions		run			run			run		
Opening pressure [MPa]	Back-pressure [MPa]	1	2	3	1	2	3	1	2	3
15	3.2	69	66	69	81	81	83	90	90	91
15	4.3	68	65	66	80	81	80	90	91	90
25	3.2	55	54	71	81	81	82	90	91	90
25	4.3	72	69	72	83	80	83	90	90	92

The energy contribution alone is not a sufficient indicator for fully characterizing our experimental setup and spray pressure conditions. Therefore, we proceed with analyzing POD spatial modes and temporal coefficients.

4.2. Spatial modes analysis

The spatial modes from the U matrix obtained from the POD analysis are a valuable source of information about the spray structure. Shadow images of the spatial modes, calculated for run 1 of each experimental setup, are presented in Fig. 9 and Fig. 10 for opening pressures of 15 MPa and 25 MPa, respectively. Selected modes are shown for backpressures of 3.2 MPa and 4.3 MPa.

In POD analysis, Mode 0 represents the overall geometric shape of the fuel spray, resulting from preprocessing data centering, while Mode 1 corresponds to the dominant structure, such as the cone shape. The number of times a spatial mode changes sign (observed as a black-to-white color transition in Fig. 9 and Fig. 10) can provide information for distinguishing between coherent dynamics and high-frequency structures, such as those associated with atomization.

Lower-order POD spatial modes represent the spray's core and primary breakup structures. The backpressure of gases in the constant-volume chamber directly influences the shape of the diesel fuel spray and its atomization. The

intensity at the center of the spatial mode provides insight into the spray's core dynamics. Furthermore, the symmetry of the mode shapes, as seen in Fig. 9 and Fig. 10, indicates that the spray fluctuates in a balanced way on both sides of the spray axis.

Higher-order POD spatial modes can represent droplet behavior, turbulence, and noise. The disintegration of the diesel fuel spray depends on instabilities caused by aerodynamic drag forces. Due to the impact of aerodynamic forces exerted by the gas, the spray surface is subject to violent disturbances, particularly in the outer regions. The edges highlighted in the spatial modes, as seen in Fig. 9 and Fig. 10, suggest that the spray boundary is dynamically active. In these regions, intense secondary breakup occurs, forming cloud-like structures composed of dispersed droplets. Simultaneously, an increase in the cone angle of the fuel spray is observed.

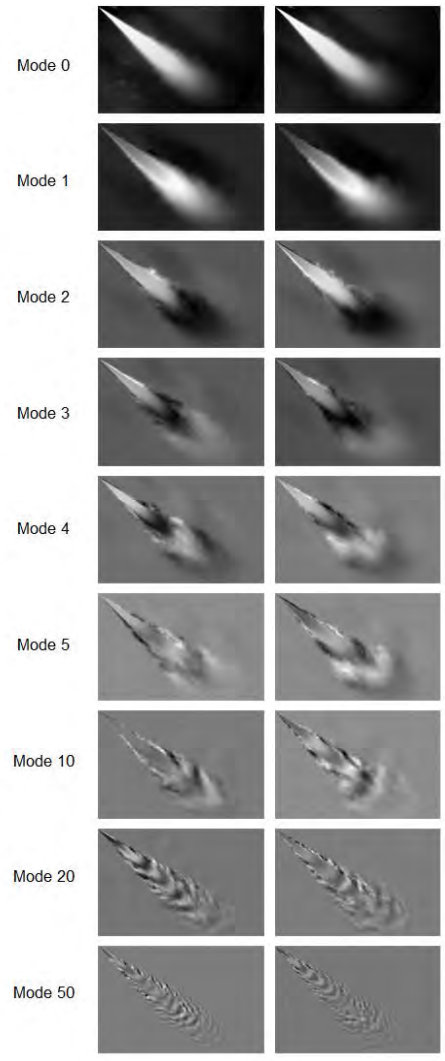

Fig. 9. Spatial mode shapes for opening pressure: 15 MPa with backpressures of 3.2 MPa (left) and 4.3 MPa (right)

Furthermore, if a mode is localized upstream, it may indicate nozzle fluctuations in higher-order modes or injection irregularities in lower-order modes. On the other hand, if the mode is localized downstream, it may point to droplet cloud dispersion or final breakup events.

The interpretation of spatial modes very much depends on the resolution of the snapshots and the physical distance represented by each image pixel. An overall interpretation for mode shapes is given in Table 4.

Table 4. Spatial modes interpretation

Modes	Interpretation
Mode 0	The mean through all snapshots, i.e., the baseline structure
Mode 1	Represents the dominant structure, like the cone shape
Lower Modes	Represent spray core and primary breakups
Higher Modes	Represent turbulence, droplet behavior, or noise

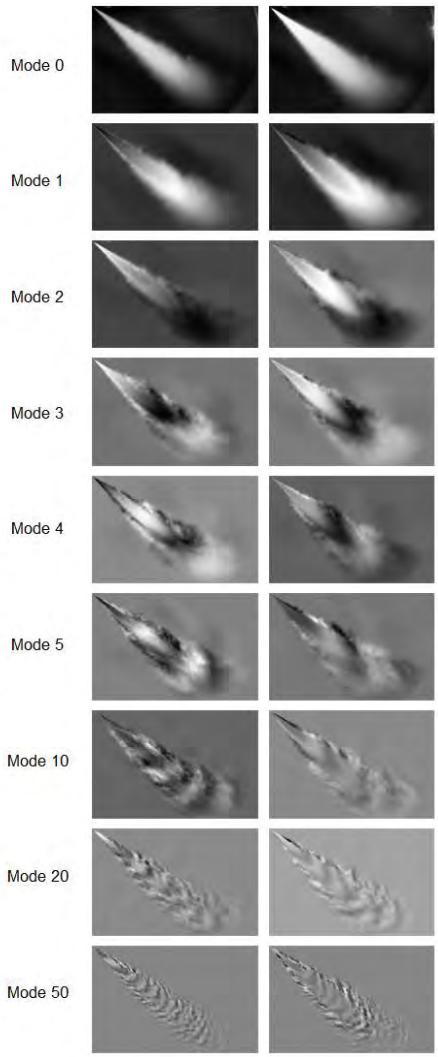

Fig. 10. Spatial mode shapes for opening pressure: 25 MPa with backpressures of 3.2 MPa (left) and 4.3 MPa (right)

4.3. Temporal coefficients analysis

For a better understanding of the dynamic behavior of the spray, we also analyze the temporal coefficients obtained from POD. By temporal coefficients analysis, it is possible to determine if the spray shows oscillatory behavior, random fluctuations, or other sudden transient events.

Temporal coefficients, calculated from run 1 of each experimental setup, for selected modes are shown in Fig. 11 and Fig. 12 for opening pressures of 15 MPa and 25 MPa,

respectively. These coefficients indicate the contribution of each spatial mode over time and reflect the underlying flow dynamics. Analysis of higher-order modes confirms the presence of complex oscillatory and transient behaviors, which are characteristic of turbulent atomization, droplet interactions, and breakup phenomena.

Additionally, spectral analysis of the temporal signals could be applied to identify dominant frequencies, offering a more quantitative measure of spray behavior.

5. Conclusions

In this work, we demonstrated the applicability of the POD method for analyzing the fuel spray atomization process. By decomposing the complex spray dynamics into spatial modes and temporal coefficients, we characterized the dominant structures and their evolution over time.

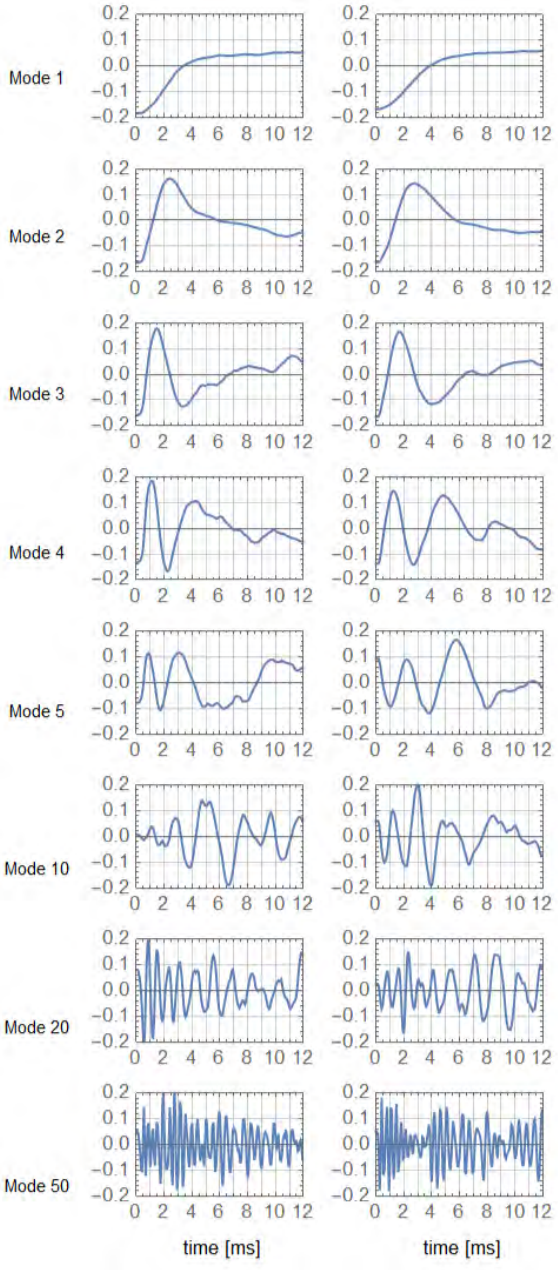

Fig. 11. Temporal POD coefficients for an opening pressure of 15 MPa and backpressures of 3.2 MPa (left) and 4.3 MPa (right)

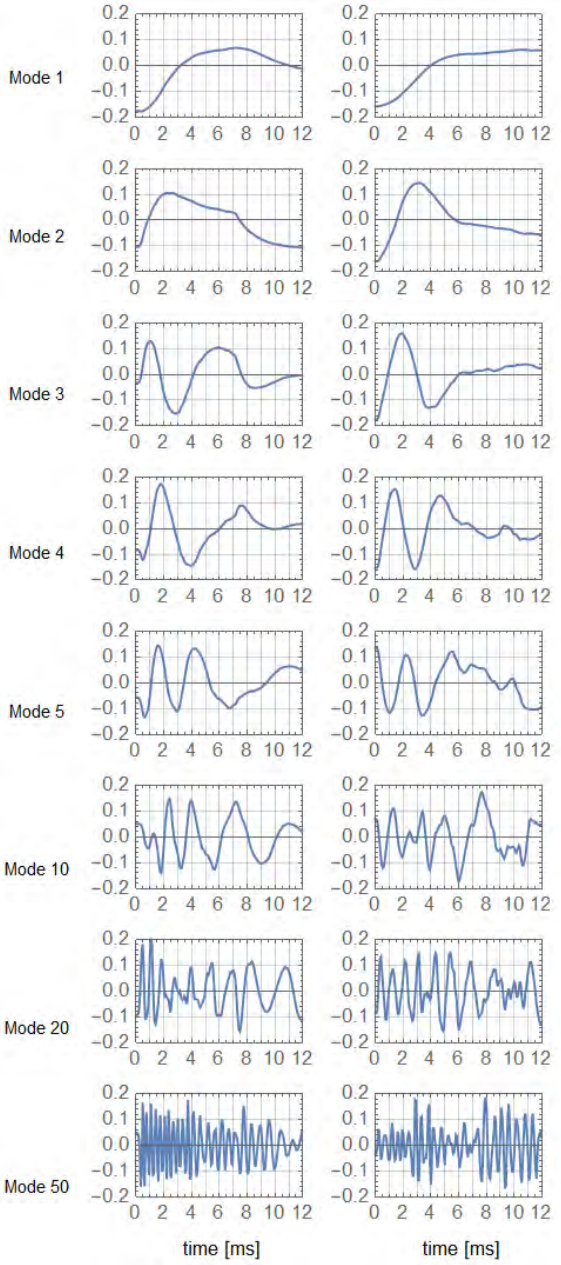

Fig. 12. Temporal POD coefficients for an opening pressure of 25 MPa and backpressures of 3.2 MPa (left) and 4.3 MPa (right)

The consistency of the POD results across repeated tests under the same operating conditions confirms the reliability of the experimental setup and POD methodology. The analysis of singular values showed that the fuel spray is largely governed by a few dominant modes, with the first mode capturing approximately 70% of the total energy under most experimental conditions. Increased backpressure in the constant volume chamber was shown to enhance spray dynamics by increasing the energy associated with secondary breakup and turbulent dispersion. The POD spatial modes provided valuable information about the effects of nozzle fluctuations, core dynamics, and droplet dispersion at different stages of spray development. The temporal coefficient analysis confirmed the presence of oscillatory and transient behaviors, representing complex atomization processes. It should be emphasized that the test results and

their analysis are valid only for the specific fuel injection parameters presented in this work and for the Mie scattering measurement method. The POD method can be used to analyze droplets in a fuel spray in terms of the general structures (modes) present. Therefore, information about which structures dominate the fuel atomization and air mixing process, depending on the injection parameters, can be utilized in the design phase of marine fuel injection systems.

This work's findings suggest that POD can be a powerful tool for optimizing the fuel atomization process in marine diesel engine injectors, supporting future efforts to design more efficient and cleaner combustion systems. It should be noted, however, that the possibility of analyzing the results of fuel spray and spray dynamics tests using POD depends on the specific optical measurement method employed.

Acknowledgments

The authors gratefully acknowledge Prof. Jerzy Kowalski for his support and collaboration, and Dr. Piotr Jaworski for his technical assistance during the experimental investigations.

Nomenclature

CI	compression ignition
CNG	compressed natural gas
DI	direct injection
LPG	liquified petroleum gas
POD	proper orthogonal decomposition
SI	spark ignition
SVD	singular value decomposition
U	spatial mode matrix
σ_i	singular value for i-th mode
Σ	singular values matrix
V	temporal coefficient matrix

Bibliography

[1] Berkooz G, Holmes P, Lumley JL. The proper orthogonal decomposition in the analysis of turbulent flows. Annu Rev Fluid Mech. 1993;25(1):539-575. https://doi.org/10.1146/annurev.fl.25.010193.002543

[2] Chen H, Hung DL, Xu M, Zhuang H, Yang J. Proper orthogonal decomposition analysis of fuel spray structure variation in a spark-ignition direct-injection optical engine. Exp Fluids. 2014;55:1-12. https://doi.org/10.1007/s00348-014-1703-y

[3] Deng J, Wang X, Wei Z, Wang L, Wang C, Chen Z. A review of NOx and SOx emission reduction technologies for marine diesel engines and the potential evaluation of liquefied natural gas fuelled vessels. Sci Total Environ. 2021; 766:144319. https://doi.org/10.1016/j.scitotenv.2020.144319

[4] Du W, Zhang Q, Zhang Z, Lou J, Bao W. Effects of injection pressure on ignition and combustion characteristics of impinging diesel spray. Appl Energy. 2018;226:1163-1168. https://doi.org/10.1016/j.apenergy.2018.06.032

[5] Ganti H, Khare P. Data-driven surrogate modeling of multiphase flows using machine learning techniques. Comput Fluids. 2020;211:104626. https://doi.org/10.1016/j.compfluid.2020.104626

[6] Grochowalska J. Analysis of the macrostructure of the fuel spray atomized with marine engine injector. Combustion Engines. 2019;179(4):80-85. https://doi.org/10.19206/CE-2019-413

[7] Grochowalska J, Jaworski P, Kapusta Ł. Analysis of the structure of the atomized fuel spray with marine diesel engine injector in the early stage of injection. Combustion Engines. 2023;195:97-103. https://doi.org/10.19206/CE-168394

[8] Hu N, Zhou P, Yang J. Reducing emissions by optimising the fuel injector match with the combustion chamber geometry for a marine medium-speed diesel engine. Transp Res D Transp Environ. 2017;53:1-16. https://doi.org/10.1016/j.trd.2017.03.024

[9] International Maritime Organization. Fourth Greenhouse Gas Study 2020. London: IMO 2020 (accessed on 2025. 05.06) https://www.imo.org/en/ourwork/Environment/Pages/Fourth-IMO-Greenhouse-Gas-Study-2020.aspx

[10] Kafar L, Merkisz J, Piaseczny L. Fuel spray model in a medium speed marine engine – a simulation. Combustion Engines. 2006;126(3):63-76. https://doi.org/10.19206/CE-117345

[11] Kapitza L, Imberdis O, Bensler HP, Willand J, Thévenin D. An experimental analysis of the turbulent structures generated by the intake port of a DISI-engine. Exp Fluids. 2010; 48:265-280. https://doi.org/10.1007/s00348-009-0736-0

[12] Kistler. Piezoresistive high pressure sensor. 2014 (accessed on 2025 May 6). https://www.kistler.com/type=669&fid=61054&model=document&callee=frontend

[13] Lewińska J, Kapusta ŁJ. Analysis of the microstructure of the fuel spray atomized by marine injector. Combustion Engines. 2017;169(2):120-124. https://doi.org/10.19206/CE-2017-221

[14] Lumley JL. Computational modeling of turbulent flows. Adv Appl Mech. 1979;18:123-176. https://doi.org/10.1016/S0065-2156(08)70266-7

[15] Ma H, Wu X, Feng F, Wang D, Yang C, Zhuo C. An experimental study on fuel spray-induced vortex-like structures. Exp Therm Fluid Sci. 2014;57:335-343. https://doi.org/10.1016/j.expthermflusci.2014.05.013

[16] Najar I, Buchholz B, Stengel B, Fink C, Hassel E. Influence of the fuel properties on the injection process and spray development in a large ship diesel engine. In: ILASS–Europe 2017, 28th Conf on Liquid Atomization and Spray Systems; 2017 Sep 6-8; Valencia, Spain. https://doi.org/10.4995/ILASS2017.2017.4787

[17] Salvador FJ, Gimeno J, De la Morena J, González-Montero LA. Experimental analysis of the injection pressure effect on the near-field structure of liquid fuel sprays. Fuel. 2021;292: 120296. https://doi.org/10.1016/j.fuel.2021.120296

[18] Soid SN, Zainal ZA. Spray and combustion characterization for internal combustion engines using optical measuring techniques – a review. Energy. 2011;36(2):724-741. https://doi.org/10.1016/j.energy.2010.11.022

[19] Viana M, Hammingh P, Colette A, Querol X, Degraeuwe B, de Vlieger I, van Aardenne J. Impact of maritime transport emissions on coastal air quality in Europe. Atmos Environ. 2014; 90:96-105. https://doi.org/10.1016/j.atmosenv.2014.03.046

[20] Weiss J. A tutorial on the proper orthogonal decomposition. In: AIAA Scitech 2019 Forum; 2019 Jan 7-11; San Diego, CA. Reston (VA): AIAA; 2019. Paper No.: AIAA 2019-3333. https://doi.org/10.2514/6.2019-3333
[21] Wrzask K, Kowalski J, Le VV, Nguyen VG, Cao DN. Fault detection in the marine engine using a support vector data description method. J Mar Eng Technol. 2024;23(6):412-422. https://doi.org/10.1080/20464177.2024.2318844
[22] Yao C, Geng P, Yin Z, Hu J, Chen D, Ju Y. Impacts of nozzle geometry on spray combustion of high pressure common rail injectors in a constant volume combustion chamber. Fuel. 2016;179:235-245. https://doi.org/10.1016/j.fuel.2016.03.097
[23] Zhang Z, Zhang P, Chen H, Wu H, Geng L, Zhang W et al. Optical study on the spray and combustion characteristics of diesel-biodiesel-alcohol blend fuels on a constant volume combustion chamber. J Energy Inst. 2024;117:101779. https://doi.org/10.1016/j.joei.2024.101779

Joanna Grochowalska, DEng. – Faculty of Mechanical Engineering and Ship Technology, Gdansk University of Technology, Poland.
e-mail: *joanna.lewinska@pg.edu.pl*

Klaudia Wrzask, DEng. – Faculty of Mechanical Engineering and Ship Technology, Gdansk University of Technology, Poland.
e-mail: *klaudia.wrzask@pg.edu.pl*

Łukasz Jan Kapusta, DEng. – Faculty of Power and Aeronautical Engineering, Warsaw University of Technology, Poland.
e-mail: *lukasz.kapusta@pw.edu.pl*

Article citation info:
Grab-Rogaliński K, Tutak W, Jamrozik A, Kociszewski A. Comparative analysis of IC diesel engine performance fueled with diesel/hydrogen and diesel/ammonia mixtures. Combustion Engines. 2026;204(1):176-183. https://doi.org/10.19206/CE-211069

Karol Grab-ROGALIŃSKI
Wojciech TUTAK
Arkadiusz JAMROZIK
Arkadiusz KOCISZEWSKI

Combustion Engines
Polish Scientific Society of Combustion Engines

Comparative analysis of IC diesel engine performance fueled with diesel/hydrogen and diesel/ammonia mixtures

ARTICLE INFO

Received: 27 May 2025
Revised: 10 September 2025
Accepted: 18 September 2025
Available online: 16 October 2025

The paper presents the results of research performed on an internal combustion diesel engine operating on a dual-fuel strategy. Fuels used during the study were diesel as a reference fuel, pure hydrogen, and ammonia as a hydrogen carrier. Fuel mixtures of diesel/hydrogen and diesel/ammonia were added to the engine, at energetic shares of 8, 12, 22, and 32% to maintain the constant engine load compared to the engine fueled with diesel. A comparison of the engine performance and the combustion process was made. Under the test conditions for all mixtures, the indication of the combustion pressure was made. The indication results were used to calculate engine performance parameters, such as IMEP, engine power, COV_{IMEP}, and thermal efficiency. They were also used to describe the combustion process, including the determination of parameters like combustion stages, 50% MFB position, and HRR. The analysis of the results shows that adding hydrogen or ammonia as a main fuel causes a much faster combustion process compared to a diesel fuel engine. With an increase in energetic share, the combustion characteristic of the diesel/hydrogen engine shows two maxima in the HRR curve, besides 32% where there is only one peak. In contrast, for the diesel/ammonia engine, there is only one maximum, where an increase in the value of the kinetic combustion phase and the delay of ignition occur.

Key words: *hydrogen, ammonia, co-combustion, combustion analysis, diesel engine*

1. Introduction

The global industrialization based on fossil fuel energy production negatively influences living organisms on our planet [17, 25]. The negative causes of industrialization are related to the emission of toxic and harmful gas compounds, greenhouse gases (GHG), which significantly influence climate change [4, 10]. One of the reasons for this is the use of worldwide transport, which is based on vehicles equipped with internal combustion (IC) engines. To prevent an increase in emissions and reduce them to zero, the European Union has introduced the Fit for 55 program [21]. To respond to that program, it is necessary to switch the technology of the IC engine, which is based on the combustion of fossil fuels, to a clean combustion technology that uses alternative fuels, such as carbon-free fuels. Carbon-free fuels can be characterized as those for which combustion doesn't lead to carbon dioxide (CO_2) emission [3], for this group of fuels, hydrogen and ammonia can be considered.

The hydrogen (H_2) as an energy carrier can be used as a fuel in pure form for IC engines, both spark-ignited (SI) and compressed-ignition (CI), and in fuel cells [8, 9, 22, 26]. Hydrogen as a fuel for IC engines has specific properties that distinguish it from fossil fuels. An important difference is in its atomic structure, where there is no carbon atom, which benefits the decrease in GHG emissions. For the mass unit, it has a very high lower heating value (LHV), which is 120 MJ/kg, which is close to three times higher than for petroleum fuels. From that point of view, it can be recognized as a fuel with big potential as a substitute for conventional fuels. However, as a gaseous fuel, it has a very low density, which implies that for a volume unit, the LHV is around 10.3 MJ/m^3, and if this value is compared with, for example, natural gas (NG), whose LHV is equal to 34.5 MJ/m^3, it is around three times lower. Hydrogen also has a very high laminar flame speed (LFS), which in normal conditions and in stoichiometric mixtures is 2.5 m/s [24]. For natural gas, the LHV value is 0.4 m/s [6], and it is nearly six times lower compared with hydrogen. Hydrogen can be a catalyst that increases the chemical reactivity of co-combusted fuels, and also because of its wide flammability limits, which are from 5 to 75% of volume, it promotes combustion of very lean co-combusted mixtures of fuels. Also, high penetration of the hydrogen flame increases the efficiency of the combustion process itself and leads to more complete combustion. However, there are several problems and challenges with hydrogen use as a fuel for IC engines, which are related to such topics as storage, transportation, and production. The production of hydrogen is generally costly and mostly done by electrolysis or by steam methane reforming. The storage technology used in transportation nowadays is based on high-pressure (350 to 700 bar) or cryogenics (1 atm; –240°C) tanks, which are expensive and advanced technologies [8]. And from that point of view, an interesting alternative can be ammonia (NH_3).

Ammonia, as a hydrogen carrier that can be treated as a fuel, also does not have a carbon atom in its structure. Thanks to that property, it can also be considered as a fuel which leads to a decrease in the emission of one of the GHGs, namely CO_2. But unfortunately, additional nitrogen in the structure promotes the emission of nitrogen oxides (NO_x). The energetic density of ammonia is higher than that of hydrogen. Ammonia compressed to 1 MPa has a volumetric energy density equal to 13.6 GJ/m^3, which is a higher value than methane, which has 10.4 GJ/m^3 at 25 MPa. Laminar flame speed for ammonia is 0.07 m/s, which is very low, and determines the character of the combustion

process; it causes an increase in ignition delay [13]. The combustion process of ammonia is prolonged, which causes, in many cases, increased emission of unburnt NH_3 [20, 31], which is also recognized as a greenhouse gas [30]. The flammability limits by volume for ammonia are lower than for pure hydrogen, and they are respectively 15 to 28%, which is wider than for petroleum fuels.

As it was mentioned, most alternative and all petroleum fuels have carbon in their structure, which means that during their combustion, as a result, we get the emission of carbon dioxide, which is responsible, among others, for greenhouse gas emissions (GHGs) [19]. Based on the analysis of hydrogen and ammonia properties, it can be stated that they can be an alternative to carbon-based fuels [16]. Those fuels can be used both in spark-ignition and compression-ignition engines. However, because of the high-octane number, which leads to a low cetane number, they are difficult to ignite in CI engines, and to do that, the pilot injection of high-reactivity fuel, such as diesel oil, should be used. The hydrogen addition increases combustion speed, which is decreased by ammonia, which has, as mentioned earlier, a low LFS compared to other fuels.

Those combined properties cause blends of diesel/hydrogen and diesel/ammonia to be very interesting as an alternative energy source for IC compression-ignition engines. The research related to the combustion of the aforementioned fuel blends is the subject of research performed by many institutions around the world. The results presented by Kanth and Debbarma [11] determined the increase in engine efficiency by 2.5% when it was fueled by a mixture of diesel and hydrogen and 1.6% when it was a mixture of diesel and biodiesel (10% v/v). They also noted a decrease in CO and UHC emissions, but accompanied by an increase in NO_x. Investigation of a dual-fuel engine powered by diesel and hydrogen was presented by Gomes Antunes et al. [7]. In this case, both fuels were directly injected into the engine cylinder. They observed an increase in engine power by 14%, and to achieve stable engine operation, they heat up the intake air. An increase in pressure and efficiency was also noted during those tests. Akra et al. [1] performed the tests with an engine fueled by a biodiesel/hydrogen mixture, and they added hydrogen to get an improvement in the combustion process. They achieved an increase in engine performance and a decrease in exhaust gas emissions except for the NO_x. The co-combustion of hydrogen with diesel and biodiesel and their mixture was tested by Köse and Acaroğlu [12]. As a result, they observed that the highest increase in engine efficiency was for an engine fueled by biodiesel with a 2.5% addition of hydrogen, and for a diesel/biodiesel with a 2.5% hydrogen mixture, maximum power output was achieved. Bjørgen et al. [2] tested an engine fueled with a mixture of diesel and NH_3, where those fuels were separately injected into the engine cylinder. The ammonia energy share was 40, 50, and 60%. The diesel injection timing was constant with the value of 15° bTDC. Advancing ammonia injection 15° before diesel injection causes an increase in ignition delay. Injection of ammonia simultaneously or after diesel injection had a positive impact on the combustion process and the smooth running of the engine. Injection at the same time of diesel and ammonia resulted in the highest efficiency value, lower ammonia slip, and decreased NO_x emission. In the research presented by Nadimi et al. [18], the results of NH_3/diesel mixtures with various ratios were presented. The tests show that increasing the ammonia energetic ratio (AER) switched combustion mode from diffusive (diesel) to premixed combustion (diesel/ammonia) in a dual-fuel engine. Increase in AER changed combustion phases. Addition of NH_3 reduces the emissions of CO_2, CO, and particle matters (PM), at the same time, causes an increase in NO_x and NH_3 emissions. Also, Liu et al.[15] tested a dual-fuel diesel engine where additional fuel, ammonia, was added. The parameters that were changed during those tests were ammonia energy fraction (AEF), diesel injection pressure, and diesel injection timing. As a result of that research, they found that an increase in AEF causes a decrease in peak pressure, an increase in combustion duration, a reduction of NO_x, soot, and CO_2 emissions, which also causes an increase in emissions of unburned ammonia UNH_3 and N_2O.

Besides the aforementioned fuel mixtures, diesel/hydrogen and diesel/ammonia, there is research being performed at an IC compression ignition engine where the mixture of those three fuels, diesel/ammonia/hydrogen, is used. Zhang et al. [32] performed the tests at full load for different energetic rates for ammonia up to 50% and hydrogen up to 8%. They found that the addition of NH_3 improves engine performance, whereas the addition of H_2 improves the combustion of the diesel/ammonia mixture. The addition of NH_3 and H_2 causes a reduction of NO_x, CO_2, and soot, but causes an increase in NH_3 emissions. The research of Wang et al. [29] was performed on a single-cylinder diesel engine at a constant speed, where the energetic fraction of hydrogen was changed from 10 to 90%. The results of those tests were that the optimal hydrogen energetic fraction was 30%, which led to a drop in NH_3 emission by almost 90% but caused an increase in NO_x emission by close to 60%. The tests on a 1-cylinder diesel engine fueled with diesel/ammonia/hydrogen blends were performed by Dhas et al. [5], where ammonia and hydrogen were added to the engine with a constant flow equal to 10 LPM (liter per minute). They found that the addition of NH_3 and H_2 improved brake thermal efficiency, reduced carbon dioxide (CO_2), hydrocarbons (HC), and smoke, but increased NO_x emissions.

As shown in the literature review, the use of diesel/hydrogen and diesel/ammonia mixtures in IC compression ignition engines gives many advantages compared to the combustion of petroleum fuels. These advantages can be observed especially in terms of engine performance, efficiency, and emission of exhaust gases, especially those based on carbon fuel combustion. As a good aspect of hydrogen and ammonia mixing with diesel, it can be pointed out that, as a carbon-free fuel, it is a clean energy source in its own right. Ammonia is much safer to transport and store, and its volumetric energy index is higher than that of hydrogen itself, making it an attractive engine fuel. On the negative side, hydrogen burns very quickly and has a very low ignition energy, which creates problems with combustion control. Rapid combustion is accompanied by large temperature increases, which increase nitrogen oxide emis-

sions. Ammonia, on the other hand, burns slowly, which can be problematic for high-speed engines. The aggressive nature of ammonia requires the use of materials resistant to its effects.

The research presented in this paper was performed on 1-cylinder diesel engines. The engine was running with constant speed and load. The addition of hydrogen and ammonia to the engine was in that manner to ensure the constant load level equal to that of a diesel-fueled engine. During the test, the engine's indication was done, and 100 consecutive cycles for each measured point were stored for combustion analysis. On the basis of measurement, the analysis of the combustion process was done, and the pressure, heat release rate, and normalized heat release curves were presented. The combustion phases were determined for each case, and the engine performance parameters, such as power, indicated efficiency, and COV_{IMEP}, were calculated and presented. The research performed in this paper presents the comparison analysis of combustion parameters between an engine fueled with diesel/hydrogen and a diesel/ammonia mixture. The research was done at the same load conditions and energetic shares of gas fuels, which gives interesting information about the combustion process of those gaseous fuels in a dual fuel engine, especially from fuel chemical properties.

2. Materials and methods

The tests were carried out on a 1-cylinder industrial dual-fuel compression-ignition engine 1CA90 powered by diesel oil and hydrogen or ammonia. The engine was air-cooled and the fuel system provided a constant injection timing of 20°CA bTDC. The engine operated at a constant rotational speed of 1500 rpm.

The engine was equipped with an indication system. An encoder with a resolution of 1 °CA was mounted on the engine crankshaft; this signal was used in the data acquisition system. Data obtained from the measuring track equipped with a pressure transducer (Kistler 6118C) and a charge amplifier (Kistler 5018A) were transferred to a PC using an A/C converter (USB-1608HS). The author's computer program allowed for real-time observation of pressure courses, released heat, HRR, temperature, combustion phases, and IMEP. The engine intake system was equipped with an air filter, a rotary flow meter (CGR-01), and a pressure pulsation damper. Hydrogen/ammonia was fed to the intake manifold in the gas phase, and its volume flow was controlled by a needle valve at the gas reducer. The gas flow was measured by a flow meter (RTU-10-300). A detailed description of the research test stand is presented in studies [27, 28].

The aim of the research was to conduct a comparative analysis of the co-combustion process of H_2/NH_3 with diesel fuel in an industrial compression-ignition engine. The research was carried out for a constant engine load defined as IMEP, whose value was 0.77 MPa. The energy share of fuels was determined from the relationship:

$$\mathrm{HEF/AEF} = \frac{d_{H2/NH3} \cdot LHV_{H2/NH3}}{d_{D100} \cdot LHV_{D100} + d_{H2/NH3} \cdot LHV_{H2/NH3}} \quad (1)$$

where: AEF – ammonia energy fraction, HEF – hydrogen energy fraction, d_{D100} – mass of diesel fuel dose per cycle, $d_{H2/NH3}$ – mass of hydrogen/ammonia dose per cycle, $LHV_{H2/NH3}$ – lower heat value of hydrogen/ammonia, MJ/kg.

IMEP was calculated based on following equation:

$$\mathrm{IMEP} = \frac{1}{V_d} \int_0^{720} p \frac{dV}{d\varphi} \quad (2)$$

where: V_d – displacement volume [m^3].

The indicated thermal efficiency can be defined as the ratio of the indicated work in the cylinder volume to the amount of heat supplied to the cylinder.

$$\mathrm{ITE} = \frac{\mathrm{IMEP} \cdot V_d}{Q_{cycle}} \cdot 100\% \quad (3)$$

where: IMEP – indicted mean effective pressure [Pa], Q_{cycle} – total heat supplied to the engine [J].

The heat release rate is one of the parameters that analysis allows to describe the combustion process in an IC engine. This parameter is determined on the basis of the in-cylinder pressure measurement. It can be calculated on the basis of the first law of thermodynamics and the equation of state. A simplification of those equations allows us to calculate the net heat release rate. A net heat release is calculated based on the following equation:

$$\frac{dQ}{d\varphi} = \frac{1}{\kappa - 1} \left[\kappa p \cdot \frac{dV}{d\varphi} + V \cdot \frac{dp}{d\varphi} \right] \quad (4)$$

where: κ – the ratio of specific heats [–], V – cylinder volume [m^3], p – in cylinder pressure [Pa].

The indicator of unrepeatability of IMEP was determined based on the following equation:

$$\mathrm{COV_{IMEP}} = \frac{\sigma_{IMEP}}{(IMEP)_{mean}} \cdot 100\% \quad (5)$$

where: σ_{IMEP} – standard deviation of IMEP.

Table 1 presents the mass and energy doses of fuels supplied to the engine for the individual analyzed measurement points.

The results show that with the increase in the share of H_2 or NH_3, the share of diesel fuel decreased so that the power generated by the engine remained at a constant level. The increase in the share of H_2/NH_3 caused the engine to require a smaller dose of energy contained in the fuel to generate the same power.

Table 1. Mass and energy doses of fuels

HEF	D100	H_2	$Q_{en(H2)}$	q_{NH2}	Q_{cycle}
	kg/h	kg/h	MJ/h	J/cycle	J/cycle
0%	1.202	0.000	0.00	0.00	1122
8%	1.018	0.0293	3.52	78.72	1029
12%	0.966	0.0467	5.60	124.54	1027
22%	0.827	0.0811	9.73	245.06	1015
32%	0.738	0.1209	14.51	322.50	1012

AEF	D100	NH_3	$Q_{en(NH3)}$	q_{NH3}	Q_{cycle}
	kg/h	kg/h	MJ/h	J/cycle	J/cycle
0%	1.202	0.000	0.00	0.00	1122
8%	1.087	0.219	4.12	91.49	1106
12%	1.044	0.319	6.01	133.58	1108
22%	0.883	0.552	10.38	256.18	1080
32%	0.759	0.788	14.82	329.34	1038

3. Results

The basis for assessing the combustion process in a piston engine is the knowledge of the pressure course in the cylinder. As part of the research, 100 consecutive engine work cycles were recorded, and the average course from the entire set of realizations was analyzed. The engine was characterized by high repeatability of subsequent cycles observed in real time during the research. Each measurement point was repeated 3 times while maintaining thermal stabilization of the engine for each change in the fuel share.

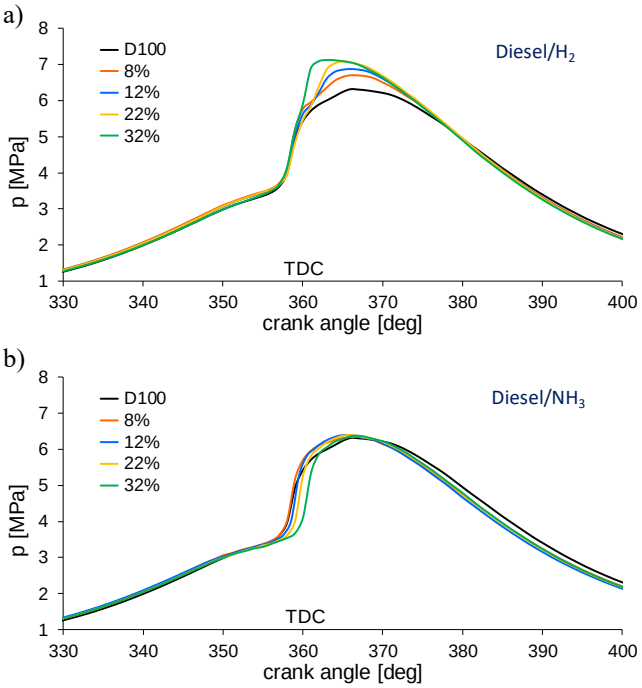

Fig. 1. Pressure curves in the engine cylinder for different H_2 (a) and NH_3 (b) proportions

Figure 1a presents a comparison of pressure courses for a dual-fuel engine fueled with diesel oil and hydrogen, and Fig. 1b with diesel oil and ammonia. It can be seen that with the increase in the share of hydrogen, the peak pressure value also increases, and this value also occurs closer to TDC. That change, because of the hydrogen properties, such as high LFS and diffusion, was expected. For the engine fueled with hydrogen, with its highest energy share, there was an increase in p_{max} by 0.76 MPa compared to the engine fueled with diesel fuel. When fueled with ammonia, the maximum pressure increase was noted for a 12% share of NH_3 and amounted to 0.05 MPa. For the ammonia fuel, a significant delay in the pressure courses is visible compared to the reference case, which is not the case for the hydrogen fuel, and it was caused by the low value of LFS of this fuel. Figure 2 presents the heat release rate courses that are the basis for assessing the combustion process.

From the HRR courses for the hydrogen-fueled engine, it can be seen that with the increase of the H_2 share, up to 22%, the combustion process takes place in two stages, after the first peak on the HRR curve, a second maximum begins to appear. Exceeding this H_2 share caused the combustion to pass into one stage of kinetic combustion with a noticeable disappearance of the diffusion part. Such behavior of a diesel/hydrogen mixture can be caused by an increase in the energetic share of the fuel, which has a low ignition energy value. Consequently, in certain cylinder conditions, the ignition of the hydrogen-air mixture occurs. The increase in HRR_{max} did not exceed 15 J/deg. For the engine fueled with ammonia, the kinetic combustion phase increased by 12 J/deg, which is similar to that of hydrogen. In this case, the nature of the HRR courses is similar for all NH_3 shares. There was a clear reduction in the diffusion combustion phase with the increase of the NH_3 share. Similarly to the pressure courses, a delay in combustion was visible with the increase of the NH_3 share. This was caused, among others, by the increase in the share of fuel with low laminar combustion speed (0.07 m/s) and high heat of vaporization (1370 kJ/kg).

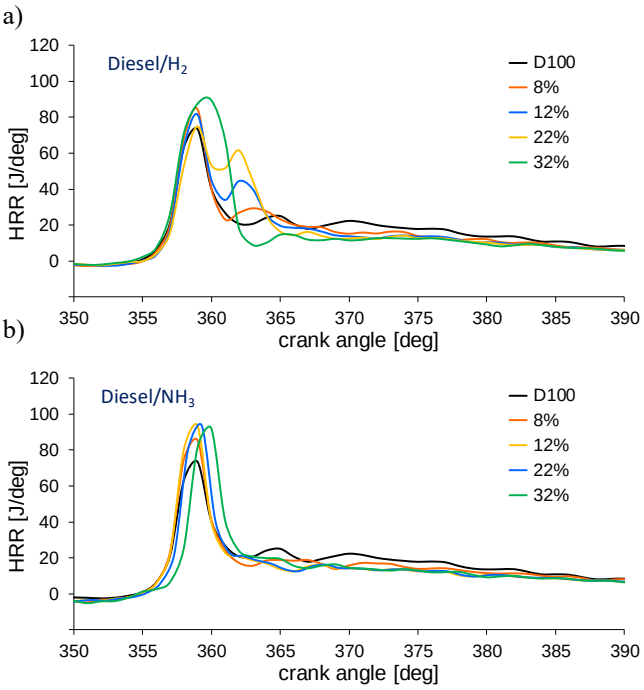

Fig. 2. Heat release rate curves for different H_2 (a) and NH_3 (b) fractions

Based on the heat release rate curves, the heat release curves were determined, which, after normalization, were used to determine characteristic combustion stages. The ignition delay time (CA10) was determined, defined as the time from the beginning of liquid fuel injection to the moment of 10% heat release. The combustion duration (CA10–90) was also determined, defined as the time from the beginning of combustion (CA10) to the moment of 90% heat release (CA90).

The determined heat release courses after normalization are shown in Fig. 3. Fueling the engine with hydrogen clearly affects the heat release course. With an increase in the H_2 share, a clear increase in heat release is visible in the initial combustion phase. Hydrogen, thanks to its high LFS value, intensifies the combustion process. For the engine fueled with NH_3, a change in the nature of heat release is also visible, but here, after the initial intensification of this process, it is clearly slowed down due to the limited flammability of ammonia.

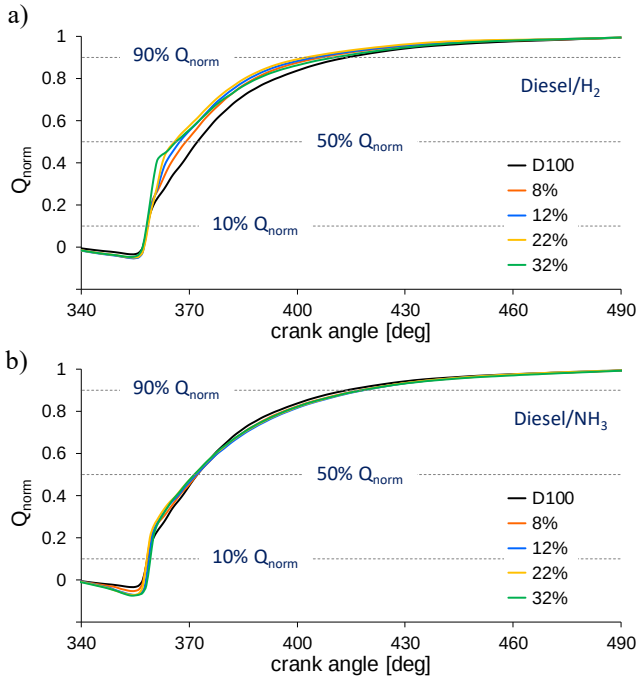

Fig. 3. Normalized heat release curves for different H_2 (a) and NH_3 (b) fractions

In Figure 3 (a and b) characteristic combustion stages are marked, 10% Q_{norm} is the ignition delay time (CA10) and 90% Q_{norm} is the conventional end of combustion time (CA90). The type of fuel is crucial for the initiation and combustion process in both spark ignition and compression ignition engines. It influences characteristic combustion phases, such as ignition delay and combustion duration. For a diesel engine, these phases are most often determined based on the curves of the total released heat.

Figure 4 shows the changes of CA10 and CA10-90 during co-combustion of diesel fuel with hydrogen and ammonia in a dual fuel engine for the analyzed ranges of H_2 and NH_3 shares. The addition of hydrogen to diesel fuel, in comparison with the addition of ammonia, caused a smaller ignition delay and shortened the combustion duration. The smaller CA10 for the diesel/hydrogen engine resulted from providing better conditions for ignition in the engine cylinder due to the improved homogeneity of the combustible mixture containing hydrogen.

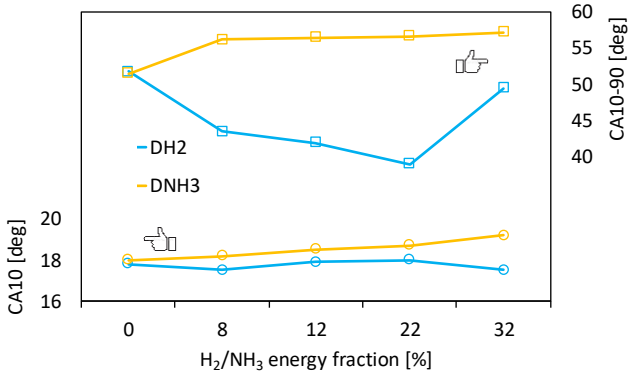

Fig. 4. Characteristic combustion stages: ignition delay (CA10) and combustion duration (CA10-90)

Easier ignition of mixtures with H_2 also resulted from the low minimum ignition energy of hydrogen (0.018 mJ), significantly lower than the minimum ignition energy of ammonia (5–8 mJ). The shorter combustion time of mixtures with H_2 added compared to NH_3 added was mainly caused by the difference in laminar flame speed values for both fuels. High peak laminar flame speed of hydrogen (2.65–3.25 m/s), which is about 40 times higher than the laminar flame speed of ammonia (0.07 m/s), intensifies combustion and helps to shorten CA10–90.

Figure 5 presents a comparison of changes in the IMEP non-repeatability coefficient for a diesel/hydrogen and diesel/ammonia dual-fuel engine. It can be seen that in both cases the COV_{IMEP} values did not exceed the 5% limit permissible for combustion engines and were comparable to the values achieved by a conventional diesel engine. For the engine combusting a mixture with the addition of NH_3, in the entire range of energy shares of this fuel, the COV_{IMEP} values were about 2%. For the engine burning a mixture with the addition of H_2, a slight increase in non-repeatability was noted for the largest 32% share of this fuel. In this case, a large amount of hydrogen in the combustible mixture caused premature ignitions in some cycles, resulting in distortion of the cycles and deepening the differences between them and the average cycle.

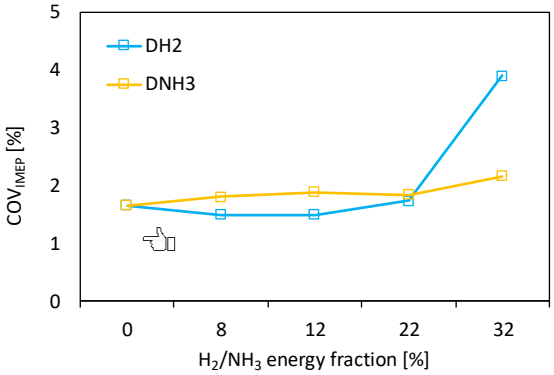

Fig. 5. Coefficient of variation for IMEP

Objective evaluation of the combustion engine operation is also possible thanks to utility indicators such as thermal efficiency (ITE) and specific energy consumption (SEC). Fig. 6 presents the curves of ITE and SEC changes obtained for the diesel/hydrogen and diesel/ammonia engines. They show that the dual-fuel engine worked more efficiently compared to the conventional diesel engine. It can also be seen that the dual-fuel engine with H_2 addition was characterized by higher efficiency and lower specific energy consumption compared to the engine fueled with NH_3. For the diesel/hydrogen engine, the shorter combustion time limited heat losses to the combustion chamber walls and contributed to reduced energy consumption and improved efficiency. For both combusted mixtures, the maximum value of ITE was observed for 12% energy share.

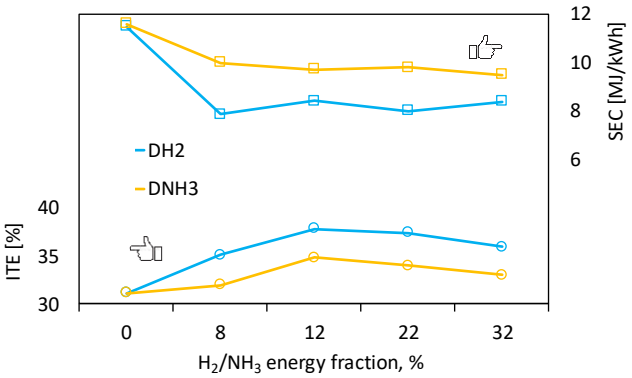

Fig. 6. Engine Thermal Efficiency (ITE) and Specific Energy Consumption (SEC)

When fueling a piston engine with conventional fuels, the basic mechanism for the formation of nitrogen oxides is the thermal mechanism. The share of hydrogen in the fuel mixture contributed to the increase in the combustion temperature and thus intensified the NO_x formation process. The data in Fig. 7 show this almost linear relationship between NO_x emissions and the share of hydrogen in combustion. For the engine fueled with the reference fuel, the NO_x concentration was 457 ppm and for a 32% share of H_2 it increased to 860 ppm, i.e. increased almost twice.

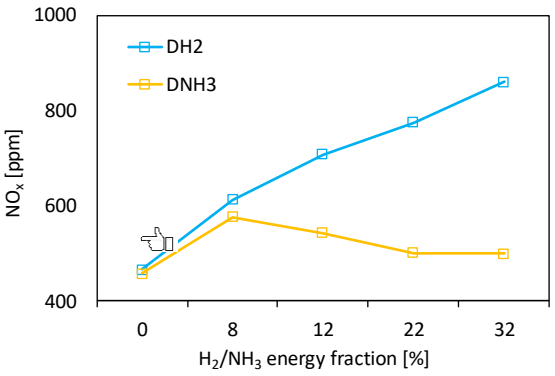

Fig. 7. NO_x concentration in exhaust gases depending on the fuel type

In the case of NH_3 engine fueling, NO_x emissions will also be affected by the thermal mechanism, but the fuel mechanism will play a significant role. Ammonia is a compound of nitrogen and hydrogen, which means that access to nitrogen in the fuel contributes to changing the nature of NO_x formation mechanisms. According to literature sources [13, 23], the deNO_x mechanism can also occur with such fuel. In the analyzed cases, for an 8% share of NH_3, the NO_x concentration increased by 120 ppm, and for a further increase in the share of NH_3, a systematic decrease in NO_x concentration was noted. One of the main benefits of using alternative fuels, such as hydrogen or ammonia, in a compression ignition engine is the reduction of carbon-based compound emissions. One of them is soot, which is a significant problem for conventional diesel engines. Figure 8 shows changes in the soot concentration in the exhaust gases of a dual-fuel engine in the analyzed range of H_2 and NH_3 shares. Emission results showed a significant reduction in soot content in the exhaust of the dual fuel engine, compared to a conventional engine fueled with diesel fuel alone. Replacing part of the diesel fuel with fuels free of elemental carbon, such as hydrogen or ammonia, in the engine cylinder reduced the possibility of incomplete fuel combustion and reduced the amount of soot in the exhaust. The diesel/hydrogen engine was characterized by lower soot emissions compared to the diesel/ammonia engine due to the better ability of H_2 to homogenize the combustible mixture and reduce fuel-rich zones in the engine cylinder.

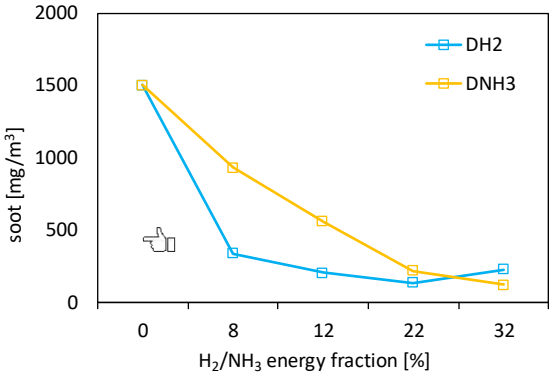

Fig. 8. The influence of H_2 and NH_3 on soot emission

4. Conclusions

As shown in this research, the addition of hydrogen or ammonia as an energy substitution for diesel fuel can be an interesting solution not only because of diesel engine performance but also the combustion process itself. On the basis of the research, the following conclusion can be drawn:

- The addition of hydrogen and ammonia to diesel fuel decreases the total energy of the cycle from 1122 kJ to 1022 kJ for diesel/hydrogen and from 1122 kJ to 1038 kJ for diesel/ammonia, to achieve the same IMEP as for diesel fuel.
- The addition of hydrogen to diesel causes an increase in the cycle's p_{max}, and that value constantly increases with the increase in hydrogen share by 0.76 MPa from 6.24 to 7.00 MPa. The ammonia addition did not cause a significant increase in p_{max}. The p_{max} was almost constant for all energy ratios, and it was around 6.24 MPa.
- The diesel/hydrogen combustion is characterized by two maxima on the HRR curve for all energy ratios except the 32% ratio, where there is only one maximum. The increase in HRR value is 15 J/deg for all cases, except for the 32% energy ratio, where HRR is 20 J/deg. The combustion of a diesel/ammonia mixture is characterized by only one maximum, indicating a combustion process closer to a kinetic one. In this case, the increase in HRR value doesn't exceed 15 J/deg for all energy ratios.
- The hydrogen addition did not affect an ignition delay (CA10), which is, for all cases, close to 17°CA, whereas the ammonia constantly increases that period from 17°CA to 19°CA, with an increase in the ammonia energetic share.
- The CA10–90 phase for hydrogen constantly decreases with an increase in energy share, and it was around

14°CA for an energy share equal to 22% from 54°CA to 40°CA. Because of an increase in unstable combustion for an energy share equal to 32% the increase in that parameter was noted to CA10–90 = 50°CA. For diesel/ammonia mixtures, there was a constant increase in the CA10–90 phase with an increase in the ammonia energy share from 54°CA to 58°CA.

- The addition of hydrogen or ammonia causes an increase in the indicated thermal efficiency, where for both combusted mixtures, the maximum value was observed for 12% energy share, and it is 38% and 34% respectively.
- The addition of ammonia did not cause any significant change in COV_{IMEP}, and the same trend was observed for all energy fractions of hydrogen, except for the last one, which was 32%. An increase in COV_{IMEP} for this energy fraction was observed. It is worth noting that the COV_{IMEP} for all tested mixtures was under 5% value.
- The emission of NO_x increases in both tested fuel mixtures. However, a more visible increase was observed for diesel/hydrogen mixtures, where the increase is from 457 ppm to 860 ppm. For diesel/ammonia mixtures, the increase in NO_x emissions was from 450 ppm to 500 ppm.
- In both cases of fuel mixtures, a decrease in soot emission was observed. In both mixtures, diesel/hydrogen and diesel/ammonia, the decrease was from a value level of 1500 ppm to 200 ppm.

The use of alternative fuel, which does not contain carbon particles in its structure, is an interesting solution to improving the combustion process and emissions of internal combustion diesel engines. Both fuels, when blended with diesel, improve ITE but also demonstrate that it is important to use their full potential, which requires controlling injection timing. The next step of the research will be the modification of the engine fuel supply system from mechanical to an electronically controlled one, which gives the possibility to change the injected fuel dose in a wider range and also provides control of the injection timing, which allows for the expansion of the field of research.

Acknowledgements

This research was funded by the Minister of Science and Higher Education of Poland from the funds dedicated to scientific research No. BS-PB-100-301/2025/P.

The authors would like to thank COLDEX company for delivering pure ammonia cylinders and substantive support in the field of safety.

Nomenclature

AEF	ammonia energy fraction
bTDC	before top dead center
CI	compression ignition
COV_{IMEP}	coefficient of variation for IMEP
HEF	hydrogen energy fraction
HRR	heat release rate
IC	internal combustion
IMEP	indicated mean effective pressure
ITE	indicated thermal efficiency
LFS	laminar flame speed
LHV	lower heating value
LPG	liquefied petroleum gas
SEC	specific energy consumption
σ_{IMEP}	standard deviation of IMEP

Bibliography

[1] Akar MA, Kekilli E, Bas O, Yildizhan S, Serin H, Ozcanli M, Hydrogen enriched waste oil biodiesel usage in compression ignition engine. Int J Hydrogen Energy. 2018;43(38): 18046-18052. https://doi.org/10.1016/j.ijhydene.2018.02.045

[2] Bjørgen KOP, Emberson DR, Løvås T. Combustion of liquid ammonia and diesel in a compression ignition engine operated in high-pressure dual fuel mode. Fuel. 2024;360: 130269. https://doi.org/10.1016/j.fuel.2023.130269

[3] Chehade G, Dincer I. Progress in green ammonia production as potential carbon-free fuel. Fuel. 2021;299:120845. https://doi.org/10.1016/j.fuel.2021.120845

[4] Chun J, McKeown J, Kang S. Impact of vehicle electrification on road roughness induced greenhouse gas (GHG) emissions. Sustainable Energy Technologies and Assessments. 2024;64:103701. https://doi.org/10.1016/j.seta.2024.103701

[5] Dhas AAG, Almoallim HS, Ganeshan S, Anbarasu A, Gavurova B. In-depth study of waste cooking oil blends with hydrogen and ammonia in internal combustion engine: Performance and emission study. Fuel. 2024;369:131663. https://doi.org/10.1016/j.fuel.2024.131663

[6] Dong C, Zhou Q, Zhang X, Zhao Q, Xu T, Hui S. Experimental study on the laminar flame speed of hydrogen/natural gas/air mixtures. Front Chem Eng China. 2010;4:417-422. https://doi.org/10.1007/s11705-010-0515-8

[7] Gomes Antunes JM, Mikalsen R, Roskilly AP, An experimental study of a direct injection compression ignition hydrogen engine. Int J Hydrogen Energy. 2009;34(15):6516-6522. https://doi.org/10.1016/j.ijhydene.2009.05.142

[8] Haddad M, Javani N. Dynamic analysis of green hydrogen production integrated with storage tanks: An economical assessment for different demands. Int J Hydrogen Energy. 2024;140:1126-1139. https://doi.org/10.1016/j.ijhydene.2024.10.024

[9] Hamedani EA, Alenabi SA, Talebi S. Hydrogen as an energy source: A review of production technologies and challenges of fuel cell vehicles. Energy Reports. 2024;12:3778-3794. https://doi.org/10.1016/j.egyr.2024.09.030

[10] Hosseini SE, Wahid MA. Development of biogas combustion in combined heat and power generation. Renew Sust Energ. 2014;40:868-875. https://doi.org/10.1016/j.rser.2014.07.204

[11] Kanth S, Debbarma S. Comparative performance analysis of diesel engine fuelled with hydrogen enriched edible and non-edible biodiesel. Int J Hydrogen Energy. 2021;46(17): 10478-10493. https://doi.org/10.1016/j.ijhydene.2020.10.173

[12] Köse H, Acaroğlu M. The effect of hydrogen addition to Cynara biodiesel on engine performance and emissions in diesel engine. Energy Sources, Part A. 2020;46(1):8455-8474. https://doi.org/10.1080/15567036.2020.1765904

[13] Kuta K, Nadimi E, Przybyła G, Żmudka Z, Adamczyk W. Ammonia CI engine aftertreatment systems design and flow simulation. Combustion Engines. 2022;190(3):3-10. https://doi.org/10.19206/CE-143158
[14] Liu J, Liu J, Experimental investigation of the effect of ammonia substitution ratio on an ammonia-diesel dual-fuel engine performance. J Cleaner Prod. 2024;434:140274. https://doi.org/10.1016/j.jclepro.2023.140274
[15] Liu J, Wang X, Zhao W, Sun P, Ji Q. Effects of ammonia energy fraction and diesel injection parameters on combustion stability and GHG emissions characteristics in a low-loaded ammonia/diesel dual-fuel engine. Fuel. 2024;360: 130544. https://doi.org/10.1016/j.fuel.2023.130544
[16] Ma BC, Liu B, Wang Y, Liu L. Analysis on the combustion performance of ammonia-hydrogen coaxial stratified injection in low speed marine engine. Appl Therm Eng. 2025; 126253. https://doi.org/10.1016/j.applthermaleng.2025.126253
[17] Monforti-Ferrario F, Crippa M, Pisoni E. Addressing the different paces of climate and air quality combustion emissions across the world. iScience. 2024;27:108686. https://doi.org/10.1016/j.isci.2023.108686
[18] Nadimi E, Przybyła G, Lewandowski MT, Adamczyk W. Effects of ammonia on combustion, emissions, and performance of the ammonia/diesel dual-fuel compression ignition engine. J Energy Inst. 2023;107:101158. https://doi.org/10.1016/j.joei.2022.101158
[19] Napolitano P, Fraioli V, Guido C, Beatrice C. Assessment of optimized calibrations in minimizing GHG emissions from a dual fuel NG/diesel automotive engine. Fuel. 2019;258: 115997. https://doi.org/10.1016/j.fuel.2019.115997
[20] Nie X, Bi Y, Shen L, Lei J, Wan W, Wang Z et al. Combustion and emission characteristics of ammonia-diesel dual fuel engine at different altitudes. Fuel. 2024;371B:132072. https://doi.org/10.1016/j.fuel.2024.132072
[21] Ovaere M, Proost S. Cost-effective reduction of fossil energy use in the European transport sector: an assessment of the Fit for 55 Package. Energy Policy. 2022;168:113085. https://doi.org/10.1016/j.enpol.2022.113085
[22] Rameez PV, Ibrahim MM. Maximizing hydrogen utilization in CI engines: an investigation of dual fuel and RCCI combustion approaches under low and mid-load conditions in a medium duty automotive engine. Energy Convers Manage. 2024;321:119100. https://doi.org/10.1016/j.enconman.2024.119100
[23] Raza H, Woo S, Kim H, Investigation of an ammonium carbamate–based SCR system for NOx reduction in diesel engines under transient conditions. Energy. 2022;251: 123918. https://doi.org/10.1016/j.energy.2022.123918
[24] Rrustemi DN, Ganippa LC, Megaritis T, Axon CJ. New laminar flame speed correlation for lean mixtures of hydrogen combustion with water addition under high pressure conditions. Int J Hydrogen Energy. 2024;63:609-617. https://doi.org/10.1016/j.ijhydene.2024.03.177
[25] Sarfaty M, Duritz N, Gould R, Mitchell M, Patel L, Paulson J et al. Organizing to advance equitable climate and health solutions: the medical society consortium on climate and health. The Journal of Climate Change and Health. 2022;7: 100174. https://doi.org/10.1016/j.joclim.2022.100174
[26] Silveira JP, Fagundez JLS, Garlet RA, Martins MES, Salau NPG, Lanzanova TDM. Hydrogen-fueled PFI SI engine investigation for near-zero NOx emissions in de-throttled and supercharged ultra-lean burn conditions. Int J Hydrogen Energy. 2024;91:800-813. https://doi.org/10.1016/j.ijhydene.2024.10.198
[27] Tutak W, Jamrozik A, Grab-Rogaliński K, Pyrc M. Effects of ammonia energy fraction on combustion stability and emissions characteristics of naturally aspired industrial dual-fuel diesel engine. Energy Convers Manage. 2024;314: 118698. https://doi.org/10.1016/j.enconman.2024.118698
[28] Tutak W, Jamrozik A, Grab-Rogaliński K. Effect of natural gas enrichment with hydrogen on combustion process and emission characteristic of a dual fuel diesel engine. Int J Hydrogen Energy. 2020;45(15):9088-9097. https://doi.org/10.1016/j.ijhydene.2020.01.080
[29] Wang B, Yang C, Wang H, Hu D, Wang Y. Effect of diesel-ignited ammonia/hydrogen mixture fuel combustion on engine combustion and emission performance. Fuel. 2023; 331(2):125865. https://doi.org/10.1016/j.fuel.2022.125865
[30] Wu B, Wang Y, Wang D, Feng Y, Jin S. Generation mechanism and emission characteristics of N_2O and NO_x in ammonia-diesel dual-fuel engine. Energy. 2023;284:129291. https://doi.org/10.1016/j.energy.2023.129291
[31] Xu L, Xu S, Bai XS, Repo JA, Hautala S, Hyvönen J. Performance and emission characteristics of an ammonia/diesel dual-fuel marine engine. Renewable and Sustainable Energy Rev. 2023;185:113631. https://doi.org/10.1016/j.rser.2023.113631
[32] Zhang Z, Hu J, Yang D, Yin Z, Lu K, Tan D. A comprehensive assessment over the environmental impact and combustion efficiency of using ammonia/hydrogen/diesel blends in a diesel engine. Energy. 2024;303:131955. https://doi.org/10.1016/j.energy.2024.131955

Karol Grab-Rogaliński, DEng. – Faculty of Mechanical Engineering, Czestochowa University of Technology, Poland.
e-mail: *k.grab-rogalinski@pcz.pl*

Prof. Arkadiusz Jamrozik, DSc., DEng. – Faculty of Mechanical Engineering, Czestochowa University of Technology, Poland.
e-mail: *arkadiusz.jamrozik@pcz.pl*

Prof. Wojciech Tutak, DSc., DEng. – Faculty of Mechanical Engineering, Czestochowa University of Technology, Poland.
e-mail: *wojciech.tutak@pcz.pl*

Arkadiusz Kociszewski, DEng. – Faculty of Mechanical Engineering, Czestochowa University of Technology, Poland.

Article citation info:
Woś P, Krzemiński A, Kuszewski H, Jakubowski M, Jaworski A, Hunicz J et al. Problems of filtration and standardization on parameter conformity of diesel fuels containing decarbonization components and processing impurities. Combustion Engines. 2026;204(1):184-191. https://doi.org/10.19206/CE-211450

Paweł WOŚ
Artur KRZEMIŃSKI
Hubert KUSZEWSKI
Mirosław JAKUBOWSKI
Artur JAWORSKI
Jacek HUNICZ
Arkadiusz RYBAK
Andrzej BORAWSKI
Dariusz SZPICA

Combustion Engines
Polish Scientific Society of Combustion Engines

Problems of filtration and standardization on parameter conformity of diesel fuels containing decarbonization components and processing impurities

ARTICLE INFO

Received: 20 June 2025
Revised: 22 September 2025
Accepted: 28 September 2025
Available online: 30 October 2025

The use of alternative fuels and fuel components derived from organic and inorganic waste enables progress toward the goals set by decarbonization policies and environmental protection, but on the other hand, it presents a number of challenges related to maintaining the operational quality of these fuels. This primarily involves achieving normative physico-chemical parameters for newly formulated blends intended for powering automotive engines, as well as identifying and effectively removing both solid and liquid contaminants specific to each fraction (component). Information concerning the chemical composition and purity of individual fuel components is essential in the context of formulating substitute fuels. This article presents the results of comparative studies on the amount of contaminants found in substitute fuel components such as hydrotreated vegetable oil (HVO), tire pyrolysis oil (TPO), and plastic-derived pyrolysis oils – polypropylene pyrolytic oil (PPO) and polystyrene oil (PSO). For diesel fuel and substitute fuels, microfiltration was carried out using membrane filters to determine the quantity of solid impurities. The aim of the study was to assess the feasibility of using these types of fuels either on their own or in blends with diesel fuel, under the assumption that they would be used directly after processing to power compression ignition engines. The research showed that the distillation process of pyrolytic oils significantly reduces the content of process-related impurities. The greatest reduction was observed for PPO, where after filtering a 50 ml sample the level of contaminants after distillation and ashing decreased from approximately 23 mg to a value close to zero.

Key words: *process contaminants, filtration, diesel fuel, hydrotreated vegetable oil (HVO), waste-based pyrolytic oils*

1. Introduction

The absence of contaminants in fuels used to power internal combustion engines is one of the most critical requirements that such fuels must meet. This is particularly important for compression ignition engines due to their high operating pressures and the extremely precise tolerances of fuel system components. Fuel injection systems used today are built to extremely precise standards and operate under very high pressure. Because of that, they are easily affected by even tiny traces of contaminants – whether solid particles or liquid residues. When such impurities get into the system, they can cause wear and tear much faster than expected, damage delicate parts, or block narrow channels. This can end up lowering engine performance, raising emissions, and leading to more frequent or expensive repairs. In this context, the presence of any foreign substances – whether particulate, chemical, or microbiological – poses a significant risk to engine reliability and durability. Therefore, these factors necessitate effective fuel filtration – not only to remove solid and microbiological contaminants but also to eliminate water, which can cause corrosion, irregular combustion, accelerated microbial growth, and degradation of fuel quality during storage and operation [24]. Effective filtration becomes even more crucial when dealing with alternative or waste-derived fuels, which may contain unique contaminants resulting from their specific production processes.

Fuel contamination is not just a problem once the fuel reaches the engine – it can start much earlier, right at the point of delivery. Tanks, pipes, and even fuel nozzles at stations are not always perfectly clean. Over time, tiny bits of rust, moisture, or grit can build up, and during refueling, some of that stuff can easily get into the vehicle's tank. It might not seem like much, but it can cause real trouble down the line. Modern injection systems, especially common rail types running at over 2000 bar, are incredibly sensitive. They are built with extreme precision, and unfortunately, that means even the smallest particles can do damage. Tests and field data have shown that one of the biggest threats to these systems comes from very small, hard particles – often inorganic. They are sharp enough to gradually wear out injectors, valves, and other precision components. As wear adds up, fuel delivery becomes inconsistent. That throws off combustion, leads to more emissions, and overall, the engine just does not perform like it should.

These days, there is growing pressure to cut down on harmful emissions like nitrogen oxides (NO_x), carbon monoxide (CO), unburned hydrocarbons (HC), particulate matter (PM), and carbon dioxide (CO_2) – which is widely recognized as a major contributor to climate change [16]. With environmental rules getting tougher and the public demanding cleaner solutions, researchers and engineers have been turning more and more to renewable fuels and bio-based

additives. What makes this option appealing is that it does not require overhauling existing engines. In most cases, only small changes to things like injection timing, air-fuel ratio, or exhaust gas recirculation are needed [19]. So, instead of replacing entire systems, we can work with what we already have. This makes renewable fuels a realistic way to lower emissions in transportation without massive costs or disruptions to current infrastructure.

Mixing bio-components into fuel can change how it behaves in more ways than one. The fuel might get thicker, and water can behave differently – sometimes staying suspended longer or forming larger droplets. How much this happens depends a lot on how the liquids interact on a surface level, like their tension [2]. These changes can be subtle but still affect how the fuel performs. People working with engines – especially in real-world settings – have noticed that biodiesel tends to plug up filters sooner than regular diesel. That seems to happen more often when there's more water involved. The way biodiesel flows and how it moves through filter media probably has something to do with it [11].

Moreover**,** the degradation process of biodiesel leads to the formation of soft particles that negatively impact filtration efficiency [4, 5, 8]. Reports from users regarding clogged fuel filters [12] and damaged engine components have prompted the development of solutions aimed at mitigating the adverse effects of biocomponent usage. One such solution is the implementation of multi-stage filtration systems, which can significantly extend filter service life [9].

Despite ongoing research, the impact of biodiesel on the filtration process remains insufficiently understood [20]. Even less is known about the behavior of newer fuel additives containing decarbonizing components such as hydrotreated vegetable oil (HVO), pyrolytic oils from used tires (TPO), and plastic-derived oils, including polypropylene pyrolytic oil (PPO) and polystyrene oil (PSO), along with the process-related contaminants associated with their production.

Some newer approaches to removing water from fuel include filters made with graphene-based materials – which are also known for their ability to kill bacteria [7]. Another solution uses filters built from fine polypropylene (PP) and polyamide (PA6) fibers. These are made using co-extrusion and delamination methods. In lab tests, they have shown better water separation than standard commercial filters, with results ranging from about 62% to 85% under the same testing conditions [22, 23].

One of the other problems that can come up when using biodiesel is contamination from glycerides – these can end up clogging fuel filters. Even a small amount of monoglycerides in the fuel can cause buildup, especially when temperatures drop [17]. Some tests [14, 15] using filters with different pore sizes – along with a modified version of the CSFT method (ASTM D7501) – showed that filters with bigger pores tend to collect fewer deposits.

At the same time, researchers have looked into whether certain materials can help improve biodiesel filterability. One study [1] tested several common adsorbents – including activated carbon, silica, and sand. Out of those, activated carbon worked best.

But monoglycerides aren't the only issue. Other substances, like sodium soaps and free sterol glycosides, also play a role in shortening filter life. According to another study [3], current fuel standards don't fully cover these problems, and there is a growing case for updating regulations to better protect fuel systems running on biodiesel.

Some studies have explored how less conventional plant oils – like karanja or palm – perform when used in fuel blends [13]. Since these oils usually come from non-edible sources, they are often seen as a good option for scaling up biofuel production without cutting into the food supply. Still, their chemical makeup is different from what is used in more common feedstocks, and that can bring up new issues with fuel cleanliness. For karanja oil in particular, research shows that doing things like esterification, transesterification, or degumming can help. These treatments reduce the amount of sticky compounds – like gums, polar residues, or heavier materials – that tend to block filters [21]. These refining steps improve fuel stability and mitigate the formation of deposits that can obstruct fuel flow under operational conditions. For example, study [20] observed that the tendency to clog the FBT filter increased exponentially with higher biodiesel content in the blend, emphasizing the sensitivity of filtration systems to biodiesel-induced contamination. Tests showed that filters used with biodiesel had about 35% more pressure drop than those with regular diesel. In simple terms – the fuel had a harder time flowing, and filters wore out quicker. That might not matter much everywhere, but in places with high biodiesel use or seasonal blends, it could turn into a real issue. On the other hand, research [13] showed that diesel locomotives running on a 20% biodiesel–palm oil mix were still filtering well after 125 hours of generator use or even after three months of traction service. So, with the right blending and processing, biodiesel can hold up well – even in tough, long-running conditions. It all comes down to making sure that processing steps match the type of feedstock used. When that is done right, it is possible to get both good engine performance and real environmental gains.

To quantitatively evaluate how effectively fuel filters retain contaminants, researchers employ a variety of analytical techniques. These include gas chromatography–mass spectrometry (GC-MS), X-ray fluorescence spectroscopy (XRF), Fourier-transform infrared spectroscopy (FTIR), and scanning electron microscopy coupled with energy-dispersive X-ray spectroscopy (SEM/EDX). Thermogravimetric analysis (TGA) is also commonly used for this purpose [4, 5].

Lab tests are useful, no doubt, but they can not always show what is really going on inside the filter. So, in a lot of cases, researchers build math-based models to help them get closer to the actual behavior [6]. These tools let them try out different combinations – fuel blends, particle size, filter material – to see what happens when everything interacts. Not under perfect conditions, but more like what would be got in the real world. It is not always exact, but it is enough to find weak spots or make early design changes that would take a lot longer to test in practice. By accounting for factors such as fluid flow dynamics, particle size distribution, mechanisms of pore blockage, and pressure

drop evolution, these models support the development of filtration systems that are both more efficient and more durable. Furthermore, predictive modeling helps reduce the time and cost of empirical testing by narrowing the range of design options before physical prototypes are constructed and validated. Nevertheless, despite these advancements, the filtration of fuels containing a wide range of additives remains a poorly understood issue that requires further detailed investigation. The growing diversity of renewable and waste-derived fuel components introduces an array of contaminant types with distinct physical and chemical properties, which may behave differently from those encountered in conventional fossil-based fuels. Some of these contaminants come from leftover by-products, materials that break down during processing, or particles that get in from raw materials or equipment. The way they interact with filter materials is still not fully understood, which makes it hard to reliably predict how well a filter will perform when different types of alternative fuels are used.

The primary objective of this study is to conduct a comparative analysis of contaminants present in selected waste-derived substitute fuels, namely hydrotreated vegetable oil (HVO), polypropylene pyrolysis oil (PPO), polystyrene pyrolysis oil (PSO), and waste tire pyrolysis oil (TPO) – in relation to conventional diesel fuel. Too many contaminants in fuel can shorten the service life of filters – both in fueling equipment at stations and inside engine systems. This not only drives up maintenance costs but also puts long-term equipment reliability at risk. In more serious cases, especially where high-precision fuel injection is used, heavy contamination may lead to unexpected breakdowns or even major engine damage. Since this area is still not well understood, and considering how strongly fuel quality affects engine performance, there is a clear need for more detailed research. Solid, real-world data are necessary – not just to help shape fuel blending guidelines, but also to support better design of filtration systems. That kind of knowledge will be key to safely and effectively including waste-based fuels in today's fuel distribution networks.

2. Research methodology

The first stage of the study focused on determining the mass of solid contaminants. Mass measurements were performed using a RADWAG WAA40/160/X/1 analytical laboratory balance, characterized by a readability of 0.01 mg and repeatability of 0.02 mg. Each fuel sample was tested in duplicate, and the results for mass and filtration time were averaged. A proprietary testing methodology was developed based on the ISO 4020 procedure.

The determination of solid impurities involved forced filtration of 50 ml of fuel through an ashless cellulose acetate (CA) membrane filter with a diameter of 47 mm and a pore size of 0.8 µm, under a vacuum of 80 kPa ±1 kPa. A standard laboratory vacuum filtration setup was used (Fig. 1), following the procedure below.

Measurement of the mass of a porcelain crucible used to hold the filter membrane:

- measurement of the crucible with the membrane prior to filtration
- placement of the membrane on the sintered disc of the vacuum filtration apparatus
- filling the glass filtration funnel with 50 ml of the test fuel
- activation of the vacuum pump and adjustment of the vacuum pressure to 80 kPa ±1 kPa
- initiation of the filtration process with simultaneous timing of the filtration duration
- transfer of the membrane into the porcelain crucible post-filtration
- measurement of the crucible mass with the membrane after filtration
- drying the crucible with the membrane at 100°C for 1 hour
- cooling of the crucible in a desiccator
- measurement of the crucible mass after drying
- placement of both the post-filtration and clean membranes in crucibles onto a hot plate heated to 550°C ±5°C for preliminary ashing
- transfer of the crucibles to a muffle furnace at 800°C ±20°C for 2 hours
- removal of the crucibles from the furnace and cooling in a desiccator for 1 hour
- measurement of the crucible masses with the ash residues
- calculation of the mass of solid contaminants based on the difference in mass before and after ashing.

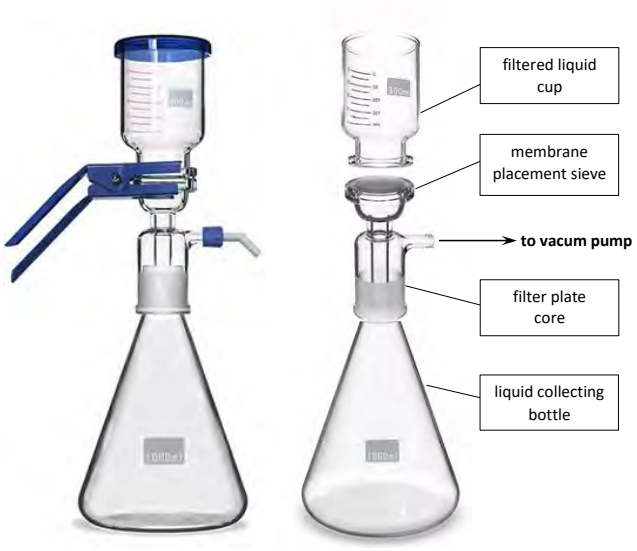

Fig. 1. A standard laboratory vacuum filtration setup used to sedimentation tests; assembled view (at left); component view (at right)

Comparative testing was performed for conventional diesel fuel and selected waste-derived substitute fuels: HVO, PPO, PSO, and TPO.

This selection of fuels represents a broad spectrum of chemical compositions and production technologies, each associated with distinct impurity profiles. Hydrotreated vegetable oil (HVO), produced via catalytic hydrotreatment, typically contains minimal contaminants due to extensive processing steps. In contrast, pyrolysis-derived oils such as PPO, PSO, and TPO generated through thermal decomposition of plastic waste or end-of-life tires can retain significant amounts of process-related impurities, including unconverted feedstock residues, oligomers, char particles, and various organic compounds. The physico-

chemical properties of the tested fuels, as well as the production technologies of the waste-derived fuels, were previously reported by the authors [10, 18], providing a comprehensive basis for understanding their behavior in filtration processes.

In the second stage of the study, atmospheric distillation was performed in accordance with the standard PN-EN ISO 3405, Petroleum and related products of synthetic or natural origin – Determination of distillation characteristics at atmospheric pressure, for PSO, TPO, and PPO. The application of this distillation process was aimed at simulating industrial-level purification steps to assess the potential of reducing contaminant loads in these fuels through relatively simple thermal separation methods. By removing the most volatile and heavy fractions, the distillation process was expected to concentrate residual contaminants and allow for a more accurate quantification of the solid impurity content remaining in the fuel.

The measurements were carried out using an OptiDist distillation apparatus (Fig. 2), which was configured according to Group 4-a configuration representative of diesel fuel – thus maintaining consistent instrument settings across all fuel samples. This standardized configuration ensured that variations in distillation behavior and residual contamination could be attributed solely to the intrinsic properties of the fuels themselves rather than to differences in test methodology. The ability to apply identical distillation parameters to both conventional and substitute fuels allowed for direct comparability and provided an objective basis for evaluating the efficacy of distillation as a contaminant-reduction technique.

Fig. 2. OptiDist distillation apparatus used to perform atmospheric distillation tests

Following the distillation process, the mass of residual contaminants in the waste-derived fuels was determined. The visual assessment of the post-distillation samples (Fig. 3) revealed notable differences in clarity and sediment content, which were indicative of the varying efficiency of impurity removal across the different fuel types. The distilled fuels were designated as follows: PSO-D, TPO-D, and PPO-D, each representing the respective distillate fraction after thermal processing. This nomenclature was adopted to distinguish between the raw and purified forms of each substitute fuel throughout the subsequent filtration analyses.

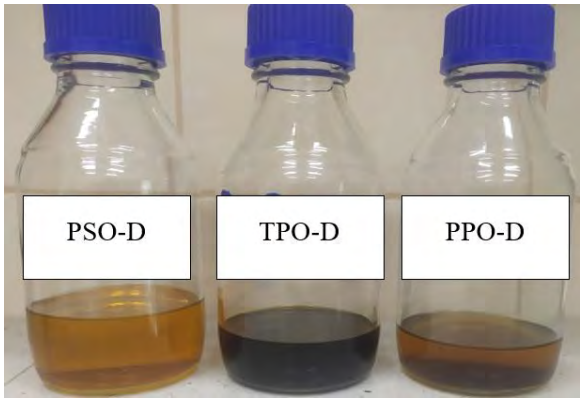

Fig. 3. Fuel samples after distillation, for which the mass of contaminants was determined

3. Analysis of research results

The objective of the study was to conduct a comparative analysis of contaminant levels in waste-derived substitute fuels relative to conventional diesel fuel, using a vacuum-assisted filtration system designed to quantify solid impurities. This method enabled a direct evaluation of the filtration load imposed by each fuel type, reflecting their respective purity levels and potential operational risks for fuel systems. Figure 4 presents the appearance of the filtration membranes following the filtration process for diesel fuel and the analyzed substitute fuels. The degree of membrane darkening serves as a visual indicator of contaminant concentration, with progressively darker membranes suggesting greater amounts of retained particulate matter. Among the tested fuels, the membrane corresponding to PPO displayed the most pronounced darkening, indicating the highest concentration of solid contaminants in this fuel. This qualitative observation was fully consistent with the quantitative results obtained from mass measurements of the retained impurities (Fig. 5), confirming PPO as the most heavily contaminated among the tested samples. Furthermore, these results were corroborated by the recorded filtration times (Fig. 6), which serve as an additional proxy for filter loading and flow resistance. Fuels with higher contaminant content exhibited longer filtration durations, reflecting increased membrane fouling and reduced permeability under the applied vacuum conditions.

As illustrated in Fig. 5, PPO resulted in the most substantial deposit on the membrane, with a recorded mass of 1.4310 g. This considerable buildup indicates a high impurity load in pyrolysis oil derived from polypropylene. The likely sources of these residues include incomplete breakdown of feedstock, carryover of solid particles, or condensation of heavier organic compounds during the thermal process. Supporting this, the filtration of PPO required over

two hours to complete, as shown in Fig. 6, highlighting severe membrane obstruction and restricted flow. In real-world systems, such conditions would likely lead to rapid filter clogging in engines and fuel dispensers.

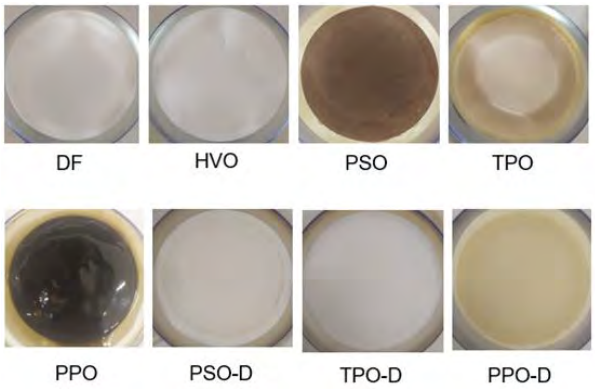

Fig. 4. Filtration membranes after the filtration process

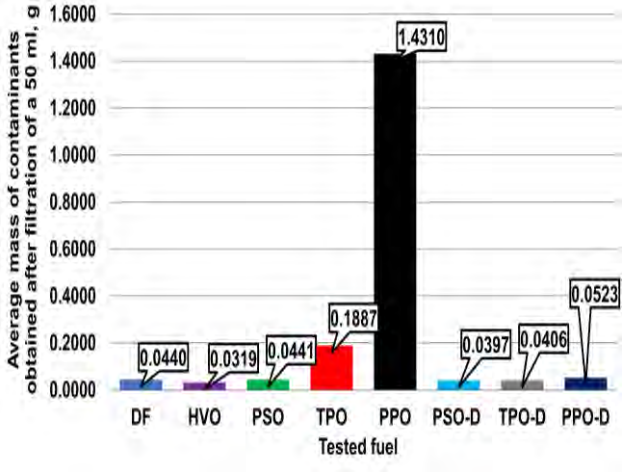

Fig. 5. Average mass of contaminants after filtration

When compared with diesel, PPO left behind a significantly larger amount of solid residues – 1.3870 g more – indicating a clearly higher filtration burden. For TPO, the retained contaminant mass reached 0.1890 g, which is 0.1450 g above the diesel benchmark. Although pyrolysis oil derived from used tires still contains a notable level of impurities, the overall load remains much lower than that associated with PPO. This difference is likely tied to variations in feedstock composition as well as operational settings during thermal conversion. The filtration process for TPO also took longer than for diesel, by approximately 1.0 ±0.1 s, pointing to a moderate increase in membrane resistance. In contrast, HVO demonstrated the cleanest profile. The amount of material deposited on the membrane for this fuel averaged 0.0319 g, which is 0.0121 g less than the value observed for diesel. This aligns with the high purity typically achieved during hydrotreatment. With such a low contaminant load, HVO can be regarded as a clean, low-risk fuel in terms of filtration system wear and performance.

In the following stage of the study, attention was turned to the distilled fuel samples – PSO-D, TPO-D, and PPO-D. After undergoing atmospheric distillation, all three fuels showed a clear drop in the amount of contaminants collected on the filtration membranes. For PSO-D and TPO-D, the measured deposit levels were similar to those found for conventional diesel, which indicates that distillation removed a large share of the particulate and processing-related impurities present in the original feedstocks. This is most likely due to the fact that the distillation process separates lighter compounds, which tend to contain fewer heavy residues or particles. While PPO-D also benefited from the distillation step, the total amount of filtered material was still slightly above that observed for diesel – by around 0.0083 g – possibly due to the persistence of trace heavier fractions in the final product. A slight difference in retained mass between PPO-D and diesel fuel was still observed, which may point to the partial persistence of high-boiling residues from the polypropylene pyrolysis process. Alongside this, notable improvements in filtration behavior were also recorded for the distilled samples. All distillates passed through the membrane faster than diesel, suggesting smoother flow and reduced membrane resistance under vacuum-assisted conditions. Among them, PPO-D had the longest filtration time at 10.3 ±0.1 seconds – still a considerable improvement compared to the much longer filtration duration seen for untreated PPO. In contrast, PSO-D showed the fastest filtration time at 4.1 ±0.1 seconds, indicating a particularly clean fraction. These results collectively confirm that atmospheric distillation has a strong positive effect on the filtration performance of fuels derived from waste, especially those obtained from plastic feedstocks.

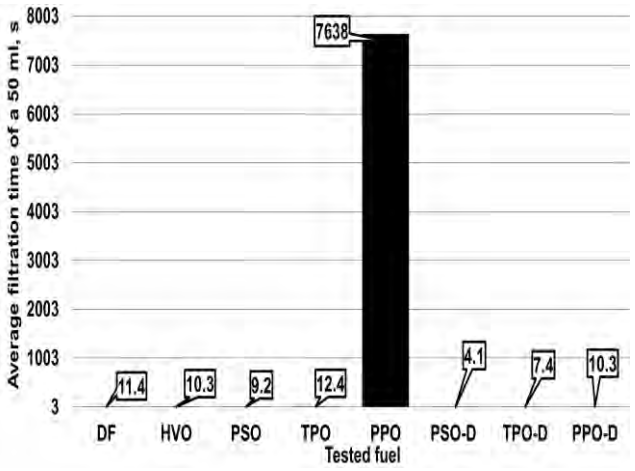

Fig. 6. Average filtration time

The graph presented in Fig. 7 illustrates the average mass of contaminants retained on the filtration membrane after filtering various fuels and their distilled fractions, followed by thermal treatment of the membranes in a muffle furnace at 100°C for 1 hour. This process allowed for the evaporation of volatile compounds.

The highest amount of contaminants retained on the filtration membrane was recorded for PPO, with a mass of 0.7504 g. Compared to diesel fuel (DF), this represents an increase of approximately 97%, highlighting the significant impurity burden associated with raw polypropylene pyrolysis oil. The substantial contaminant mass suggests that the pyrolysis of polypropylene generates not only condensable

hydrocarbons but also considerable amounts of solid residues, char particles, and high-molecular-weight by-products that are difficult to remove without additional refining steps. A lower, though still elevated, contaminant mass was observed for TPO, which exhibited 0.1178 g of retained contaminants, an increase of approximately 83% relative to DF. This elevated level likely reflects the presence of tire-derived inorganic fillers, carbon black, and metallic residues often encountered in waste tire processing streams. PSO presented a considerably lower contaminant mass of 0.0254 g, corresponding to approximately 21% more than diesel fuel, suggesting that the pyrolysis of polystyrene yields a cleaner product in terms of solid impurities compared to other waste-derived feedstocks.

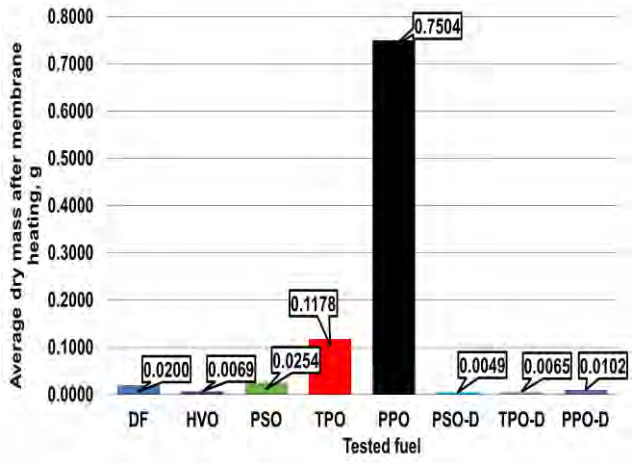

Fig. 7. Average mass of contaminants after heating of the filter membrane

In contrast, the lowest levels of contamination were observed for HVO (0.0069 g), confirming once again the high purity of this hydrotreatment-derived fuel. Among the distilled fuels, contaminant levels were further reduced, with PSO-D (0.0049 g), TPO-D (0.0065 g), and PPO-D (0.0102 g) demonstrating significantly improved filtration cleanliness compared to their raw counterparts. These results reinforce the beneficial role of atmospheric distillation in removing impurities, particularly from pyrolysis-derived fuels, and suggest that simple distillation can serve as an effective initial purification step prior to fuel utilization or blending.

The final stage of the study involved ashing the filtration membranes, followed by thermal treatment of the residue at 800°C ±20°C for 2 hours in a muffle furnace. This high-temperature treatment allowed for the complete combustion of organic matter, isolating only the inorganic solid residues. The mass of these residues serves as a reliable indicator of non-volatile inorganic contaminants, including metals, ash-forming minerals, and refractory compounds that could contribute to long-term engine wear or deposit formation.

Figure 9 summarizes the results concerning the average mass of contaminants remaining after the ashing and heat treatment of the membrane samples, providing a more detailed characterization of the nature and persistence of solid impurities in the tested fuels.

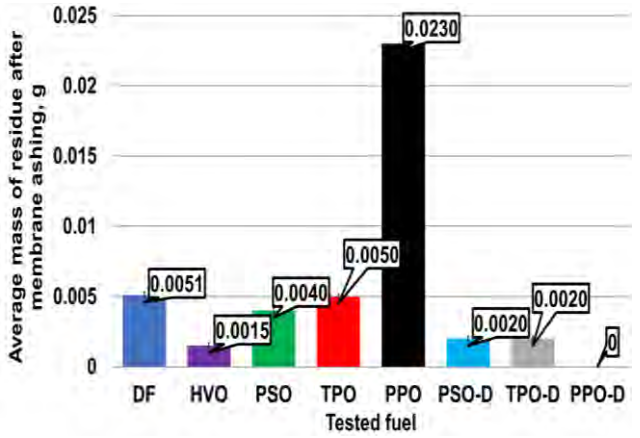

Fig. 8. Average mass of residue after filtration membrane ashing followed by high-temperature drying

PPO stood out among all the tested fuels by leaving the largest quantity of ash after combustion, with 0.0230 g of residue recorded. Compared to diesel fuel (DF), this represents an increase of approximately 360%, indicating that polypropylene pyrolysis oil retains notable amounts of non-volatile inorganic material even after the organic content has been burned off. Such residues are most likely composed of metals, remnants of catalysts, or thermally resistant char substances often formed as by-products during the thermal breakdown of plastic waste. In contrast, HVO samples showed the least contamination, with ash content averaging 80% lower than in diesel, pointing to a much cleaner composition. The results for HVO once again demonstrated its exceptionally high purity. Practically no ash remained after the ashing procedure, which reflects the effectiveness of hydrotreatment in eliminating both organic and inorganic contaminants. Thanks to this high degree of cleanliness, HVO can be considered well suited for use in modern injection systems, with little risk of filter blockage or injector deposits.

In the case of PPO-D, no solid residue was detected after ashing. This indicates that atmospheric distillation was successful in removing almost all non-volatile contaminants from the original pyrolysis fraction. The result further supports the idea that distillation may serve as a straightforward but efficient method for cleaning up plastic-derived pyrolytic oils. For raw PSO, the post-ashing mass was approximately 20% lower than that of diesel, pointing to a naturally low concentration of thermally stable inorganic matter in polystyrene-derived fuels. TPO, in contrast, left behind 0.0050 g of ash, essentially matching the result obtained for diesel. This finding reflects the typical complexity of tire-based fuels, which often contain both carbonaceous residues and mineral-based additives. Distilled versions of these fuels – PSO-D and TPO-D – exhibited significantly improved cleanliness. The amount of residual ash dropped by about 60% compared to diesel. This reduction not only confirms a lower total level of contaminants but also shows that distillation is particularly effective at removing substances that would otherwise remain as ash after combustion. These improvements highlight the potential of distillation to prepare waste-based pyrolysis fuels for

use in diesel engines without posing additional operational risks.

4. Conclusions

Based on the conducted research, the following conclusions can be drawn:

- the lowest mass of contaminants was recorded for HVO, confirming the high degree of purification achieved through hydrotreatment, which effectively eliminates both organic and inorganic impurities
- PSO and diesel fuel (DF) exhibited comparable levels of solid contaminants, suggesting that polystyrene-derived pyrolysis oil, even in its raw form, contains relatively few non-volatile residues that could challenge filtration systems
- the filtration time of the tested fuels closely correlated with the mass of retained impurities, demonstrating that increasing contaminant load directly impacts filtration performance and resistance to flow
- the highest contaminant levels were found in PPO and TPO, reflecting the more complex composition and impurity profiles of polypropylene and tire-derived pyrolysis oils, which contain significant solid residues, char particles, and refractory compounds
- distillation proved to be an effective method for reducing process-related contaminants in pyrolytic oils derived from plastics and used car tires; the significant reduction in both organic and inorganic impurities after distillation demonstrates the practical value of this relatively simple purification step in improving the filterability and potential usability of waste-derived fuels.

The results of this study clearly indicate that, due to their high impurity content, raw waste-based pyrolytic oils are not suitable for direct application as fuels in diesel engines, as their use would likely lead to rapid filter clogging, injector fouling, and accelerated wear of precision fuel system components. However, as demonstrated by the experimental data, atmospheric distillation may serve as a viable and technically straightforward method for purifying such fuels. The resulting distillate fractions exhibit substantially improved purity, making them potential candidates for use either as standalone fuels or as blending components with conventional diesel or HVO. Nevertheless, while the reduction of solid contaminants is a crucial step toward the practical application of waste-derived fuels, their full suitability for diesel engine operation requires further comprehensive research. Additional investigations should address other critical fuel parameters, such as lubricity, cetane number, chemical stability, and the formation of combustion deposits, all of which directly influence combustion processes, emissions, long-term engine durability, and ope-rational safety.

Acknowledgements

The research leading to these results has received funding from the commissioned task entitled “Polytechnic Network VIA CARPATIA named after President of the Republic of Poland Lech Kaczynski”, financed by a special purpose grant from the Minister of Science and Higher Education contract no: MEiN/2022/DPI/2575, MEiN/2022/DPI/2577, MEiN/2022/DPI/2578, activity “ISKRA – building inter-university research teams”.

Nomenclature

CA	cellulose acetate membrane
DF	diesel fuel
HVO	hydrotreated vegetable oil
PPO	polypropylene pyrolysis oil
PPO-D	distillated polypropylene pyrolysis oil
PSO	polystyrene pyrolysis oil
PSO-D	distillated polystyrene pyrolysis oil
TPO	waste tire pyrolysis oil
TPO-D	distillated waste tire pyrolysis oil

Bibliography

[1] Abd Malek MNF, Veerappan V, Ab Rahim MH, Maniam GP. Various adsorbents to improve the filterability of biodiesel. Phys Chem Earth 2020;120:102910. https://doi.org/doi:10.1016/j.pce.2020.102910

[2] Arounia H, Farooq U, Goswami P, Vengadasalam K, Wilson M, Kapur N et al. Biodiesel and its challenges for nonwoven coalescence filter media. American Filtration and Separations Society Fall Conference 2015, AFS 2015: Advanced Technologies in Filter Media. 2015.

[3] Cardeño F, Lapuerta M, Rios L, Agudelo JR. Reconsideration of regulated contamination limits to improve filterability of biodiesel and blends with diesel fuels. Renew Energy. 2020;159:138-147. https://doi.org/10.1016/j.renene.2020.06.079

[4] Csontos B, Bernemyr H, Pach M, Hittig H. Analysis of the interaction between soft particles and fuel filter media. SAE Int J Fuels Lubr. 2021;14(3):256-264. https://doi.org/10.4271/04-14-03-0010

[5] Csontos B, Hittig H, Pach M, Bernemyr H, Erlandsson A. A measurement of fuel filters’ ability to remove soft particles, with a custom-built fuel filter rig. SAE Technical Paper. 2020-01-2130. 2020. https://doi.org/10.4271/2020-01-2130

[6] Eker OF, Camci F, Jennions IK. Physics-based prognostic modelling of filter clogging phenomena. Mech Syst Signal Process. 2016;75:395-412. https://doi.org/10.1016/j.ymssp.2015.12.011

[7] Górska-Włodarczyk W. Problemy separacji wody z oleju napędowego (in Polish). Biul WAT. 2020;69(4):43-56. https://doi.org/10.5604/01.3001.0015.3624

[8] Haryono I, Suryantoro MT, Kurniawan A, Ma’ruf M, Rochmanto B, Setiapraja H et al. The effect of contaminants and temperatures of a high-palm-oil biodiesel blend on the lifetime of a diesel fuel filter. Energies. 2025;18(1):219. https://doi.org/10.3390/en18010219

[9] Haryono I, Suryantoro MT, Rochmanto B, Kurniawan A, Rohman AT, Ma’ruf M et al. An effective three level filtration system for improved contaminant removal in high ratio biodiesel blends. Evergreen. 2023;10(3):667-674. https://doi.org/10.5109/7151711

[10] Hunicz J, Krzaczek P, Gęca M, Rybak A, Mikulski M. Comparative study of combustion and emissions of diesel

engine fuelled with FAME and HVO. Combustion Engines. 2021;184(1):72-78. https://doi.org/10.19206/CE-135066
[11] Komariah LN, Hadiah F, Aprianjaya F, Nevriadi F. Biodiesel effects on fuel filter: assessment of clogging characteristics. J Phys Conf Ser. 2018;1095(1):012017. https://doi.org/10.1088/1742-6596/1095/1/012017
[12] Lapuerta M, Rodríguez-Fernández J, Fernández-Rodríguez D, Patiño-Camino R. Cold flow and filterability properties of n-butanol and ethanol blends with diesel and biodiesel fuels. Fuel. 2018;224:552-555. https://doi.org/10.1016/j.fuel.2018.03.083
[13] Maruf M, Haryono I. An effect of biodiesel (B20) on life time locomotive fuel filter. Maj Ilm Pengkajian Ind. 2023; 13(3):134-142. https://doi.org/10.29122/mipi.v13i3.3787
[14] Paryanto I, Budianta IA, Alifia KCH, Hidayatullah IM, Darmawan MA, Judistira AA et al. Modelling of fuel filter clogging of B20 fuel based on the precipitate measurement and filter blocking test. Chem Engineering. 2022;6(6):84. https://doi.org/10.3390/chemengineering6060084
[15] Paryanto I, Rismana E, Arbianto AD, Prakoso T, Gozan M. The effect of fuel filter pore size on B20 fuel filter clogging at low-temperature condition. IOP Conf Ser Earth Environ Sci. 2020;520(1):012002. https://doi.org/10.1088/1755-1315/520/1/012002
[16] Pielecha I, Szwajca F, Stępień Z. Potential of ethanol and butanol in reducing deposits of SIDI engine injectors. Combustion Engines. 2023;194(3):21-31. https://doi.org/10.19206/CE-167898
[17] Pramudito Y, Fathurrahman NA, Auzani AS, Wibowo CS, Anggarani R, Soemanto A et al. Comparative analysis of filterability behavior of B30 and B40 biodiesel blends on various porosity and dimension of fuel filter. Int J Renew Energy Dev. 2023;12(4):849-858. https://doi.org/10.14710/ijred.2023.52801
[18] Rybak A, Hunicz J, Szpica D, Mikulski M, Gęca M, Woś P. Comparative analysis of waste-derived pyrolytic fuels applied in a contemporary compression ignition engine. Combustion Engines. 2024;198:74-81. https://doi.org/10.19206/ce-186697
[19] Sitnik LJ, Sroka ZJ, Andrych-Zalewska M. The impact on emissions when an engine is run on fuel with a high heavy alcohol content. Energies 2021;14:41. https://doi.org/10.3390/en14010041
[20] Thangamani S, Sundaresan SN, Kannappan SS, Barawkar VT, Jeyaseelan T. Impact of biodiesel and diesel blends on the fuel filter: a combined experimental and simulation study. Energy. 2021;227:120526. https://doi.org/10.1016/j.energy.2021.120526
[21] Vora R, Kadam V, Thangaraja J. Experimental investigation on the filtration characteristics of a commercial diesel filter operated with raw and processed karanja-diesel blends. Sādhanā. 2020;45(1):13. https://doi.org/10.1007/s12046-020-01394-2
[22] Wang J, Ayyar R, Olah A, Baer E. Processing-structure–property relationships of novel fibrous filters produced by a melt-process. J Mater Sci. 2016;51(1):134-147. https://doi.org/10.1007/s10853-015-9380-7
[23] Wang J, Ponting M, Zhang C, Olah A, Baer E. Fuel filtration properties and mechanism of a novel fibrous filter produced by a melt-process. J Membr Sci. 2017;526:1-10. https://doi.org/10.1016/j.memsci.2016.12.040
[24] Yoshino FJ, Marques GA, Ferrari F. Water separation challenge for Brazilian diesel engine. SAE Technical Paper. 2013-01-1693. 2013. https://doi.org/10.4271/2013-01-1693

Paweł Woś, DSc., DEng. – Faculty of Mechanical Engineering and Aeronautics, Rzeszów University of Technology, Poland.
e-mail: *pwos@prz.edu.pl*

Artur Jaworski, DEng. – Faculty of Mechanical Engineering and Aeronautics, Rzeszów University of Technology, Poland.
e-mail: *ajaworsk@prz.edu.pl*

Artur Krzemiński, DEng. – Faculty of Mechanical Engineering and Aeronautics, Rzeszów University of Technology, Poland.
e-mail: *akrzeminski@prz.edu.pl*

Prof. Jacek Hunicz, DSc., DEng. – Faculty of Mechanical Engineering, Lublin University of Technology, Poland.
e-mail: *j.hunicz@pollub.pl*

Hubert Kuszewski, DSc., DEng. – Faculty of Mechanical Engineering and Aeronautics, Rzeszów University of Technology, Poland.
e-mail: *hkuszews@prz.edu.pl*

Arkadiusz Rybak, MEng. – Faculty of Mechanical Engineering, Lublin University of Technology, Poland.
e-mail: *a.rybak@pollub.pl*

Mirosław Jakubowski, DEng. – Faculty of Mechanical Engineering and Aeronautics, Rzeszow University of Technology, Poland.
e-mail: *mjakubow@prz.edu.pl*

Andrzej Borawski, DSc., DEng. – Faculty of Mechanical Engineering, Bialystok University of Technology, Poland.
e-mail: *a.borawski@pb.edu.pl*

Dariusz Szpica, DSc., DEng. – Faculty of Mechanical Engineering, Bialystok University of Technology, Poland.
e-mail: *d.szpica@pb.edu.pl*

Article citation info:
Bednarski M, Sikora M, Orliński P. Analysis of the current lubricant requirements of the latest combustion engines. Combustion Engines. 2026;204(1):192-199. https://doi.org/10.19206/CE-211331

Mateusz BEDNARSKI
Mieczysław SIKORA
Piotr ORLIŃSKI

Combustion Engines
Polish Scientific Society of Combustion Engines

Analysis of the current lubricant requirements of the latest combustion engines

ARTICLE INFO

Received: 16 June 2025
Revised: 25 September 2025
Accepted: 25 September 2025
Available online: 30 October 2025

The advancement of combustion engines is driven by stricter emission regulations (e.g., Euro/EPA standards), requiring innovations in lubrication. Modern oils must ensure wear protection, emission system compatibility (e.g., DPFs) and fuel efficiency. This paper analyzes updates to ACEA, API, and OEM specifications, focusing on oxidation resistance, low-SAPS formulations, and fuel economy. The trend toward low-viscosity oils (0W-20, 0W-16) reduces friction but challenges lubrication under high loads. The study evaluates these changes' impact on engine durability and future oil development amid tightening sustainability and emission norms. This article will analyze lubricant requirements for passenger cars.

Key words: *engine oils, lubricant standards, API, ACEA, OEM*

1. Introduction

Modern emission requirements (Euro 6/VI standards, EPA Tier 3 regulations) have fundamentally dictated the evolution of internal combustion engine designs, resulting in significant modifications to their operational parameters [14]. Stringent limits on harmful emissions have necessitated combustion process optimization, consequently leading to increased thermomechanical stresses in contemporary powertrain units. This technological transformation has directly influenced the tightening of quality criteria for engine lubricants. In response to these challenges, standardized classification systems (OEM, ACEA, API, SAE) have implemented precise specifications defining:

– Physicochemical parameters of lubricants
– Application ranges for different powertrain types
– Operational boundary conditions (including temperature operating ranges).

The article aims to summarize the current requirements for engine oils set by car manufacturers and industry associations.

2. Engine oil requirements

Engine oil requirements have evolved significantly alongside advancements in powertrain technology and increased machinery accessibility [1]. Initial formulations focused primarily on providing adequate lubrication for naturally aspirated engines with limited service intervals (typically 3000–5000 km) [2]. Industrialization and stringent emission regulations (Euro 6d, EPA Tier 3) have fundamentally transformed lubricant development priorities [3]:

– Increased mechanical/thermal loads (peak cylinder pressures > 200 bar)
– Advanced aftertreatment compatibility (DPF, SCR, GPF systems)
– Extended drain intervals (up to 30,000 km in OEM specifications)
– Restriction of hazardous additives:
  • Zinc dialkyldithiophosphate (ZDDP) reduction to ≤ 0.08% P [3]
  • Sulfated ash limits < 0.8% in Low SAPS formulations [2].

Modern engines increases power density. Table 1 shows comparison between two turbochargered ~2000 cm³ spark ignition engines.

Table 1. Spark ignition engines comparison

Parameter	Lancia Delta HF (1987-1994)	VW EA888 Gen3
Displacement	1995 cm³	1984 cm³
Power Output	158 kW @ 5750 rpm	245 kW @ 6500 rpm
Torque	314 Nm @ 2500 rpm	420 Nm @ 2000 rpm

Power density increase necessitates:

– Piston ring coatings (CrN, MoS_2, DLC) [15]
– Reduced ring pack width (1.2 mm → 0.8 mm)
– Aluminum engine blocks with plasma-sprayed cylinder liners.

One of the next requirements for modern engines is a change in the friction reduction strategy. Modern engines employ low-viscosity oils (SAE 0W-20 replacing 5W-30), variable displacement oil pumps and electronically controlled cooling jets. All organizations describe extended drain oil capability (circa 30,000 km for passenger cars). An extended interval most often causes changes in oil parameters:

– Base number retention (TBN > 50% of initial value)
– Oxidation stability (RPVOT > 150 min) [4]
– Soot handling capacity (< 3% dispersion efficiency loss).

Due to the increase of combustion temperatures and operating temperatures, the oil specification requires:

– CCS viscosity < 6200 mPa·s @ –35°C (SAE 0W)
– HTHS viscosity > 2.6 mPa·s @ 150°C
– Flash point > 230°C.

Emission standards forced some other oil features like: Fuel dilution resistance (< 5% viscosity change at 7% fuel contamination) [15] and aftertreatment compatibility features for example, low SAPS formulation, where the following parameters are limited:

- Phosphorus: 600–800 ppm
- Sulfur: < 0.3%
- Sulfated ash: < 0.5%.

3. Industry standards

3.1. API standards [2]

The American Petroleum Institute (API) has established a standardized engine oil quality classification system, which utilizes a two-letter alphanumeric code to designate performance specifications, where the first letter indicates engine type:

- "S" (Spark Ignition): gasoline/petrol engines (quality progression: SA → SB → SC → SD → SE → SF → SG → SH → SJ → SL → SM → SN → SP → SQ). Note: Each subsequent letter denotes improved performance requirements
- "C" (Compression Ignition): diesel engine (quality progression: CA → CB → CC → CD → CD-II → CE → CF → CF-2 → CF-4 → CG-4 → CH-4 → CI-4 → CJ-4 → CK-4 → FA-4.

Suffix designations: "II" or "2": Applicable to two-stroke diesel engines "4" or no suffix: Applicable to four-stroke diesel engines.

The second letter follows alphabetical progression, with each advancement indicating stricter performance benchmarks (e.g., SN > SM > SL).

FA-4 is a specialized category for fuel-efficient, lower-viscosity diesel oils (HTHS 2.9–3.2 mPa·s).

Obsolete classifications (e.g., SA–SH) remain documented but are no longer certified for modern applications. This system ensures backward compatibility where applicable while mandating compliance with evolving OEM and regulatory requirements.

3.2. Analysis of the evolution of API standards

Table 2 shows API spark ignition oil standards with key advancements.

Table 2. API classification system for gasoline engine oils

API Class	Introduction Year	Key Advancements
SG	1988	Basic oxidation stability, wear protection
SJ	1996	Improved deposit control, phosphorus limits (0.1% max)
SL	2001	Enhanced high-temperature deposit protection
SM	2004	Improved oxidation resistance, extended drain capability
SN	2010	Turbocharger protection, fuel economy improvement
SN PLUS	2018	LSPI (Low-Speed Pre-Ignition) prevention
SP	2020	Advanced LSPI protection, enhanced fuel economy

Critical changes in API Spark ignition oil requirements:

- Phosphorus content reduction (SJ (1996): ≤ 0.1% to SP: ≤ 0.08% due to catalyst protection
- HTHS value decreased from ≥ 2.6 mPa·s to ≥ 2.3 mPa·s (SN) and ≥ 1.7 mPa·s (SP for 0W-16)
- Deposit control (TEOST 33C test limit increased from 30 mg (SM) to 35 mg (SP))
- Fuel economy improvement (sequence VIE test introduced in SP specification and minimum 0.5–1.5% improvement over previous generations.

API standards also introduce requirements resulting from the engine design and limiting its wear and aftertreatment systems wear:

- SN and later standards include specific tests for turbocharger deposit control and high-temperature stability (150°C+ conditions)
- LSPI prevention (SN Plus introduced first test – sequence IX, API SP reduced 50% of LSPI events vs. API SN (due to special additive formulation and Ca/Mo balance
- SP reduced sulfated ash (≤ 1.0%), sulfur content (≤ 0.4%), and phosphorus (≤ 0.08%).

The latest API spark ignition oil requirements have a performance test:

- Sequence IVA: Valve train wear protection
- Sequence VH: Sludge and varnish control
- Sequence VIII: Bearing corrosion
- Sequence IX: LSPI prevention
- Sequence VIE/VID: Fuel economy measurement.

and requires physical parameters:

- Noack volatility: ≤ 15%
- Shear stability: ≤ 10% viscosity loss
- Foaming tendency: < 10 ml/50 ml/10 ml (Seq I/II/III).

The API SQ specification, introduced in 2025, tightened the API SP requirements. Table 3 shows selected differences.

Table 3. API SP/SQ differences

Parameter	API SP	API SQ
LSPI Prevention	50% reduction vs. SN	Enhanced testing protocols
Wear protection	Sequence IVA (valvetrain)	New sequence X (bearing/cylinder tests)
Oxidation stability	ASTM D7528 (TEOST MHT-4)	Stricter deposit limits
Hybrid compatibility	No specific requirements	Fuel dilution resistance
SAPS limits	Phosphorus ≤ 0.08%, sulfur ≤ 0.4%	Further reduced additive restrictions
HTHS viscosity	≥ 2.9 mPa·s (5W-30)	Lower viscosities permitted (0W-12)
Fuel economy	Sequence VIE	Enhanced friction reduction

Technical Improvements in API SQ:

- Enhanced deposit control (30% better high-temperature deposit prevention vs. SP (per ASTM D7097))
- Advanced additive chemistry (optimized calcium/molybdenum ratios for LSPI protection)
- Extended drain capability (improved TBN retention (+15% vs. SP in ASTM D2896).

This analysis includes how API classifications have consistently addressed issues that occur in gasoline technology due to turbocharging, fuel control, and emission configuration control in recent specifications. Moving from SJ to SP means 60% deposit control and 40% attack protec-

tion based on standard test protocols and reduced fuel consumption through the HTHS parameter. Near-term development in the context of hybrid vehicles and engine anti-wear protection in water-in-oil conditions. New API SQ spec will be the base for some OEM specs for Ford Eco-Boost engines and VW EA888 Gen4 engines. Figure 1 shows graphical differences between API standards.

Fig. 1. API spark ignition standards [13]

3.3. ACEA standards

The Association des Constructeurs Européens d'Automobiles (ACEA) [2] establishes rigorous performance standards for engine lubricants, reflecting the evolving demands of modern powertrain technologies and stringent Euro 7 emission regulations. This classification system is structured to address three critical operational domains: durability, emissions compatibility, and energy efficiency.

Modern emission requirements (Euro 6/VI standards, EPA Tier 3 regulations) have fundamentally dictated the evolution of internal combustion engine designs, resulting in significant modifications to their operational parameters. Stringent limits on harmful emissions have necessitated combustion process optimization, consequently leading to increased thermomechanical stresses in contemporary powertrain units. This technological transformation has directly influenced the tightening of quality criteria for engine lubricants. In response to these challenges, standardized classification systems (OEM, ACEA, API, SAE) have implemented precise specifications defining:

- Physicochemical parameters of lubricants
- Application ranges for different powertrain types
- Operational boundary conditions (including temperature operating ranges).

ACEA introduced 4 different oil specification ranges:

- A for gasoline engines
- B for light-duty diesel engines
- C for all engines with aftertreatment systems
- E for heavy-duty diesel engines.

3.4. Analysis of differences of ACEA standards

ACEA describes oil specification by oil parameters, and real engine test [15]:

- viscosity (HTHS measured per CEC L-36-90 (150°C, shear rate 10^6 s^{-1}))
- shear stability measured per (CEC L-14-93, ASTM D6278/D7109) – oils must retain viscosity grade after 30 shear cycles
- volatility (noack evaporation – CEC L-40-93 – maximum mass loss after 1 h at 250°C should be less than 13% depending on spec. (minimum ≤ 11% for C3, C4)
- total base number (TBN) – ASTM D2896/D4739 (minimum ≥ 6.0 mgKOH/g)
- elastomer compatibility (CEC L-112-16 – evaluates seal material degradation after 7-day immersion in fresh oil)
- piston cleanliness & turbo deposits (CEC L-111-16 – EP6CDT – minimum RL259 merit rating for piston deposits)
- Low-temperature sludge & varnish (ASTM D8256 – sequence VH ≥ 7.6 merit for average engine sludge)
- valvetrain wear (ASTM D8350 – sequence IVB ≤ 3.3 mm^3 max intake lifter wear)
- soot handling (CEC L-106-14 – DV6C viscosity increase ≤ 2.5 mm^2/s at 5.5% soot)
- engine wear (CEC L-099-08 – OM646LA camshaft wear ≤ 120 µm)
- piston cleanliness & ring sticking (CEC L-117-20 – VW TDI zero ring sticking, deposits ≥ RL276 – 5 merit)
- low-speed pre-ignition (LSPI – ASTM D829 ≤ 5 pre-ignition events (C6/C7))
- timing chain wear (ASTM D8279 – sequence X ≤ 0.085% elongation.

Tables 4 and 5 show selected results. A and B classes are High SAPS oils, C class is Low/Mid SAPS oil. Tables contain results from the latest ACEA revision.

Figure 2 and 3 show graphical differences between all C and A/B 2023 ACEA specs.

Table 4. ACEA 2023 A/B parameters

Parameter	A3/B4-23	A5/B5-23	A7/B7-23
HTHS	≥ 3.5 mPa·s	2.9–3.5 mPa·s	2.9–3.5 mPa·s
TBN	≥ 10.0 mgKOH/g	≥ 8.0 mgKOH/g	≥ 6.0 mgKOH/g
LSPI Protection	Not required	Not required	Sequence IX ≤ 5 events
Key Application	Conventional turbo	Fuel-efficient ICE	High-performance DI

Table 5. ACEA 2023 C parameters

Parameter	C2-23	C3-23	C5-23
HTHS	≥ 2.9 mPa·s	≥ 3.5 mPa·s	2.6–2.9 mPa·s
Sulfated ash	≤ 0.8%	≤ 0.8%	≤ 0.8%
Phosphorus	0.07–0.09%	0.07–0.09%	0.07–0.09%
Fuel economy	M111 ≥2.5%	Not required	2ZR-FXE ≥0.3%

Fig. 2. 2023 ACEA C standards [13]

Fig. 3. 2023 ACEA C standards [13]

3.5. Analysis of the evolution of ACEA standards

ACEA Oil Sequences, established by the European Automobile Manufacturers' Association, have undergone iterative revisions since their inception in 1996. These updates reflect advancements in [2, 7, 9, 11]:

- Engine technology (e.g., turbocharging, hybridization)
- Emission regulations (Euro norms, aftertreatment compatibility)
- Material compatibility (low-SAPS formulations, elastomer resilience).

Milestones of ACEA revisions:

- 1996 First standardized classification (A/B for gasoline/diesel, C for catalyst-compatible oils), introducing HTHS viscosity as a critical parameter, A3/B3 emphasized shear stability for extended drain intervals
- 2007 split A5/B5 into A5/B5-04 (lower HTHS: 2.9–3.5 mPa·s) for fuel economy, added C4 (ultra-low SAPS: Ash ≤ 0.5%, P ≤ 0.09%)
- 2013 introduced C5 with HTHS ≥ 2.6 mPa·s for reduced friction, mandated Sequence IIIG (ASTM D7320) for oxidation stability
- 2021 A7/B7 debuted with LSPI (low-speed pre-ignition) protection, C6 combined fuel economy with turbocharger deposit control
- 2023 C7 introduced with HTHS ≥ 2.3 mPa·s (ultra-low viscosity for hybrids), stricter LSPI limits (ASTM D8291) for GDI engines.

Table 5 shows the Comparative Analysis of ACEA specs.

Figures 4, 5 and 6 show the evolution of selected ACEA specs.

Table 5. Changes in ACEA specs

Parameter	1996–2004	2007–2016	2021–2023
HTHS viscosity	A3/B3: ≥ 3.5 mPa·s	A5/B5: 2.9–3.5 mPa·s	C7: ≥ 2.3 mPa·s
SAPS limits	Not standardized	C4: Ash ≤ 0.5%	C6: Mid-SAPS
LSPI protection	N/A	A7/B7 introduced	≤ 5 events (ASTM D8291)
Diesel Soot handling	Sequence IIIE	DV4 (CEC L-78-99)	DV6C (CEC L-106-14)

Fig. 4. 2023 ACEA A5/B5 evolution [13]

Fig. 5. 2023 ACEA C2 evolution [13]

Fig. 6. 2023 ACEA A3/B4 evolution [13]

4. OEM oil specifications

OEM (Original Equipment Manufacturer) oil standards constitute a set of technical requirements imposed directly by automotive manufacturers such as BMW, Ford, Mercedes-Benz, and others on lubricants intended for specific engine designs used in their vehicles. Unlike ACEA and API classifications, which provide broad industry-wide benchmarks, OEM specifications are more stringent as they address the precise engineering demands of particular engines or engine families within a manufacturer's lineup.

Overview of selected OEM oil specifications

The BMW Longlife-17 FE+ (LL-17 FE+) specification is a premium engine oil standard based on ACEA C5 developed by BMW Group for modern gasoline and diesel engines. It emphasizes fuel efficiency (FE), extended drain intervals, and enhanced engine protection, particularly for vehicles equipped with particulate filters (GPF/DPF) and turbocharged direct-injection engines.

Key performance requirements [8, 12]:

– Low high-temperature high-shear (HTHS) viscosity (≤ 2.9 mPa·s) to reduce friction and improve efficiency, – Formulated with advanced friction modifiers to meet FE+ (fuel economy plus) requirements
– Compatible with BMW's condition-based service (CBS) system, allowing extended oil change intervals (up to 30,000 km or 2 years, depending on driving conditions)
– Enhanced oxidation stability to prevent oil degradation under high temperatures
– Low SAPS (sulphated ash, phosphorus, sulfur) formulation for compatibility with particular filters
– Improved wear protection (e.g., turbocharger bearings, timing chains)
– Primarily synthetic (group III+/PAO/ester-based) for superior thermal stability
– Advanced additive package with anti-wear agents (e.g., optimized ZDDP levels), detergents & dispersants to prevent deposits, anti-foaming & corrosion inhibitors.

Table 6 shows a comparison between different BMW oil specs. Figure 7 and 8 shows the difference between the different BMW OEM spec and ACEA base of this spec.

Table 6. BMW engine oil comparison

Specification	HTHS Viscosity	SAPS Level	Key applications
LL-17 FE+	≤ 2.9 mPa·s	Mid SAPS	GPF/DPF engines, hybrids
LL-04	≥ 3.5 mPa·s	Low SAPS	Older diesels (DPF-equipped)
LL-01 FE	~3.5 mPa·s	High SAPS	Pre-2020 gasoline engines

Fig. 7. BMW LL 17 FE+ vs. ACEA C5 [13]

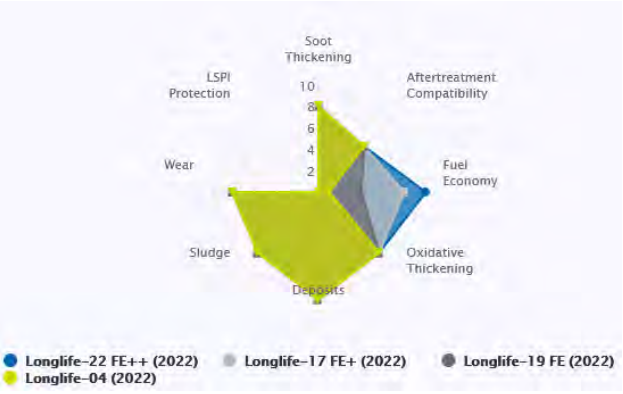

Fig. 8. Comparison of BMW specs [13]

The VW 508.00 (gasoline) and VW 509.00 (diesel) specifications represent Volkswagen Group's latest engine oil standards for vehicles produced since 2019. These specs were developed for WLTP/RDE-compliant engines, particle filter-equipped vehicles (GPF/DPF), and extended drain interval systems.

Key performance requirements:

– SAE 0W-20 grade mandated
– HTHS viscosity 2.6–2.9 mPa·s (lower than previous VW standards)

– Optimized for energy efficiency (FE++ classification)
– Up to 30,000 km/2 years' service intervals
– Compatible with VW's flexible service regime
– Sulphated ash ≤ 0.8%, phosphorus ≤ 0.05%, sulfur ≤ 0.2%
– Enhanced engine protection (special anti-wear additives for: timing chain systems, turbocharger bearings, direct injection components
– Improved oxidation stability for hybrid applications.

Additionally, this specification requires full synthetic (Group III+/PAO) base oils.

Table 9 shows comparison between different VW oil specs. Figure 9 shows comparison of VW specs.

Table 8. BMW engine oil comparison [5]

Specification	HTHS Viscosity	SAPS Level	Key Applications
LL-17 FE+	≤ 2.9 mPa·s	Mid SAPS	GPF/DPF engines, hybrids
LL-04	≥ 3.5 mPa·s	Low SAPS	Older diesels (DPF-equipped)
LL-01 FE	~3.5 mPa·s	High SAPS	Pre-2020 gasoline engines

Table 9. VW engine oil comparison

Specification	Viscosity	SAPS Level	Key Applications
508.00/509.00	0W-20	Ultra-Low	GPF/DPF (2019+)
504.00/507.00	5W-30	Low	Pre-WLTP vehicles
502.00/505.00	5W-40	High	Older generations

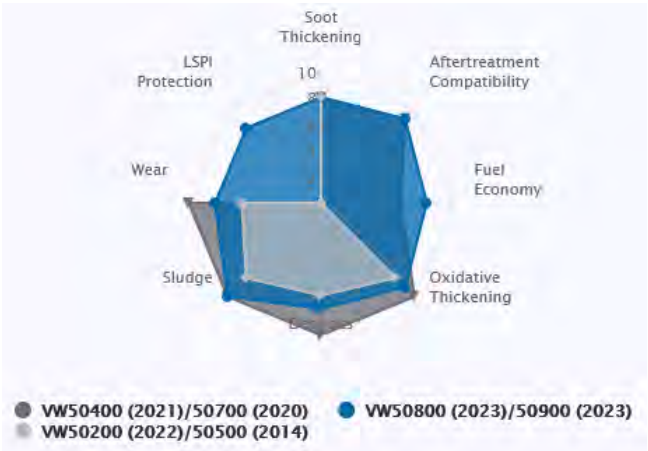

Fig. 9. Comparison of VW specs [13]

5. Specific lubricant requirements for internal combustion engines in hybrid electric vehicles

5.1. Introduction

Conventional internal combustion engines (ICEs) are designed to operate under relatively stable load and temperature conditions. In hybrid electric vehicles (HEVs, PHEVs), the ICE operates in a fundamentally new, dynamic environment that presents a unique set of challenges for engine lubricants. The necessity to cooperate with an electric motor, frequent start-stop cycles, and operation at low-load ranges significantly impact oil degradation and the formation of specific contaminants. This chapter details the key requirements for lubricants intended for use in hybrid engines, focusing on issues related to fuel dilution, oxidation and wear.

5.2. Characterization of ICE operation in a hybrid system and its impact on lubricant

The primary difference in the operation of a hybrid engine is its discontinuous and often brief operation. The engine is started and stopped multiple times during a single drive cycle to cooperate with or recharge the electric motor. This leads to several key phenomena [10]:

– Reduced operating temperature: the ICE in a hybrid system often operates within its optimal but relatively low-load range, resulting in a lower average oil sump temperature compared to conventional engines. Low temperature hinders the evaporation of condensed water and unburned fuel that enters the crankcase (a phenomenon known as fuel dilution).
– Frequent start-stop cycles: each start-up event is associated with momentary, intense boundary wear, as the oil film has not yet fully protected all tribological pairs. The repeated nature of this cycle accelerates the degradation of anti-wear additives and the base oil itself.
– Prolonged engine-off periods: when the vehicle is driven solely by electric power, the ICE cools down completely. During these periods, combustion by-products and water can condense into the oil, leading to the formation of acids and sludge

5.3. Main challenges and requirements for engine lubricants

5.3.1. Fuel dilution

This is one of the most critical challenges in hybrid engines, particularly in those with gasoline direct injection (GDI). During frequent cold starts, fuel injected into the cylinder partially washes down the liner walls and enters the crankcase. The low operating temperature of the engine prevents its effective evaporation. A high degree of fuel dilution (above 5–10%) reduces the oil's viscosity, leading to increased wear and risk of bearing damage. Furthermore, gasoline degrades performance additives and lowers the oil's flash point, posing a potential safety hazard.

Requirement: lubricants for hybrid engines must exhibit high volatility performance (low Noack volatility) and viscosity stability in the presence of diluents to maintain an adequate lubricating film.

5.3.2. Oxidation and acid contamination

Despite a generally lower bulk oil temperature, local temperatures in the combustion chamber and exhaust system remain very high. While a conventional engine operates stably after reaching its operating temperature, a hybrid engine repeatedly undergoes rapid heating and cooling phases. These thermal cycles promote oil oxidation. Additionally, condensed water and combustion blow-by gases (oxides of sulfur and nitrogen) form acids that attack metallic surfaces and lead to corrosion.

Requirement: exceptionally high thermal-oxidative stability and a robust total base number (TBN) are necessary to neutralize acids formed over extended oil drain intervals.

5.3.3. Wear and wear protection

Frequent starts mean repeated periods of operation under boundary lubrication conditions, where the protection from anti-wear additives (e.g., ZDDP) is crucial [10,11]. Concurrently, modern emission standards limit the use of some traditional additive chemistries. Furthermore, a weakened oil film due to fuel dilution further increases the risk of adhesive and abrasive wear.

Requirement: the lubricant must contain an advanced package of anti-wear and friction modifier additives that provide immediate protection at start-up, are resistant to fuel dilution, and meet environmental regulations. Manufacturers' requirements specifically for hybrid vehicles are not observed. Manufacturers typically require API SP/SQ and ACEA C5. In the case of OEM specifications, hybrid vehicles use oils identical to those used in conventional engines.

6. Conclusions

The automotive lubrication industry has undergone a paradigm shift in engine oil specifications, driven by increasingly stringent emissions regulations and rapid technological advancements in powertrain design. Our comprehensive analysis reveals that while API and ACEA specifications continue to provide fundamental performance benchmarks, OEM-specific requirements have emerged as the dominant force shaping lubricant formulations. This evolution reflects the growing complexity of modern engine architectures and aftertreatment systems.

The industry-wide transition to ultra-low viscosity grades (0W-20, 0W-16 and lower) represents a critical response to WLTP and RDE emission protocols [6, 12]. However, this shift has introduced significant technical challenges in maintaining adequate engine protection while achieving fuel economy targets. The reduction of HTHS viscosity to $\leq$ 2.3 mPa·s necessitates the development of advanced anti-wear additives, including molybdenum dithiocarbamate compounds and precision-formulated ZDDP packages, to prevent boundary lubrication failures. Simultaneously, the prevalence of turbocharged gasoline direct injection (TGDI) engines has made Low-Speed Pre-Ignition (LSPI) mitigation a paramount concern, driving the creation of new test protocols.

The electrification of vehicle powertrains has introduced unprecedented formulation challenges. Modern hybrid systems require lubricants capable of withstanding $\geq$ 15% fuel dilution. OEMs are responding with proprietary test methods that frequently precede ACEA/API updates by 12-18 months. While ACEA C6 (2022) and API SP provide partial harmonization, they lack the engine-specific validation sequences and aftertreatment compatibility requirements mandated by leading automakers.

Looking ahead, the industry must prioritize several key development areas. Next-generation friction modifiers stable below 100°C are essential for optimizing cold-start fuel economy, while advanced soot-handling dispersants will be critical for extending DPF service intervals. The establishment of OEM-collaborative test benches for hybrid-specific wear modes and high-throughput screening methods for LSPI inhibitor development should be considered urgent infrastructure investments.

The impending transition to synthetic fuels and hydrogen combustion systems will necessitate fundamental reformulation of lubricant chemistries. Key focus areas include enhanced high-temperature stability (>150°C bulk oil temperatures) and novel additive packages compatible with emerging seal and gasket materials. The formation of industry consortia to develop standardized lubricants test methods and bio-based base oil specifications should be prioritized to ensure a cohesive transition to alternative propulsion technologies.

In conclusion, the lubrication industry stands at an inflection point, where the traditional boundaries between mechanical protection, emissions compliance, and energy efficiency are being radically redefined. Success in this new paradigm will require unprecedented collaboration between additive chemists, OEM engineers, and testing organizations to develop solutions that meet the competing demands of tomorrow's powertrain technologies.

Nomenclature

HTHS	high temperature high share	SI	spark ignition
SAPS	sulfated ash phosphorus and sulfur	DI	direct injection
ACEA	European Automobile Manufacturers' Association	LSPI	low-speed pre-ignition
API	American Petroleum Institute		

Bibliography

[1] American Petroleum Institute. API 1509: Engine Oil Licensing and Certification System. 18th ed. Washington, DC: API 2022.

[2] American Petroleum Institute. API 1509: Engine Oil Licensing and Certification System. 19th ed. Washington, DC: API Publishing Services 2024.

[3] ASTM International. ASTM D2272-14(2019): Standard test method for oxidation stability of steam turbine oils by rotating pressure vessel. West Conshohocken, PA: ASTM 2019.

[4] ASTM International. ASTM D4951-14(2019): Standard classification and specification for automotive service greases. West Conshohocken, PA: ASTM 2019.

[5] BMW Group. Engine oil specifications: technical service bulletin. Munich: BMW Group 2023.

[6] Chłopek Z, Biedrzycki J, Lasocki J, Wójcik P. Assessment of the impact of dynamic states of an internal combustion engine on its operational properties. Eksploat Niezawodn. 2015;17(1):35-41. https://doi.org/10.17531/ein.2015.1.5

[7] European Automobile Manufacturers' Association. ACEA European Oil Sequences 2021. Brussels: ACEA 2021.

[8] European Automobile Manufacturers' Association. ACEA European Oil Sequences for Light-Duty Engines. Brussels: European Automobile Manufacturers' Association; 2023.

https://www.acea.auto/files/2023_ACEA_oil_sequences_light-duty_engines.pdf (accessed on 10.05.2025).
[9] European Parliament, Council of the European Union. Regulation (EU) 2018/858 on the approval and market surveillance of motor vehicles and their trailers. Official Journal of the European Union. 2018;L151:1-218.
[10] Growney D, Joedicke A, Williams M, Robin M, Mainwaring R, Davies M. Hybrid electric vehicle engine operation and engine oil degradation: a research approach. SAE Int J Fuels Lubr. 2024;17(1):3-16. https://doi.org/10.4271/04-17-01-0001
[11] Hybrid-Specific Lube. Lube Media 2023. https://www.lube-media.com/wp-content/uploads/Hybrid-Specific-Lube-WEB-ONLY-Article-Jan23.pdf (accessed on 10.05.2025).
[12] Japanese Automobile Standards Organization. JASO GLV-1: Light Vehicle Gasoline Engine Oil Standard. Tokyo: JASO 2016.
[13] Lubrizol's RELPERF Tool. Wickliffe, OH: The Lubrizol Corporation. https://online.lubrizol.com/relperftool/pc.html (accessed on 10.05.2025).
[14] Stępień Z. Vehicle related non exhaust particle emissions – Euro 7 requirements. Combustion Engines. 2024;199(4):15-29. https://doi.org/10.19206/CE-190606
[15] Volkswagen AG. VW 508 00/509 00: Engine Oil Quality Standard. Wolfsburg: Volkswagen AG 2023.

Mateusz Bednarski, MEng. – Faculty of Automotive and Construction Machinery Engineering, Warsaw University of Technology, Poland.
e-mail: *mateusz.bednarski@pw.edu.pl*

Mieczysław Sikora, MEng. – Faculty of Automotive and Construction Machinery Engineering, Warsaw University of Technology, Poland.
e-mail: *mieczyslaw.sikora@pw.edu.pl*

Prof. Piotr Orliński, DSc., DEng. – Faculty of Automotive and Construction Machinery Engineering, Warsaw University of Technology, Poland.
e-mail: *piotr.orlinski@pw.edu.pl*

Article citation info:
Magryta P, Barański G, Biały M. Acoustic source identification and knock detection in a Wankel engine operating on gasoline and hydrogen fuels. Combustion Engines. 2026;204(1):200-207. https://doi.org/10.19206/CE-210988

Paweł MAGRYTA
Grzegorz BARAŃSKI
Michał BIAŁY

Combustion Engines
Polish Scientific Society of Combustion Engines

Acoustic source identification and knock detection in a Wankel engine operating on gasoline and hydrogen fuels

ARTICLE INFO

Received: 16 May 2025
Revised: 9 September 2025
Accepted: 16 September 2025
Available online: 7 October 2025

This study presents an experimental investigation into the acoustic emissions of a Wankel rotary engine fueled by three distinct injection strategies: unleaded gasoline (E10), hydrogen with water addition (H_2W), and pure hydrogen (H_2). Measurements were carried out on an engine test bench under steady-state operating conditions. The analysis encompassed both sound pressure levels and frequency-domain characteristics of the acoustic signals. A microphone array in conjunction with CAE Noise Inspector software was used to capture and analyse noise emissions originating from the combustion chamber. The results revealed distinct variations in acoustic behaviour depending on the fuel type. Notably, the engine powered by pure hydrogen exhibited the highest amplitude of emitted combustion noise, potentially attributable to knocking combustion phenomena. The study underscores that fuel selection has a significant impact on the acoustic signature of the Wankel engine. Furthermore, the adopted measurement methodology proved effective in identifying combustion-related sound patterns and provides a foundation for future optimisation of rotary engines operating on alternative fuels.

Key words: *Wankel, knocking, noise, sound, hydrogen*

1. Introduction

The Wankel engine, due to its unique rotary piston design, is an interesting alternative to conventional piston engines. Its advantages, such as high-power output at a compact size and smooth operation, make it applicable in various fields of technology. In recent years, the growing interest in alternative fuels, including hydrogen, has led to intensive research into the use of this gas as an environmentally friendly energy source for internal combustion engines. Both of these considerations make the use of an alternative fuel such as hydrogen for a Wankel engine a legitimate challenge. In such a case, one of the problems to be solved is the occurrence of knock combustion during the operation of the power unit. Knock combustion in internal combustion engines was first described by Harry Ricardo. This undesirable phenomenon involves the premature ignition of the fuel-air mixture due to contact with the superheated walls of the combustion chamber. An analysis of the scientific literature reveals that the problem of knock combustion is the subject of intensive research not only in Wankel engines. The literature points to various methods of detecting this phenomenon, including the analysis of pressure pulsations in the combustion chamber, the measurement of mechanical vibrations of engine components, and the use of advanced diagnostic systems. In particular, amplitude-frequency analysis makes it possible to precisely determine the intensity and characteristics of knock combustion, so that measures can be taken to eliminate it. In spark-ignition (SI) engines, knocking combustion manifests itself in high-frequency pressure pulsations, which can lead to mechanical damage and reduced efficiency of the power unit [24].

Knock combustion, as a result, can lead to negative consequences for engine operation [9]. The causes of knock combustion, such as abnormal ignition, high temperature and pressure in the combustion chamber, allow the selection of appropriate detection and control methods. It is also worth emphasising the importance of optimising the combustion process to prevent knock combustion and ensure proper engine operation.

One of the main parameters affecting the formation of knock combustion is the temperature occurring in the combustion chamber [16]. Higher temperatures can increase the propensity for this phenomenon to occur. Currently, the mechanisms of knock combustion initiation under different thermal conditions are being analysed to better understand this complex process. The results of the research indicate that the temperature in the combustion chamber must be controlled to minimise the risk of knocking combustion.

As pressure and temperature increase, the mixture may self-ignite at specific points in the combustion chamber. These self-ignition points interact with the flame front in an uncontrolled manner, causing pressure and temperature oscillations. The rapidly changing pressure amplitude can lead to potential engine damage [6, 32]. The process of knock initiation, recorded using a camera for recording rapidly changing phenomena, is shown in the Fig. 1.

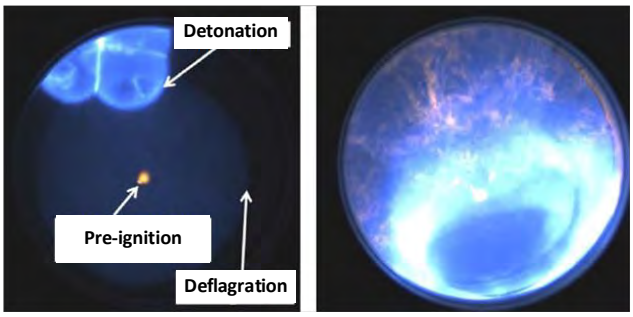

Fig. 1. Screenshots from the recording of rapidly changing measurements for engine operation with knocking combustion [15]

Wankel engines are characterised by a rather specific combustion process due to their design. The tendency for knocking combustion in a Wankel engine differs from that in piston engines, which means that current research on hydrogen combustion may not be directly applicable to this type of engine. Therefore, research on hydrogen combustion in piston engines is more common, but its results are not easily transferable to Wankel engines. [1, 2, 5, 14, 21, 26].

The occurrence of knocking combustion is also influenced by other engine operating parameters such as engine speed, engine load and the composition of the fuel-air mixture [17]. The available experimental results allow us to determine the optimal engine operating conditions that minimise the risk of knock combustion. The importance of precise control of the combustion process to ensure stability and efficiency should be emphasised here.

For example, the authors of the article [20] presented a way to improve the efficiency of a spark-ignition engine with an increased compression ratio. They proposed to counteract knocking combustion by dosing fuel with an increased octane number. The publication also presents the idea of measurements, the test stand and the results obtained. Changing from traditional fuel to hydrogen fuel can affect the intensity of the combustion process. The specific properties of hydrogen that distinguish it from traditional hydrocarbon fuels reveal the potential benefits and challenges of using hydrogen as a fuel in internal combustion engines, including its impact on knocking combustion. The publication [18] highlights the need to adapt engine design and operating parameters to the specifics of hydrogen combustion.

It is not only hydrogen that affects the possibility of knock combustion. The paper [27] presents a preliminary study of the intensity of knock combustion in a large methanol engine. The effectiveness of five conventional indicators of knock combustion intensity (MAPO, IMPO, AE, MVTD, and HRR) was examined at 50%, 75% and 87.5% load of a methanol-hydrogen engine with an average speed. The MAPO index was shown to be the most suitable for knock combustion analysis.

Various methods are used to detect knock combustion in internal combustion engines. The article [12] describes a simple knock combustion sensor tester. The article also presents information that most knock combustion processes oscillate in frequency ranges from 5000 to 15,000 Hz, and the presented sensor can record up to 37,000 Hz.

Another method is presented in the article [3], where the concept of using low-cost and readily available Arduino microprocessor modules and the Matlab computing package to detect knocking combustion in spark-ignition engines is presented. The tests were carried out for a typical range of vibration frequencies characteristic of knock combustion. The tests were performed for two piezoelectric sensors with linear characteristics, which indicated the need for signal amplifiers in the target measurement system. According to the authors, the measurement methods used cannot satisfactorily handle the piezoelectric sensors used. Sampling frequencies of microprocessor modules communicating directly with Matlab software turned out to be much lower than the hardware capabilities. This justifies the need to use another type of method for detecting knock combustion, such as a microphone array.

On the other hand, the article [10] presented a method for the detection of knock combustion in gasoline engines based on the Hilbert-Huang transformation. This analysis technique allowed the decomposition of the signal into individual components, which enabled precise information about the combustion process. Analysis of the pressure signal using the Hilbert-Huang transform allowed accurate monitoring and evaluation of the combustion process of the fuel-air mixture.

Another method used to analyse knock combustion is the use of the optical signal from the combustion chamber. The article [23] presents research conducted on a modified single-cylinder engine equipped with an optical sensor with direct access to the combustion chamber. Spectral analysis of the flame in the combustion chamber, taking into account chemiluminescence phenomena, made it possible to assess the intensity of knock combustion. The results confirmed the possibility of detecting and evaluating the intensity of knock combustion based on optical signal analysis.

Sound recording methods of internal combustion engines are also used to detect and analyse the phenomenon of knock combustion. They make it possible to evaluate the intensity of knock combustion. Acoustic methods are widely used in the analysis of internal combustion engines. The article [25] presents an acoustic analysis of a single-cylinder diesel engine using magnetised blends of biodiesel and diesel fuel. The effect of biodiesel percentage (0; 5; 10 and 20%) and magnetic field strength (0; 5300 and 7000 G) on engine noise was studied. The results of the analysis of variance confirmed significant differences between the tested fuel blends and magnetic levels at the 1% probability level.

On the other hand, the article [30] proposes a method for the separation and identification of diesel engine noise sources, which combines the binaural noise localisation method and the blind source separation method. The method can effectively separate and identify combustion noise and piston impact noise of a diesel engine. The results show that the frequency of combustion noise and piston impact noise are concentrated at 4350 Hz and 1988 Hz, respectively. Compared with the blind source separation method, the proposed method has better separation and identification results, and the separation results have fewer interfering components from other noises.

An interesting idea for acoustic analysis is the method presented in the article [7], where the correlation between airborne sound and structure-borne sound in a diesel engine was analysed. It was shown how structure-borne sound signals can be used to evaluate engine noise. The study showed a high correlation between airborne sound and structure-borne sound. The article suggests that analysis of structure-borne sound can be useful in diesel engine management systems for noise control.

As mentioned earlier, there are also publications describing the correlation between knock combustion and combustion noise. The article [31] describes a correlation method based on time-frequency masking theory. The proposed method simultaneously takes into account the effects

of time and frequency masking, which allows for a more accurate analysis of knock noise. The method has been successfully applied to the objective evaluation of diesel engine knock noise and verified by subjective evaluation. The results of the study show the potential of the new method in the objective evaluation of the noise quality of diesel engines.

Some authors also present methods for diagnosing engine damage based on noise intensity analysis. In the publication [29], the noises of an EFI gasoline engine in normal and damaged states were measured, and their sound intensity level (SIL) contours were calculated by interpolation to preliminarily investigate the possibility of SIL-based EFD. An incomplete WPA model consisting of a five-level discrete wavelet transform (DWT) and a four-level WPA was developed and applied to the measured noise signals to extract engine damage features. A multi-layer ANN model was used to classify engine damage using the extracted noise features. The results presented here suggest that noise-based WPA-ANN models are effective for engine damage diagnosis.

Changing the fuel also affects the combustion noise emitted by a working engine. The paper [22] investigated the combustion noise characteristics of a diesel engine with hydrogen added to the intake air. The noise of the engine with 10 % vol. hydrogen added to the intake air was lower than that of the engine with diesel alone at late fuel injection times. A transient combustion noise generation model was introduced to discuss the noise characteristics based on the conversion of energy from combustion impact to noise through structural vibration. The results showed that maximum combustion impact energy had a dominant effect on maximum engine noise power for each cycle.

On the other hand, the paper [11] investigated the combustion noise characteristics of hydrogen reciprocating engines, in which the authors found an opportunity to reduce combustion noise. The results showed that increasing the air-fuel equivalence ratio, ignition delay, and exhaust gas recirculation ratio produced favourable acoustic effects, with the air-fuel equivalence ratio being the most effective, with a possible noise reduction of up to 20 dB.

In summary, the identification of the combustion noise amplitude of knock combustion in a hydrogen-powered Wankel engine is a key aspect in the context of monitoring and optimising the combustion process of such a power unit. However, the use of hydrogen presents several technological challenges, one of the most serious of which is the phenomenon of knocking combustion [4]. In the case of hydrogen-powered Wankel engines, this problem becomes even more complex due to hydrogen's specific properties, such as high combustion velocity and propensity for self-ignition [28].

This article presents the results of a study on identifying the amplitude of the sound of knocking combustion in a hydrogen-powered Wankel engine. This research was based on the analysis of the amplitude and frequency of sounds recorded in real time at constant engine operating conditions. Based on the data obtained, an evaluation was made of the primary and alternative fuels on the intensity of the sound amplitude. Further parts of the article include a detailed description of the research methodology, analysis of the results obtained and conclusions regarding the possibility of the occurrence of knock combustion in a Wankel engine.

2. Methodology

2.1. Engine description

The object of the study was the Aixro XR 50 Wankel engine (Fig. 2). It is a naturally aspirated, four-stroke, spark-ignition engine offered by the German company Aixro GmbH. It is a single-rotor four-stroke unit with a displacement of 294 cm^3. It achieves a power equal to 33 kW (for a rotational speed of 8750 rpm), the maximum torque produced by the engine is 39 Nm (for a rotational speed of 7500 rpm), and the permissible rotational speed is 10,800 rpm. At the factory, the manufacturer equips the engine with a carburettor power system and a magnetoinduction ignition system with a fixed ignition advance angle. The basic technical parameters of the engine are shown in Table 1.

Table 1. Basic technical data of the research engine [8]

Parameter	Value	Unit
Manufacturer/designation	AIXRO GmbH / XR50	–
Type	4-stroke with a single rotor	–
Max. power (8750 rpm)	33	kW
Max. torque (4500 rpm)	35	Nm
Max. speed	11.000	rpm
Combustion chamber capacity	294	cm^3
Ignition type	Magneto ignition with a fixed timing	–
Fuel	Automotive gasoline with a 2% addition of lubricating oil	–
Mass	17	kg

To carry out the tests, the power unit was fueled with the original fuel (motor gasoline) and hydrogen gas. Therefore, the engine was equipped with additional systems. Here we can distinguish: a system of indirect injection into the intake manifold, both original fuel and hydrogen fuel, and a lubricating oil metering system (the factory engine was fed with a mixture of lubricating oil and fuel). The magnetoinductive ignition system was replaced by an electronic ignition system. The engine was also retrofitted with an electronically controlled throttle and a water injection system for the intake manifold. An electronic ECU was also developed to integrate the measurement sensors installed on the test unit and to precisely control the actuators. To precisely dispense the gaseous fuel, a hydrogen supply system was developed. This system consisted of a battery of gaseous fuel storage tanks, three stages of pressure reduction from 200 to 1 bar (due to the remote location of the tank battery from the test facility), a fuel storage tank, a fuel mass flow meter and a fuel injector. A water injection system was also developed for the intake manifold of the test facility. This system consisted of a demineralised water tank, a pump, a pressure regulator and an injector. The coolant was injected into the intake manifold, just after the air throttle and the gasoline and hydrogen injectors. The test

stand with the AIXRO XR50 engine installed allows full calibration and adjustment of the fuel supply, lubrication, and ignition systems.

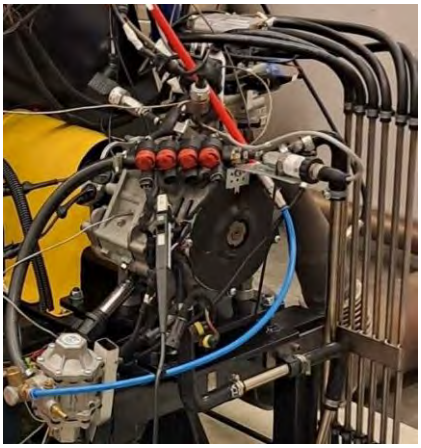

Fig. 2. AIXRO XR50 engine on the test bench

2.2. Acoustic camera

The approach used for measuring noise sources involved utilising the Noise Inspector software in conjunction with an acoustic camera provided by CAE Systems & Software. This sophisticated equipment transforms sound into visual representations, such as images or videos. Through this method, noise-emitting sources become distinguishable and their precise locations can be swiftly identified [9]. Thanks to this visual representation, the identification of noise origins can occur in real-time. The system is adept at both detecting noise sources and quantifying their intensity in terms of emitted sound pressure. By visualising noise sources in images or videos, the time required for measurements is substantially reduced compared to traditional methods [13]. The apparatus comprises an array of 16 microphones arranged in a single plane, with an HD camera centrally positioned (Fig. 3). Additional components include modules for signal and image processing. The entire system is linked to a portable computer. A diagram of the entire test setup is shown in Fig. 4.

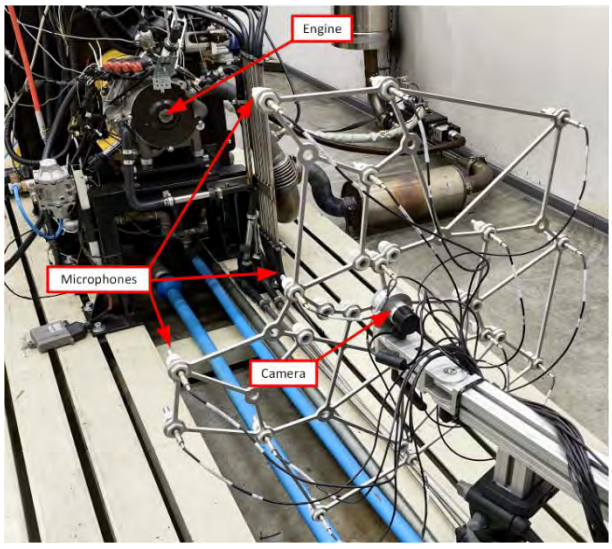

Fig. 3. Engine and acoustic camera

Key components of the Noise Inspector system are [19]:

- microphone array
- Microsoft LifeCam Studio 1080p HD camera
- 16 G.R.A.S. 40PH one-dimensional microphones
- ICP data acquisition module PXIe-1073 from National Instruments
- PXI-4496 measurement card
- portable computer
- CAE Noise Inspector V6.0 software.

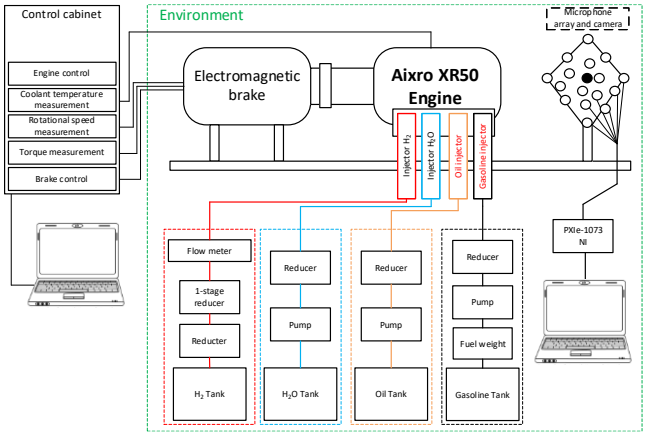

Fig. 4. Measurement station diagram

This measurement technique offers exceptional convenience. The modular architecture of the Noise Inspector system ensures adaptability to meet specific requirements. Notable benefits of the acoustic camera include [19]:

- a single measurement suffices, eliminating the need for multiple readings
- greater accuracy compared to conventional measuring microphones
- non-intrusive operation, allowing measurements without disrupting equipment functionality (e.g., in industrial environments)
- rapid measurement process, typically taking only a few minutes
- generation of noise source maps, facilitating identification of unwanted noise origins
- capability to pinpoint specific system components responsible for noise and assess noise levels
- no requirement for work stoppages at the measurement location
- effective identification of noise sources even in reverberant settings
- suitability for both indoor and outdoor measurements.

The fundamental working principle of the acoustic camera system involves capturing noise sources across different acoustic levels. A unique feature of this system is its ability to adjust the focus level after the measurement, enabling the production of multiple acoustic images without the need for repeated measurements. Furthermore, the live preview function offers immediate access to preliminary measurement data in real-time [13].

2.3. Measurement conditions

The test plan included performing tests at three different engine operating conditions labelled sequentially:

– E10 – feeding with unleaded 95 gasoline
– H_2W – hydrogen feed with water added
– H_2 fueling with pure hydrogen.

The second power strategy concerned hydrogen fueling with the addition of water, i.e. to lower the combustion temperature of the mixture and thus mitigate the process of knocking combustion, a water injection map was developed when fueling with hydrogen to maximise the use of the gaseous fuel – to obtain the highest possible mechanical power generated by the engine. The third strategy involved feeding pure hydrogen with no water input.

Three separate noise recordings (3 seconds each) were made for each trial, following one after the other. In addition, the noise of the accessories when the engine was turned off (electro-brake, ventilation, stand cooling, etc.) was recorded in a separate trial.

The tests were performed for engine operating parameters:

– speed 5000 rpm
– torque of 10 Nm
– hydrogen flow in H_2W and H_2 tests 290 l/min.

In all tests, the engine was in the same thermodynamic state. The tests were performed at short intervals, which eliminated the influence of external factors. The acoustic camera was 1.1 meters away from the engine.

3. Research results

Figure 5 shows the average value of noise amplitude as a function of its frequency. The curves represent 3 different supply conditions of the Wankel engine E10, H_2W, and H_2 (each averaged from three separate samples). For the analysis, four frequency ranges were selected in which the greatest difference in noise amplitudes is noticeable, and at the same time, the source of the noise comes from the engine:

– 4000–6000 Hz
– 6000–8000 Hz
– 8000–12,000 Hz
– 12,000–22,000 Hz.

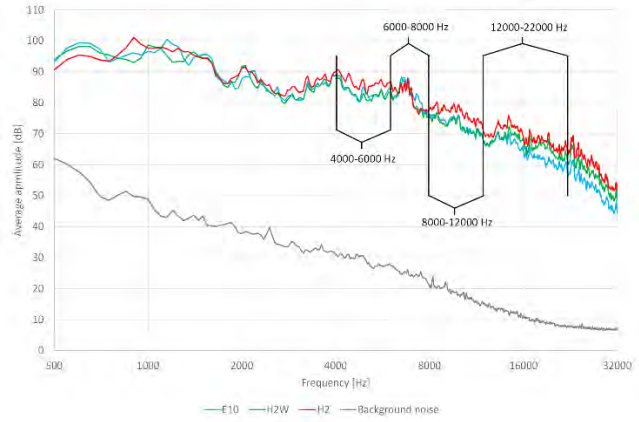

Fig. 5. Average value of noise amplitude as a function of its frequency for three different engine operating conditions

Ranges below 4000 Hz were discarded because no significant difference in the noise amplitude waveform for different samples was noticed there. The maximum value that was analysed was also limited to 22,000 Hz, because the higher frequency range of noise is inaudible to humans. Figure 3 also shows the noise of accessories (electro-brake cooling, ventilation, etc.) recorded when the engine was not running.

To further visualise the differences presented in Fig. 5, a plot of Fig. 6 was made showing the differences in sound amplitude values, respectively, between the

– H_2W supply, and E10 supply
– H_2 supply, and H_2W supply.

As can be seen in Fig. 6, the differences between H_2W and E10 supply are not as large as those between H_2 and H_2W supply. When switching from E10 to H_2W fuel, a reduction in noise amplitude is noticeable in the range of 4000 to 12,000 Hz. On the other hand, an increase in noise amplitude occurred in the range of 12,000 to 22,000 Hz. The situation is different when changing from H_2W fuel to H_2. In this case, an increase in noise amplitude was noticed in all four tested ranges from 4000 to 22,000 Hz, by about a maximum of 6 dB.

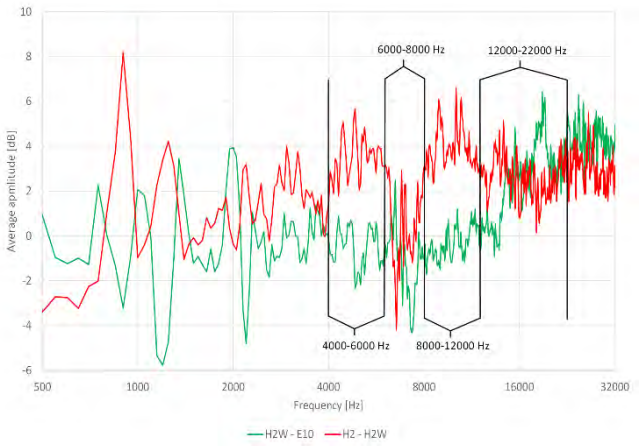

Fig. 6. Variations in the average value of noise amplitude as a function of its frequency for three different engine operating conditions

To highlight these differences, an additional analysis was performed showing the exact average values of the noise amplitude in each range and for each type of fuel supply. Figure 7 shows a larger value of the average amplitude for the H_2 supply in the ranges from 4000–6000 and 8000–22,000 Hz. On the other hand, in the frequency range of 6000–8000 Hz, the E10 supply has the highest value of average amplitude. Figure 7 also indicates the value of the standard deviation from the three trials conducted for each engine supply strategy.

The pure hydrogen supply (H_2) generates the highest combustion noise emissions in the ranges: 4000–6000 Hz, 8000–12,000 Hz, and 12,000–22,000 Hz, reaching maximum values of 86.55 dB, 76.31 dB, and 68.83 dB, respectively (Fig. 7). This indicates a rather dynamic course of heat generation in the engine combustion chamber.

Since the trend of increased noise amplitude for the H_2 supply is noticeable from the previous results, it was also decided to analyse the maximum noise values. Figure 8 shows the maximum noise values recorded during each test.

The difference in the amplitude level of the H_2 supply is also evident in this parameter.

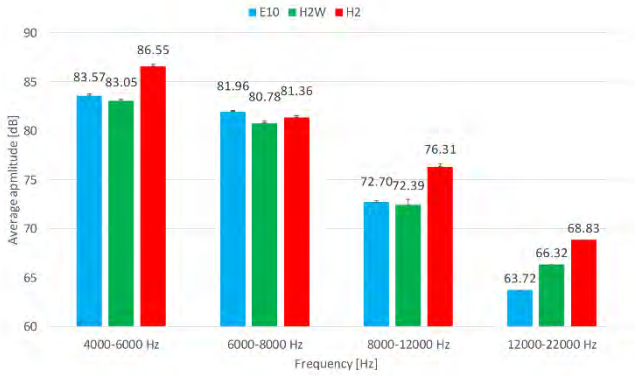

Fig. 7. Average value of noise amplitude for selected frequency ranges for three different engine operating conditions

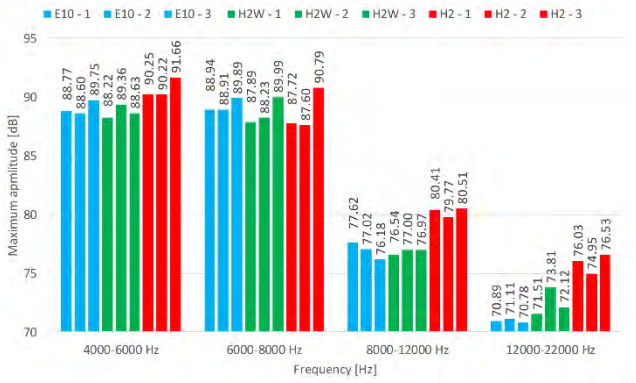

Fig. 8. Maximum noise amplitude values for selected frequency ranges from all tests for three different engine operating conditions

The acoustic noise analysis system also allows localisation of the noise source in the recorded image. For this purpose, the program performs interpolation of the noise amplitude level in the selected frequency range and applies these values to the recorded image. The system has 16 independent microphones, which makes it possible to accurately analyse the location of the noise source. Figure 9 shows the results of such analysis for selected frequency ranges. Unfortunately, the software does not allow the presentation of results averaged from several measurements, so it was decided to present the results from measurement no. 3 for each type of engine fuel supply strategy. Figure 9 also shows the maximum noise values for each sample. Note that the legend of the results was selected individually for each frequency range. As can be seen from the presented results, each noise location corresponds to the location of the Wankel engine body. In addition, the difference in the amplitude level of the noise is visible, which is the same as the previously presented results in the form of waveforms or graphs. It was not decided to present the results in the 12,000–22,000 Hz frequency range graphically due to the lack of visualisation of the focused source of the noise.

4. Conclusions

This article presents the methodology and results of acoustic testing of a rotary piston engine, the Wankel Aixro XR50, fueled with three different fuel strategies: motor gasoline only (E10), hydrogen with water (H_2W), and hydrogen gas only (H_2). The use of an acoustic camera during the study made it possible to analyse in detail the sources of noise and their location for different frequency ranges. Experimental studies showed that the greatest differences in noise emission occurred in the high frequency range (above 8000 Hz), especially when the engine was supplied with pure gaseous hydrogen (H_2).

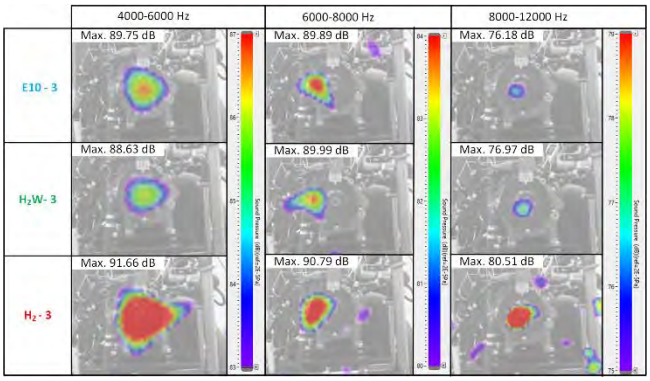

Fig. 9. Noise source localisation for selected frequency ranges for three different engine operating conditions

The supply of hydrogen with the addition of an injected dose of water (H_2W) allowed for the reduction of the intensity of noise, which confirms the effectiveness of supplying water to the combustion chamber in reducing noise, and thus in mitigating contact combustion of the gas-fueled engine. In addition, it can be concluded that water injection in the case of gaseous hydrogen fueling reduces noise intensity levels, particularly evident in the high frequency range (8000–22,000 Hz), and noise source location maps confirm that the dominant source of noise emissions is within the chamber where the heat generation process takes place, regardless of the power supply strategy, but the intensity level is clearly highest for pure hydrogen fuel (H_2). By using an advanced measurement system, it was possible to quickly and precisely identify the source of the noise, which can provide a basis for further optimisation of the design and power strategy of Wankel engines using alternative energy sources, especially hydrogen gas. As part of future research, we plan to conduct a comprehensive analysis of the noise source using Noise Inspector and measure the pressure in the combustion chamber, which will enable precise identification and characterisation of the knocking phenomenon.

Acknowledgements

The project/research was financed in the framework of the Lublin University of Technology funds, conducting scientific activities FD – discipline fund, funded by the Polish Ministry of Science and Higher Education – Article 365(2) of July 20, 2018.

Nomenclature

AE	average energy	HRR	heat release rate based on the knock metric
ANN	artificial neural network	IMPO	integral of modulus of pressure oscillations
DWT	discrete wavelet transform	MAPO	maximum amplitude of pressure oscillations
ECU	electronic control unit	MVTD	minimum value of the third derivative
EFD	early fault detection	SI	spark ignition
EFI	electronic fuel injection	SIL	speech interference level
HD	high definition	WPA	wavelet package analysis

Bibliography

[1] Amrouche F, Erickson P, Park J, Varnhagen S. An experimental investigation of hydrogen-enriched gasoline in a Wankel rotary engine. Int J Hydrogen Energy. 2014;39: 8525-8534. https://doi.org/10.1016/j.ijhydene.2014.03.172

[2] Amrouche F, Erickson PA, Varnhagen S. Extending the lean operation limit of a gasoline Wankel rotary engine using hydrogen enrichment. Int J Hydrogen Energy. 2016;41:14261-14271. https://doi.org/10.1016/j.ijhydene.2016.06.250

[3] Aromiński A. Preliminary concept of knock determination using Arduino modules, piezoelectric sensors and Matlab software. Logistyka. 2014;6:1505-1514.

[4] Biały M, Wendeker M, Gęca M. Identyfikacja spalania stukowego w silniku Wankla zasilanym paliwem wodorowym (in Polish). Autobusy, Technika, Eksploatacja, Systemy transpotowe 2012;4.

[5] Brzeżański M, Mareczek M, Noga M. Conversion of an internal combustion engine to supply of hydrogen or other gaseous fuels. Combustion Engines. 2025;202(3):162-168. https://doi.org/10.19206/CE-207877

[6] Cabezas M, Vorraro K, Liu G, Menaca X, Im R, Turner H. Numerical analysis of hydrogen injection and mixing in Wankel rotary engines. SAE Technical Paper. 2023-24-0069. 2023. https://doi.org/10.4271/2023-24-0069

[7] Decker M, Lucas S, Leist T, Gühmann C. Noise analysis of a diesel engine based on structure-borne sound signals. IFAC Proceedings Volumes. 2010;43(18):603-605. https://doi.org/10.3182/20100913-3-US-2015.00037

[8] Engine data sheet: AXRO XR-50. https://www.aixro.co.uk/buy-a-good-used-aixro-xr50-wankel-karting-engine

[9] Fiołka J. Detekcja spalania stukowego w silnikach benzynowych oparta na metodzie HVD (in Polish). Przegląd Elektrotechniczny. 2021;97(3). https://doi.org/10.15199/48.2021.03.29

[10] Fiołka J. Usage of Hilbert-Huang transform for knock detection in spark ignition engines (in Polish). Elektronika: konstrukcje, technologie, zastosowania. 2013;54(10).

[11] Fu T, Günther M, Pischinger S, Heuer S, Steffens C. Investigation of the combustion noise of hydrogen piston engines. Int J Hydrogen Energy. 2024;87:148-158. https://doi.org/10.1016/j.ijhydene.2024.08.478

[12] Gutten M, Jurcik J, Cichy A, Roj J. The analysis of a combustion engine knock control system. Pomiary Automatyka Kontrola. 2014;60(10).

[13] Kamera akustyczna Noise Inspector dla szybkiej lokalizacji źródeł hałasu. www.wibroakustyka.com.pl

[14] Karim Sharifi S, Azarshab M, Khoshnam A. Experimental investigation of hydrogen fueled Wankel engine from the point of view of relationship between knock, flame velocity, flow velocity and combustion velocity. Int J Smart Energy Technol Environ Eng. 2024;3(1):23-37. https://doi.org/10.61186/setee.3.1.23

[15] Kasseris E. Knock limits in spark ignited direct injected engines using gasoline/ethanol blends. Massachusetts Institute of Technology 2011.

[16] Kordzliński C, Reiman M, Sendyka B, Trajdos H. Badania wpływu temperatury mieszanki paliwowo-powietrznej na widmo amplitudowo-częstotliwościowe silników o zapłonie iskrowym (in Polish). Zeszyty Naukowe Politechniki Śląskiej. Transport 1986;829(3).

[17] Lasocki J. Engine knock detection and evaluation: a review. Proceedings of the Institute of Vehicles. 2016;109(5):41-50.

[18] Lasocki J, Orliński P, Wojs MK, Owczuk M, Matuszewska A. Hydroxyl radicals as an indicator of knocking combustion in the dual-fuel compression-ignition engine. Combustion Engines. 2017;168(1):178-185. https://doi:10.19206/CE-2017-129

[19] Magryta P, Skiba K, Czyż Z. Identification of noise generated by driving set of autogyro using an acoustic camera. Advances in Science and Technology. 2017;11(4):247-251. https://doi.org/10.12913/22998624/80825

[20] Malewicz K, Ligus G, Wasilewski M. Experimental research of the increased compression ratio engine. Logistyka. 2015;44706-4714.

[21] Matla J, Kaźmierczak A, Haller P, Trocki M. Hydrogen as a fuel for spark ignition combustion engines – state of knowledge and concept. Combustion Engines. 2024;196(1): 73-79. https://doi.org/10.19206/CE-171541

[22] Nguyen TA, Mikami M. Effect of hydrogen addition to intake air on combustion noise from a diesel engine. Int J Hydrogen Energy. 2013;38(10):4153-4162. https://doi.org/10.1016/j.ijhydene.2013.01.082

[23] Piernikarski D, Hunicz J, Komsta H. Detection of knocking combustion in a spark ignition engine using optical signal from the combustion chamber. Eksploat Niezawodn. 2013; 15(3):214-220.

[24] Różycki A. Zjawisko stuku w silniku spalinowym o zapłonie samoczynnym zasilanym dwupaliwowo (in Polish). Technika Transportu Szynowego koleje, tramwaje, metro 2013;10.

[25] Sadegh S, Kobra H. Acoustic analysis of a single-cylinder diesel engine using magnetized biodiesel-diesel fuel blends. Heliyon. 2020;6:e05113. https://doi.org/10.1016/j.heliyon.2020.e05113

[26] Stępień Z. Analysis of the prospects for hydrogen-fuelled internal combustion engines. Combustion Engines. 2024; 197(2):32-41. https://doi.org/10.19206/CE-174794

[27] Suijs W, De Graeve R, Verhelst S. An exploratory study of knock intensity in a large-bore heavy-duty methanol engine. Energy Conv Manag. 2024;302:118089. https://doi.org/10.1016/j.enconman.2024.118089

[28] Szwaja S. Hydrogen resistance to knock combustion in spark ignition internal combustion engines. Combustion Engines. 2011:144(1):13-19. https://doi.org/10.19206/CE-117118

[29] Wang YS, Liu NN, Guo H, Wang XL. An engine-fault-diagnosis system based on sound intensity analysis and wavelet packet pre-processing neural network. Eng Appl Artif Intell. 2020;94:103765. https://doi.org/10.1016/j.engappai.2020.103765

[30] Yao J, Xiang Y, Qian S, Li S, Wu S. Noise source separation of diesel engine by combining binaural sound localization method and blind source separation method. Mech Syst Signal Pr. 2017;96:303-320. https://doi.org/10.1016/j.ymssp.2017.04.027

[31] Yun DU, Lee SK. Objective evaluation of the knocking sound of a diesel engine considering the temporal and frequency masking effect simultaneously. J Sound Vib. 2017; 397:282-297. https://doi.org/10.1016/j.jsv.2017.03.005

[32] Zhi W, Hui L, Reitz RD. Knocking combustion in spark-ignition engines. Prog Energy Combust Sci. 2017;61:78-112. https://doi.org/10.1016/j.pecs.2017.03.004

Paweł Magryta, MEng. – Faculty of Mechanical Engineering, Lublin University of Technology, Poland.
e-mail: *p.magryta@pollub.pl*

Grzegorz Barański, DEng. – Faculty of Mechanical Engineering, Lublin University of Technology, Poland.
e-mail: *g.baranski@pollub.pl*

Michał Biały, DEng. – Faculty of Engineering Science, John Paul II University in Biała Podlaska, Poland.
e-mail: *m.bialy@dyd.akademiabialska.pl*

Kolokacja
Serwery dedykowane
Cloud
Backup
Wirtualne serwery

WWW.DATACENTER.PNT.OPOLE.PL

Inżynieria odwrotna
Projektowanie CAD
Badania i pomiary
Symulacje komputerowe

WWW.LAB.PNT.OPOLE.PL

Park Naukowo-Technologiczny w Opolu sp. z o.o.
ul. Technologiczna 2
45-839 Opole

tel.: +48 884 883 627,
email: biuro@pnt.opole.pl
www.pnt.opole.pl

NIP: 7543069732
REGON: 161506358
KRS: 0000449086
BDO: 000530146

PNT
PARK NAUKOWO-TECHNOLOGICZNY W OPOLU

Łukasiewicz
Institute
of Aviation

ROCKET TECHNOLOGIES

Suborbital Rocket
ILR-33 AMBER 2K

SATELLITE TECHNOLOGIES

SPARK (Spacecraft Platform Architecture for Research and Key-enabling missions)

AVIATION TECHNOLOGIES

Aerobatic Glider I-45 JAY

The Łukasiewicz Research Network – Institute of Aviation
offers a wide range of specialized research, engineering services and products. We provide comprehensive solutions, ranging from dedicated analyzes, simulations, engineering design, through the selection, testing and certification of materials and structures, to rapid prototyping and additive manufacturing.

al. Krakowska 110/114, 02-256 Warsaw, Poland
e-mail: info@ilot.lukasiewicz.gov.pl / www.ilot.lukasiewicz.gov.pl

Publisher:

Polish Scientific Society of Combustion Engines

ISSN: 2300-9896
eISSN: 2658-1442

Combustion Engines

Polskie Towarzystwo Naukowe Silników Spalinowych

www.combustion-engines.eu